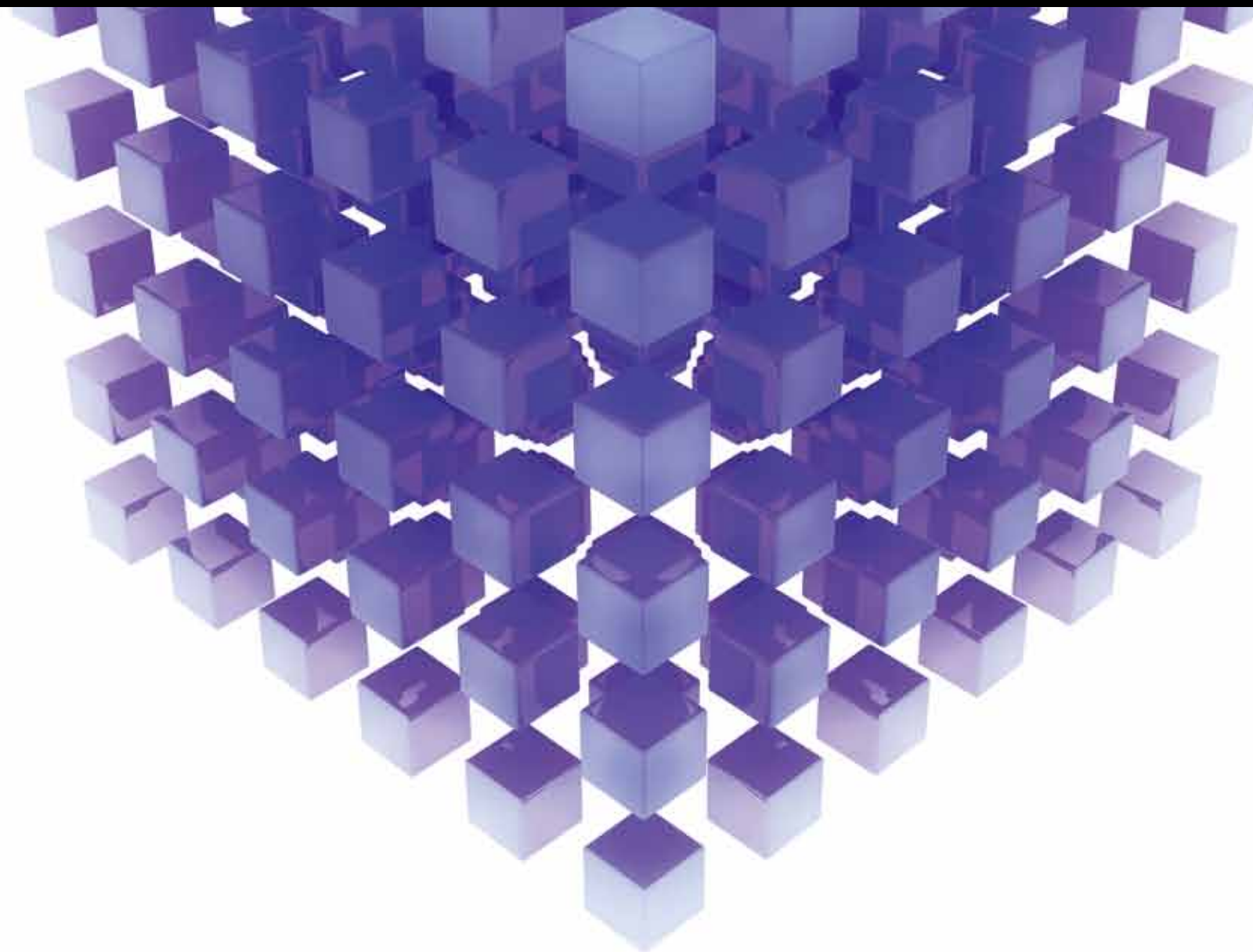


MATHEMATICAL PROBLEMS IN ENGINEERING

# NEW DEVELOPMENTS IN FLUID MECHANICS AND ITS ENGINEERING APPLICATIONS

GUEST EDITORS: OLUWOLE DANIEL MAKINDE, WAQAR AHMED KHAN,  
AND TIRIVANHU CHINYOKA





---

# **New Developments in Fluid Mechanics and Its Engineering Applications**

Mathematical Problems in Engineering

---

## **New Developments in Fluid Mechanics and Its Engineering Applications**

Guest Editors: Oluwole Daniel Makinde, Waqar Ahmed Khan,  
and Tirivanhu Chinyoka



---

Copyright © 2013 Hindawi Publishing Corporation. All rights reserved.

This is a special issue published in “Mathematical Problems in Engineering.” All articles are open access articles distributed under the Creative Commons Attribution License, which permits unrestricted use, distribution, and reproduction in any medium, provided the original work is properly cited.

## Editorial Board

- M. Abd El Aziz, Egypt  
E. M. Abdel-Rahman, Canada  
R. K. Abu Al-Rub, USA  
Sarp Adali, South Africa  
Salvatore Alfonzetti, Italy  
Igor Andrianov, Germany  
Sebastian Anita, Romania  
W. Assawinchaichote, Thailand  
Erwei Bai, USA  
Ezzat G. Bakhoun, USA  
José M. Balthazar, Brazil  
R. K. Bera, India  
C. Bérenguer, France  
Jonathan N. Blakely, USA  
Stefano Boccaletti, Spain  
Stephane P.A. Bordas, USA  
Daniela Boso, Italy  
M. Boutayeb, France  
Michael J. Brennan, UK  
Salvatore Caddemi, Italy  
Piermarco Cannarsa, Italy  
Jose E. Capilla, Spain  
Carlo Cattani, Italy  
M. M. Cavalcanti, Brazil  
Diego J. Celentano, Chile  
Mohammed Chadli, France  
Arindam Chakraborty, USA  
Yong-Kui Chang, China  
Michael J. Chappell, UK  
Kui Fu Chen, China  
Xinkai Chen, Japan  
Kue-Hong Chen, Taiwan  
Jyh-Horng Chou, Taiwan  
Slim Choura, Tunisia  
C. Cruz-Hernandez, Mexico  
Swagatam Das, India  
Filippo de Monte, Italy  
Antonio Desimone, Italy  
Yannis Dimakopoulos, Greece  
Baocang Ding, China  
Joao B. R. Do Val, Brazil  
Daoyi Dong, Australia  
B. Dubey, India  
Horst Ecker, Austria  
M. Onder Efe, Turkey  
Elmetwally Elabbasy, Egypt  
A. Elías-Zúñiga, Mexico  
Anders Eriksson, Sweden  
Vedat S. Erturk, Turkey  
Moez Feki, Tunisia  
Ricardo Femat, Mexico  
Robertt A. Valente, Portugal  
C. Fuerte-Esquivel, Mexico  
Zoran Gajic, USA  
Ugo Galvanetto, Italy  
Furong Gao, Hong Kong  
Xin-Lin Gao, USA  
Behrouz Gatmiri, Iran  
Oleg V. Gendelman, Israel  
Didier Georges, France  
P. Gonçalves, Brazil  
Oded Gottlieb, Israel  
Fabrizio Greco, Italy  
Quang Phuc Ha, Australia  
M. R. Hajj, USA  
Tony S. W. Hann, Taiwan  
Thomas Hanne, Switzerland  
K. R. (Stevanovic) Hedrih, Serbia  
M.I. Herreros, Spain  
Wei-Chiang Hong, Taiwan  
Jaromir Horacek, Czech Republic  
Huabing Huang, China  
Chuangxia Huang, China  
Gordon Huang, Canada  
Yi Feng Hung, Taiwan  
Hai-Feng Huo, China  
Asier Ibeas, Spain  
Anuar Ishak, Malaysia  
Reza Jazar, Australia  
Zhijian Ji, China  
Jun Jiang, China  
J. J. Judice, Portugal  
Tadeusz Kaczorek, Poland  
Tamas Kalmar-Nagy, USA  
Tomasz Kapitaniak, Poland  
Hamid Reza Karimi, Norway  
Metin O. Kaya, Turkey  
Nikolaos Kazantzis, USA  
Farzad Khani, Iran  
K. Krabbenhoft, Australia  
Ren-Jieh Kuo, Taiwan  
Jurgen Kurths, Germany  
Claude Lamarque, France  
Usik Lee, Korea  
Marek Lefik, Poland  
Stefano Lenci, Italy  
Roman Lewandowski, Poland  
Shanling Li, Canada  
Ming Li, China  
Jian Li, China  
Shihua Li, China  
Teh-Lu Liao, Taiwan  
Panos Liatsis, UK  
Shueei M. Lin, Taiwan  
Yi-Kuei Lin, Taiwan  
Jui-Sheng Lin, Taiwan  
Yuji Liu, China  
Wanquan Liu, Australia  
Bin Liu, Australia  
Paolo Lonetti, Italy  
V. C. Loukopoulos, Greece  
Junguo Lu, China  
Chien-Yu Lu, Taiwan  
Alexei Mailybaev, Brazil  
M. K. Maiti, India  
O. D. Makinde, South Africa  
R. Martinez-Guerra, Mexico  
Driss Mehdi, France  
Roderick Melnik, Canada  
Xinzhu Meng, China  
Yuri V. Mikhlin, Ukraine  
G. Milovanovic, Serbia  
Ebrahim Momoniat, South Africa  
Trung Nguyen Thoi, Vietnam  
Hung Nguyen-Xuan, Vietnam  
Ben T. Nohara, Japan  
Sotiris K. Ntouyas, Greece  
Gerard Olivar, Colombia  
Claudio Padra, Argentina  
Bijaya Ketan Panigrahi, India  
Francesco Pellicano, Italy  
Matjaz Perc, Slovenia  
Vu Ngoc Phat, Vietnam  
M. do Rosário Pinho, Portugal  
A. Pogromsky, The Netherlands

Seppo Pohjolainen, Finland  
Stanislav Potapenko, Canada  
Sergio Preidikman, USA  
Carsten Proppe, Germany  
Hector Puebla, Mexico  
Justo Puerto, Spain  
Dane Quinn, USA  
K. R. Rajagopal, USA  
Gianluca Ranzi, Australia  
Sivaguru Ravindran, USA  
G. Rega, Italy  
Pedro Ribeiro, Portugal  
J. Rodellar, Spain  
R. Rodriguez-Lopez, Spain  
A. J. Rodriguez-Luis, Spain  
Ignacio Romero, Spain  
Hamid Ronagh, Australia  
Carla Roque, Portugal  
R. R. García, Spain  
Manouchehr Salehi, Iran  
Miguel A. Sanjuán, Spain  
Ilmar F. Santos, Denmark  
Nickolas S. Sapidis, Greece  
E. J. Sapountzakis, Greece  
Bozidar Sarler, Slovenia  
Andrey V. Savkin, Australia  
Massimo Scalia, Italy  
Mohamed A. Seddeek, Egypt  
A. P. Seyranian, Russia  
Leonid Shaikhet, Ukraine

Cheng Shao, China  
Bo Shen, Germany  
Jian-Jun Shu, Singapore  
Zhan Shu, UK  
Dan Simon, USA  
Luciano Simoni, Italy  
Grigori M. Sisoiev, UK  
Christos H. Skiadas, Greece  
Davide Spinello, Canada  
Sri Sridharan, USA  
Rolf Stenberg, Finland  
Changyin Sun, China  
Jitao Sun, China  
Xi-Ming Sun, China  
Andrzej Swierniak, Poland  
Yang Tang, Germany  
Allen Tannenbaum, USA  
Cristian Toma, Romania  
Irina N. Trendafilova, UK  
Alberto Trevisani, Italy  
Jung-Fa Tsai, Taiwan  
K. Vajravelu, USA  
Victoria Vampa, Argentina  
Josep Vehi, Spain  
Stefano Vidoli, Italy  
Xiaojun Wang, China  
Dan Wang, China  
Youqing Wang, China  
Yongqi Wang, Germany  
Cheng C. Wang, Taiwan

Moran Wang, China  
Yijing Wang, China  
Gerhard-Wilhelm Weber, Turkey  
J. S. Witteveen, The Netherlands  
Kwok-Wo Wong, Hong Kong  
Ligang Wu, China  
Zhengguang Wu, China  
Gongnan Xie, China  
Wang Xing-yuan, China  
Xi Frank Xu, USA  
Xuping Xu, USA  
Jun-Juh Yan, Taiwan  
Xing-Gang Yan, UK  
Suh-Yuh Yang, Taiwan  
Mahmoud T. Yassen, Egypt  
Mohammad I. Younis, USA  
Bo Yu, China  
Huang Yuan, Germany  
S.P. Yung, Hong Kong  
Ion Zaballa, Spain  
A. M. Zenkour, Saudi Arabia  
Jianming Zhan, China  
Xu Zhang, China  
Yingwei Zhang, China  
Lu Zhen, China  
Liancun Zheng, China  
Jian Guo Zhou, UK  
Zexuan Zhu, China  
Mustapha Zidi, France

# Contents

**New Developments in Fluid Mechanics and Its Engineering Applications**, Oluwole Daniel Makinde, Waqar Ahmed Khan, and Tirivanhu Chinyoka  
Volume 2013, Article ID 797390, 3 pages

**Influence of Thermal Radiation on Unsteady Free Convection MHD Flow of Brinkman Type Fluid in a Porous Medium with Newtonian Heating**, Farhad Ali, Ilyas Khan, Sami Ul Haq, and Sharidan Shafie  
Volume 2013, Article ID 632394, 13 pages

**Unsteady Hydromagnetic Rotating Flow through an Oscillating Porous Plate Embedded in a Porous Medium**, I. Khan, A. Khan, A. Farhad, M. Qasim, and S. Sharidan  
Volume 2013, Article ID 508431, 8 pages

**Heat Transfer and Mass Diffusion in Nanofluids over a Moving Permeable Convective Surface**, Muhammad Qasim, Ilyas Khan, and Sharidan Shafie  
Volume 2013, Article ID 254973, 7 pages

**Numerical Simulation on the Effect of Turbulence Models on Impingement Cooling of Double Chamber Model**, Zhenglei Yu, Tao Xu, Junlou Li, Hang Xiu, and Yun Li  
Volume 2013, Article ID 170317, 8 pages

**Travelling Waves Solution of the Unsteady Flow Problem of a Rarefied Nonhomogeneous Charged Gas Bounded by an Oscillating Plate**, Taha Zakaraia Abdel Wahid  
Volume 2013, Article ID 503729, 13 pages

**DSMC Prediction of Particle Behavior in Gas-Particle Two-Phase Impinging Streams**, Min Du, Changsui Zhao, Bin Zhou, and Yingli Hao  
Volume 2013, Article ID 254082, 11 pages

**Performance Analysis of High-Speed Deep/Shallow Recessed Hybrid Bearing**, Lei Wang and Shuyun Jiang  
Volume 2013, Article ID 918767, 9 pages

**Feature-Parameter-Criterion for Predicting Lean Blowout Limit of Gas Turbine Combustor and Bluff Body Burner**, Hongtao Zheng, Zhibo Zhang, Yajun Li, and Zhiming Li  
Volume 2013, Article ID 939234, 17 pages

**Time-Splitting Procedures for the Numerical Solution of the 2D Advection-Diffusion Equation**, A. R. Appadu and H. H. Gidey  
Volume 2013, Article ID 634657, 20 pages

**Model of Infiltration of Spent Automotive Catalysts by Molten Metal in Process of Platinum Metals Recovery**, Agnieszka Fornalczyk, Slawomir Golak, and Mariola Saturnus  
Volume 2013, Article ID 461085, 7 pages

**A Fractal Model for the Maximum Droplet Diameter in Gas-Liquid Mist Flow**, Xiao-Hua Tan, Jian-Yi Liu, Xiao-Ping Li, Guang-Dong Zhang, and Chuan Tang  
Volume 2013, Article ID 532638, 6 pages

**Framework for the Shape Optimization of Aerodynamic Profiles Using Genetic Algorithms**, D. López, C. Angulo, I. Fernández de Bustos, and V. García  
Volume 2013, Article ID 275091, 11 pages

**Nonlinear Characteristics of Helicopter Rotor Blade Airfoils: An Analytical Evaluation**, Constantin Rotaru  
Volume 2013, Article ID 503858, 9 pages

**The Use of Fractional Order Derivative to Predict the Groundwater Flow**, Abdon Atangana and Necdet Bildik  
Volume 2013, Article ID 543026, 9 pages

**Unsteady Analyses of a Control Valve due to Fluid-Structure Coupling**, Yudong Xie, Yong Wang, Yanjun Liu, Fang Cao, and Yongcheng Pan  
Volume 2013, Article ID 174731, 7 pages

**The Flow of a Variable Viscosity Fluid down an Inclined Plane with a Free Surface**, M. S. Tshehla  
Volume 2013, Article ID 754782, 8 pages

**A New Numerical Approach of MHD Flow with Heat and Mass Transfer for the UCM Fluid over a Stretching Surface in the Presence of Thermal Radiation**, S. Shateyi and G. T. Marewo  
Volume 2013, Article ID 670205, 8 pages

**Analytical Solution of Flow and Heat Transfer over a Permeable Stretching Wall in a Porous Medium**, M. Dayyan, S. M. Seyyedi, G. G. Domairry, and M. Gorji Bandpy  
Volume 2013, Article ID 682795, 10 pages

**Calculation Analysis of Pressure Wave Velocity in Gas and Drilling Mud Two-Phase Fluid in Annulus during Drilling Operations**, Yuanhua Lin, Xiangwei Kong, Yijie Qiu, and Qiji Yuan  
Volume 2013, Article ID 318912, 17 pages

**Spectral Local Linearisation Approach for Natural Convection Boundary Layer Flow**, S. S. Motsa, Z. G. Makukula, and S. Shateyi  
Volume 2013, Article ID 765013, 7 pages

**Gel Characteristics of Urea-Formaldehyde Resin under Shear Flow Conditions**, Dang-liang Wang, Han-ying Bai, and Gao Yue  
Volume 2013, Article ID 748176, 5 pages

**On the Comparison between Compact Finite Difference and Pseudospectral Approaches for Solving Similarity Boundary Layer Problems**, P. G. Dlamini, S. S. Motsa, and M. Khumalo  
Volume 2013, Article ID 746489, 15 pages

**Radiation and Magnetohydrodynamics Effects on Unsteady Free Convection Flow in a Porous Medium**, Sami Ulhaq, Ilyas Khan, Farhad Ali, and Sharidan Shafie  
Volume 2013, Article ID 148410, 7 pages

**CFD Simulation of Heat Transfer and Friction Factor Augmentation in a Circular Tube Fitted with Elliptic-Cut Twisted Tape Inserts**, Sami D. Salman, Abdul Amir H. Kadhum, Mohd S. Takriff, and Abu Bakar Mohamad

Volume 2013, Article ID 163839, 7 pages

**Shock Wave Solutions for Some Nonlinear Flow Models Arising in the Study of a Non-Newtonian Third Grade Fluid**, Taha Aziz, R. J. Moitsheki, A. Fatima, and F. M. Mahomed

Volume 2013, Article ID 602902, 6 pages

**Hydromagnetic Stagnation-Point Flow towards a Radially Stretching Convectively Heated Disk**,

S. Shateyi and O. D. Makinde

Volume 2013, Article ID 616947, 8 pages

**MHD Boundary Layer Flow due to Exponential Stretching Surface with Radiation and Chemical Reaction**, Y. I. Seini and O. D. Makinde

Volume 2013, Article ID 163614, 7 pages

**Entropy Generation Analysis in a Variable Viscosity MHD Channel Flow with Permeable Walls and Convective Heating**, A. S. Eegunjobi and O. D. Makinde

Volume 2013, Article ID 630798, 12 pages

**Boundary Layer Flow Past a Wedge Moving in a Nanofluid**, Waqar A. Khan and I. Pop

Volume 2013, Article ID 637285, 7 pages

## Editorial

# New Developments in Fluid Mechanics and Its Engineering Applications

**Oluwole Daniel Makinde,<sup>1</sup> Waqar Ahmed Khan,<sup>2</sup> and Tirivanhu Chinyoka<sup>3</sup>**

<sup>1</sup> Faculty of Military Science, Stellenbosch University, Private Bag X2, Saldanha 7395, South Africa

<sup>2</sup> Department of Engineering Sciences, Pakistan Navy Engineering College, National University of Sciences & Technology, Karachi 75350, Pakistan

<sup>3</sup> Center for Research in Computational and Applied Mechanics, University of Cape Town, Rondebosch 7701, South Africa

Correspondence should be addressed to Oluwole Daniel Makinde; makinded@gmail.com

Received 8 December 2013; Accepted 8 December 2013

Copyright © 2013 Oluwole Daniel Makinde et al. This is an open access article distributed under the Creative Commons Attribution License, which permits unrestricted use, distribution, and reproduction in any medium, provided the original work is properly cited.

Fluid mechanics is an active field of research with many unsolved or partially solved problems in science and engineering. Fluid mechanics can be mathematically complex. Sometimes the problems can best be solved by numerical methods, typically using computers. Fluids have the ability to transport matter and its properties as well as transmit force; therefore fluid mechanics is a subject that is particularly open to cross-fertilization with other sciences and disciplines of engineering. The subject of fluid mechanics is highly relevant in such domains as mechanical, chemical, petrochemical, civil, metallurgical, biological, and ecological engineering.

The original papers explored in this special issue include a wide variety of topics such as boundary layer flows, nanofluids dynamics, heat and mass transfer, combustion theory hydromagnetic flows, gas dynamics, computational fluid dynamics, thermodynamics analysis, aerodynamics, and non-Newtonian flows. In “*Travelling waves solution of the unsteady flow problem of a rarefied nonhomogeneous charged gas bounded by an oscillating plate*,” T. Zakaraia and A. Wahid solved the initial-boundary value problem of the Rayleigh flow applied to the system of two-component plasma (positive ions + electrons), bounded by an oscillating plate. The ratios between the different contributions of the internal energy changes are predicted via the extended Gibbs equation for both diamagnetic and paramagnetic plasmas. In “*DSMC prediction of particle behavior in gas-particle two-phase impinging streams*,” M. Du et al. investigated the behaviour of gas-particle two-phase impinging streams

(GPISs). The collisional interaction of particles was taken into account by means of a modified direct simulation Monte Carlo (DSMC) method based on a Lagrangian approach and the modified Nanbu method. The results indicate that the particle distribution in GPIS can be divided into three zones: particle-collision zone, particle-jetting zone, and particle-scattering zone. In “*Performance analysis of high-speed deep/shallow recessed hybrid bearing*,” L. Wang and S. Jiang presented a theoretical analysis of the performance of deep/shallow recessed hybrid bearing. By adopting bulk flow theory, the turbulent Reynolds equation and energy equation are modified and solved numerically. The results indicate that the load capacity and drag torque increase as the depth becomes shallower and the width ratio (half angle of deep recess versus half angle of shallow recess) becomes smaller. In “*Feature-parameter-criterion for predicting lean blowout limit of gas turbine combustor and bluff body burner*,” H. Zheng et al. proposed a new method named Feature-Parameter-Criterion (FPC) for predicting Lean blowout (LBO) limit using computational fluid dynamics (CFD) software FLU-ENT. The results show that the simulation of LBO limit based on FPC is in good agreement with the experiment data (the errors are about 5%). In “*Time-splitting procedures for the numerical solution of the 2D advection-diffusion equation*,” A. R. Appadu and H. H. Gidey presented a spectral analysis of the dispersive and dissipative properties of two time-splitting procedures, namely, locally one-dimensional (LOD) Lax-Wendroff and LOD (1, 5) for the numerical solution of the

2D advection-diffusion equation. An optimization technique is implemented to find the optimal value of temporal step size that minimizes the dispersion error for both schemes when the spatial step is chosen as 0.025. In “*Model of infiltration of spent automotive catalysts by molten metal in process of platinum metals recovery*,” A. Fornalczyk et al. analysed the model for the washing-out process of precious metals from spent catalysts by the use of molten lead in which the metal flow is caused by the rotating electromagnetic field and the Lorentz force. The developed model enabled analysis of the impact of spacing between the catalysts and the supply current on the degree of catalyst infiltration by the molten metal. In “*A fractal model for the maximum droplet diameter in gas-liquid mist flow*,” X. H. Tan et al. made use of fractal theory to describe liquid droplet size distribution in gas-liquid mist flow. The results reveal that maximum droplet diameter decreases with an increase in gas superficial velocity but increases with an increase in liquid superficial velocity. Droplet fractal dimension also increases with an increase in gas superficial velocity but decreases with an increase in liquid superficial velocity. In “*Framework for the shape optimization of aerodynamic profiles using genetic algorithms*,” D. López et al. developed a framework for the shape optimization of aerodynamics profiles using computational fluid dynamics (CFD) and genetic algorithms. The results obtained demonstrated the effectiveness of the developed tool. In “*Nonlinear characteristics of helicopter rotor blade airfoils: an analytical evaluation*,” C. Rotaru examined the effect of unsteadiness on airfoil operating under nominally attached flow conditions away from stall using Theodorsen’s theory, where the aerodynamic response (lift and pitching moment) is considered as a sum of noncirculatory and circulatory parts. The apparent mass contributions to the forces and pitching moments, which are proportional to the instantaneous motion, are included as part of the quasi-steady result. In “*The use of fractional order derivative to predict the groundwater flow*,” A. N. Atangana and Bildik derived the analytical solution of the time-fractional groundwater flow equation (TFGFE) via the Laplace-Carson transform method and the generalized Wright function. This solution obtained is in perfect agreement with the data observed from the pumping test performed by the Institute for Groundwater Study on one of its borehole settled on the test site of the University of the Free State. In “*Unsteady analyses of a control valve due to fluid-structure coupling*,” Y. Xie et al. analysed the coupling mechanism between the structure and the fluid system at the control valve numerically. The results help understand the processes that occur in the valve flow path leading to the pressure control instability observed in the control valve in the combined cycle power plants (CCPP). In “*The flow of a variable viscosity fluid down an inclined plane with a free surface*,” M. S. Tshehla investigated the combined effects of convective heating and temperature dependent variable viscosity on fluid flowing down an inclined plane with a free surface. The model problem is tackled numerically; graphical results are displayed and discussed quantitatively. In “*A new numerical approach of MHD flow with heat and mass transfer for the UCM fluid over a stretching surface in the presence of thermal radiation*,” S. Shateyi and G. T. Marewo made

use of spectral relaxation method in order to numerically investigate the magnetohydrodynamic boundary layer flow with heat and mass transfer of an incompressible upper-convected Maxwell fluid over a stretching sheet in the presence of viscous dissipation and thermal radiation as well as chemical reaction. The results are obtained for velocity, temperature, concentration, skin friction, and Nusselt number. In “*Analytical solution of flow and heat transfer over a permeable stretching wall in a porous medium*,” M. Dayyan et al. investigated the boundary layer flow through a porous medium over a stretching porous wall with respect to first and second laws of thermodynamics for both isothermal and isoflux cases. It is shown that the rate of heat transfer increases with Reynolds number, Prandtl number, and suction to the surface. In “*Calculation analysis of pressure wave velocity in gas and drilling mud two-phase fluid in annulus during drilling operations*,” Y. Lin et al. proposed a united wave velocity model based on pressure gradient equations in drilling operations, gas-liquid two-fluid model, the gas-drilling mud equations of state, and small perturbation theory. It is shown that the drop of pressure causes an increase in void fraction along the flow direction. The wave velocity tends to increase with the increase in back pressure and the decrease of gas influx rate and angular frequency, significantly in low range. In “*Spectral local linearisation approach for natural convection boundary Layer flow*,” S. S. Motsa et al. utilised a spectral local linearisation method (SLLM) to numerically solve a model problem describing natural convection boundary layer flow with domain transformation. A comparative study between the SLLM and existing results in the literature was carried out to validate the results. The method has shown to be a promising efficient tool for nonlinear boundary value problems as it gives converging results after few iterations. In “*Gel characteristics of urea-formaldehyde resin under shear flow conditions*,” D. Wang et al. investigated the gel characteristics of urea-formaldehyde resin (UFR) chemical grout under shear flow conditions experimentally using an apparatus which consists of a magnetic stirrer and a viscometer. The results show that the grouting flow rate influences the gelling time. Faster flow rates will cause longer gelling time, which means that the time for the grout to gel during the flowing process under shear flow conditions is longer than that under static conditions. In “*On the comparison between compact finite difference and pseudospectral approaches for solving similarity boundary layer problems*,” P. G. Dlamini et al. presented a comparison of the compact finite difference approach against the pseudospectral approach in solving similarity boundary layer problems. It is shown that the results of the two approaches are comparable in terms of accuracy for small systems of equations. For larger systems of equations, the proposed compact finite difference approaches are more accurate than the spectral-method-based approaches. In “*Radiation and magnetohydrodynamics effects on unsteady free convection flow in a porous medium*,” S. Ulhaq et al. examined the unsteady MHD free convection flow near an exponentially accelerated infinite vertical plate through porous medium with uniform heat flux in the presence of thermal radiation. Exact solutions are obtained by the Laplace transform method. The effects of pertinent parameters such

as the radiation parameter, Grashof number, Prandtl number, and time on velocity, temperature, and skin friction are shown graphically and discussed quantitatively. In “*CFD simulation of heat transfer and friction factor augmentation in a circular tube fitted with elliptic-cut twisted tape inserts*,” S. D. Salman et al. presented a numerical simulation of swirling flow in a tube induced by elliptic-cut and classical twist tape inserts using CFD package (FLUENT-6.3.26). The results show that the heat transfer rate and friction factor in the tube equipped with elliptic-cut twist tape (ECT) are significantly higher than those fitted with classical twist tape (CTT). In “*Shock wave solutions for some nonlinear flow models arising in the study of a non-Newtonian third grade fluid*,” T. Aziz et al. presented a new class of closed-form shock wave solutions for some nonlinear problems arising in the study of a third grade fluid model using the Lie symmetry reduction technique. In “*Hydromagnetic stagnation-point flow towards a radially stretching convectively heated disk*,” S. Shateyi and O. D. Makinde presented a numerical solution for steady MHD stagnation-point flow and heat transfer of an electrically conducted incompressible viscous fluid over a convectively heat and radially stretching disk surface. Pertinent results on the effects of various thermophysical parameters on the velocity and temperature fields as well as local skin friction and local Nusselt number are discussed in detail and shown graphically and/or in tabular form. In “*MHD boundary layer flow due to exponential stretching surface with radiation and chemical reaction*,” Y. I. Seini and O. D. Makinde investigated the combined effects of thermal radiation and first order homogeneous chemical reaction on hydromagnetic boundary layer flow of a viscous, steady, and incompressible fluid over an exponential stretching sheet. It was found that the rate of heat transfer at the surface decreases with increasing values of the transverse magnetic field parameter and the radiation parameter. In “*Entropy generation analysis in a variable viscosity MHD channel flow with permeable walls and convective heating*,” A. S. Egunjobi and O. D. Makinde numerically analysed inherent irreversibility in a steady flow of an incompressible variable viscosity electrically conducting fluid through a channel with permeable walls and convective surface boundary conditions. The results revealed that entropy generation minimization can be achieved by appropriate combination of the regulated values of thermophysical parameters controlling the flow systems. In “*Boundary layer flow past a wedge moving in a nanofluid*,” W. A. Khan and I. Pop numerically studied the problem of steady boundary layer flow of nanofluid past a stretching wedge with a parallel free stream velocity. It is found that the velocity at the surface increases/decreases with stretching/shrinking parameters while the temperature increases with both Brownian motion and thermophoresis parameters.

Thus, the papers in this special issue, representing a broad spectrum of both theoretical and experimental approaches and areas of investigation, demonstrate the wide array of new development in fluid mechanics and its engineering applications. We are certain that the papers published in this special issue will contribute to advancement of knowledge in the field of fluid mechanics and provide scientists, engineers,

industries, research scholars, and practitioners’ latest theoretical and technological achievements in fluid mechanics and its various engineering applications.

## Acknowledgments

We would like to thank the authors for their contribution and the reviewers for their collaboration.

Oluwole Daniel Makinde  
Waqar Ahmed Khan  
Tirivanhu Chinyoka

## Research Article

# Influence of Thermal Radiation on Unsteady Free Convection MHD Flow of Brinkman Type Fluid in a Porous Medium with Newtonian Heating

Farhad Ali,<sup>1</sup> Ilyas Khan,<sup>1,2</sup> Sami Ul Haq,<sup>1</sup> and Sharidan Shafie<sup>1</sup>

<sup>1</sup> Department of Mathematical Sciences, Faculty of Science, Universiti Teknologi Malaysia (UTM), 81310 Johor Bahru, Johor, Malaysia

<sup>2</sup> College of Engineering Majmaah University, P.O. Box 66, Majmaah 11952, Saudi Arabia

Correspondence should be addressed to Sharidan Shafie; [sharidan@utm.my](mailto:sharidan@utm.my)

Received 20 June 2013; Revised 13 September 2013; Accepted 13 September 2013

Academic Editor: Waqar Khan

Copyright © 2013 Farhad Ali et al. This is an open access article distributed under the Creative Commons Attribution License, which permits unrestricted use, distribution, and reproduction in any medium, provided the original work is properly cited.

The focus of this paper is to analyze the influence of thermal radiation on some unsteady magnetohydrodynamic (MHD) free convection flows of an incompressible Brinkman type fluid past a vertical flat plate embedded in a porous medium with the Newtonian heating boundary condition. The fluid is considered as a gray absorbing-emitting but nonscattering medium and the Rosseland approximation in the energy equations is used to describe the radiative heat flux for optically thick fluid. For a detailed analysis of the problem, four important situations of flow due to (i) impulsive motion of the plate (ii) uniform acceleration of the plate (iii) nonuniform acceleration of the plate, and (iv) highly nonuniform acceleration of the plate are considered. The governing equations are first transformed into a system of dimensionless equations and then solved analytically using the Laplace transform technique. Numerical results for temperature and velocity are shown graphically, while skin friction and Nusselt number are computed in tables. The results show that temperature and velocity increase on increasing radiation and Newtonian heating parameters. However, the results of magnetic and porosity parameters on velocity are found quite opposite.

## 1. Introduction

Generally speaking, a free convection flow field is a self-sustained flow driven by the presence of a temperature gradient. Extensive research work has been published on free convection flow past a vertical plate for different boundary conditions (see [1–10] and the references therein). Perhaps, it is due to their numerous applications in engineering, geophysical and astrophysical environments, geothermal energy, oil reservoir modelling, building insulation, food processing, and grain storage. Most of these existing studies have used the usual boundary conditions of constant wall temperature or constant heat flux. However, in many practical situations it was realized that the convection flow can also be set up by the Newtonian heating from the surface known as conjugate convective flow [11]. The Newtonian heating situation occurs in many important engineering devices such as in heat exchanger where the conduction in solid tube wall is greatly

influenced by the convection in the fluid flowing over it and in conjugate heat transfer around fins where the conduction within the fin and the convection in the fluid surrounding it are simultaneously analyzed in order to obtain the vital design information [12]. In view of these applications various researchers are involved in dealing with the Newtonian heating problems via numerical or analytical techniques.

Chaudhary and Jain [13, 14] investigated the problem of unsteady free convection flow of an incompressible viscous fluid for different motions of the plate with the Newtonian heating condition and obtained the exact solutions using the Laplace transform technique. Recently, Guchhait et al. [15] reinvestigated the problem of Chaudhary and Jain [14] numerically by using the Crank-Nicolson implicit finite-difference scheme. Mebine and Adigio [16] obtained an exact solution for unsteady free convection flow of an incompressible viscous optically thin fluid past an impulsively started vertical porous plate with the Newtonian heating. Salleh et al.

[17, 18] analyzed numerically the steady boundary layer flow and heat transfer over a horizontal circular cylinder and over a stretching sheet with the Newtonian heating. Narahari and Ishak [19] investigated the influence of thermal radiation on unsteady free convection flow past a moving vertical plate with Newtonian heating. Recently Akbar and Nadeem [20] studied mixed convective MHD peristaltic flow of a Jeffrey nanofluid with the Newtonian heating. Narahari and Yunus [21] performed an analytical study of free convection flow near an impulsively started infinite vertical plate with Newtonian heating in the presence of thermal radiation and constant mass diffusion. The closed-form exact solutions were obtained by the Laplace transform method.

On the other hand, the study of MHD flows has important technological and geothermal applications in cooling of nuclear reactors, liquid metals fluid, power generation system, aerodynamics, and engineering problems. The study of MHD flow with heat transfer also plays an important role in biological sciences. In addition, the flow through a porous medium is of great physical interest because of its various applications found in hydrology for the sand structures in earth, in filter beds for purification of drinking water and sewage, in chemical engineering for the permeation chromatography, filtering of gases, and liquids chromatography, and in petroleum technology for the production of petroleum and gases. Having such motivation, Hayat et al. [22] analyzed MHD stagnation point flow of a Jeffery fluid past a stretching surface with the Newtonian heating. Lesnic et al. [23, 24] analyzed the free convection flow in a porous medium generated by Newtonian heating. In another study, Lesnic et al. [25] considered the steady free convection boundary layer flow along a semi-infinite plate, slightly inclined to the horizontal and embedded in a porous medium with the flow generated by Newtonian heating. Furthermore, radiative convective flows are frequently encountered in many environmental and scientific processes such as aeronautics, fire research, and heating and cooling of channels. Radiation and thermal diffusion effects on MHD free convection flow of an incompressible viscous fluid near an oscillating plate embedded in a porous medium were considered by Khan et al. [26]. Radiation and porosity effects on the MHD flow past an oscillating vertical plate with uniform heat flux were presented by Samiulhaq et al. [27]. Mohammed et al. [28] discussed analytical solutions of MHD natural convection transients flow near an oscillating plate emerged in a porous medium.

Most of the above studies with Newtonian heating conditions are performed for viscous fluids and numerical or exact solutions are obtained. However, such studies for non-Newtonian fluids are very few, especially those that are solved for exact solutions. Non-Newtonian fluids problems on the other hand are of great and increasing interest for the last five decades. Such fluids differ from the Newtonian fluids in that the relationship between the shear stress and flow field is more complicated. Examples of the non-Newtonian fluids are coal water, food products, inks, glues, soaps, and polymer solutions [29–33]. Therefore, in the present investigation we have chosen Brinkman type fluid as a non-Newtonian fluid. This model was first used by Brinkman in [34, 35]. Later,

several authors have used the Brinkman model in describing several types of flows through a porous medium. Among them, Hsu and Cheng [36] studied the natural convection about a semi-infinite vertical flat plate in a porous medium using Brinkman model. Varma and Babu [37], Gorla et al. [38], and Rajagopal [39] also used Brinkman model in their studies. By using Brinkman type fluid, Fetecău et al. [40] reported some interesting results. They used Fourier sine transform and obtained exact solutions for some unsteady motions. Recently, this problem was reinvestigated by Ali et al. [41] and they established some new types of exact solutions using Laplace transform.

Motivated by above studies, the present research aims to analyze the influence of thermal radiation on unsteady MHD free convection flow of Brinkman type fluid past a vertical plate embedded in a porous medium with Newtonian heating. To the best of authors' knowledge such study is not available in the literature and the present work claims to fill this space. Moreover, for a detailed analysis of the problem four different types of plate motion are considered. As a result, the following flow situations known as (i) flow induced by an impulsive motion of the plate, (ii) flow due to uniform acceleration of the plate, (iii) flow due to nonuniform acceleration of the plate, and (iv) flow due to highly nonuniform acceleration of the plate are discussed. Exact solutions of momentum and energy equations are obtained by using Laplace transform technique. They satisfy all imposed initial and boundary conditions and can easily be reduced to the similar solutions for hydrodynamic Brinkman type and Newtonian fluids. Analytical as well as numerical results for skin friction and Nusselt number are provided. Graphical results are presented and discussed for various physical parameters. Applications of the present problem are diverse. Because this work presents a new research on free convection flow of Brinkman type fluid for some fundamental fluid motions, therefore this problem can be extended for more complicated studies on Brinkman type fluid in various porous media. Furthermore, the exact solutions obtained in this study will assist scientist and engineers as they can use them as a check of correctness for numerical or approximate solutions of complicated flow problems.

## 2. Mathematical Formulation and Solution of the Problem

Let us consider unsteady free convection flow of an incompressible and electrically conducting fluid of Brinkman type [40]. It is assumed that the plate occupies the half porous space  $y > 0$  over an infinite vertical flat plate situated in the  $(x, z)$  plane of a Cartesian coordinate system  $x, y$ , and  $z$ . The  $x$ -axis is taken along the vertical plate and the  $y$ -axis is taken normal to the plate. A uniform magnetic field of strength  $B_0$  is transversely applied to the plate in the outward direction. The applied magnetic field is assumed to be strong enough so that the induced magnetic field due to the fluid motion is weak and can be neglected. As mentioned by Cramer and Pai [42], this assumption is physically justified for partially ionized fluids and metallic

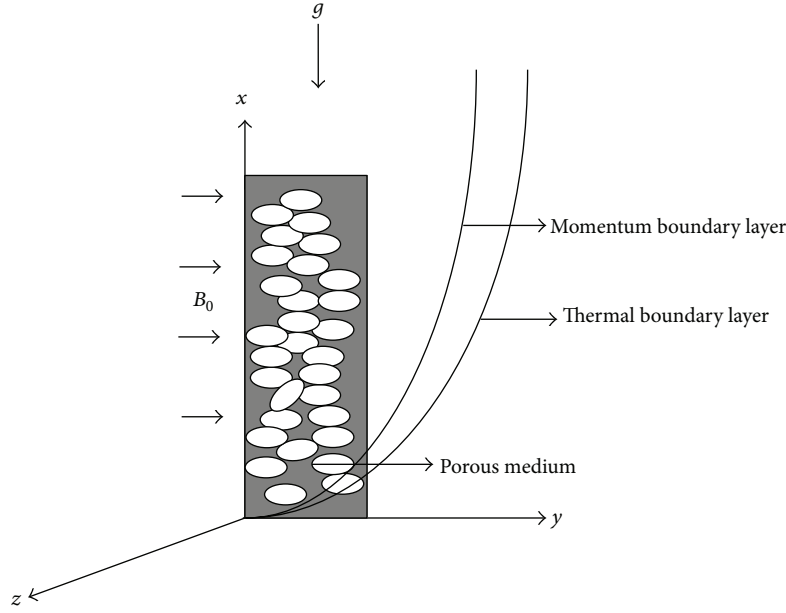


FIGURE 1: Physical model and coordinates system.

liquids because of their small magnetic Reynolds number. Since there is no applied or polarization voltage imposed on the flow field, therefore the electric field due to polarization of charges is zero. Initially, both the plate and fluid are at rest with constant temperature  $T_\infty$ . After time  $t = 0^+$ , the flow is caused by translating the plate in its plane with time-dependent velocity  $At^n$  against the gravitational field. It is assumed that the rate of heat transfer from the surface is directly proportional to the local surface temperature  $T$ . Due to the shear, the fluid is gradually moved and its velocity is of the form

$$\mathbf{v} = \mathbf{v}(y, t) = u(y, t) \mathbf{i}, \quad (1)$$

where  $\mathbf{i}$  is the unit vector in the flow direction. The physical model is shown in Figure 1.

In addition to the above assumptions, we assume that the internal dissipation is absent and the usual Boussinesq approximation is taken into consideration. Moreover, the pressure gradient in the flow direction is compensated by the gradient of the hydrostatic pressure gradient of the fluid. As a result the governing equations of momentum and energy are derived as follows:

$$\begin{aligned} \frac{\partial u(y, t)}{\partial t} + \beta u(y, t) &= \nu \frac{\partial^2 u(y, t)}{\partial y^2} - \frac{\sigma B_0^2 u(y, t)}{\rho} \\ &- \frac{\nu \phi u(y, t)}{k} + g \beta_T (T - T_\infty), \end{aligned} \quad (2)$$

$$\rho c_p \frac{\partial T}{\partial t} = k_1 \frac{\partial^2 T}{\partial y^2} - \frac{\partial q_r}{\partial y}, \quad (3)$$

where  $T$  is the temperature of the fluid,  $\nu = \mu/\rho$  ( $\mu$  is the viscosity and  $\rho$  is the constant density of the fluid) is the kinematic viscosity,  $\sigma$  is the electrical conductivity of the

fluid,  $\beta = \alpha/\rho$  ( $\alpha$  is the drag coefficient that is usually assumed to be positive),  $\phi$  is the porosity parameter,  $k$  is the permeability parameter,  $\beta_T$  is the volumetric coefficient of thermal expansion,  $g$  is the acceleration due to gravity,  $T_\infty$  is the free stream temperature,  $c_p$  is the specific heat of the fluid at a constant pressure,  $k_1$  is the thermal conductivity, and  $q_r$  is the radiative flux along the  $y$ -axis.

The initial and boundary conditions relevant to the present flow situation are

$$t \leq 0 : u(y, t) = 0, \quad T(y, t) = T_\infty; \quad y > 0,$$

$$t > 0 : u(0, t) = At^n, \quad \frac{\partial T(0, t)}{\partial y} = -h_s T, \quad (4)$$

$$u(\infty, t) = 0, \quad T(\infty, t) = T_\infty,$$

where  $n \geq 0$  is constant and  $h_s$  is the heat transfer parameter for Newtonian heating. The radiative heat flux term in (3) is simplified using the Rosseland approximation as

$$q_r = -\frac{4\sigma_1}{3k_2} \frac{\partial T^4}{\partial y}, \quad (5)$$

where  $\sigma_1$  is the Stefan-Boltzmann constant and  $k_2$  is the mean absorption coefficient. It is assumed that the temperature differences inside the flow are sufficiently small such that  $T^4$  may be expressed as a linear function of the temperature, and then by expanding  $T^4$  about  $T_\infty$  using Taylor series and neglecting the higher order terms, we get

$$T^4 \cong 4T_\infty^3 T - 3T_\infty^4. \quad (6)$$

Now (3) after using (5) and (6) takes the following form:

$$\rho c_p \frac{\partial T}{\partial t} = k_1 \left( 1 + \frac{16\sigma T_\infty^3}{3k_1 k_2} \right) \frac{\partial^2 T}{\partial y^2}. \quad (7)$$

By introducing the following dimensionless variables

$$\begin{aligned} v_n &= \frac{u}{(\nu^n A)^{1/(2n+1)}}, & \xi &= y \left( \frac{A}{\nu^{n+1}} \right)^{1/(2n+1)}, \\ \tau &= t \left( \frac{A^2}{\nu} \right)^{1/(2n+1)}, \\ \beta_n &= \beta \left( \frac{\nu}{A^2} \right)^{1/(2n+1)}, & \theta &= \frac{T - T_\infty}{T_\infty}, \end{aligned} \quad (8)$$

into (2)–(4) and (7), we obtain the following dimensionless system:

$$\frac{\partial v_n(\xi, \tau)}{\partial \tau} = \frac{\partial^2 v_n(\xi, \tau)}{\partial \xi^2} - \beta_n v_n(\xi, \tau) - H v_n(\xi, \tau) + \text{Gr} \theta(\xi, \tau), \quad (9)$$

$$\text{Pr} \frac{\partial \theta}{\partial \tau} = (1 + R) \frac{\partial^2 \theta}{\partial \xi^2}, \quad (10)$$

$$\tau \leq 0 : v_n(\xi, \tau) = 0, \quad \theta(\xi, \tau) = 0; \quad \xi > 0,$$

$$\tau > 0 : v_n(0, \tau) = \tau^n, \quad \frac{\partial \theta(0, \tau)}{\partial \xi} = -\gamma(1 + \theta), \quad (11)$$

$$v_n(\infty, \tau) = 0, \quad \theta(\infty, \tau) = 0,$$

where  $\gamma$  is the Newtonian heating parameter. Using the Laplace transform technique, (9)–(11) give the following transformed solutions:

$$\begin{aligned} \bar{v}_n(\xi, q) &= \frac{\Gamma(n+1)}{q^{n+1}} e^{-\xi\sqrt{q+H}} + a_1 \frac{e^{-\xi\sqrt{q+H}}}{\sqrt{q}-d} + a_2 \frac{e^{-\xi\sqrt{q+H}}}{q} \\ &+ a_3 \frac{e^{-\xi\sqrt{q+H}}}{\sqrt{q}} - a_4 \frac{e^{-\xi\sqrt{q+H}}}{q-H_1} - a_5 \frac{\sqrt{q} e^{-\xi\sqrt{q+H}}}{q-H_1} \\ &- a_1 \frac{e^{-\xi\sqrt{q\bar{a}}}}{\sqrt{q}-d} - a_2 \frac{e^{-\xi\sqrt{q\bar{a}}}}{q} - a_3 \frac{e^{-\xi\sqrt{q\bar{a}}}}{\sqrt{q}} \\ &+ a_4 \frac{e^{-\xi\sqrt{q\bar{a}}}}{q-H_1} + a_5 \frac{\sqrt{q} e^{-\xi\sqrt{q\bar{a}}}}{q-H_1}, \end{aligned} \quad (12)$$

$$\bar{\theta}(\xi, q) = \frac{d}{q(\sqrt{q}-d)} e^{-\xi\sqrt{q\bar{a}}}, \quad (13)$$

where

$$\begin{aligned} \beta_n &= \beta \left( \frac{\nu}{A^2} \right)^{1/(2n+1)}, & M^2 &= \frac{\sigma B_0^2}{\rho} \left( \frac{\nu}{A^2} \right)^{1/(2n+1)}, \\ \frac{1}{K} &= \frac{\nu \phi}{k} \left( \frac{\nu}{A^2} \right)^{1/(2n+1)}, & \text{Gr} &= \frac{g \beta_T T_\infty}{(A^3 \nu^{n-1})^{1/(2n+1)}}, \\ \gamma &= h_s \left( \frac{\nu^{n+1}}{A} \right)^{1/(2n+1)}, & \text{Pr} &= \frac{\mu c_p}{k_1}, & R &= \frac{16 \sigma T_\infty^3}{3 k_1 k_2}, \\ H &= M^2 + \frac{1}{K}, & H_1 &= \frac{H}{a-1}, \\ a &= \frac{\text{Pr}}{1+R}, & d &= \frac{\gamma}{\sqrt{a}}, \\ \text{Gr}_1 &= \frac{\text{Gr} d}{a-1}, & a_1 &= \frac{\text{Gr}_1}{d^2(d^2-H_1)}, \\ a_2 &= \frac{\text{Gr}_1}{d H_1}, & a_3 &= \frac{\text{Gr}_1}{d^2 H_1}, \\ a_4 &= \frac{\text{Gr}_1 d}{H_1(d^2-H_1)}, & a_5 &= \frac{\text{Gr}_1}{H_1(d^2-H_1)}. \end{aligned} \quad (14)$$

The Laplace inverse of (13) results in

$$\begin{aligned} \theta(\xi, \tau) &= \exp(d^2 \tau - \gamma \sqrt{a} d) \text{erf} c \left[ \frac{\gamma \sqrt{a}}{2 \sqrt{\tau}} - d \sqrt{\tau} \right] \\ &- \text{erf} c \left[ \frac{\gamma \sqrt{a}}{2 \sqrt{\tau}} \right]. \end{aligned} \quad (15)$$

For a detailed analysis of (12), we are considering the following four cases.

### 3. Flow Induced by an Impulsive Motion of the Plate

For an impulsive motion of the plate ( $n = 0$ ), (12) yields

$$\begin{aligned} \bar{v}_0(\xi, q) &= \frac{1}{q} e^{-\xi\sqrt{q+H}} + a_1 \frac{e^{-\xi\sqrt{q+H}}}{\sqrt{q}-d} + a_2 \frac{e^{-\xi\sqrt{q+H}}}{q} \\ &+ a_3 \frac{e^{-\xi\sqrt{q+H}}}{\sqrt{q}} - a_4 \frac{e^{-\xi\sqrt{q+H}}}{q-H_1} - a_5 \frac{\sqrt{q} e^{-\xi\sqrt{q+H}}}{q-H_1} \\ &- a_1 \frac{e^{-\xi\sqrt{q\bar{a}}}}{\sqrt{q}-d} - a_2 \frac{e^{-\xi\sqrt{q\bar{a}}}}{q} - a_3 \frac{e^{-\xi\sqrt{q\bar{a}}}}{\sqrt{q}} \\ &+ a_4 \frac{e^{-\xi\sqrt{q\bar{a}}}}{q-H_1} + a_5 \frac{\sqrt{q} e^{-\xi\sqrt{q\bar{a}}}}{q-H_1}. \end{aligned} \quad (16)$$

The solution of (16), after taking the Laplace inverse, is given by

$$\begin{aligned}
 v_0(\xi, \tau) = & f_1(\xi, \tau, H) + a_2 f_1(\xi, \tau, H) - a_2 f_1(\xi, \tau, 0) \\
 & - a_4 e^{H_1 t} f_1(\xi, \tau, H + H_1) + a_4 e^{H_1 t} f_1(\xi \sqrt{a}, \tau, H_1) \\
 & - a_1 f_2(\xi \sqrt{a}, \tau, d) + 2 f_6(\xi, z, \tau, H) \\
 & + 2 d f_7(\xi, z, \tau, H) + 2 f_8(\xi, z, \tau, H) \\
 & - 2 f_9(\xi, z, \tau, H) - 2 H_1 f_{10}(\xi, z, \tau, H) \\
 & - f_{11}(\xi, z, \tau, H) + 2 f_{12}(\xi, z, \tau, H) \\
 & + 2 H_1 f_{13}(\xi, z, \tau, H).
 \end{aligned} \tag{17}$$

#### 4. Flow due to Uniform Acceleration of the Plate

For the uniform acceleration of the plate ( $n = 1$ ), (12) yields

$$\begin{aligned}
 \bar{v}_1(\xi, q) = & \frac{1}{q^2} e^{-\xi \sqrt{q+H}} + a_1 \frac{e^{-\xi \sqrt{q+H}}}{\sqrt{q-d}} + a_2 \frac{e^{-\xi \sqrt{q+H}}}{q} \\
 & + a_3 \frac{e^{-\xi \sqrt{q+H}}}{\sqrt{q}} - a_4 \frac{e^{-\xi \sqrt{q+H}}}{q-H_1} \\
 & - a_5 \frac{\sqrt{q} e^{-\xi \sqrt{q+H}}}{q-H_1} - a_1 \frac{e^{-\xi \sqrt{q} a}}{\sqrt{q-d}} \\
 & - a_2 \frac{e^{-\xi \sqrt{q} a}}{q} - a_3 \frac{e^{-\xi \sqrt{q} a}}{\sqrt{q}} + a_4 \frac{e^{-\xi \sqrt{q} a}}{q-H_1} \\
 & + a_5 \frac{\sqrt{q} e^{-\xi \sqrt{q} a}}{q-H_1}.
 \end{aligned} \tag{18}$$

The solution of (18), after taking the Laplace inverse, is given by

$$\begin{aligned}
 v_1(\xi, \tau) = & a_2 f_1(\xi, \tau, H) - a_2 f_1(\xi \sqrt{a}, \tau, 0) \\
 & - a_4 e^{H_1 t} f_1(\xi, \tau, H + H_1) + a_4 e^{H_1 t} f_1(\xi \sqrt{a}, \tau, H_1) \\
 & - a_1 f_2(\xi \sqrt{a}, \tau, d) + f_3(\xi, \tau, H) + 2 f_6(\xi, z, \tau, H) \\
 & + 2 d f_7(\xi, z, \tau, H) + 2 f_8(\xi, z, \tau, H) \\
 & - 2 f_9(\xi, z, \tau, H) - 2 H_1 f_{10}(\xi, z, \tau, H) \\
 & - f_{11}(\xi, z, \tau, H) + 2 f_{12}(\xi, z, \tau, H) \\
 & + 2 H_1 f_{13}(\xi, z, \tau, H).
 \end{aligned} \tag{19}$$

#### 5. Flow due to Nonuniform Acceleration of the Plate

For the nonuniform acceleration of the plate ( $n = 2$ ), (12) yields

$$\begin{aligned}
 \bar{v}_2(\xi, q) = & \frac{1}{q^3} e^{-\xi \sqrt{q+H}} + a_1 \frac{e^{-\xi \sqrt{q+H}}}{\sqrt{q-d}} + a_2 \frac{e^{-\xi \sqrt{q+H}}}{q} \\
 & + a_3 \frac{e^{-\xi \sqrt{q+H}}}{\sqrt{q}} - a_4 \frac{e^{-\xi \sqrt{q+H}}}{q-H_1} - a_5 \frac{\sqrt{q} e^{-\xi \sqrt{q+H}}}{q-H_1} \\
 & - a_1 \frac{e^{-\xi \sqrt{q} a}}{\sqrt{q-d}} - a_2 \frac{e^{-\xi \sqrt{q} a}}{q} - a_3 \frac{e^{-\xi \sqrt{q} a}}{\sqrt{q}} \\
 & + a_4 \frac{e^{-\xi \sqrt{q} a}}{q-H_1} + a_5 \frac{\sqrt{q} e^{-\xi \sqrt{q} a}}{q-H_1}.
 \end{aligned} \tag{20}$$

The solution of (20), after taking the Laplace inverse, is given by

$$\begin{aligned}
 v_2(\xi, \tau) = & a_2 f_1(\xi, \tau, H) - a_2 f_1(\xi \sqrt{a}, \tau, 0) \\
 & - a_4 e^{H_1 t} f_1(\xi, \tau, H + H_1) \\
 & + a_4 e^{H_1 t} f_1(\xi \sqrt{a}, \tau, H_1) \\
 & - a_1 f_2(\xi \sqrt{a}, \tau, d) + f_4(\xi, \tau, H) \\
 & + 2 f_6(\xi, z, \tau, H) + 2 d f_7(\xi, z, \tau, H) \\
 & + 2 f_8(\xi, z, \tau, H) - 2 f_9(\xi, z, \tau, H) \\
 & - 2 H_1 f_{10}(\xi, z, \tau, H) - f_{11}(\xi, z, \tau, H) \\
 & + 2 f_{12}(\xi, z, \tau, H) + 2 H_1 f_{13}(\xi, z, \tau, H).
 \end{aligned} \tag{21}$$

#### 6. Flow due to Highly Nonuniform Acceleration of the Plate

In this case,  $n = 3$  and (12) yields

$$\begin{aligned}
 \bar{v}_3(\xi, q) = & \frac{1}{q^4} e^{-\xi \sqrt{q+H}} + a_1 \frac{e^{-\xi \sqrt{q+H}}}{\sqrt{q-d}} + a_2 \frac{e^{-\xi \sqrt{q+H}}}{q} \\
 & + a_3 \frac{e^{-\xi \sqrt{q+H}}}{\sqrt{q}} - a_4 \frac{e^{-\xi \sqrt{q+H}}}{q-H_1} - a_5 \frac{\sqrt{q} e^{-\xi \sqrt{q+H}}}{q-H_1} \\
 & - a_1 \frac{e^{-\xi \sqrt{q} a}}{\sqrt{q-d}} - a_2 \frac{e^{-\xi \sqrt{q} a}}{q} - a_3 \frac{e^{-\xi \sqrt{q} a}}{\sqrt{q}} \\
 & + a_4 \frac{e^{-\xi \sqrt{q} a}}{q-H_1} + a_5 \frac{\sqrt{q} e^{-\xi \sqrt{q} a}}{q-H_1}.
 \end{aligned} \tag{22}$$

The solution of (22), after taking the Laplace inverse, is given by

$$\begin{aligned} v_3(\xi, \tau) = & a_2 f_1(\xi, \tau, H) - a_2 f_1(\xi \sqrt{a}, \tau, 0) \\ & - a_4 e^{H_1 t} f_1(\xi, \tau, H + H_1) + a_4 e^{H_1 t} f_1(\xi \sqrt{a}, \tau, H_1) \\ & - a_1 f_2(\xi \sqrt{a}, \tau, d) + f_5(\xi, \tau, H) + 2f_6(\xi, z, \tau, H) \\ & + 2df_7(\xi, z, \tau, H) + 2f_8(\xi, z, \tau, H) \\ & - 2f_9(\xi, z, \tau, H) - 2H_1 f_{10}(\xi, z, \tau, H) \\ & - f_{11}(\xi, z, \tau, H) + 2f_{12} + 2H_1 f_{13}, \end{aligned} \quad (23)$$

where

$$\begin{aligned} f_1(y, t, w) = & \frac{1}{2} \left( e^{-y\sqrt{w}} \operatorname{erfc} \left[ \frac{y}{2\sqrt{t}} - \sqrt{wt} \right] \right. \\ & \left. + e^{y\sqrt{w}} \operatorname{erfc} \left[ \frac{y}{2\sqrt{t}} + \sqrt{wt} \right] \right), \\ f_2(y, t, w) = & \frac{1}{\sqrt{\pi t}} \exp \left( -\frac{y^2}{4t} \right) \\ & + w \exp(-yw + w^2 t) \operatorname{erfc} \left[ \frac{y}{2\sqrt{t}} - w\sqrt{t} \right], \\ f_3(y, t, w) = & \frac{1}{2} \left( \left( t - \frac{y}{2\sqrt{w}} \right) e^{-\xi\sqrt{w}} \operatorname{erfc} \left[ \frac{y}{2\sqrt{t}} - \sqrt{wt} \right] \right. \\ & + \left( t + \frac{y}{2\sqrt{w}} \right) e^{y\sqrt{w}} \\ & \left. \times \operatorname{erfc} \left[ \frac{y}{2\sqrt{t}} + \sqrt{wt} \right] \right), \\ f_4(y, t, w) = & \frac{1}{4} \left( \left( t^2 - \frac{yt}{\sqrt{w}} + \frac{y^2}{4w} + \frac{y}{4w\sqrt{w}} \right) \right. \\ & \left. \times e^{-y\sqrt{w}} \operatorname{erfc} \left[ \frac{y}{2\sqrt{t}} - \sqrt{wt} \right] \right) \\ & + \left( t^2 + \frac{yt}{\sqrt{w}} + \frac{y^2}{4w} - \frac{y}{4w\sqrt{w}} \right) \\ & \left. \times e^{y\sqrt{w}} \operatorname{erfc} \left[ \frac{y}{2\sqrt{t}} + \sqrt{wt} \right] \right), \\ f_5(y, t, w) = & \frac{1}{6} \left( \frac{3y}{4w^2} - \frac{yt}{w} \right) \sqrt{\frac{t}{w}} \exp \left( \frac{y^2}{4t} - wt \right) \\ & + \left( -\frac{y^2}{32w^2} - \frac{y^2 t}{16w} + \frac{t^3}{12} \right) \\ & \times e^{-y\sqrt{w}} \operatorname{erfc} \left[ \frac{y}{2\sqrt{t}} - \sqrt{wt} \right] \end{aligned}$$

$$\begin{aligned} & + e^{y\sqrt{w}} \operatorname{erfc} \left[ \frac{y}{2\sqrt{t}} + \sqrt{wt} \right] \\ & \times \left( -\frac{y}{32w^2\sqrt{w}} - \frac{y^2}{96w\sqrt{w}} \right. \\ & \left. + \frac{yt}{16w\sqrt{w}} - \frac{yt^2}{8\sqrt{w}} \right) \\ & \times \left( e^{-y\sqrt{w}} \operatorname{erfc} \left[ \frac{y}{2\sqrt{t}} - \sqrt{wt} \right] \right. \\ & \left. + e^{y\sqrt{w}} \operatorname{erfc} \left[ \frac{y}{2\sqrt{t}} + \sqrt{wt} \right] \right), \end{aligned}$$

$$f_6(\xi, z, \tau, H)$$

$$= \frac{a_1}{\pi} \int_{\xi/2\sqrt{\tau}}^{\infty} \frac{\exp(-z^2 - H(\xi^2/4z^2))}{\sqrt{\tau - (\xi^2/4z^2)}} dz,$$

$$\begin{aligned} f_7(\xi, z, \tau, H) = & \frac{a_1}{\sqrt{\pi}} \int_{(\xi/2\sqrt{\tau})}^{\infty} \exp \left( -z^2 - H \frac{\xi^2}{4z^2} \right. \\ & \left. + d^2 \tau - d^2 \frac{\xi^2}{4z^2} \right) \\ & \times \operatorname{erfc} \left[ -d \sqrt{\tau - \frac{\xi^2}{4z^2}} \right] dz \end{aligned}$$

$$f_8(\xi, z, \tau, H) = \frac{a_3}{\pi} \int_{\xi/2\sqrt{\tau}}^{\infty} \frac{\exp(-z^2 - H(\xi^2/4z^2))}{\sqrt{\tau - (\xi^2/4z^2)}} dz,$$

$$f_9(\xi, z, \tau, H) = \frac{a_5}{\pi} \int_{\xi/2\sqrt{\tau}}^{\infty} \frac{\exp(-z^2 - H(\xi^2/4z^2))}{\sqrt{\tau - (\xi^2/4z^2)}} dz,$$

$$\begin{aligned} f_{10}(\xi, z, \tau, H) = & \frac{a_5}{\sqrt{\pi}} \int_{\xi/2\sqrt{\tau}}^{\infty} \exp \left( -z^2 - H \frac{\xi^2}{4z^2} \right. \\ & \left. + H_1 \tau - H_1 \frac{\xi^2}{4z^2} \right) \\ & \times \operatorname{erfc} \left[ \sqrt{H_1 \left( \tau - \frac{\xi^2}{4z^2} \right)} \right] dz, \end{aligned}$$

$$f_{11}(\xi, z, \tau, H) = \exp \left( \frac{\xi^2 a}{4\tau} \right),$$

$$f_{12}(\xi, z, \tau, H) = \frac{a_5 \sqrt{a}}{\pi} \int_{\xi/2\sqrt{\tau}}^{\infty} \frac{\exp(-z^2 a)}{\sqrt{\tau - (\xi^2/4z^2)}} dz,$$

$$f_{13}(\xi, z, \tau, H) = \frac{a_5 \sqrt{a}}{\sqrt{\pi}} \int_{\xi/2\sqrt{\tau}}^{\infty} \exp \left( -z^2 a + H_1 \tau \right)$$

$$\begin{aligned} & -H_1 \frac{\xi^2}{4z^2} \Big) \\ & \times \operatorname{erf} \left[ \sqrt{H_1 \left( \tau - \frac{\xi^2}{4z^2} \right)} \right] dz. \end{aligned} \tag{24}$$

### 7. Special Cases

The following solutions from the literature appear as the limiting cases of our general solutions.

#### 7.1. Absence of Thermal Effects

7.1.1. *Case I: Impulsive Motion of the Plate.* By eliminating the convective term  $Gr = 0$  together with MHD and porosity effects ( $M = 0$  and  $K \rightarrow \infty$ ; that is,  $H = \beta_0$ ) in (17), we get

$$v_0 = f_1(\xi, \tau, \beta_0), \tag{25}$$

which is in quite agreement with [40, Equation (2.7)] when  $\nu = U = 1$ . Furthermore by putting  $\beta_0 = 0$ , (25) reduces to

$$v_{0N} = f_1(\xi, \tau, 0), \tag{26}$$

which is the well-known solution of Newtonian fluid [40, Equation (2.8)] for the impulsive motion of the plate obtained by a different technique.

7.1.2. *Case II: Accelerated Motion of the Plate.* In this case when convective term  $Gr = 0$  with  $M = 0$  and  $K \rightarrow \infty$ , (19) reduces to

$$v_1 = f_3(\xi, \tau, \beta_1), \tag{27}$$

which is in complete agreement with [41, Equation (15)] for accelerated motion of the plate.

*Skin Friction.* The expressions for skin frictions  $\tau_0$  and  $\tau_1$  evaluated from (17) and (19), respectively, are given by

$$\begin{aligned} \tau_0 &= - \left. \frac{\partial v_0(\xi, \tau)}{\partial \xi} \right|_{\xi=0} = -g_1(\tau, H) - a_2 g_1(\tau, H) \\ &+ a_2 g_1(\tau, 0) + a_4 e^{H_1 \tau} g_1(\tau, H + H_1) \\ &- a_4 \sqrt{a} e^{H_1 \tau} g_1(\tau, H_1) \\ &+ a_1 \sqrt{a} g_2(\tau, d), \\ \tau_1 &= - \left. \frac{\partial v_1(\xi, \tau)}{\partial \xi} \right|_{\xi=0} = -a_2 g_1(\tau, H) + a_2 g_1(\tau, 0) \\ &+ a_4 e^{H_1 \tau} g_1(\tau, H + H_1) \\ &- a_4 \sqrt{a} e^{H_1 \tau} g_1(\tau, H_1) \\ &+ a_1 \sqrt{a} g_2(\tau, d) - g_3(\tau, H), \end{aligned} \tag{28}$$

where

$$\begin{aligned} g_1(t, w) &= \left. \frac{\partial f_1}{\partial y}(y, t, w) \right|_{y=0} \\ &= - \frac{e^{-wt} (1 + e^{wt} \sqrt{w} \sqrt{\pi t} \operatorname{erf}[\sqrt{wt}])}{\sqrt{\pi t}}, \\ g_2(t, w) &= \left. \frac{\partial f_2}{\partial y}(y, t, w) \right|_{y=0} \\ &= \frac{a_1 \sqrt{a} d (-1 - 2de^{d^2 t} \sqrt{\pi t} + de^{d^2 t} \sqrt{\pi t} \operatorname{erfc}[d\sqrt{t}])}{\sqrt{\pi t}}, \\ g_3(t, w) &= \left. \frac{\partial f_3}{\partial y}(y, t, w) \right|_{y=0} \\ &= - \frac{e^{-wt} \sqrt{t}}{\sqrt{\pi}} - \frac{(1 + 2tw) \operatorname{erf}[\sqrt{wt}]}{2\sqrt{w}}. \end{aligned} \tag{29}$$

*Nusselt Number.* The rate of heat transfer evaluated from (15) is given by

$$\begin{aligned} \operatorname{Nu} &= - \left. \frac{\partial \theta(\xi, \tau)}{\partial \xi} \right|_{\xi=0} = \gamma \left[ \frac{1}{\theta(0, \tau)} + 1 \right] \\ &= \gamma \left[ \frac{1}{e^{d^2 \tau} (1 + \operatorname{erf}[d\sqrt{\tau}]) - 1} + 1 \right]. \end{aligned} \tag{30}$$

### 8. Graphical Results and Discussion

In this paper, the influence of thermal radiation on unsteady free convection flow of MHD Brinkman type fluid past a vertical plate in a porous medium is studied with Newtonian heating condition. Four different types of motions in terms of different boundary conditions on velocity are discussed. Exact solutions are obtained by means of Laplace transforms. Straightforward computations show that the velocities  $v_0(y, t)$ ,  $v_1(y, t)$ ,  $v_2(y, t)$ , and  $v_3(y, t)$  given by (17), (19), (21), and (23) and temperature (15), respectively, satisfy both the governing equations and all imposed initial and boundary conditions. As a special case when  $\beta_n$  ( $n = 0-3$ )  $\rightarrow 0$ , the solutions that have been established reduce to the well-known solutions for Newtonian fluids. It is worthy pointing out that solutions corresponding to hydrodynamic motion of Brinkman fluid in a nonporous medium can also be obtained as a limiting case. In order to study the physical aspects of the problem, the analytical results for velocities  $v_0(\xi, \tau)$  and  $v_1(\xi, \tau)$  due to impulsive motion and uniform acceleration as well as for temperature distribution are plotted graphically in Figures 2–12, whereas the numerical results of skin friction and Nusselt number for different flow parameters are shown in Tables 1 and 2. The parameters entering into the problem are Prandtl number  $Pr$ , magnetic

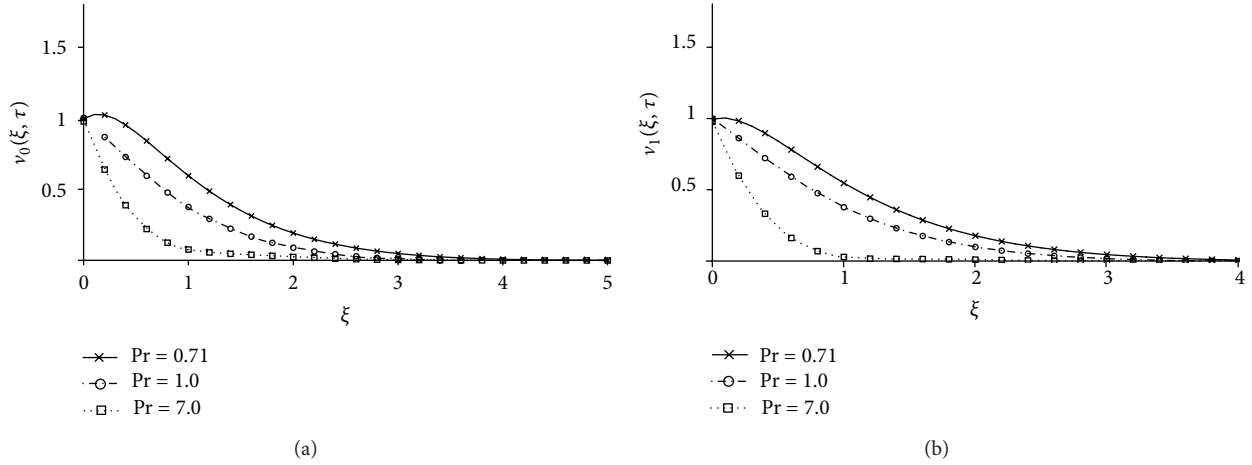


FIGURE 2: Velocity profiles for different values of  $Pr$  where  $M = 2, K = 1, Gr = 0.5, R = 1, \gamma = 1, \beta_0 = \beta_1 = 1,$  and  $\tau = 1.$

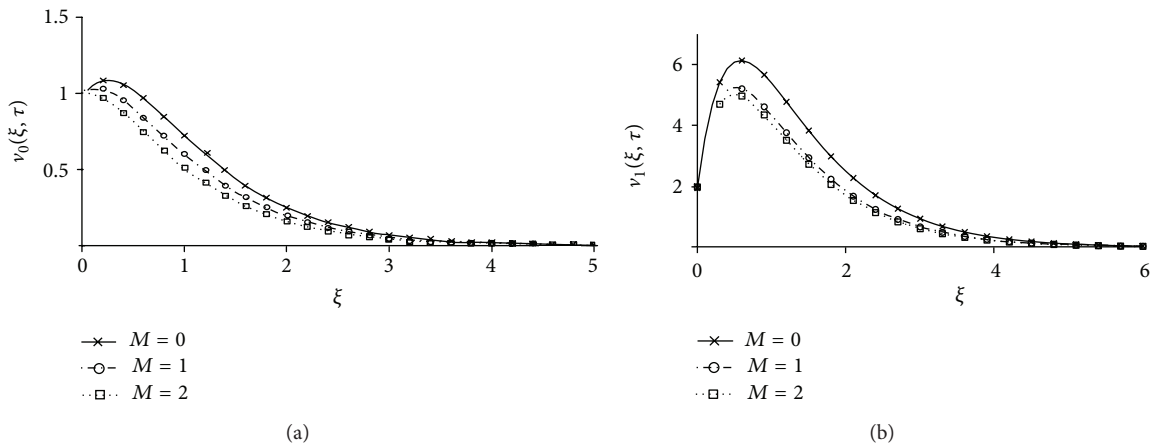


FIGURE 3: Velocity profiles for different values of  $M$  where  $Pr = 0.71, K = 1, Gr = 0.5, R = 1, \gamma = 1, \beta_0 = \beta_1 = 1,$  and  $\tau = 1.$

TABLE 1: Variation in skin friction  $\tau_0$  and  $\tau_1$ .

Pr	M	K	Gr	R	$\gamma$	$\beta_0$	$\beta_1$	$\tau$	$\tau_0$	$\tau_1$
0.71	1	1	0.5	1	0.2	1	1	1	2.029	2.314
<b>1</b>	1	1	0.5	1	0.2	1	1	1	2.035	2.320
0.71	<b>2</b>	1	0.5	1	0.2	1	1	1	2.656	2.860
0.71	1	<b>2</b>	0.5	1	0.2	1	1	1	1.910	2.218
0.71	1	1	<b>1</b>	1	0.2	1	1	1	2.324	2.608
0.71	1	1	0.5	<b>2</b>	0.2	1	1	1	2.025	2.310
0.71	1	1	0.5	1	<b>0.4</b>	1	1	1	2.089	2.373
0.71	1	1	0.5	1	0.2	<b>2</b>	<b>2</b>	1	2.255	2.504
0.71	1	1	0.5	1	0.2	1	1	<b>2</b>	2.038	4.059

The bold values show the comparison (increase or decrease) with the fixed values (not bold) of the same column for the corresponding parameters given at the top of the column on the skin frictions ( $\tau_0$  and  $\tau_1$ ).

parameter  $M$ , porosity parameter  $K$ , Grashof number  $Gr$ , radiation parameter  $R$ , Newtonian heating parameter  $\gamma$ , dimensionless time  $\tau$ , and Brinkman parameter  $\beta_n$  ( $n = 0, 1$ ).

TABLE 2: Variation in Nusselt number  $Nu$ .

Pr	R	$\gamma$	$\tau$	$Nu$
0.71	1	0.2	1	0.305
<b>7</b>	1	0.2	1	0.284
0.71	<b>2</b>	0.2	1	0.340
0.71	1	<b>0.4</b>	1	1.040
0.71	1	0.2	<b>2</b>	0.375

The bold values show the comparison (increase or decrease) with the fixed values (not bold) of the same column for the corresponding parameters given at the top of the column on Nusselt number ( $Nu$ ).

Figure 2 is plotted to see the effect of  $Pr$  on velocity in cases of impulsive motion  $v_0(\xi, \tau)$  and uniform acceleration  $v_1(\xi, \tau)$  of the plate. Three different values of  $Pr = 0.71, 1,$  and  $7$  are chosen such that physically they correspond to air, electrolytic solution, and water, respectively. It is clear from this figure that velocity decreases for both impulsive motion and accelerated motion of the plate as  $Pr$  increases. Physically, it is true due to the fact that an increase in Prandtl number  $Pr$  increases viscosity of

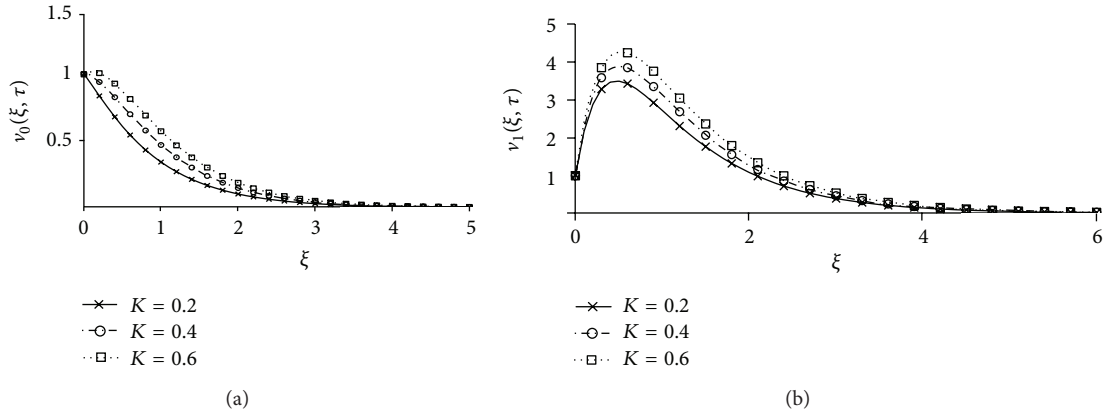


FIGURE 4: Velocity profiles for different values of  $K$  where  $M = 2$ ,  $Pr = 0.71$ ,  $Gr = 0.5$ ,  $R = 1$ ,  $\gamma = 1$ ,  $\beta_0 = \beta_1 = 1$ , and  $\tau = 1$ .

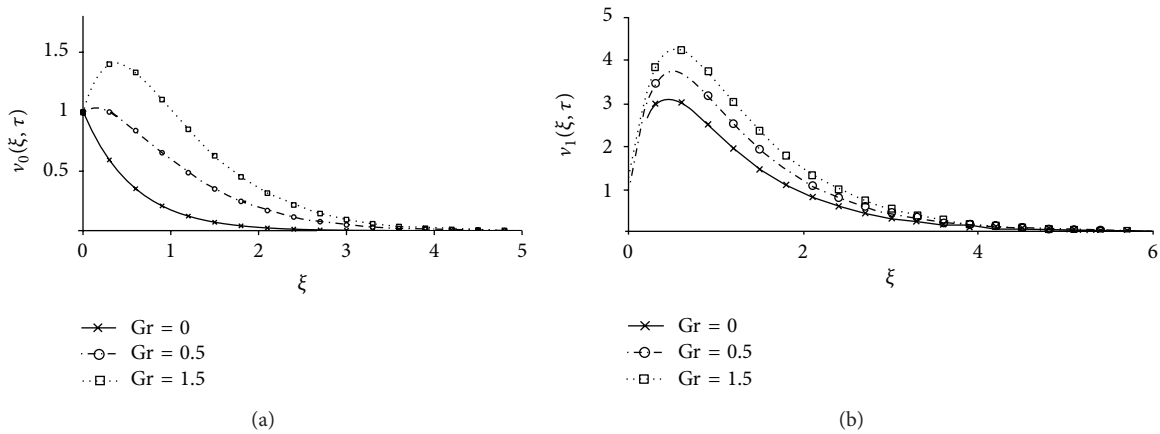


FIGURE 5: Velocity profiles for different values of  $Gr$  where  $M = 2$ ,  $K = 1$ ,  $Pr = 0.71$ ,  $R = 1$ ,  $\gamma = 1$ ,  $\beta_0 = \beta_1 = 1$ , and  $\tau = 1$ .

the fluid. Hence, the fluid becomes thick and consequently velocity decreases. Figure 3 is prepared to see the effects of the magnetic parameter  $M$  on velocity profiles for impulsive and accelerated motions of the plate. It is observed that velocity in both cases decreases when  $M$  is increased. This physical interpretation of the velocity is an indication that the increasing values of magnetic parameter  $M$  make the resistive forces strong enough so that they can oppose the fluid motion and as a result velocity decreases. This figure also shows the comparison of hydrodynamic velocity to hydromagnetic velocity of Brinkman fluid. In the absence of magnetic effects the velocity is maximum. Furthermore, it is observed that the momentum boundary layer thickness for the impulsive motion is greater compared to uniformly accelerated motion. However, the magnitude of velocity in case of uniformly accelerated motion is greater than that of impulsive motion.

Figure 4 is plotted to show the effects of porosity parameter  $K$  on the velocities  $v_0(\xi, \tau)$  and  $v_1(\xi, \tau)$ . It appears from this figure that with increasing values of  $K$ , velocity increases for both impulsive and uniformly accelerated motions. Physically, it is true because increasing  $K$  reduces the drag force and causes the velocity profiles to increase. Thus increasing value of the porosity

parameter  $K$  yields an effect opposite to that of the magnetic parameter  $M$ . Figure 5 shows the effect of Grashof number  $Gr$  on the velocities for the cases of impulsive and uniformly accelerated motions. It is observed that an increase in Grashof number  $Gr$  leads to increasing both types of velocities  $v_0(\xi, \tau)$  and  $v_1(\xi, \tau)$  due to enhancement in buoyancy force. It is true because thermal Grashof number signifies the relative effect of thermal buoyancy force to viscous hydrodynamic force. Increase of Grashof number  $Gr$  means increase of temperature gradient ( $T_w - T_\infty$ ) due to which the contribution from the buoyancy near the plate becomes significant and hence a short rise in the velocity near the plate is observed. Physically,  $Gr = 0$  corresponds to the absence of free convection current and  $Gr > 0$  means heating of the fluid or cooling of the plate by natural convection. For the positive values of  $Gr$ , heat is conducted away from the vertical plate into the fluid which increases the temperature and thereby enhances the buoyancy force.

The graphs showing the variations of radiation parameter  $R$  on the velocities  $v_0(\xi, \tau)$  and  $v_1(\xi, \tau)$  are displayed in Figure 6. We found that in both cases the velocity increases as  $R$  increases. Physically, it is true, as higher radiation occurs when temperature is higher and ultimately velocity

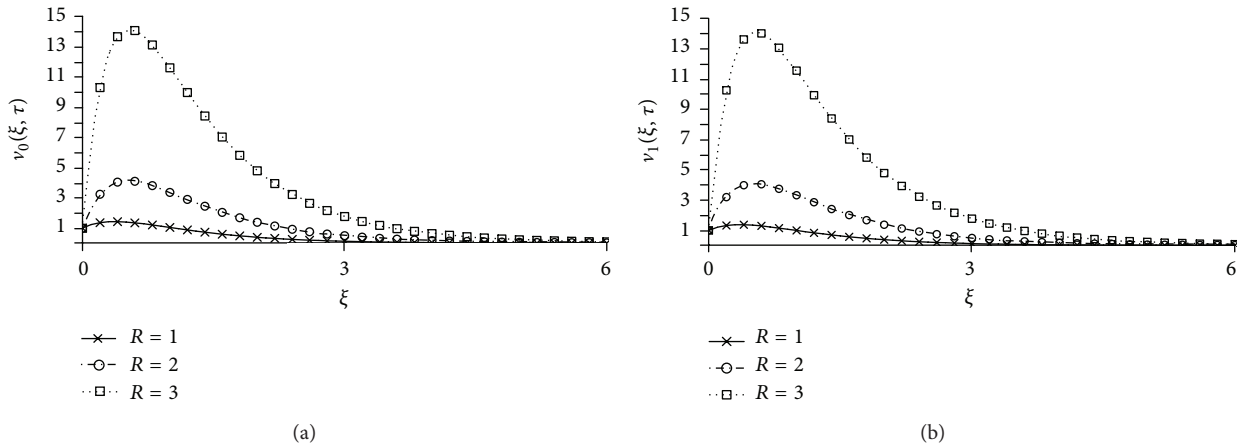


FIGURE 6: Velocity profiles for different values of  $R$  where  $M = 2, K = 1, Gr = 0.5, Pr = 0.71, \gamma = 1, \beta_0 = \beta_1 = 1,$  and  $\tau = 1$ .

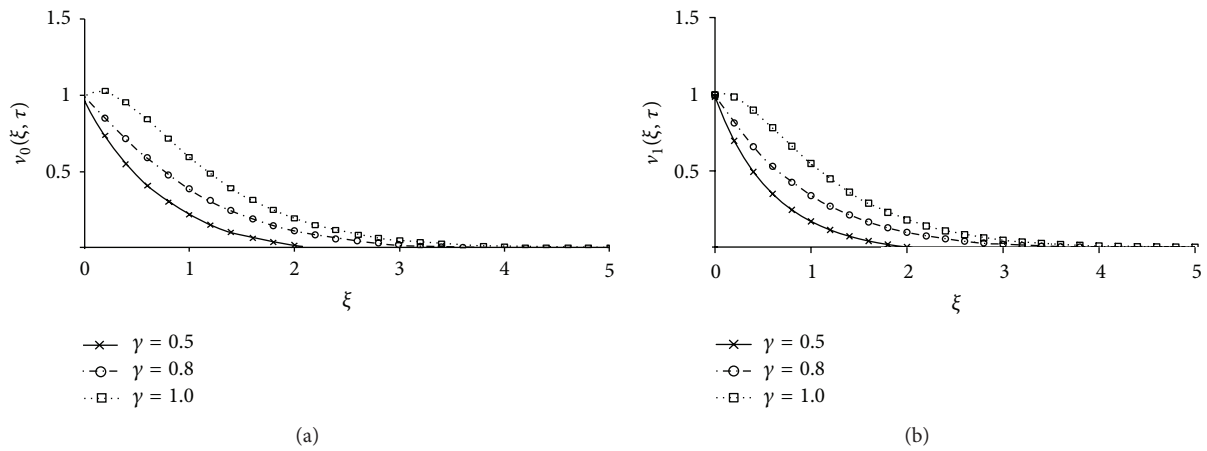


FIGURE 7: Velocity profiles for different values of  $\gamma$  where  $M = 2, K = 1, Gr = 0.5, R = 1, Pr = 0.71, \beta_0 = \beta_1 = 1,$  and  $\tau = 1$ .

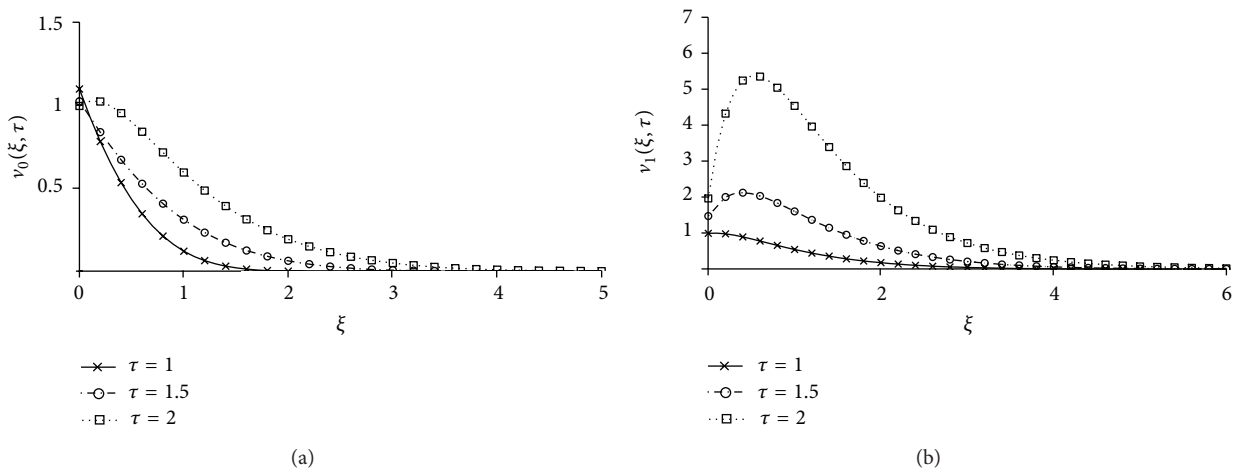


FIGURE 8: Velocity profiles for different values of  $\tau$  where  $M = 2, K = 1, Gr = 0.5, R = 1, \gamma = 1, \beta_0 = \beta_1 = 1,$  and  $Pr = 0.71$ .

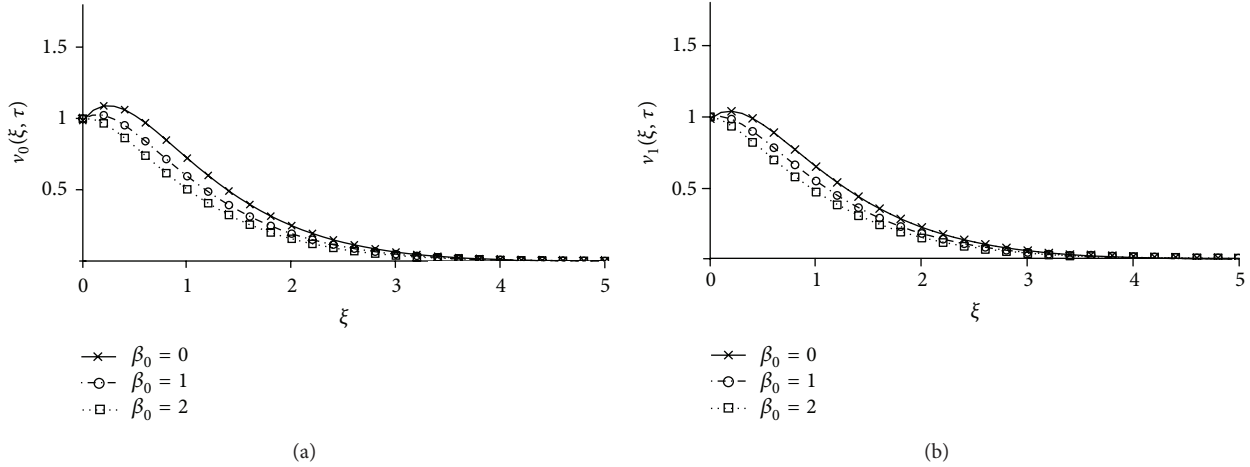


FIGURE 9: Velocity profiles for different values of  $\beta_0$  and  $\beta_1$  where  $M = 2, K = 1, Gr = 0.5, R = 1, \gamma = 1, Pr = 0.71,$  and  $\tau = 1.$

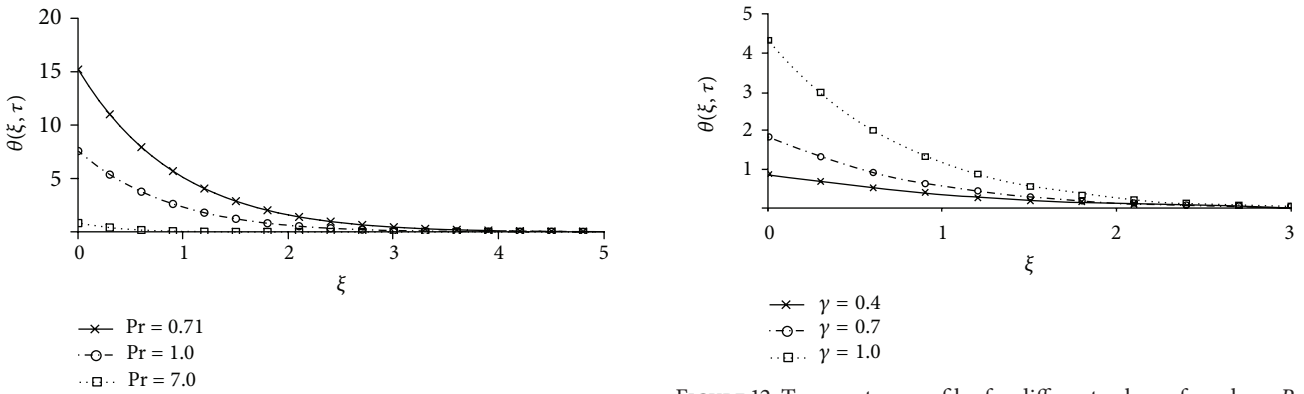


FIGURE 10: Temperature profiles for different values of  $Pr$  where  $R = 1, \gamma = 1,$  and  $\tau = 1.$

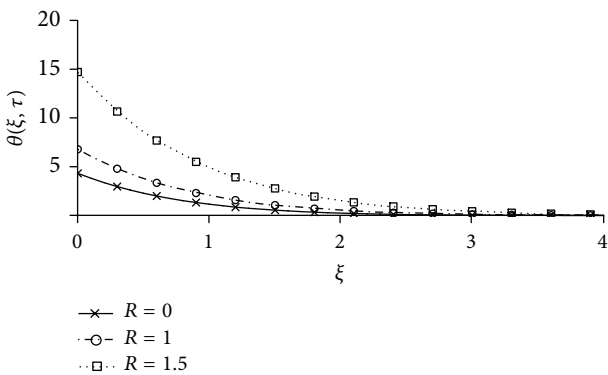


FIGURE 11: Temperature profiles for different values of  $R$  where  $Pr = 0.71, \gamma = 1,$  and  $\tau = 1.$

risers. Figure 7 is plotted to show the influence of conjugate parameter  $\gamma$  on velocities  $v_0(\xi, \tau)$  and  $v_1(\xi, \tau)$ . We observe that velocity increases in both figures as  $\gamma$  increases. The influence of dimensionless time  $\tau$  on velocity is shown in Figure 8. It is seen from this figure that velocity

increases when  $\tau$  increases. Furthermore, both of these velocities  $v_0(\xi, \tau)$  and  $v_1(\xi, \tau)$  satisfy the given boundary conditions (see (11)). This proves the accuracy of our obtained results. The effects of Brinkman parameter  $\beta_n$  ( $n = 0, 1$ ) on the flow due to impulsive and uniformly accelerated motions of the plate are studied in Figure 9. We observe that velocity decreases as  $\beta$  increases. Physically, it is true in the sense that the Brinkman type fluid can move slowly due to the drag properties of the fluid.

Figure 10 is sketched to show the effects of Prandtl number  $Pr$  on temperature profiles. Three different values of  $Pr = 0.71, 1,$  and  $7$  that physically correspond to air, electrolytic solution, and water are chosen. It is observed that increasing values of  $Pr$  lead to a fall in the temperature. A similar behavior was also expected due to the fact that at smaller values of  $Pr$  fluids possess high thermal conductivity and heat diffuses away from the surface faster than at higher values of  $Pr$ . Thus the boundary layer becomes thicker and consequently temperature decreases when  $Pr$  is increased.

Figure 11 is plotted to show the influence of radiation parameter  $R$  on the temperature profiles. It is found that temperature shows an increasing behavior as  $R$  increases. Physically, a similar effect was also expected because the

radiation parameter  $R$  signifies the relative contribution of conduction heat transfer to thermal radiation transfer. The temperature profiles for different values of the Newtonian heating parameter  $\gamma$  are plotted in Figure 12. We observe that temperature profiles increase when  $\gamma$  increases. It is due to the fact that, as we increase  $\gamma$ , it results in an increase in the heat transfer rate from the surface which raises the temperature.

The numerical results for skin friction and Nusselt are shown in Tables 1 and 2. Table 1 is prepared to show the effects of  $Pr$ ,  $M$ ,  $K$ ,  $Gr$ ,  $R$ ,  $\gamma$ ,  $\beta_0$ ,  $\beta_1$ , and  $\tau$  on the skin frictions  $\tau_0$  and  $\tau_1$  corresponding to impulsive and uniformly accelerated motions of the plate, respectively. It is observed that both  $\tau_0$  and  $\tau_1$  increase when the values of  $Pr$ ,  $M$ ,  $\tau$ , and  $\beta$  are increased. However, this behavior is quite opposite for radiation parameter  $R$ , conjugate parameter  $\gamma$ , permeability parameter  $K$ , and Grashof number  $Gr$ . Table 2 represents the numerical results for the rate of heat transfer in terms of Nusselt number  $Nu$  for different values of Prandtl number  $Pr$ , radiation parameter  $R$ , and conjugate parameter  $\gamma$ . It is found that the rate of heat transfer decreases with the increasing values of  $Pr$  and increases when  $R$ ,  $\gamma$ , and  $\tau$  are increased.

## 9. Conclusions

The exact solutions for the unsteady free MHD convection flow of an incompressible Brinkman fluid past a vertical plate in a porous medium with radiation effects and Newtonian heating condition are obtained using the Laplace transform technique. For a detailed discussion of the problem, four important flow situations are discussed. It was observed from the analytical and graphical results that the obtained solutions satisfy the imposed initial and boundary conditions as well as the basic equations of the present problem. The analytical results of velocity corresponding to the impulsive and uniformly accelerated motions of the plate together with temperature are plotted graphically, whereas the numerical results for skin friction and Nusselt number are provided in tables. From the present analysis, we observed the following:

- (i) The effects of  $M$  and  $K$  on the velocities are quite opposite.
- (ii) The magnitude of velocity for uniformly accelerated motion is greater than the magnitude for the impulsive motion of the plate.
- (iii) In the absence of free convection velocity shows the highest amplitude.
- (iv) Increasing thermal radiation increases velocity.
- (v) Velocities increase for large values of the Newtonian heating parameter.
- (vi) Velocities are increasing functions of time.
- (vii) Increasing non-Newtonian fluid parameter  $\beta$  decreases fluid velocity.
- (viii) The temperature increases for large values of  $R$  and  $\gamma$ .
- (ix) The solutions in [40, 41] appear as the limiting cases of the present solutions.

## Acknowledgment

The authors would like to acknowledge the Research Management Centre, UTM, for the financial support through vote nos. 4F109 and 04h27 for this research.

## References

- [1] P. Chandran, N. C. Sacheti, and A. K. Singh, "Unsteady hydro-magnetic free convection flow with heat flux and accelerated boundary motion," *Journal of the Physical Society of Japan*, vol. 67, no. 1, pp. 124–129, 1998.
- [2] P. Chandran, N. C. Sacheti, and A. K. Singh, "Natural convection near a vertical plate with ramped wall temperature," *Heat and Mass Transfer*, vol. 41, no. 5, pp. 459–464, 2005.
- [3] R. Muthucumaraswamy, "Natural convection on flow past an impulsively started vertical plate with variable surface heat flux," *Far East Journal of Applied Mathematics*, vol. 14, no. 1, pp. 99–119, 2004.
- [4] R. Muthucumaraswamy, P. Chandrakala, and S. A. Raj, "Radiative heat and mass transfer effects on moving isothermal vertical plate in the presence of chemical reaction," *International Journal of Applied Mechanics and Engineering*, vol. 11, no. 3, pp. 639–646, 2006.
- [5] R. Muthucumaraswamy and A. Vijayalakshmi, "Effects of heat and mass transfer on flow past an oscillating vertical plate with variable temperature," *International Journal of Applied Mathematics and Mechanics*, vol. 4, no. 1, pp. 59–65, 2008.
- [6] R. Muthucumaraswamy, "Chemical reaction effects on vertical oscillating plate with variable temperature," *Chemical Industry and Chemical Engineering Quarterly*, vol. 16, no. 2, pp. 167–173, 2010.
- [7] G. S. Seth, M. S. Ansari, and R. Nandkeolyar, "MHD natural convection flow with radiative heat transfer past an impulsively moving plate with ramped wall temperature," *Heat and Mass Transfer*, vol. 47, no. 5, pp. 551–561, 2011.
- [8] P. Chandrakala and P. N. Bhaskar, "Thermal radiation effects on MHD flow past a vertical oscillating plate," *International Journal of Applied Mechanics and Engineering*, vol. 14, no. 2, pp. 349–358, 2009.
- [9] P. Chandrakala, "Radiation effects on flow past an impulsively started vertical oscillating plate with uniform heat flux," *International Journal of Dynamics of Fluids*, vol. 6, pp. 209–215, 2010.
- [10] P. Chandrakala and P. N. Bhaskar, "Radiation effects on oscillating vertical plate with uniform heat flux and mass diffusion," *International Journal of Fluids Engineering*, vol. 4, pp. 1–11, 2012.
- [11] J. H. Merkin, "Natural-convection boundary-layer flow on a vertical surface with newtonian heating," *International Journal of Heat and Fluid Flow*, vol. 15, no. 5, pp. 392–398, 1994.
- [12] M. Z. Salleh, R. Nazar, and I. Pop, "Numerical solutions of free convection boundary layer flow on a solid sphere with newtonian heating in a micropolar fluid," *Meccanica*, vol. 47, no. 5, pp. 1261–1269, 2012.
- [13] R. C. Chaudhary and P. Jain, "Unsteady free convection boundary-layer flow past an impulsively started vertical surface with newtonian heating," *Romanian Journal of Physics*, vol. 51, pp. 911–925, 2006.
- [14] R. C. Chaudhary and P. Jain, "An exact solution to the unsteady free-convection boundary-layer flow past an impulsively started vertical surface with newtonian heating," *Journal of Engineering Physics and Thermophysics*, vol. 80, no. 5, pp. 954–960, 2007.

- [15] S. K. Guchhait, S. Das, and R. N. Jana, "Unsteady free convective flow past a moving vertical porous plate with newtonian heating," *International Journal of Engineering Science and Technology*, vol. 4, no. 7, pp. 3236–3245, 2012.
- [16] P. Mebine and E. M. Adigio, "Unsteady free convection flow with thermal radiation past a vertical porous plate with newtonian heating," *Turkish Journal of Physics*, vol. 33, no. 2, pp. 109–119, 2009.
- [17] M. Z. Salleh, R. Nazar, and I. Pop, "Boundary layer flow and heat transfer over a stretching sheet with newtonian heating," *Journal of the Taiwan Institute of Chemical Engineers*, vol. 41, no. 6, pp. 651–655, 2010.
- [18] M. Z. Salleh, R. Nazar, N. M. Arifin, I. Pop, and J. H. Merkin, "Forced-convection heat transfer over a circular cylinder with newtonian heating," *Journal of Engineering Mathematics*, vol. 69, no. 1, pp. 101–110, 2011.
- [19] M. Narahari and A. Ishak, "Radiation effects on free convection flow near a moving vertical plate with newtonian heating," *Journal of Applied Sciences*, vol. 11, no. 7, pp. 1096–1104, 2011.
- [20] N. S. Akbar and S. Nadeem, "Mixed convective magnetohydrodynamic peristaltic flow of a Jeffrey nanofluid with newtonian heating," *Zeitschrift für Naturforschung*, vol. 68, pp. 433–441, 2013.
- [21] M. Narahari and M. N. Yunus, "Free convection flow past an impulsively started infinite vertical plate with newtonian heating in the presence of thermal radiation and mass diffusion," *Turkish Journal of Engineering and Environmental Sciences*, vol. 35, no. 3, pp. 187–198, 2011.
- [22] T. Hayat, M. Awais, and A. Alsaedi, "Newtonian heating and magnetohydrodynamic effects in flow of a Jeffery fluid over a radially stretching surface," *International Journal of Physical Sciences*, vol. 7, no. 21, pp. 2838–2844, 2012.
- [23] D. Lesnic, D. B. Ingham, and I. Pop, "Free convection boundary-layer flow along a vertical surface in a porous medium with newtonian heating," *International Journal of Heat and Mass Transfer*, vol. 42, no. 14, pp. 2621–2627, 1999.
- [24] D. Lesnic, D. B. Ingham, and I. Pop, "Free convection from a horizontal surface in a porous medium with newtonian heating," *Journal of Porous Media*, vol. 3, no. 3, pp. 227–235, 2000.
- [25] D. Lesnic, D. B. Ingham, I. Pop, and C. Storr, "Free convection boundary-layer flow above a nearly horizontal surface in a porous medium with newtonian heating," *Heat and Mass Transfer*, vol. 40, no. 9, pp. 665–672, 2004.
- [26] I. Khan, K. Fakhar, and S. Shafie, "Magnetohydrodynamic free convection flow past an oscillating plate embedded in a porous medium," *Journal of the Physical Society of Japan*, vol. 80, no. 10, Article ID 104401, 2011.
- [27] S. U. Haq, C. Fetecau, I. Khan, F. Ali, and S. Shafie, "Radiation and porosity effects on the magnetohydrodynamic flow past an oscillating vertical plate with uniform heat flux," *Zeitschrift für Naturforschung A*, vol. 67a, pp. 572–580, 2012.
- [28] A. H. Mohammed, I. Khan, and S. Shafie, "Exact solutions of MHD natural convection transient flow near an oscillating plate emerged in a porous medium," *Jurnal Teknologi*, vol. 57, no. 1, pp. 1–16, 2012.
- [29] W. A. Khan and I. Pop, "Boundary-layer flow of a nanofluid past a stretching sheet," *International Journal of Heat and Mass Transfer*, vol. 53, no. 11–12, pp. 2477–2483, 2010.
- [30] W. A. Khan and A. Aziz, "Natural convection flow of a nanofluid over a vertical plate with uniform surface heat flux," *International Journal of Thermal Sciences*, vol. 50, no. 7, pp. 1207–1214, 2011.
- [31] O. D. Makinde, W. A. Khan, and Z. H. Khan, "Buoyancy effects on MHD stagnation point flow and heat transfer of a nanofluid past a convectively heated stretching/shrinking sheet," *International Journal of Heat and Mass Transfer*, vol. 62, pp. 526–533, 2013.
- [32] N. S. Akbar and S. Nadeem, "Simulation of heat transfer on the peristaltic flow of a Jeffrey-six constant fluid in a diverging tube," *International Communications in Heat and Mass Transfer*, vol. 38, no. 2, pp. 154–159, 2011.
- [33] N. S. Akbar and S. Nadeem, "Characteristics of heating scheme and mass transfer on the peristaltic flow for an Eyring-Powell fluid in an endoscope," *International Journal of Heat and Mass Transfer*, vol. 55, no. 1–3, pp. 375–383, 2012.
- [34] H. C. Brinkman, "A calculation of the viscous force exerted by a flowing fluid on a dense swarm of particles," *Applied Scientific Research*, vol. 1, no. 1, pp. 27–34, 1949.
- [35] H. C. Brinkman, "On the permeability of media consisting of closely packed porous particles," *Applied Scientific Research*, vol. 1, no. 1, pp. 81–86, 1949.
- [36] C. T. Hsu and P. Cheng, "The Brinkman model for natural convection about a semi-infinite vertical flat plate in a porous medium," *International Journal of Heat and Mass Transfer*, vol. 28, no. 3, pp. 683–697, 1985.
- [37] S. V. Varma and M. S. Babu, "Brinkman model for MHD viscous incompressible flow through a porous channel," *Indian Journal of Pure and Applied Mathematics*, vol. 16, no. 7, pp. 796–806, 1985.
- [38] R. S. R. Gorla, M. A. Mansour, and M. Gaid Sahar, "Natural convection from a vertical plate in a porous medium using Brinkman's model," *Transport in Porous Media*, vol. 36, no. 3, pp. 357–371, 1999.
- [39] K. R. Rajagopal, "On a hierarchy of approximate models for flows of incompressible fluids through porous solids," *Mathematical Models and Methods in Applied Sciences*, vol. 17, no. 2, article 215, 2007.
- [40] C. Fetecău, C. Fetecău, and M. A. Imran, "On stokes problems for fluids of Brinkman type," *Mathematical Reports*, vol. 13, no. 1, pp. 15–26, 2011.
- [41] F. Ali, I. Khan, Samiulhaq, and S. Shafie, "A note on new exact solutions for some unsteady flows of Brinkman-type fluids over a plane wall," *Zeitschrift für Naturforschung A*, vol. 67, pp. 377–380, 2012.
- [42] K. R. Cramer and S. I. Pai, *Magnetofluid Dynamics For Engineers and Applied Physicists*, McGraw-Hill, New York, NY, USA, 1973.

## Research Article

# Unsteady Hydromagnetic Rotating Flow through an Oscillating Porous Plate Embedded in a Porous Medium

I. Khan,<sup>1,2</sup> A. Khan,<sup>1</sup> A. Farhad,<sup>1</sup> M. Qasim,<sup>3</sup> and S. Sharidan<sup>1</sup>

<sup>1</sup> Department of Mathematical Sciences, Faculty of Science, Universiti Teknologi Malaysia, 81310 Skudai, Malaysia

<sup>2</sup> College of Engineering, Majmaah University, P.O. Box 66, Majmaah 11952, Saudi Arabia

<sup>3</sup> Department of Mathematics, COMSATS Institute of Information Technology, Park Road, Chak Shahzad, Islamabad 44000, Pakistan

Correspondence should be addressed to S. Sharidan; sharidan@utm.my

Received 23 July 2013; Revised 2 October 2013; Accepted 9 October 2013

Academic Editor: Tirivanhu Chinyoka

Copyright © 2013 I. Khan et al. This is an open access article distributed under the Creative Commons Attribution License, which permits unrestricted use, distribution, and reproduction in any medium, provided the original work is properly cited.

This paper investigates unsteady hydromagnetic flow of a viscous fluid in a rotating frame. The fluid is bounded by an oscillating porous plate embedded in a porous medium. The Laplace transform and Fourier sine transform methods are employed to find the exact solutions. They satisfy all imposed initial and boundary conditions and as special cases are reduced to some published results from the literature. The graphical results are plotted for different values of pertinent parameters and some interesting conclusions are made.

## 1. Introduction

Stokes' problem for the flow of an incompressible, viscous fluid over an oscillating plane serves as a benchmark in the literature of fluid dynamics [1]. It admits an exact analytical solution. The Stokes' problem not only is of fundamental theoretical interest but also occurs in many applied problems [2]. The transient solutions in terms of tabulated functions for the flow of viscous fluid due to oscillating boundary have been expressed by Panton [3]. Later, in 2000, Erdogan [4] studied the unsteady flow of Newtonian fluid past an oscillating horizontal plane wall and obtained the exact solutions. Fetecau et al. [5] presented new exact solutions corresponding to Stokes' second problem for both small and large times. Erdoğan and Imrak [6] made comparative study for the solution of Stokes' second problem by employing two different transform methods. They expressed transient solutions in terms of tabulated functions.

On the other hand, flow through porous media is very prevalent in nature and, therefore, has become a principal interest of researchers in many scientific and engineering studies. For example, one can refer to the books of Pop and Ingham [7], Ingham et al. [8], Ingham and Pop [9], Vafai [10], and Nield and Bejan [11] for the detailed literature on this topic. Moreover, the rotating flow through porous media has

been the subject of many studies in the last few decades due to their wide range of applications in cosmological and geophysical fluid dynamics, astrophysics, meteorology, petroleum, and hydrology to study the movement of underground water (Jana et al. [12]). According to Hayat et al. [13], the analysis of the effects of rotation and magnetic field in fluid flows has been an active area of research because of its geophysical and technological applications such as the MHD power generator and boundary layer flow control. Based on this motivation, Das et al. studied in [14] the simultaneous effects of rotation and magnetic field on the flow of a second grade fluid between two parallel plates. Bearing in mind the importance of MHD and porosity in a rotating fluid, Hayat et al. [15, 16], Abelman et al. [17], Sahoo et al. [18], Seth et al. [19], and Farhad et al. [20] studied the hydromagnetic flow of rotating fluids in porous media. Recently, Jana et al. [21] studied the unsteady flow of viscous fluid through a porous medium bounded by a porous plate in a rotating system.

In order to further discuss the work of Jana et al. [21] and to make closer relations between this study and practical engineering, we study in this work hydromagnetic rotating flow of a viscous fluid bounded by an oscillating porous plate embedded in a porous medium. The governing mathematical problem is solved by using the Laplace transform and Fourier sine transform methods. The expressions for velocity and skin

friction in case of cosine and sine oscillations of the plate are obtained. The analytical results are plotted and discussed. The results of Jana et al. [21] are recovered as a special case from our obtained solutions. The present study is useful in astronomy to study the rotating motion of astrophysical objects such as magnetic stars.

## 2. Mathematical Formulation of the Problem

Consider the unsteady flow of an incompressible viscous fluid occupying the upper porous half-space of the  $(x, y)$  plane. The fluid is bounded by a porous plate at  $z = 0$  such that the positive  $z$ -axis is taken normal to the plate and the  $x$ -axis is taken parallel to the plate. We consider the hydromagnetic flow induced in the fluid in the presence of a uniform magnetic field of strength  $B_0$  applied in a direction normal to the plate by means of the plate oscillations in its plane (Hayat et al. [13]). The electric field due to polarization of charges is neglected. Both of the fluid and plate are in a state of rigid body rotation with constant angular velocity  $\Omega = \Omega \hat{\mathbf{k}}$ ;  $\hat{\mathbf{k}}$  is a unit vector in the  $z$ -direction. The geometry of the problem is shown in Figure 1. Initially, for  $t \leq 0$ , both of the fluid and plate are at rest. At time  $t = 0^+$ , the lower plate suddenly starts to move in its own plane with oscillating velocity in the flow direction. Under these assumptions, the equations of momentum in a rotating frame along the  $x$ - and  $y$ -directions are [18–20]

$$\frac{\partial u}{\partial t} - w_0 \frac{\partial u}{\partial z} - 2\Omega v = \nu \frac{\partial^2 u}{\partial z^2} - \frac{\nu \phi}{k} u - \frac{\sigma B_0^2}{\rho} u, \quad z, t > 0, \quad (1)$$

$$\frac{\partial v}{\partial t} - w_0 \frac{\partial v}{\partial z} + 2\Omega u = \nu \frac{\partial^2 v}{\partial z^2} - \frac{\nu \phi}{k} v - \frac{\sigma B_0^2}{\rho} v, \quad z, t > 0,$$

where  $u$  and  $v$  are the velocity components in  $x$ - and  $y$ -directions,  $w_0$  is the suction velocity at the plate,  $\nu$  is the kinematic viscosity,  $t$  is the time,  $\sigma$  is the electrical conductivity,  $B_0$  is the applied magnetic field,  $\rho$  is the fluid density,  $\phi$  is the porosity, and  $k$  is the permeability of the porous medium.

The corresponding initial and boundary conditions are

$$u = v = 0; \quad t \leq 0, \quad (2)$$

$$u = UH(t) \cos(\omega_0 t) \quad \text{or} \quad U \sin(\omega_0 t); \quad (3)$$

$$v = 0; \quad \text{at } z = 0; \quad t > 0,$$

$$u \rightarrow 0; \quad v \rightarrow 0 \quad \text{as } z \rightarrow \infty; \quad t > 0, \quad (4)$$

in which  $U$  is the constant plate velocity,  $\omega_0$  is the frequency of oscillation of the plate, and  $H(t)$  is the Heaviside function.

Defining  $F = u + iv$ , the above system of equations reduces to

$$\frac{\partial F}{\partial t} - w_0 \frac{\partial F}{\partial z} + 2i\Omega F = \nu \frac{\partial^2 F}{\partial z^2} - \frac{\nu \phi}{k} F - \frac{\sigma B_0^2}{\rho} F, \quad z, t > 0,$$

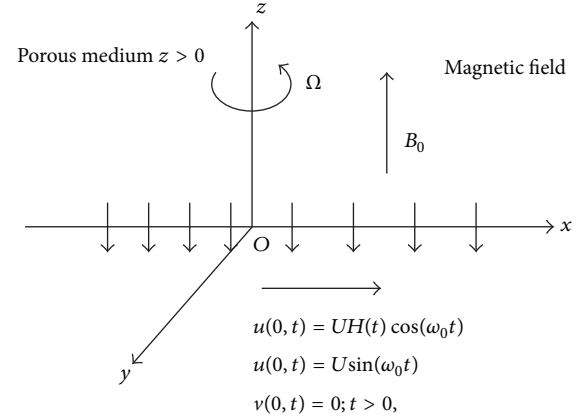


FIGURE 1: Geometry of the problem.

$$F(z, 0) = 0; \quad t \leq 0,$$

$$F(0, t) = UH(t) \cos(\omega_0 t) \quad \text{or} \quad U \sin(\omega_0 t); \quad t > 0$$

$$F \rightarrow 0 \quad \text{as } z \rightarrow \infty; \quad t > 0. \quad (5)$$

Introducing the following dimensionless variables (see Jana et al. [21]):

$$G = \frac{F}{U}, \quad \xi = \frac{zU}{\nu}, \quad \tau = \frac{U^2 t}{\nu}, \quad \omega = \frac{\omega_0 \nu}{U^2}, \quad (6)$$

the dimensionless problem takes the following form:

$$\frac{\partial G}{\partial \tau} - S \frac{\partial G}{\partial \xi} + 2i\eta G = \frac{\partial^2 G}{\partial \xi^2} - M^2 G - \frac{1}{K} G, \quad (7)$$

$$G(\xi, 0) = 0; \quad \tau \leq 0, \quad (8)$$

$$G(0, \tau) = H(\tau) \cos(\omega \tau) \quad \text{or} \quad \sin(\omega \tau); \quad \tau > 0, \quad (9)$$

$$G(\infty, \tau) = 0; \quad \tau > 0, \quad (10)$$

$$M^2 = \frac{\sigma B_0^2 \nu}{\rho U^2}, \quad \frac{1}{K} = \frac{\nu^2 \phi}{k U^2}, \quad \eta = \frac{\Omega \nu}{U^2}, \quad S = \frac{w_0}{U}, \quad (11)$$

where  $M$ ,  $K$ ,  $\eta$ , and  $S$  are the magnetic, permeability, rotation, and suction parameters, respectively.

## 3. Solution of the Problem by Using Laplace Transform

Taking the Laplace transform of (7) and using the initial condition (8), we get the following transformed differential equation:

$$\frac{d^2 \bar{G}(\xi, q)}{d\xi^2} + S \frac{d\bar{G}(\xi, q)}{d\xi} - \left[ q + M^2 + \frac{1}{K} + 2i\eta \right] \bar{G}(\xi, q) = 0, \quad (12)$$

where  $q$  is the transform parameter. In view of the boundary conditions (9) and (10), the Laplace transform  $\bar{G}(\xi, q)$  of  $G(\xi, \tau)$  has to satisfy the following conditions:

$$\bar{G}(0, q) = \frac{q}{q^2 + \omega^2} \quad \text{or} \quad \bar{G}(0, q) = \frac{\omega}{q^2 + \omega^2}, \quad (13)$$

$$\bar{G}'(0, q) = 0. \quad (14)$$

Solution of (12) under the boundary conditions (13) and (14) yields

$$\bar{G}_c(\xi, q) = \frac{1}{2} e^{-\xi S/2} \left\{ \frac{1}{q + i\omega} e^{-\xi \sqrt{q+a}} + \frac{1}{q - i\omega} e^{-\xi \sqrt{q+a}} \right\}, \quad (15)$$

respectively,

$$\bar{G}_s(\xi, q) = \frac{1}{2i} e^{-\xi S/2} \left\{ -\frac{1}{q + i\omega} e^{-\xi \sqrt{q+a}} + \frac{1}{q - i\omega} e^{-\xi \sqrt{q+a}} \right\}, \quad (16)$$

where the subscripts  $c$  and  $s$  denote the cosine and sine oscillations of the plate and

$$a = \frac{S^2}{4} + \frac{1}{K} + M^2 + 2i\eta. \quad (17)$$

Now, in order to find the inverse Laplace transform of (15) and (16), we use formula (A4) from the Appendix of Farhad et al. [20]; hence, we get the following solutions:

$$\begin{aligned} G_c(\xi, \tau) &= \frac{H(\tau) e^{-\xi S/2}}{4} \\ &\times \left[ e^{-i\omega\tau} \left\{ e^{-\xi \sqrt{a-i\omega}} \operatorname{erfc} \left( \frac{\xi}{2\sqrt{\tau}} - \sqrt{(a-i\omega)\tau} \right) \right. \right. \\ &\quad \left. \left. + e^{\xi \sqrt{a-i\omega}} \operatorname{erfc} \left( \frac{\xi}{2\sqrt{\tau}} + \sqrt{(a-i\omega)\tau} \right) \right\} \right] \\ &+ \frac{H(\tau) e^{-\xi S/2}}{4} \\ &\times \left[ e^{i\omega\tau} \left\{ e^{-\xi \sqrt{a+i\omega}} \operatorname{erfc} \left( \frac{\xi}{2\sqrt{\tau}} - \sqrt{(a+i\omega)\tau} \right) \right. \right. \\ &\quad \left. \left. + e^{-\xi \sqrt{a+i\omega}} \operatorname{erfc} \left( \frac{\xi}{2\sqrt{\tau}} + \sqrt{(a+i\omega)\tau} \right) \right\} \right], \quad (18) \end{aligned}$$

respectively,

$$\begin{aligned} G_s(\xi, \tau) &= \frac{e^{-\xi S/2}}{4i} \\ &\times \left[ -e^{-i\omega\tau} \left\{ e^{-\xi \sqrt{a-i\omega}} \operatorname{erfc} \left( \frac{\xi}{2\sqrt{\tau}} - \sqrt{(a-i\omega)\tau} \right) \right. \right. \\ &\quad \left. \left. + e^{\xi \sqrt{a-i\omega}} \operatorname{erfc} \left( \frac{\xi}{2\sqrt{\tau}} + \sqrt{(a-i\omega)\tau} \right) \right\} \right] \\ &+ \frac{e^{-\xi S/2}}{4i} \left[ e^{i\omega\tau} \left\{ e^{-\xi \sqrt{a+i\omega}} \operatorname{erfc} \left( \frac{\xi}{2\sqrt{\tau}} - \sqrt{(a+i\omega)\tau} \right) \right. \right. \\ &\quad \left. \left. + e^{\xi \sqrt{a+i\omega}} \operatorname{erfc} \left( \frac{\xi}{2\sqrt{\tau}} + \sqrt{(a+i\omega)\tau} \right) \right\} \right]. \quad (19) \end{aligned}$$

#### 4. Solution of the Problem by Using Fourier Sine Transform

Now, applying Fourier sine transform to (12) and using boundary conditions (13) and (14), we obtain

$$\bar{G}_c(\zeta, q) = \frac{\sqrt{2}(\zeta + \zeta S)q}{(\zeta^2 + \zeta^2 S + q + a)(q^2 + \omega^2)}, \quad (20)$$

respectively,

$$\bar{G}_s(\zeta, q) = \frac{\sqrt{2}(\zeta + \zeta S)\omega}{(\zeta^2 + \zeta^2 S + q + a)(q^2 + \omega^2)}, \quad (21)$$

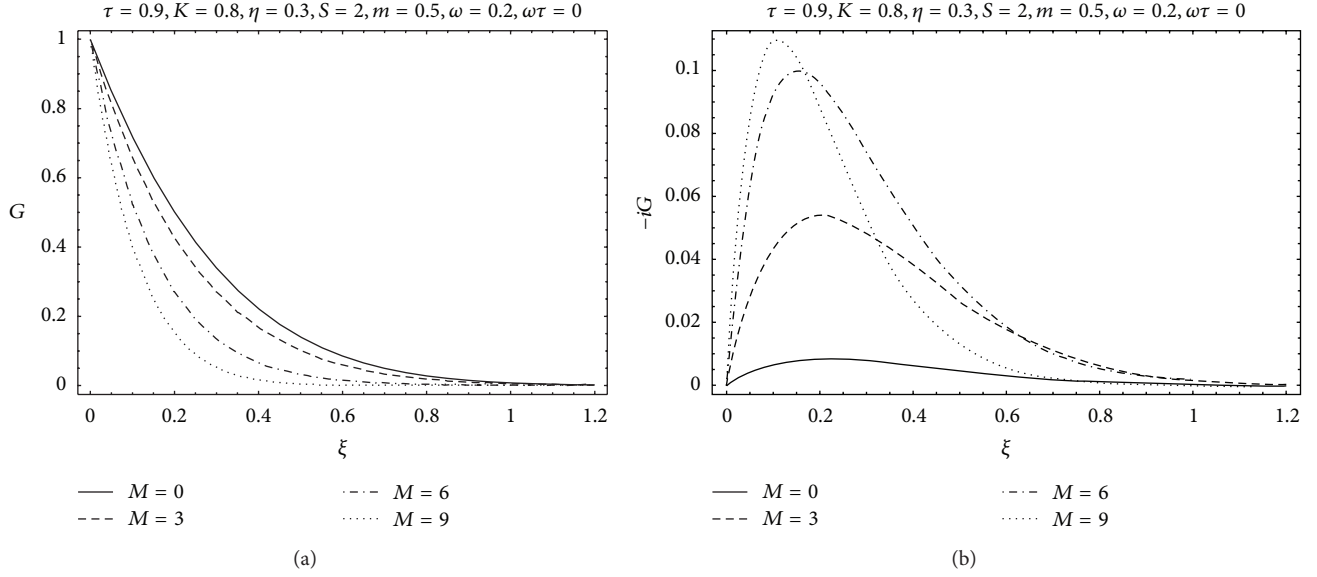
where  $\bar{G}(\zeta, q)$  denotes Fourier sine transform of  $\bar{G}(\xi, q)$ .

Now, we take the inverse Fourier sine transform of (20), which yields

$$G_c(\xi, q) = \frac{2\sqrt{2}q}{\pi(q^2 + \omega^2)} \int_0^\infty \frac{(\zeta + \zeta S)}{(\zeta^2 + \zeta^2 S + q + a)} \sin(\zeta\xi) d\zeta. \quad (22)$$

Taking the inverse Laplace transform of (22), we obtain

$$\begin{aligned} G_c(\xi, \tau) &= \frac{2}{\pi} \int_0^\infty \frac{\zeta(\zeta^2 + \zeta^2 S + a) e^{-(\zeta^2 + \zeta^2 S + a)\tau}}{((\zeta^2 + \zeta^2 S + a)^2 + \omega^2)} \\ &\quad \times \sin(\zeta\xi) d\zeta \\ &- \frac{2}{\pi} \int_0^\infty \frac{\zeta S(\zeta^2 + \zeta^2 S + a) e^{-(\zeta^2 + \zeta^2 S + a)\tau}}{((\zeta^2 + \zeta^2 S + a)^2 + \omega^2)} \\ &\quad \times \sin(\zeta\xi) d\zeta \end{aligned}$$

FIGURE 2: Profiles of velocity for different values of  $M$ .

$$\begin{aligned}
& + \frac{2}{\pi} \int_0^{\infty} \frac{\zeta (\zeta^2 + \zeta^2 S + a)}{((\zeta^2 + \zeta^2 S + a)^2 + \omega^2)} \\
& \quad \times \cos(\omega\tau) \sin(\zeta\xi) d\zeta \\
& + \frac{2}{\pi} \int_0^{\infty} \frac{\zeta\omega}{((\zeta^2 + \zeta^2 S + a)^2 + \omega^2)} \\
& \quad \times \sin(\omega\tau) \sin(\zeta\xi) d\zeta \\
& + \frac{2}{\pi} \int_0^{\infty} \frac{\zeta S (\zeta^2 + \zeta^2 S + a)}{((\zeta^2 + \zeta^2 S + a)^2 + \omega^2)} \\
& \quad \times \cos(\omega\tau) \sin(\zeta\xi) d\zeta \\
& + \frac{2}{\pi} \int_0^{\infty} \frac{\zeta S \omega}{((\zeta^2 + \zeta^2 S + a)^2 + \omega^2)} \\
& \quad \times \sin(\omega\tau) \sin(\zeta\xi) d\zeta.
\end{aligned} \tag{23}$$

Similarly for the sine oscillation of the boundary we get from (21) the following:

$$\begin{aligned}
G_s(\xi, \tau) &= \frac{2}{\pi} \int_0^{\infty} \frac{\zeta \omega e^{-(\zeta^2 + \zeta^2 S + a)\tau}}{((\zeta^2 + \zeta^2 S + a)^2 + \omega^2)} \sin(\zeta\xi) d\zeta \\
& - \frac{2}{\pi} \int_0^{\infty} \frac{\zeta\omega}{((\zeta^2 + \zeta^2 S + a)^2 + \omega^2)} \cos(\omega\tau) \sin(\zeta\xi) d\zeta
\end{aligned}$$

$$\begin{aligned}
& + \frac{2}{\pi} \int_0^{\infty} \frac{\zeta (\zeta^2 + \zeta^2 S + a) \omega}{((\zeta^2 + \zeta^2 S + a)^2 + \omega^2)} \sin(\omega\tau) \sin(\zeta\xi) d\zeta \\
& + \frac{2}{\pi} \int_0^{\infty} \frac{\zeta S \omega e^{-(\zeta^2 + \zeta^2 S + a)\tau}}{((\zeta^2 + \zeta^2 S + a)^2 + \omega^2)} \sin(\zeta\xi) d\zeta \\
& - \frac{2}{\pi} \int_0^{\infty} \frac{\zeta S \omega}{((\zeta^2 + \zeta^2 S + a)^2 + \omega^2)} \cos(\omega\tau) \sin(\zeta\xi) d\zeta \\
& + \frac{2}{\pi} \int_0^{\infty} \frac{\zeta S (\zeta^2 + \zeta^2 S + a)}{((\zeta^2 + \zeta^2 S + a)^2 + \omega^2)} \sin(\omega\tau) \sin(\zeta\xi) d\zeta.
\end{aligned} \tag{24}$$

The nondimensional shear stresses  $\tau_c$  and  $\tau_s$  at the plate  $\xi = 0$ , due to cosine and sine oscillations of the plate, are obtained from (18) and (19) as follows:

$$\begin{aligned}
\tau_c &= -(\tau_x + i\tau_y) \\
&= -\frac{H(\tau) e^{-at - i\omega\tau}}{4\sqrt{\pi\tau}} \\
&\quad \times \left[ (-4e^{i\omega\tau} - S\sqrt{\pi\tau}e^{a\tau} - S\sqrt{\pi\tau}e^{a\tau + 2i\omega\tau} \right. \\
&\quad - 2e^{a\tau} \sqrt{(a - i\omega)\pi\tau} - 2e^{a\tau + 2i\omega\tau} \sqrt{(a + i\omega)\pi\tau} \\
&\quad + 2e^{a\tau} \sqrt{(a - i\omega)\pi\tau} \operatorname{erfc}(\sqrt{(a - i\omega)\tau}) \\
&\quad \left. + 2\sqrt{(a + i\omega)\pi\tau} e^{a\tau + 2i\omega\tau} \operatorname{erfc}(\sqrt{(a + i\omega)\tau}) \right],
\end{aligned}$$

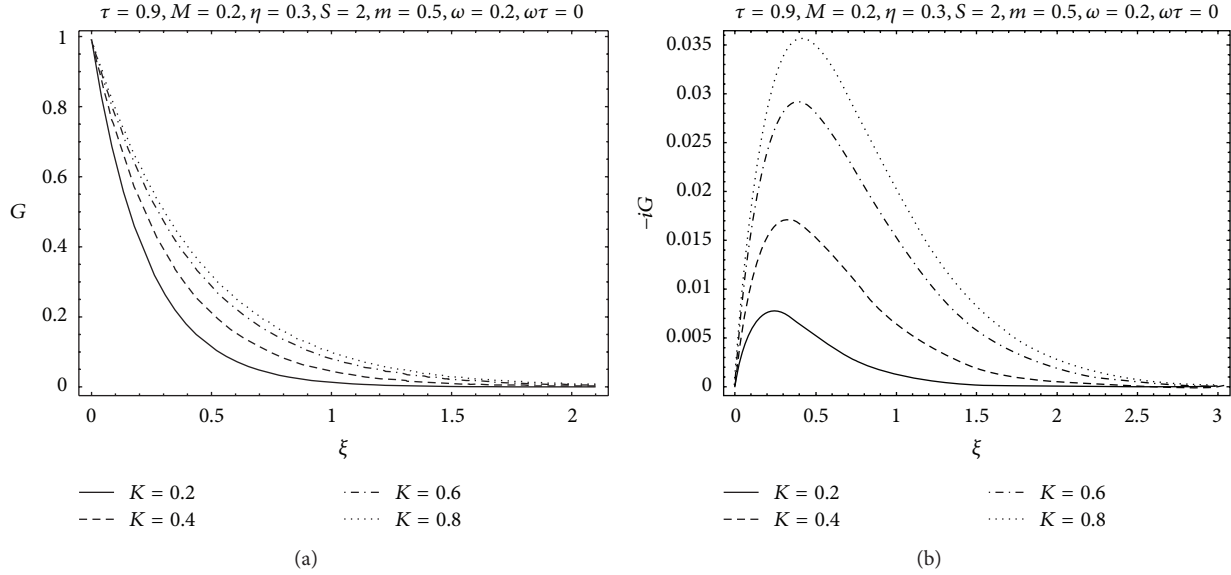


FIGURE 3: Profiles of velocity for different values of  $K$ .

$$\begin{aligned}
 \tau_s &= -(\tau_x + i\tau_y) \\
 &= \frac{ie^{-at-i\omega\tau}}{4\sqrt{\pi\tau}} \\
 &\times \left[ (-4e^{i\omega\tau} - S\sqrt{\pi\tau}e^{a\tau} - S\sqrt{\pi\tau}e^{a\tau+2i\omega\tau} \right. \\
 &\quad - 2e^{a\tau}\sqrt{(a-i\omega)\pi\tau} - 2e^{a\tau+2i\omega\tau}\sqrt{(a+i\omega)\pi\tau} \\
 &\quad + 2e^{a\tau}\sqrt{(a-i\omega)\pi\tau}\operatorname{erfc}\left(\sqrt{(a-i\omega)\tau}\right) \\
 &\quad \left. + 2\sqrt{(a+i\omega)\pi\tau}e^{a\tau+2i\omega\tau}\operatorname{erfc}\left(\sqrt{(a+i\omega)\tau}\right) \right]. \tag{25}
 \end{aligned}$$

**5. Special Cases**

In order to verify the correctness of our obtained solutions, it is important to note that (18) and (19) satisfy the governing equation and the imposed initial and boundary conditions. Further, these solutions are more general comparing to the existing solutions in the literature. In this section, we derive some special cases of these solutions. The solution given by (18) for hydrodynamic fluid ( $M = 0$ ) over an impulsively moved plate ( $\omega = 0$ ) reduces to the following form:

$$\begin{aligned}
 G(\xi, \tau) &= \frac{H(\tau)e^{-\xi S/2}}{2} \\
 &\times \left[ e^{-\xi\sqrt{S^2/4+1/K+2i\eta}} \right. \\
 &\quad \left. \times \operatorname{erfc}\left(\frac{\xi}{2\sqrt{\tau}} - \sqrt{\left(\frac{S^2}{4} + \frac{1}{K} + 2i\eta\right)\tau}\right) \right]
 \end{aligned}$$

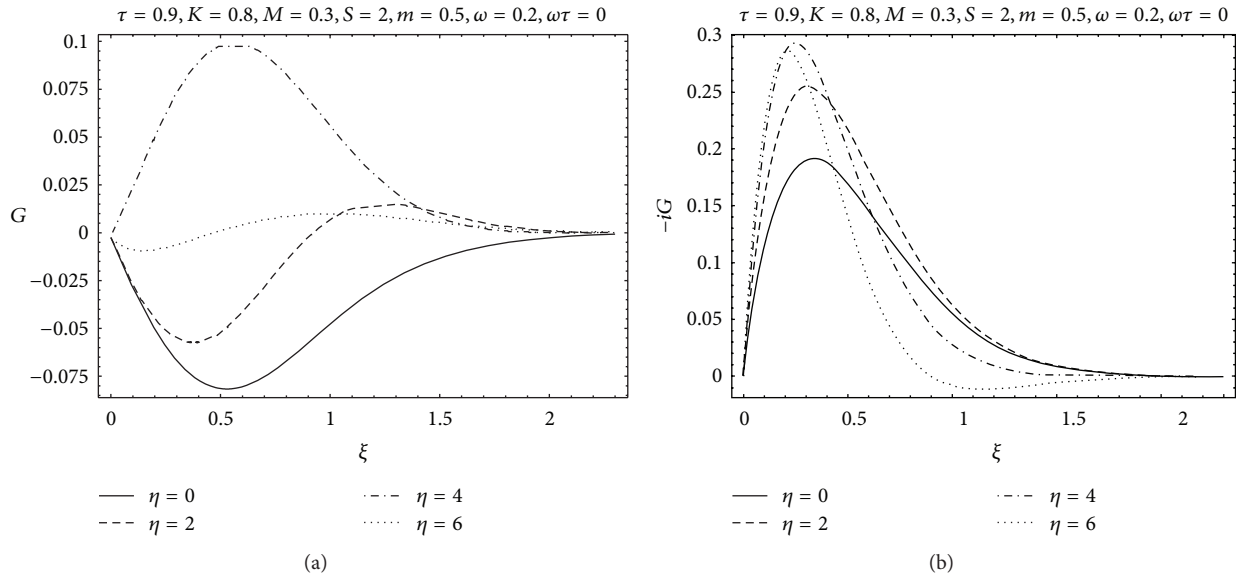
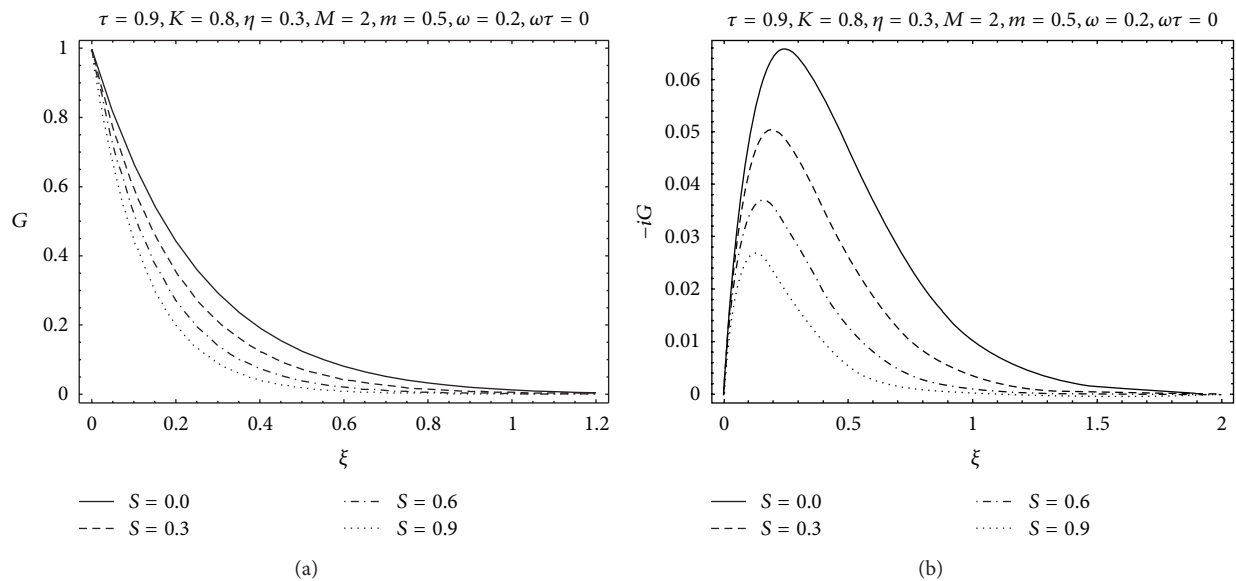
$$\begin{aligned}
 &+ e^{\xi\sqrt{S^2/4+1/K+2i\eta}} \\
 &\times \operatorname{erfc}\left(\frac{\xi}{2\sqrt{\tau}} + \sqrt{\left(\frac{S^2}{4} + \frac{1}{K} + 2i\eta\right)\tau}\right), \tag{26}
 \end{aligned}$$

which is identical to the solution given by (13), obtained by Jana et al. [21]. Further, the present solution given by (18) for suddenly moved plate ( $\omega = 0$ ) reduces to the solution (19) obtained by Farhad et al. [20] in the absence of Hall current and slip boundary condition. Hence this provides a useful mathematical check to our calculi.

**6. Results and Discussion**

The exact solutions for the unsteady hydromagnetic flow of viscous fluid bounded by a porous plate in a porous medium are obtained. The analytical results are displayed for various values of emerging parameters such as Hartmann number  $M$ , permeability parameter  $K$ , rotation parameter  $\eta$ , suction parameter  $S$ , and phase angle  $\omega\tau$ . Figures 2–6 are plotted for the cosine velocity given by (18). In these figures, (a) and (b) show the real and imaginary parts of velocity.

Figure 2 is prepared to show the variation of velocity for different values of Hartmann number  $M$ . It is found that the real part of velocity and boundary layer thickness decreases with increasing values of Hartmann number. It is due to the fact that the application of transverse magnetic field results a resistive type force (called Lorentz force) similar to drag force and upon increasing the values of  $M$ , the drag force increases which leads to the deceleration of the flow. However, it is observed that this behavior is quite opposite for the imaginary part of velocity. Figure 3 reveals that the presence of porous medium increases the resistance to flow thus reducing its

FIGURE 4: Profiles of velocity for different values of  $\eta$ .FIGURE 5: Profiles of velocity for different values of  $S$ .

velocity. It may also be expected due to the fact that increasing values of  $K$  reduces the friction forces which assists the fluid considerably to move fast and increases the boundary layer thickness. The graphs for the rotation parameter are plotted in Figure 4. It is observed that the real part of velocity increases when  $\eta$  is increased. However, when observed carefully, it is found from Figure 4(b) that the behavior of imaginary part of velocity is more oscillatory in nature. The velocity increases first and then decreases when  $\eta$  is increased.

Figure 5 shows the effect of suction parameter  $S$  on the flow through a porous medium in a rotating frame. Clearly, the absolute value of velocity and boundary layer thickness for both real and imaginary parts of velocity decrease with

an increase in suction parameter. The variation of velocity for different values of phase angle  $\omega\tau$  is shown in Figure 6. It is found that the real part of velocity decreases with increasing phase angle  $\omega\tau$ . Two different values of the phase angle  $\omega\tau = 0\pi$  and  $\pi/2$  are chosen. It is interesting to note that, when  $\omega\tau = 0\pi$ , the real part of velocity is 1 which corresponds to the impulsive motion of the plate. Moreover, for  $\omega\tau = \pi/2$ , the real part of velocity is 0. The absolute value of the imaginary part of velocity is increasing with increasing phase angle  $\omega\tau$ . Furthermore, for large values of  $\xi$ , that is,  $\xi \rightarrow \infty$ , both of the real and imaginary parts of velocity are approaching zero. The graphical behavior in this figure is in accordance with the imposed boundary conditions (3) and (4). Moreover, it

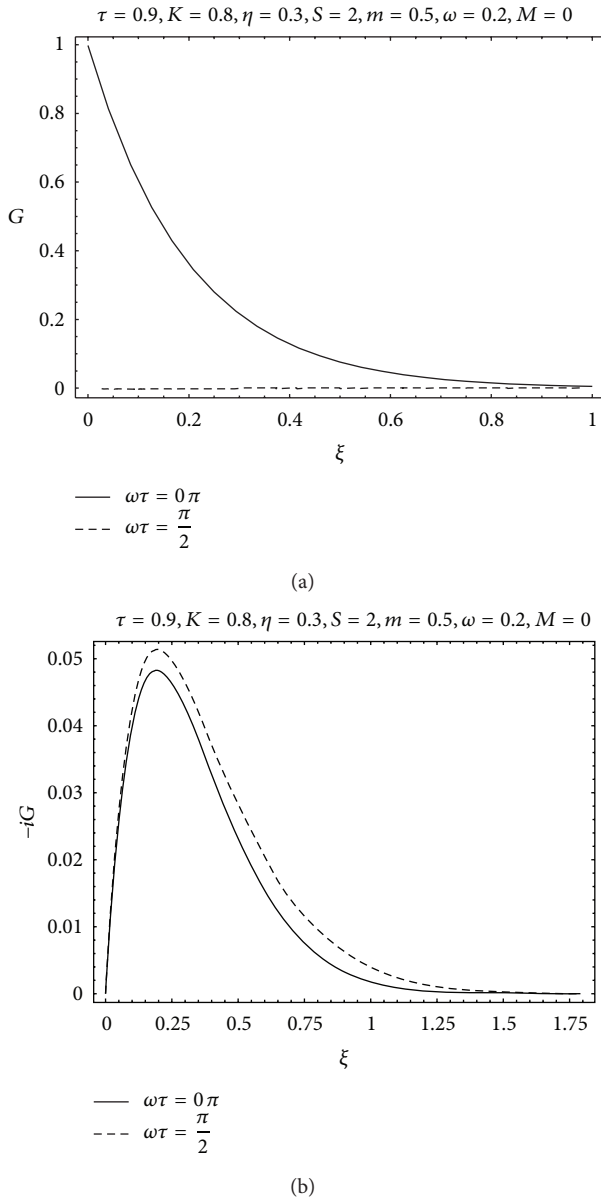


FIGURE 6: Profiles of velocity for different values of  $\omega\tau$ .

is interesting to note from Figure 6 that for a hydrodynamic fluid and impulsive motion of the plate, that is, when  $M = 0$  and  $\omega = 0$ , the graph for velocity matches with that of Jana et al. [21], which ensures the accuracy of the obtained analytical results.

### 7. Conclusions

The unsteady hydromagnetic rotating flow of viscous fluid bounded by an oscillating porous plate embedded in a porous medium is studied. The Laplace transform and Fourier sine transform methods are used for finding the solutions of the problem. The analytical results for nondimensional velocity and skin friction are obtained. The graphical results are

plotted. The results show that velocity increases with increasing rotation parameter and permeability parameter whereas it decreases with increasing Hartmann number, suction parameter, and phase angle. Moreover, as the permeability of the medium increases, the velocity field increases in the boundary layer. Thus we can control the velocity field by introducing porous medium in a rotating system.

### References

- [1] H. Schlichting, *Grenzschicht Theorie*, Braun, Karlsruhe, Germany, 8th ed edition, 1982.
- [2] N. Tokuda, "On the impulsive motion of a flat plate in a viscous fluid," *Journal of Fluid Mechanics*, vol. 33, no. 4, pp. 657–672, 1968.
- [3] R. Panton, "The transient solution for Stokes's oscillating plane: a solution in terms of tabulated functions," *Journal of Fluid Mechanics*, vol. 31, no. 4, pp. 819–825, 1968.
- [4] M. E. Erdogan, "Note on an unsteady flow of a viscous fluid due to an oscillating plane wall," *International Journal of Non-Linear Mechanics*, vol. 35, no. 1, pp. 1–6, 2000.
- [5] C. Fetecau, D. Vieru, and C. Fetecau, "A note on the second problem of Stokes for Newtonian fluids," *International Journal of Non-Linear Mechanics*, vol. 43, no. 5, pp. 451–457, 2008.
- [6] M. E. Erdoğan and C. E. Imrak, "On the comparison of the solutions obtained by using two different transform methods for the second problem of Stokes for Newtonian fluids," *International Journal of Non-Linear Mechanics*, vol. 44, no. 1, pp. 27–30, 2009.
- [7] I. Pop and D. B. Ingham, *Convective Heat Transfer: Mathematical and Computational Modeling of Viscous Fluids and Porous Media*, Pergamon, Oxford, UK, 2001.
- [8] D. B. Ingham, A. Bejan, E. Mamut, and I. Pop, *Emerging Technologies and Techniques in Porous Media*, Kluwer Academic, Dordrecht, The Netherlands, 2004.
- [9] D. B. Ingham and I. Pop, *Transport Phenomena in Porous Media*, Pergamon, Oxford, UK, 2005.
- [10] K. Vafai, *Handbook of Porous Media*, Taylor & Francis, New York, NY, USA, 2005.
- [11] D. A. Nield and A. Bejan, *Convection in Porous Media*, Springer, New York, NY, USA, 3rd edition, 2006.
- [12] M. Jana, S. Das, and R. N. Jana, "Unsteady Couette flow through a porous medium in a rotating system," *Open Journal of Fluid Dynamics*, vol. 2, pp. 149–158, 2012.
- [13] T. Hayat, S. Nadeem, A. M. Siddiqui, and S. Asghar, "An oscillating hydromagnetic non-Newtonian flow in a rotating system," *Applied Mathematics Letters*, vol. 17, no. 6, pp. 609–614, 2004.
- [14] S. Das, S. L. Maji, M. Guria, and R. N. Jana, "Unsteady MHD Couette flow in a rotating system," *Mathematical and Computer Modelling*, vol. 50, no. 7-8, pp. 1211–1217, 2009.
- [15] T. Hayat, C. Fetecau, and M. Sajid, "Analytic solution for MHD Transient rotating flow of a second grade fluid in a porous space," *Nonlinear Analysis: Real World Applications*, vol. 9, no. 4, pp. 1619–1627, 2008.
- [16] T. Hayat, C. Fetecau, and M. Sajid, "On MHD transient flow of a Maxwell fluid in a porous medium and rotating frame," *Physics Letters A*, vol. 372, no. 10, pp. 1639–1644, 2008.
- [17] S. Abelman, E. Momoniat, and T. Hayat, "Steady MHD flow of a third grade fluid in a rotating frame and porous space," *Nonlinear Analysis: Real World Applications*, vol. 10, no. 6, pp. 3322–3328, 2009.

- [18] S. N. Sahoo, J. P. Panda, and G. C. Dash, "Hydromagnetic oscillatory flow and heat transfer of a viscous liquid past a vertical porous plate in a rotating medium," *Indian Journal of Science and Technology*, vol. 3, pp. 817–821, 2010.
- [19] G. S. Seth, M. S. Ansari, and R. Nandkeolyar, "Unsteady hydro-magnetic Couette flow within porous plates in a rotating system," *Advances in Applied Mathematics and Mechanics*, vol. 2, no. 3, pp. 286–302, 2010.
- [20] A. Farhad, M. Norzieha, S. Sharidan, I. Khan, and Samiulhaq, "Hydromagnetic rotating flow in a porous medium with slip condition and Hall current," *International Journal of Physical Sciences*, vol. 7, no. 10, pp. 1540–1548, 2012.
- [21] M. Jana, S. L. Maji, S. Das, and R. N. Jana, "Unsteady flow of viscous fluid through a porous medium bounded by a porous plate in a rotating system," *Journal of Porous Media*, vol. 13, no. 7, pp. 645–653, 2010.

## Research Article

# Heat Transfer and Mass Diffusion in Nanofluids over a Moving Permeable Convective Surface

Muhammad Qasim,<sup>1</sup> Ilyas Khan,<sup>2,3</sup> and Sharidan Shafie<sup>2</sup>

<sup>1</sup> Department of Mathematics, COMSATS Institute of Information Technology, Park Road, Chak Shahzad, Islamabad 44000, Pakistan

<sup>2</sup> Department of Mathematical Sciences, Faculty of Science, Universiti Teknologi Malaysia (UTM), Johor Barhu, 81310 Skudai, Malaysia

<sup>3</sup> College of Engineering Majmaah University, P.O. Box 66, Majmaah 11952, Saudi Arabia

Correspondence should be addressed to Ilyas Khan; ilyaskhanqau@yahoo.com

Received 14 July 2013; Revised 13 September 2013; Accepted 13 September 2013

Academic Editor: Waqar Khan

Copyright © 2013 Muhammad Qasim et al. This is an open access article distributed under the Creative Commons Attribution License, which permits unrestricted use, distribution, and reproduction in any medium, provided the original work is properly cited.

Heat transfer and mass diffusion in nanofluid over a permeable moving surface are investigated. The surface exhibits convective boundary conditions and constant mass diffusion. Effects of Brownian motion and thermophoresis are considered. The resulting partial differential equations are reduced into coupled nonlinear ordinary differential equations using suitable transformations. Shooting technique is implemented for the numerical solution. Velocity, temperature, and concentration profiles are analyzed for different key parameters entering into the problem. Performed comparative study shows an excellent agreement with the previous analysis.

## 1. Introduction

Usually, the conventional heat transfer fluids such as oil, water, and ethylene glycol mixtures are poor heat transfer fluids because of their poor thermal conductivity. Therefore, several attempts have been made by many researchers to enhance the thermal conductivity of these fluids by suspending nano/microparticles in liquids. Amongst them Choi [1] was the first who introduced a fluid with enhanced thermal conductivity known as nanofluid. At present, the flow problem involving nanofluids has attracted the investigators to the field. These fluids are engineered colloidal suspensions of nanoparticles (nanometer-sized particles of metals, oxides, nitrides, carbides, or nanotubes) in the ordinary base fluid. Thermal conductivity of nanofluids is higher than the base fluids. Such fluids over a moving surface with heat transfer seem to be very important in microelectronics, fuel cells, hybrid-powered engines, and pharmaceutical processes. It should be pointed out that several metallurgical processes involve the cooling of continuous strips or filaments by drawing them through a nanofluid [2]. Having that in mind, the boundary layer flows of nanofluids have been studied

through different approaches, in the recent attempts [3–15] there has been an increasing interest of the recent researchers in the studies of boundary layer flows over a moving surface with heat transfer. This interest in fact stems from several applications of such flows in aerodynamic extrusion process, paper production, food process, glass fiber production, metallurgical process, and so forth. Sakiadis [16] made an initial attempt for boundary layer flow induced by a continuous solid surface moving with constant speed. Tsou et al. [17] extended the work of Sakiadis [16] to heat transfer concept in the boundary layer flow on a continuous moving surface. Abdelhafez [18] studied the boundary layer flow over a continuous moving flat surface in a parallel free stream. He studied the case when surface and free stream move in the same direction. Afzal et al. [19] revisited similar problem and reported the case when the surface and free stream move in the opposite directions. Ishak et al. [20] extended the work of Afzal et al. [19] by considering viscous dissipation and mass transfer effects. They investigated both the cases when surface and free stream move in the same direction and opposite directions. They obtained the numerical solution of the problem by a finite difference scheme known as Keller

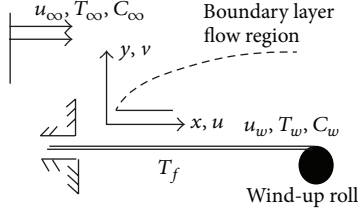


FIGURE 1: Physical flow model.

box method. Very recently, Aziz [21] obtained a similarity solution for Blasius flow of a viscous fluid employing convective boundary conditions. Hayat et al. [22] investigated the flow of Maxwell fluid over a stretching sheet with convective boundary conditions. Some more interesting problems with convective boundary conditions have been reported [23–29].

The present paper concentrates on the numerical study of the boundary layer flow of a nanofluid over a permeable moving surface. Mathematical model is constructed in the presence of Brownian and thermophoresis effects. Governing nonlinear analysis is computed by shooting method. Results are compared and analyzed in detail.

## 2. Problem Statement

We study flow of nanofluid over a moving permeable surface with constant velocity  $u_w$  in the parallel direction of the uniform free stream velocity  $u_\infty$ . The constant temperature and concentration of wall are,  $T_w$  and  $C_w$ , respectively. The ambient values of temperature and concentration are respectively,  $T_\infty$  and  $C_\infty$ . In Cartesian coordinate system,  $x$ - and  $y$ -axes are chosen parallel and perpendicular to the moving surface (see Figure 1).

The boundary layer equations (in absence of viscous dissipation) for the physical problems under examination are

$$\frac{\partial u}{\partial x} + \frac{\partial v}{\partial y} = 0, \quad (1)$$

$$u \frac{\partial u}{\partial x} + v \frac{\partial u}{\partial y} = -\frac{1}{\rho_f} \frac{\partial p}{\partial x} + \nu \frac{\partial^2 u}{\partial y^2}, \quad (2)$$

$$u \frac{\partial T}{\partial x} + v \frac{\partial T}{\partial y} = \alpha \frac{\partial^2 T}{\partial y^2} + \tau \left[ D_B \left( \frac{\partial C}{\partial y} \frac{\partial T}{\partial y} \right) + \frac{D_T}{T_\infty} \left( \frac{\partial T}{\partial y} \right)^2 \right], \quad (3)$$

$$u \frac{\partial C}{\partial x} + v \frac{\partial C}{\partial y} = D_B \frac{\partial^2 C}{\partial y^2} + \frac{D_T}{T_\infty} \frac{\partial^2 T}{\partial y^2}, \quad (4)$$

where  $u$  and  $v$  are the components of the velocity along the  $x$ - and  $y$ -directions, respectively,  $\rho_f$  is the density of the base fluid,  $\nu$  ( $= \mu/\rho_f$ ) is the kinematic viscosity,  $\alpha$  is the thermal diffusivity,  $D_B$  is the Brownian motion coefficient,  $D_T$  is the thermophoretic diffusion coefficient, and  $\tau = ((\rho c)_p/(\rho c)_f)$  is the ratio of effective heat capacity of the nanoparticle material to the heat capacity of the fluid.

The boundary conditions in view of physics of the present problem are

$$\begin{aligned} u &= u_w, & v &= v_w, \\ -k \frac{\partial T}{\partial y} &= h_f (T_f - T), & C &= C_w \quad \text{at } y = 0, \\ u &\rightarrow u_\infty, & T &\rightarrow T_\infty, \\ C &\rightarrow C_\infty \quad \text{as } y \rightarrow \infty. \end{aligned} \quad (5)$$

It seems worth mentioning to point out that  $u_w = 0$  corresponds to the Blasius problem and for  $u_\infty = 0$  we have the Sakiadis problem. Here  $h$  is the heat transfer coefficient and  $T_f$  is the convective fluid temperature below the moving surface. A stream of cold fluid at temperature  $T_\infty$  moving over the right surface of the plate with uniform velocity  $u_\infty$  while the left surface of the plate is heated below by the convection from the hot fluid of temperature  $T_f$  which provides a heat transfer coefficient  $h_f$ . As a result, convective boundary conditions arise.

We define the dimensionless quantities given by

$$\psi = \sqrt{x\nu U} f(\eta), \quad \theta(\eta) = \frac{T - T_\infty}{T_f - T_\infty}, \quad (6)$$

$$\phi(\eta) = \frac{C - C_\infty}{C_w - C_\infty}, \quad \eta = \sqrt{\frac{U}{x\nu}} y,$$

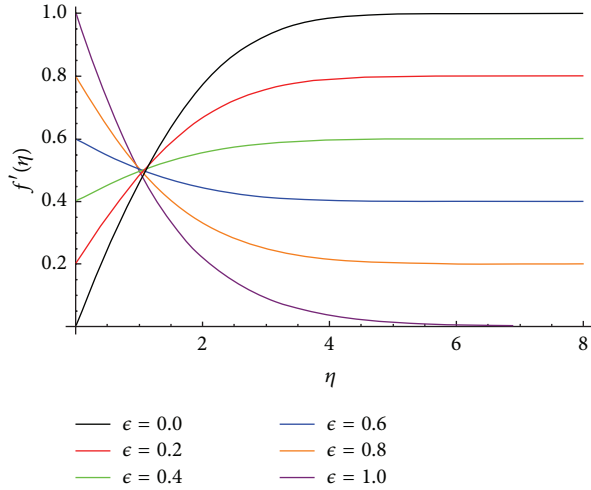
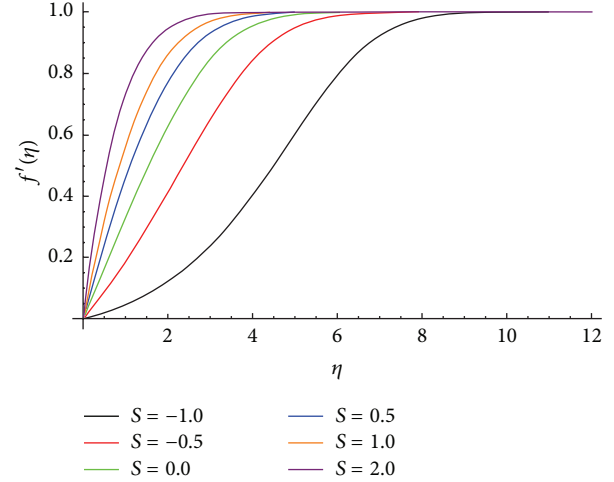
where  $U = u_w + u_\infty$ , and the free stream function  $\psi$  satisfies

$$u = \frac{\partial \psi}{\partial y}, \quad v = -\frac{\partial \psi}{\partial x}. \quad (7)$$

The above expression also satisfies the continuity equation (1) and (2)–(5) are reduced to the following forms:

$$\begin{aligned} f''' + \frac{1}{2} f f'' &= 0, \\ \theta'' + \frac{\text{Pr}}{2} f \theta' + \text{Pr} N_b \theta' \phi' + \text{Pr} N_t \theta'^2 &= 0, \\ \phi'' + \frac{\text{Le}}{2} f \phi' + \frac{N_t}{N_b} \theta'' &= 0, \\ f(0) = S, \quad f'(0) = \epsilon, \quad f'(\infty) = 1 - \epsilon, \\ \theta'(0) = -\gamma(1 - \theta(0)), \quad \theta(\infty) &\rightarrow 0, \\ \phi(0) = 1, \quad \phi(\infty) &= 0. \end{aligned} \quad (8)$$

Here primes denote differentiation with respect to  $\eta$ ,  $f(0) = S$  with  $S > 0$  corresponding to suction case and  $S < 0$  implying injection,  $\text{Pr}$  ( $= \nu/\alpha$ ) is the Prandtl number,  $\text{Le}$  ( $= \nu/D_B$ ) is the Lewis number,  $N_b$  ( $= (\rho c)_p D_B (C_w - C_\infty)/(\rho c)_f \nu$ ) is the Lewis number,  $N_b$  ( $= (\rho c)_p D_B (C_w - C_\infty)/(\rho c)_f \nu$ ) is the Lewis number,  $N_t$  ( $= (\rho c)_p D_T (T_f - T_\infty)/(\rho c)_f T_\infty \nu$ ) is the thermophoresis parameter,  $\gamma = (h_f/k\sqrt{\nu x/U})$  is the Biot number, and  $\epsilon$  ( $= u_w/U$ ) is the velocity ratio parameter. Further we noticed that  $\epsilon = 0$  corresponds


 FIGURE 2: Velocity profile  $f'(\eta)$  for various values of  $\epsilon$  when  $S = 1.0$ .

 FIGURE 3: Velocity profile  $f'(\eta)$  for various values of  $S$  when  $\epsilon = 0.0$ .

to the flow over a stationary surface caused by the free stream velocity while  $\epsilon = 1$  is subjected to a moving plate in an ambient fluid, respectively. The case  $0 < \epsilon < 1$  holds when the plate and fluid are moving in the same direction. If  $\epsilon < 0$ , the free stream is directed towards the positive  $x$ -direction, while the plate moves towards negative  $x$ -direction. On the other hand, if  $\epsilon > 1$ , the free stream is directed towards negative  $x$ -direction, while the plate moves towards the positive  $x$ -direction. Here we only discussed the case when  $0 \leq \epsilon \leq 1$ .

Expressions for the local Nusselt number  $Nu_x$  and the local Sherwood number  $Sh_x$  are

$$\begin{aligned} Nu_x &= \frac{xq_w}{k(T_w - T_\infty)}, \\ Sh_x &= \frac{xj_w}{D_B(C_w - C_\infty)}, \end{aligned} \quad (9)$$

where the wall heat flux  $q_w$  and the mass flux  $j_w$  are given by

$$\begin{aligned} q_w &= -k \left( \frac{\partial T}{\partial y} \right)_{y=0}, \\ j_w &= -D_e \left( \frac{\partial C}{\partial y} \right)_{y=0}. \end{aligned} \quad (10)$$

Dimensionless form of (10) is given by

$$\begin{aligned} (Re_w - Re_\infty)^{-1/2} Nu_x &= -\theta'(0), \\ (Re_w - Re_\infty)^{-1/2} Sh_x &= -\phi'(0), \end{aligned} \quad (11)$$

where the Reynolds numbers are defined as

$$Re_w = \frac{u_w x}{\nu}, \quad Re_\infty = \frac{u_\infty x}{\nu}. \quad (12)$$

### 3. Results and Discussion

Here the velocity, temperature, and concentration profiles are analyzed for the velocity ratio  $\epsilon$ , suction parameter  $S$ , Brownian motion parameter  $N_b$ , thermophoresis parameter  $N_t$ , and

Lewis number  $Le$ . Such theme is achieved through the plots of Figures 2–12 which are sketched. Figure 2 describes the effect of  $\epsilon$  on  $f'$ . It is found that initially  $f'$  decreases, but after  $\eta = 1.0$ , it increases when  $\epsilon$  decreases. Figures 3 and 4 study the influence of  $S$  on  $f'$  when  $\epsilon = 0.0$  and  $\epsilon = 0.3$ , respectively. The boundary layer thickness is found to decrease with the increasing values of  $S$ . Sucking fluid particles through porous wall reduces the growth of the boundary layer. This is quite reliable as the fact that suction causes reduction in the boundary layer thickness. Hence a porous character of wall provides a powerful mechanism for controlling the momentum boundary layer thickness. Influence of parameter  $\gamma$  on dimensionless temperature  $\theta$  is seen in Figure 5. A gradual increase in  $\gamma$  increases the thermal boundary layer thickness. This is expected because the thermal resistance on the hot fluid side is proportional to  $h_f$ . Hence when  $\gamma$  increases, the hot fluid side convection decreases and consequently the surface temperature increases. Also for  $\alpha \rightarrow \infty$ , the result approaches the classical solution for the constant surface temperature. For fixed values of cold fluid properties and free stream velocity,  $\alpha$  at any location  $x$  is directly proportional to heat transfer coefficient associated with the hot fluid, namely,  $h_f$ . The thermal resistance on the hot fluid side is inversely proportional to  $h_f$ . Thus when  $\alpha$  increases, then hot fluid side convection resistance decreases and, consequently, the surface temperature increases [21]. Figure 6 elucidates the effects of  $S$  on  $\theta$ . Temperature field  $\theta$  decreases when  $S$  increases. The thermal boundary layer thickness also decreases by increasing  $S$ . Effects of thermophoresis parameter  $N_t$  and Brownian motion parameter  $N_b$  on the temperature  $\theta$  are shown in Figures 7 and 8. An appreciable increase in the temperature and thermal boundary layer thickness is noticed with an increase in  $N_t$  and  $N_b$ . The Brownian motion of nanoparticles contributes to thermal conduction enhancement and hence both the temperature and thermal boundary layer thickness increase. It is also noticed that such increase is larger in the case of  $N_b$  when compared with  $N_t$ . Figure 9 illustrates the effect of Lewis number  $Le$  on mass fraction field  $\phi$ . An increase in  $Le$  leads to

TABLE 1: Values of  $\theta(0)$  and  $-\theta'(0)$  for various values of  $\gamma$  when  $N_b = 0 = N_t = S = \epsilon = 0.0$ .

$\gamma$	$\theta(0)$		$-\theta'(0)$		$\theta(0)$		$-\theta'(0)$	
	[21]	Present	[21]	Present	[21]	Present	[21]	Present
		Pr = 0.1				Pr = 10		
0.05	0.2536	0.25362	0.0373	0.03733	0.0643	0.06427	0.0468	0.04683
0.10	0.4046	0.40463	0.0594	0.05941	0.1208	0.12075	0.0879	0.08778
0.20	0.5761	0.57613	0.848	0.84821	0.2155	0.21552	0.1569	0.15685
0.40	0.7310	0.73104	0.1076	0.10762	0.3546	0.35458	0.2582	0.25823
0.60	0.8030	0.80306	0.1182	0.11824	0.4518	0.45177	0.3289	0.32877
0.80	0.8446	0.84463	0.1243	0.12434	0.5235	0.52354	0.3812	0.38134
1	0.8717	0.87172	0.1283	0.12833	0.5787	0.57868	0.4213	0.42125
5	0.9714	0.97144	0.1430	0.14395	0.8729	0.87289	0.6356	0.63558
10	0.9855	0.98554	0.1450	0.14597	0.9321	0.93207	0.6787	0.67856
20	0.9927	0.99275	0.1461	0.14607	0.9649	0.96491	0.7026	0.70246

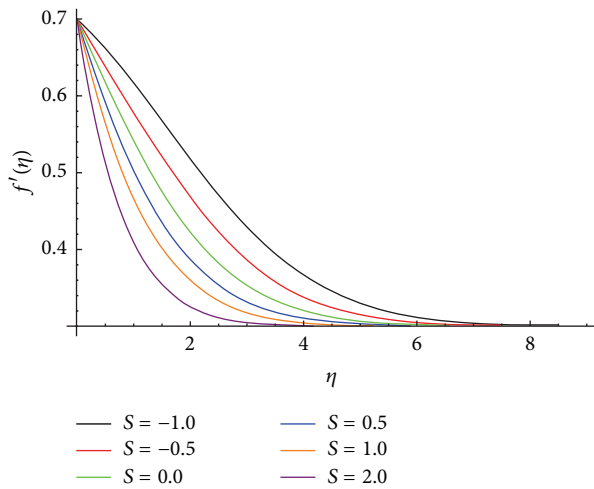


FIGURE 4: Velocity profile  $f'(\eta)$  for various values of  $S$  when  $\epsilon = 0.0$ .

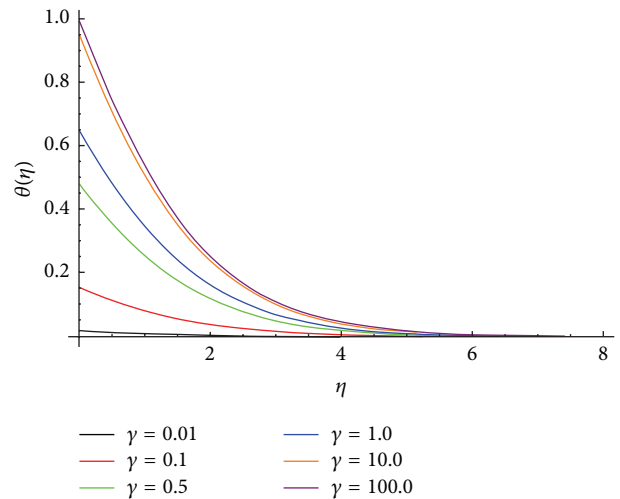


FIGURE 5: Temperature profile  $\theta(\eta)$  for various values of  $\gamma$  when  $Pr = 0.7$ ,  $S = 1.0$ ,  $N_t = N_b = 0.1$ , and  $\epsilon = 0.3$ .

a decrease in molecular diffusivity. Thus increasing the values of  $Le$  gradually decreases the concentration of boundary layer. Figures 10 and 11 are plotted to show the effects of thermophoresis parameter  $N_t$  and Brownian motion parameter  $N_b$ , respectively, on concentration of field  $\phi$ . It is observed that an increase in  $N_b$  increases the concentration boundary layer whereas an increase in  $N_t$  causes a decrease in  $\phi$ . Figure 12 shows the effect of  $\gamma$  on the mass fraction field  $\phi$ . It is also observed that  $N_t = 0 = N_b$  corresponds to the case when there is no transport driven by the moment of nanoparticles from the surface to the fluid. Further for  $\epsilon = 0.0$ , our results are in excellent agreement with those presented in [21] (see Table 1).

**3.1. Conclusions.** An incompressible two-dimensional boundary layer flow of nanofluids past a permeable moving surface with convective boundary conditions is studied numerically. The governing boundary layer equations are converted into highly nonlinear coupled ordinary differential equations using some suitable transformations. The resulting

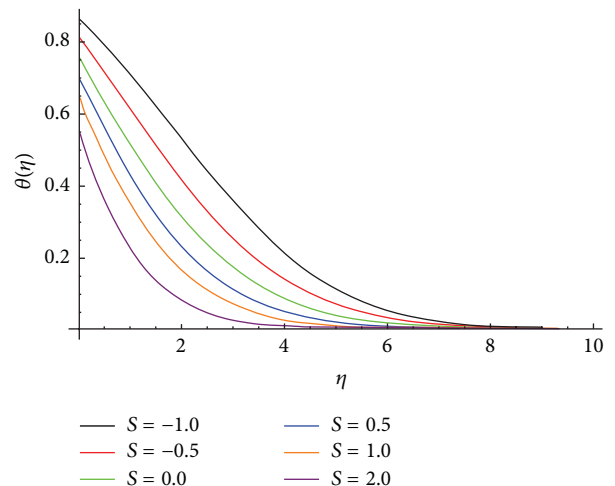


FIGURE 6: Temperature profile  $\theta(\eta)$  for various values of  $S$  when  $Pr = 0.7$ ,  $\gamma = 1.0$ ,  $N_b = 0.2$ ,  $Le = 5.0$ , and  $\epsilon = 0.3$ .

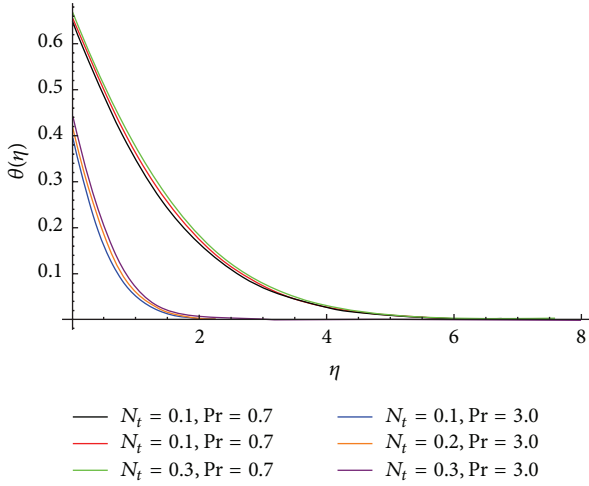


FIGURE 7: Temperature profile  $\theta(\eta)$  for various values of  $N_t$  when  $Pr = 0.7$ ,  $\gamma = 1.0$ ,  $N_b = 0.2$ ,  $Le = 5.0$ , and  $\epsilon = 0.3$ .

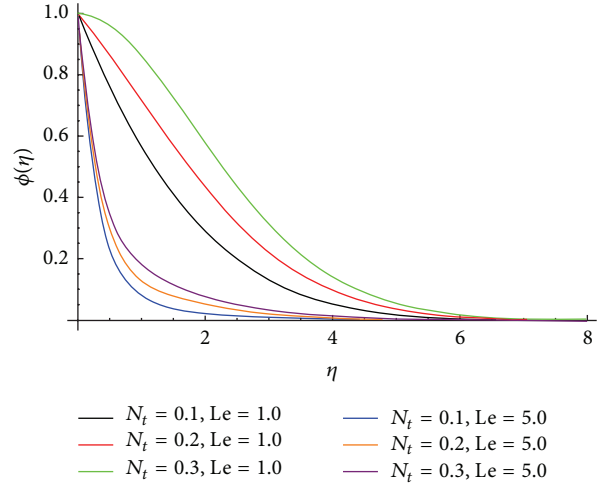


FIGURE 10: Concentration profile  $\phi(\eta)$  for various values of  $N_t$  when  $Pr = 0.7$ ,  $\gamma = 1.0$ ,  $N_b = 0.3$ , and  $\epsilon = 0.3$ .

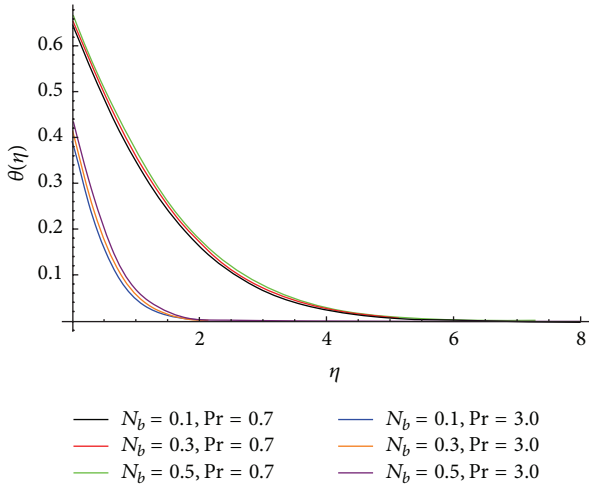


FIGURE 8: Temperature profile  $\theta(\eta)$  for various values of  $N_b$  when  $Pr = 0.7$ ,  $\gamma = 1.0$ ,  $N_t = 0.3$ ,  $Le = 5.0$ , and  $\epsilon = 0.3$ .

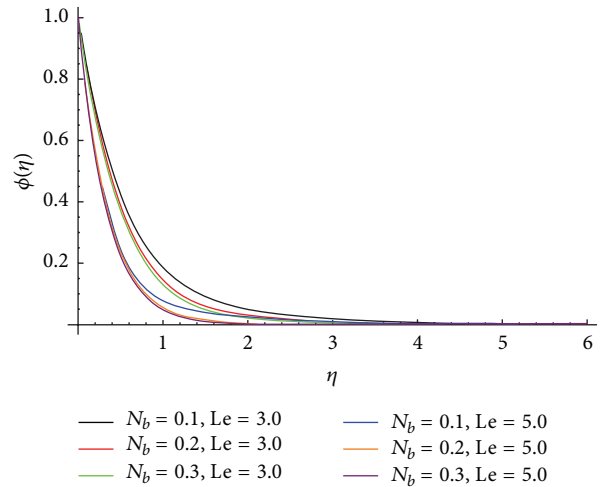


FIGURE 11: Concentration profile  $\phi(\eta)$  for various values of  $N_b$  when  $Pr = 0.7$ ,  $\gamma = 1.0$ ,  $N_t = 0.3$ , and  $\epsilon = 0.3$ .

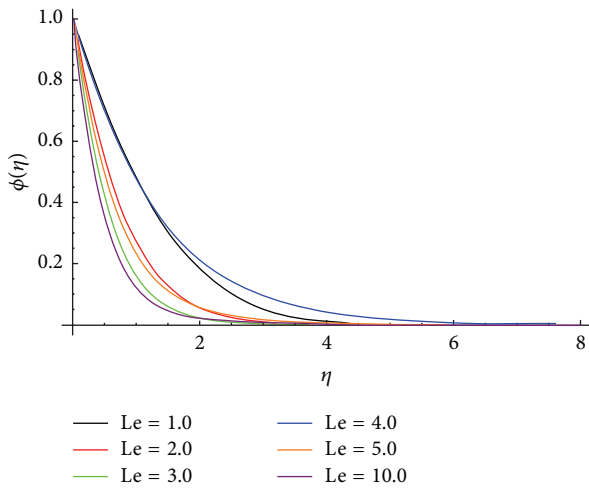


FIGURE 9: Concentration profile  $\phi(\eta)$  for various values of  $Le$  when  $Pr = 0.7$ ,  $\gamma = 1.0$ ,  $N_t = 0.3$ ,  $N_b = 0.1$ , and  $\epsilon = 0.3$ .

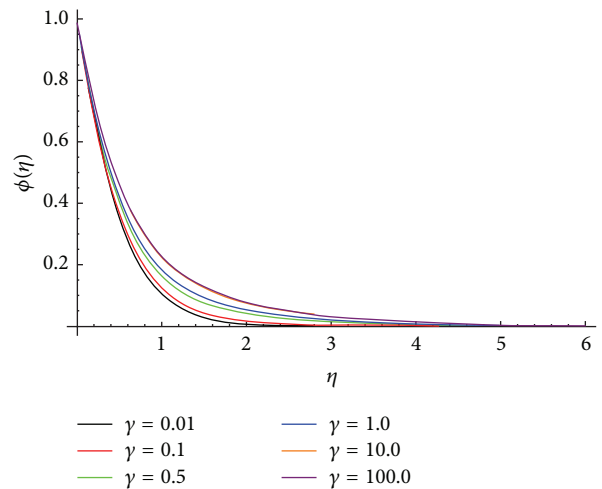


FIGURE 12: Concentration profile  $\phi(\eta)$  for various values of  $\gamma$  when  $Pr = 0.7$ ,  $N_b = 0.1$ ,  $N_t = 0.3$ , and  $\epsilon = 0.3$ .

equations are solved numerically using shooting technique. Based on the results, the following conclusions are drawn.

- (i)  $f'$  decreases initially, but after  $\eta = 1.0$ , it increases when  $\epsilon$  decreases.
- (ii) Boundary layer thickness decreases with the increasing values of  $S$ .
- (iii) Porous character of wall provides a powerful mechanism for controlling the momentum of boundary layer thickness.
- (iv) As  $\gamma$  increases, it increases the thermal boundary layer thickness.
- (v) Temperature decreases when  $S$  increases.
- (vi) Temperature and thermal boundary layer thickness increase with increasing  $N_t$  and  $N_b$ .
- (vii) An increase in  $N_b$  increases the concentration of boundary layer whereas an increase in  $N_t$  causes a decrease in  $\phi$ .
- (viii) Results in [21] are found to be special cases of the present work.

## References

- [1] S. Choi, "Enhancing thermal conductivity of fluids with nanoparticle," in *Developments and Applications of Non-Newtonian Flows*, D. A. Siginer and H. P. Wang, Eds., vol. 66, pp. 99–105, ASME, FED, 1995.
- [2] A. B. Rosmila, R. Kandasamy, and I. Muhaimin, "Lie symmetry group transformation for MHD natural convection flow of nanofluid over linearly porous stretching sheet in presence of thermal stratification," *Applied Mathematics and Mechanics*, vol. 33, no. 5, pp. 593–604, 2012.
- [3] J. Buongiorno, "Convective transport in nanofluids," *Journal of Heat Transfer*, vol. 128, no. 3, pp. 240–250, 2006.
- [4] P. Rana and R. Bhargava, "Flow and heat transfer of a nanofluid over a nonlinearly stretching sheet: a numerical study," *Communications in Nonlinear Science and Numerical Simulation*, vol. 17, no. 1, pp. 212–226, 2012.
- [5] R. Kandasamy, P. Loganathan, and P. P. Arasu, "Scaling group transformation for MHD boundary-layer flow of a nanofluid past a vertical stretching surface in the presence of suction/injection," *Nuclear Engineering and Design*, vol. 241, no. 6, pp. 2053–2059, 2011.
- [6] M. A. A. Hamad and M. Ferdows, "Similarity solution of boundary layer stagnation-point flow towards a heated porous stretching sheet saturated with a nanofluid with heat absorption/generation and suction/blowing: a Lie group analysis," *Communications in Nonlinear Science and Numerical Simulation*, vol. 17, no. 1, pp. 132–140, 2012.
- [7] A. Mahdy, "Unsteady mixed convection boundary layer flow and heat transfer of nanofluids due to stretching sheet," *Nuclear Engineering and Design*, vol. 249, pp. 248–255, 2012.
- [8] M. I. Anwar, I. Khan, S. Sharidan, and M. Z. Salleh, "Conjugate effects of heat and mass transfer of nanofluids over a nonlinear stretching sheet," *International Journal of Physical Sciences*, vol. 7, pp. 4081–4092, 2012.
- [9] M. I. Anwar, I. Khan, M. Z. Salleh, A. Hasnain, and S. Sharidan, "Magnetohydrodynamic effects on stagnation-point flow of Nanofluids towards a non-linear stretching sheet," *Wulfenia Journal*, vol. 19, pp. 367–383, 2012.
- [10] W. A. Khan and I. Pop, "Boundary layer flow past a stretching surface in a porous medium saturated by a nanofluid: Brinkman-Forchheimer model," *PLoS ONE*, vol. 7, no. 10, Article ID e47031, 2012.
- [11] O. D. Makinde, W. A. Khan, and Z. H. Khan, "Buoyancy effects on MHD stagnation point flow and heat transfer of a nanofluid past a convectively heated stretching/shrinking sheet," *International Journal of Heat and Mass Transfer*, vol. 62, pp. 526–533, 2013.
- [12] S. Nadeem, R. U. Haq, and Z. H. Khan, "Numerical solution of non-Newtonian nanofluid flow over a stretching sheet," *Applied Nanoscience* 07/s13204-013-0235-8.
- [13] A. Aziz and W. A. Khan, "Natural convective boundary layer flow of a nanofluid past a convectively heated vertical plate," *International Journal of Thermal Sciences*, vol. 52, no. 1, pp. 83–90, 2012.
- [14] S. Nadeem, R. Mehmood, and N. S. Akbar, "Non-orthogonal stagnation point flow of a nano non-Newtonian fluid towards a stretching surface with heat transfer," *International Journal of Heat and Mass Transfer*, vol. 57, pp. 679–689, 2013.
- [15] W. A. Khan, A. Aziz, and N. Uddin, "Buongiorno model for nanofluid blasius flow with surface heat and mass fluxes," *Journal of Thermophysics and Heat Transfer*, vol. 27, no. 1, pp. 134–141, 2013.
- [16] B. C. Sakiadis, "Boundary-layer behavior on continuous solid surfaces: I. Boundary-layer equations for two-dimensional and axisymmetric flow," *AIChE Journal*, vol. 7, pp. 26–28, 1961.
- [17] F. K. Tsou, E. M. Sparrow, and R. J. Goldstein, "Flow and heat transfer in the boundary layer on a continuous moving surface," *International Journal of Heat and Mass Transfer*, vol. 10, no. 2, pp. 219–235, 1967.
- [18] T. A. Abdelhafez, "Skin friction and heat transfer on a continuous flat surface moving in a parallel free stream," *International Journal of Heat and Mass Transfer*, vol. 28, no. 6, pp. 1234–1237, 1985.
- [19] N. Afzal, A. Badaruddin, and A. A. Elgarvi, "Momentum and heat transport on a continuous flat surface moving in a parallel stream," *International Journal of Heat and Mass Transfer*, vol. 36, no. 13, pp. 3399–3403, 1993.
- [20] A. Ishak, R. Nazar, and I. Pop, "The effects of transpiration on the flow and heat transfer over a moving permeable surface in a parallel stream," *Chemical Engineering Journal*, vol. 148, no. 1, pp. 63–67, 2009.
- [21] A. Aziz, "A similarity solution for laminar thermal boundary layer over a flat plate with a convective surface boundary condition," *Communications in Nonlinear Science and Numerical Simulation*, vol. 14, no. 4, pp. 1064–1068, 2009.
- [22] T. Hayat, S. A. Shehzad, M. Qasim, and S. Obaidat, "Steady flow of Maxwell fluid with convective boundary conditions," *Zeitschrift fur Naturforschung A*, vol. 66, no. 6-7, pp. 417–422, 2011.
- [23] O. D. Makinde, "Thermal stability of a reactive viscous flow through a porous-saturated channel with convective boundary conditions," *Applied Thermal Engineering*, vol. 29, no. 8-9, pp. 1773–1777, 2009.
- [24] O. D. Makinde and A. Aziz, "MHD mixed convection from a vertical plate embedded in a porous medium with a convective boundary condition," *International Journal of Thermal Sciences*, vol. 49, no. 9, pp. 1813–1820, 2010.

- [25] W. A. Khan and R. S. R. Gorla, "Mixed convection of water at 4°C along a wedge with a convective boundary condition in a porous medium," *Special Topics and Reviews in Porous Media*, vol. 2, no. 3, pp. 227–236, 2011.
- [26] M. A. A. Hamad, M. J. Uddin, and A. I. M. Ismail, "Investigation of combined heat and mass transfer by Lie group analysis with variable diffusivity taking into account hydrodynamic slip and thermal convective boundary conditions," *International Journal of Heat and Mass Transfer*, vol. 55, no. 4, pp. 1355–1362, 2012.
- [27] N. A. Yacob, A. Ishak, I. Pop, and K. Vajravelu, "Boundary layer flow past a stretching/shrinking surface beneath an external uniform shear flow with a convective surface boundary condition in a nanofluid," *Nanoscale Research Letters*, vol. 6, article 314, 2011.
- [28] O. D. Makinde, T. Chinyoka, and L. Rundora, "Unsteady flow of a reactive variable viscosity non-Newtonian fluid through a porous saturated medium with asymmetric convective boundary conditions," *Computers & Mathematics with Applications*, vol. 62, no. 9, pp. 3343–3352, 2011.
- [29] R. C. Bataller, "Radiation effects for the Blasius and Sakiadis flows with a convective surface boundary condition," *Applied Mathematics and Computation*, vol. 206, no. 2, pp. 832–840, 2008.

## Research Article

# Numerical Simulation on the Effect of Turbulence Models on Impingement Cooling of Double Chamber Model

Zhenglei Yu, Tao Xu, Junlou Li, Hang Xiu, and Yun Li

College of Mechanical Science & Engineering, Jilin University, Changchun 130025, China

Correspondence should be addressed to Yun Li; [yunjlu@sina.com](mailto:yunjlu@sina.com)

Received 5 August 2013; Revised 17 October 2013; Accepted 17 October 2013

Academic Editor: Waqar Khan

Copyright © 2013 Zhenglei Yu et al. This is an open access article distributed under the Creative Commons Attribution License, which permits unrestricted use, distribution, and reproduction in any medium, provided the original work is properly cited.

Investigation of the effects of impingement cooling for the different turbulence models and study of the aerodynamic behavior of a simplified transition piece model (TP) are the two themes of this paper. A model (double chamber model) of a one-fourth cylinder is designed which could simulate the transition piece structure and performance. The relative strengths and drawbacks of renormalization group theory  $k - \varepsilon$  (RNG), the realizable  $k - \varepsilon$  (RKE), the  $v^2 - f$ , the shear stress transport  $k - \omega$  (SST), and large-eddy simulation (LES) models are used to solve the closure problem. The prediction of the inner wall temperature, cooling effectiveness, and velocity magnitude contours in various conditions are compared in five different turbulence models. Surprisingly, the  $v^2 - f$  and SST models can produce even better predictions of fluid properties in impinging jet flows. It is recommended as the best compromise between solution speed and accuracy.

## 1. Introduction

Given the large number of sustained operational hours required for industrial turbines, two important demands placed on such engines are component life and overall engine performance. These demands are somewhat conflicting because high temperatures are required at turbine combustor in order to achieve high performance; however, increasing combustor outlet temperature in turn reduced component life, high repair costs, and downtime costs. Impingement cooling is an enhanced heat transfer method capable of cooling a transition piece (TP) without injecting cool air directly into the gas chamber. Cooling the transition piece from the gas inlet enables engineers to dissipate the heat load and maintains more uniform temperatures in the turbine region needed for efficient turbine [1].

In the example of turbine cooling applications [2], impinging jet flows may be used to cool several different sections of the engine such as the combustor case (combustor can walls), turbine case/liner, and the critical high temperature turbine blades. General applications and performance of impinging jets had been discussed in a number of reviews [3–6]. The jet impingement angle has an effect on heat transfer and was studied frequently [3, 4]. Göppert et al. [5]

investigated the effects of an unstable precessing jet over a fixed target plate. Hwang et al. [6] altered the flow pattern in the initial shearing layer by using coaxial jets.

Numerical modeling of impinging jet flows and heat transfer is employed widely for prediction, sensitivity analysis, and device design. Finite element, finite difference, and finite volume computational fluid dynamics (CFD) models of impinging jets have succeeded in making rough predictions of heat transfer coefficients and velocity fields. Turbulent impinging jet CFD employs practically all available numerical methods that will be critically reviewed in the following sections.

An earlier critical review of this topic was conducted by Polat et al. [7] in 1989. Since that date, the variety of numerical models have been established and computational research in predicting the physical behavior of impinging jets. Tzeng et al. [8] compared seven low Re modifications of the  $k - \varepsilon$  model using a confined turbulent slot jet array problem with three adjacent jets at  $H/B = 1$ . Heck et al. [9] showed the RNG model that provided a close match of Nu in the wall-jet region but an error up to 10% in the stagnation region. Modeling by Cziesla et al. [10] demonstrated the ability of LES to predict local Nu under a slot jet within 10% of experimental measurements. Silieti et al. [11] investigated the numerical

prediction of cooling effectiveness in 2D and 3D gas turbine end walls/shrouds for the cases of conjugate and adiabatic heat transfer models. They considered different cooling hole geometries, that is, cooling slots, cylindrical, and fan-shaped cooling holes at different blowing ratios. They incorporated the effects of different turbulence models in predicting the surface temperature and hence the cooling effectiveness.

There is a great interest in the application of impingement cooling to protect the transition piece from high temperature gas streams. The model created in the paper looks like a quarter torus with the curved double chambers simulating the structure of the transition piece. The relative strengths and drawbacks of renormalization group theory  $k - \varepsilon$  model (RNG), the realizable  $k - \varepsilon$  model (RKE), the  $v^2 - f$  model, the shear stress transport  $k - \omega$  model (SST), and large-eddy simulation model (LES) for impinging jet flow and heat transfer are compared. As well, the velocity and temperature fields, in addition to centerline and two-dimensional impingement cooling effectiveness, will be presented.

## 2. Turbulence Models

**2.1. The Renormalization Group Theory  $k - \varepsilon$  Model (RNG).** The RNG  $k - \varepsilon$  turbulence model is derived from the instantaneous Navier-Stokes equations, using a mathematical technique called renormalization group (RNG) methods, borrowed from quantum mechanics. The analytical derivation results in a model with constants different from those in the standard  $k - \varepsilon$  model, and it results in additional terms and functions in the transport equations for the turbulent kinetic energy ( $k$ ) and for dissipation rate ( $\varepsilon$ ). A more comprehensive description of RNG theory and its application to turbulence can be found in [12, 13]. The governing equations for this model are as follows:

$k$  equation

$$\rho \frac{Dk}{Dt} = \frac{\partial}{\partial x_j} \left[ \left( \mu + \frac{\mu_t}{\sigma_k} \right) \frac{\partial k}{\partial x_j} \right] + \mu_t S^2 \quad (1)$$

$$- \rho \varepsilon - g_i \frac{\mu_t}{\rho \text{Pr}_k} \frac{\partial \rho}{\partial x_i} - 2\rho \varepsilon \frac{k}{\gamma RT},$$

$\varepsilon$  equation

$$\rho \frac{D\varepsilon}{Dt} = \frac{\partial}{\partial x_j} \left[ \left( \alpha_\tau \mu_{\text{eff}} \right) \frac{\partial \varepsilon}{\partial x_j} \right] + \frac{\varepsilon}{k} \left( C_{1\tau} \mu_\tau S^2 - \rho \varepsilon C_{2\tau}^* \right), \quad (2)$$

where  $D/Dt$  is the convective (or substantial time) derivative,

$$\frac{D}{Dt} = \frac{\partial}{\partial t} + \vec{V} \cdot \nabla, \quad (3)$$

and  $S$  is related to the mean strain tensor,  $S_{ij} = (1/2)(\partial u_i/\partial x_j + \partial u_j/\partial x_i)$ , as  $S = \sqrt{2S_{ij}S_{ij}}$ ,  $C_{1\tau} = 1.42$ ,  $C_{2\tau} = 1.68$ ,  $C_\mu = 0.0845$ ,  $\eta = S(k/\varepsilon)$ ,  $\mu_t = \rho C_\mu (k^2/\varepsilon)$ , and  $C_{2\tau}^* = C_{2\tau} + ((C_\mu \rho \eta^3 (1 - (\eta_1/\eta_0)))/(1 + \beta \eta^3))$ .

**2.2. The Realizable  $k - \varepsilon$  Model (RKE).** The term realizable means that the model satisfies certain mathematical constraints on the normal stresses consistent with the physics

of turbulent flows. In this model, the  $k$  equation is the same as in RNG model; however  $C_\mu$  is not a constant and varies as a function of mean velocity field and turbulence ( $0.09$  in log-layer  $S(k/\varepsilon) = 3.3$ ,  $0.05$  in shear layer of  $S(k/\varepsilon) = 6$ ). The equation is based on a transport equation for the mean-square vorticity fluctuation [14] as

$$\rho \frac{D\varepsilon}{Dt} = \frac{\partial}{\partial x_j} \left[ \left( \mu + \frac{\mu_t}{\sigma} \right) \frac{\partial \varepsilon}{\partial x_j} \right] + C_1 S \rho \varepsilon - C_2 \frac{\rho \varepsilon^2}{k + \sqrt{v\varepsilon}}, \quad (4)$$

where  $C_1 = \max[0.43, \eta/(\eta + 1)]$  and  $C_2 = 1.0$ . This model is designed to avoid unphysical solutions in the flow field.

**2.3. The  $v^2 - f$  Model.** Durbin's  $v^2 - f$  model, also known as the "normal velocity relaxation model," has shown some of the best predictions to date, with calculated Nu values falling within the spread of experimental data [15]. The  $v^2 - f$  model uses an eddy viscosity to increase stability with two additional differential equations beyond those of the  $k - \varepsilon$  model, forming a four-equation model. The additional equations are defined as

$$\frac{Dk}{Dt} = \frac{\partial}{\partial x_j} \left[ \left( \nu + \nu' \right) \frac{\partial k}{\partial x_j} \right] + 2\nu' S_{ij} S_{ij} - \varepsilon,$$

$$\nu' = C_\mu \overline{v^2} T_{\text{scale}},$$

$$\frac{D\varepsilon}{Dt} = \frac{c'_{\varepsilon 1} 2\nu' S_{ij} S_{ij} - c_{\varepsilon 2} \varepsilon}{T_{\text{scale}}} + \frac{\partial}{\partial x_j} \left[ \left( \nu + \frac{\nu'}{\sigma_\varepsilon} \right) \frac{\partial \varepsilon}{\partial x_j} \right],$$

$$\frac{D\nu^2}{Dt} = k f_{\text{wall}} - \overline{\nu^2} \frac{\varepsilon}{k} + \frac{\partial}{\partial x_j} \left[ \left( \nu + \nu' \right) \frac{\partial \nu^2}{\partial x_j} \right],$$

$$f_{\text{wall}} - L_{\text{scale}}^2 \frac{\partial}{\partial x_j} \frac{\partial f}{\partial x_j} = \frac{(C_1 - 1) \left( (2/3) - (\overline{\nu^2}/k) \right)}{T_{\text{scale}}} + \frac{C_2 2\nu' S_{ij} S_{ij}}{k}, \quad (5)$$

$$L_{\text{scale}} = C_L \max \left( \min \left( \frac{k^{3/2}}{\varepsilon}, \frac{1}{\sqrt{3}} \frac{k^{3/2}}{\nu^2 C_\mu \sqrt{2S_{ij} S_{ij}}} \right), C_\mu \left( \frac{\nu^3}{\varepsilon} \right)^{1/4} \right),$$

$$T_{\text{scale}} = \min \left( \max \left( \frac{k}{\varepsilon}, 6 \sqrt{\frac{\nu}{\varepsilon}} \right), \frac{\alpha}{\sqrt{3}} \frac{k}{\nu^2 C_\mu \sqrt{2S_{ij} S_{ij}}} \right),$$

$$c'_{\varepsilon 1} = 1.44 \left( 1 + 0.045 \sqrt{\frac{k}{\nu^2}} \right),$$

where  $C_\mu = 0.19$ ,  $c_{\varepsilon 2} = 1.9$ ,  $\sigma_\varepsilon = 1.3$ ,  $C_1 = 1.4$ ,  $C_2 = 0.3$ ,  $C_\eta = 70.0$ ,  $C_L = 0.3$ , and  $\alpha = 0.6$ . Similar equations exist for predicting the transport of a scalar (e.g., thermal energy) with a  $\text{Pr}'$  as a function of  $\nu$  and  $\nu'$ .

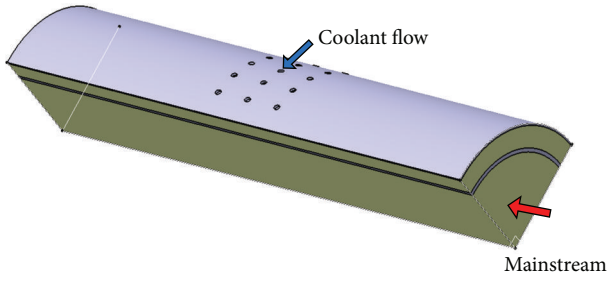


FIGURE 1: Impingement-cooling concave model.

2.4. *The Shear Stress Transport  $k - \omega$  Model (SST)*. There are two major ways in which the SST model differs from the standard  $k - \omega$  model. The first is the gradual change from the standard  $k - \omega$  model in the inner region of the boundary layer to a high Reynolds-number version of the  $k - \epsilon$  model in the outer part of the boundary layer. The second is the modified turbulent viscosity formulation to account for the transport effects of the principal turbulent shear stress. The SST (shear stress transport) model consists of the zonal (blended)  $k - \omega/k - \epsilon$  equations and clips of turbulent viscosity so that turbulent stress stays within what is dictated by structural similarity constant. The  $k$  equation is the same as the standard  $k - \omega$  model whereas the resulting blended equation for  $\omega$  is [16]

$$\rho \frac{D\omega}{Dt} = \frac{\gamma}{\nu_t} \tau_{ij} \frac{\partial U_i}{\partial x_j} - \rho \beta \omega^2 + \frac{\partial}{\partial x_j} \left[ \left( \mu + \frac{\mu_\tau}{\sigma_\omega} \right) \frac{\partial \omega}{\partial x_j} \right] + 2\rho (1 - F_1) \sigma_{\omega 2} \frac{1}{\omega} \frac{\partial k}{\partial x_j} \frac{\partial \omega}{\partial x_j}, \quad (6)$$

where  $F_1 = 1$  in the inner layer and  $F_1 \rightarrow 0$  in the outer layer, and  $\sigma_{\omega 2} = 1.168$ .

2.5. *Large-Eddy Simulation (LES)*. Large-eddy simulation (LES) is a technique intermediate between the direct simulation of turbulent flows and the solution of the Reynolds-averaged equations. In LES the contribution of the large, energy-carrying structures to momentum and energy transfer is computed exactly; well only the effect of the smallest scales of turbulence is modeled. Since the small scales tend to be more homogeneous and universal and less affected by the boundary conditions than the large ones, there is hope that their models can be simpler and require fewer adjustments when applied to different flows than similar models for the RANS equations [17, 18].

### 3. Computational Model, Boundary Conditions, and Grid

3.1. *Model Description*. Transition piece develops heat transformation on both internal and external walls to eliminate resonant frequency concerns. As well the transition piece conducts gas flow directly from the corresponding combustion liners toward the first stage of the gas turbine

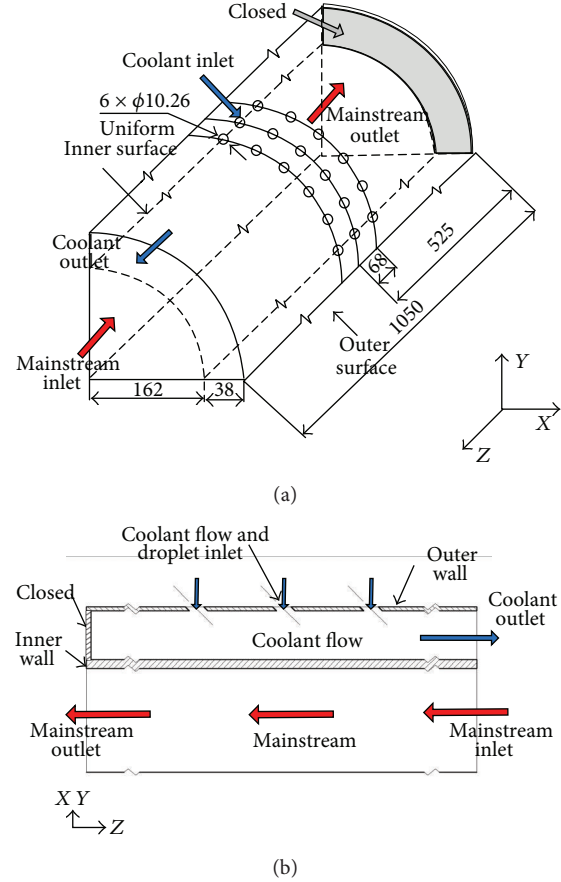


FIGURE 2: Computational domain showing boundary conditions.

(stator). The discrete coolant jets, forming a protective film chamber on the side of transition piece, are drawn from the upstream compressor in an operational gas turbine engine. From the supply plenum, the coolant is ejected through the several rows of discrete holes over the external boundary layer against the local high thermal conduction on the other side of the transition pieces [19]. The model, as a one-fourth cylinder, could simulate the transition piece's structure and performance, to elaborate the turbulence effect on the impingement-cooling performance over a concave surface (see Figure 1) [4].

A schematic diagram of the flow domain along with boundary conditions and dimensions is given in Figure 2(a). As shown in the figure, the one-fourth cylinder model has two layers of chambers with a length of 1050 mm and an outer radius and an inner radius of 200 mm and 162 mm, respectively. In the diagram, one side of the outer chamber called the coolant chamber is closed; contrarily, both sides of the mainstream chamber as the inner chamber are unfolding in which gas could flow through from one side to the other. There are 18 holes distributed uniformly in three rows on the surface of the outer wall. The distance between the two rows is 68 mm and the diameter of all the holes is about 10.26 mm. In this scenario, the velocity of the coolant flow is set at 6 m/s; the temperatures of the coolant flow and the mainstream flow are set as 300 K and 1300 K, respectively.

TABLE 1: Boundary conditions.

Component	Boundary conditions	Magnitude
Mainstream inlet	Mass flux rate	31.46 (kg/s)
	Gas temperature	1300 (K)
	Turbulent intensity	5 (%)
	Hydraulic diameter	0.324 (m)
	Pressure	1.512 (MPa)
Mainstream outlet	Turbulent intensity	5 (%)
	Hydraulic diameter	0.324 (m)
	Convection coefficient	10 (W/m <sup>2</sup> K)
	Air temperature	300 (K)
	Pressure	1.4552 (MPa)
Coolant chamber	Pressure recovery coefficient	0.95
	Turbulent intensity	5 (%)
	Hydraulic diameter	0.01026 (m)

**3.2. Boundary Conditions.** Boundary conditions are applied to specific faces within the domain to specify the flow and thermal variables that dictate conditions within the model. Figure 2(a) discloses the boundary conditions used in the model in which the cooling air and gas are moving along, respectively, in the two layers of chambers in opposite directions. In the cooling chamber, the simulation is performed by using air as the cooling flow, while velocity and temperature are set on the jet holes, with pressure on the exit. In another chamber, it is assumed that the mainstream is a mixture of O<sub>2</sub>, H<sub>2</sub>O, CO<sub>2</sub>, N<sub>2</sub>, and some rare gases. The model created is considered as boundary condition (Table 1) [4]. Assumption of the solid wall of the quarter torus is formed with a hypothesis of negligible thermal resistance by conduction; the thermal properties of the material were considered by Nimonic 263.

**3.3. Meshing and Simulation Procedures.** The computational domain incorporates the model, the HEXA mesh in the software, ICEM/CFD, used to generate the structured multiblock and the body-fitted grid system. In this study, the grid system associated with the parts of the mainstream and the coolant supply plenum is H-type. Figure 3 shows the grids of the computational domain, and the total number of the cells for the 3D domain is 776,828. Local grid refinement is used near the hole regions.

The wall  $Y$ -plus (7) is a nondimensional number similar to local Reynolds number, determining whether the influences in the wall-adjacent cells are laminar or turbulent, hence indicating the part of the turbulent boundary layer that they resolve:

$$y^+ = \frac{u_{\text{rair}} y}{\nu_{\text{air}}}. \quad (7)$$

The subdivisions of the near-wall region in a turbulent boundary layer can be summarized as follows [20]:

- (a)  $y^+ < 5$ : in the viscous sublayer region (velocity profiles are assumed to be laminar and viscous stress dominates the wall shear),

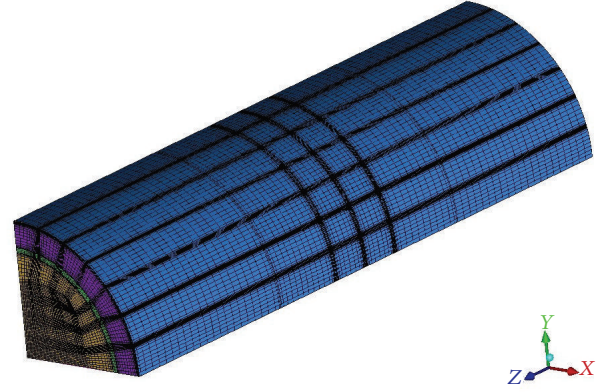
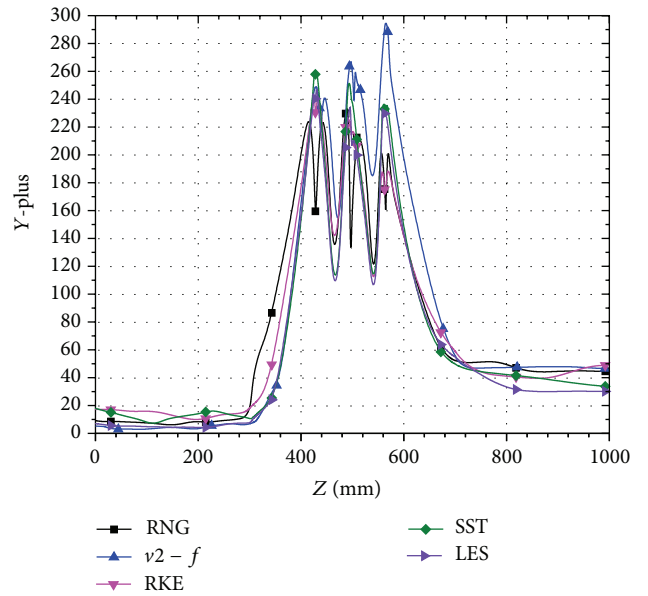


FIGURE 3: Meshes.

FIGURE 4:  $Y$ -plus distribution on the inner wall surface.

- (b)  $5 < y^+ < 30$ : buffer region (both viscous and turbulent shear dominate),
- (c)  $30 < y^+ < 300$ : fully turbulent portion or log-law region (corresponds to the region where turbulent shear predominates).

As it can be seen in Figure 4, for all cases, all nodes on the inner wall surface have the  $Y$ -plus value smaller than 300.

This study is using a commercial CFD code based on the control-volume method, ANSYS-FLUENT 12.0.16, which in order to predict temperature, impingement-cooling effectiveness, and velocity fields. All runs were made on a PC cluster with sixteen Pentium-4 3.0 GHz personal computers. The convergence criteria of the steady-state solution are judged by the reduction in the mass residual by a factor of 6, typically, in 2000 iterations.

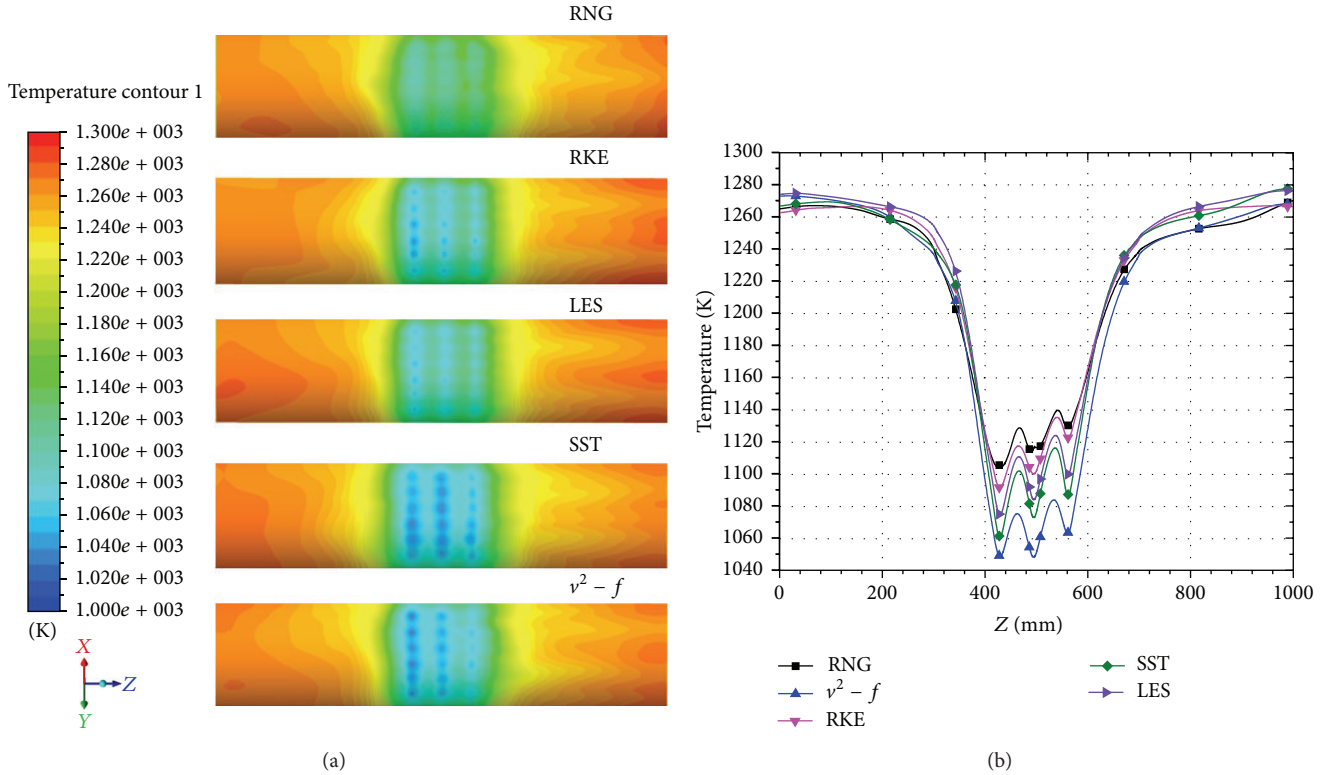


FIGURE 5: Comparative analysis of inner wall temperature using different turbulence models: (a) temperature distribution of inner wall; (b) temperature along the center line.

## 4. Results and Discussion

**4.1. Inner Wall Temperature.** Figure 5 shows the temperature contours predicted by five turbulence models. The figure illustrates that the temperature at the starting point of the wall is high and then starts to go down. The starting point is cooled by the coolant holes at the curve  $Z = 430$  mm on the outer wall while the same temperature is maintained throughout the coolant holes. After the coolant strikes the inner wall, there are vortexes formed. The jet impingement and the vortex formed out of the coolant flow cool the surface of the inner wall. The delicate color region (orange, yellow, and green region) is approximately the region where the coolant strikes the inner wall after being reflected by the coolant holes, in which the inner wall is cooled purely by impingement cooling. These figures confirm that the  $v^2 - f$  model has well simulation of heat transfer in the double chamber model. The calculated temperature at the center line of the inner wall is presented in Figure 5(b); there is a difference among the predictions of SST, LES, and RKE models. Both the temperature contours and the color lines have the same trend in the five turbulence models whereas the calculated temperatures between  $Z = 400$  and  $600$  mm are diverse for all turbulence models. All turbulence models continue to predict similar wall temperatures, while the RNG model underpredicts the temperature by up to 5%–8% in the same location.

**4.2. Cooling Effectiveness.** To define cooling effectiveness, the surface temperature downstream of the cooling hole has to be measured. The adiabatic cooling effectiveness ( $\eta$ ) is used to examine the performance of cooling. The definition of  $\eta$  is

$$\eta = \frac{T_m - T_{aw}}{T_m - T_c}, \quad (8)$$

where  $T_m$  is the mainstream hot gas inlet temperature, which is a fixed value for calculation of the adiabatic cooling effectiveness of any location, and  $T_c$  is the temperature of the coolant, which is assigned as a constant of 300 K in this issue.  $T_{aw}$  is the adiabatic wall temperature [21].

Figures 6(a) and 6(b) exhibit the comparison of cooling effectiveness on distribution and averaged cooling effectiveness along the  $z$ -axis, respectively. It could be concluded that the effectiveness is high at the beginning of the film while decreasing gradually in downstream. The distribution of the cooling effectiveness of the  $v^2 - f$  and SST model cases is significantly different. The centerline effectiveness by using the five turbulence model cases is shown in Figure 6(b). Overall, particularly the  $v^2 - f$  model gave better results compared to other models. Values of cooling effectiveness compare with the RNG model case, there is an approximately 30% difference in  $v^2 - f$  model case.

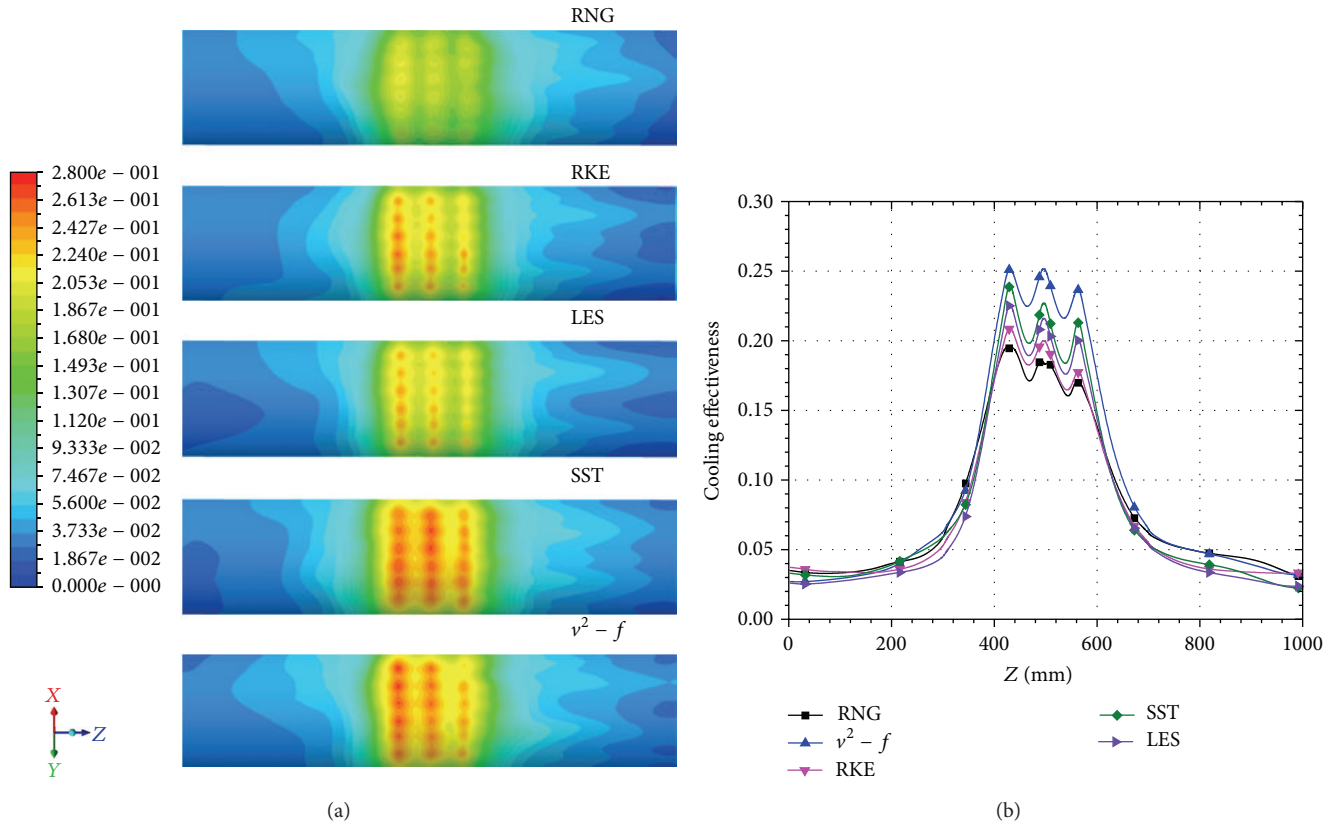


FIGURE 6: Comparative analysis of cooling effectiveness in five turbulence models: (a) cooling effectiveness distribution of inner wall; (b) averaged cooling effectiveness.

**4.3. Characteristics of the Flow Field.** Since the thermal field of a jet-in-crossflow interaction is dictated by the hydrodynamics, the flow field results were predicted by five turbulence models. Figure 7(a) shows the velocity contours at the section plane of coolant chamber. As it can be seen, all models predicted the low momentum region along the downstream edge and the corresponding high momentum or jetting region along the upstream edge within the cooling holes. The predicted reattachment region by SST and  $v^2 - f$  model cases is approximately at the inlet of the cooling chamber, whereas LES, RKE, and RNG predict a larger separation bubble and the flow separates behind the cooling holes. The computed near inner wall velocity contours (m/s) along the centerline plane are shown in Figure 7(b), where the turbulence closure was simulated using the five different turbulence models. All predictions are extremely close to each other with a skewed upstream velocity profile.

The actual computational cost will of course vary with model complexity and computing power. With the parallel computing resources of a desktop computer available at the time of writing, six Pentium-4 typically 3 GHz processors, for a high-resolution two-dimensional problem, the steady time-averaged eddy viscosity models (RNG, RKE) will have computation times of a few hours (0.5–1.5). In comparison, the more complex SST and  $v^2 - f$  could take 2–4 hours

depending on how smoothly the model converges. Based on recent work, unsteady LES models have computation times at least two orders of magnitude higher; a well-resolved three-dimensional LES impinging jet model could take a day to provide a solution.

## 5. Conclusion

A numerical simulation has been performed to study the flow and heat transfer of impinging cooling on the double chamber model, and a comparative study, indicating the ability of five turbulence models, is presented. The research of turbulence model tasks is important to improve the design and resulting performance of impinging jets.

During this investigation, numerical simulation is impacted with five turbulence models, which has some practical value for real processing and guiding significance for theory. To date, the SST and  $v^2 - f$  models offer the best results for the least amount of computation time. It is very important to consider the effect of heat conduction within the metal on the predictions of an accurate surface temperature and hence impingement-cooling effectiveness. The validation of the present study has confirmed angle cases and will be employed in future studies of impingement-cooling parameters optimization.

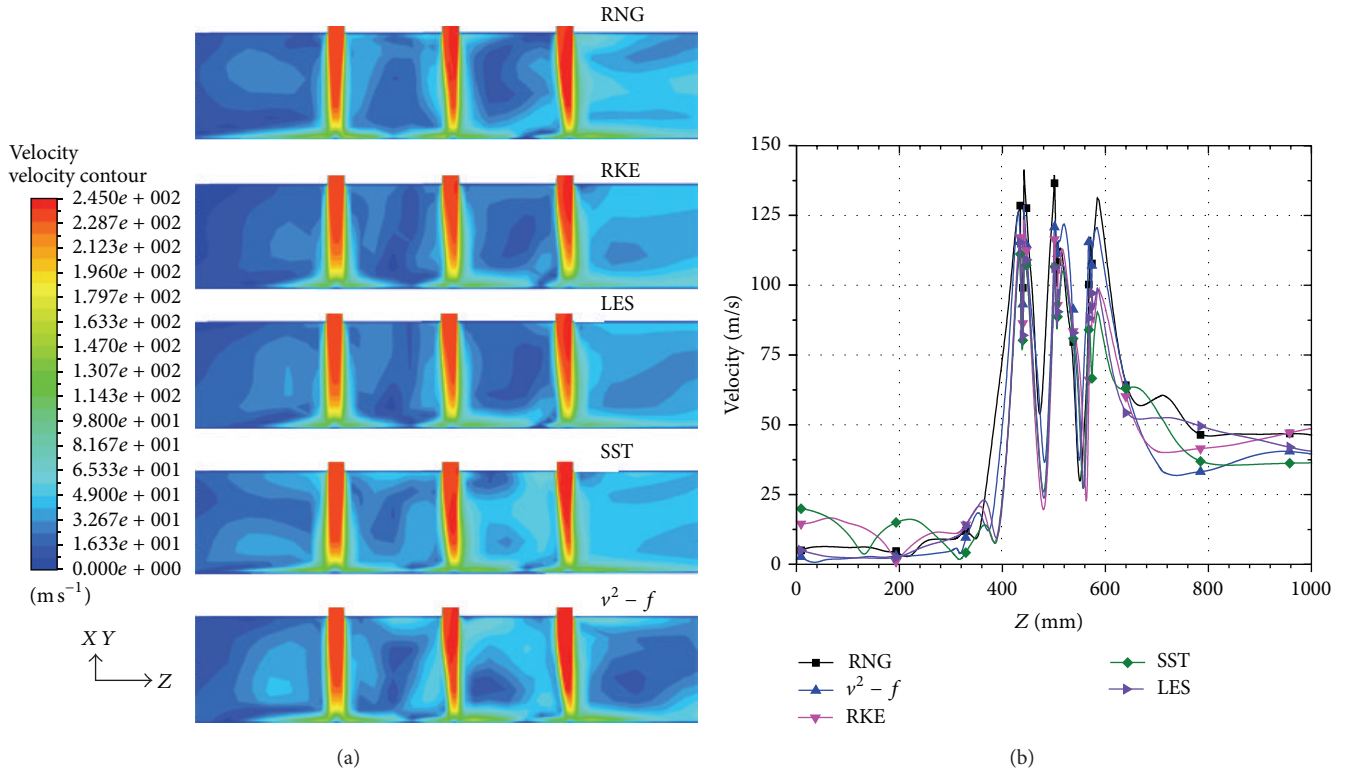


FIGURE 7: Coolant velocity contours predicted by various turbulence models: (a) X-Y cross-section velocity distribution; (b) averaged coolant velocity.

**Nomenclature**

- $D_a$ : Diameter of coolant chamber
- $D_g$ : Diameter of mainstream chamber
- $L$ : Length of the model
- $T$ : Absolute static temperature
- $X, Y, Z$ : Nondimensional coordinates in diameter, spanwise, and mainstream directions.

*Greek Symbols*

- $\eta$ : Cooling effectiveness.

*Suffixes*

- $m$ : Mainstream flow
- $c$ : Coolant flow
- $aw$ : Adiabatic wall.

**Conflict of Interests**

The authors declare that there is no conflict of interests.

**Acknowledgment**

This research is supported by the Technology Development of Jilin Province (no. 20126001).

**References**

- [1] J. C. Han, S. Dutta, and S. V. Ekkad, *Gas Turbine Heat Transfer and Cooling Technology*, Taylor and Francis, New York, NY, USA, 2000.
- [2] N. Zuckerman and N. Lior, "Impingement heat transfer: correlations and numerical modeling," *Journal of Heat Transfer*, vol. 127, no. 5, pp. 544–552, 2005.
- [3] A. A. Tawfek, "Heat transfer studies of the oblique impingement of round jets upon a curved surface," *Heat and Mass Transfer*, vol. 38, no. 6, pp. 467–475, 2002.
- [4] Z. L. Yu, T. Xu, J. L. Li, L. Ma, and T. S. Xu, "Comparison of a series of double chamber model with various hole angles for enhancing cooling effectiveness," *International Communications in Heat and Mass Transfer*, vol. 44, pp. 38–44, 2013.
- [5] S. Göppert, T. Gürtler, H. Mocikat, and H. Herwig, "Heat transfer under a precessing jet: effects of unsteady jet impingement," *International Journal of Heat and Mass Transfer*, vol. 47, no. 12-13, pp. 2795–2806, 2004.
- [6] S. D. Hwang, C. H. Lee, and H. H. Cho, "Heat transfer and flow structures in axisymmetric impinging jet controlled by vortex pairing," *International Journal of Heat and Fluid Flow*, vol. 22, no. 3, pp. 293–300, 2001.
- [7] S. Polat, B. Huang, A. S. Mujumdar, and W. J. M. Douglas, "Numerical flow and heat transfer under impinging jets: a review," *Annual Review of Numerical Fluid Mechanics and Heat Transfer*, vol. 2, pp. 157–197, 1989.
- [8] P. Y. Tzeng, C. Y. Soong, and C. D. Hsieh, "Numerical investigation of heat transfer under confined impinging turbulent slot jets," *Numerical Heat Transfer A*, vol. 35, no. 8, pp. 903–924, 1999.

- [9] U. Heck, U. Fritsching, and K. Bauckhage, "Fluid flow and heat transfer in gas jet quenching of a cylinder," *International Journal of Numerical Methods for Heat and Fluid Flow*, vol. 11, no. 1, pp. 36–49, 2001.
- [10] T. Cziesla, G. Biswas, H. Chattopadhyay, and N. K. Mitra, "Large-eddy simulation of flow and heat transfer in an impinging slot jet," *International Journal of Heat and Fluid Flow*, vol. 22, no. 5, pp. 500–508, 2001.
- [11] M. Silieti, E. Divo, and A. J. Kassab, "Film cooling effectiveness from a single scaled-up fan-shaped hole a CFD simulation of adiabatic and conjugate heat transfer models," in *Proceedings of the ASME Turbo Expo: Power for Land, Sea, and Air*, pp. 431–441, June 2005, paper no. GT2005-68431.
- [12] S. H. Park, S. W. Park, S. H. Rhee, S. B. Lee, J.-E. Choi, and S. H. Kang, "Investigation on the wall function implementation for the prediction of ship resistance," *International Journal of Naval Architecture and Ocean Engineering*, vol. 5, no. 1, pp. 33–46, 2013.
- [13] S.-E. Kim and S. H. Rhee, "Efficient engineering prediction of turbulent wing tip vortex flows," *Computer Modeling in Engineering and Sciences*, vol. 62, no. 3, pp. 291–309, 2010.
- [14] Z. L. Yu, T. Xu, J. L. Li, T. S. Xu, and Y. Tatsuo, "Computational analysis of droplet mass and size effect on mist/air impingement cooling performance," *Advances in Mechanical Engineering*, vol. 2013, Article ID 181856, 8 pages, 2013.
- [15] M. Behnia, S. Parneix, Y. Shabany, and P. A. Durbin, "Numerical study of turbulent heat transfer in confined and unconfined impinging jets," *International Journal of Heat and Fluid Flow*, vol. 20, no. 1, pp. 1–9, 1999.
- [16] T. H. Park, H. G. Choi, J. Y. Yoo, and S. J. Kim, "Streamline upwind numerical simulation of two-dimensional confined impinging slot jets," *International Journal of Heat and Mass Transfer*, vol. 46, no. 2, pp. 251–262, 2003.
- [17] Y. Huang, S. Wang, and V. Yang, "Systematic analysis of lean-premixed swirl-stabilized combustion," *AIAA Journal*, vol. 44, no. 4, pp. 724–740, 2006.
- [18] V. Moureau, P. Domingo, and L. Vervisch, "From large-eddy simulation to direct numerical simulation of a lean premixed swirl flame: filtered laminar flame-PDF modeling," *Combustion and Flame*, vol. 158, no. 7, pp. 1340–1357, 2011.
- [19] J. Benoit, C. Johnston, and M. Zingg, "Enhancing gas turbine power plant profitability: chronic transition piece and turbine part failures in some 501F gas turbines led to a replacement part redesign," *Power Engineering*, vol. 111, no. 11, pp. 140–144, 2007.
- [20] M. Moshfeghi, Y. J. Song, and Y. H. Xie, "Effects of near-wall grid spacing on SST-K- $\omega$  model using NREL Phase VI horizontal axis wind turbine," *Journal of Wind Engineering and Industrial Aerodynamics*, vol. 107, pp. 94–105, 2012.
- [21] H. Wu, J. Wang, and Z. Tao, "Evaluation of predicted heat transfer on a transonic vane using  $v^2 - f$  turbulence models," *Journal of Thermal Science and Technology*, vol. 6, no. 3, pp. 424–435, 2011.

## Research Article

# Travelling Waves Solution of the Unsteady Flow Problem of a Rarefied Nonhomogeneous Charged Gas Bounded by an Oscillating Plate

**Taha Zakaraia Abdel Wahid**

*Mathematics and Statistics Department, El-Madina Higher Institution of Administration and Technology, El-Madina Academy, Egypt*

Correspondence should be addressed to Taha Zakaraia Abdel Wahid; [taha\\_zakaraia@yahoo.com](mailto:taha_zakaraia@yahoo.com)

Received 21 May 2013; Revised 17 September 2013; Accepted 22 September 2013

Academic Editor: Tirivanhu Chinyoka

Copyright © 2013 Taha Zakaraia Abdel Wahid. This is an open access article distributed under the Creative Commons Attribution License, which permits unrestricted use, distribution, and reproduction in any medium, provided the original work is properly cited.

The extension of the previous paper (Abdel Wahid and Elagan, 2012) has been made for a nonhomogeneous charged rarefied gas mixture (two-component plasma) instead of a single electron gas. Therefore, the effect of the positive ion collisions with electrons and with each other is taken into consideration, which was ignored, as an approximation, in the earlier work. Thus, we will have four collision terms (electron-electron, electron-ion, ion-ion, and ion-electron) instead of one term, as was studied before. These collision terms are added together with a completely additional system of differential equations for ions. This study is based on the solution of the Bhatnager-Gross-Krook (BGK) model of the Boltzmann kinetic equation coupled with Maxwell's equations. The initial-boundary value problem of the Rayleigh flow problem applied to the system of the two-component plasma (positive ions + electrons), bounded by an oscillating plate, is solved. This situation, for the best of my knowledge, is presented from the molecular viewpoint for the first time. For this purpose, the traveling wave solution method is used to get the exact solution of the nonlinear partial differential equations. In addition, the accurate formula of the whole four-collision frequency terms is presented. The distinction and comparisons between the perturbed and the equilibrium velocity distribution functions are illustrated. Definitely, the equilibrium time for electrons and for ions is calculated. The relation between those times and the relaxation time is deduced for both species of the mixture. The ratios between the different contributions of the internal energy changes are predicted via the extended Gibbs equation for both diamagnetic and paramagnetic plasmas. The results are applied to a typical model of laboratory argon plasma.

## 1. Introduction

A development of the previous paper [1] is introduced. The nonstationary Krook kinetic equation model for a rarefied charged binary gas mixture is solved, instead of the single gas. Analytically, the Bhatnager-Gross-Krook (BGK) model of the kinetic equation is applied. The travelling wave solution method is used to get the exact solution of the nonlinear partial differential equations. These equations were produced from applying the moment method to the unsteady BGK equation. Now we should solve eight nonlinear partial differential equations, which represent an arduous task. This situation, for the best of our knowledge, is presented in this paper for the first time. The unsteady solution for a binary charged gas mixture (two-component plasma) gives the

problem a great generality and more applications. Taking into consideration the effect of the positive ions on the behavior of electrons, which was not observed in the previous work [1], this effect becomes a pressing matter in some physical situation; see, for example, [2]. The problem is investigated, with the new circumstance, to follow the behavior of the macroscopic properties of the gas such as the mean velocity, the shear stress, and the viscosity coefficient. The important quantities together with both the induced electric and magnetic fields are investigated for the two-component mixture, with respect to both distance and time. This new study is done to examine the behavior of electrons and positive ions in the microscale. This is performed using the kinetic Boltzmann equation coupled with Maxwell's equation. An important novel thermodynamic treatment of the system is concluded.

The behavior of the nonequilibrium thermodynamic distribution functions for both positive ions and electrons, in different cases, is illustrated. Such treatment holds for the first time for a nonhomogeneous charged gas mixture bounded by oscillating plate. The calculated velocities are substituted into the corresponding two-stream Maxwellian distribution functions permitting us to investigate the nonequilibrium thermodynamic properties of the system (gas particles + the oscillating plate). The entropy, entropy flux, entropy production, thermodynamic forces, and kinetic coefficients are obtained. The verification of the Boltzmann H-theorem, Le Chatelier principle, and the second law of thermodynamic is examined. The ratios between the different contributions of the internal energy change based upon the total derivatives of the extensive parameters estimated via the Gibbs formula.

The behavior of charged gases in nonequilibrium states has received considerable attention from the standpoint of understanding the characteristics of nonequilibrium phenomena [3]. The kinetic theory has contributed not only to the understanding of nonequilibrium transport phenomena in gases, but also to the development of general nonequilibrium statistical physics. It is well accepted that the Boltzmann equation [3–8] is one of the most reliable kinetic models for describing nonequilibrium phenomena in gas phase. Following its success and usefulness, The Boltzmann equation is widely used in order to describe various gas-phase transport phenomena such as plasma gases, granular gases, polyatomic gases, relativistic gases, thermal radiation affected by gases, and chemically reacting gases [9–15]. The kinetic equation of gas flow based on the Boltzmann equation has obvious peculiarities in comparison with the macroscopic description found by using the Navier-Stokes equations; see [4, 13].

For planar flows, the oscillating Couette problem has many analogies with Stokes' second problem, which involves a flat plate oscillating in an unbounded medium. Stokes [16] first solved this problem in 1851 and later it was solved by Rayleigh [17] in 1911. Stokes' second problem is one of the simplest configurations to study the behavior of a nonequilibrium gas responding to a plate oscillating in its own plane [18]. A comprehensive study has been carried out with the linearized Bhatnagar-Gross-Krook (BGK) equation over a wide range of Knudsen numbers [19]. The effect of the oscillation frequency on the amplitudes and phases of the velocity and shear stress was reported. In order to improve our understanding of time-periodic, shear driven gas flows, oscillatory Couette flow provides an ideal test case. It has been studied extensively using kinetic theory (Sharipov and Kalempa [20]; Park et al. [21]; Hadjiconstantinou [22]; Emerson et al. [23]; Doi [24]). A brief comparison of the linearized R13 (LR13) equations with DSMC data (Hadjiconstantinou [22]) was carried out by Taheri et al. [25]. Although oscillatory Couette flow is a simple case, it has many related applications in a variety of MEMS devices, for example, the Tang resonator (Tang et al. [26]). A proper understanding of flow phenomena in resonators will therefore help to improve the performance and quality factor (Frangi et al. [27]). In this study, the extended continuum governing equations are employed to compute the details of Stokes' second problem and oscillatory planar Couette flow

in the early transition regime. The purpose of the paper is to analyze and assess the dynamic response capability of the higher-order moment equations for oscillatory flow and compare against the available kinetic data. Gu and Emerson [18] presented results using three different continuum-based models to study oscillatory flow in the transition regime. Data obtained from numerical solutions of the Boltzmann equation and the direct simulation Monte Carlo method are used to assess the ability of the continuum models to capture important rarefaction effects.

The objective of this paper is to seek the unsteady exact solution of the Boltzmann kinetic equation of an inhomogeneous charged gas mixture bounded by an oscillating plate, for the first time. The initial-boundary value problem of the Rayleigh flow problem, applied to the system of the two-component plasma (positive ions + electrons), is solved to determine the macroscopic parameters such as the mean velocity, shear stress, and viscosity coefficient, together with the induced electric and magnetic fields. The investigation of the collisions mutual effects of ions with electrons, in the form of the ion distribution function, is completely operated. The light will be shed upon the effects of collisions of electrons with ions in the form of the electrons distribution function. Using the estimated distribution functions, it is of fundamental physical importance to deliberate the irreversible thermodynamic behavior of the diamagnetic and paramagnetic plasma gas. The results are applied to a typical model of laboratory argon plasma. The agreements of the results with the preceding theoretical studies are clarified.

## 2. The Physical Problem and Mathematical Formulation

Let us assume that the upper half of the space ( $y \geq 0$ ), which is bounded by an infinite flat plate ( $y = 0$ ), is filled with a nonhomogeneous mixture of charged particles of electrons and positive ions. An infinite flat plate is fixed at  $y = 0$ , and parallel to the  $xz$ -plane. The plate oscillates harmonically in the  $x$  direction with frequency  $\beta$ ; that is, the velocity of the plate depends on the time  $t$  as follows:

$$V_w = R_e [U_0 \exp(-i\beta t)] = U_0 \text{Cos}(\beta t), \quad (1)$$

where the symbol  $R_e$  denotes the real part of complex expression. The quantity  $U_0$  is the velocity amplitude, which is assumed to be small when compared with the thermal molecular velocity  $V_{Te}$  of the gas. The charged gas is initially in absolute equilibrium and the wall is at rest. Then the plate starts to oscillate suddenly in its own plane with a velocity  $U_0 \text{Cos}(\beta t)$  along the  $x$ -axis ( $U_0$  and  $\beta$  are constants). Moreover, the plate is considered impermeable, uncharged, and an insulator. The whole system (electrons + ions + plate) is kept at constant temperature. All physical quantities are defined in the Nomenclatures.

Let the forces  $\vec{f}_e$  and  $\vec{f}_i$  acting on each electron and ion respectively be given by [28–30]

$$\begin{aligned}\vec{f}_e &= -e\vec{E}_e - \frac{e}{c_0} (\vec{c} \wedge \vec{B}_e), \\ \vec{f}_i &= e\vec{E}_i + \frac{e}{c_0} (\vec{c} \wedge \vec{B}_i).\end{aligned}\quad (2)$$

The directions of the considered physical quantities are as follows:

$$\begin{aligned}\vec{V}_\alpha &\equiv (V_{x\alpha}, 0, 0), & \vec{J}_\alpha &\equiv (q_\alpha n V_{x\alpha}, 0, 0), \\ \vec{E}_\alpha &\equiv (E_{x\alpha}, 0, 0), & \vec{B}_\alpha &\equiv (0, 0, B_{z\alpha}),\end{aligned}\quad (3)$$

where  $\alpha = e$  for electrons and  $\alpha = i$  for ions.

The  $V_{x\alpha}$ ,  $E_{x\alpha}$ ,  $B_{z\alpha}$ , and  $J_{x\alpha}$  are functions of  $y$  and  $t$  that satisfy Maxwell's equations. The distribution function  $F(y, c, t)$  of the particles for the plasma gas can be obtained from the Bhatnager-Gross-Krook (BGK) model [31] of the kinetic Boltzmann's equation as

$$\frac{\partial F_e}{\partial t} + \vec{c} \cdot \frac{\partial F_e}{\partial \vec{r}} + \frac{\vec{f}_e}{m_e} \cdot \frac{\partial F_e}{\partial \vec{c}} \quad (4)$$

$$= \nu_{ee} (F_{0e} - F_e) + \nu_{ei} (\overline{F_{0e}} - F_e) \text{ for electrons,}$$

$$\frac{\partial F_i}{\partial t} + \vec{c} \cdot \frac{\partial F_i}{\partial \vec{r}} + \frac{\vec{f}_i}{m_i} \cdot \frac{\partial F_i}{\partial \vec{c}} \quad (5)$$

$$= \nu_{ii} (F_{0i} - F_i) + \nu_{ie} (\overline{F_{0i}} - F_i) \text{ for ions,}$$

where  $F_{0\alpha} = n_\alpha (2\pi RT_\alpha)^{-3/2} \exp(-(\vec{c} - \vec{V}_\alpha)^2 / 2RT_\alpha)$  and  $\overline{F_{0\alpha}} = n_\alpha (2\pi \overline{RT}_\alpha)^{-3/2} \exp(-(\vec{c} - \overline{\vec{V}}_\alpha)^2 / 2\overline{RT}_\alpha)$ .

The quantities  $n_\alpha$ ,  $\vec{V}_\alpha$  and  $T_\alpha$  are the number density, mean drift velocity, and effective temperature obtained by taking moments of  $F_\alpha$ . Some latitude in the definition of  $\overline{T}_\alpha$  and  $\overline{\vec{V}}_\alpha$  is possible; one choice is in [32]

$$\overline{T}_e = T_i, \quad \overline{T}_i = T_e, \quad \overline{\vec{V}}_e = \vec{V}_i, \quad \overline{\vec{V}}_i = \vec{V}_e. \quad (6)$$

The particles are reflected from the plate with a full velocity accommodation; that is, the plasma particles are reflected with the plate velocity so that the boundary conditions are  $V_{x2\alpha}(0, t) = U_0 \cos(\beta t)$  for  $t > 0$ , where  $V_{x2\alpha} = V_{x\alpha}$  as  $c_y > 0$  and  $V_{x\alpha}$  is finite as  $y \rightarrow \infty$  for both ions and electrons.

Substituting from (2), (3), and (6) into (4) and (5) one obtains

$$\frac{\partial F_e}{\partial t} + c_y \frac{\partial F_e}{\partial y} - \frac{eB_{ez}}{m_e c_0} \left( c_y \frac{\partial F_e}{\partial c_x} - c_x \frac{\partial F_e}{\partial c_y} \right) + \frac{eE_{ex}}{m_e} \frac{\partial F_e}{\partial c_x} \quad (7)$$

$$= \nu_{ee} (F_{0e} - F_e) + \nu_{ei} (F_{0i} - F_e), \text{ for electrons,}$$

$$\frac{\partial F_i}{\partial t} + c_y \frac{\partial F_i}{\partial y} + \frac{eB_{iz}}{m_i c_0} \left( c_y \frac{\partial F_i}{\partial c_x} - c_x \frac{\partial F_i}{\partial c_y} \right) - \frac{eE_{ix}}{m_i} \frac{\partial F_i}{\partial c_x} \quad (8)$$

$$= \nu_{ii} (F_{0i} - F_i) + \nu_{ie} (F_{0e} - F_i), \text{ for ions,}$$

where  $\nu_{ee}$ ,  $\nu_{ei}$ ,  $\nu_{ii}$ , and  $\nu_{ie}$  are electron-electron, electron-ion, ion-ion, and ion-electron collision frequencies, respectively, which are given by [32–35]

$$\begin{aligned}\nu_{ee} &= \left( \frac{4\sqrt{\pi} n_e e^4 \text{Log}[\Lambda_{ee}]}{3\sqrt{m_e} K_B^{3/2} T_e^{3/2}} \right), \\ \nu_{ei} &= \left( \frac{4\sqrt{2\pi} n_i e^4 Z^2 \text{Log}[\Lambda_{ei}]}{3\sqrt{m_e} K_B^{3/2} T_e^{3/2}} \right), \\ \nu_{ii} &= \left( \frac{4\sqrt{\pi} n_i e^4 Z^4 \text{Log}[\Lambda_{ii}]}{3\sqrt{m_i} K_B^{3/2} T_i^{3/2}} \right), \\ \nu_{ie} &= \left( \frac{m_e}{m_i} \frac{4\sqrt{2\pi} n_e e^4 Z^2 \text{Log}[\Lambda_{ie}]}{3\sqrt{m_e} K_B^{3/2} T_e^{3/2}} \right),\end{aligned}\quad (9)$$

where  $\lambda_{De} = \lambda_{Di} = \lambda_D$ ,  $\text{Log}[\Lambda] = \text{Log}[4\pi n \lambda_D^3]$  and  $Z$  are the Coulomb Logarithms and the degree of ionization, respectively.

The model of the cone of influence suggested by Lee's moment method [36–40] for the solution of the Boltzmann's equation is employed here. Let us write the solution of (4) and (5), as suggested by Kashmarov in the form

$$F_\alpha = \begin{cases} F_{1\alpha} = n_\alpha (2\pi RT_\alpha)^{-3/2} \left( 1 + \frac{c_x V_{x1\alpha}}{RT_\alpha} \right) \exp\left(\frac{-c^2}{2RT_\alpha}\right) & \text{for } c_y < 0, \\ F_{2\alpha} = n_\alpha (2\pi RT_\alpha)^{-3/2} \left( 1 + \frac{c_x V_{x2\alpha}}{RT_\alpha} \right) \exp\left(\frac{-c^2}{2RT_\alpha}\right) & \text{for } c_y > 0, \end{cases} \quad (10)$$

where  $V_{x1\alpha}$  and  $V_{x2\alpha}$  are four unknown functions of time  $t$  and the distance variable  $y$ .

Using Grad's moment method multiplying (7) and (8) by  $Q_j(\vec{c})$ . Integrating over all values of  $\vec{c}$ , we can obtain the transfer equations for electrons and ions, respectively, in the form

$$\begin{aligned}\frac{\partial}{\partial t} \int Q_j F_e d\vec{c} + \frac{\partial}{\partial y} \int c_y Q_j F_e d\vec{c} + \frac{eE_{xe}}{m_e} \\ \times \int F_e \frac{\partial Q_j}{\partial c_x} d\vec{c} - \frac{eB_{ze}}{m_e c_0} \int \left( c_x \frac{\partial Q_j}{\partial c_y} - c_y \frac{\partial Q_j}{\partial c_x} \right) d\vec{c} \quad (11)\end{aligned}$$

$$= \nu_{ee} \int (F_{0e} - F_e) Q_j d\vec{c} + \nu_{ei} \int (F_{0i} - F_e) Q_j d\vec{c},$$

$$\begin{aligned}\frac{\partial}{\partial t} \int Q_j F_i d\vec{c} + \frac{\partial}{\partial y} \int c_y Q_j F_i d\vec{c} - \frac{eE_{ix}}{m_i} \\ \times \int F_i \frac{\partial Q_j}{\partial c_x} d\vec{c} + \frac{eB_{iz}}{m_i c_0} \int \left( c_x \frac{\partial Q_j}{\partial c_y} - c_y \frac{\partial Q_j}{\partial c_x} \right) d\vec{c} \quad (12)\end{aligned}$$

$$= \nu_{ii} \int (F_{0i} - F_i) d\vec{c} + \nu_{ie} \int (F_{0e} - F_i) Q_j d\vec{c}.$$

The integrals over the velocity distance are evaluated from the relation

$$\int Q_j(\vec{c}) F_\alpha d\vec{c} = \int_{-\infty}^{\infty} \int_{-\infty}^0 \int_{-\infty}^{\infty} Q_j F_{1\alpha} d\vec{c} + \int_{-\infty}^{\infty} \int_0^{\infty} \int_{-\infty}^{\infty} Q_j F_{2\alpha} d\vec{c}, \quad (13)$$

where  $Q_j = Q_j(\vec{c})$ ,  $j = 1, 2$ , and  $d\vec{c} = dc_x dc_y dc_z$ , where  $c_x$ ,  $c_y$ , and  $c_z$  are the particles velocities components along  $x$ -,  $y$ -, and  $z$ -axes, respectively. Moreover,  $E_\alpha$  and  $B_\alpha$  may be obtained from Maxwell's equation, for electrons as follows:

$$\begin{aligned} \frac{\partial E_{xe}}{\partial y} - \frac{1}{c_0} \frac{\partial B_{ze}}{\partial t} &= 0, \\ \frac{\partial B_{ze}}{\partial y} - \frac{1}{c_0} \frac{\partial E_{xe}}{\partial t} - \frac{4\pi n_e}{c_0} V_{xe} &= 0. \end{aligned} \quad (14)$$

For ions we obtain

$$\begin{aligned} \frac{\partial E_{xi}}{\partial y} - \frac{1}{c_0} \frac{\partial B_{zi}}{\partial t} &= 0, \\ \frac{\partial B_{zi}}{\partial y} - \frac{1}{c_0} \frac{\partial E_{xi}}{\partial t} + \frac{4\pi n_i}{c_0} V_{xi} &= 0, \end{aligned} \quad (15)$$

where  $n_\alpha = \int F_\alpha d\vec{c}$ ,  $n_\alpha V_{x\alpha} = \int c_x F_\alpha d\vec{c}$ , with the initial and boundary conditions

$$E_{x\alpha}(y, 0) = B_{z\alpha}(y, 0) = 0; \quad (16)$$

$E_{x\alpha}(y, t)$ ,  $B_{z\alpha}(y, t)$  are finite as  $y \rightarrow \infty$ .

We introduce the dimensionless variables defined by

$$\begin{aligned} t &= t' \tau_{ie}, & y &= y' \left( \frac{\tau_{ie} V_{Te}}{\sqrt{2\pi}} \right), \\ V_{x\alpha} &= V'_{x\alpha} V_{Te}, & \tau_{xy\alpha} &= \tau'_{xy\alpha} V_{Te}, & \text{Ma} &= \frac{U_0}{V_{Te}}, \\ B_{z\alpha} &= B'_{z\alpha} \left( \frac{\sqrt{2\pi} m_e c_0}{e \tau_{ie}} \right), & E'_{x\alpha} &= E'_{x\alpha} \left( \frac{m_e V_{Te}}{e \tau_{ie}} \right), \end{aligned} \quad (17)$$

$$\rho_\alpha = n_\alpha m_\alpha, \quad V_{Te} = \sqrt{\frac{2K_B T_e}{m_e}},$$

$$\varepsilon = \frac{m_e}{m_i}, \quad dU_\alpha = dU'_\alpha (K_B T_e),$$

$$F_{j\alpha} = F'_{j\alpha} n_e (2\pi R T_e)^{-3/2}, \quad j = 0, 1, 2.$$

For  $\text{Ma}^2 \ll 1$  (low Mach number), we can assume that the density and the temperature variation at each point of the flow and at any time are negligible; that is,  $n_\alpha = 1 + O(\text{Ma}^2)$  and  $T_\alpha = 1 + O(\text{Ma}^2)$ . Put

$$\begin{aligned} V_{x\alpha} &= \frac{1}{2} (V_{x1\alpha} + V_{x2\alpha}), \\ \tau_{xy\alpha} &= \frac{P_{xy\alpha}}{\rho_\alpha U_0 \sqrt{R T_e} / 2\pi} = (V_{x2\alpha} - V_{x1\alpha}), \end{aligned} \quad (18)$$

where  $P_{xy\alpha}$  is the shear stress [11] that is defined by  $P_{xy\alpha} = m \int (c_x - V_x) c_y F_\alpha d\vec{c}$ .

Using the dimensionless variable, if we neglect terms of order  $O(\text{Ma}^2)$ , (11) for  $Q_1 = c_x$  and  $Q_2 = c_x c_y$  is:

$$\frac{\partial V'_{xe}}{\partial t'} + \frac{\partial \tau'_{xye}}{\partial y'} - E'_{xe} = 0, \quad (19)$$

$$\frac{\partial \tau'_{xye}}{\partial t'} + 2\pi \frac{\partial V'_{xe}}{\partial y'} + \left( \frac{\nu_{ee}}{\nu_{ie}} + \frac{\nu_{ei}}{\nu_{ie}} \right) \tau'_{xye} = 0.$$

Similarly, (12) becomes:

$$\frac{\partial V'_{xi}}{\partial t'} + \frac{\partial \tau'_{xyi}}{\partial y'} + \varepsilon E'_{xi} = 0, \quad (20)$$

$$\frac{\partial \tau'_{xyi}}{\partial t'} + 2\pi \frac{\partial V'_{xi}}{\partial t'} + \left( \frac{\nu_{ii}}{\nu_{ie}} + \frac{\nu_{ie}}{\nu_{ie}} \right) \tau'_{xyi} = 0,$$

with the initial and boundary conditions

$$\begin{aligned} V'_{x\alpha}(y', 0) &= \tau'_{xy\alpha}(y', 0) = 0, \\ 2V'_{x\alpha}(0, t') + \tau'_{xy\alpha}(0, t') &= 2\text{Ma} \cos(\beta_1 t'); \end{aligned} \quad (21)$$

$V'_{x'}$ ,  $\tau'_{xy}$  are finite as  $y \rightarrow \infty$ ,  $\beta_1 = \beta \tau_{ie}$ .

In the expressions for the transport coefficients mentioned previously, the fact that the plasma is neutral was used [33], writing  $n = n_e = Zn_i$ ,  $T = T_e = T_i$ , and  $Z = 1$ , which exploited the fact that the ratio  $m_e/m_i$  is small. Thus, the ratio between the four distinguished collision frequencies can be rewritten in a form that referred to  $\nu_{ee}$  in formulas (9)

$$\nu_{ee} : \nu_{ei} : \nu_{ii} : \nu_{ie} = 1 : \sqrt{2} : \sqrt{\frac{m_e}{m_i}} : \frac{m_e}{m_i} = 1 : \sqrt{2} : \sqrt{\varepsilon} : \varepsilon. \quad (22)$$

Therefore,  $\nu_{ee} \sim \nu_{ei} \gg \nu_{ii} \gg \nu_{ie}$ ; the first of these gross inequalities arises because thermal ion speeds are less than thermal electron speeds by the factor  $\sqrt{m_e/m_i}$  if  $T_e \approx T_i$ , and so the ions take longer period of time to meet each other. The second one reflects the fact that the electrons are not very effective in deflecting the much heavier ions.

For the sake of simplicity, henceforth, we drop the dash over the dimensionless variables. Therefore, we have the following initial-boundary value problem for electrons (neglecting the displacement current) [30]:

$$\frac{\partial V_{xe}}{\partial t} + \frac{\partial \tau_{xye}}{\partial y} - E_{xe} = 0, \quad (23)$$

$$\frac{\partial \tau_{xye}}{\partial t} + 2\pi \frac{\partial V_{xe}}{\partial y} + \left( \frac{1}{\sqrt{\varepsilon}} + \sqrt{\frac{2}{\varepsilon}} \right) \tau_{xye} = 0, \quad (24)$$

$$\frac{\partial E_{xe}}{\partial y} - \frac{\partial B_{ze}}{\partial t} = 0, \quad (25)$$

$$\frac{\partial B_{ze}}{\partial y} - \alpha_{0e} V_{xe} = 0, \quad \text{where } \alpha_{0e} = \left( \frac{V_{Te}^2 \tau_{ie}^2 e^2 n_e}{m_e c_0^2} \right), \quad (26)$$

with the initial and boundary conditions

$$\begin{aligned} V_{xe}(y, 0) = \tau_{xye}(y, 0) = E_{xe}(y, 0) = B_{ze}(y, 0) = 0, \\ 2V_{xe}(0, t) + \tau_{xye}(0, t) = 2Ma \cos(\beta_1 t), \quad \text{for } t > 0; \end{aligned} \quad (27)$$

$$V_{xe}, \tau_{xye}, E_{xe}, B_{ze} \quad \text{are finite as } y \rightarrow \infty.$$

In addition, we have the following initial-boundary problem for ions (neglecting the displacement current):

$$\frac{\partial V_{xi}}{\partial t} + \frac{\partial \tau_{xyi}}{\partial y} + \varepsilon E_{xi} = 0, \quad (28)$$

$$\frac{\partial \tau_{xyi}}{\partial t} + 2\pi \frac{\partial V_{xi}}{\partial y} + (\sqrt{\varepsilon} + 1) \tau_{xyi} = 0, \quad (29)$$

$$\frac{\partial E_{xi}}{\partial y} - \frac{\partial B_{zi}}{\partial t} = 0, \quad (30)$$

$$\frac{\partial B_{zi}}{\partial y} + \alpha_{0i} V_{xi} = 0, \quad \text{where } \alpha_{0i} = \left( \frac{V_{Te}^2 \tau_{ie}^2 e^2 n_i}{m_e c_0^2} \right). \quad (31)$$

Since  $n_i = n_e$ ; thus, henceforth, we put  $\alpha_{0i} = \alpha_{0e} = \alpha_0$ .

We can reduce our basic (23)–(26), for electrons, after some analytical manipulations to a single equation as follows:

$$\begin{aligned} \frac{\partial^4 V_{xe}(y, t)}{\partial t^2 \partial y^2} - 2\pi \frac{\partial^4 V_{xe}(y, t)}{\partial t^4} - A_c \frac{\partial^3 V_{xe}(y, t)}{\partial t \partial y^2} \\ - \alpha_0 \frac{\partial^2 V_{xe}(y, t)}{\partial t^2} - \alpha_0 A_c \frac{\partial V_{xe}(y, t)}{\partial t} = 0, \end{aligned} \quad (32)$$

where  $A_c = ((1/\sqrt{\varepsilon}) + \sqrt{2/\varepsilon})$ .

Similarly, the basic (28)–(31) can be reduced for ions to obtain

$$\begin{aligned} \frac{\partial^4 V_{xi}(y, t)}{\partial t^2 \partial y^2} - 2\pi \frac{\partial^4 V_{xi}(y, t)}{\partial t^4} - B_c \frac{\partial^3 V_{xi}(y, t)}{\partial t \partial y^2} \\ - \alpha_0 \varepsilon \frac{\partial^2 V_{xi}(y, t)}{\partial t^2} - \alpha_0 \varepsilon B_c \frac{\partial V_{xi}(y, t)}{\partial t} = 0, \end{aligned} \quad (33)$$

where  $B_c = (\sqrt{\varepsilon} + 1)$ .

### 3. Solution of the Initial-Boundary Value Problem

The traveling wave solution method [41, 42] is used, considered

$$\xi = ly - mt, \quad (34)$$

to make all the dependent variables as functions of  $\xi$ . Here  $l$  and  $m$  are transformation constants, which do not depend on the properties of the fluid but as parameters to be determined

by the boundary and initial conditions [41]. Using (34) we obtain the derivatives

$$\begin{aligned} \frac{\partial}{\partial t} = -m \frac{\partial}{\partial \xi}, \quad \frac{\partial}{\partial y} = l \frac{\partial}{\partial \xi}, \quad \frac{\partial^a}{\partial t^a} = (-1)^a m^a \frac{\partial^a}{\partial \xi^a}, \\ \frac{\partial^a}{\partial y^a} = l^a \frac{\partial^a}{\partial \xi^a}, \end{aligned} \quad (35)$$

where  $a$  is a positive integer.

Substituting from (34)–(35) into (32), we have

$$\begin{aligned} (m^2 l^2 - 2\pi m^4) \frac{d^4 V_{xe}(\xi)}{d\xi^4} + A_c m l^2 \frac{d^3 V_{xe}(\xi)}{d\xi^3} \\ - \alpha_0 m^2 \frac{d^2 V_{xe}(\xi)}{d\xi^2} + \alpha_0 A_c m \frac{dV_{xe}(\xi)}{d\xi} = 0. \end{aligned} \quad (36)$$

The boundary and initial conditions became

$$\begin{aligned} E_{xe}(\xi = 0) = B_{ze}(\xi = 0) = \tau_{xye}(\xi = 0) = 0, \\ 2V_{xe}(\xi = -m) + \tau_{xye}(\xi = -m) = 2Ma \cos(\beta_1), \\ \text{at } y = 0, \text{ e.g., } t = 1; \end{aligned} \quad (37)$$

$$V_{xe}, \tau_{xye}, E_{xe}, B_{ze} \quad \text{are finite as } \xi \rightarrow -\infty.$$

Now we have an ordinary differential Equation (36) with the boundary and initial conditions (37). Next, let us solve (33) by using the same tackling. Substituting from expressions (34)–(35) into (33), we get

$$\begin{aligned} (m^2 l^2 - 2\pi m^4) \frac{d^4 V_{xi}(\xi)}{d\xi^4} + B_c m l^2 \frac{d^3 V_{xi}(\xi)}{d\xi^3} \\ - \alpha_0 \varepsilon m^2 \frac{d^2 V_{xi}(\xi)}{d\xi^2} + \alpha_0 \varepsilon B_c m \frac{dV_{xi}(\xi)}{d\xi} = 0, \end{aligned} \quad (38)$$

with the corresponding boundary and initial conditions

$$\begin{aligned} E_{xi}(\xi = 0) = B_{zi}(\xi = 0) = \tau_{xyi}(\xi = 0) = 0, \\ 2V_{xi}(\xi = -m) + \tau_{xyi}(\xi = -m) = 2Ma \cos(\beta_1); \\ V_{xi}, \tau_{xyi}, E_{xi}, B_{zi} \quad \text{are finite as } \xi \rightarrow -\infty. \end{aligned} \quad (39)$$

The two ordinary, fourth order homogeneous differential equations (36) and (38) can be solved exactly by the help of symbolic computer software, with their boundary and initial conditions (37) and (39). The sought solutions will be applied to a typical model of laboratory argon plasma.

### 4. The Investigation of the Behavior of the Internal Energy Change

The studying of the behavior of the internal energy change for the physical systems presents a great importance in science. The extended Gibbs relation for electrons and ions is introduced to study the internal energy change for the system,

based on the solution of the nonstationary Boltzmann equation [43]. It includes the electromagnetic field energy as a part of the complete energy balance. This procedure distinguishes the charged gas into paramagnetic and diamagnetic ones. If there are unpaired electrons in the molecular orbital diagram, the gas is paramagnetic. If all electrons are paired, the gas is considered as a diamagnetic one. We should write the internal energy balance, including the electromagnetic field energy, to get the work term in the first law of thermodynamics as follows.

- (a) For paramagnetic plasma, the internal energy change is expressed in terms of the extensive quantities  $S_\alpha$ ,  $P_\alpha$ , and  $M_\alpha$ , which are the thermodynamic coordinates corresponding to the conjugate intensive quantities  $T_\alpha$ ,  $E_\alpha$ , and  $B_\alpha$ , respectively. The three contributions in the internal energy change in the Gibbs formula we have

$$dU_\alpha = dU_{S_\alpha} + dU_{P_\alpha} + dU_{M_\alpha}, \quad (40)$$

where  $dU_{S_\alpha} = T dS_\alpha$  is the internal energy change due to the variation of the entropy, which is written in dimensionless form as

$$S_\alpha = -\pi^{3/2} \left[ (V_{x1\alpha}^2 + V_{x2\alpha}^2) - \frac{3}{2} \right], \quad (41)$$

$dU_{P_\alpha} = E_\alpha dP_\alpha$  is the internal energy change due to variation of polarization, and  $dU_{M_\alpha} = B_\alpha dM_\alpha$  is the internal energy change due to the variation of magnetization, here  $M$  is calculated from the equation [44]

$$\frac{\partial S_\alpha}{\partial M_\alpha} = -\frac{B_\alpha}{T_\alpha} \implies M_\alpha = - \int \left( \frac{T_\alpha}{B_\alpha} \frac{\partial S_\alpha}{\partial y} \right)_t dy. \quad (42)$$

Introduce the dimensionless variables  $U'_\alpha = U_\alpha / K T_\alpha$ ,  $M'_\alpha = M_\alpha (1/e_\alpha \tau_{ei} V_{Te})$ ,  $P'_\alpha = P_\alpha (1/e_\alpha \tau_{ei} V_{Te})$  in the Gibbs formula to get (after dropping the primes)

$$dU_\alpha = dS_\alpha + f_{\alpha 1} E_\alpha dP_\alpha + f_{\alpha 1} B_\alpha dM_\alpha. \quad (43)$$

- (b) On the other hand, if the plasma is diamagnetic, the internal energy change due to the extensive variables  $S$ ,  $P$ , and  $B$  represents the thermodynamic coordinates conjugate to the intensive quantities  $T$ ,  $E$ , and  $M$ , respectively; therefore, we have three contributions in the internal energy change in the Gibbs formula given by

$$dU_\alpha = dU_{S_\alpha} + dU_{P_\alpha} + dU_{B_\alpha}, \quad (44)$$

where  $dU_{B_\alpha} = -M_\alpha dB_\alpha$  is the internal energy change due to the variation of the induced magnetic induction, where  $M_\alpha = T_\alpha (\partial S_\alpha / \partial B_\alpha)$ . Hence, the dimensionless form for  $dU$  in this case takes the following form:

$$dU_\alpha = dS_\alpha + f_{\alpha 1} E_\alpha dP_\alpha - f_{\alpha 1} M_\alpha dB_\alpha, \quad (45)$$

where

$$f_1 = \left( \frac{m_e V_{Te}^2}{K T_0} \right), \quad dS_\alpha = \left( \frac{\partial S_\alpha}{\partial r} \right) \delta y + \left( \frac{\partial S_\alpha}{\partial t} \right) \delta t; \quad (46)$$

$$\delta y = 1, \quad \delta t = 4.35 \approx t_{eqe}.$$

## 5. Discussion

In this problem, the unsteady behavior of an inhomogeneous mixture of charged gas, bounded by an oscillating plate, is investigated. This study is based on the kinetic theory via the BGK model of the Boltzmann equation. Our computations are performed according to typical data for argon plasma as a paramagnetic medium in the case of the argon gas losing single electrons subjected to the following conditions and parameters:  $K_B = 1.3807 \cdot 10^{-16}$  erg/K,  $T_0 = 600$  K,  $n_e = 7 \cdot 10^{16}$  cm<sup>-3</sup>,  $d = 3.84 \cdot 10^{-8}$  cm (diameter of the argon atom); the electron rest mass, mass of ions, and charge are  $m_e = 9.093 \cdot 10^{-28}$  gm,  $m_i = 6.633 \cdot 10^{-23}$  gm,  $e = 4.8 \cdot 10^{-10}$  esu, which are used to calculate electron-ion relaxation time  $\tau_{ie} = 1.4859 \cdot 10^{-10}$  sec. The dimensionless parameter is  $\alpha_0 = 7.9 \cdot 10^{-2}$  and the mean free path of the electrons  $\lambda_{ie} = 2.110^{-3}$  cm compared to the electron Debye length.

Consider  $\lambda_{De} = (K_B T_0 / 4\pi n_e e^2)^{1/2} = 6.39 \cdot 10^{-7}$  cm,  $f_1 = 2$ . Using the idea of the shooting numerical calculation method, the transformation constants are evaluated to obtain  $m = 2.8$ ,  $l = -1.2$ , and the plate Mach number  $Ma = 6.5 \cdot 10^{-2}$ .

The fundamental and the essential inequalities, which we must bear in mind when analyzing the results, are

$$m_i \gg m_e \quad \text{makes} \quad \varepsilon^2 = \frac{m_e}{m_i} = 1.37 \cdot 10^{-5}, \quad (I-a)$$

$$\tau_{ee} : \tau_{ei} : \tau_{ii} : \tau_{ie} = 1 : 7.07 \cdot 10^{-1} : 2.69 \cdot 10^2 : 5.15 \cdot 10^4$$

$$\implies \tau_{ee} \sim \tau_{ei} \ll \tau_{ii} \ll \tau_{ie}. \quad (I-b)$$

These inequalities will control the major behavior of both electrons and positive ions in the rest of the discussion. Figure 1(a) clarifies that in the course of time the perturbed velocity distribution functions  $F_1$  and  $F_2$  approach to the equilibrium velocity distribution function  $F_0$  at  $y = 0.003$ , for example. The ions are still departing from equilibrium very slowly; see Figure 1(b).

A comparison between Figures 1(a) and 1(b) shows that the collisions of ions with electrons have a very little effect on the form of the ions nonequilibrium distribution function. On the other hand, collisions of electrons with ions have an important effect on the form of the electrons nonequilibrium distribution function, which is in a good agreement with the well-known study of Braginskii [33]. This is because the transfer of momentum from ions to electrons occurs in about the same time  $\sim \tau_{ei}$  as the transfer of the energy; hence, ion-electron momentum transfer is small compared with ion-ion momentum transfer. The transfer of momentum from electrons to ions occurs in a time of the same order  $\sim \tau_{ee}$  as electron-electron transfer time, so that collisions of electrons

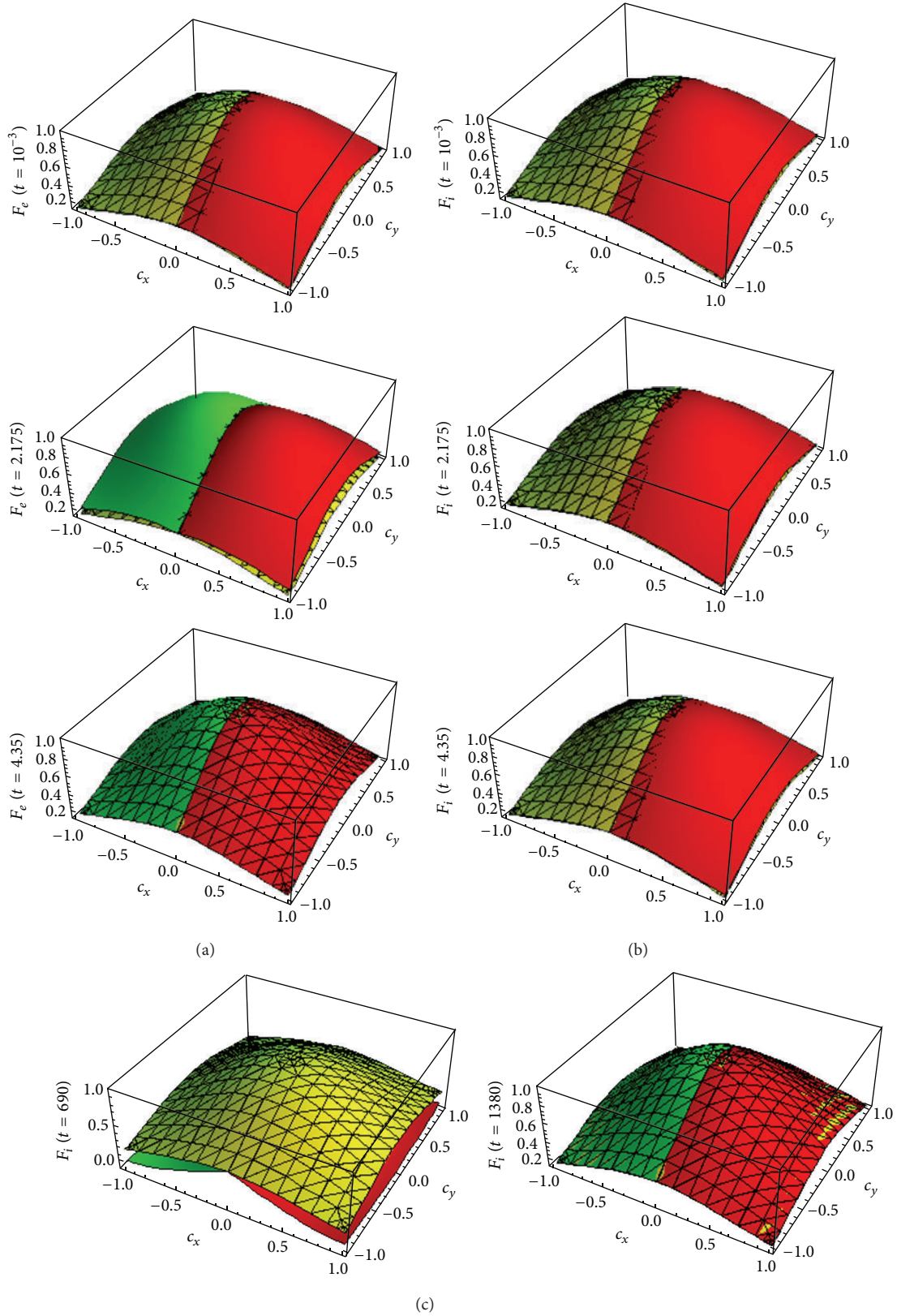


FIGURE 1: (a) The comparison between the combined perturbed dimensionless velocity distribution functions for electrons  $F_e$  ( $F_{1e}$  (green),  $F_{2e}$  (red)) and electrons equilibrium velocity distribution function  $F_{0e}$  (grid) at  $t = 10^{-3}$ , 2.175, and 4.35 for a fixed  $y$  value (0.003) with the Mach number of the plate  $Ma = 0.065$ . (b) The comparison between the combined perturbed dimensionless velocity distribution functions for ions  $F_i$  ( $F_{1i}$  (green),  $F_{2i}$  (red)) and ions equilibrium velocity distribution function  $F_{0i}$  (grid) at  $t = 10^{-3}$ , 2.175, and 4.35 for a fixed  $y$  value (0.003) with the Mach number of the plate  $Ma = 0.065$ . (c) The comparison between the combined perturbed dimensionless velocity distribution functions for ions  $F_i$  ( $F_{1i}$  (gray),  $F_{2i}$  (black)) and ions equilibrium dimensionless velocity distribution function  $F_{0i}$  (grid) at  $t = 690$ , 1380 for a fixed  $y$  value (0.003) with the Mach number of the plate  $Ma = 0.065$ .

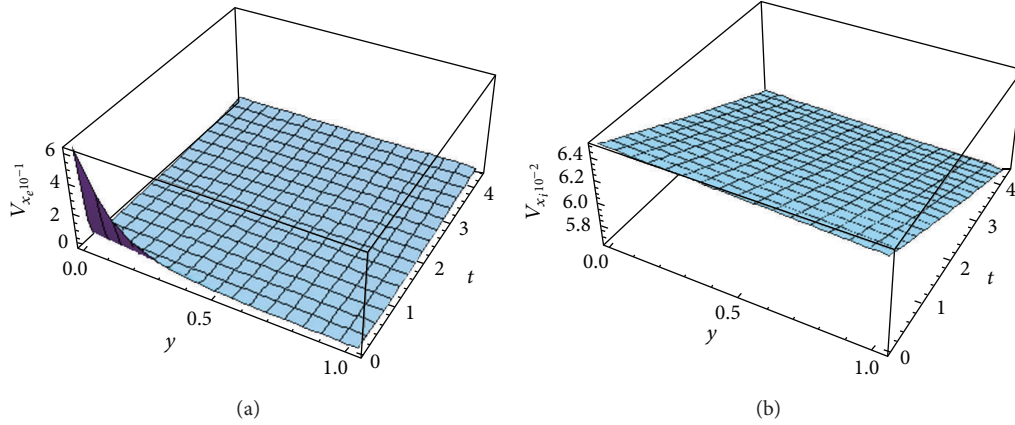


FIGURE 2: The dimensionless velocity versus space  $y$  and time  $t$ : (a)  $V_{xe}$ ; (b)  $V_{xi}$ .

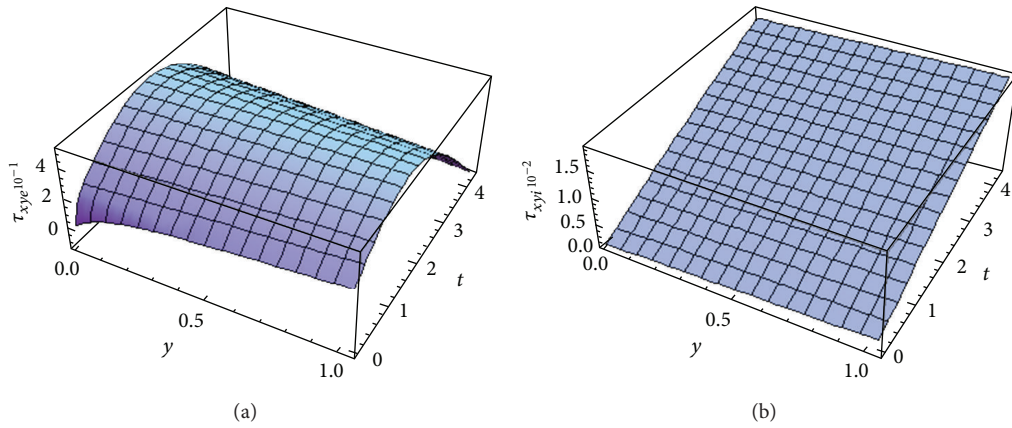


FIGURE 3: The dimensionless shear stress versus space  $y$  and time  $t$ : (a)  $\tau_{xye}$ ; (b)  $\tau_{xyi}$ .

with the ions affect the electrons nonequilibrium distribution function.

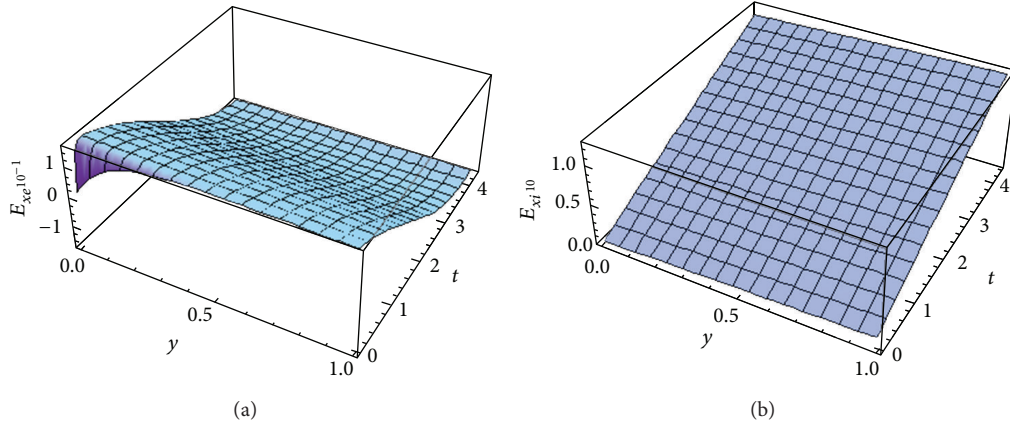
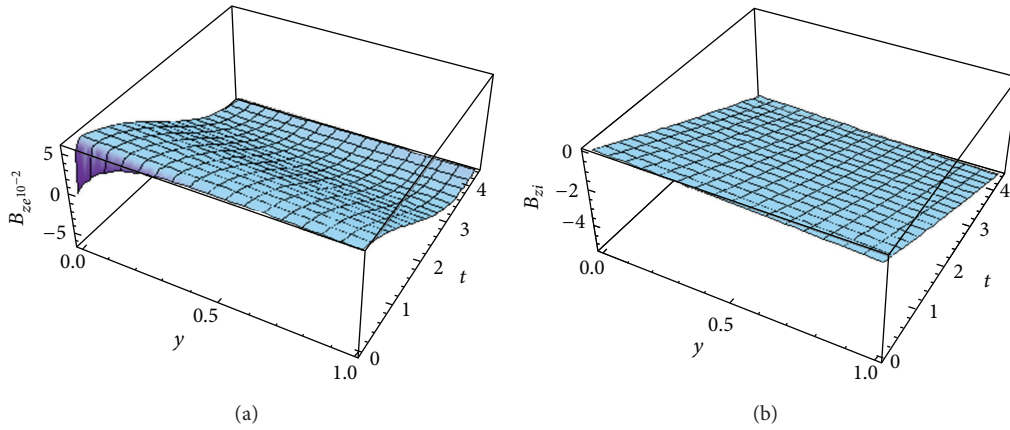
Figures 1(a) and 1(b) indicate that the lighter species (electrons) in the mixture of gases reach equilibrium before the heavier one (positive ions) that is in a qualitative agreement with the investigation made by Galkin [45]. Figure 1(a) makes it clear that the time needed for the electrons to reach equilibrium is ( $t_{eq} \sim 4.35$ ) which will be taken into consideration, henceforth.

In a relative long period, for example,  $t = 690$ , the departure of positive ions from equilibrium becomes obvious; the distinction between ions equilibrium distribution function and their nonequilibrium distribution function becomes substantial. After a relatively long time the heavy species (positive ions) reach equilibrium at  $t \cong 1380$ ; see Figure 1(c).

All Figures 1(a) and 1(b) to 8(a) and 8(b) shed light upon the boundary and initial conditions for both electrons and ions hold. As revealed in Figures 2(a) and 2(b) at the vicinity of the suddenly oscillating plate the mean velocities for both electrons and positive ions have a value = Ma of the oscillating plate which satisfies the conditions of the problem. The  $V_{xe}$  gets a severe decrement with time while  $V_{xi}$  shows a gradually linear decrement; this is due to two reasons, firstly, because thermal ion speeds are less than the thermal electron

speeds, by the amount  $\sqrt{m_e/m_i}$  as  $T_e \cong T_i$ , and so ions take longer time to encounter each other while electrons do not. Secondly, this behavior reflects the fact that the electrons are not very effective in deflecting the much heavier ions, while ions have a very successful effect on electrons motion, referring to inequalities (I-a) and (I-b). Therefore, the change of all kinetic and thermodynamic variables belongs to the positive ions that has unnoticed nonlinear gradually slow changes; see Figures 1(b) to 8(b). This is in a qualitative agreement with the previous paper [15].

The shear stress  $\tau_{xye}$  is beginning from zero value. It is increasing nonlinearly towards its maximum value at  $t \sim 0.5t_{eqe}$ . After that, it decreases with the same behavior until it vanishes; see Figure 3(a). This is according to the behavior of the electrons velocity itself. Since the deviation from equilibrium is small, the electron gas is rarefied and the flow is slow. Thus, the gas is Newtonian [46]. It follows that the viscosity  $\mu_\alpha = -\tau_{xy\alpha}/(\partial V_{x\alpha}/\partial y)$  represents the resistance to the motion. It gradually increases nonlinearly as the gas particles move away from the plate for ions  $\mu_i$ . The  $\mu_e$  approaches zero for electrons except at a small time interval around  $t \sim 0.5t_{eqe}$ ; this is due to the corresponding maximum value of  $\tau_{xye}$  in the same time interval.


 FIGURE 4: The dimensionless induced electric field versus space  $y$  and time  $t$ : (a)  $E_{xe}$ ; (b)  $E_{xi}$ .

 FIGURE 5: The dimensionless induced electric field versus space  $y$  and time  $t$ : (a)  $B_{ze}$ ; (b)  $B_{zi}$ .

The electrons induced electric field has a sudden increase in the beginning until it reaches its maximum value ( $E_{xe\text{Max}} \sim 0.1$ ) due to the sudden oscillation of the plate itself. It decreases nonlinearly until it vanishes at  $t \sim 0.5t_{eqe}$ . After that, it changes its direction until the same maximum value  $E_{xe\text{Max}} \sim -0.1$  in the opposite direction. It is pushing electrons towards equilibrium. This is because of the famous le Chatelier principle that states, “If the system going away from equilibrium, its particles take the behavior that decreases the departure from equilibrium” that is pushing the system towards equilibrium again; see Figure 4(a). The same behavior holds for electrons induced magnetic field; see Figure 5(a).

Upon passing through a plasma, a charged particle (electron) losses (or gains) part of its energy because of the interaction with the surroundings (positive ions) due to plasma polarization and collisions. The energy loss (or gain) of an electron is determined by the work of the forces acting on the electrons in the plasma by the electromagnetic field generated by the moving particles themselves [47], since the suddenly oscillating plate causes work to be done on the gas, changing the internal energy of the gas  $U$ . As shown in Figures 6–8, the change in the internal energy due to the variation of entropy and polarization varies smoothly

with time by the energy lost to and gained from the ions and plate, respectively. The change in internal energy varies chaotically because of the intensive variables, corresponding to paramagnetic plasma; at the end each tends to zero.

## 6. Conclusions

The solution of the unsteady BGK equation in the case of an inhomogeneous rarefied charged gas, bounded by an oscillating plate, is investigated. We use the method of moments of the two-sided distribution function together with Maxwell’s equations. This is developed within the restrictions of small deviation from equilibrium, rarified gas mixture, and slow flow. This solution allows for the calculation of the components of the velocity of the flow for both electrons and positive ions. Inserting them into the suggested two-sided distribution functions and analyzing the results, it is found that:

- (a) the lighter species (electrons) of the gas mixture reaches equilibrium before the heavy one (positive ions), which is in a qualitative agreement with Galkin [37];

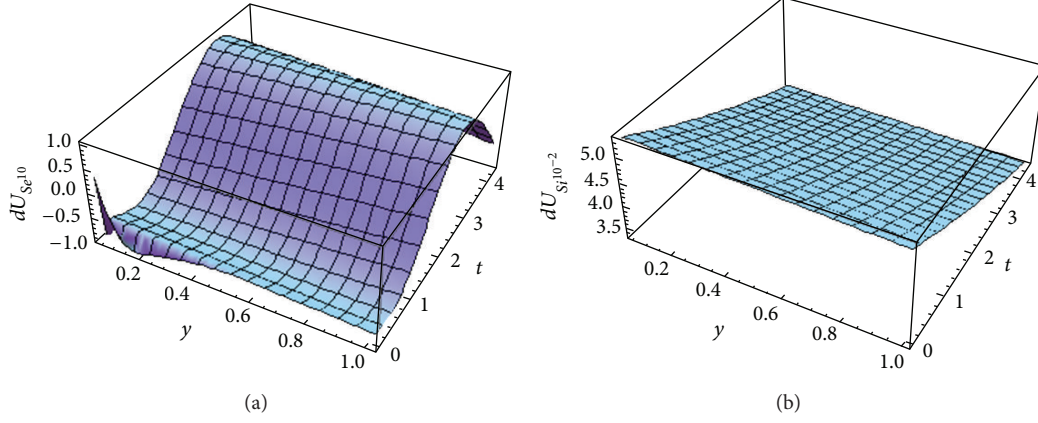


FIGURE 6: The dimensionless internal energy change versus space  $y$  and time  $t$ : (a)  $dU_{se}$ ; (b)  $dU_{si}$ .

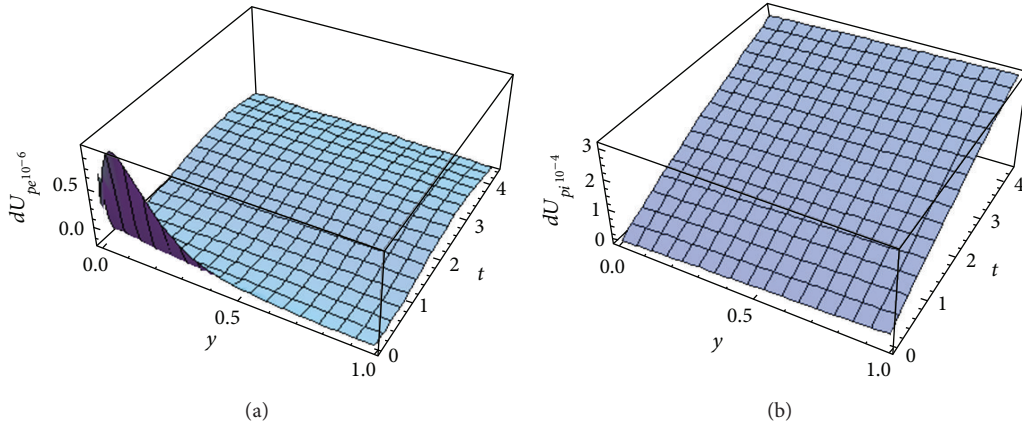


FIGURE 7: The dimensionless internal energy change versus space  $y$  and time  $t$ : (a)  $dU_{pe}$ ; (b)  $dU_{pi}$ .

- (b) definitely, the equilibrium times for electrons and for ions are calculated. The relation between those times and the relaxation time for both species of the mixture is deduced. We proved that the collision of ions with electrons has very little effect on the form of the ions nonequilibrium distribution function. On the other hand, we found that the collisions of electrons with ions have an important effect on the form of the electrons nonequilibrium distribution function, which is in a qualitative agreement with the study done by Park et al. [21];
- (c) the ratio between the time that electrons ( $t_{eqe} \cong 4.35$ ) and ions ( $t_{eqi} \cong 1380$ ) need to reach equilibrium is approximately equal to the same order of the reverse ratio of the ion-ion collision frequency to the mean value of the electron-electron and electron-ion collision frequencies; that is,  $t_{eqi}/t_{eqe} \cong ((\nu_{ee} + \nu_{ei})/2)/\nu_{ii}$ . This conclusion is different from the situation when the plate is moving with damping velocity and not oscillating; see the previous paper [15].

The predictions, estimated using Gibbs' equation, reveal that the following order of maximum magnitude ratios between the different contributions to the internal energy

change based on the total derivatives of the extensive parameters is, for ions

$$dU_{Si} : dU_{pi} : dU_{pari} = 1 : 0.6 \times 10^{-2} : 0.8 \times 10^{-4}. \quad (47)$$

It is concluded that the effect of the changes of the internal energies for positive ions  $dU_{pi}$  and  $dU_{pari}$  due to electric and magnetic fields are small in comparison with  $dU_{Se}$ . This happens with the recognition of the fact that these fields are self-induced by the sudden motion of the oscillating plate.

The same conclusion is applied in the case of electrons such that

$$dU_{Se} : dU_{pe} : dU_{pare} = 1 : 10^{-6} : 10^{-2}. \quad (48)$$

## Nomenclature

- $\vec{B}$ : The induced magnetic field vector
- $B$ : The induced magnetic field
- $\vec{E}$ : The induced electric vector
- $E$ : The induced electric field
- $F$ : The velocity distribution function

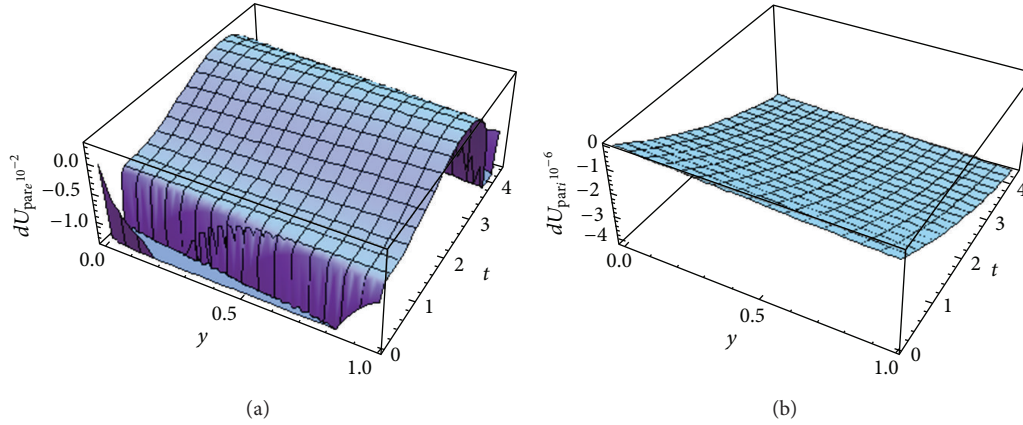


FIGURE 8: The dimensionless internal energy change versus space  $y$  and time  $t$ : (a)  $dU_{\text{pare}}$ ; (b)  $dU_{\text{pari}}$ .

$F_0$ : The local Maxwellian distribution function  
 $F_1$ : Distribution function for going downward particles  $c_y < 0$   
 $F_2$ : Distribution function for going upward particles  $c_y > 0$   
 $J$ : The current density  
 $K_B$ : Boltzmann's constant (Erg/K<sup>0</sup>)  $1.38 \cdot 10^{-16}$   
 $Ma$ : The plate Mach number  
 $M$ : Specific magnetization  
 $P$ : Polarization  
 $R$ : The gas constant  
 $S$ : Entropy per unit mass  
 $T$ : The temperature  
 $U$ : The internal energy of the gas  
 $U_0$ : Plate initial velocity  
 $V_x$ : The mean velocity  
 $V_{x1}$ : The mean velocity related to  $F_1$   
 $V_{x2}$ : The mean velocity related to  $F_2$   
 $V$ : Gas volume  
 $V_{Te}$ : Thermal velocity of electrons  
 $V_{Ti}$ : Thermal velocity of ions  
 $c_0$ : The speed of light  
 $c$ : The velocity of the particles  
 $d$ : Particle diameter  
 $e$ : The electron charge  
 $\vec{f}$ : Lorantz's force vector  
 $m_e$ : Electron mass  
 $m_i$ : Ion mass  
 $n$ : The mean density  
 $n_e$ : Electrons concentration  
 $n_i$ : Ions concentration  
 $p$ : Pressure  
 $\vec{r}$ : The position vector of the particle  
 $t$ : Time variable  
 $\vec{u}$ : The mean velocity of the particle  
 $dU_S$ : The internal energy change due to the variation of entropy  
 $dU_P$ : The internal energy change due to the variation of polarization  
 $dU_{\text{par}}$ : The internal energy change due to the variation of magnetization

$dU_{\text{dia}}$ : The internal energy change due to the variation of the induced magnetic field  
 $y$ : Displacement variable  
 $Z$ : Ionization.

*Superscripts*

$t$  : Dimensionless variable.

*Subscripts*

$e$  : Related to electrons  
 $i$  : Related to ions  
 $q$  : Equilibrium  
 $\alpha$  : =  $e$  for electrons or =  $i$  for ions.

*Greek Letters*

$\tau$  : The relaxation time  
 $\tau_{xy}$ : The shear stress  
 $\mu$  : Viscosity coefficient  
 $\lambda$  : The mean free path  
 $\alpha_0$ : Dimensionless parameter  
 $B$ : Frequency  
 $\nu$  : Collision frequency  
 $\varepsilon$  : Mass ratio  
 $\lambda$  : Mean free path  
 $\lambda_D$ : Debye radius.

**References**

[1] T. Z. Abdel Wahid and S. K. Elagan, "Kinetic treatment for the exact solution of the unsteady Rayleigh flow problem of a rarefied homogeneous charged gas bounded by an oscillating plate," *Canadian Journal of Physics*, vol. 90, no. 10, pp. 987–998, 2012.  
 [2] D. D. Millar, "Ion currents, ion-neutral collisions and plasma transport phenomena," *Australian Journal of Physics*, vol. 29, no. 4, pp. 249–261, 1976.  
 [3] K. Hyeon-Deuk, "Two-dimensional nonlinear nonequilibrium kinetic theory under steady heat conduction," *Physical Review E*, vol. 71, no. 4, Article ID 041203, 19 pages, 2005.

- [4] V. V. Aristov, *Methods of Direct Solving the Boltzmann Equation and Study of Non-Equilibrium*, vol. 60 of *Fluid Mechanics and Its Applications*, Kluwer Academic, Dordrecht, The Netherlands, 2001.
- [5] C. Cercignani, *Theory and Application of the Boltzmann Equation*, Scottish Academic Press, Edinburgh, UK, 1975.
- [6] S. Chapman and T. G. Cowling, *The Mathematical Theory of Non-Uniform Gases*, Cambridge University Press, Cambridge, UK, 1970.
- [7] V. P. Shidlovskiy, *Introduction to Dynamics of Rarefied Gases*, Elsevier, New York, NY, USA, 1967.
- [8] G. Lebon, D. Jou, and J. Casas-Vázquez, *Understanding Non-Equilibrium Thermodynamics: Foundations, Applications, Frontiers*, Springer, Berlin, Germany, 2008.
- [9] B. C. Eu, *Kinetic Theory and Irreversible Thermodynamics*, John Wiley & Sons, New York, NY, USA, 1992.
- [10] V. M. Zhdanov and V. I. Roldughin, "Non-equilibrium thermodynamics and kinetic theory of rarefied gases," *Physica-Uspekhi*, vol. 41, no. 4, pp. 349–378, 1998.
- [11] A. M. Abourabia and T. Z. Abdel Wahid, "Solution of the Krook kinetic equation model and non-equilibrium thermodynamics of a rarefied gas affected by a non-linear thermal radiation field," *Journal of Non-Equilibrium Thermodynamics*, vol. 36, no. 1, pp. 75–98, 2011.
- [12] A. M. Abourabia and T. Z. Abdel Wahid, "Kinetic and thermodynamic treatments of a neutral binary gas mixture affected by a nonlinear thermal radiation field," *Canadian Journal of Physics*, vol. 90, no. 2, pp. 137–149, 2012.
- [13] A. M. Abourabia and T. Z. Abdel Wahid, "The unsteady Boltzmann kinetic equation and non-equilibrium thermodynamics of an electron gas for the Rayleigh flow problem," *Canadian Journal of Physics*, vol. 88, no. 7, pp. 501–511, 2010.
- [14] T. Z. Abdel Wahid, "Kinetic and thermodynamic treatment for the exact solution of the unsteady Rayleigh flow problem of a rarefied homogeneous charged gas," *Journal of Non-Equilibrium Thermodynamics*, vol. 37, no. 2, pp. 119–141, 2012.
- [15] A. M. Abourabia and T. Z. Abdel Wahid, "Kinetic and thermodynamic treatment for the Rayleigh flow problem of an inhomogeneous charged gas mixture," *Journal of Non-Equilibrium Thermodynamics*, vol. 37, no. 1, pp. 1–25, 2012.
- [16] G. G. Stokes, *On the Effect of the Internal Friction of Fluids on the Motion of Pendulums*, vol. 9 of *Transactions of the Cambridge Philosophical Society*, 1851.
- [17] L. Rayleigh, "On the motion of solid bodies through viscous liquid," *Philosophical Magazine*, vol. 21, no. 126, pp. 697–711, 1911.
- [18] X. J. Gu and D. R. Emerson, "Modeling oscillatory flows in the transition regime using a high-order moment method," *Microfluidics and Nanofluidics*, vol. 10, no. 2, pp. 389–401, 2011.
- [19] F. Sharipov and D. Kalempa, "Oscillatory Couette flow at arbitrary oscillation frequency over the whole range of the Knudsen number," *Microfluidics and Nanofluidics*, vol. 4, no. 5, pp. 363–374, 2008.
- [20] F. Sharipov and D. Kalempa, "Gas flow near a plate oscillating longitudinally with an arbitrary frequency," *Physics of Fluids*, vol. 19, no. 1, Article ID 017110, 2007.
- [21] J. H. Park, P. Bahukudumbi, and A. Beskok, "Rarefaction effects on shear driven oscillatory gas flows: a direct simulation Monte Carlo study in the entire Knudsen regime," *Physics of Fluids*, vol. 16, no. 2, pp. 317–330, 2004.
- [22] N. G. Hadjiconstantinou, "Oscillatory shear-driven gas flows in the transition and free-molecular-flow regimes," *Physics of Fluids*, vol. 17, no. 10, Article ID 100611, 2005.
- [23] D. R. Emerson, X. J. Gu, S. K. Stefanov, S. Yuhong, and R. W. Barber, "Nonplanar oscillatory shear flow: from the continuum to the free-molecular regime," *Physics of Fluids*, vol. 19, no. 10, Article ID 107105, 2007.
- [24] T. Doi, "Numerical analysis of oscillatory Couette flow of a rarefied gas on the basis of the linearized Boltzmann equation," *Vacuum*, vol. 84, no. 5, pp. 734–737, 2009.
- [25] P. Taheri, A. S. Rana, M. Torrilhon, and H. Struchtrup, "Macroscopic description of steady and unsteady rarefaction effects in boundary value problems of gas dynamics," *Continuum Mechanics and Thermodynamics*, vol. 21, no. 6, pp. 423–443, 2009.
- [26] W. C. Tang, T. C. H. Nguyen, and R. T. Howe, "Laterally driven polysilicon resonant microstructures," *Sensors and Actuators*, vol. 20, no. 1-2, pp. 25–32, 1989.
- [27] A. Frangi, A. Ghisi, and L. Coronato, "On a deterministic approach for the evaluation of gas damping in inertial MEMS in the free-molecule regime," *Sensors and Actuators A*, vol. 149, no. 1, pp. 21–28, 2009.
- [28] A. H. Khater and A. E. El-Sharif, "Analytical solutions of the Rayleigh flow problem for a rarefied gas of a nonhomogeneous system of charged particles," *Physica A*, vol. 150, no. 3, pp. 592–613, 1988.
- [29] A. H. Khater and A. E. El-Sharif, "Analytical solutions of the Rayleigh flow problem for a highly rarefied gas of a homogeneous system of charged particles," *Astrophysics and Space Science*, vol. 146, no. 1, pp. 157–162, 1988.
- [30] E. M. Purcell, *Electricity and Magnetism*, McGraw-Hill, Singapore, 3rd edition, 1965.
- [31] P. L. Bhatnagar, E. P. Gross, and M. Krook, "A model for collision processes in gases. I. Small amplitude processes in charged and neutral one-component systems," *Physical Review*, vol. 94, no. 3, pp. 511–525, 1954.
- [32] J. D. Huba, *NRL Plasma Formulary*, Navel Research Laboratory, Washington, DC, USA, 2011.
- [33] S. I. Braginskii, "Transport processes in a plasma," in *Reviews of Plasma Physics*, vol. 1, p. 205, Consultants Bureau, New York, NY, USA, 1965.
- [34] I. H. Hutchinson, *Introduction to Plasma Physics*, 2001, <http://silas.psfc.mit.edu/introplasma/index.html>.
- [35] T. J. M. Boyd and J. J. Sanderson, *The Physics of Plasmas*, Cambridge University Press, New York, NY, USA, 2003.
- [36] H. Grad, "On the kinetic theory of rarefied gases," *Communications on Pure and Applied Mathematics*, vol. 2, pp. 331–407, 1949.
- [37] L. Lees, "Kinetic theory description of rarefied gas flow," *Journal of the Society for Industrial and Applied Mathematics*, vol. 13, pp. 278–311, 1965.
- [38] L. Lees and C. Y. Liu, "Kinetic-theory description of conductive heat transfer from a fine wire," *The Physics of Fluids*, vol. 5, pp. 1137–1148, 1962.
- [39] E. Wasserstrom, C. H. Su, and R. F. Probstein, "Kinetic theory approach to electrostatic probes," *Physics of Fluids*, vol. 8, no. 1, pp. 56–72, 1965.
- [40] A. G. El-Sakka, R. A. Abdellatif, and S. A. Montasser, "Free molecular flow of rarefied gas over an oscillating plate under a periodic external force," *Astrophysics and Space Science*, vol. 109, no. 2, pp. 259–270, 1985.
- [41] J. Gratton, S. M. Mahajan, and F. Minotti, *Non Newtonian Gravity Creeping Flow*, International Centre for Theoretical Physics, Trieste, Italy, 1988.

- [42] G. Nugroho, A. M. S. Ali, and Z. A. Abdul Karim, "Toward a new simple analytical formulation of Navier-Stokes equations," *World Academy of Science*, vol. 39, pp. 110–114, 2009.
- [43] F. Sharipov, "Reciprocal relations based on the non-stationary Boltzmann equation," *Physica A*, vol. 391, no. 5, pp. 1972–1983, 2012.
- [44] P. Ván, "Thermodynamic stability of dia- and paramagnetic materials," *Periodica Polytechnica*, vol. 42, no. 2, pp. 97–102, 1998.
- [45] V. S. Galkin, "Application of the Chapman-Enskog method to the case of a binary two-temperature gas mixture," *Izvestiya Akademii Nauk SSSR. Mekhanika Zhidkosti i Gaza*, vol. 2, no. 6, pp. 38–41, 1971.
- [46] C. O. Bennett and J. E. Myers, *Moment, Heat and Mass Transfer*, McGraw-Hill, Singapore, 3rd edition, 1988.
- [47] A. G. Sitenko, *Electromagnetic Fluctuation in Plasma*, Academic Press, New York, NY, USA, 1967.

## Research Article

# DSMC Prediction of Particle Behavior in Gas-Particle Two-Phase Impinging Streams

Min Du,<sup>1,2</sup> Changsui Zhao,<sup>2</sup> Bin Zhou,<sup>3</sup> and Yingli Hao<sup>3</sup>

<sup>1</sup> School of Energy and Power Engineering, Jiangsu University, Zhenjiang 212013, China

<sup>2</sup> Key Laboratory of Energy Thermal Conversion and Control of Ministry of Education, School of Energy and Environment, Southeast University, Nanjing 210096, China

<sup>3</sup> Institute of Space Science and Technology, Southeast University, Nanjing 210096, China

Correspondence should be addressed to Min Du; [dumin@mail.uj.edu.cn](mailto:dumin@mail.uj.edu.cn) and Changsui Zhao; [cszhao@seu.edu.cn](mailto:cszhao@seu.edu.cn)

Received 30 May 2013; Revised 30 September 2013; Accepted 30 September 2013

Academic Editor: Waqar Khan

Copyright © 2013 Min Du et al. This is an open access article distributed under the Creative Commons Attribution License, which permits unrestricted use, distribution, and reproduction in any medium, provided the original work is properly cited.

Devices with impinging streams have been employed in various fields of chemical engineering, as a means of intensifying heat and mass transfer processes. The particle behavior in gas-particle two-phase impinging streams (GPISs), which is of essential importance for the research of transfer processes, was simulated by an Eulerian-Lagrangian approach in this paper. Collisional interaction of particles was taken into account by means of a modified direct simulation Monte Carlo (DSMC) method based on a Lagrangian approach and the modified Nanbu method. A quantitative agreement was obtained between the predicted results and the experimental data in the literature. The particle motion behavior and the distributions of particle concentration and particle collision positions were presented reasonably. The results indicate that the particle distribution in GPIS can be divided into three zones: particle-collision zone, particle-jetting zone, and particle-scattering zone. Particle collisions occur mainly in the particle-collision zone, which obviously results in a few particles penetrating into the opposite stream. The interparticle collision rate and the particle concentration reach their maximum values in the particle-collision zone, respectively. The maximum value of the particle concentration increases with the increasing inlet particle concentration according to a logarithmic function. The interparticle collision rate is directly proportional to the square of local particle concentration.

## 1. Introduction

The earliest emergence of impinging streams (ISs) can be traced back to the development and application of the Koppers-Totzek gasifier in 1953, and its scientific concept was proposed by Elperin [1] in the early 1960s. In an original gas-particle two-phase IS (GPIS), two gas-particle streams impinge against each other at high velocity. Particles from one stream penetrate into the other, which increases the relative velocity between the particles and the gas and prolongs the mean residence time of particles. This phenomenon yields the effect of intensifying the interphase heat and mass transfer in particulate systems [2]. Therefore, the GPIS devices have a broad application in many industrial processes, such as coal gasification, combustion, and drying [3]. The particle behavior in GPIS is of essential importance for research of the transfer processes; however, it is difficult to study by

experimental means. This study will focus on the particle behavior in GPIS, such as particle motion and particle collision, from a viewpoint of mathematical modeling.

There are two classical models in simulation of gas-particle flow, the Eulerian-Eulerian two-fluid model which treats particles as a continuous phase and the Eulerian-Lagrangian particle trajectory model which tracks individual particles. For the former model, it is difficult to give different characteristics of particle motion, interparticle collisions, and interactions between gas and particles in different zones in GPIS, because this model is based on all kinds of hypotheses. Therefore, the particle trajectory model, which needs fewer assumptions, is used in this study to calculate the gas turbulence and the motion of individual particle. On the other hand, an important character in GPIS is the severe interparticle interaction which plays a significant role in the characteristics of the particle motion and concentration

distribution. Therefore, the effect of collisions between particles should be taken into consideration in addition to the particle-fluid interaction in the numerical study of GPIS.

Many models have been reported for GPIS. In earlier studies, Kitron et al. [4] applied the particle Boltzmann transport equation [5, 6] including interparticle collisions to the study of GPIS. The Monte Carlo method was then used to solve this equation to obtain the velocity distribution of particle phase. However, the solution process of this method was too complex to be applied to the engineering practice. Guo et al. [7] and Ni et al. [8] used a Markov chain stochastic model to predict the residence time distribution of gas and particle in an opposed multiburner (OMB) gasifier. Other researchers [9–13] proposed various single-particle dynamics models to analyze the motion behavior of single particles in GPIS. These models neglected the interaction between particles and cannot give the particle collision effect.

The direct simulation Monte Carlo (DSMC) method, based on a Lagrangian approach developed in rarefied gas dynamics for handling collisions of a large number of gas molecules [14, 15], is an effective method of dealing with particle motion and collisions in dense gas-particle two-phase flow [16, 17]. The authors of this paper first applied the DSMC method, called as the traditional DSMC method in this paper, to GPIS to deal with the interparticle collision with acceptable computational cost [18]. Li et al. [19] then established a 3D model of the impinging zone of an OMB gasifier with DSMC method. This model reveals the concentration and the mean velocity profiles of particles in the impinging zone. Nevertheless, the particle flow has its own characteristics in GPIS, such as nonuniform distributions of particle concentration and particle collision positions, and a period of short time required for a particle to pass through the impinging zone. According to these characteristics of multiple spatial scales and multiple time scales, the DSMC method is modified to be more suitable to the numerical study of GPIS as in our earlier work [20]. This modified DSMC method is not restricted to flow field cells in the calculation of particle motion and collisions, and the particle time step in this method is adaptive and calculated using local particle parameters, such as the particle concentration and the velocities of particles nearby. In this work, this modified DSMC method is validated quantitatively using experimental results in the literature. Then, this method is applied to the numerical study of the particle behavior in GPIS. The distributions of particle concentration and particle collision positions are analyzed based on the calculation results. More specifically, the effect of the inlet particle mass flow rate will also be given. These results lay the foundations for further heat and mass transfer study in GPIS.

## 2. Mathematical Model

Real processes in practical engineering GPIS are very complex generally, which include multiphase flow, heat and mass transfer, and chemical reactions sometimes. To simplify the issue, the following assumptions are made in the present modeling: (1) heat and mass transfer is ignored in flow

process; (2) no chemical reactions are considered; and (3) particles are treated as rigid hard spheres with the same diameter.

*2.1. Gas-Particle Two-Phase Flow.* An Eulerian-Lagrangian approach is adopted to describe the gas-particle two-phase flow in GPIS as mentioned above. The interactions between gas phase and particle phase are determined by means of Newtonian third law. Therefore, four-way coupling between discrete phase and continuous phase is carried out. The key features of the mathematical model are briefly described as follows.

*2.1.1. Governing Equations for Gas Phase.* The gas flow field in GPIS is generally a turbulent flow field with backflows, and it is calculated using the realizable  $k - \varepsilon$  model [21] in this simulation. In this model, the conservation equations for mass and momentum can be written as follows:

$$\frac{\partial \rho_g}{\partial t} + \nabla \cdot (\rho_g \mathbf{u}) = 0, \quad (1)$$

$$\frac{\partial (\rho_g \mathbf{u})}{\partial t} + \nabla \cdot (\rho_g \mathbf{u} \mathbf{u}) = -\nabla p + \nabla \cdot (\boldsymbol{\tau}) + \rho_g \mathbf{g} + \mathbf{F}_g, \quad (2)$$

where  $\mathbf{F}_g$  is the external body forces that arise from interaction with the particle phase, which results in the momentum exchanges between the gas and particle phases. And  $\mathbf{F}_g$  is calculated from the reverse action of particles. To close (2), the modeled transport equations for the turbulence kinetic energy,  $k$ , and its dissipation rate,  $\varepsilon$ , are

$$\begin{aligned} \frac{\partial (\rho_g k)}{\partial t} + \nabla \cdot (\rho_g k \mathbf{u}) &= \nabla \cdot \left[ \left( \frac{\mu + \mu_t}{\sigma_k} \right) \nabla k \right] + G_k + G_b \\ &\quad - \rho_g \varepsilon - Y_M, \\ \frac{\partial (\rho_g \varepsilon)}{\partial t} + \nabla \cdot (\rho_g \varepsilon \mathbf{u}) &= \nabla \cdot \left[ \left( \frac{\mu + \mu_t}{\sigma_\varepsilon} \right) \nabla \varepsilon \right] \\ &\quad + \frac{\rho_g C_1 S \varepsilon - \rho_g C_2 \varepsilon^2}{k + \sqrt{\nu \varepsilon}} + \frac{C_{1\varepsilon} C_{3\varepsilon} G_b \varepsilon}{k}, \end{aligned} \quad (3)$$

where  $C_1 = \max[0.43, \eta/(\eta + 5)]$ ;  $\eta = Sk/\varepsilon$ ;  $\mu_t = \rho_g C_\mu k^2/\varepsilon$ ;  $S = (2S_{ij}S_{ij})^{1/2}$ ; and  $G_k = \mu_t S^2$  represents the generation of turbulence kinetic energy due to the mean velocity gradients.  $G_b$  is the generation of turbulence kinetic energy due to buoyancy.  $Y_M$  represents the contribution of the fluctuating dilatation in compressible turbulence to the overall dissipation rate. The model constants are  $C_{1\varepsilon} = 1.44$ ,  $C_2 = 1.9$ ,  $\sigma_k = 1.0$ , and  $\sigma_\varepsilon = 1.2$  [22].

*2.1.2. Particle Motion Equations.* In GPIS, the spherical particles are entrained by gas flow. The translational motion of a particle in the gas phase is governed by Newton's second law of motion and can be written as

$$\frac{m_p d\mathbf{v}_p}{dt} = \mathbf{F}_d + \mathbf{F}, \quad (4)$$

where  $\mathbf{F}$  is an additional force term used in the simulation, including virtual mass force, pressure gradient force, and Saffman's lift force. In addition,  $\mathbf{F}_d$  represents the drag force of gas phase acting on the particle which is the most important force acting on the particle calculated using the following equation:

$$\mathbf{F}_d = 0.125\pi D_p \mu C_d \text{Re} (\mathbf{u} - \mathbf{v}). \quad (5)$$

The drag coefficient,  $C_d$ , is determined by the following equation:

$$C_d = \begin{cases} \frac{24}{\text{Re}} \left(1 + \frac{1}{6} \text{Re}^{2/3}\right) & \text{Re} \leq 1000, \\ 0.424 & \text{Re} > 1000, \end{cases} \quad (6)$$

where  $\text{Re}$  is the relative Reynolds number, which is defined as

$$\text{Re} \equiv \frac{\rho_g D_p |\mathbf{u} - \mathbf{v}|}{\mu}. \quad (7)$$

**2.2. Interparticle Collision.** The modified DSMC method, based on a gridless approach and local time stepping with automatic adaption, is applied for modeling the interparticle collisions in GPIS here. The basic ideas of this method are as follows:

- (1) real particles are replaced by smaller number of sampled particles. And the trajectories of sampled particles are calculated. In this way, the computer memory and computation time can be saved significantly. This item is just the same as the traditional DSMC method;
- (2) sampled particle motion is decoupled into the movement and collision processes as the traditional DSMC method. Sampled particle movement obeys the single particle motion model, and the collision process follows the interparticle collision dynamics. In the modified DSMC method, the particle time step, that is, the time required for a particle in each movement, is adaptive, which is different from the traditional DSMC method;
- (3) collision pairs are found through the theory of collision probability instead of using trajectories as the traditional DSMC method. Nevertheless, the calculation of the collision probability between particles and the searching of collision pairs is based on the spherical region generated from the local particle parameters rather than the flow field cells.

To update the particle time step, the local collision mean-free path, that is, the average distance a particle travels between collisions with other moving particles, is calculated firstly using the following equation:

$$L = \frac{v_p}{v}, \quad (8)$$

where  $v_p$  is the velocity magnitude of the particle being tracked.  $v$  is the collision frequency, that is, the number of

collisions occurred in unit time, which is obtained according to the local distribution of particles. To satisfy the "principle of uncoupling" in the modified DSMC method, the particle time step  $\Delta t_p$  is given by

$$\Delta t_p = \min \left[ \frac{L}{3v_x}, \frac{L}{3v_y}, \frac{L}{3v_z} \right], \quad (9)$$

where  $v_x$ ,  $v_y$ , and  $v_z$  are components of particle velocity  $\mathbf{v}_p$ .  $\Delta t_g$  is the time step for gas phase.

In the modified DSMC method, the collision pairs are found through the spherical region, that is, searching scope, with the particle tracked being considered as center and  $r$  as its radius given below

$$r = \max [v_p \Delta t_p, v_{r,\max} \Delta t_p], \quad (10)$$

where  $v_{r,\max}$  is the maximum value of relative velocity between the particle being tracked and the sampled particles nearby. Then, the probability of collision between particle  $i$  being tracked and particle  $j$  during a time step  $\Delta t_p$  is calculated by

$$P_{ij} = \frac{0.25\pi (D_i + D_j)^2 |\mathbf{G}^{(0)}| n_{p,j} \Delta t_p}{V}, \quad (11)$$

where  $D_i$  and  $D_j$  are the diameters of particle  $i$  and particle  $j$ , respectively.  $\mathbf{G}^{(0)}$  is the relative velocity vector between particles  $i$  and  $j$ .  $n_{p,j}$  is the real particle number represented by the sampled particle  $j$ .  $V$  is the volume of the searching scope and equal to  $4\pi r^3/3$ .

The modified Nanbu method [23] is used to search a candidate collision partner  $j$ , which probably collide with particle  $i$  in the searching scope during a time step  $\Delta t_p$ , and decide whether the collision occurs. First, a random number  $R$  with a uniform distribution from zero to unity is extracted from a generator. The candidate collision partner  $j$  is selected according to

$$j = \text{int} [R \times N] + 1, \quad j \neq i, \quad (12)$$

where  $\text{int}[R \times N]$  is defined as the integer part of  $R \times N$  and  $N$  is the total number of all sampled particles in the searching scope. If the relation

$$R > \frac{j}{N} - P_{ij} \quad (13)$$

is satisfied, particle  $i$  would collide with particle  $j$  during the time step  $\Delta t_p$ , and the velocities of particles  $i$  and  $j$  are replaced with the postcollision velocities, but without changing their positions. The post-velocities of the two particles are as follows:

$$\text{when } (\mathbf{n} \cdot \mathbf{G}^{(0)} / |\mathbf{G}_{ct}^{(0)}|) < 1 / (\xi(1 + e))$$

$$\mathbf{v}_i = \frac{\mathbf{v}_i^{(0)} - (\mathbf{n} + \xi \mathbf{t})(\mathbf{n} \cdot \mathbf{G}^{(0)})(1 + e) m_j}{m_i + m_j}, \quad (14)$$

$$\mathbf{v}_j = \frac{\mathbf{v}_j^{(0)} + (\mathbf{n} + \xi \mathbf{t})(\mathbf{n} \cdot \mathbf{G}^{(0)})(1 + e) m_i}{m_i + m_j},$$

when  $(\mathbf{n} \cdot \mathbf{G}^{(0)})/|\mathbf{G}_{ct}^{(0)}| \geq 1/(\xi(1+e))$

$$\mathbf{v}_i = \frac{\mathbf{v}_i^{(0)} - [(1+e)(\mathbf{n} \cdot \mathbf{G}^{(0)})\mathbf{n} + |\mathbf{G}_{ct}^{(0)}|\mathbf{t}]m_j}{m_i + m_j},$$

$$\mathbf{v}_j = \frac{\mathbf{v}_j^{(0)} + [(1+e)(\mathbf{n} \cdot \mathbf{G}^{(0)})\mathbf{n} + |\mathbf{G}_{ct}^{(0)}|\mathbf{t}]m_i}{m_i + m_j},$$
(15)

where  $\mathbf{n}$  is the normal unit vector directed from particle  $i$  to particle  $j$  at the moment on contact.  $\mathbf{t}$  is the unit vector in the tangential direction.  $\mathbf{G}_{ct}^{(0)}$  is the tangential component of the relative velocity.

**2.3. Numerical Solution.** The numerical solutions of the gas-particle two-phase flow, including the governing equations for gas continuous phase, motion equations for sampled particles, and the momentum exchanges between two phases, are obtained using the CFD code FLUENT. The calculations of particle time step and interparticle collision process are performed using self-written program in VC language, which is taken as self-defined function (UDF) embedded in the calculation of gas-particle two-phase flow in GPIS. To obtain the rapid convergence of the calculation of gas-solid two-phase flow, the gas flow field is calculated to be convergent first, and then the particles are introduced. When a particle reaches the outlet, the particle tracking is terminated. If the number of particles in GPIS does not change greatly, the calculation is assumed to be convergent.

### 3. Model Validation

To validate the established model, two experimental cases (Case 1 and Case 2) in the literature [24] are calculated first. Figure 1 shows the schematic diagram of the experimental apparatus with two opposed nozzles. The inner diameter of either nozzle was 8 mm. The distance between two nozzles was 140 mm. Particles were conveyed by air into the nozzles. The parameters of the gas and particle phases injecting from nozzles for two cases are also summarized in Table 1.

The coordinate system is shown in Figure 1. The origin of the coordinate system is placed on the midpoint of the line connecting the two nozzles. The axial direction  $x$ -axis is on the horizontal line through nozzle axes and defined as positive rightward. The  $x$ -axis is called the axial line of the GPIS device. Figure 2 shows the meshed geometry for the calculation domain, and the domain is meshed with about 80000 hexahedral cells. The mesh refinement in the zone between two nozzles is carried out to raise the accuracy of gas phase solutions because of the big variation gradients of various variables in this zone. The minimum mesh size is about 1.3 mm.

Figure 3 shows the comparison between experimental and simulated dimensionless particle concentration profiles along the axial line, in which  $C_0$  is the particle concentration at the outlet of nozzle. It can be seen that the particle concentration decreases sharply with the increasing distance from the outlet of nozzle along the axial line because of dispersion, and it increases obviously near the center

TABLE 1: Conditions and parameters used in simulation.

Parameter	Value
Gas phase	
Gas type	Air
Inlet velocity	100 m/s
Apparatus	
Nozzle diameter, $d$	8 mm
Distance between nozzles, $l$	140 mm
Particle spray angle	14°
Mass ratio of gas particle	1
Particle phase	
Particle shape	Sphere
Density	2500 kg/m <sup>3</sup>
Restitution coefficient, $e$	0.9
Friction coefficient, $\xi$	0.2
Inlet velocity	25 m/s (Case 1) 55 m/s (Case 2)
Average diameter, $D_p$	77 $\mu$ m (Case 1) 33 $\mu$ m (Case 2)

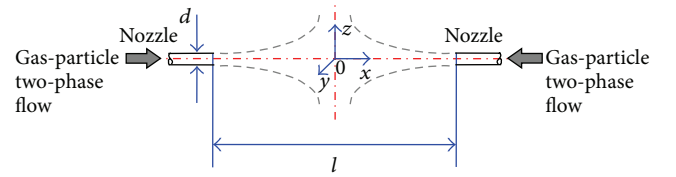


FIGURE 1: Schematic diagram of the experimental apparatus.

because of the particle collisions. The predicted results of the particle concentration are in reasonable agreement with the experimental data, which indicates the validity of the present method.

### 4. Results and Discussion

Figure 4 shows the sketch of a laboratory-scale GPIS device with two opposed nozzles [25]. The impinging chamber is made of stainless steel of 0.5 m in diameter. The distance between the two nozzles ( $l$ ) is set to 200 mm; both nozzles have a diameter of 42 mm. The outlet diameter of the impinging chamber is relatively small to collect particles. The following part of work is to model the particle behavior in the impinging zone. To reduce the computational cost, the calculation domain is located near the nozzles framed by the black dash-line rectangle as shown in Figure 4. The calculation domain is meshed with hexahedral cells. The mesh refinement in the zone near the height of nozzles is carried out to raise the accuracy of gas phase solutions. In order to obtain grid-independent solutions, several mesh sizes, that is, 62740, 142394, and 274836, were tested. The results of the particle concentration along the axial line computed using 142394 and 274836 meshes were closer to each other; the maximum differences in the predicted results were indeed less than 10%. On the other hand, finer meshes required excessive computational time; therefore, mesh size of 142394 was selected in this study (see Figure 4).

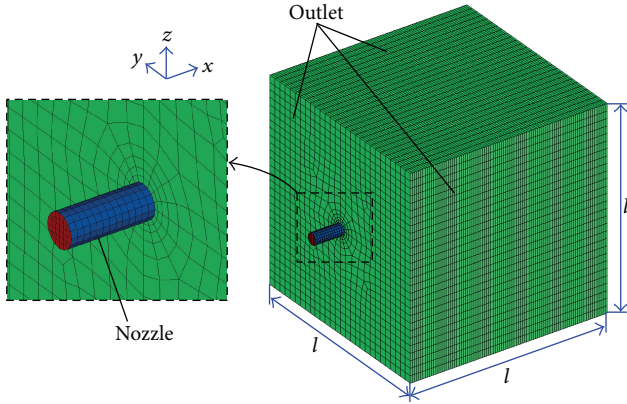
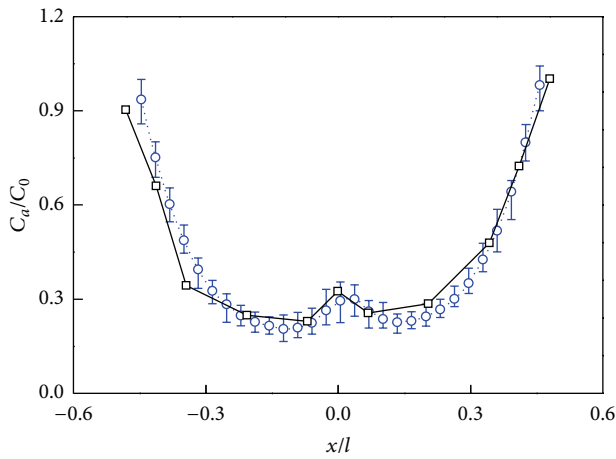
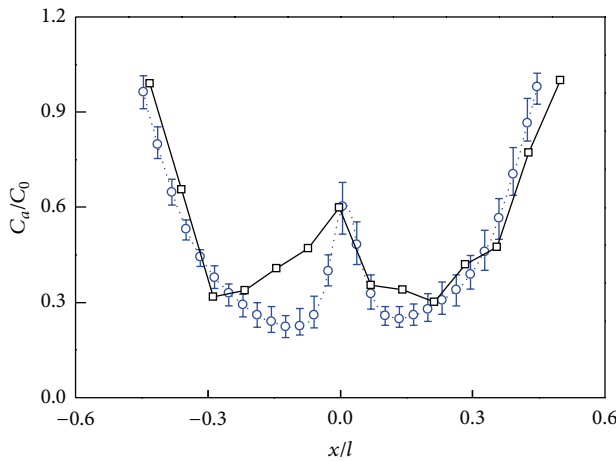


FIGURE 2: Grid model and the drawing of partial enlargement.



···· Simulation results  
 —□— Experimental results

(a) Case 1



···· Simulation results  
 —□— Experimental results

(b) Case 2

FIGURE 3: Comparison between experimental and simulated dimensionless particle concentration profiles along the axial line.

TABLE 2: Conditions and parameters used in simulation.

Parameter	Value
Size of computational domain	
Distance between nozzles, $l$	400 mm
Nozzle diameter, $d$	42 mm
Calculating parameter [19]	
Restitution coefficient, $e$	0.9
Friction coefficient, $\xi$	0.2
Gas time step, $\Delta t_g$	$1 \times 10^{-4}$ s
Particle spray angle <sup>a</sup>	$0^\circ$
Initial condition for inlet <sup>b</sup>	
Particle inlet velocity	20 m/s
Particle density	2450 kg/m <sup>3</sup>
Particle average diameter	200 $\mu$ m
Gas type	Air
Gas inlet velocity	25 m/s
Gas density	1.2 kg/m <sup>3</sup>
Inlet particle mass flow rate (single nozzle), $W_p$	0.01, 0.02, 0.027, 0.035, 0.04, 0.045, 0.05, 0.054, 0.06, 0.07, 0.08, 0.09, 0.1, 0.11, 0.12, 0.14, 0.16, 0.18, 0.2, 0.25, 0.3, 0.4, 0.5, 0.6, 0.7, 0.8, 0.9, 1 kg/s
Initial condition for outlet	
Pressure	101325 Pa

<sup>a</sup>To reduce the effect of dispersion on the particle behavior, the particle spray angle is set to  $0^\circ$ .

<sup>b</sup>The gas-solid two-phase flow is fully developed at the outlet of nozzle.

The parameters used in the simulation are summarized in Table 2 with reference to the parameters used practically. The boundary conditions are “velocity-inlet” and “outflow” for inlet and outlet, respectively. All walls are treated as nonslip boundaries in the lateral direction for the gas phase with standard wall function. To obtain the rapid convergence of the calculation of gas-solid two-phase flow, the gas flow field is calculated to be convergent first, and then the particles are introduced. When a particle reaches the outlet, the particle tracking is terminated. If the number of particles in GPIS does not change greatly, the calculation is assumed to be convergent.

The coordinate system is shown in Figure 4. The origin of the coordinate system is placed on the midpoint of the line connecting two nozzles. The rightward  $x$ -axis on the nozzle axes is called the axial line of the GPIS device. In addition, coordinate surface  $yz$  is called impinging plane.

**4.1. Particle Motion Behavior.** Figure 5 shows the particle position distribution at different moments for the case with  $W_p = 0.2$  kg/s in which the colormap denotes the particle residence time, and Figure 6 shows the velocity distribution of particles between two nozzles. From those two figures, it is found that the particle velocity remains about the same before the time point 0.01 s at which two particle flows

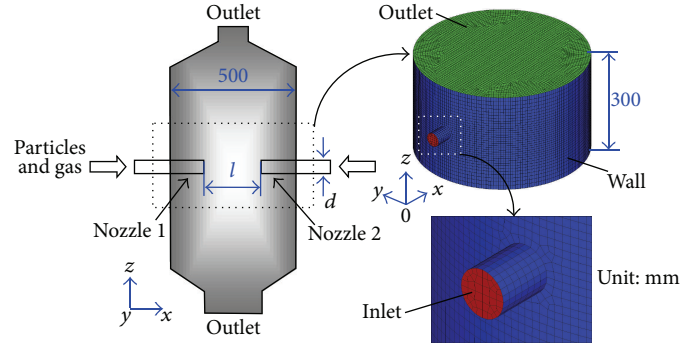


FIGURE 4: Sketch of a laboratory-scale GPIS device and grid meshing of calculation domain.

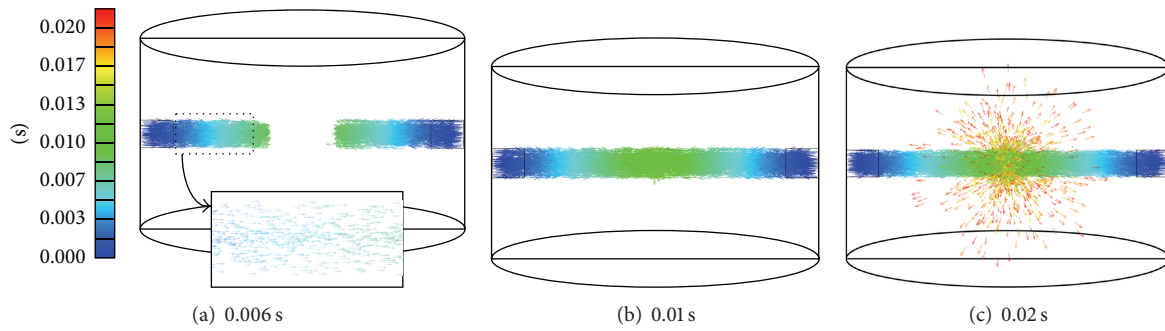


FIGURE 5: Particle position distributions at different time moments,  $W_p = 0.2 \text{ kg/s}$ .

start to meet each other near the origin of the coordinate system. This is mainly because that the collision between particles is caused by difference in particle velocities. Before this time point, particles move towards the impinging plane along the axial direction. The velocity difference between neighboring particles is small, which results in the small interparticle collision probability. In addition, the change in particle velocities is not obvious due to the small impacting impulse if two particles collide with each other.

When two gas-particle flows with a great number of particles meet each other at 0.01 s in the area around the origin of the coordinate system, particles from the opposite streams collide with each other violently. This area is called impingement zone generally. The collisions in this zone increase the velocity components in the impinging plane and decrease the axial velocity components of particles. Therefore, particles cannot pass through this area and penetrate into the opposite stream easily. These particles spread out from this area after several collisions as the particle position distribution at 0.02 s shown in Figure 5(c).

**4.2. Particle Concentration Distribution.** Figure 7 shows the residence time distribution of particles between two nozzles. It is found that the violent particle collisions increase the particle residence time in the impingement zone. In other words, the violent particle collision makes the particles accumulate in this zone, which results in the highest particle concentration near the origin as shown in Figure 8. And the high particle concentration strengthens the particle collision

in turn. After particles leave the impingement zone in all directions, the particle concentration decreases drastically because of the increasing volume occupied by the particles.

Figure 9 shows the particle concentration profiles along the axial line for different inlet particle mass flow rates. It can be seen that particle concentration along the axial line increases with the increasing inlet particle mass flow rate reasonably. For a certain case, the particles injected into the device move towards the impinging plane along the axial line and the collisions with neighboring particles obviously can not change the particle paths as mentioned above. Therefore, the particle concentration does not change significantly along the axial line in the areas between either the nozzle or the impingement zone. In the impingement zone, the particle concentration increases sharply and reaches a maximum value near the origin due to the particle collisions. The relation between the maximal particle concentration  $C_{\max}$  in the impingement zone and the inlet particle concentration  $C_0$  is drawn in Figure 10. It can be seen that the maximum value  $C_{\max}$  of particle concentration increases sharply with the increasing inlet particle concentration  $C_0$  for lower  $C_0$ . The relative particle concentration, ratio of  $C_{\max}$  and  $C_0$ , also increases sharply at first. With the further increase in  $C_0$ , the increase in  $C_{\max}$  with  $C_0$  tends to slow down, and the ratio of  $C_{\max}$  and  $C_0$  decreases obviously. The change of  $C_{\max}$  with  $C_0$  can be fitted by a logarithmic function with a correlation coefficient 0.9860 as follows:

$$C_{\max} = a \ln(C_0 + b) - c, \quad (16)$$

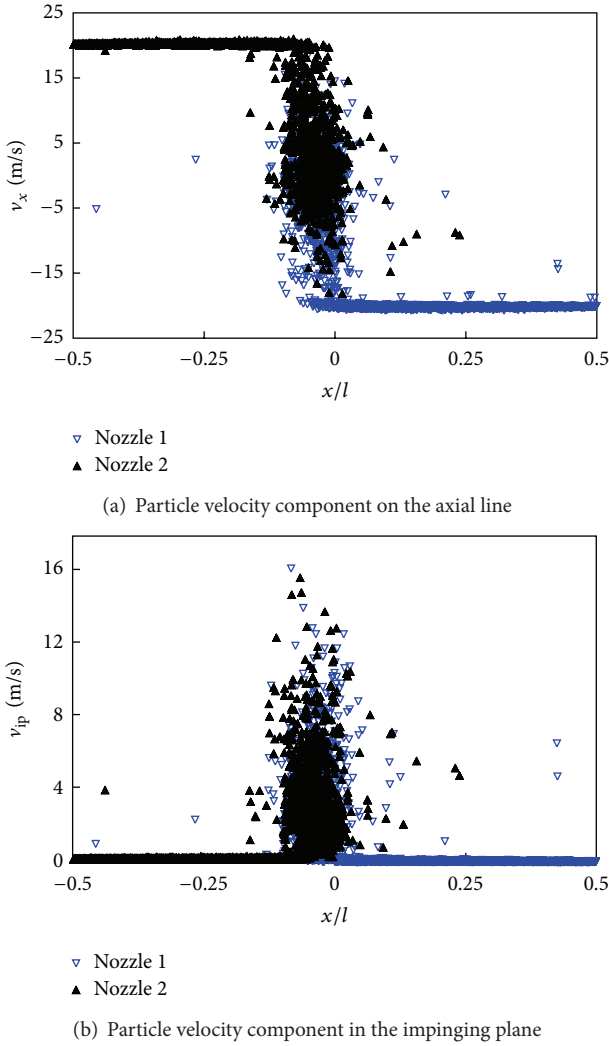


FIGURE 6: Particle velocity distribution between two nozzles,  $W_p = 0.2 \text{ kg/s}$ ,  $t = 0.8 \text{ s}$ .

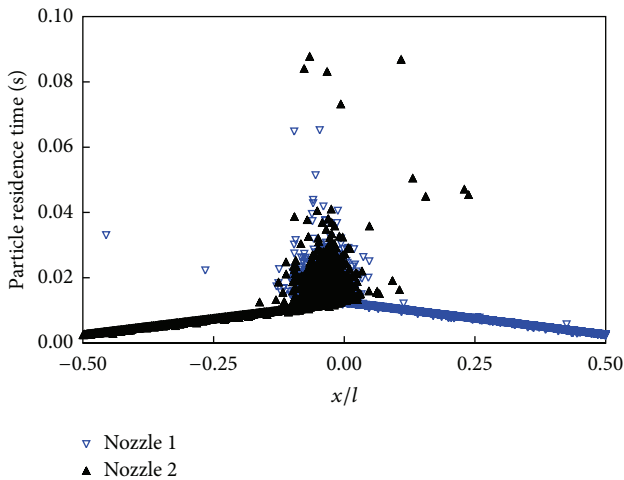


FIGURE 7: Particle residence time distribution between two nozzles,  $W_p = 0.2 \text{ kg/s}$ ,  $t = 0.8 \text{ s}$ .

where  $a = 46.317$ ,  $b = 1.6264$ , and  $c = 22.527$ . The ratio of  $C_{\max}$  with  $C_0$  reaches the maximum value as  $C_0 = 7.2 \text{ kg/m}^3$ .

**4.3. Particle Collision Position Distribution.** Figure 11 shows the distribution of particle collision positions in 0.01 s for the case with  $W_p = 0.09 \text{ kg/s}$ , where one red point represents one collision occurring there. In the 0.01 s, there are 184059 collisions between sampled particles in total. According to the distribution of particle collision positions, the particle distribution can be divided into three zones: particle-collision zone, particle-jetting zone, and particle-scattering zone. The statistical result shows that particle collisions occur mainly in the particle-collision zone in which the number of collisions accounts for about 90% of the total. The particle-collision zone is an ellipsoid whose center is located at the origin of coordinates. The shorter axis on  $x$ -axis and the longer axis on  $y$ -axis of the ellipsoid are about  $0.075l$  and  $0.1l$  for the case with  $W_p = 0.09 \text{ kg/s}$ , respectively. In this zone, particles from the opposite streams collide with each other violently, which causes two results. First, particle collisions make the particles accumulate in this zone, which results in the highest particle concentration shown in Figure 8. Second, particle collisions make the particles spread out from this zone to the whole device. Between the particle-collision zone and two nozzles, the two long and narrow zones are called particle-jetting zone. Although the particle concentration in this zone is high, the smaller collision probability between particles caused by small velocity difference results in the smaller number of collisions in these two zones. The broad zone outside the particle-collision zone and the particle-jetting zones is called the particle-scattering zone. Particles spreading out from the particle-collision zone scatter quickly in this zone. The collision probability between particles in this zone is small because of the low particle concentration shown in Figure 8. Therefore, there are only a few collisions occurring near the particle-collision zone and few collisions occur in the area away from the particle-collision zone.

Figure 12 shows the profiles of interparticle collision rate  $N_c$  along the axial line for different inlet particle mass flow rates, where the interparticle collision rate  $N_c$  is defined as the number of interparticle collisions per unit time per unit volume. It is found that the profiles of interparticle collision rate along the axial line for different inlet particle mass flow rates are similar to those of particle concentration shown in Figure 9, and the maximum value of the interparticle collision rate is reached in the particle-collision zone due to the violent collisions. This phenomenon indicates that the interparticle collision rate has direct relation with the particle concentration, and the violent particle collisions occur in the particle-collision zone with high particle concentration. Figure 13 shows the relation between the average interparticle collision rate at the nozzle outlet and the local particle concentration for different cases. The fitting curve is as follows:

$$N_{c,0} = a \times C_0^{2 \pm 0.00316}, \quad (17)$$

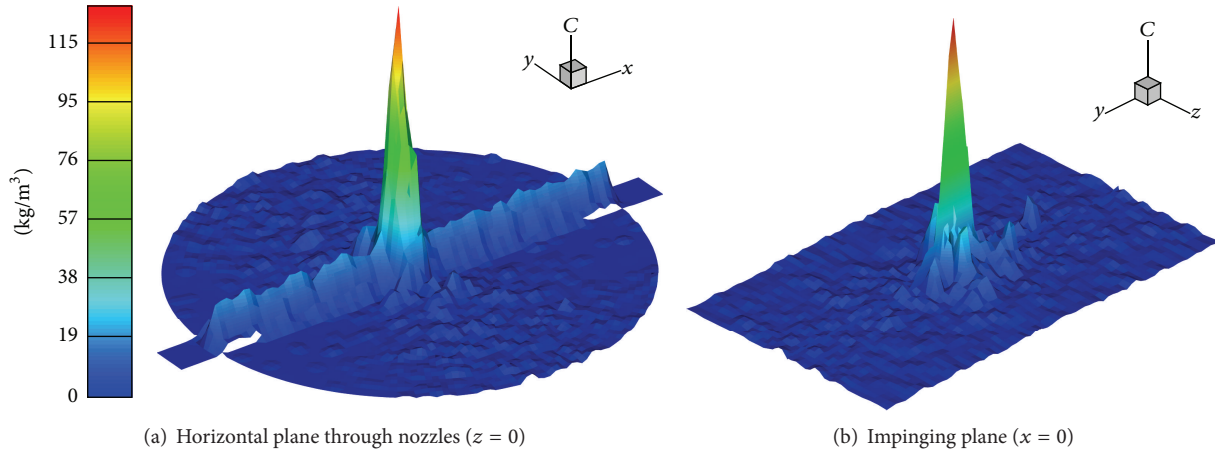


FIGURE 8: Particle concentration distribution,  $W_p = 0.2 \text{ kg/s}$ ,  $t = 0.8 \text{ s}$ .

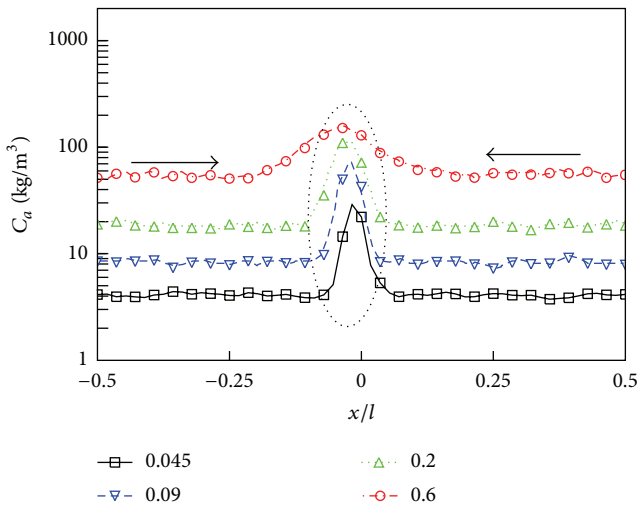


FIGURE 9: Particle concentration profiles along the axial line for different inlet particle mass flow rates.

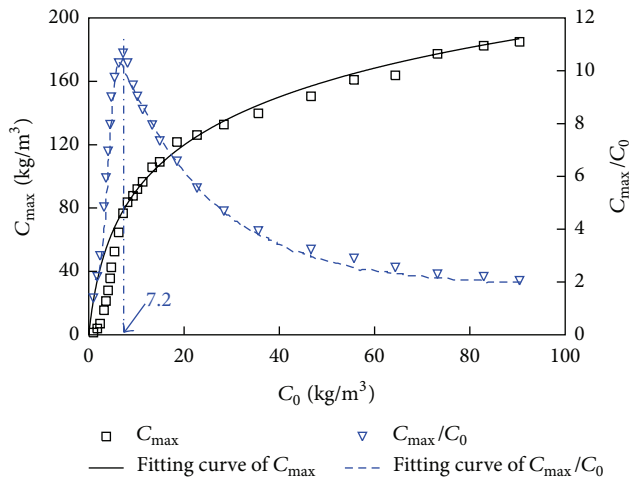


FIGURE 10: Maximal particle concentration in impingement zone versus inlet particle concentration.

where  $a$  is a constant and equal to  $1.48 \times 10^8$ . The correlation coefficient of this fitting curve is 0.9966. From this formula, it can be seen that the interparticle collision rate is directly proportional to the square of particle concentration, which is in accordance with the statement in the literature [26].

### 5. Conclusions

The modified direct simulation Monte Carlo (DSMC) method is applied to predict the particle behavior in GPIS in this work. The main results are as follows:

- (1) according to the distribution of particle collision positions, the particle distribution can be divided into three zones: particle-collision zone, particle-jetting zone, and particle-scattering zone. Particle collisions occur mainly in the particle-collision zone, and the distribution of particle collision positions is very similar to the particle concentration distribution;
- (2) for GPIS, a few particles penetrate into the opposite stream due to the violent particle collisions and almost all particles spread out from the particle-collision zone;
- (3) the particle concentration and the interparticle collision rate along the axial line have a similar variation trend. They increase sharply and reach their maximum values near the origin in the particle-collision zone. The maximum value of the particle concentration increases with the increasing inlet particle concentration according to a logarithmic function. The interparticle collision rate is directly proportional to the square of local particle concentration.

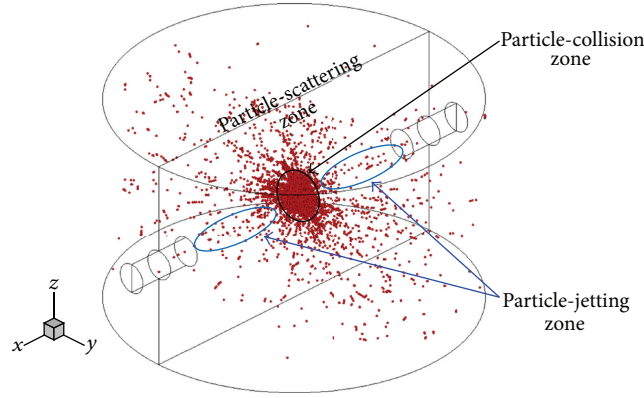


FIGURE 11: Statistical result of particle collision positions in 0.01 s,  $W_p = 0.09$  kg/s.

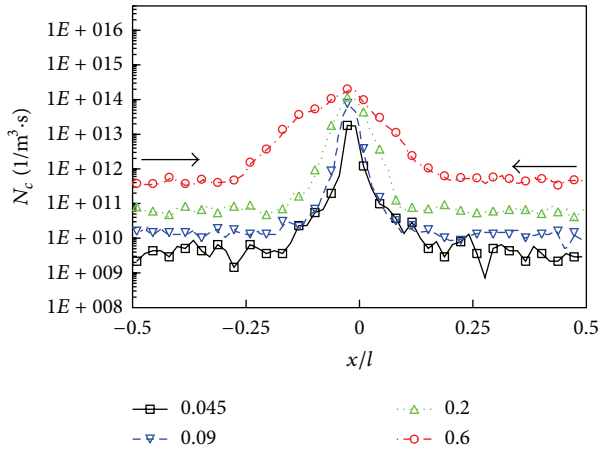


FIGURE 12: Profiles of interparticle collision rate  $N_c$  along the axial line for different inlet particle mass flow rates.

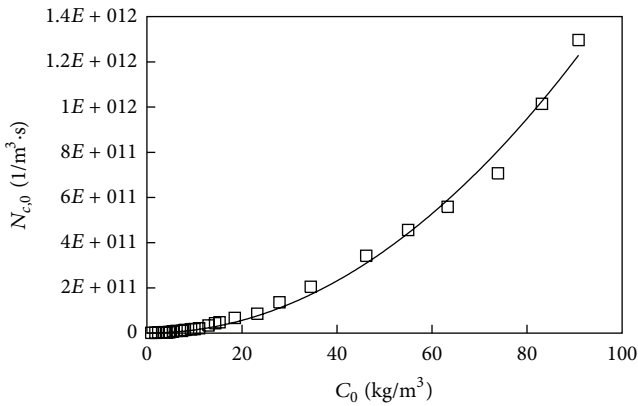


FIGURE 13: Interparticle collision rate at the nozzle outlet versus local particle concentration.

### Nomenclature

- $a, b, c$ : Constants in fitting curve
- $C$ : Particle concentration,  $\text{kg/m}^3$
- $C_1, C_2, C_{1\epsilon}, C_{3\epsilon}$ : Constants in turbulence model
- $C_a$ : Particle concentration on the axial line,  $\text{kg/m}^3$
- $C_d$ : Drag coefficient
- $D$ : Diameter of particle, m
- $d$ : Diameter of nozzle, mm
- $e$ : Coefficient of restitution
- $\mathbf{F}$ : Force vector, N
- $\mathbf{g}$ : Acceleration vector of gravity
- $\mathbf{G}$ : Relative velocity vector, m/s
- $k$ : Turbulence kinetic energy,  $\text{m}^2/\text{s}^2$
- $L$ : Collision mean-free path, m
- $l$ : Distance between nozzles, mm
- $m$ : Mass of particle, kg
- $N$ : The number of the sampled particles
- $N_c$ : Interparticle collision rate,  $1/\text{m}^3\text{-s}$
- $\mathbf{n}$ : Normal unit vector
- $n_p$ : Number of real particles represented by a sampled particle
- $p$ : Static pressure, Pa
- $P$ : Collision probability
- $R$ : Random number on interval  $[0, 1]$
- $\text{Re}$ : Relative Reynolds number
- $r$ : Radius of searching scope, m
- $t$ : Simulation time, s
- $\mathbf{t}$ : Tangential unit vector
- $\Delta t$ : Time step, s
- $\mathbf{u}$ : Gas velocity vector, m/s
- $u$ : Gas velocity magnitude, m/s
- $V$ : Volume of searching scope,  $\text{m}^3$
- $\mathbf{v}$ : Particle velocity vector, m/s
- $v$ : Particle velocity magnitude, m/s
- $W_p$ : Inlet particle mass flow rate for single nozzle, kg/s.

### Greek Letters

$\varepsilon$ :	Turbulent dissipation rate
$\mu$ :	Dynamic viscosity, kg/m-s
$\mu_t$ :	Turbulent viscosity, kg/m-s
$\xi$ :	Friction coefficient of Coulomb's friction law
$\rho$ :	Gas density, kg/m <sup>3</sup>
$\sigma_k, \sigma_\varepsilon$ :	Inverse effective turbulent Prandtl numbers for $k$ and $\varepsilon$
$\tau$ :	Stress tensor
$\nu$ :	Collision frequency.

### Superscripts

(0): Before the collision.

### Subscripts

0:	At nozzle outlet
$ct$ :	Tangential direction
$d$ :	Drag force
$g$ :	Gas phase
$i, j$ :	Sampled particle No.
$ip$ :	Impinging plane
$k$ :	Turbulent kinetic energy
max:	Maximum value
$p$ :	Particle
$r$ :	Relative velocity
$x, y, z$ :	Vector direction
$\varepsilon$ :	Turbulent dissipation rate.

### Acknowledgments

The financial supports from the National Natural Science Foundation of China (no. 50976024), the National Basic Research Program of China (no. 2010CB227002), the Natural Science Foundation of Jiangsu Province (no. BK20130520), and the Senior Expert Fund of Jiangsu University (no. 11JDG152) are greatly appreciated.

### References

- [1] I. T. Elperin, "Heat and mass transfer in opposing currents," *Journal of Engineering Physics*, vol. 6, pp. 62–68, 1961.
- [2] T. Kudra and A. S. Mujumdar, "Impingement stream dryers for particles and pastes," *Drying Technology*, vol. 7, no. 2, pp. 219–266, 1989.
- [3] T. Swasdisevi, S. Devahastin, S. Thanasookprasert, and S. Soponronnarit, "Comparative evaluation of hot-air and superheated-steam impinging stream drying as novel alternatives for paddy drying," *Drying Technology*, vol. 31, no. 6, pp. 717–725, 2013.
- [4] A. Kitron, T. Elperin, and A. Tamir, "Monte Carlo simulation of gas-solids suspension flows in impinging streams reactors," *International Journal of Multiphase Flow*, vol. 16, no. 1, pp. 1–17, 1990.
- [5] F. E. C. Culick, "Boltzmann equation applied to a problem of two-phase flow," *The Physics of Fluids*, vol. 7, pp. 1898–1904, 1964.
- [6] S. I. Pai, "Fundamental equations of a mixture of gas and small spherical solid particles from simple kinetic theory," *Revue Roumaine des Sciences Techniques*, vol. 19, pp. 605–621, 1974.
- [7] Q. Guo, Q. Liang, J. Ni, S. Xu, G. Yu, and Z. Yu, "Markov chain model of residence time distribution in a new type entrained-flow gasifier," *Chemical Engineering and Processing*, vol. 47, no. 12, pp. 2061–2065, 2008.
- [8] J. J. Ni, Q. F. Liang, Q. H. Guo, Z. Yu, and G. S. Yu, "Stochastic modeling of the particle residence time distribution in an opposed multi-burner gasifier," *Chemical Engineering and Technology*, vol. 31, no. 10, pp. 1487–1493, 2008.
- [9] A. Tamir, *Impinging Stream Reactors: Fundamental and Application*, Elsevier, Amsterdam, The Netherlands, 1994.
- [10] S. M. Hosseinalipour and A. S. Mujumdar, "Superheated steam drying of a single particle in an impinging stream dryer," *Drying Technology*, vol. 13, no. 5–7, pp. 1279–1303, 1995.
- [11] G. F. Carrier, F. E. Fendell, S. F. Fink IV, and C. N. Folley, "Particle transport in a counter-flow," *Combustion and Flame*, vol. 126, no. 3, pp. 1630–1639, 2001.
- [12] Y. T. Xu, H. Q. Tang, S. F. Ye, Z. P. Cai, Y. S. Xie, and Y. F. Chen, "Three dimensional numerical simulation of gas-solid flows in impinging streams reactor," *Computers and Applied Chemistry*, vol. 24, no. 11, pp. 1511–1515, 2007.
- [13] H. J. Liu, C. Zou, Z. W. Tian, and C. G. Zheng, "Motions of single particle in the impinging streams," *Journal of Huazhong University of Science and Technology*, vol. 35, no. 5, pp. 106–109, 2008.
- [14] F. J. Alexander and A. L. Garcia, "The direct simulation Monte Carlo method," *Computers in Physics*, vol. 11, no. 6, pp. 588–593, 1997.
- [15] G. A. Bird, *Gas Dynamics and the Direct Simulation of Gas Flows*, Oxford University Press, Oxford, UK, 1994.
- [16] L. Huilin, S. Zhiheng, J. Ding, L. Xiang, and L. Huanpeng, "Numerical simulation of bubble and particles motions in a bubbling fluidized bed using direct simulation Monte-Carlo method," *Powder Technology*, vol. 169, no. 3, pp. 159–171, 2006.
- [17] Y. Tsuji, T. Tanaka, and S. Yonemura, "Cluster patterns in circulating fluidized beds predicted by numerical simulation (discrete particle model versus two-fluid model)," *Powder Technology*, vol. 95, no. 3, pp. 254–264, 1998.
- [18] M. Du, Y. Hao, and X. Liu, "Application of DSMC method in large-scale gas-solid two-phase impinging streams," *CIESC Journal*, vol. 60, no. 8, pp. 1950–1958, 2009.
- [19] C. Li, Z. H. Dai, W. F. Li, J. L. Xu, and F. C. Wang, "3D numerical study of particle flow behavior in the impinging zone of an Opposed Multi-Burner gasifier," *Powder Technology*, vol. 225, pp. 118–123, 2012.
- [20] M. Du, C. Zhao, B. Zhou, H. Guo, and Y. Hao, "A modified DSMC method for simulating gas-particle two-phase impinging streams," *Chemical Engineering Science*, vol. 66, no. 20, pp. 4922–4931, 2011.
- [21] W. Q. Tao, *Numerical Heat Transfersecond*, Xi'an Jiaotong University Press, Xi'an, China, 2nd edition, 2001.
- [22] FLUENT 6.0 User's Guide Book, Fluent Inc., 2001.
- [23] R. Illner and H. Neunzert, "On simulation methods for the Boltzmann equation," *Transport Theory and Statistical Physics*, vol. 16, no. 2–3, pp. 141–154, 1987.
- [24] Z. G. Sun, *Study on multiphase opposed jets and dense gas-solid two-phase coaxial jets [Ph.D. thesis]*, East China University of Science, Xuhui, China, 2009.

- [25] T. Zhang, M. Du, B. Zhou, L. H. Shen, and Y. L. Hao, "Experimental study on coaxial gas-solid two impinging stream drying," *Journal of Engineering Thermophysics*, vol. 32, no. 11, pp. 1910–1912, 2011.
- [26] X.-J. Liu, L. Shi, and X.-C. Xu, "Activities of dense particle-gas two-phase flow modeling in Eulerian-Lagrangian approach," *Chinese Journal of Computational Mechanics*, vol. 24, no. 2, pp. 166–172, 2007.

## Research Article

# Performance Analysis of High-Speed Deep/Shallow Recessed Hybrid Bearing

**Lei Wang and Shuyun Jiang**

*School of Mechanical Engineering, Southeast University, Nanjing 211189, China*

Correspondence should be addressed to Shuyun Jiang; [jiangshyseu@gmail.com](mailto:jiangshyseu@gmail.com)

Received 10 June 2013; Accepted 5 November 2013

Academic Editor: Tirivanhu Chinyoka

Copyright © 2013 L. Wang and S. Jiang. This is an open access article distributed under the Creative Commons Attribution License, which permits unrestricted use, distribution, and reproduction in any medium, provided the original work is properly cited.

The present paper proposes a theoretical analysis of the performance of deep/shallow recessed hybrid bearing. It is intended that, on the basis of the numerical results drawn from this study, appropriate shallow recess depth and width can be determined for use in the bearing design process. By adopting bulk flow theory, the turbulent Reynolds equation and energy equation are modified and solved numerically including concentrated inertia effects at the recess edge with different depth and width of shallow recess. The results indicate that the load capacity, drag torque increases as the depth of shallow recess is shallower and the width ratio (half angle of deep recess versus half angle of shallow recess) is smaller. In contrast, the flow rate decreases as the depth of shallow recess is shallower and the width ratio is smaller. Nevertheless, the appropriate design of the depth and width of shallow recess might well induce the performance of high-speed deep/shallow recessed hybrid bearing.

## 1. Introduction

The hybrid journal bearings provide superior performance characteristics such as minimum friction, large fluid film stiffness, good damping characteristics, and smooth relative motion. Due to the characteristics of excellent stiffness and damping, good rotational accuracy, low friction, and long life, they can be an attractive alternative to rolling bearings in high-speed machine tool spindle [1, 2]. The hybrid bearings have many types, the deep/shallow recess bearings are a common form of hybrid bearings, and the hydrodynamic effects of these bearings are greatly improved and have the merits of larger load capacity, higher stiffness, and superior stability than many other types of hybrid bearings. Despite all that, the main drawback of these bearings is large heat generation in high-speed condition; therefore, the low-viscosity fluid is adopted in the high-speed deep/shallow recess hybrid bearing to satisfy the demands of high-speed machine tool spindle since the low viscosity can significantly reduce the friction loss and heat generation.

During the last few decades, the theoretical analysis of the hybrid bearings with deep/shallow recesses has been carried out and reported in the literature. Among the first studies

were the principles of these bearings [3]. Also the static and dynamic characteristics of deep/shallow recessed hybrid bearings were studied, respectively, with different structure of bearing [4–6], different restrictors [7], various recess shapes [8, 9], and considering different flow regime and operational condition [10]. The depth and width of shallow recess were a key design parameter for hybrid bearings with deep/shallow recess. The following review details some important investigation carried out for the influence of shallow recess depth and width on the hybrid bearings.

Chen et al. [11, 12] studied the influence of the shallow recess depth on the performance of hybrid bearing with orifice compensated and capillary compensated. Compared to the conventional deep recess bearing, they put forward the design criterion of shallow recess depth about the hybrid bearing. Helene et al. [13] presented the theoretical analysis of the pressure pattern in a two-dimensional recess of a hybrid journal bearing. They introduced the ratio of the recess depth versus the film thickness. Six values of this ratio are considered, ranging from 4 (shallow recess) to 152 (deep recess), and presented in a systematic manner giving a clear insight of the flow effects intervening in the recess and of their mutual interaction with laminar and turbulent conditions.

The above references have been instrumental to the present development. Due to the high surface speed, the high-speed hybrid bearing with deep/shallow recesses using the low-viscosity fluid is always operated in the turbulent flow regime; meanwhile the inertia effects are also pronounced, especially the concentrated inertia effects at the edge of deep recess. To the best knowledge of authors, a thorough scan of the available literature reveals that there does not exist any comprehensive study related to the performance of the high-speed deep/shallow recessed hybrid bearing with different depth and width of shallow recess considering the turbulent flow regime and inertia effects in thermohydrodynamic lubrication analysis.

In the present study, an analysis is conducted and solutions are provided for the effects of the depth and width of shallow recess on the performance of the high-speed deep/shallow recessed hybrid bearing. By adopting bulk flow theory, the turbulent Reynolds equation and energy equation are modified and solved numerically including concentrated inertia effects at the deep recess edge with different eccentricity ratios.

## 2. Theoretical Analysis

**2.1. The Geometry of High-Speed Hybrid Bearing with Deep/Shallow Recesses.** Figure 1 shows the geometry of high-speed hybrid bearing with four deep/shallow recesses and feed orifices. The deep/shallow recess is comprised of two parts, the shallow recess and deep recess; the pressurized fluid is supplied into the deep recess through orifice, a flow from deep recess into the shallow recess and film land.

**2.2. Turbulent Reynolds Equation.** The generalized nondimensional Reynolds equation for the turbulent flow regime can be written as

$$\frac{\partial}{\partial \theta} \left( G_x \frac{\bar{H}^3}{\bar{\mu}} \frac{\partial \bar{p}}{\partial \theta} \right) + \left( \frac{D}{L} \right)^2 \frac{\partial}{\partial \bar{z}} \left( G_z \frac{\bar{H}^3}{\bar{\mu}} \frac{\partial \bar{p}}{\partial \bar{z}} \right) = \Lambda \frac{\partial \bar{H}}{\partial \theta} + \sigma \frac{\partial \bar{H}}{\partial \tau}, \quad (1)$$

where nondimensional parameters are defined by

$$\begin{aligned} \theta &= \frac{x}{R}, & \bar{z} &= \frac{z}{L/2}, & \bar{H} &= \frac{h}{c}, & \bar{p} &= \frac{p}{p_s}, \\ \bar{\mu} &= \frac{\mu}{\mu_0}, & \tau &= \omega_p \cdot t, & \Lambda &= \frac{\mu_0 \cdot \omega \cdot R^2}{2p_s c^2}, & \sigma &= \frac{\mu_0 \cdot \omega_p \cdot R^2}{p_s \cdot c^2}, \end{aligned} \quad (2)$$

where the turbulent coefficients  $G_x$  and  $G_z$  depend on the fluid velocity field and are smaller than 1/12 which is the value they take in the case of laminar flow.

**2.3. The Bulk Flow Model for Turbulent Lubrication.** Returning to the Navier-Stokes equations for a turbulent thin film

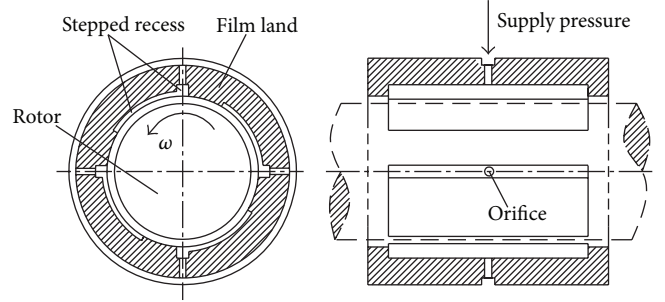


FIGURE 1: Geometry of the high-speed hybrid bearing with deep/shallow recesses.

and disregarding the inertia terms, after integration, the bulk-flow speed components can be expressed in the following form [14]:

$$V_x = -G_x \frac{h^2}{\mu} \frac{\partial p}{\partial x} + \frac{U}{2}, \quad V_z = -G_z \frac{h^2}{\mu} \frac{\partial p}{\partial z}. \quad (3)$$

Here  $V_x$  and  $V_z$  are the mean values across the film of the stochastic averages of the fluid velocity components. Following the bulk flow theory of Hirs, the pressure gradient depends on the bulk flow velocity [15]:

$$\begin{aligned} -h \frac{\partial \bar{p}}{\partial x} &= \frac{\mu}{h} \left\{ \frac{1}{2} (k_J + k_B) V_x + k_J \frac{U}{2} \right\}, \\ -h \frac{\partial \bar{p}}{\partial z} &= \frac{\mu}{h} \left\{ \frac{1}{2} (k_J + k_B) V_z \right\}, \end{aligned} \quad (4)$$

where the turbulent shear parameters at shaft and bearing ( $k_J$ ,  $k_B$ ) are defined in terms of the flow Reynolds numbers relative to the rotating shaft and stationary bearing surfaces:

$$k_J = 0.066 \text{Re}_J^{0.75}, \quad k_B = 0.066 \text{Re}_B^{0.75}. \quad (5)$$

The flow Reynolds numbers relative to the rotating shaft and stationary bearing surfaces are

$$\begin{aligned} \text{Re}_B &= \frac{\rho h}{\mu} [V_x^2 + V_z^2]^{1/2}, \\ \text{Re}_J &= \frac{\rho h}{\mu} [(V_x - U)^2 + V_z^2]^{1/2}. \end{aligned} \quad (6)$$

Comparing (3), (4) the turbulent coefficients are obtained as

$$\begin{aligned} G_x &= \min \left[ \frac{1}{12}; \frac{2V_x - U}{(k_J + k_B)V_x - k_J U} \right], \\ G_z &= \min \left[ \frac{1}{12}; \frac{2}{(k_J + k_B)} \right]. \end{aligned} \quad (7)$$

**2.4. The Concentrated Inertia Effects at the Edge of Deep Recess.** The local acceleration of fluid film from a deep recess into shallow recess and film land causes a sudden pressure drop in the high-speed condition [16, 17]; the pressure at the entrance

to shallow recess and film land is modeled from Bernoulli's equation as

$$p_e = p_r - \frac{\rho V_{x,z}^2}{2} (1 + \xi) \quad (V_{x,z} \cdot n > 0). \quad (8)$$

Note that the entrance loss coefficient  $\xi$  is expressed as the empirical (edge) entrance loss coefficients.

**2.5. Energy Equation.** The energy equation under adiabatic conditions in turbulent flow regime is obtained as follows:

$$\rho \left[ \frac{\partial (c_v T h V_x)}{\partial x} + \frac{\partial (c_v T h V_z)}{\partial z} \right] = \tau_{xy}|_0 U - \tau_{xy}|_0^h V_x - \tau_{zy}|_0^h V_z, \quad (9)$$

where

$$\begin{aligned} \tau_{xy}|_0 &= \frac{h}{2} \frac{\partial p}{\partial x} + \frac{\mu}{4h} [k_b V_x - (V_x - U) k_j], \\ \tau_{xy}|_0^h &= -\frac{\mu}{h} \left( k_x V_x - k_j \frac{U}{2} \right), \\ \tau_{zy}|_0^h &= -\frac{\mu}{h} (k_z V_z). \end{aligned} \quad (10)$$

The energy equation becomes in nondimensional form:

$$\begin{aligned} \rho \left[ \frac{\partial (c_v \bar{T} H V_x)}{\partial \theta} + \left( \frac{D}{L} \right) \frac{\partial (c_v \bar{T} H V_z)}{\partial (Z)} \right] \\ = \left[ \frac{p_s}{2T_s} \frac{\bar{H}\bar{P}}{\partial \theta} \right] U + \left[ \frac{\mu_0 R}{c^2 T_s} \frac{\bar{\mu}}{4\bar{H}} [k_b V_x - (V_x - U) k_j] \right] U \\ + \left[ \frac{\mu_0 R}{c^2 T_s} \frac{\bar{\mu}}{H} \left( k_x V_x - k_j \frac{U}{2} \right) \right] V_x + \frac{\mu_0 R}{c^2 T_s} \frac{\bar{\mu}}{H} (k_z V_z) V_z, \end{aligned} \quad (11)$$

where  $\bar{T} = T/T_s$ .

The fluid viscosity is considered to vary with temperature according to the following formulae:

$$\mu = b e^{-a(t-t_0)}. \quad (12)$$

**2.6. Drag Torque.** The turbulent wall shear stress at the journal surface based on bulk flow theory is given by [18]

$$\tau_{xy}|_0 = \frac{h}{2} \frac{\partial p}{\partial x} + \frac{\mu}{4h} (V_x k_b - (V_x - \omega R) \cdot k_j). \quad (13)$$

The drag torque is given by integration of the wall shear stress at the journal surface:

$$T_f = \int_{-L/2}^{-L/2} \int_0^{2\pi R} \tau_{yx} R dx dz. \quad (14)$$

**2.7. Mass Conservation at a Deep Recess.** The continuity equation at the deep recess is defined by the global balance between the flow through the orifice restrictor ( $Q_{in}$ ), the

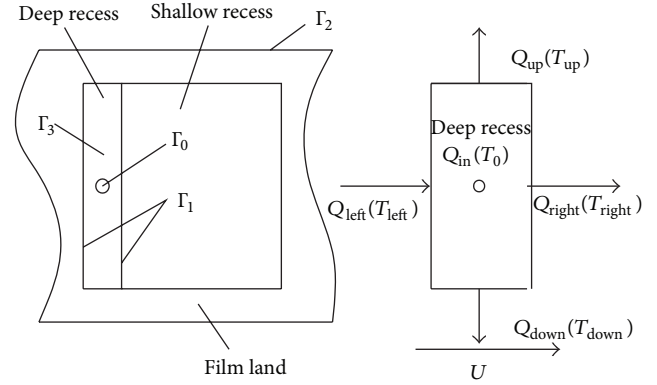


FIGURE 2: Boundary conditions and conceptual description of global flow rate and energy balance at a deep recess.

recess outflow into the shallow recess and film land ( $Q_{out}$ ), and the time rate of mass changing due to squeeze effect ( $Q_j$ ). The recess flow continuity equation is expressed as

$$Q_{in} = Q_{out} + Q_j, \quad (15)$$

where the flow through the orifice restrictor is

$$Q_{in} = A_0 C_d \sqrt{\frac{2(p_s - p_r)}{\rho}}. \quad (16)$$

The recess outflow into the shallow recess and film land is comprised of two parts, the flow across axial and circumferential boundaries of the deep recess:

$$Q_{out} = Q_{outa} + Q_{outc}. \quad (17)$$

The time rate of mass changing due to squeeze effect is determined as follows:

$$Q_j = A_r \frac{\partial h}{\partial t}. \quad (18)$$

**2.8. Global Energy Balance Equation at a Deep Recess.** The energy leaving the boundary of the deep recess must be equal to the energy flowing into the deep recess (Figure 2); that is,

$$E_{in} = E_{out}. \quad (19)$$

- (1) The energy flowing into the deep recess is comprised of two parts, the carry-over of hot fluid from upstream to downstream of the deep recess and the fresh fluid from the supply source into the deep recess volume [19]:

$$E_{in} = q_{in} T_s + q_{left} T_{left}. \quad (20)$$

- (2) The energy leaving the boundary of the deep recess is expressed as

$$E_{out} = q_{right} T_{right} + q_{up} T_{up} + q_{down} T_{down}. \quad (21)$$

TABLE 1: The parameters of high-speed deep/shallow recessed hybrid bearing.

Bearing diameter (mm)	Bearing length (mm)	Orifice diameter (mm)
$D = 60$	$L = 60$	$d_c = 1$
Rotor speed (rpm)	Depth of deep recess (mm)	Inlet temperature (°)
$\omega = 30000$	$h_p = 0.5$	$T_0 = 20$
Half angle of recess (°)	Depth of shallow recess (mm)	Width ratio of shallow recess
$\theta = 0-30$	$h_r = 0.01-0.05$	$k = 0.25-4$
Radial clearance ( $\mu\text{m}$ )	Viscosity (pa·s)	Supply pressure (Mpa)
$c = 20$	$\mu_0 = 0.001$	$P_s = 3$

$k$  is the width ratio,  $k = \theta_d : \theta_s, \theta_d$ : half angle of deep recess, and  $\theta_s$ : half angle of shallow recess. When  $k = 0$  or  $k = \infty$ , the deep/shallow recess is changed to shallow or deep recess.

**2.9. Boundary Conditions.** The boundary conditions for the pressure and temperature fields on the high-speed deep/shallow recessed hybrid bearing which are shown in Figure 2 are expressed as follows.

### 2.9.1. Pressure Boundary Conditions

- (1) The pressure at the ends of the bearing is taken to be equal to the ambient pressure. Thus,

$$p|_{\Gamma=\Gamma_2} = P_a. \quad (22)$$

- (2) The depth of deep recess is much greater than the film thickness; it is assumed that the pressure in each deep recess is uniform and equal to

$$p|_{\Gamma=\Gamma_3} = P_r. \quad (23)$$

- (3) Fluid inertia at the edges of deep recess is treated through a Bernoulli-type relationship.

- (4) The supply pressure is equal to

$$p|_{\Gamma=\Gamma_0} = P_s. \quad (24)$$

- (5) On the  $360^\circ$  extended film land, the pressure field is continuous and single-valued in the circumferential direction:

$$p(\theta, z) = P(\theta + 2\pi, z). \quad (25)$$

### 2.9.2. Temperature Boundary Conditions

- (1) The temperature of the deep recess and edges is obtained as described above; that is,

$$T|_{\Gamma=\Gamma_3} = T_r, \quad T|_{\Gamma=\Gamma_1} = T_r. \quad (26)$$

- (2) The supply temperature is equal to

$$T|_{\Gamma=\Gamma_0} = T_s. \quad (27)$$

- (3) On the  $360^\circ$  extended film land, temperature field is continuous and single-valued in the circumferential direction:

$$T(\theta, z) = T(\theta + 2\pi, z). \quad (28)$$

## 3. Result and Discussion

The parameters of high-speed deep/shallow recessed hybrid bearing are chosen from Table 1.

**3.1. Fluid-Film Pressure Distribution.** The distribution of fluid-film pressure along circumferential direction at axial midplane is shown in Figure 3. It is observed from the figure that the hydrodynamic effects of high-speed hybrid bearing with deep/shallow recesses are significant and the peak pressure is higher as the width ratio decreases; the shallow recessed bearing ( $k = 0$ ) has the maximum peak pressure; however, the pressure distribution changes slowly and has no peak pressure along circumferential direction for the deep recessed bearing ( $k = \infty$ ) since the hydrodynamic effects are the lowest; meanwhile the pressure has a sharp decrease at the downstream edge of deep recess due to the concentrated inertia effects. Furthermore, from Figure 7(b), it can be seen that the hydrodynamic effects of high-speed deep/shallow recessed hybrid bearing are more pronounced as the depth of shallow recess is shallower. The peak pressure is located at the downstream of shallow recess.

**3.2. Fluid-Film Temperature Distribution.** The profile of fluid-film temperature along circumferential direction at axial midplane is depicted in Figure 4. It is noticed that the bearing temperature rise increases as the depth of shallow recess is shallower and the width ratio is smaller due to the increase of drag torque and the reduction of flow rate caused by hydrodynamic effects. The temperature is found higher at almost all the points along circumferential directions for the shallow recessed bearing and has the maximum peak value (almost  $60^\circ$ ); however, due to the large flow rate the temperature rise of deep recessed bearing changes not obviously and the value of temperature is not beyond  $30^\circ$  which showed the advantages of hybrid bearing using the low viscosity fluid under the high-speed condition. Further, it is also observed that the temperature rise of high-speed hybrid bearing with deep/shallow recesses is high (almost  $60^\circ$ ) with the shallower depth of shallow recess ( $h_r = 10 \mu\text{m}$ ) and the smaller width ratio ( $k = 1:4$ ) due to the combination of hydrodynamic and turbulent effects.

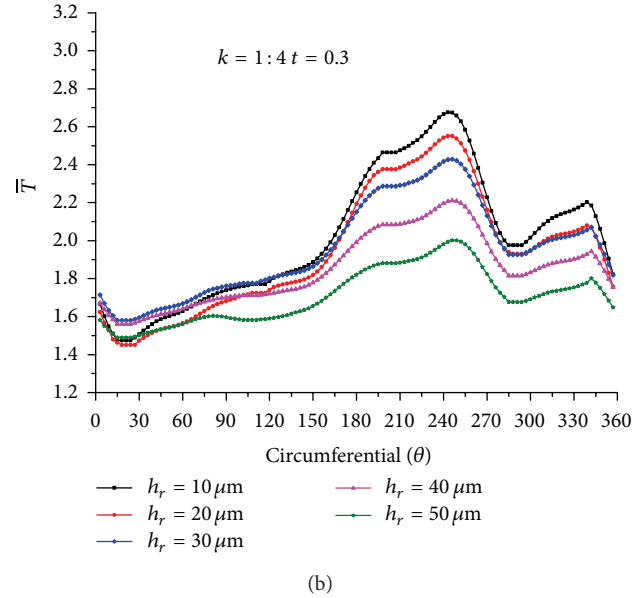
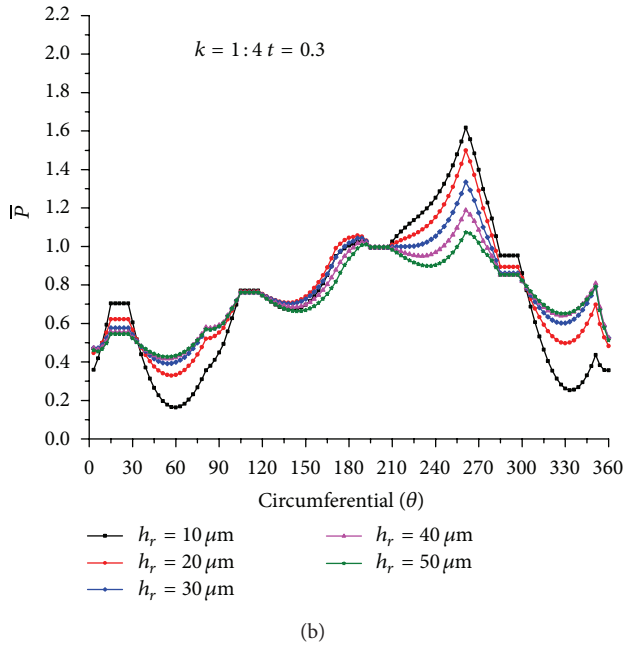
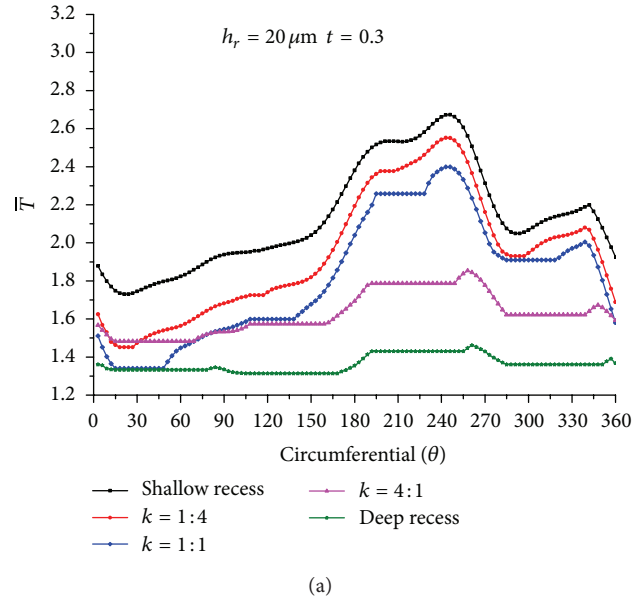
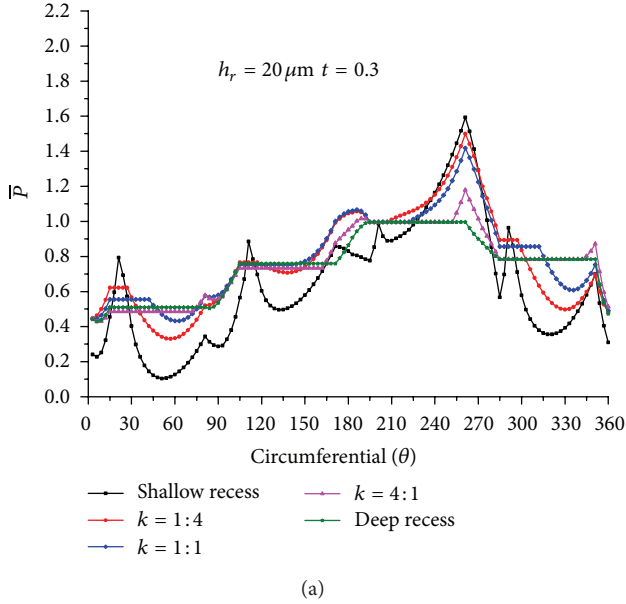


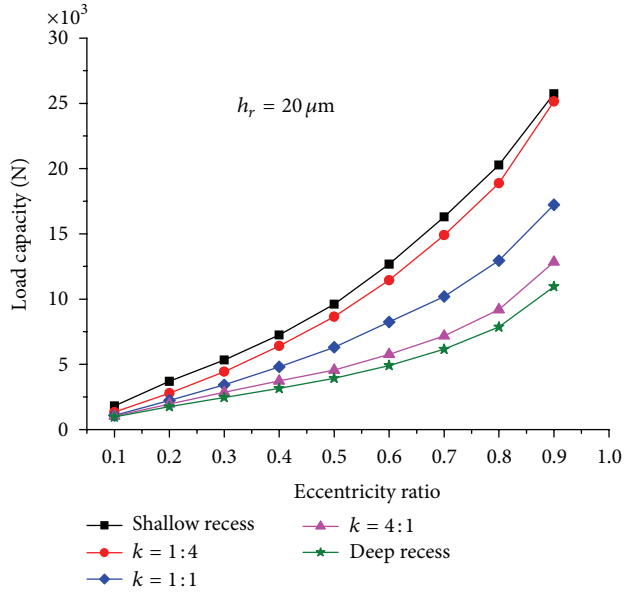
FIGURE 3: Pressure distribution for the high-speed deep/shallow recessed hybrid bearing.

FIGURE 4: Temperature distribution for the high-speed deep/shallow recessed hybrid bearing.

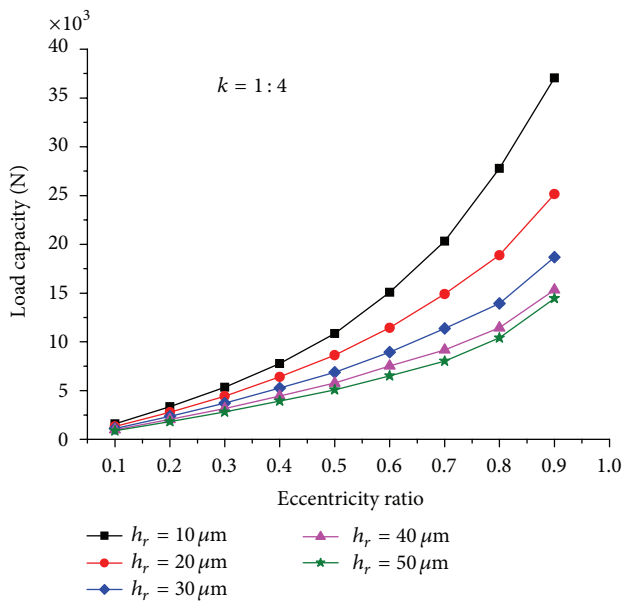
**3.3. Static Load Capacity.** Figure 5 shows the static load capacity of high-speed deep/shallow recessed hybrid bearing versus the eccentricity ratio. Note that the static load capacity exhibits a remarkable enhancement as the eccentricity ratio is larger owing to the increase of hydrodynamic effects. The static load capacity increases as the depth of shallow recess is shallower and the width ratio is smaller; meanwhile, the static load capacity of deep/shallow recessed bearing is larger than the deep recessed bearing and almost twice as large as deep recessed bearing for smaller width ratio ( $k = 1:4$ ) at large eccentricity ratio ( $\varepsilon > 0.7$ ). It can be explained that the predominance of hydrodynamic effects gets over hydrostatic

effects with the increase of eccentricity ratio. Moreover, when the width ratio becomes smaller ( $k = 1:4$ ) or larger ( $k = 4:1$ ), the static load capacity of deep/shallow recessed bearing is close to the shallow recessed bearing or the deep recessed bearing, respectively.

**3.4. Attitude Angle.** Figure 6 shows the attitude angle of high-speed hybrid bearing with deep/shallow recesses against the eccentricity ratio. It can be seen that the attitude angle decreases with the eccentricity ratio except for the deep recessed bearing. The attitude angle is larger with the shallower depth of shallow recess and the smaller width ratio especially for small eccentricity ratio due to the increase of hydrodynamic effects. Further, the attitude angle of shallow



(a)

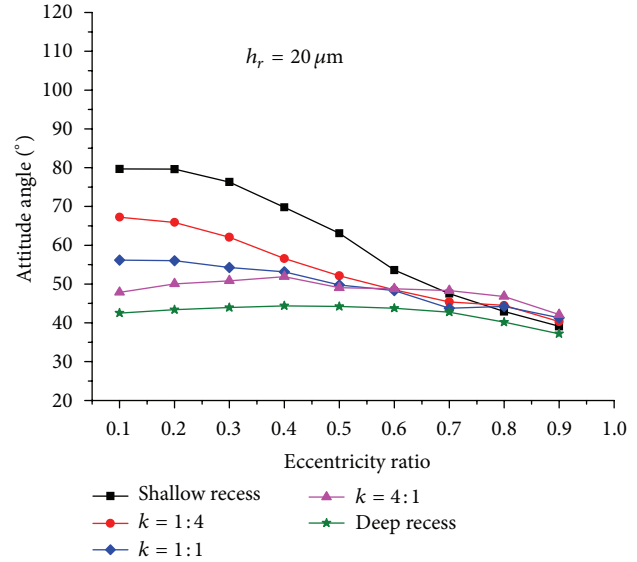


(b)

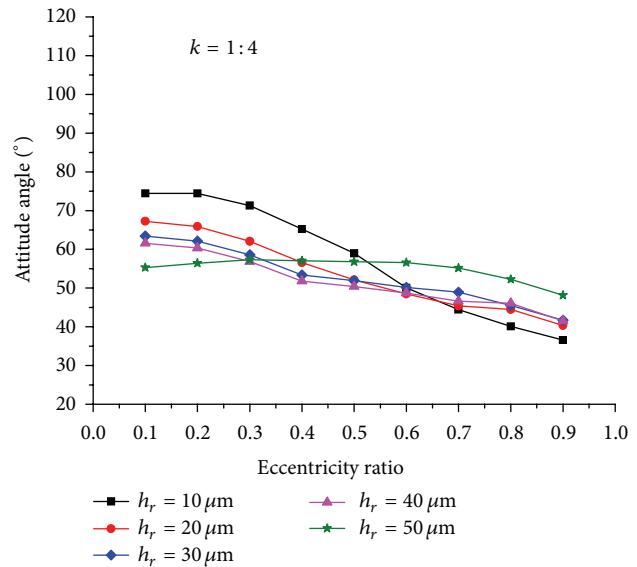
FIGURE 5: Static load capacity versus eccentricity ratio.

recessed bearing is the largest ( $80^\circ$ ) at lower eccentricity ratio ( $\epsilon < 0.3$ ) and decreases rapidly with the increase of eccentricity ratio; however, the attitude angle of deep recessed bearing is almost constant at lower eccentricity ratio ( $\epsilon < 0.3$ ) and decreases slightly at large eccentricity ratio ( $\epsilon > 0.7$ ).

**3.5. Flow Rate.** The eccentricity ratio as a function of the flow rate is shown in Figure 7. It can be found that the flow rate has almost the same value as that of the eccentricity ratio. There is a reduction in the flow rate as the width ratio is smaller since the hydrostatic effects decrease and the flow rate of deep recessed bearing is almost twice as large as



(a)



(b)

FIGURE 6: Attitude angle versus eccentricity ratio.

the shallow recessed bearing. Moreover, with the increase of eccentricity ratio, the flow rate of deep/shallow recessed and shallow recessed bearing has a tiny increase, while the flow rate of deep recessed bearing decreases slowly. Furthermore, as the depth of shallow recess is deeper, the turbulent effects increase at the shallow recess region and the flow rate also increases which is seen in Figure 7(b).

**3.6. Drag Torque.** The drag torque of high-speed deep/shallow recessed hybrid bearing as a function of the eccentricity ratio is presented in Figure 8. The drag torque has almost the same value as the eccentricity ratio is lower and slightly increases as the eccentricity ratio is larger ( $\epsilon > 0.7$ ). Similarly, The drag torque is larger (twice as big as the deep recessed

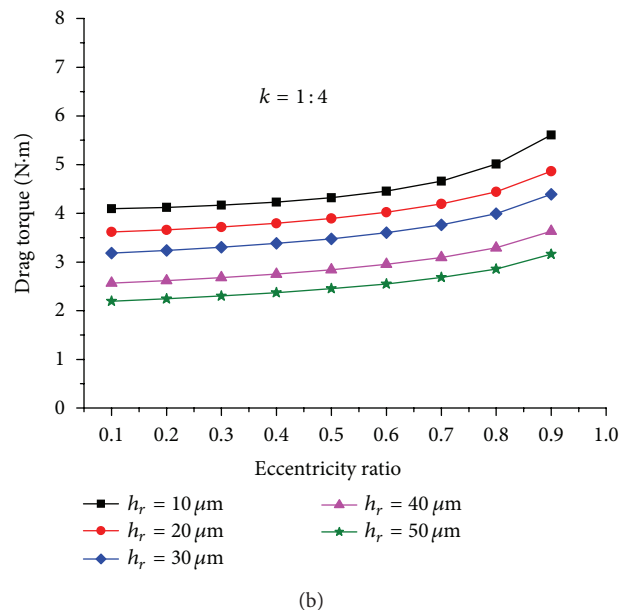
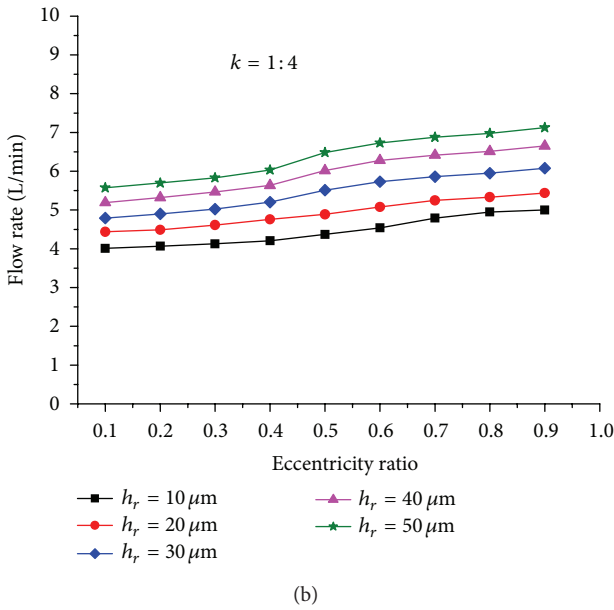
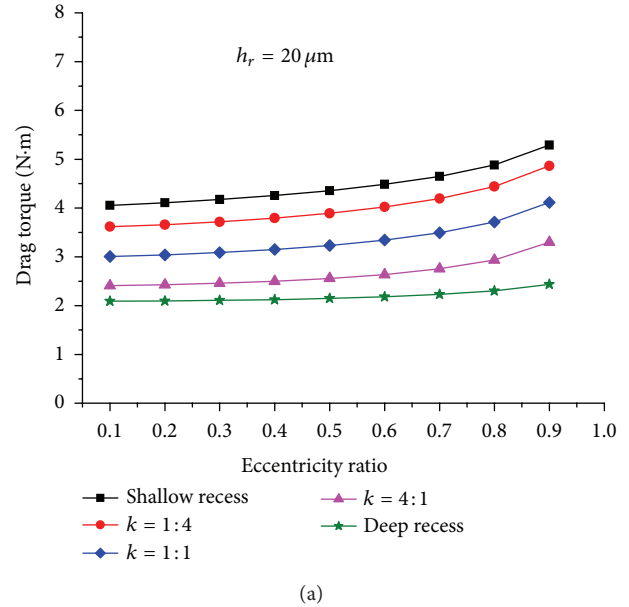
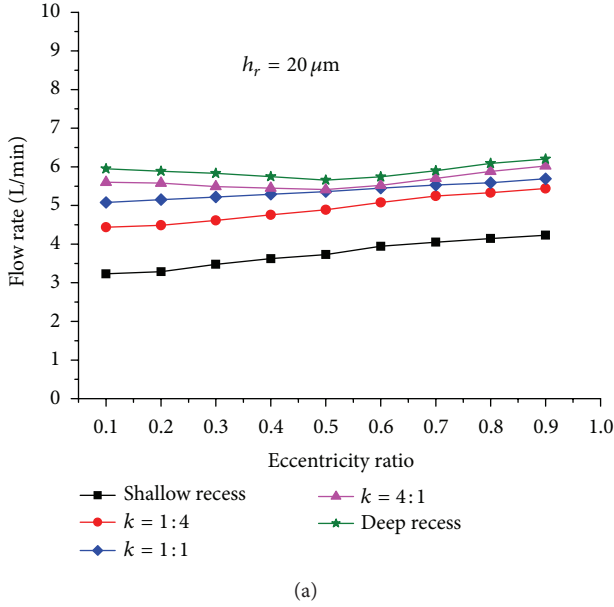


FIGURE 7: Flow rate versus eccentricity ratio.

FIGURE 8: Drag torque versus eccentricity ratio.

bearing) with the shallower depth of shallow recess and the smaller width ratio due to the increase of wall shear stress. Furthermore, the drag torque of deep recessed bearing is the smallest (2 N/m) owing to the larger deep recess; contrarily the drag torque is the largest (4 N/m) for the shallow recessed bearing.

#### 4. Conclusion

An analysis is conducted and solutions are provided for the effects of the depth and width of shallow recess on the performance of the high-speed deep/shallow recessed hybrid bearing. By adopting bulk flow theory, the turbulent Reynolds equation and energy equation are modified and

solved numerically including concentrated inertia effects at the deep recess edge with different eccentricity ratios. The following conclusions can be obtained.

- (1) The depth and width of shallow recess significantly affect the pressure and temperature distribution of the high-speed deep/shallow recessed hybrid bearing. The pressure and temperature rise of the deep/shallow recessed hybrid bearing increases with the shallower recess depth and the smaller width ratio.
- (2) The load capacity of the high-speed deep/shallow recessed hybrid bearing significantly increases as well as the flow rate reduces and the drag torque increases with the shallower recess depth and the smaller width

ratio especially at large eccentricity ratio. In contrast, the flow rate decreases as the depth of shallow recess is shallower and the width ratio is smaller.

- (3) In summary, from the view for the high-speed deep/shallow recessed hybrid bearing design, when the eccentricity ratio is large ( $\epsilon > 0.4$ ), the depth of shallow recess should be designed shallower ( $h_r < 30 \mu\text{m}$ ) and the width ratio should also be designed smaller ( $k < 1:1$ ) for the high-speed deep/shallow recessed hybrid bearing; otherwise, the deeper shallow recess and the larger width ratio are required in order to reduce the friction power consumption and simplify the design and manufacturing.

## Nomenclature

$h$ :	Film thickness
$\bar{H}$ :	Nondimensional film thickness
$\theta$ :	Angular coordinate
$\omega$ :	Journal rotating speed
$\rho$ :	Density of lubricant
$p_e$ :	Pressure at deep recess edge
$G_x, G_z$ :	Turbulent coefficients of circumferential and axial turbulent coefficients
$k_f, k_B$ :	Turbulent shear parameters at shaft and bearing
$V_x, V_z$ :	Bulk flow circumferential and axial velocities
$\tau_{xy}, \tau_{zy}$ :	Wall shear stresses
$\tau_{xy} _0$ :	Turbulent wall shear stress at shaft surface
$T_R$ :	Drag torque
$A_0$ :	Orifice sectional area
$d_c$ :	Diameter of orifice
$A_r$ :	Recess area
$C_d$ :	Empirical orifice discharge coefficients
$Q_{in}, Q_{out}$ :	The flow through the orifice restrictor and the deep recess outflow into the film land
$Q_{outc}, Q_{outa}$ :	Circumferential and radial mass flow
$E_{in}, E_{out}$ :	The energy flowing into the deep recess and leaving the boundary of the deep recess
$T_s$ :	Water inlet temperature
$T_r$ :	Temperature within deep recess and downstream edge
$T_{left}$ :	Temperature in upstream edge
$\xi$ :	Empirical recess-edge entrance loss coefficients.

## Subscripts

$s$ :	Supply condition
$r$ :	Bearing recesses
$B, J$ :	Bearing and shaft.

## Acknowledgments

The authors gratefully acknowledge the support of the National Science Foundation through Grant nos. 50775036, 11172065 and Jiangsu University-Industry Collaboration Project through Grant no. BY2012199.

## References

- [1] E. Abele, Y. Altintas, and C. Brecher, "Machine tool spindle units," *CIRP Annals*, vol. 59, no. 2, pp. 781–802, 2010.
- [2] W. Xiong, X. Yang, L. Lv, and J. Yuan, "Review on key technology of hydrodynamic and hydrostatic high-frequency motor spindles," *Journal of Mechanical Engineering*, vol. 45, no. 9, pp. 1–18, 2009.
- [3] W. B. Rowe, "A theoretical and experimental investigation of self compensated externally pressurized thrust bearings," in *Proceedings of the 6th Symposium on Gas Bearing*, 1974.
- [4] G. Hong, L. Xinmin, W. Xiaoling, and C. Shaoqi, "Performance of flat capillary compensated deep/shallow pockets hydrostatic/hydrodynamic journal-thrust floating ring bearing," *Tribology Transactions*, vol. 52, no. 2, pp. 204–212, 2009.
- [5] H. Guo, S. Lin Zhang, and S. Qi Cen, "Theoretical and experimental study on dynamic coefficients and stability for a hydrostatic/hydrodynamic conical bearing," *Journal of Tribology*, vol. 131, pp. 701–708, 2009.
- [6] D. Pan, Z. Yabin, and X. Hua, "The structure of new journal hybrid bearing for high-speed machine spindle and its performance," *Lubrication Engineering*, vol. 34, no. 2, pp. 11–14, 2009.
- [7] C.-H. Chen, Y. Kang, Y.-N. Huang, C.-H. Chu, and J.-T. Teng, "The restrictive effects of capillary compensation on the stability of the Jeffcott rotor-hybrid bearing system," *Tribology International*, vol. 35, no. 12, pp. 849–855, 2002.
- [8] W. Chen, F. Wang, and Y. Zhang, "The flow field simulation of a novel water-lubricated hybrid bearing for high-speed spindle," in *Proceedings of the STLE/ASME International Joint Tribology Conference (IJTC '10)*, pp. 91–93, October 2010.
- [9] N. Heinrichson, I. F. Santos, and A. Fuerst, "The influence of injection pockets on the performance of tilting-pad thrust bearings—part I. Theory," *Journal of Tribology*, vol. 129, no. 4, pp. 895–903, 2007.
- [10] H. Guo, S. Lin Zhang, and S. Qi Cen, "Research on static characteristics of deep/shallow pockets hybrid bearing under laminar and turbulent mixed regimes," in *Advanced Materials Research, Materials Processing Technology*, vol. 291–294, pp. 1516–1520, 2011.
- [11] C.-H. Chen, Y. Kang, Y.-P. Chang, H.-H. Lee, and P.-C. Shen, "Influences of recess depth on the stability of the Jeffcott rotor supported by hybrid bearings with orifice restrictors," *Industrial Lubrication and Tribology*, vol. 57, no. 1, pp. 41–51, 2005.
- [12] C. H. Chen, Y. Kang, Y.-P. Chang, Y.-P. Wang, and H.-H. Lee, "Influence of restrictor on stability of the rigid rotor-hybrid bearing system," *Journal of Sound and Vibration*, vol. 297, no. 3–5, pp. 635–648, 2006.
- [13] M. Helene, M. Arghir, and J. Frene, "Numerical study of the pressure pattern in a two-dimensional hybrid journal bearing recess, laminar, and turbulent flow results," *Journal of Tribology*, vol. 125, no. 2, pp. 283–290, 2003.
- [14] G. G. Hirs, "A bulk-flow theory for turbulence in lubricant films," *Journal of Lubrication Technology*, vol. 95, no. 2, pp. 137–146, 1973.
- [15] B. J. Hamrock, S. R. Schmid, and B. O. Jacobson, *Fundamentals of Fluid Film Lubrication*, 2004.
- [16] V. N. Constantinescu and S. Galetuse, "Pressure drop due to inertia forces in step bearings," *Journal of Lubrication Technology*, vol. 98, no. 1, pp. 167–174, 1976.
- [17] J. Frène, M. Arghir, and V. Constantinescu, "Combined thin-film and Navier-Stokes analysis in high Reynolds number

lubrication," *Tribology International*, vol. 39, no. 8, pp. 734–747, 2006.

- [18] A. Z. Szeri, *Fluid Film Lubrication: Theory and Design*, Cambridge University Press, 1998.
- [19] S. M. Chun and D.-H. Ha, "Study on mixing flow effects in a high-speed journal bearing," *Tribology International*, vol. 34, no. 6, pp. 397–405, 2001.

## Research Article

# Feature-Parameter-Criterion for Predicting Lean Blowout Limit of Gas Turbine Combustor and Bluff Body Burner

Hongtao Zheng,<sup>1</sup> Zhibo Zhang,<sup>1</sup> Yajun Li,<sup>2</sup> and Zhiming Li<sup>1</sup>

<sup>1</sup> College of Power and Energy Engineering, Harbin Engineering University, Harbin 150001, China

<sup>2</sup> China Shipbuilding Industry Corporation, No. 703 Research Institute, Harbin 150078, China

Correspondence should be addressed to Hongtao Zheng; zhenghongtao9000@163.com

Received 25 June 2013; Accepted 22 September 2013

Academic Editor: Tirivanhu Chinyoka

Copyright © 2013 Hongtao Zheng et al. This is an open access article distributed under the Creative Commons Attribution License, which permits unrestricted use, distribution, and reproduction in any medium, provided the original work is properly cited.

Lean blowout (LBO) limit is one of the most important combustor parameters. A new method named Feature-Parameter-Criterion (FPC) for predicting LBO limit has been put forward in the present work. A computational fluid dynamics (CFD) software FLUENT has been used to simulate the process of LBO of gas turbine combustor and bluff body burner. And “M” flame has been proposed as the portent for predicting lean blowout of gas turbine combustor. Effects of flow velocity, air temperature, droplet averaged-diameter, and flow distribution between swirlers and primary holes on the LBO limit of gas turbine combustor have been researched by use of Feature-Parameter-Criterion in this paper. The effects of fuel air mixture velocity and different structures on bluff body LBO limit have also been analyzed in the present work by use of FPC. The results show that the simulation of LBO limit based on FPC is in good agreement with the experiment data (the errors are about 5%) and this method is reliable for engineering applications.

## 1. Introduction

Gas turbine is one of the most important fluid machineries in the engineering field, and bluff body burner is widely used in engine combustors to stabilize flames [1]. There are many core problems, such as heat and mass transfer, CO<sub>2</sub> and NO<sub>x</sub> emission, and lean blowout, to be researched. Due to increasingly stringent emission requirements, modern gas turbine combustors usually work under lean operating conditions [2] for lowering combustion temperature and reducing the production rate of NO<sub>x</sub>. The operation near the lean blowout (LBO) limit, however, may result in undesirable combustion characteristics, such as flashback and combustion instabilities due to the partial flame extinction and dynamic fluctuations of heat release rate, which will lead to low combustion efficiency and poor operability of the combustor.

Experimental studies on combustor performance of gas turbine are essential, but huge experimental measurements are expensive and time consuming. Numerical methods provide a reasonable approach for combustor performance prediction, heat and mass transfer process, chemical reaction recurrence, and transient response [3, 4]. At the same time, some advanced mathematical models [5, 6] have been

presented. In addition, the Reynolds-Averaged Navier-Stokes (RANS) based approach has been widely used in device design and optimization due to its lower requirement in computational spending and its acceptable precision prediction of time-averaged flow properties [7, 8]. RANS approach can provide quality instruction for combustor design [9]. But for lean blowout limit predicting, advanced method should be used to match up with RANS approach.

On predicting lean blowout in gas turbine combustor, there are three main methods at present: experimental research method, empirical formula method, and numerical simulation method. In experimental research, Marinov et al. [2, 10–12] and Yuan et al. [13–16] did effective work in their respective fields. But the experimental research method needs high-precision measuring equipment and the cost is high. Being subject to experiment condition, it would unlikely obtain inner parameters distribution and changes law in gas turbine combustor. In empirical formula, A. H. Lefebvre and D. R. Ballal Lefebvre [17] and Meller [18] proposed the semiempirical formula based on heat balance model and the characteristic time model. Rizk and Mongia [19, 20] proposed the multidimensional empirical analysis method. Rizk and Mongia [21] revised Lefebvre's

semiempirical formula and put it into computational fluid dynamics field. The advantages of empirical formula method are high-precision and convenience, but they are only aimed at certain combustion and bring poor universality. In numerical simulation, Kim et al. [22] researched the lean blowout limit of bluff body burner with large eddy simulation technology, and some of the works were mainly focused on bluff body stabilized flames as summarized in a recent review by Shanbhogue et al. [23]. Kumaran and Shet found that the LBO limit depends on aeroengine parameters including swirl number [24]. Furthermore the LBO limit can be extended to addition of hydrogen [25, 26]. Cai et al. proposed the fuel steady stepwise method to predict the LBO limit, and predictions were in agreement with corresponding experimental data [27]. However, most of researches did not propose appropriate criterion for predicting lean blowout limit. CAI Wenxiang's method was only aimed at annular combustor and could not be used in other combustor style.

A new method named Feature-Parameter-Criterion (FPC) for predicting LBO limit of gas turbine combustor and bluff body burner has been put forward in this paper. A new parameter named as feature-parameter, detailed prediction principle, and lean blowout process have been shown firstly. And then comparison between numerical simulation results and experimental data has been made to test and verify the accuracy of Feature-Parameter-Criterion.

## 2. Geometry and Mathematical Models

The present work is based on an annular combustor of gas turbine and a type of bluff body burner.

The geometry of annular combustor which burn oil C7H16 has been shown in Figure 1. It is composed of diffuser, swirler, primary holes, nozzle, cooling holes, and flame tube. The length of diffuser is 150 mm, and the length and diameter of flame tube are separately 250 mm and 100 mm. There are 10 primary holes with 10 mm-diameter for each and 40 cooling holes with 8 mm-diameter for each. Air is supplied axially through "Air-inlet" (1522 mm<sup>2</sup> for area) and divided into two parts: one part of air passes over the swirler to help atomizing fuel and form a central recirculation zone (CRZ) in the downstream of swirler; the other part of air flows into the primary holes and cooling holes. The purpose is forming combustion flow field and protecting flame tube. Combustion occurs within the flame tube and all the emissions discharge through outlet. In order to improve grid quality and save the calculation resources, periodic boundary condition and Hexa-Core grid technology are used in this paper. The middle section of the grid is shown in Figure 2.

Boundary conditions of annular combustor are as follows:

operation pressure: 4.2 MPa;

air-inlet:

velocity: 50 m/s–90 m/s,

temperature: 285 K–530 K;

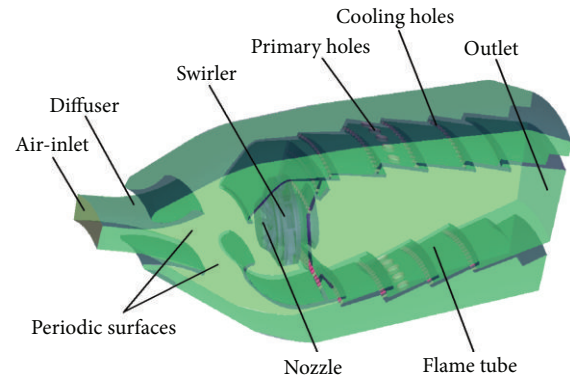


FIGURE 1: Geometry of annular combustor.

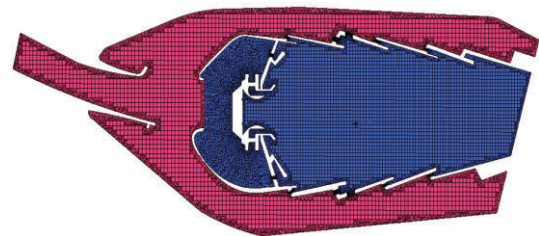


FIGURE 2: The middle section of the grid of annular combustor.

nozzle:

fuel: liquid kerosene (C7H16),

fuel air ratio: 0.00415–0.0187,

temperature: 300 K,

droplet averaged-diameter: 30  $\mu\text{m}$ –160  $\mu\text{m}$ ; the oil-fired droplet follows Rosin-Rammler (R-R) Function;

outlet: pressure outlet;

Wall: one group of wall is periodic, adiabatic boundary, and others are no-slip, adiabatic boundary.

With reference to [28] the structure of axisymmetric and coaxial bluff body is used in this paper. The central mixture (air + liquefied petroleum gas (LPG)) is supplied axially through a central axial tube with 4.9 mm diameter for single hole. The coflowing (coaxial) air passes over disk stabilizer with diameter of 55 mm or conical bluff body with the angle of 30 degree–90 degree. The disk stabilizer is placed into the interior of a burner pipe with the diameter of 82 mm. In this way, the edge of the central axial tube and the burner pipe can be ensured to be in the same vertical plane. The burner is confined in a combustor of 152.4 mm diameter by a cooling jacket. The geometrical structure of bluff body burner is shown in Figure 3. To improve the calculation accuracy, block structure grid technology is used for bluff body burner. The middle section of the grid is shown in Figure 4.

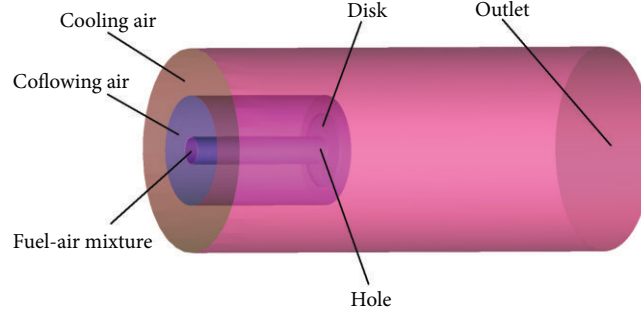


FIGURE 3: Geometry of bluff body burner.

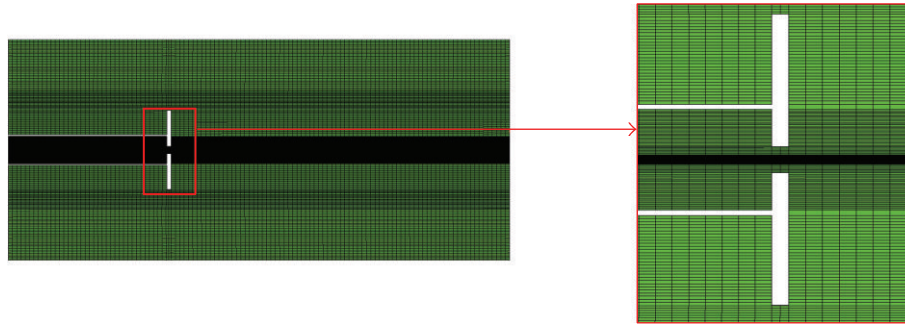


FIGURE 4: The middle section of the grid of bluff body burner.

Boundary conditions of bluff body burner are as follows:

- operation pressure: 0.1 MPa;
- fuel air mixture:
  - velocity: 23.8 m/s–42.3 m/s,
  - temperature: 300 K;
  - air + liquefied petroleum gas (LPG);
- Coflowing air:
  - velocity: 4.8 m/s,
  - temperature: 300 K;
- cooling air:
  - velocity: 4.8 m/s,
  - temperature: 300 K;
- outlet: pressure outlet;
- wall: the maximum cylinder wall is pressure outlet; others are no-slip, adiabatic boundary.

In combustion flows, conservation equations for mass, momentum, energy, species, state, and turbulence are solved. All the primary equations which are used in this paper are as follows (ignore radiation and gravitation).

Mass conservation equation:

$$\nabla \cdot (\rho \vec{V}) = S_m. \quad (1)$$

Momentum conservation equation:

$$\nabla \cdot (\rho \vec{V} \vec{V}) = -\nabla p + \nabla \cdot \tau + \vec{F}. \quad (2)$$

Energy conservation equations:

$$\begin{aligned} \nabla \cdot (\rho \vec{V} E) = \nabla \cdot \left( -\vec{q} - \rho \vec{V} + \tau \cdot \vec{V} - \sum_{i=1}^{N_s} h_i \vec{J}_i \right) \\ + S_h + q_p. \end{aligned} \quad (3)$$

Species transport equation:

$$\nabla \cdot (\rho \vec{V} m_i) = -\nabla \cdot \vec{J}_i + R_i + Q_i. \quad (4)$$

Realizable  $k$ - $\epsilon$  models:

$$\begin{aligned} \nabla \cdot (\rho \vec{V} k) = \nabla \cdot (\Gamma_k \nabla k) + G_k + G_b - \rho \epsilon - Y_k + S_k, \\ \nabla \cdot (\rho \vec{V} \epsilon) = \nabla \cdot (\Gamma_\epsilon \nabla \epsilon) + \rho C_1 S_\epsilon - \rho C_2 \frac{\epsilon^2}{k + \sqrt{\nu \epsilon}} \\ + C_{1\epsilon} \frac{\epsilon}{k} C_{3\epsilon} G_b + S_\epsilon. \end{aligned} \quad (5)$$

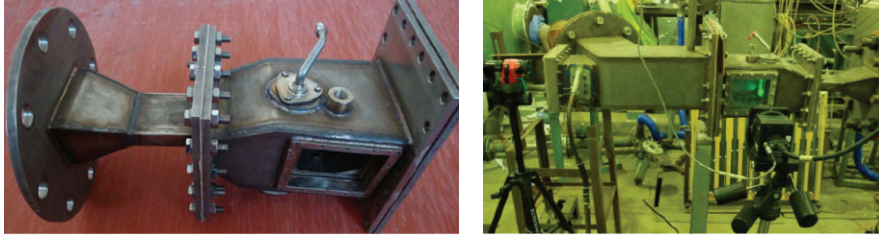


FIGURE 5: Experimental apparatus of gas turbine combustor.

RNG  $k$ - $\epsilon$  models:

$$\begin{aligned} \frac{\partial}{\partial x_i} (\rho k u_i) &= \frac{\partial}{\partial x_j} \left( \alpha_k \mu_{\text{eff}} \frac{\partial k}{\partial x_j} \right) \\ &+ G_k + G_b - \rho \epsilon - Y_M + S_k, \\ \frac{\partial}{\partial x_i} (\rho \epsilon u_i) &= \frac{\partial}{\partial x_j} \left( \alpha_\epsilon \mu_{\text{eff}} \frac{\partial \epsilon}{\partial x_j} \right) \\ &+ C_{1\epsilon} \frac{\epsilon}{k} (G_k + C_{3\epsilon} G_b) \\ &- C_{2\epsilon} \rho \frac{\epsilon^2}{k} - R_\epsilon + S_\epsilon. \end{aligned} \quad (6)$$

Eddy-dissipation (ED) combustion model was used to simulate the combustion chemical reaction of gas turbine combustor in this paper. The net rate of production of species  $i$  due to reaction  $R_{i,r}$  is given by the smaller of the two expressions below:

$$\begin{aligned} R_{i,r} &= v'_{i,r} M_{w,i} A \rho \frac{\epsilon}{k} \min R \left( \frac{Y_R}{v'_{R,r} M_{w,R}} \right), \\ R_{i,r} &= v'_{i,r} M_{w,i} A B \rho \frac{\epsilon}{k} \frac{\sum p Y_P}{\sum_j v''_{j,r} M_{w,j}}. \end{aligned} \quad (7)$$

Cone injection and Rosin-Rammler (R-R) Function were used to simulate the fuel droplet diameter distribution of C7H16 in annular combustor. R-R Function of oil atomization characteristic is as follows:

$$R = \exp \left[ - \left( \frac{d}{\bar{d}} \right)^h \right]. \quad (8)$$

### 3. Validations of Mathematical Models

In order to verify the accuracy of mathematical models which were used in this paper, the comparison has been done with experiment results. This paper and [28, 29] have the same combustor structure and condition parameters. Experimental apparatus of [29] has been shown in Figure 5.

**3.1. Validations of Independence of Grid Size.** In numerical simulations, firstly the study on grid independence is performed to determine the best grid with the highest accuracy.

For the annular combustor of the gas turbine, Table 1 shows 9 kinds of grid size ranging from 2.1 mm to 4.0 mm (the number of the grid varies from  $4.4e + 06$  to  $2.1e + 06$ ). The FLUENT is used for monitoring the outlet average temperature ( $T_{\text{out}}$ ) and combustion efficiency ( $\eta$ ) in order to verify the grid size accuracy. Table 1 indicates that the change rate of outlet temperature is only 0.88% when grid size is 2.6 mm and the change rate of combustion efficiency is only 0.81% when grid size is 2.9 mm. With integrated consideration of these two parameters, the grid size of 2.6 mm is chosen in this paper.

For bluff body burner, Table 2 shows 7 kinds of grid size range which range from 1.1 mm to 3.0 mm (the grid number varies from  $7.82e + 05$  to  $5.69e + 06$ ) in this paper. Outlet average temperature ( $T_{\text{out}}$ ) and average velocity of a special point (it is in the axis, and the distance between it and disk is 40 mm,  $V_{40}$ ) have been monitored by using FLUENT to verify the accuracy of grid size. From the table, it can conclude that grid size  $\Delta = 1.7$  mm should be the best chosen in this paper.

### 3.2. Validations of Turbulence Combustion Model

**3.2.1. Validations for Annular Combustor of Gas Turbine.** To improve the accuracy of simulation, at first, the turbulence combustion models should be validated.

Fuel oxidation was modeled by one-step global reaction:



The reaction rate proposed by fluent database according to Arrhenius is as follows:

$$\begin{aligned} \omega &= \frac{d [\text{C}_7\text{H}_{16}]}{dt} = -2.868 \times 10^{-9} e^{-15107/T} \\ &\times [\text{C}_7\text{H}_{16}]^{0.25} [\text{O}_2]^{1.5} \end{aligned} \quad (10)$$

Figure 6 shows the comparison between the results of different turbulence models and experiment data. More specifically, turbulence models including realizable  $k$ -epsilon model (RKE), RNG  $k$ -epsilon model (RNG), Reynolds stress model (RSM), and large eddy simulation model (LES) are chosen to validate the accuracy. It indicates that the curves by using RNG  $k$ -epsilon model and LES model have the same trend as from experimental data. When  $x < 75$  mm, RNG  $k$ -epsilon model can get better results. And when  $x > 150$  mm, the error between the numerical result and the experiment data by using LES model is extremely small. Under other conditions, the two kinds of models can obtain almost same curves.

TABLE 1: Grid size independence validation of annular combustor.

Grid size/mm	$T_{out}/K$	Rate of change/%	$\eta$	Rate of change/%	Grid amount
4	1373.23	—	0.97	—	2100314
3.7	1486.62	8.26%	0.985	1.55%	2447927
3.5	1374.54	7.54%	0.97	1.52%	2890137
3.3	1457.32	6.02%	0.982	1.24%	3143522
3.1	1399.51	3.97%	0.993	1.12%	3325334
2.9	1372.03	1.96%	0.985	0.81%	3605722
2.6	1360.02	0.88%	0.978	0.71%	3891140
2.3	1371.92	0.87%	0.984	0.61%	4020562
2.1	1380.54	0.63%	0.987	0.30%	4415871

TABLE 2: Grid size independence validation of bluff body burner.

Grid size/mm	$T_{out}/K$	Rate of change/%	$V_{40}$	Rate of change/%	Grid amount
3.0	851.07	—	23.28	—	782198
2.5	865.31	1.67%	24.97	7.26%	1365165
2.2	842.63	2.62%	25.49	2.08%	1965144
2.0	835.51	0.84%	25.23	1.02%	2496055
1.7	830.24	0.63%	25.46	0.91%	3325334
1.4	834.97	0.57%	25.31	0.59%	4047064
1.1	831.26	0.44%	25.17	0.55%	5693193

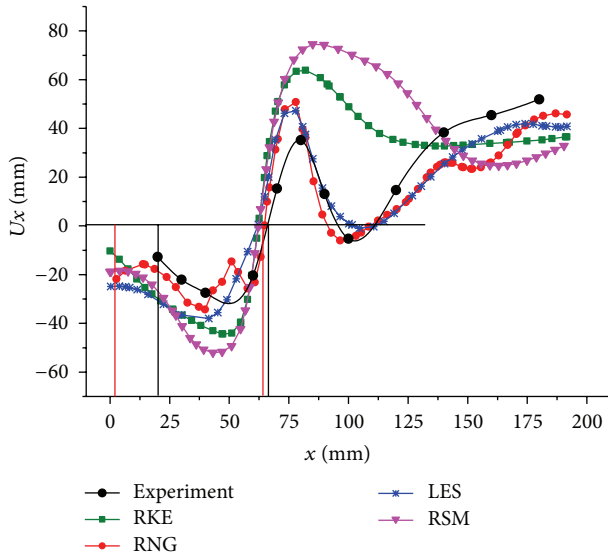


FIGURE 6: Profile of  $U_x$  of cold field in the middle axis.

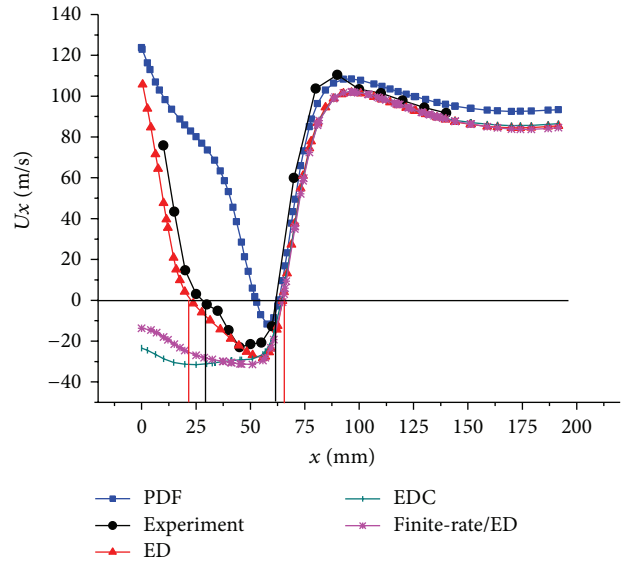


FIGURE 7: Profile of  $U_x$  of combustion field in the middle axis.

Figure 7 shows the comparison between the results of different combustion models and experiment data. More specifically, combustion models include probability density function model (PDF), eddy-dissipation model (ED), eddy-dissipation concept model (EDC), and finite-rate/eddy-dissipation model (Finite-Rate/ED). From the figure it can be concluded that when  $x < 75$  mm, only ED model could fit the experiment data. When  $x > 75$  mm, the simulated results with all combustion models are the same. As known to all, the character of central recirculation zone (CRZ) is  $U_x < 0$ .

The region of CRZ is also shown in Figure 6. It indicates that the region of CRZ simulated with ED is almost same as experiment data.

As shown above, it can be concluded that RNG  $k$ -epsilon turbulence model and ED combustion model are the best choice in numerical simulation of gas turbine annular combustor in this paper.

3.2.2. *Validations for Bluff Body Burner.* In the numerical simulation of bluff body burner, four different turbulence

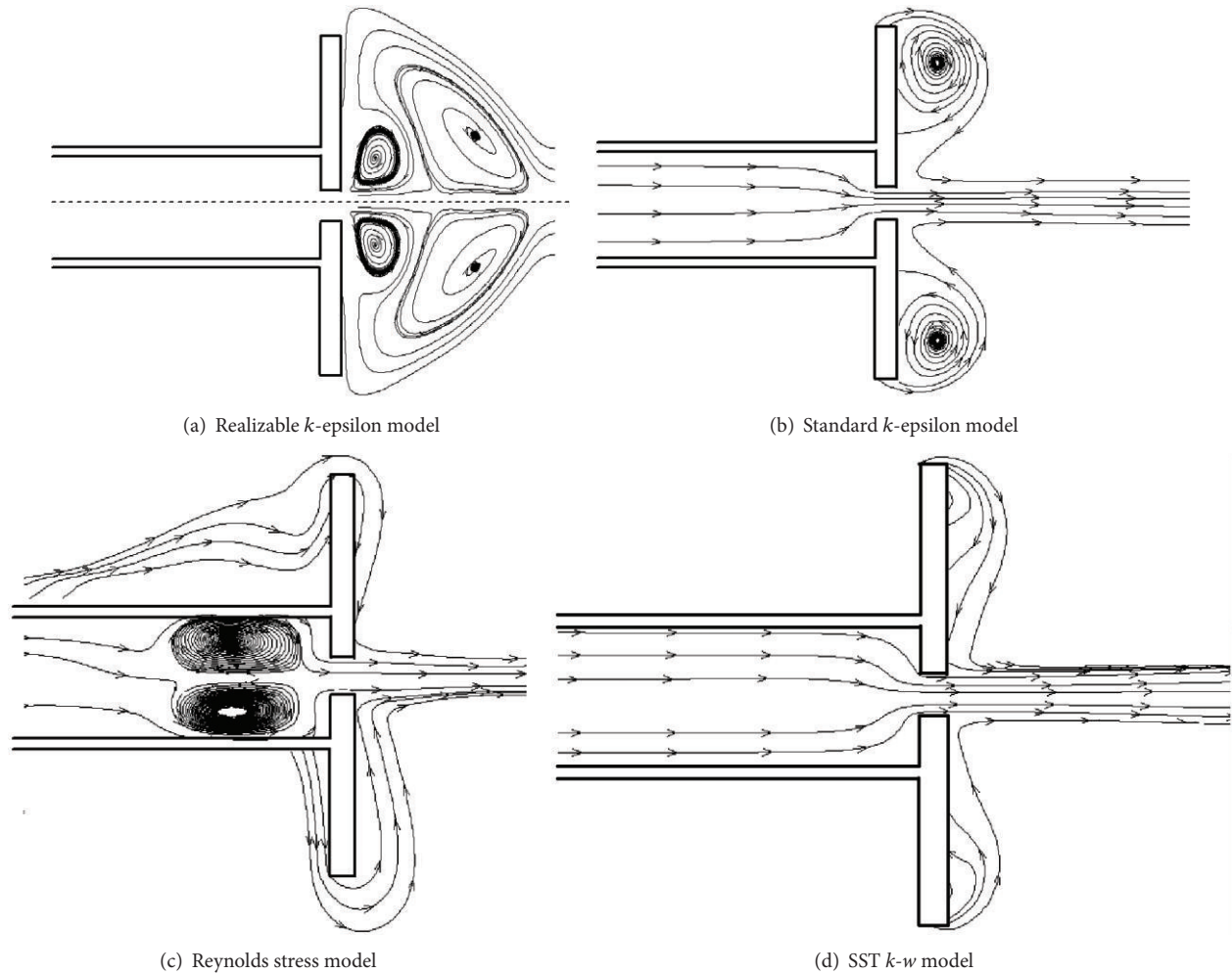


FIGURE 8: Streamline of cold flow field with different turbulence models.

models (RKE model, SKE model, RSM model, and SST  $k-w$  model are included) and four different combustion models (ED model, EDC model, PDF model, and Finite-Rate/ED model) have been compared.

The GRI-MECH 3.0 detailed chemical reaction mechanism, consisting of 325 elementary reactions involving 53 species, was used as the first part of the mechanism and describes the reaction chemistry of  $\text{CH}_4$ . The second part of the mechanism was taken from [30] and involved the reactions of C2–C4 hydrocarbon fuels considered herein. The reaction rates that appear as source terms in the species transport equations are computed based on Arrhenius rate expressions.

Figure 8 shows the different streamline of cold flow field near disk stabilizer using different turbulence models when fuel air mixture velocity is 24 m/s and coflowing air velocity is 4.8 m/s. As is well-known, there are vortices in the downstream of bluff body (disk in this geometry), so RSM model and model are improper. Roquemore et al. [31] found the coaxial air that converges toward the centerline downstream of the bluff body can form a wake region, which extends approximately one bluff body diameter downstream

the stabilizer edge. A toroidal recirculating flow region is formed within the wake region by the interaction of the outer coaxial air with the central-jet flow. The streamline of cold flow field with RKE model accords with Roquemore's research conclusions. So RKE model is the best choice in numerical simulation of bluff body burner.

The generalized finite-rate chemistry formulation is suitable for a wide range of applications including laminar or turbulent reaction systems, and combustion systems with premixed, nonpremixed, or partially premixed flames [28]. Figure 9 shows the profile of temperature in the middle axis with different combustion models. More specifically, combustion models in numerical simulation bluff body burner include probability density function model (PDF), eddy-dissipation model (ED), eddy-dissipation concept model (EDC), and finite-rate/eddy-dissipation model (Finite-Rate/ED). From the figure we can conclude that Finite-Rate/ED model can fit the data of reference suitably.

As shown above, it can be concluded that RKE turbulence model and Finite-Rate/ED combustion model are the best choice in numerical simulation of bluff body burner in this paper.

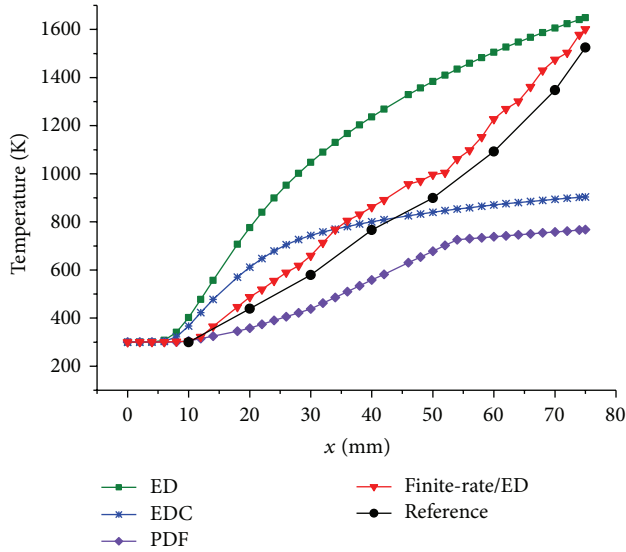


FIGURE 9: Profile of temperature in the middle axis with different combustion models.

## 4. Feature-Parameter-Criterion

**4.1. Feature-Section and Feature-Parameter.** In combustors, vortex breakdown of the swirling flow and cross-section extension at the outlet of nozzle will lead to formation of central recirculation zones (CRZ). CRZ is a simply connected zone which is composed of some surfaces whose feature is axial velocity  $u = 0$ . These zones transfer hot combustion products back to the nozzle, which enhances the ignition of unburned gas and thereby stabilizes the flame. With the reduction of inlet fuel air ratio, combustion efficiency and average temperature of flow field will decrease accordingly. Unburned gas flows into CRZ, which causes the average temperature of CRZ to decrease further, meanwhile the sparking distance will increase. When this distance exceeds the region of CRZ, fresh mixed gas could not be heated up by high-temperature gas of CRZ and overmuch fresh mixed gas (temperature is not high enough) flows into CRZ. It induces average temperature of CRZ decrease fast and lean blowout appears.

So the temperature change of CRZ seems to be the best standard of blowout. But in practical process, blowout in primary zone happens earlier than CRZ and the region of temperature decreasing of CRZ is little. It costs too much time if monitor the temperature changes of CRZ. And the prediction accuracy is unacceptable. Moreover, CRZ cannot stand for the changing regularity of whole combustor. To solve the above problems, a surface named Feature-Section which is tangent to the CRZ has been defined in this paper. It has been shown in Figure 10. Of course, under different fuel air ratio, the position and length of CRZ may change, so the position of Feature-Section may also change at the same time. The advantages of Feature-Section are, as next to the CRZ, it can reflect changing regularity of parameters in CRZ downstream sensitively; at the same time, it can monitor

more area than CRZ, so it can stand for the combustion characteristic of whole combustor objectively.

To describe the relationship between the change rate of average temperature and change rate of fuel air ratio, a new variable named feature-parameter  $\Gamma$  is defined as follows:

$$\Gamma = \frac{|(T_{n+1} - T_n) / T_n|}{|(\varphi_{n+1} - \varphi_n) / \varphi_n|}. \quad (11)$$

With the change of fuel flow and average temperature, feature-parameter  $\Gamma$  will also change. The more intensely the average temperature of feature section ( $T$ ) changes, the more greatly  $\Gamma$  varies. Among them, subscript  $n + 1$  represents current value and  $n$  represents previous value. And  $T$  represents average temperature in feature section.

With the decrease of fuel air ratio, average temperature of feature-section will also lower. But this change keeps small at the time of stable combustion, so the feature-parameter  $\Gamma$  will remain unchanged. As is well-known, blowout will occur suddenly and there is an obvious change on average temperature of feature-section. Thus, there should be an inflection point on the curves of average temperature and feature-parameter. As Figure 11 has shown, point A and point B are the inflection points which correspond to the lean blowout fuel air ratio.

**4.2. Prediction Process.** Numerical prediction of LBO is consistent with actual lean blowout process. Firstly, to numerically calculate two-phase combustion flow field which is far away from lean blowout points and obtain fuel air ratio  $\varphi_0$  and the average temperature  $T_0$ . Then to reduce fuel air ratio to  $\varphi_1$ , recalculate two phase combustion flow field, and obtain the relevant average temperature  $T_1$ . And obtain the feature-parameter  $\Gamma$  by using formula (11). To repeat this calculation till  $\varphi_{n+1}$ . If  $\Gamma_{n+1} > 5$ ,  $\varphi_{n+1}$  will be affirmed as fuel air ratio of lean blowout. If  $\Gamma_{n+1} \leq 5$ , take  $\varphi_{n+1}$  as  $\varphi_n$ , reduce fuel air ratio and make the recalculation. The prediction process is shown as Figure 12.

## 5. Results and Analysis

**5.1. Lean Blowout of Annular Combustor of Gas Turbine.** Lean blowout process, “M” flame, and some effect factors on lean blowout of combustor of gas turbine have been discussed in this paper.

**5.1.1. Blowout Process of Annular Combustor and “M” Flame.** Table 3 shows the results of LBO limit for an annular model combustor by using Feature-Parameter-Criterion. It shows that the LBO in this condition is 0.00415. The error of this result is 4.48% with experimental data.

Figure 13 shows the experiment [32] and simulation images of blowout process. The analysis of the images indicates that (a) the prediction of lean blowout process with FPC is in agreement with corresponding experimental image, and (b) there is an obvious portent before lean blowout—“M” flame.

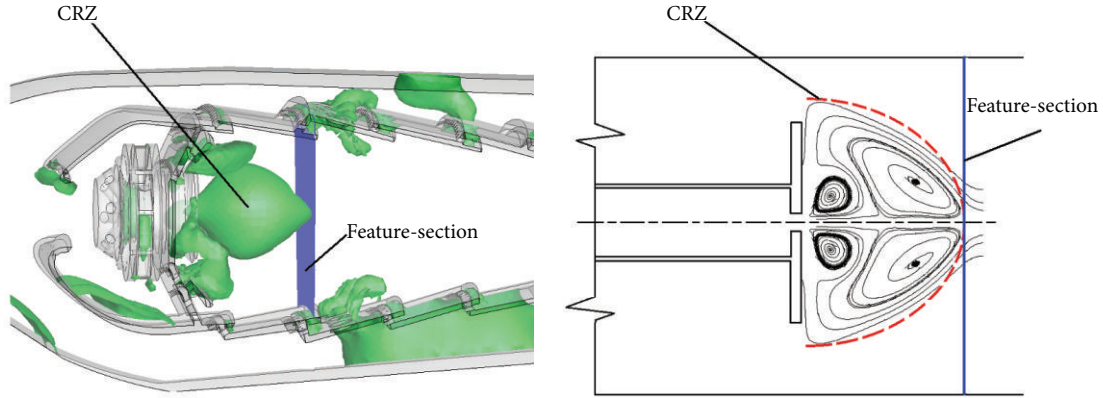


FIGURE 10: Schematic diagram of feature-section and CRZ.

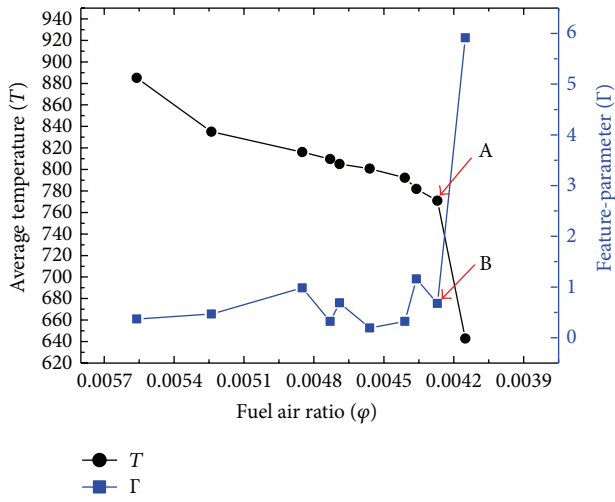


FIGURE 11: Changes of average temperature, feature-parameter, and fuel air ratio in a typical lean blowout course.

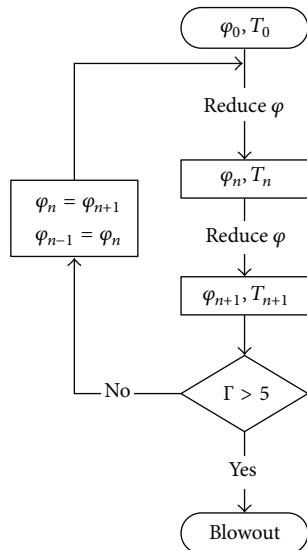


FIGURE 12: Prediction process of Feature-Parameter-Criterion.

TABLE 3: Prediction of LBO limit for gas turbine annular combustor.

	$\phi$	$T$	$\Delta\phi$	$\Gamma$
0	0.0187	1050.745	—	—
1	0.0125	996.971	0.3316	0.154
2	0.0098	974.352	0.216	0.105
$n - 1$	0.00436	781.842	0.0113	1.1593
$n$	0.00427	770.964	0.0206	0.0674
$n + 1$	0.00415	642.851	0.0281	5.913

The formation reasons for “M” flame are as follows.

- Because of central recirculation zone, there appears high negative velocity on the center of the axial line. When fuel air ratio is low, the back-flowed low-temperature air will flow into the center and compel the central to become short. Thus, “M” flame appears.
- A hollow and conical shape presents for the oil droplet (As shown in Figure 14), which makes more fuel going into the central area and less fuel going to the axial line of the flame tube. Thus, under the blowout conditions, the sufficient combustion cannot be ensured, which causes “M” flame. The distribution of oil droplet is shown intuitively in Figure 14.

Figure 15 shows the changes of flame front when fuel air ratio of annular combustor decreases gradually. In this process, with the decrease of the temperature of primary zone, flame front (contours of 2000 K is used as a symbol) changes into “M” shape gradually. Because of this “M” flame, the decrease speed rate of temperature in central point is more than that in other points of flame front. So it also induces the process of collapsing of flame and lean blowout.

Figure 16 shows the contours of three typical temperature distribution when lean blowout occurs.

- There is an obvious portent before lean blowout appears, “M” flame shape. The temperature of this primary flame is 2600 K. It means even though combustor works under lean blowout conditions, there is also high-temperature zone on the center of

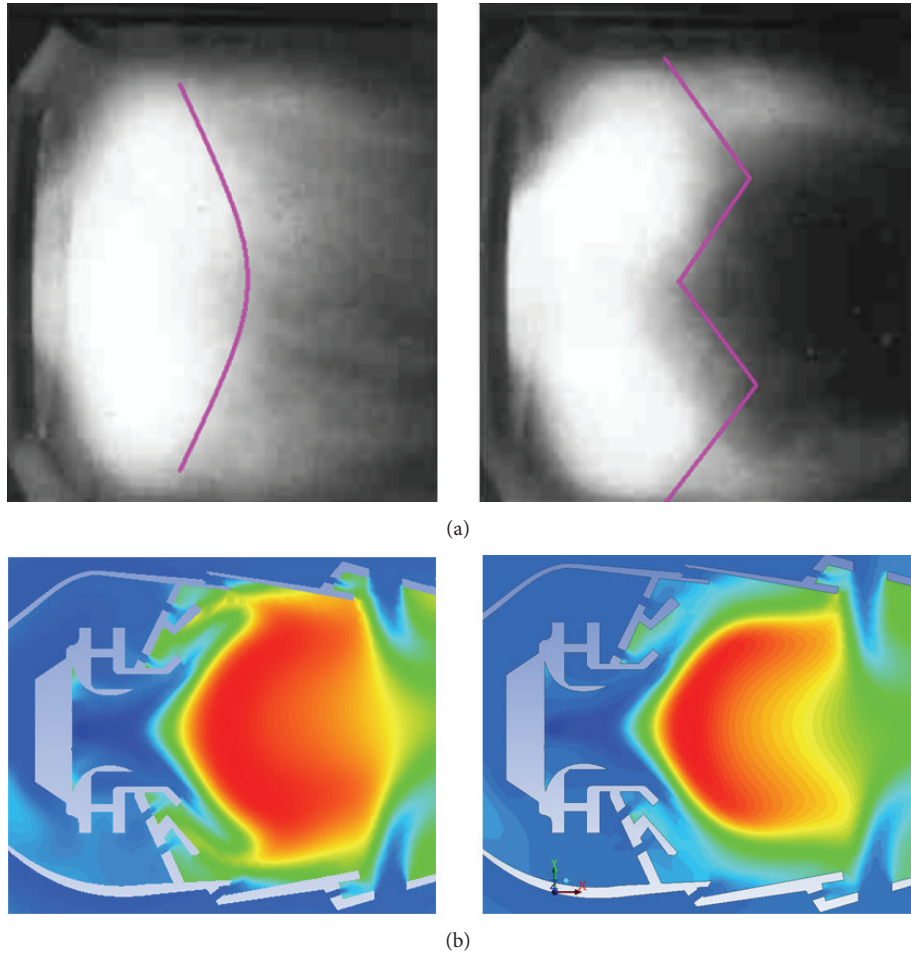


FIGURE 13: Experiment and simulation images of blowout process.

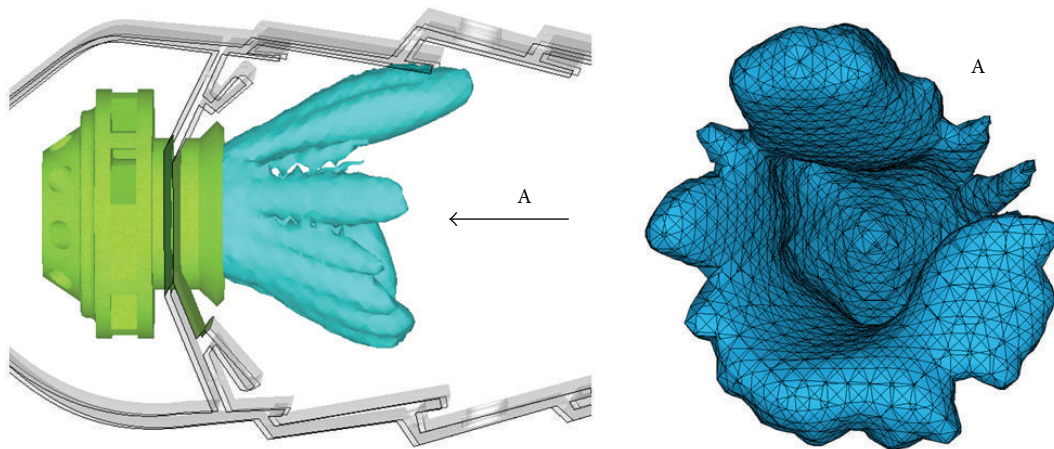


FIGURE 14: Distribution of oil droplet.

combustor. But the area of this zone is small, the diameter is quarter of flame tube.

(b) The previous experiment proves that there is no obvious flame boundary outside the primary flame front, but there exists a zone filled with high-temperature

mixing gas which is shown in Figure 15, the zone equal-temperature is indicated by 2200 K.

(c) Some cold air with temperature of 1300 K insulates the high-temperature zone and flame tube. It protects the metal wall and extends the life of the flame tube.

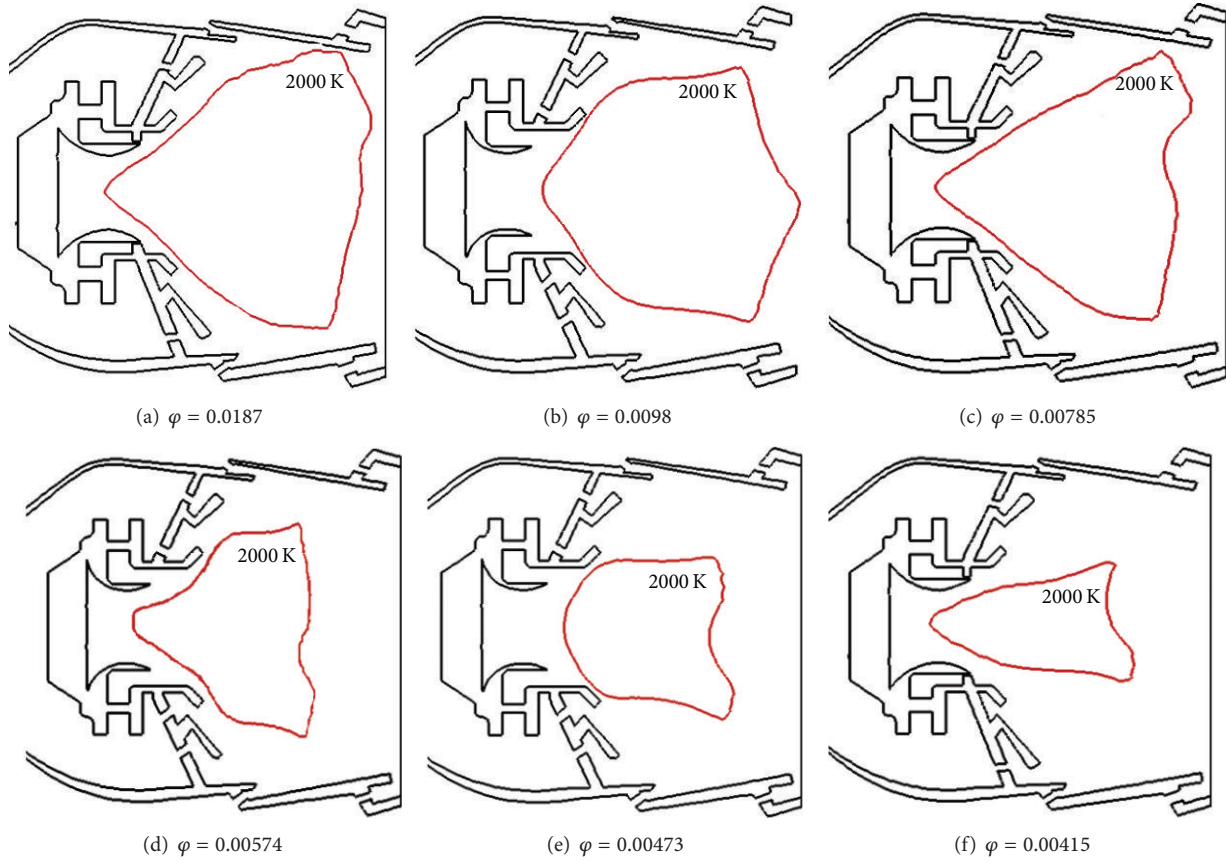


FIGURE 15: Changes of flame front with decreasing of fuel air ratio.

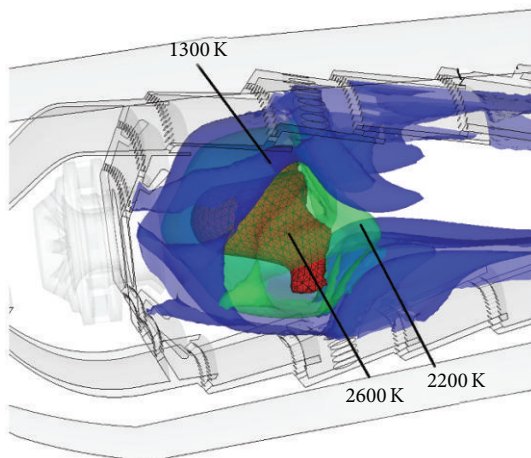


FIGURE 16: Contours of three typical temperatures.

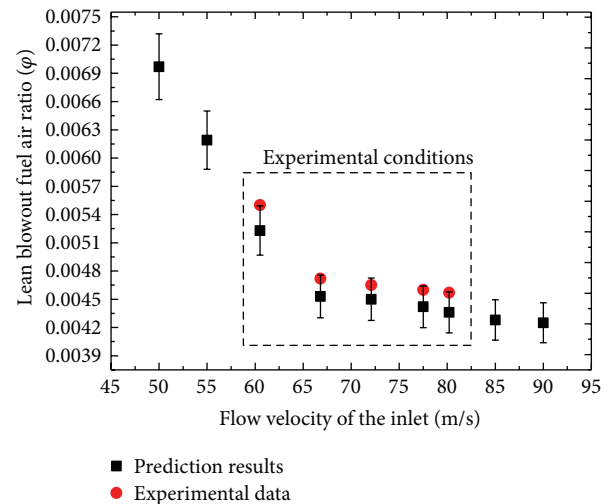


FIGURE 17: Effect of flow velocity of the inlet on lean blowout fuel air ratio.

### 5.1.2. Factors in Lean Blowout of Gas Turbine Combustor.

Numerical prediction of LBO under different flow velocity of the inlet and different temperature of air has been done in this paper by using Feature-Parameter-Criterion. The prediction results are compared with experimental data [33] for testing and verifying the accuracy of this new method. The results are shown in Figures 17 and 18.

Figure 17 shows the effects of flow velocity on LBO limit. It shows that lean blowout fuel air ratio will decline gradually as flow velocity is increased. The reason is that high-velocity air will disperse oil droplet into large space, and which will benefit the mixture between air and fuel. So the lean blowout

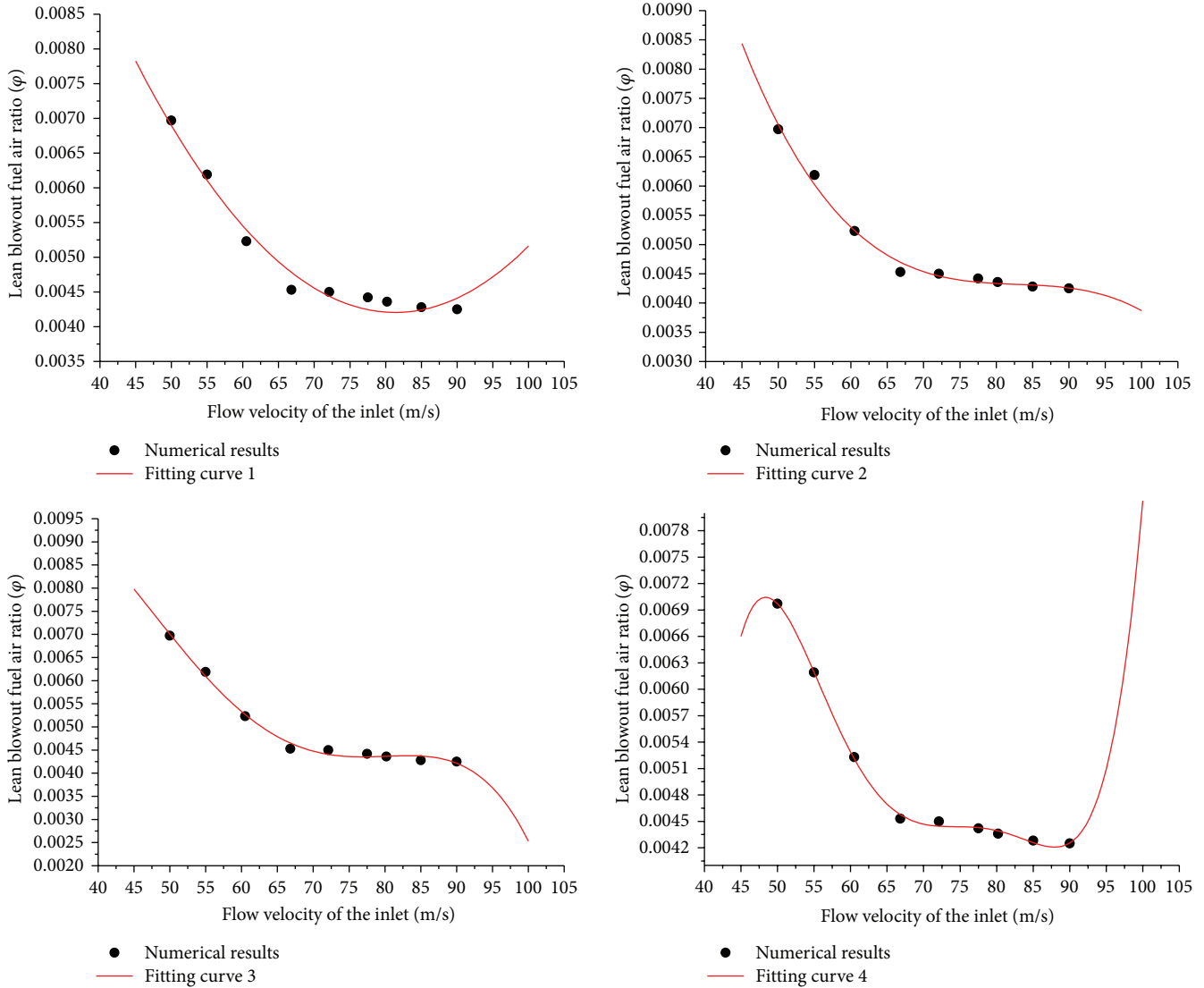


FIGURE 18: Curves of lean blowout fuel air ratio versus of flow velocity of the inlet and fitting curve.

fuel air ratio decreases. The max error between experimental data and prediction results is 5.01%, it can be accepted.

For describing above relationship between flow velocity of the inlet ( $V$ ) and lean blowout fuel air ratio ( $\varphi$ ), fitting formula of polynomials function could be assumed as follows:

$$\varphi = a \times V^5 + b \times V^4 + c \times V^3 + d \times V^2 + e \times V + f. \quad (12)$$

Fitting of the numerical data results by Least Square Method, the value of  $a, b, c, d, e, f$  can be gained as shown in Table 4. Figure 18 shows the numerical results, and the different fitting curve originated from fitting formula. It can be concluded that the error and trend of curve of cubic

polynomial is the best. And the final function which describe  $\varphi$  and  $V$  is shown below:

$$\varphi_3 = -2.97 \times 10^{-9}V^4 + 7.6 \times 10^{-7}V^3 - 6.83 \times 10^{-5}V^2 + 0.00242V - 0.0197. \quad (13)$$

Figure 19 shows the effects of air temperature on LBO limit. It shows that when air temperature is less than 397 K, lean blowout fuel air ratio declines gradually as air temperature is increased. The reason is (a) high-temperature air makes the well effect of oil droplet evaporation. The well mixture of air and fuel makes the well performance of combustor and makes the lower lean blowout fuel air ratio. (b) With the increasing of air temperature, heat requirement of CRZ decreases and most of energy can be used to keep stable combustion of primary combustion zone. So the combustor will not blowout quickly.

TABLE 4: Value of constant about lean blowout fuel air ratio and flow velocity of the inlet.

	$a$	$b$	$c$	$d$	$e$	$f$
$\varphi_1$	0	0	0	$2.74 \times 10^{-6}$	$-4.46 \times 10^{-4}$	0.02235
$\varphi_2$	0	0	$-7.24 \times 10^{-8}$	$1.8 \times 10^{-5}$	-0.0015	0.04592
$\varphi_3$	0	$-2.97 \times 10^{-9}$	$7.6 \times 10^{-7}$	$-6.83 \times 10^{-5}$	0.00242	-0.0197
$\varphi_4$	$4.67 \times 10^{-10}$	$-1.66 \times 10^{-7}$	$2.34 \times 10^{-5}$	-0.00162	0.0549	-0.72262

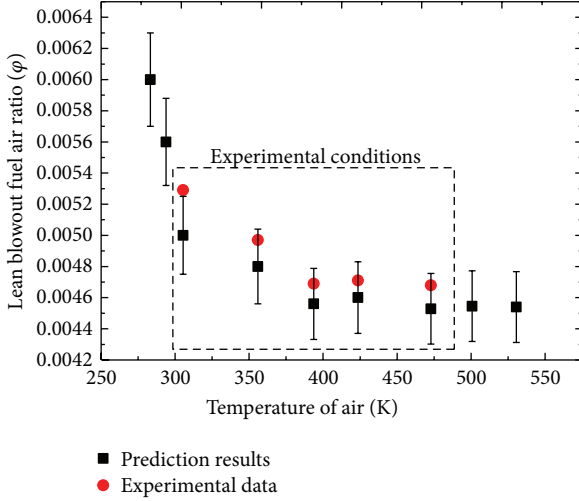


FIGURE 19: Effect of air temperature on lean blowout fuel air ratio.

But if air temperature is over the critical point (397 K), oil droplets which are in primary zone evaporate completely in a short time with the action of high-temperature air. Even raise the air temperature, it does not promote the mixing of fuel and air. So LBO fuel air ratio does not change as air temperature is increasing. If air temperature is less than 300 K, lean blowout fuel air ratio is over 0.0055, it is inadmissible by gas turbine combustor.

Figure 20 shows the relationship between droplet averaged-diameter ( $d_s$ ) and lean blowout fuel air ratio in different initial flow temperature.

When initial flow temperature is 423 K, the analysis of the figure indicates that with the increasing of droplet averaged-diameter, lean blowout fuel air ratio undergoes three different processes.

- When  $d_s < 70 \mu\text{m}$ , LBO fuel air ratio almost remains unchanged as droplet averaged-diameter is increased. The reason is that droplet averaged-diameter is small and the droplet life is short. Most of the droplets evaporate quickly and could only arrive at the edge of central recirculation zone. So air and fuel can mix with each other well and LBO fuel air ratio remains unchanged.
- When  $70 \mu\text{m} < d_s < 90 \mu\text{m}$  (point C is a turning-point), LBO fuel air ratio declines quickly as droplet averaged-diameter is increased and reaches to the minimum value at  $90 \mu\text{m}$  (point D). The reason is with the increasing of droplet averaged-diameter,

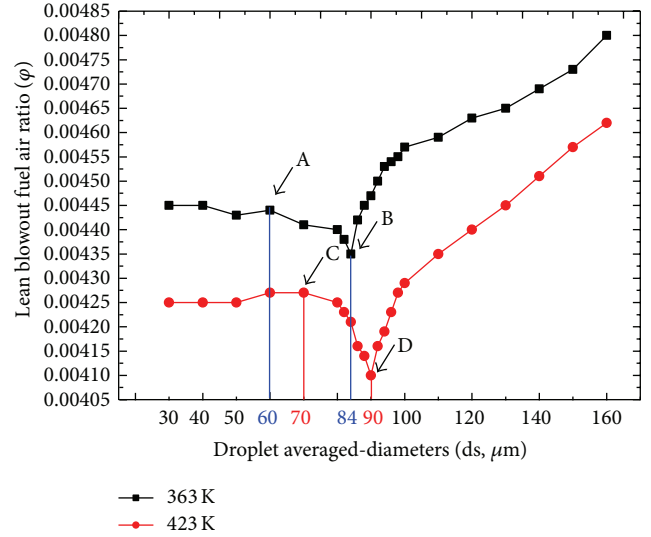


FIGURE 20: Effects of fuel droplet averaged-diameters on lean blowout fuel air ratio in different initial flow temperature.

some large-sized droplets arrive at the center of CRZ and burn there. As the flame presents “M” shape, temperature in the center line decreases slowest and they can transport energy to other zones of the combustor. So LBO fuel air ratio declines.

- When  $d_s > 90 \mu\text{m}$ , LBO fuel air ratio rises quickly as droplet averaged-diameter is increased. Because at this time, droplets averaged-diameter increases further and large-sized droplets cannot evaporate completely at CRZ. With the effect of inertia force, some large-sized droplets go through CRZ and arrive at the edge of primary combustion zone. These droplets take away the energy of CRZ and make the temperature of CRZ decrease. It induces the lean blowout phenomenon and makes LBO fuel air ratio rise quickly.

To explain the above phenomenon and reasons intuitively, distribution of oil droplet at different averaged-diameters is shown in Figure 21. When  $d_s = 50 \mu\text{m}$ , droplets only distribute in front of combustor (almost at the edge of CRZ). When  $d_s = 90 \mu\text{m}$ , some droplets do not evaporate and arrive at the center of CRZ. When  $d_s = 150 \mu\text{m}$ , most of droplets go through CRZ and arrive at the edge of primary combustion zone. The distribution of oil droplet affects the temperature of combustor and induces the different changes of lean blowout limit.

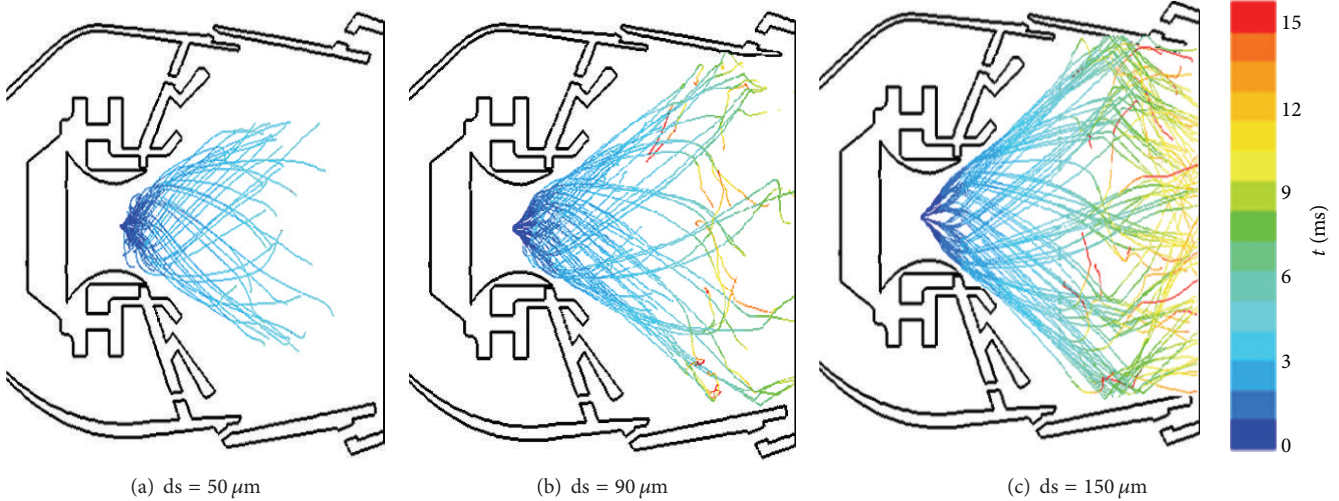


FIGURE 21: Distribution of droplet at different averaged-diameters.

As the evaporation rate of droplets also is affected by turbulent mixing and flow temperature, so some comparison has been done in this paper. When initial flow temperature is 363 K, the basic trend of curve is the same. But when initial flow temperature is lower, turning-points are  $60 \mu\text{m}$  and  $84 \mu\text{m}$  (point A and point B are the turning-points). They are smaller than the high-temperature results. The reason is that lower initial flow temperature cannot make fuel droplet evaporation in a short time, so some large-sized droplets arrive at the center of CRZ and they can transport energy to other zones of the combustor. It is benefiting the combustion stability. So LBO fuel air ratio declines quicker than higher initial flow temperature.

The effects of flow distribution between swirlers and primary holes have been researched in this paper. Then comparison between simulated results and experimental data has been shown.

Table 5 shows a detailed scheme of this research.

“Half” and “Full” in Table 5 mean the difference of airflow volume through homologous parts. For example, Figure 22 shows the sketch of decrease of air into primary holes [34]. For different scheme, pressure of outlet and total flow of combustor are not the same. In this paper, average value method has been used to eliminate the influence of these differences. Specifically, in the experiment, the researchers test 3 times for each scheme and show the average value for revising the error.

All the final results of different schemes are shown in Figure 23. It shows that

- (a) Reducing airflow volume through swirlers will extend stabilized combustion region. And the influence of oblique-hole is more than swirl-vane on lean blowout. The reason is when combustor works near blowout condition, the volume of flame is small; air for droplet atomization and combustion mainly comes from oblique-hole which is near the nozzle. So the changes of airflow volume through oblique-hole will affect blowout directly.

TABLE 5: Experimental and simulated scheme.

Scheme number	Oblique-hole swirler	Swirl-vane	Primary holes
1	Half	Half	
2	Full	Half	Half
3	Half	Full	
4	Full	Full	
5	Full	Full	
6	Half	Full	Full
7	Half	Half	

- (b) Lean blowout fuel air ratio will improve by decreasing airflow volume through primary holes and it is bad for the stabilized combustion performance.
- (c) The max error (structure 7) between experiment and simulation is 5.43%. It shows that the predictions of Feature-Parameter-Criterion are in agreement with corresponding experimental dates.

5.2. Lean Blowout of Bluff Body Burner. Lean blowout process and some factors in lean blowout of bluff body burner have been discussed in this part.

5.2.1. Blowout Process of Bluff Body Burner. Table 6 shows the results of LBO limit for bluff body burner by using Feature-Parameter-Criterion (fuel air mixture velocity is 23.8 m/s and coflowing air velocity is 4.8 m/s). It shows that the LBO limit in this condition is 0.00854. The experiment value is 0.00817 and the error is 4.51%.

Figure 24 shows the experiment [28] and simulation images of blowout process about bluff body burner. The flame is originally slender and relatively long. When the fuel air mixture is relatively low (24 m/s), flame ignition begins at a short quenching distance downstream from the disk and a lengthy rich flame is observed. If this velocity increases and exceeds 30 m/s, the flame became shorter and the boundary

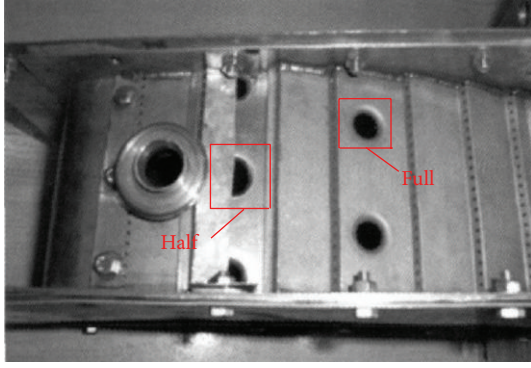


FIGURE 22: Sketch of decrease of air into primary holes.

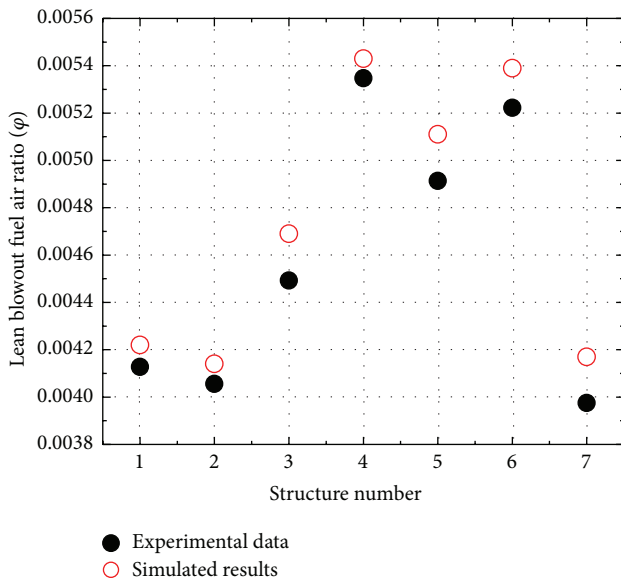


FIGURE 23: Experimental data and simulated results of blowout fuel air ratio with different structures.

of high-temperature flame reduces. Further increase velocity would shorten the flame further and concentrate the flame near disk.

**5.2.2. Factors in Lean Blowout of Bluff Body Burner.** Figure 25 shows the changes of lean blowout fuel air ratio at different fuel air mixture velocities it can conclude that (a) lean blowout fuel air ratio will rise as fuel air mixture velocity is increased. The reason is high velocity of fuel air mixture could destroy vortex near disk and lead to unstable combustion of bluff body burner. So the lean blowout performance worsens and the lean blowout fuel air ratio increases. (b) The error between prediction results with Feature-Parameter-Criterion and experimental data is about 5% and the accuracy is acceptable.

Five different structures of bluff body burner are shown in Figure 26. In general, there are two kinds of structures: cone and disk. The angles of cone changes from 30 to 90. Figure 27 shows the changes of lean blowout fuel air ratio at

TABLE 6: Prediction of LBO limit for bluff body burner.

	$\varphi$	$T$	$\Delta\varphi$	$\Gamma$
0	0.02554	1205	—	—
1	0.02409	1185	0.057	0.292
2	0.02264	1173	0.060	0.168
$n - 1$	0.01104	1159	0.512	0.023
$n$	0.00979	1146	0.113	0.099
$n + 1$	0.00854	413	0.128	5.009

different structures. It can conclude that (a) lean blowout fuel air ratio will rise as cone angle is increased. So the smaller angle of cone benefits the stability of combustion. (b) When fuel air mixture velocity is less than 39.7 m/s, the lean blowout performance of cone 90-degree is almost the same with disk; when this velocity is higher (more than 39.7 m/s), disk is the worst structure for stable combustion.

## 6. Conclusion

A new method named Feature-Parameter-Criterion (FPC) has been put forward in this paper for predicting lean blowout limit. The effects of operation condition (such as flow velocity, air temperature, droplet average-diameter, and flow distribution between swirlers and primary holes) on LBO limit of gas turbine combustor have been researched. Then the influences of fuel air mixture velocity and bluff body structures on bluff body burner's LBO limit have also been analyzed by use of FPC. The results showed that "M" flame could be the portent for predicting lean blowout of gas turbine combustor. The simulation of LBO limit based on FPC is in good agreement with the experiment data (the errors are about 5%), and this method is reliable for engineering applications. Other conclusions are as follows.

- (1) Lean blowout fuel air ratio declines gradually as flow velocity is increased. The fitting formula is  $\varphi = -2.97 \times 10^{-9}V^4 + 7.6 \times 10^{-7}V^3 - 6.83 \times 10^{-5}V^2 + 0.00242V - 0.0197$ .
- (2) As air temperature increases, when air temperature is less than 397 K, LBO fuel air ratio declines gradually, and when air temperature is over the critical point (397 K), lean blowout fuel air ratio remains unchanged.
- (3) When initial flow temperature is 423 K, as droplet averaged-diameter is increased, if  $ds < 70 \mu\text{m}$ , LBO fuel air ratio almost remains unchanged, and if  $70 \mu\text{m} < ds < 90 \mu\text{m}$ , LBO fuel air ratio decline quickly and reaches to the minimum value at  $90 \mu\text{m}$ , as well as if  $ds > 90 \mu\text{m}$ , LBO fuel air ratio rise quickly. When initial flow temperature is 363 K, the basic trend of curve is the same. But the value of turning-points is smaller than the high-temperature results.
- (4) Reducing airflow volume through swirlers will extend stabilized combustion region. And LBO fuel air ratio

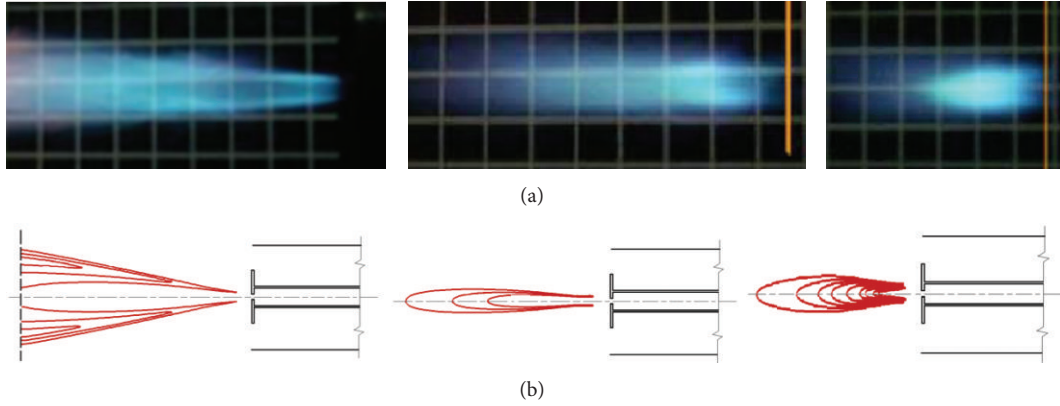


FIGURE 24: Experiment and simulation images of blowout process about bluff body burner.

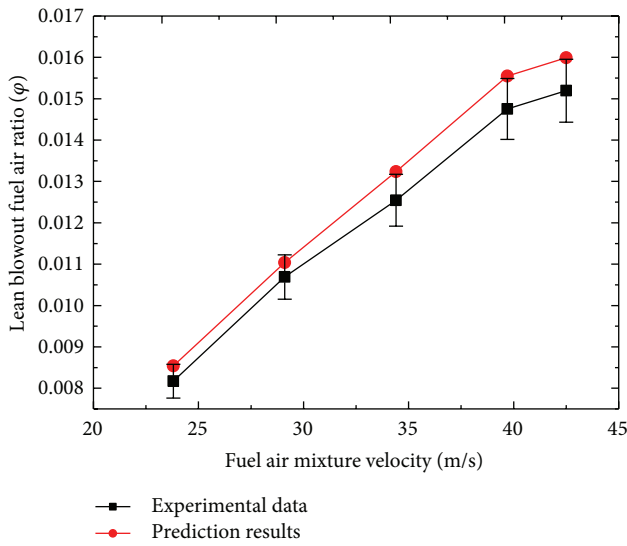


FIGURE 25: Effect of fuel air mixture velocity on lean blowout fuel air ratio.

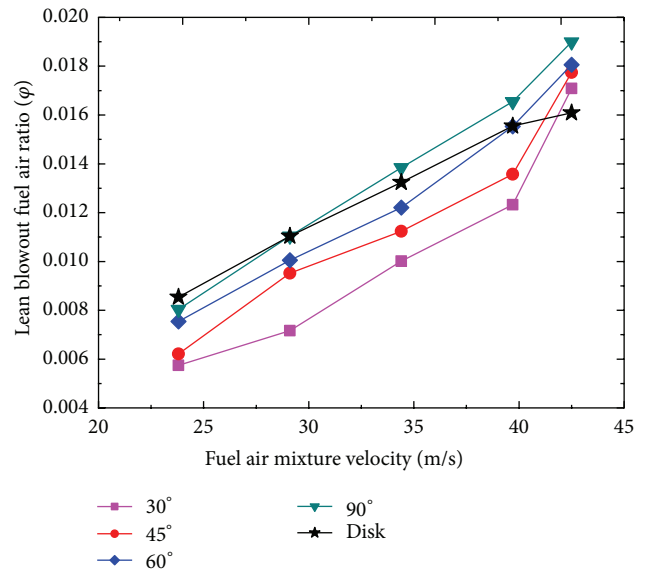


FIGURE 27: Effect of cone angle and disk on lean blowout fuel air ratio.

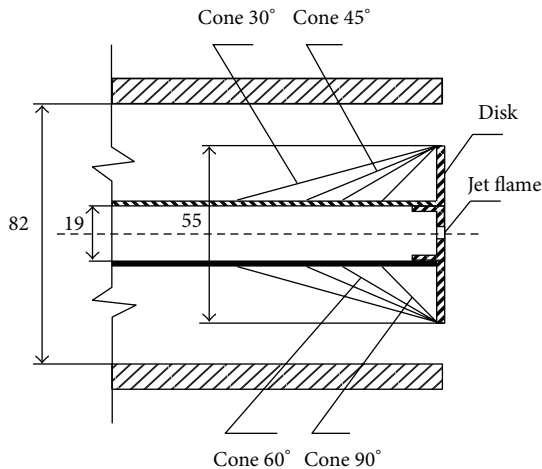


FIGURE 26: Schematic of different structures of bluff body burner.

will improve by decreasing airflow volume through primary holes.

(5) Lean blowout fuel air ratio will rise as fuel air mixture velocity and cone angle are increased.

**Nomenclatures**

- $\rho$ : Density ( $\text{kg}\cdot\text{m}^{-3}$ )
- $\bar{V}$ : Velocity ( $\text{m}\cdot\text{s}^{-1}$ )
- $S_m$ : Mass added to the continuous phase from the dispersed second phase and any user-defined sources
- $p$ : Static pressure (Pa)
- $\tau$ : Stress tensor
- $\vec{F}$ : External body forces or user-defined sources
- $\vec{q}$ : Radiation heat flux ( $\text{J}\cdot\text{m}^{-2}\cdot\text{s}^{-1}$ )

- $R_i$ : Net rate of production of species  $i$  by chemical reaction
- $Q_i$ : Rate of creation by addition from the dispersed phase plus any user-defined sources
- $k$ : Turbulent kinetic energy ( $\text{m}^2 \cdot \text{s}^{-2}$ )
- $\varepsilon$ : Kinetic energy dissipation rate ( $\text{m}^2 \cdot \text{s}^{-3}$ )
- $G_k$ : Generation of turbulence kinetic energy due to the mean velocity gradients
- $G_b$ : Generation of turbulence kinetic energy due to buoyancy
- $Y_k$ : Contribution of the fluctuating dilatation in compressible turbulence to the overall dissipation rate
- $S_k$ : User-Defined source terms
- $S_\varepsilon$ : User-Defined source terms
- $C_{1\varepsilon}$ : An empirical constant equals to 1.44
- $C_{2\varepsilon}$ : An empirical constant equals to 1.92
- $C_{3\varepsilon}$ : An empirical constant equals to 0
- $Y_p$ : Mass fraction of any product species
- $Y_R$ : Mass fraction of a particular reactant
- $A$ : An empirical constant equals to 4.0
- $B$ : An empirical constant equals to 0.5
- $T$ : Average temperature in feature section (K)
- $\varphi$ : Fuel air ratio
- $V$ : Axial velocity (m/s)
- $\Gamma$ : Feature parameter.

## Acknowledgments

Hongtao Zheng, Zhibo Zhang, and all the other authors acknowledge the contribution of the staff's advices and also appreciate the authors in the references.

## References

- [1] Y. Li, H. Zheng, and L. Cai, "Numerical simulation on hydrogen lean-blowout limit in bluff-body burner," *International Journal of Advancements in Computing Technology*, vol. 3, no. 10, pp. 232–239, 2011.
- [2] M. Stohr, I. Boxx, and C. Carter, "Dynamics of lean blowout of a swirl-stabilized flame in a gas turbine model combustor," *Proceedings of the Combustion Institute*, vol. 33, pp. 2953–2960, 2011.
- [3] W. A. Khan and A. Aziz, "Transient heat transfer in a functionally graded convecting longitudinal fin," *Heat and Mass Transfer*, vol. 48, no. 10, pp. 1745–1753, 2012.
- [4] A. Aziz and W. A. Khan, "Natural convective boundary layer flow of a nanofluid past a convectively heated vertical plate," *International Journal of Thermal Sciences*, vol. 52, no. 1, pp. 83–90, 2012.
- [5] O. D. Makinde, T. Chinyoka, and R. S. Lebelo, "Numerical investigation into CO<sub>2</sub> emission, O<sub>2</sub> depletion, and thermal decomposition in a reacting slab," *Mathematical Problems in Engineering*, vol. 2011, Article ID 208426, 19 pages, 2011.
- [6] O. D. Makinde and T. Chinyoka, "Analysis of unsteady flow of a variable viscosity reactive fluid in a slit with wall suction or injection," *Journal of Petroleum Science and Engineering*, vol. 94–95, pp. 1–11, 2012.
- [7] H. C. Mongia, "Recent progress in comprehensive modeling of gas turbine combustion," in *Proceedings of the 46th AIAA Aerospace Sciences Meeting and Exhibit*, January 2008, AIAA paper no. 2008-1445.
- [8] Y.-F. Cui, G. Xu, C.-Q. Nie, and W.-G. Huang, "Application of numerical simulation in the design of gas turbine combustor for burning syngas," *Proceedings of the Chinese Society of Electrical Engineering*, vol. 26, no. 16, pp. 109–116, 2006.
- [9] M. Boileau, G. Staffelbach, B. Cuenot, T. Poinso, and C. Bérat, "LES of an ignition sequence in a gas turbine engine," *Combustion and Flame*, vol. 154, no. 1-2, pp. 2–22, 2008.
- [10] S. Marinov, M. Kern, K. Merkle et al., "On swirl stabilized flame characteristics near the weak extinction limit," in *Proceedings of the ASME Turbo Expo 2010: Power for Land, Sea, and Air*, vol. 2, pp. 259–268, June 2010.
- [11] T. M. Muruganandam and J. M. Seitzman, "Fluid mechanics of lean blowout precursors in gas turbine combustors," *International Journal of Spray and Combustion Dynamics*, vol. 4, no. 1, pp. 29–60, 2012.
- [12] S. Zhu and S. Acharya, "An experimental study of lean blowout with hydrogen-enriched fuels," *Journal of Engineering for Gas Turbines and Power*, vol. 134, no. 4, Article ID 041507, 2012.
- [13] Y.-X. Yuan, Y.-Z. Lin, and G.-E. Liu, "The effect of flow field and fuel spray of combustor with swirl cup on lean blowout limit in idle condition," *Journal of Aerospace Power*, vol. 19, no. 3, pp. 332–337, 2004.
- [14] Q.-H. Xu, Y.-Z. Lin, G.-E. Liu, and Z.-P. Wang, "Research on the high-temperature rise combustor lean blow-out and smoke emission characteristics," *Journal of Aerospace Power*, vol. 20, no. 4, pp. 636–640, 2005.
- [15] X.-X. Dang, J.-X. Zhao, and H.-H. Ji, "Experimental study of effects of geometric parameters on combustion performance of dual-stage swirler combustor," *Journal of Aerospace Power*, vol. 22, no. 10, pp. 1639–1645, 2007.
- [16] H.-S. Hu, J.-X. Zhao, J.-P. Zhong, R.-W. Jiang, and M.-Z. Yin, "A new adjustment method of combustor outlet temperature field," *Journal of Aerospace Power*, vol. 22, no. 8, pp. 1222–1226, 2007.
- [17] A. H. Lefebvre and D. R. Ballal Lefebvre, *Gas Turbine Combustion: Alternative Fuels and Emissions*, CRC Press, New York, NY, USA, 2010.
- [18] A. M. Meller, *Design of Modern Turbine Combustor*, Academic Press, London, UK, 1990.
- [19] N. K. Rizk and H. C. Mongia, "A 3d analysis of gas turbine combustor," AIAA paper no. 89-2888, 1989.
- [20] H. C. Mongia, "Combining Lefebvre's correlations with combustor CFD," in *Proceedings of the 40th AIAA/ASME/SAE/ASEE Joint Propulsion Conference and Exhibit*, 2004, AIAA paper no. 2004-3544.
- [21] N. K. Rizk and H. C. Mongia, "Gas turbine combustor design methodology," in *Proceedings of the 22nd AIAA/ASME/SAE/ASEE Joint Propulsion Conference*, 1986, AIAA paper no. 86-1531.
- [22] W.-W. Kim, J. J. Lienau, P. R. van Slooten, M. B. Colket III, R. E. Malecki, and S. Syed, "Towards modeling lean blow out in gas turbine flameholder applications," *Journal of Engineering for Gas Turbines and Power*, vol. 128, no. 1, pp. 40–48, 2006.
- [23] S. J. Shanbhogue, S. Husain, and T. Lieuwen, "Lean blowoff of bluff body stabilized flames: scaling and dynamics," *Progress in Energy and Combustion Science*, vol. 35, no. 1, pp. 98–120, 2009.
- [24] K. Kumaran and U. S. P. Shet, "Effect of swirl on lean flame limits of pilot-stabilized open premixed turbulent flames," *Combustion and Flame*, vol. 151, no. 1-2, pp. 391–395, 2007.

- [25] Q. Zhang, D. R. Noble, S. J. Shanbhogue, and T. Lieuwen, "Impacts of hydrogen addition on near-lean blowout dynamics in a swirling combustor," in *Proceedings of the ASME Turbo Expo 2007: Power for Land, Sea, and Air*, pp. 189–198, Montreal, Canada, May 2007, ASME paper no. GT2007-27308.
- [26] P. Strakey, T. Sidwell, and J. Ontko, "Investigation of the effects of hydrogen addition on lean extinction in a swirl stabilized combustor," *Proceedings of the Combustion Institute*, vol. 31, no. 2, pp. 3173–3180, 2007.
- [27] W.-X. Cai, J.-X. Zhao, H.-S. Hu, X.-X. Dang, and X.-S. Wu, "Numerical prediction of lean blowout in aero-engine combustor," *Journal of Aerospace Power*, vol. 25, no. 7, pp. 1478–1484, 2010.
- [28] K. M. Shebl, "Experimental blowout limits and computational flow field of axial single and multijet flames," *Journal of Engineering for Gas Turbines and Power*, vol. 130, no. 5, Article ID 054505, 2008.
- [29] X. Dang, *Experimental investigation and numerical simulation of a gas turbine annular combustor with dual-stage swirler [Dissertation]*, Nanjing University of Aeronautics and Astronautics, Nanjing, China, 2009.
- [30] Z. Qin, V. V. Lissianski, H. Yang, W. C. Gardiner, S. G. Davis, and H. Wang, "Combustion chemistry of propane: a case study of detailed reaction mechanism optimization," *Proceedings of the Combustion Institute*, vol. 28, no. 2, pp. 1663–1669, 2000.
- [31] W. M. Roquemore, R. P. Bradley, J. S. Stutrud, C. M. Reeves, and L. Krishnamurthy, "Preliminary evaluation of a combustor for use in modeling and diagnostics development," ASME paper no. 80-GT-93, 1980.
- [32] Y.-X. Yuan, Y.-Z. Lin, G.-E. Liu, G. Hu, and J. Gong, "The effect of fuel-circumferential-staging on lean blowout limit at idle condition," *Journal of Aerospace Power*, vol. 18, no. 5, pp. 639–644, 2003.
- [33] Z. Zhang, *Experimental study on fuel spray characteristics in model combustor [Dissertation]*, Nanjing University of Aeronautics and Astronautics, Nanjing, China, 2009.
- [34] H.-P. Xu, F. Wang, Y. Huang, and Y.-F. Zhang, "Effects of flow split among swirlers and primary holes on the lean blowoff limits of a combustor with swirl cup," *Journal of Aerospace Power*, vol. 24, no. 2, pp. 347–352, 2009.

## Research Article

# Time-Splitting Procedures for the Numerical Solution of the 2D Advection-Diffusion Equation

A. R. Appadu<sup>1</sup> and H. H. Gidey<sup>1,2</sup>

<sup>1</sup> Department of Mathematics and Applied Mathematics, University of Pretoria, Pretoria 0002, South Africa

<sup>2</sup> African Institute for Mathematical Sciences (AIMS), 6 Road Melrose Road, Muizenberg 7945, Cape Town, South Africa

Correspondence should be addressed to A. R. Appadu; rao.appadu@up.ac.za

Received 5 June 2013; Accepted 12 August 2013

Academic Editor: Waqar Khan

Copyright © 2013 A. R. Appadu and H. H. Gidey. This is an open access article distributed under the Creative Commons Attribution License, which permits unrestricted use, distribution, and reproduction in any medium, provided the original work is properly cited.

We perform a spectral analysis of the dispersive and dissipative properties of two time-splitting procedures, namely, locally one-dimensional (LOD) Lax-Wendroff and LOD (1, 5) [9] for the numerical solution of the 2D advection-diffusion equation. We solve a 2D numerical experiment described by an advection-diffusion partial differential equation with specified initial and boundary conditions for which the exact solution is known. Some errors are computed, namely, the error rate with respect to the  $L_1$  norm, dispersion and dissipation errors. Lastly, an optimization technique is implemented to find the optimal value of temporal step size that minimizes the dispersion error for both schemes when the spatial step is chosen as 0.025, and this is validated by numerical experiments.

## 1. Introduction

The advection-diffusion equation is a parabolic partial differential equation combining the diffusion and advection (convection) equations, which describes physical phenomena where particles, energy, or other physical quantities are transferred inside a physical system due to two processes: diffusion and advection [1]. The numerical solution of advection-diffusion equation plays an important role in many fields of science and engineering. These include the transport of air and groundwater pollutants, oil reservoir flow [2], heat transfer in draining film, flow through porous media, the dispersion of pollutants in rivers and streams, long range transport of pollutants in the atmosphere, thermal pollution in river systems, and dispersion of dissolved salts in groundwater [3].

The 3D advection-diffusion equation is given by

$$\frac{\partial u}{\partial t} + \beta_x \frac{\partial u}{\partial x} + \beta_y \frac{\partial u}{\partial y} + \beta_z \frac{\partial u}{\partial z} = \alpha_x \frac{\partial^2 u}{\partial x^2} + \alpha_y \frac{\partial^2 u}{\partial y^2} + \alpha_z \frac{\partial^2 u}{\partial z^2}, \quad (1)$$

where  $\beta_x$ ,  $\beta_y$ , and  $\beta_z$  are the velocity components of advection in the directions of  $x$ ,  $y$ , and  $z$ , respectively, and  $\alpha_x$ ,  $\alpha_y$ ,

and  $\alpha_z$  are the coefficients of diffusivity in the  $x$ -,  $y$ -, and  $z$ -directions, respectively.

This study deals with the 2D advection-diffusion equation,

$$\frac{\partial u}{\partial t} + \beta_x \frac{\partial u}{\partial x} + \beta_y \frac{\partial u}{\partial y} = \alpha_x \frac{\partial^2 u}{\partial x^2} + \alpha_y \frac{\partial^2 u}{\partial y^2}, \quad (2)$$

where  $0 < t \leq T$ , in the domain  $0 \leq x \leq 1$ ,  $0 \leq y \leq 1$ , with specified initial and boundary conditions.

Dehghan [3] proposed two time-splitting procedures for the solution of the two-dimensional transport equation. The time-splitting procedure used is the locally-one dimensional (LOD) in proceeding from one time step to the next step. LOD replaces the complicated multidimensional partial differential equations by a sequence of solutions of simpler one-dimensional partial differential equations. The originality in this work is that we perform a spectral analysis of the dispersion and dissipation properties of the two schemes at some values of the temporal and spatial step sizes. 3D plots of the relative phase error per unit time step (RPE) and the modulus of the amplification factor (AFM) versus phase angles in  $x$ - and  $y$ -directions are obtained. We then use optimization strategies to compute the optimal values of

the temporal step size for the two schemes when the spatial step size is 0.025. We then validate this result by performing a 2D numerical experiment with specified initial and boundary conditions. Lastly, we have the conclusion and references.

## 2. Numerical Dispersion and Dissipation

Dissipation reduces the amplitude of sinusoids in a Fourier series. This is caused by the presence of derivatives like  $u_{xx}$  and  $-u_{xxxx}$  in the modified equation [4]. On the other hand, the amplitude of sinusoids in a Fourier series is increased by antidissipation. Derivatives like  $-u_{xx}$  and  $u_{xxxx}$  in the modified equation are generally antidissipative. Dispersion affects the speed of sinusoids in a Fourier series causing phase lag or phase lead and is caused due to the presence of odd-order derivatives in the modified equation [4].

The modulus of the amplification factor (AFM) is a measure of the stability of a scheme and it is also used to measure the dissipative characteristics of the scheme. If the modulus of the amplification factor is equal to one, a disturbance neither grows nor damps [5]. If the modulus of the amplification factor is greater than one, then the scheme is unstable [6]; if it is less than one, damping occurs [7]. The partial differential equation given by (2) is dissipative in nature due to the terms  $u_{xx}$  and  $u_{yy}$ .

The relative phase error (RPE) is a measure of the dispersive characteristics of a scheme. The relative phase error of a scheme approximating the 1D advection-diffusion equation is given by

$$\text{RPE} = -\frac{1}{c\omega} \arctan\left(\frac{\Im(\xi)}{\Re(\xi)}\right), \quad (3)$$

where  $c$  is the Courant number,  $\omega$  is phase angle,  $\xi$  is the amplification factor of the numerical scheme approximating the 1D advection-diffusion equation, and  $\Re(\xi)$  and  $\Im(\xi)$  are the real and imaginary parts of  $\xi$ , respectively [8].

We extend the work on the relative phase error in [8] for the case of the 2D advection-diffusion equation. The relative phase error for a numerical scheme approximating (2) is obtained on substituting  $u$  by  $\exp(I(\omega_1 t - \theta_1 x - \theta_2 y))$  [9], where  $I = \sqrt{-1}$ ,  $t$  is the time,  $\theta_1$  and  $\theta_2$  are wavenumbers in the directions of  $x$  and  $y$ , respectively, and  $\omega_1$  is the dispersion relation. Thus, we get

$$\begin{aligned} \frac{\partial u}{\partial t} &= I\omega_1 \exp(I(\omega_1 t - \theta_1 x - \theta_2 y)), \\ \frac{\partial u}{\partial x} &= -I\theta_1 \exp(I(\omega_1 t - \theta_1 x - \theta_2 y)), \\ \frac{\partial u}{\partial y} &= -I\theta_2 \exp(I(\omega_1 t - \theta_1 x - \theta_2 y)), \\ \frac{\partial^2 u}{\partial x^2} &= -(\theta_1)^2 \exp(I(\omega_1 t - \theta_1 x - \theta_2 y)), \\ \frac{\partial^2 u}{\partial y^2} &= -(\theta_2)^2 \exp(I(\omega_1 t - \theta_1 x - \theta_2 y)). \end{aligned} \quad (4)$$

On substituting (4) into (2), we obtain

$$\omega_1 = \beta_x \theta_1 + \beta_y \theta_2 + (\alpha_x (\theta_1)^2) I + (\alpha_y (\theta_2)^2) I. \quad (5)$$

The exact phase velocity is  $\Re(\omega_1)/\text{wavenumber}$  and we obtain

$$\text{exact phase velocity} = \frac{\beta_x \theta_1 + \beta_y \theta_2}{\text{wavenumber}}. \quad (6)$$

The amplification factor can be written as  $\xi = \xi_1 + I\xi_2$ , where  $\xi_1$  and  $\xi_2$  are the real and imaginary parts of  $\xi$ , respectively. Also, we can express  $\xi$  as  $\xi = \exp(-bk)$ , where  $k$  is time step and  $b$  is exponential growth rate [9]. Thus, we obtain

$$b = \frac{1}{k} \log\left(\frac{\xi_1 - I\xi_2}{\xi_1^2 + \xi_2^2}\right). \quad (7)$$

The numerical phase velocity is calculated as  $\Im(b)/\text{wavenumber}$  and we get

$$\text{numerical phase velocity} = \frac{-(1/k) \arctan(\xi_2/\xi_1)}{\text{wavenumber}}. \quad (8)$$

The relative phase error is the ratio of the numerical phase velocity to the exact phase velocity [10]. It is calculated as

$$\text{RPE} = -\frac{1}{k(\beta_x \theta_1 + \beta_y \theta_2)} \arctan\left(\frac{\xi_2}{\xi_1}\right). \quad (9)$$

The phase angles in the directions of  $x$  and  $y$  are given by  $\omega_x = \Delta x \theta_1$  and  $\omega_y = \Delta y \theta_2$ , respectively. Hence, the relative phase error is

$$\text{RPE} = -\frac{1}{c_x \omega_x + c_y \omega_y} \arctan\left(\frac{\xi_2}{\xi_1}\right), \quad (10)$$

where  $c_x = \beta_x k / \Delta x$  and  $c_y = \beta_y k / \Delta y$  are the Courant numbers in the directions of  $x$  and  $y$ , respectively.

## 3. Time-splitting Procedures and Numerical Experiments

The domain we consider is  $x, y \in [0, 1]$ . We divide the spatial interval  $[0, 1]$  along  $x$ - and  $y$ -directions into  $N$  and  $M$  nodes, respectively, such that  $(N-1)\Delta x = 1$  and  $(M-1)\Delta y = 1$  and also divide the time interval  $[0, T]$  into  $P$  grid points such that  $(P-1)\Delta t = T$ . Then the grid points  $(x_i, y_j, t_n)$  are defined by

$$\begin{aligned} x_i &= i\Delta x, \quad i = 1, 2, \dots, N, \\ y_j &= j\Delta y, \quad j = 1, 2, \dots, M, \\ t_n &= n\Delta t, \quad n = 1, 2, \dots, P. \end{aligned} \quad (11)$$

For simplification we take  $\Delta x = \Delta y = h$ . Let  $\Delta t = k$ ; then the parameters  $h$  and  $k$  represent the spatial and temporal grid spacing, respectively. We denote the approximated value of  $u$  at the grid point  $(i, j, n)$  by  $u_{i,j}^n$ .

3.1. *Time-Splitting Procedures.* Since one-dimensional schemes are easier to use than two-dimensional schemes, (2) is split into the following two one-dimensional equations:

$$\frac{1}{2} \frac{\partial u}{\partial t} + \beta_x \frac{\partial u}{\partial x} = \alpha_x \frac{\partial^2 u}{\partial x^2}, \quad (12)$$

$$\frac{1}{2} \frac{\partial u}{\partial t} + \beta_y \frac{\partial u}{\partial y} = \alpha_y \frac{\partial^2 u}{\partial y^2}. \quad (13)$$

Each of (12) and (13) can be solved over half of a time step to be used for the complete 2D advection-diffusion equation, using the procedures developed for the 1D advection-diffusion equation.

Some work on time-splitting procedures can be found in [3, 11]. In this paper, we refer to [3] on how a 2D advection-diffusion equation is converted into two 1D advection-diffusion equations using the locally one-dimensional (LOD) time-splitting procedure. Solving (12) and (13) in each half time step is equivalent to solving the following equations over a full-time step:

$$\frac{\partial u}{\partial t} + \beta_x \frac{\partial u}{\partial x} = \alpha_x \frac{\partial^2 u}{\partial x^2}, \quad (14)$$

$$\frac{\partial u}{\partial t} + \beta_y \frac{\partial u}{\partial y} = \alpha_y \frac{\partial^2 u}{\partial y^2}. \quad (15)$$

Then we can use the schemes used for solving the 1D advection-diffusion equation to solve (14) and (15).

3.2. *Numerical Experiments.* In [12], different explicit and implicit finite differences schemes are used to solve the 1D advection-diffusion equation

$$\frac{\partial u}{\partial t} + \frac{\partial u}{\partial x} = 0.01 \frac{\partial^2 u}{\partial x^2}. \quad (16)$$

Three values of the cell Reynolds number, namely,  $R_\Delta = 2, 4,$  and  $8,$  are used for the numerical experiments. In [3], the time-splitting procedure is used to solve the two-dimensional transport equation in the region  $0 \leq x \leq 1, 0 \leq y \leq 1,$  with

$$\alpha_x = \alpha_y = \alpha = 0.01, \quad \beta_x = \beta_y = \beta = 0.8 \quad (17)$$

and with the following boundary and initial conditions:

$$g_0(x, t) = \frac{1}{4t+1} \exp \left[ -\frac{(x-0.8t-0.5)^2}{0.01(4t+1)} - \frac{(0.8t+0.5)^2}{0.01(4t+1)} \right], \quad (18)$$

$$g_1(x, t) = \frac{1}{4t+1} \exp \left[ -\frac{(x-0.8t-0.5)^2}{0.01(4t+1)} - \frac{(0.5-0.8t)^2}{0.01(4t+1)} \right], \quad (19)$$

$$h_0(y, t) = \frac{1}{4t+1} \exp \left[ -\frac{(0.8t+0.5)^2}{0.01(4t+1)} - \frac{(y-0.8t-0.5)^2}{0.01(4t+1)} \right], \quad (20)$$

$$h_1(y, t) = \frac{1}{4t+1} \exp \left[ -\frac{(0.5-0.8t)^2}{0.01(4t+1)} - \frac{(y-0.8t-0.5)^2}{0.01(4t+1)} \right], \quad (21)$$

$$f(x, y) = \exp \left[ -\frac{(x-0.5)^2}{0.01} - \frac{(y-0.5)^2}{0.01} \right], \quad (22)$$

for which the exact solution is

$$u(x, y, t) = \frac{1}{4t+1} \exp \left[ -\frac{(x-0.8t-0.5)^2}{0.01(4t+1)} - \frac{(y-0.8t-0.5)^2}{0.01(4t+1)} \right]. \quad (23)$$

We consider two time-splitting procedures LOD Lax-Wendroff and LOD (1, 5) to solve (2) with  $\alpha_x = \alpha_y = \alpha = 0.01$  and  $\beta_x = \beta_y = \beta = 0.8,$  subject to the boundary conditions (18)–(22) at time  $T = 0.3.$

We consider two values of  $R_\Delta; R_\Delta = 2$  and  $R_\Delta = 4.$  Since  $c = 0.8k/h$  and  $s = 0.01k/h^2,$  we have  $R_\Delta = 80h.$  Thus for  $R_\Delta = 2$  and  $4,$  we have  $h = 0.025$  and  $h = 0.05,$  respectively. When  $h = 0.025,$  we have  $c = 32k$  and  $s = 16k$  and for  $h = 0.05$  we have  $c = 16k$  and  $s = 4k.$

3.3. *Quantification of Errors from Numerical Results.* In this subsection, we describe how errors from numerical results can be quantified into dispersion and dissipation by a technique devised by Takacs [13].

The total mean square error in the 1D case [13] is calculated as

$$E_{\text{TMS}} = \frac{1}{N} \sum_{i=1}^N (u_i - v_i)^2, \quad (24)$$

where  $u_i$  is the exact solution,  $v_i$  is the numerical solution at a grid point  $i,$  and  $N$  is the number of grid points. The total mean square error can be expressed as

$$\begin{aligned} \frac{1}{N} \sum_{i=1}^N (u_i - v_i)^2 &= \frac{1}{N} \sum_{i=1}^N (u_i - \bar{u})^2 + \frac{1}{N} \sum_{i=1}^N (v_i - \bar{v})^2 \\ &+ \frac{2}{N} \sum_{i=1}^N u_i \bar{u} + \frac{2}{N} \sum_{i=1}^N v_i \bar{v} - \frac{1}{N} \sum_{i=1}^N (\bar{u})^2 \\ &- \frac{1}{N} \sum_{i=1}^N (\bar{v})^2 - \frac{2}{N} \sum_{i=1}^N u_i v_i. \end{aligned} \quad (25)$$

The right hand side of (25) can be rewritten as

$$\sigma^2(u) + \sigma^2(v) + 2(\bar{u})^2 + 2(\bar{v})^2 - (\bar{u})^2 - (\bar{v})^2 - \frac{2}{N} \sum_{i=1}^N u_i v_i, \quad (26)$$

where  $\sigma^2(u)$  and  $\sigma^2(v)$  denote the variance of  $u$  and  $v$ , respectively, and  $\bar{u}$  and  $\bar{v}$  denote the mean values of  $u$  and  $v$ , respectively. Then we have

$$\begin{aligned} E_{\text{TMS}} &= \sigma^2(u) + \sigma^2(v) + ((\bar{u})^2 - 2\bar{u}\bar{v} + (\bar{v})^2) \\ &\quad + \left( 2\bar{u}\bar{v} - \frac{2}{N} \sum_{i=1}^N u_i v_i \right) \\ &= \sigma^2(u) + \sigma^2(v) + (\bar{u} - \bar{v})^2 - 2 \left( \frac{1}{N} \sum_{i=1}^N u_i v_i - \bar{u}\bar{v} \right). \end{aligned} \quad (27)$$

Therefore,

$$\frac{1}{N} \sum_{i=1}^N (u_i - v_i)^2 = \sigma^2(u) + \sigma^2(v) + (\bar{u} - \bar{v})^2 - 2\text{Cov}(u, v), \quad (28)$$

where  $\text{Cov}(u, v) = (1/N)(\sum_{i=1}^N u_i v_i - \bar{u}\bar{v})$ .

The total mean square error can be expressed as

$$\begin{aligned} \frac{1}{N} \sum_{i=1}^N (u_i - v_i)^2 &= (\sigma(u) - \sigma(v))^2 \\ &\quad + (\bar{u} - \bar{v})^2 + 2(1 - \rho)\sigma(u)\sigma(v), \end{aligned} \quad (29)$$

where  $\rho = \text{Cov}(u, v)/(\sigma(u)\sigma(v))$  is the coefficient of correlation.

The term  $2(1 - \rho)\sigma(u)\sigma(v)$  measures the dispersion error and the term  $(\sigma(u) - \sigma(v))^2 + (\bar{u} - \bar{v})^2$  measures the dissipation error.

We extend the work on quantification of errors in [14, 15] for the 2D case. The total mean square error for the 2D case is calculated as

$$E_{\text{TMS}} = \frac{1}{NM} \sum_{j=1}^M \sum_{i=1}^N (u_{i,j} - v_{i,j})^2, \quad (30)$$

where  $u_{i,j}$  and  $v_{i,j}$  are the exact and numerical solutions at a grid point  $(i, j)$ , respectively, and

$$\begin{aligned} &\frac{1}{NM} \sum_{j=1}^M \sum_{i=1}^N (u_{i,j} - v_{i,j})^2 \\ &= \frac{1}{NM} \sum_{j=1}^M \sum_{i=1}^N (u_{i,j}^2 - 2u_{i,j}v_{i,j} + v_{i,j}^2) \\ &= \frac{1}{NM} \left( \sum_{j=1}^M \sum_{i=1}^N u_{i,j}^2 + \sum_{j=1}^M \sum_{i=1}^N v_{i,j}^2 - 2 \sum_{j=1}^M \sum_{i=1}^N u_{i,j}v_{i,j} \right). \end{aligned} \quad (31)$$

Since

$$\begin{aligned} \sum_{j=1}^M \sum_{i=1}^N (u_{i,j} - \bar{u})^2 &= \sum_{j=1}^M \sum_{i=1}^N (u_{i,j}^2 - 2u_{i,j}\bar{u} + \bar{u}^2), \\ \sum_{j=1}^M \sum_{i=1}^N (v_{i,j} - \bar{v})^2 &= \sum_{j=1}^M \sum_{i=1}^N (v_{i,j}^2 - 2v_{i,j}\bar{v} + \bar{v}^2), \end{aligned} \quad (32)$$

we have

$$\begin{aligned} E_{\text{TMS}} &= \frac{1}{NM} \left[ \sum_{j=1}^M \sum_{i=1}^N (u_{i,j} - \bar{u})^2 + \sum_{j=1}^M \sum_{i=1}^N (v_{i,j} - \bar{v})^2 \right. \\ &\quad + 2 \sum_{j=1}^M \sum_{i=1}^N u_{i,j}\bar{u} + 2 \sum_{j=1}^M \sum_{i=1}^N v_{i,j}\bar{v} \\ &\quad \left. - 2 \sum_{j=1}^M \sum_{i=1}^N u_{i,j}v_{i,j} - \sum_{j=1}^M \sum_{i=1}^N \bar{u}^2 - \sum_{j=1}^M \sum_{i=1}^N \bar{v}^2 \right] \\ &= \sigma^2(u) + \sigma^2(v) + 2\bar{u}^2 + 2\bar{v}^2 \\ &\quad - \frac{2}{NM} \sum_{j=1}^M \sum_{i=1}^N u_{i,j}v_{i,j} - \bar{u}^2 - \bar{v}^2 \\ &= \sigma^2(u) + \sigma^2(v) + (\bar{u}^2 - 2\bar{u}\bar{v} + \bar{v}^2) \\ &\quad + 2\bar{u}\bar{v} - \frac{2}{NM} \sum_{j=1}^M \sum_{i=1}^N u_{i,j}v_{i,j} \\ &= \sigma^2(u) + \sigma^2(v) + (\bar{u} - \bar{v})^2 \\ &\quad - 2 \left[ \frac{1}{NM} \sum_{j=1}^M \sum_{i=1}^N u_{i,j}v_{i,j} - \bar{u}\bar{v} \right] \\ &= \sigma^2(u) + \sigma^2(v) + (\bar{u} - \bar{v})^2 - 2\text{Cov}(u, v). \end{aligned} \quad (33)$$

Hence,

$$E_{\text{TMS}} = (\sigma(u) - \sigma(v))^2 + (\bar{u} - \bar{v})^2 + 2(1 - \rho)\sigma(u)\sigma(v), \quad (34)$$

where  $\rho = \text{Cov}(u, v)/(\sigma(u)\sigma(v))$ . The dissipation error is  $(\sigma(u) - \sigma(v))^2 + (\bar{u} - \bar{v})^2$  and the dispersion error is  $2(1 - \rho)\sigma(u)\sigma(v)$ .

The error rate with respect to  $L_1$  norm for  $x, y \in [0, 1]$  is calculated as

$$E_{\text{num}} = \frac{1}{(N-1)(M-1)} \sum_{j=1}^M \sum_{i=1}^N |u_{i,j} - v_{i,j}|. \quad (35)$$

#### 4. Construction of the LOD Lax-Wendroff Procedure

We use the following approximations in the first time step of the LOD procedure [3]:

$$\frac{\partial u}{\partial t} \Big|_{i,j}^n \approx \frac{u_{i,j}^{n+(1/2)} - u_{i,j}^n}{\Delta t},$$

$$\begin{aligned}\frac{\partial u}{\partial x}\Big|_{i,j}^n &\simeq \frac{(1-\gamma_x)(u_{i,j}^n - u_{i-1,j}^n) + \gamma_x(u_{i+1,j}^n - u_{i,j}^n)}{\Delta x}, \\ \frac{\partial^2 u}{\partial x^2}\Big|_{i,j}^n &\simeq \frac{u_{i+1,j}^n - 2u_{i,j}^n - u_{i-1,j}^n}{(\Delta x)^2},\end{aligned}\quad (36)$$

where  $\gamma_x$  is the spatial weighting factor in the direction of  $x$ . The following approximations are used for the second step of the LOD procedure:

$$\begin{aligned}\frac{\partial u}{\partial t}\Big|_{i,j}^{n+(1/2)} &\simeq \frac{u_{i,j}^{n+1} - u_{i,j}^{n+(1/2)}}{\Delta t}, \\ \frac{\partial u}{\partial y}\Big|_{i,j}^{n+(1/2)} &\simeq \frac{(1-\gamma_y)(u_{i,j}^{n+(1/2)} - u_{i,j-1}^{n+(1/2)}) + \gamma_y(u_{i,j+1}^{n+(1/2)} - u_{i,j}^{n+(1/2)})}{\Delta y}, \\ \frac{\partial^2 u}{\partial y^2}\Big|_{i,j}^{n+(1/2)} &\simeq \frac{u_{i,j+1}^{n+(1/2)} - 2u_{i,j}^{n+(1/2)} - u_{i,j-1}^{n+(1/2)}}{(\Delta y)^2},\end{aligned}\quad (37)$$

where  $\gamma_y$  is the spatial weighting factor in the direction of  $y$ . By using the following relationships

$$\begin{aligned}c_x &= \frac{\beta_x k}{h}, & s_x &= \frac{\alpha_x k}{h^2}, & \gamma_x &= \frac{1-c_x}{2}, \\ c_y &= \frac{\beta_y k}{h}, & s_y &= \frac{\alpha_y k}{h^2}, & \gamma_y &= \frac{1-c_y}{2},\end{aligned}\quad (38)$$

the finite difference formula for the first half time step of the LOD Lax-Wendroff procedure is given by

$$\begin{aligned}u_{i,j}^{n+(1/2)} &= \frac{1}{2}(2s_x + c_x + c_x^2)u_{i-1,j}^n + (1-2s_x - c_x^2)u_{i,j}^n \\ &\quad + \frac{1}{2}(2s_x - c_x + c_x^2)u_{i+1,j}^n.\end{aligned}\quad (39)$$

At the second half time step the finite difference is given by

$$\begin{aligned}u_{i,j}^{n+1} &= \frac{1}{2}(2s_y + c_y + c_y^2)u_{i,j-1}^{n+(1/2)} + (1-2s_y - c_y^2)u_{i,j}^{n+(1/2)} \\ &\quad + \frac{1}{2}(2s_y - c_y + c_y^2)u_{i,j+1}^{n+(1/2)},\end{aligned}\quad (40)$$

where

$$\begin{aligned}u_{i,j-1}^{n+(1/2)} &= \frac{1}{2}(2s_x + c_x + c_x^2)u_{i-1,j-1}^n + (1-2s_x - c_x^2)u_{i,j-1}^n \\ &\quad + \frac{1}{2}(2s_x - c_x + c_x^2)u_{i+1,j-1}^n, \\ u_{i,j+1}^{n+(1/2)} &= \frac{1}{2}(2s_x + c_x + c_x^2)u_{i-1,j+1}^n + (1-2s_x - c_x^2)u_{i,j+1}^n \\ &\quad + \frac{1}{2}(2s_x - c_x + c_x^2)u_{i+1,j+1}^n.\end{aligned}\quad (41)$$

We obtain a single expression for  $u_{i,j}^{n+1}$  in a complete time step as follows:

$$\begin{aligned}u_{i,j}^{n+1} &= \frac{1}{4}(2s_y + c_y + c_y^2)(2s_x + c_x + c_x^2)u_{i-1,j-1}^n \\ &\quad + \frac{1}{2}(2s_y + c_y + c_y^2)(1-2s_x - c_x^2)u_{i,j-1}^n \\ &\quad + \frac{1}{4}(2s_y + c_y + c_y^2)(2s_x - c_x + c_x^2)u_{i+1,j-1}^n \\ &\quad + \frac{1}{2}(1-2s_y - c_y^2)(2s_x + c_x + c_x^2)u_{i-1,j}^n \\ &\quad + (1-2s_y - c_y^2)(1-2s_x - c_x^2)u_{i,j}^n \\ &\quad + \frac{1}{2}(1-2s_y - c_y^2)(2s_x - c_x + c_x^2)u_{i+1,j}^n \\ &\quad + \frac{1}{4}(2s_y - c_y + c_y^2)(2s_x + c_x + c_x^2)u_{i-1,j+1}^n \\ &\quad + \frac{1}{2}(2s_y - c_y + c_y^2)(1-2s_x - c_x^2)u_{i,j+1}^n \\ &\quad + \frac{1}{4}(2s_y - c_y + c_y^2)(2s_x - c_x + c_x^2)u_{i+1,j+1}^n.\end{aligned}\quad (42)$$

To find the modified equation of the scheme, we first find Taylor's expansion of each term in (42) about  $u_{i,j}^n$ . The Taylor series expansion of  $u_{i,j}^{n+1}$  is given by

$$u_{i,j}^{n+1} = u + k u_t + \frac{k^2}{2} u_{tt} + \frac{k^3}{6} u_{ttt} + \frac{k^4}{4!} u_{tttt} + \dots \quad (43)$$

The Taylor series expansions for some grid points about  $u_{i,j}^n$  are given as follows:

$$\begin{aligned}u_{i-1,j-1}^n &= u - hu_x - hu_y + \frac{h^2}{2} [u_{xx} + 2u_{xy} + u_{yy}] \\ &\quad - \frac{h^3}{6} [u_{xxx} + 3u_{xxy} + 3u_{xyy} + u_{yyy}] \\ &\quad + \frac{h^4}{4!} [u_{xxxx} + 4u_{xxxxy} + 6u_{xxyy} \\ &\quad \quad + 4u_{xyyy} + u_{yyyy}] + \dots,\end{aligned}$$

$$\begin{aligned}
u_{i-1,j}^n &= u - hu_x + \frac{h^2}{2}u_{xx} - \frac{h^3}{6}u_{xxx} + \frac{h^4}{4!}u_{xxxx} + \dots, \\
u_{i,j-1}^n &= u - hu_y + \frac{h^2}{2}u_{yy} - \frac{h^3}{6}u_{yyy} + \frac{h^4}{4!}u_{yyyy} + \dots, \\
u_{i-1,j+1}^n &= u - hu_x + hu_y + \frac{h^2}{2} [u_{xx} - 2u_{xy} + u_{yy}] \\
&\quad - \frac{h^3}{6} [u_{xxx} - 3u_{xxy} + 3u_{xyy} - u_{yyy}] \\
&\quad + \frac{h^4}{4!} [u_{xxxx} - 4u_{xxxy} + 6u_{xxyy} \\
&\quad\quad - 4u_{xyyy} + u_{yyyy}] + \dots, \\
u_{i+1,j-1}^n &= u + hu_x - hu_y + \frac{h^2}{2} [u_{xx} - 2u_{xy} + u_{yy}] \\
&\quad - \frac{h^3}{6} [-u_{xxx} + 3u_{xxy} - 3u_{xyy} + u_{yyy}] \\
&\quad + \frac{h^4}{4!} [u_{xxxx} - 4u_{xxxy} \\
&\quad\quad + 6u_{xxyy} - 4u_{xyyy} + u_{yyyy}] + \dots, \\
u_{i+1,j}^n &= u + hu_x + \frac{h^2}{2}u_{xx} + \frac{h^3}{6}u_{xxx} + \frac{h^4}{4!}u_{xxxx} + \dots, \\
u_{i,j+1}^n &= u + hu_y + \frac{h^2}{2}u_{yy} + \frac{h^3}{6}u_{yyy} + \frac{h^4}{4!}u_{yyyy} + \dots, \\
u_{i+1,j+1}^n &= u + hu_x + hu_y + \frac{h^2}{2} [u_{xx} + 2u_{xy} + u_{yy}] \\
&\quad + \frac{h^3}{6} [u_{xxx} + 3u_{xxy} + 3u_{xyy} + u_{yyy}] \\
&\quad + \frac{h^4}{4!} [u_{xxxx} + 4u_{xxxy} + 6u_{xxyy} \\
&\quad\quad + 4u_{xyyy} + u_{yyyy}] + \dots.
\end{aligned} \tag{44}$$

Using (2), we convert the temporal derivatives  $u_{tt}$ ,  $u_{ttt}$ , and  $u_{tttt}$  into spatial derivatives. We thus have

$$\begin{aligned}
u_{tt} &= \alpha_x^2 u_{xxxx} + \alpha_y^2 u_{yyyy} + \alpha_x \alpha_y [u_{xxyy} + u_{yyxx}] \\
&\quad - 2\alpha_x \beta_x u_{xxx} - 2\alpha_y \beta_y u_{yyy} - \alpha_x \beta_y [u_{xxy} + u_{yxx}] \\
&\quad - \alpha_y \beta_x [u_{xyy} + u_{yyx}] + \beta_x^2 u_{xx} + \beta_y^2 u_{yy} \\
&\quad + \beta_x \beta_y [u_{xy} + u_{yx}] + \dots, \\
u_{ttt} &= 3\alpha_x \beta_x^2 u_{xxxx} + 3\alpha_y \beta_y^2 u_{yyyy} \\
&\quad + \alpha_x \beta_y^2 [u_{yyxx} + u_{yxyy} + u_{xxyy}] \\
&\quad + \alpha_y \beta_x^2 [u_{xxyy} + u_{yyxx} + u_{xyyx}]
\end{aligned}$$

$$\begin{aligned}
&\quad + \alpha_y \beta_x \beta_y [2u_{yyyx} + u_{yyxy} + 2u_{xyyy} + 2u_{yxyy}] \\
&\quad + \alpha_x \beta_x \beta_y [2u_{yxxx} + 2u_{xxxy} + u_{xxyx} + 2u_{xyxx}] \\
&\quad - \beta_x^3 u_{xxx} - \beta_x \beta_y^2 [u_{yyx} + u_{yxy} + u_{xyy}] \\
&\quad - \beta_y^3 u_{yyy} - \beta_x^2 \beta_y [u_{xxy} + u_{xyx} + u_{yxx}] + \dots, \\
u_{tttt} &= \beta_x [\beta_x^3 u_{xxxx} + \beta_x^2 \beta_y [u_{xxyx} + u_{xyxx} + u_{yxxx}] \\
&\quad + \beta_x \beta_y^2 [u_{yyxx} + u_{yxyx} + u_{xyyx}] + \beta_y^3 u_{yyyy}] \\
&\quad + \beta_y [\beta_y^3 u_{yyyy} + \beta_y^2 \beta_x [u_{yyxy} + u_{yxyy} + u_{xyyy}] \\
&\quad + \beta_y \beta_x^2 [u_{xxyy} + u_{xyxy} + u_{yxyx}] + \beta_x^3 u_{xxxx}] + \dots.
\end{aligned} \tag{45}$$

Then on substituting the Taylor series expansions of each term of the difference scheme we get the following modified equation for the LOD Lax-Wendroff

$$\begin{aligned}
u_t + \beta_x u_x + \beta_y u_y &= \alpha_x u_{xx} + \alpha_y u_{yy} - \frac{1}{6} \beta_x h^2 (1 - c_x^2 - 6s_x) u_{xxx} \\
&\quad - \frac{1}{6} \beta_y h^2 (1 - c_y^2 - 6s_y) u_{yyy} \\
&\quad - \frac{h^3}{24} [-2s_x - c_x^2 + 12s_x c_x^2 + 12s_x^2 + c_x^4] u_{xxxx} \\
&\quad - \frac{h^3}{24} [-2s_y - c_y^2 + 12s_y c_y^2 + 12s_y^2 + c_y^4] u_{yyyy} + \dots.
\end{aligned} \tag{46}$$

The scheme is second order accurate in space and the leading error terms are dispersive in nature (presence of odd-order derivatives  $u_{xxx}$  and  $u_{yyy}$ ). As the time and spatial increments go to zero, the modified equation (46) reduces to its original equation, that is, (2). Hence LOD Lax-Wendroff is consistent.

We now study the spectral analysis of the dispersive and dissipative properties of the scheme for the case  $c_x = c_y = c$  and  $s_x = s_y = s$ . To obtain the amplification factor we use the Von Neumann stability analysis by substituting  $u_{i,j}^n$  by  $\xi^n \exp(I(i\omega_x + j\omega_y))$  in (42), where  $I = \sqrt{-1}$ . We thus have

$$\begin{aligned}
\xi &= \frac{1}{4} (2s_y + c_y + c_y^2) (2s_x + c_x + c_x^2) \exp(-I(\omega_x + \omega_y)) \\
&\quad + \frac{1}{2} (2s_y + c_y + c_y^2) (1 - 2s_x - c_x^2) \exp(-I\omega_y) \\
&\quad + \frac{1}{4} (2s_y + c_y + c_y^2) (2s_x - c_x + c_x^2) \exp(I(\omega_x - \omega_y)) \\
&\quad + \frac{1}{2} (1 - 2s_y - c_y^2) (2s_x + c_x + c_x^2) \exp(-I\omega_x) \\
&\quad + (1 - 2s_y - c_y^2) (1 - 2s_x - c_x^2)
\end{aligned}$$

$$\begin{aligned}
& + \frac{1}{2} (1 - 2s_y - c_y^2) (2s_x - c_x + c_x^2) \exp(I\omega_x) \\
& + \frac{1}{4} (2s_y - c_y + c_y^2) (2s_x + c_x + c_x^2) \exp(-I(\omega_x - \omega_y)) \\
& + \frac{1}{2} (2s_y - c_y + c_y^2) (1 - 2s_x - c_x^2) \exp(I\omega_y) \\
& + \frac{1}{4} (2s_y - c_y + c_y^2) (2s_x - c_x + c_x^2) \exp(I(\omega_x + \omega_y)). \tag{47}
\end{aligned}$$

The real and imaginary parts of the amplification factor are given by

$$\begin{aligned}
\text{Real}(\xi) &= 1 + 4sc^2 \cos(\omega_x) \cos(\omega_y) + c^4 \cos(\omega_x) \cos(\omega_y) \\
& + 4s^2 \cos(\omega_x) \cos(\omega_y) - 4sc^2 \cos(\omega_y) \\
& - c^2 \sin(\omega_x) \sin(\omega_y) + 4s^2 + 4sc^2 - 4sc^2 \cos(\omega_x) \\
& + c^2 \cos(\omega_x) - c^4 \cos(\omega_x) + 4s \cos(\omega_x) \\
& + 2s \cos(\omega_y) + 2s \cos(\omega_x) - 4s^2 \cos(\omega_y) \\
& - 4s^2 \cos(\omega_x) - 2c^2 + c^2 \cos(\omega_y) \\
& - c^4 \cos(\omega_y) + c^4 - 4s, \\
\text{Imag}(\xi) &= -c^3 \cos(\omega_x) \sin(\omega_y) + 2sc \sin(\omega_x) \\
& + 2sc \sin(\omega_y) - 2sc \cos(\omega_x) \sin(\omega_y) \\
& - 2sc \sin(\omega_x) \cos(\omega_y) - c \sin(\omega_x) + c^3 \sin(\omega_x) \\
& - c \sin(\omega_y) + c^3 \sin(\omega_y) - c^3 \sin(\omega_x) \cos(\omega_y), \tag{48}
\end{aligned}$$

respectively. The modulus of the amplification factor, AFM, is obtained as

$$\text{AFM} = \sqrt{(\Re(\xi))^2 + (\Im(\xi))^2}. \tag{49}$$

We find the region of stability using the approach of Hindmarsh et al. [16] and Sousa [17]. We consider the case when  $\omega_x = \omega_y = \pi$  and  $\omega_x \rightarrow 0$  and  $\omega_y \rightarrow 0$ . When  $\omega_x = \omega_y = \pi$ , (49) gives

$$|\xi| = \sqrt{1 + 16sc^2 - 4c^2 + 4c^4 + 16s^2 - 8s}. \tag{50}$$

From the Von Neumann stability analysis, the scheme is stable if and only if  $|\xi| \leq 1$ . Thus, we get

$$1 + 16sc^2 - 4c^2 + 4c^4 + 16s^2 - 8s \leq 1. \tag{51}$$

On simplification, we get

$$\left| s + \frac{2c^2 - 1}{4} \right| \leq \frac{1}{4}, \tag{52}$$

which reduces to

$$s \leq \frac{1 - c^2}{2}. \tag{53}$$

When  $\omega_x \rightarrow 0$  and  $\omega_y \rightarrow 0$ , we use the following approximations:

$$\begin{aligned}
\cos(\omega_x) &\simeq 1 - \frac{\omega_x^2}{2}, & \cos(\omega_y) &\simeq 1 - \frac{\omega_y^2}{2}, \\
\sin(\omega_x) &\simeq \omega_x, & \sin(\omega_y) &\simeq \omega_y.
\end{aligned} \tag{54}$$

We consider (49) and use the approximations in (54) to obtain

$$|\xi|^2 \simeq 1 - 2s(\omega_x^2 + \omega_y^2). \tag{55}$$

Thus LOD Lax-Wendroff is stable if  $-2s \leq 0$ . Therefore, we have

$$s \geq 0. \tag{56}$$

On combining (53) and (56), we obtain the region of stability for the LOD Lax-Wendroff procedure as

$$0 \leq s \leq \frac{1 - c^2}{2}. \tag{57}$$

We choose  $\alpha = 0.01$  and  $\beta = 0.8$  [3]. For  $h = 0.025$  from (57), we have

$$0 \leq \frac{0.01k}{(0.025)^2} \leq \frac{1 - (0.8k/0.025)^2}{2}. \tag{58}$$

On solving for  $k$ , we get

$$0 \leq k \leq 0.0193. \tag{59}$$

Therefore, for  $h = 0.025$ , the stability region for the LOD Lax-Wendroff procedure is  $0 \leq k \leq 0.0193$ . We choose  $k$  such that  $0.3/k$  is an integer as for our numerical experiments,  $T = 0.3$ . Then  $0.3/k$  gives the number of time intervals. We choose  $k = 0.005, 0.01, 3/160$ , and  $1/60$ .

For  $h = 0.05$ , we have  $c = 16k$  and  $s = 4k$ . When  $\omega_x = \pi$  and  $\omega_y = \pi$ , using (51) we get

$$0 \leq 1 - 32k + 1638k^3 - 768k^2 + 262144k^4 \leq 1, \tag{60}$$

which gives

$$0 \leq k \leq 0.0487985. \tag{61}$$

Therefore, for  $h = 0.05$ , LOD Lax-Wendroff is stable if  $0 \leq k \leq 0.0487985$ . We then choose some values of  $k \in (0, 0.048)$  for the numerical experiments. for our numerical experiments.

3D plots of the modulus of the amplification factor versus phase angles in  $x$ - and  $y$ -directions for some different values of  $h$  and  $k$  are depicted in Figures 1 and 2. 2D plots of the modulus of the amplification factor versus  $\omega_x$ , when  $\omega_y = 0$ , are shown in Figure 3. The scheme is in general less dissipative at  $h = 0.05$  as compared to  $h = 0.025$ . Out of the eight combinations of values of  $h$  and  $k$ , the scheme is

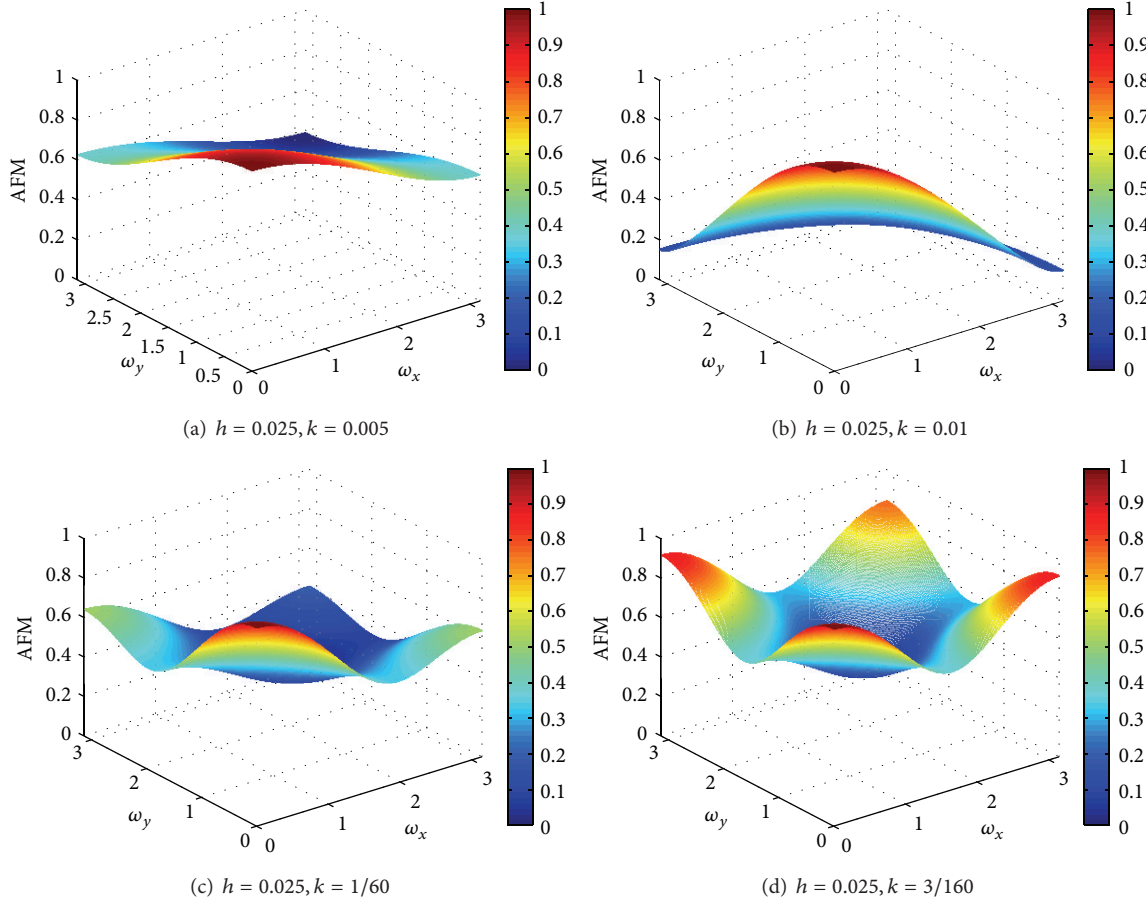


FIGURE 1: Plots of modulus of amplification factor versus phase angle in  $x$ -direction,  $\omega_x$ , versus phase angle in  $y$ -direction,  $\omega_y$ , at  $h = 0.025$  with some different values of  $k$  for the LOD Lax-Wendroff scheme.

least dissipative when  $h = 0.05$  and  $k = 0.005$  and it is most dissipative when  $h = 0.025$  and  $k = 0.01$ .

Figures 4 and 5 show the 3D plots of the relative phase error versus  $\omega_x$  versus  $\omega_y$  for some different values of  $h$  and  $k$ . Figure 6 shows the 2D plots of the relative phase error versus  $\omega_x$ , for the case  $\omega_y = 0$  at  $h = 0.025$  and  $h = 0.05$ . For  $h = 0.025$ , we observe phase lag behaviour at  $k = 0.01$  and  $k = 0.005$  and phase lead behaviour at  $k = 1/60$  and  $k = 3/160$ . For  $h = 0.05$ , we have phase lag behaviour at  $k = 0.005, 0.01, 0.02$ , and  $0.03$ . The scheme is least dispersive when  $h = 0.05; k = 0.03$  and  $h = 0.025; k = 0.01$ . In the following section, we consider the LOD (1, 5) scheme.

## 5. LOD (1, 5) Explicit Procedure

In this procedure the following approximations are used in the first half time step [3]:

$$\frac{\partial u}{\partial t} \Big|_{i,j}^n \approx \frac{u_{i,j}^{n+(1/2)} - u_{i,j}^n}{\Delta t},$$

$$\begin{aligned} \frac{\partial u}{\partial x} \Big|_{i,j}^n &\approx \left( \frac{12s_x + 2c_x^2 - 3c_x - 2}{12} \right) \left( \frac{u_{i+2,j}^n - u_{i,j}^n}{2\Delta x} \right) \\ &+ \left( \frac{12s_x + 2c_x^2 + 3c_x - 2}{12} \right) \left( \frac{u_{i,j}^n - u_{i-2,j}^n}{2\Delta x} \right) \\ &- \left( \frac{c_x^2 + 6s_x - 4}{12} \right) \left( \frac{u_{i+1,j}^n - u_{i-1,j}^n}{2\Delta x} \right), \\ \frac{\partial^2 u}{\partial x^2} \Big|_{i,j}^n &\approx \left( \frac{-c_x^4 + 4c_x^2 - 12s_x^2 - 12s_x c_x^2 + 8s_x}{6s_x} \right) \\ &\times \left( \frac{u_{i+1,j}^n - 2u_{i,j}^n + u_{i-1,j}^n}{(\Delta x)^2} \right) \\ &+ \left( \frac{c_x^4 - 4c_x^2 + 12s_x^2 + 12s_x c_x^2 - 2s_x}{6s_x} \right) \\ &\times \left( \frac{u_{i+2,j}^n - 2u_{i,j}^n + u_{i-2,j}^n}{4(\Delta x)^2} \right). \end{aligned} \quad (62)$$

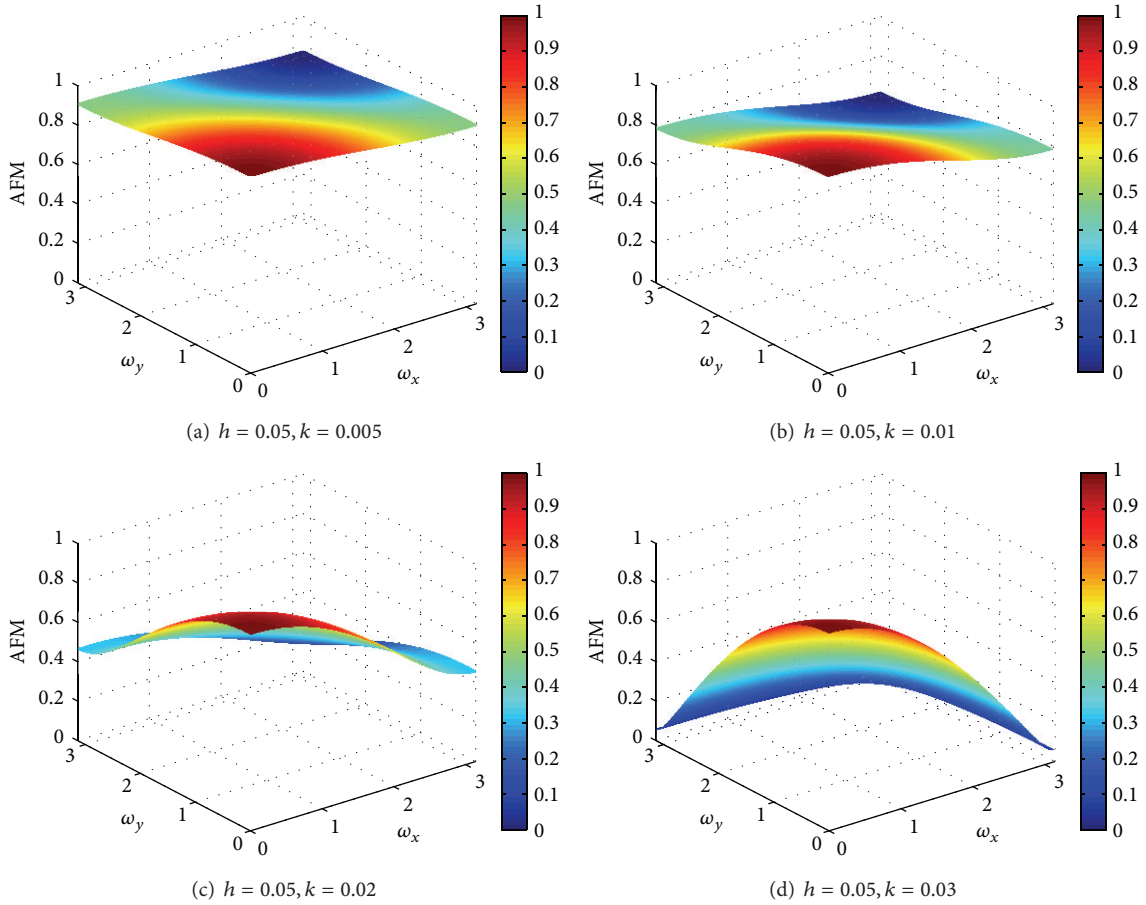


FIGURE 2: Plots of modulus of amplification factor versus phase angle in  $x$ -direction,  $\omega_x$ , versus phase angle in  $y$ -direction,  $\omega_y$ , at  $h = 0.05$  with some different values of  $k$  for the LOD Lax-Wendroff scheme.

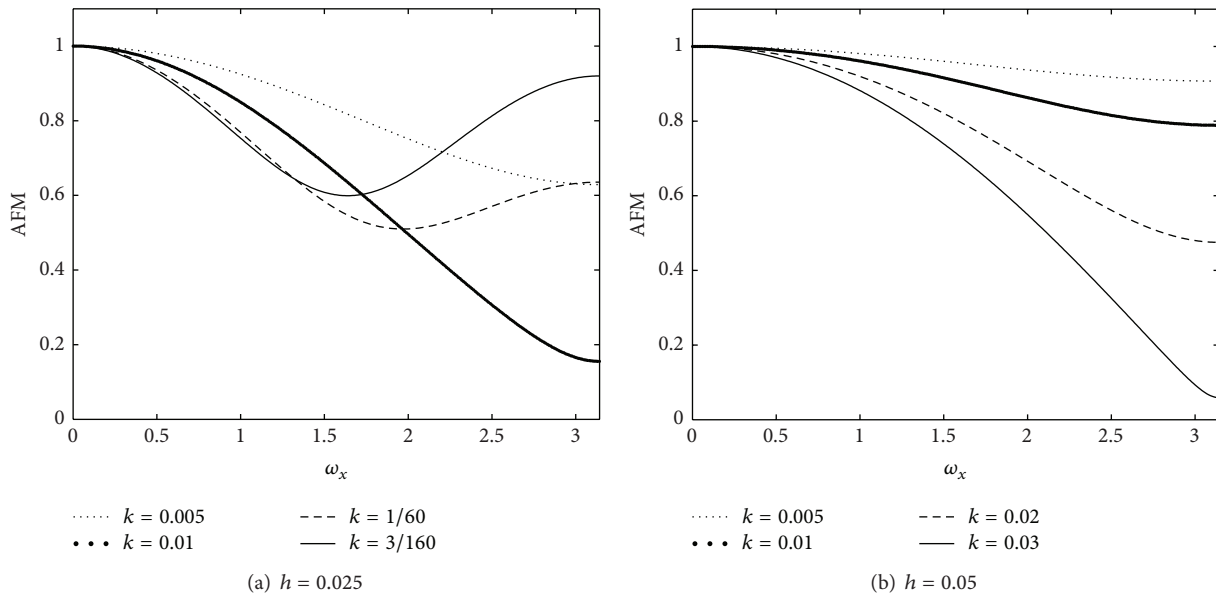


FIGURE 3: Plots of modulus of amplification factor versus  $\omega_x$  when  $\omega_y = 0$  at  $h = 0.025$  and  $h = 0.05$  with some different values of  $k$  for the LOD Lax-Wendroff scheme.

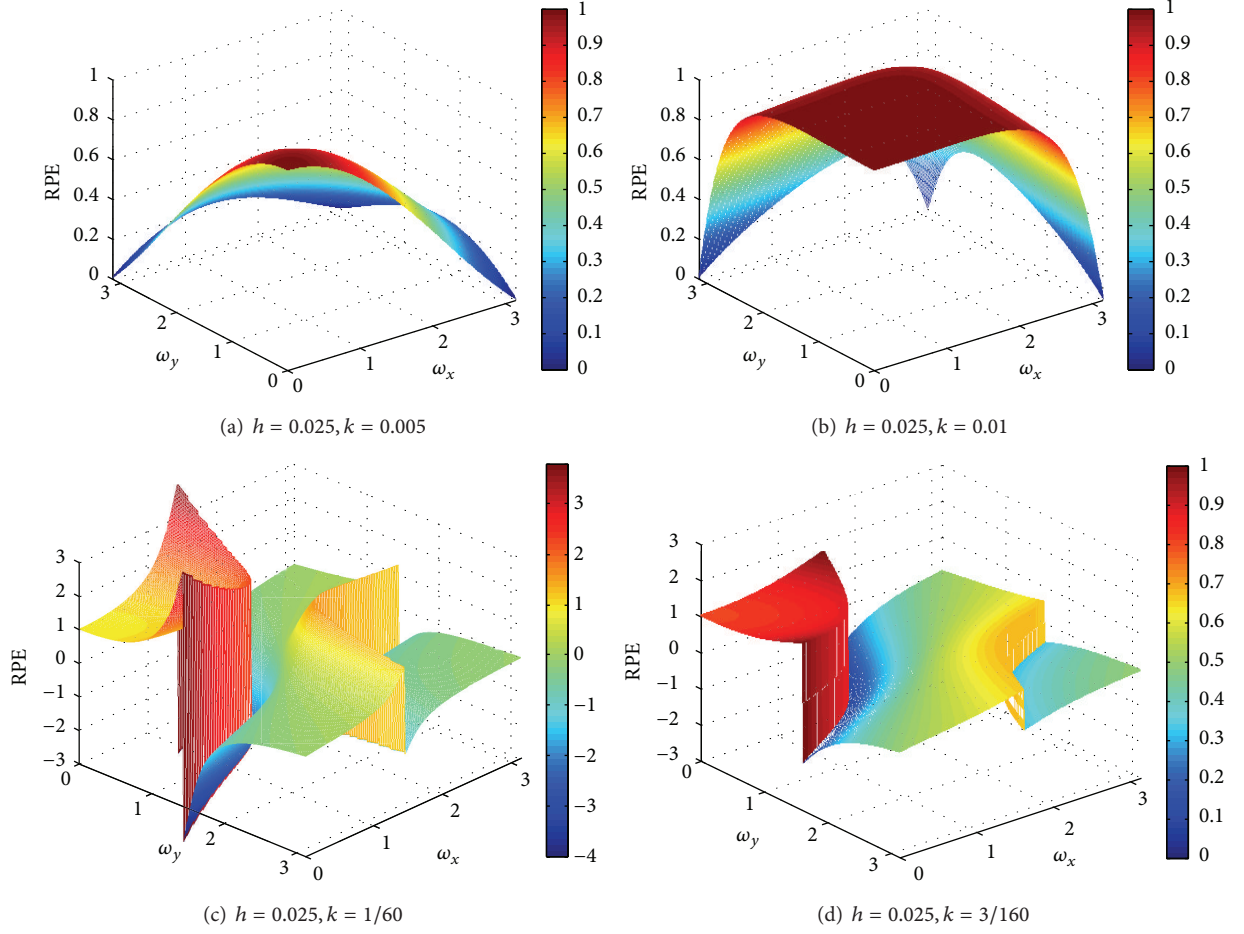


FIGURE 4: Plots of relative phase error versus phase angle in  $x$ -direction ( $\omega_x$ ) versus phase angle in  $y$ -direction ( $\omega - y$ ), at  $h = 0.025$  with some different values of  $k$  for the LOD Lax-Wendroff scheme.

On substituting (62) into (14), we get the following finite difference equation for the first half time step:

$$u_{i,j}^{n+1/2} = A_x u_{i-2,j}^n + B_x u_{i-1,j}^n + C_x u_{i,j}^n + D_x u_{i+1,j}^n + E_x u_{i+2,j}^n, \quad (63)$$

where

$$\begin{aligned} A_x &= \frac{1}{24} (12s_x (s_x + c_x^2) + 2s_x (6c_x - 1) \\ &\quad + c_x (c_x - 1)(c_x + 1)(c_x + 2)), \\ B_x &= -\frac{1}{6} (12s_x (s_x + c_x^2) + 2s_x (3c_x - 4) \\ &\quad + c_x (c_x - 2)(c_x + 1)(c_x + 2)), \\ C_x &= \frac{1}{4} (12s_x (s_x + c_x^2) - 10s_x \\ &\quad + (c_x - 1)(c_x - 2)(c_x + 1)(c_x + 2)), \end{aligned}$$

$$\begin{aligned} D_x &= -\frac{1}{6} (12s_x (s_x + c_x^2) - 2s_x (3c_x + 4) \\ &\quad + c_x (c_x - 2)(c_x - 1)(c_x + 2)), \\ E_x &= \frac{1}{24} (12s_x (s_x + c_x^2) - 2s_x (6c_x + 1) \\ &\quad + c_x (c_x - 1)(c_x + 1)(c_x - 2)). \end{aligned} \quad (64)$$

The following approximations are used in the second half time step:

$$\begin{aligned} \frac{\partial u}{\partial t} \Big|_{i,j}^{n+(1/2)} &\simeq \frac{u_{i,j}^{n+1} - u_{i,j}^{n+(1/2)}}{\Delta t}, \\ \frac{\partial u}{\partial x} \Big|_{i,j}^{n+(1/2)} &= \left( \frac{12s_y + 2c_y^2 - 3c_y - 2}{12} \right) \left( \frac{u_{i,j+2}^{n+(1/2)} - u_{i,j}^{n+(1/2)}}{2\Delta y} \right) \end{aligned}$$

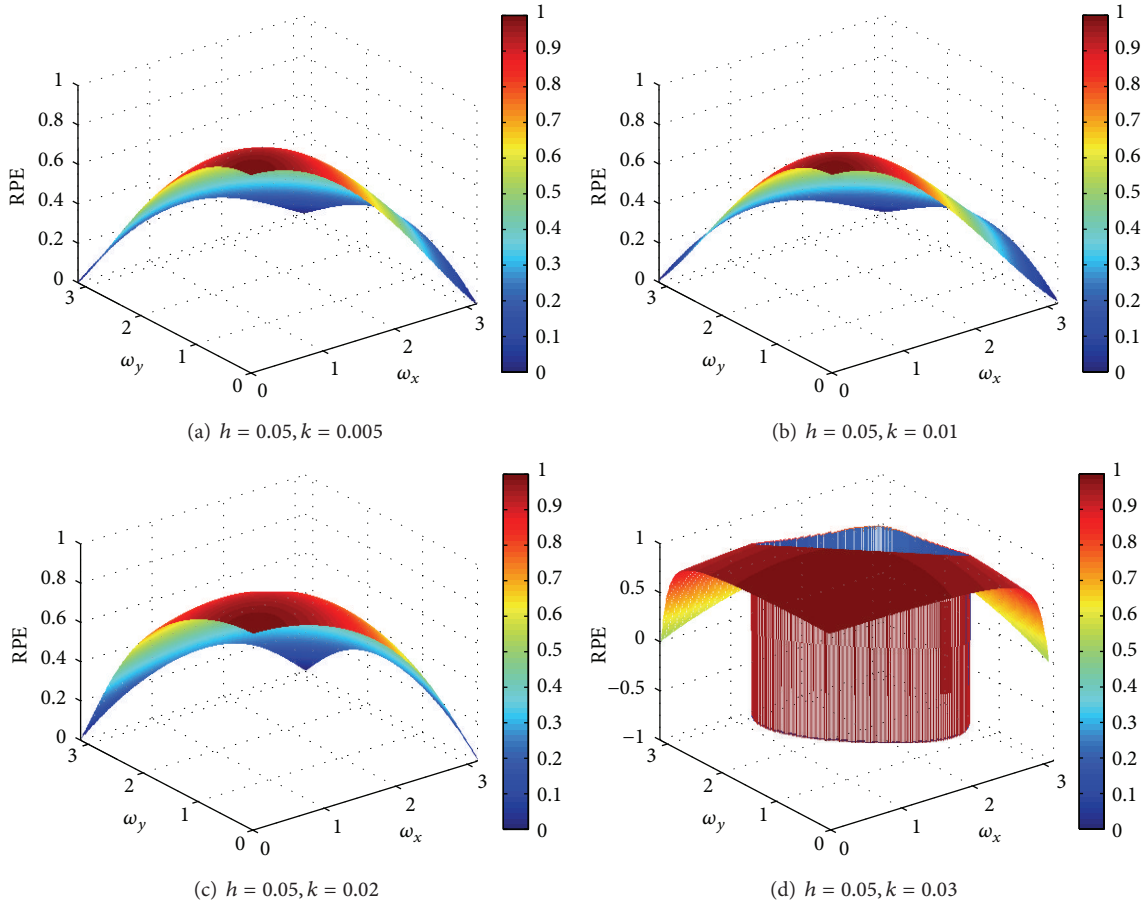


FIGURE 5: Plots of relative phase error versus  $\omega_x$  versus  $\omega_y$ , at  $h = 0.05$  with some different values of  $k$  for the LOD Lax-Wendroff scheme.

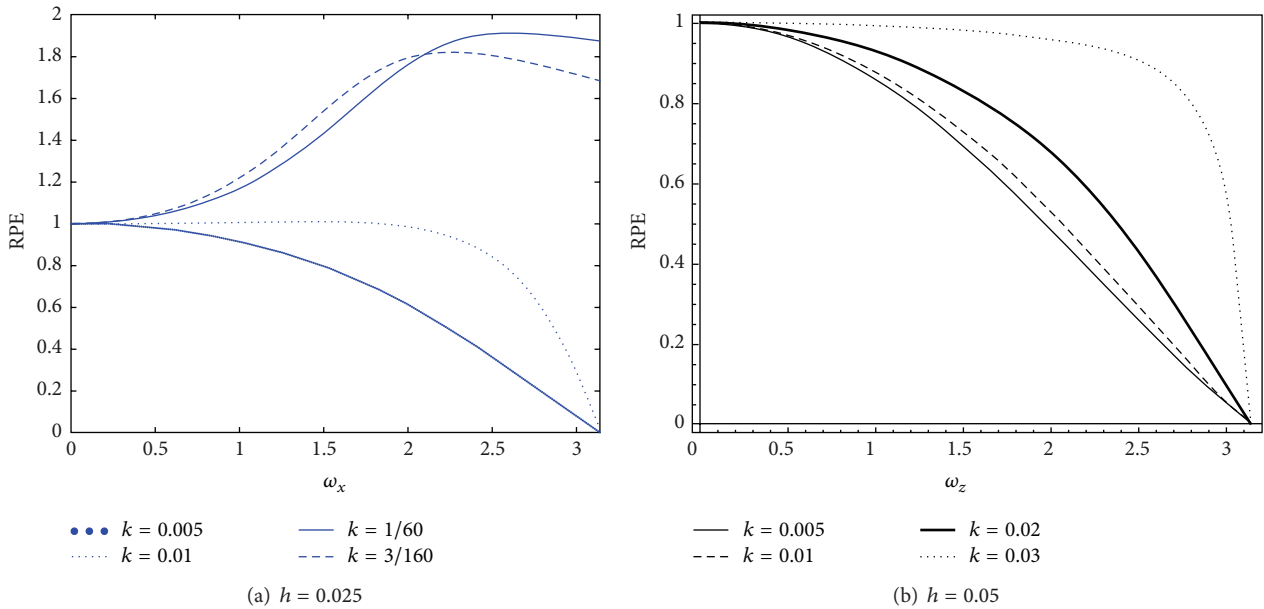


FIGURE 6: Plots of relative phase error versus  $\omega_x$  when  $\omega_y = 0$  at  $h = 0.025$  and  $h = 0.05$  with some different values of  $k$  for the LOD Lax-Wendroff scheme.

$$\begin{aligned}
& + \left( \frac{12s_y + 2c_y^2 + 3c_y - 2}{12} \right) \left( \frac{u_{i,j}^{n+(1/2)} - u_{i,j-2}^{n+(1/2)}}{2\Delta y} \right) \\
& - \left( \frac{c_y^2 + 6s_y - 4}{12} \right) \left( \frac{u_{i,j+1}^{n+(1/2)} - u_{i,j-1}^{n+(1/2)}}{2\Delta y} \right), \\
\frac{\partial^2 u}{\partial y^2} \Big|_{i,j}^{n+(1/2)} & \approx \left( \frac{-c_y^4 + 4c_y^2 - 12s_y^2 - 12s_y c_y^2 + 8s_y}{6s_y} \right) \\
& \times \left( \frac{u_{i,j+1}^{n+(1/2)} - 2u_{i,j}^{n+(1/2)} + u_{i,j-1}^{n+(1/2)}}{(\Delta y)^2} \right) \\
& + \left( \frac{c_y^4 - 4c_y^2 + 12s_y^2 + 12s_y c_y^2 - 2s_y}{6s_y} \right) \\
& \times \left( \frac{u_{i,j+2}^{n+(1/2)} - 2u_{i,j}^{n+(1/2)} + u_{i,j-2}^{n+(1/2)}}{4(\Delta y)^2} \right). \tag{65}
\end{aligned}$$

Then on substituting (65) into (15), we get the following difference equation for the second half time step:

$$\begin{aligned}
u_{i,j}^{n+1} & = A_y u_{i,j-2}^{n+(1/2)} + B_y u_{i,j-1}^{n+(1/2)} + C_y u_{i,j}^{n+(1/2)} \\
& + D_y u_{i,j+1}^{n+(1/2)} + E_y u_{i,j+2}^{n+(1/2)}, \tag{66}
\end{aligned}$$

where

$$\begin{aligned}
A_y & = \frac{1}{24} \left( 12s_y (s_y + c_y^2) + 2s_y (6c_y - 1) \right. \\
& \quad \left. + c_y (c_y - 1) (c_y + 1) (c_y + 2) \right), \\
B_y & = -\frac{1}{6} \left( 12s_y (s_y + c_y^2) + 2s_y (3c_y - 4) \right. \\
& \quad \left. + c_y (c_y - 2) (c_y + 1) (c_y + 2) \right), \\
C_y & = \frac{1}{4} \left( 12s_y (s_y + c_y^2) - 10s_y \right. \\
& \quad \left. + (c_y - 1) (c_y - 2) (c_y + 1) (c_y + 2) \right), \tag{67} \\
D_y & = -\frac{1}{6} \left( 12s_y (s_y + c_y^2) - 2s_y (3c_y + 4) \right. \\
& \quad \left. + c_y (c_y - 2) (c_y - 1) (c_y + 2) \right), \\
E_y & = \frac{1}{24} \left( 12s_y (s_y + c_y^2) - 2s_y (6c_y + 1) \right. \\
& \quad \left. + c_y (c_y - 1) (c_y + 1) (c_y - 2) \right).
\end{aligned}$$

The complete LOD (1, 5) scheme is given by

$$\begin{aligned}
u_{i,j}^{n+1} & = A_y A_x u_{i-2,j-2}^n + A_y B_x u_{i-1,j-2}^n + A_y C_x u_{i,j-2}^n \\
& + A_y D_x u_{i+1,j-2}^n + A_y E_x u_{i+2,j-2}^n \\
& + B_y A_x u_{i-2,j-1}^n + B_y B_x u_{i-1,j-1}^n + B_y C_x u_{i,j-1}^n \\
& + B_y D_x u_{i+1,j-1}^n + B_y E_x u_{i+2,j-1}^n \\
& + C_y A_x u_{i-2,j}^n + C_y B_x u_{i-1,j}^n + C_y C_x u_{i,j}^n \\
& + C_y D_x u_{i+1,j}^n + C_y E_x u_{i+2,j}^n \\
& + D_y A_x u_{i-2,j+1}^n + D_y B_x u_{i-1,j+1}^n + D_y C_x u_{i,j+1}^n \\
& + D_y D_x u_{i+1,j+1}^n + D_y E_x u_{i+2,j+1}^n \\
& + E_y A_x u_{i-2,j+2}^n + E_y B_x u_{i-1,j+2}^n + E_y C_x u_{i,j+2}^n \\
& + E_y D_x u_{i+1,j+2}^n + E_y E_x u_{i+2,j+2}^n. \tag{68}
\end{aligned}$$

The Taylor series expansion of the terms on the right hand side of (68) about  $u_{i,j}^n$  is given as follows:

$$\begin{aligned}
u_{i+a,j+b}^n & = u + ah u_x + bh u_y + \frac{h^2}{2} (a^2 u_{xx} + 2ab u_{xy} + b^2 u_{yy}) \\
& + \frac{h^3}{6} (a^3 u_{xxx} + 3a^2 b u_{xxy} + 3ab^2 u_{xyy} + b^3 u_{yyy}) \\
& + \frac{h^4}{24} (a^4 u_{xxxx} + 4a^3 b u_{xxxxy} + 6a^2 b^2 u_{xxyy} \\
& \quad + 4ab^3 u_{xyyyy} + b^4 u_{yyyyy}) \\
& + \frac{h^5}{120} (a^5 u_{xxxxx} + 5a^4 b u_{xxxxy} \\
& \quad + 10a^3 b^2 u_{xxxyy} + 10a^2 b^3 u_{xxyyy} \\
& \quad + 5ab^4 u_{xyyyy} + b^5 u_{yyyyy}) + \dots, \tag{69}
\end{aligned}$$

for  $a = -2, -1, 0, 1, 2$  and  $b = -2, -1, 0, 1, 2$ .

We obtain the following modified equation:

$$\begin{aligned}
u_t + \beta_x u_x + \beta_y u_y & = \alpha_x u_{xx} + \alpha_y u_{yy} \\
& + \frac{\beta_x h^4}{120} (60s_x^2 + 20s_x c_x^2 + c_x^4 \\
& \quad - 5c_x^2 + 4 - 30s_x) u_{xxxxx} \\
& + \frac{\beta_y h^4}{120} (60s_y^2 + 20s_y c_y^2 + c_y^4 \\
& \quad - 5c_y^2 + 4 - 30s_y) u_{yyyyy} + \dots. \tag{70}
\end{aligned}$$

The scheme is essentially dispersive as the leading error terms are dispersive in nature due to the presence of the odd-order derivative terms  $u_{xxxxx}$  and  $u_{yyyyy}$ . Also, the scheme is consistent and it is fourth order accurate in space.

The amplification factor of the LOD (1, 5) scheme is given by

$$\begin{aligned} \xi = & A_y [A_x \exp(I(-2\omega_x - 2\omega_y)) + B_x \exp(I(-\omega_x - 2\omega_y)) \\ & + C_x \exp(-2I\omega_y) \\ & + D_x \exp(I(\omega_x - 2\omega_y)) + E_x \exp(I(2\omega_x - 2\omega_y))] \\ & + B_y [A_x \exp(I(-2\omega_x - \omega_y)) + B_x \exp(I(-\omega_x - \omega_y)) \\ & + C_x \exp(-I\omega_y) + D_x \exp(I(\omega_x - \omega_y)) \\ & + E_x \exp(I(2\omega_x - \omega_y))] \\ & + C_y [A_x \exp(-2I\omega_x) + B_x \exp(-I\omega_x) \\ & + C_x + D_x \exp(I\omega_x) + E_x \exp(2I\omega_x)] \\ & + D_y [A_x \exp(I(-2\omega_x + \omega_y)) + B_x \exp(-I(\omega_x + \omega_y)) \\ & + C_x \exp(I\omega_y) + D_x \exp(I(\omega_x + \omega_y)) \\ & + E_x \exp(I(2\omega_x + \omega_y))] \\ & + E_y [A_x \exp(I(-2\omega_x + 2\omega_y)) \\ & + B_x \exp(I(-\omega_x + 2\omega_y)) + C_x \exp(2I\omega_y) \\ & + D_x \exp(I(\omega_x + 2\omega_y)) \\ & + E_x \exp(I(2\omega_x + 2\omega_y))]. \end{aligned} \quad (71)$$

We consider  $c_x = c_y = c$  and  $s_x = s_y = s$ . We use the Von Neumann stability analysis and the approach of Hindmarsh et al. [16] to obtain the stability region. When  $\omega_x = \omega_y = \pi$ , on simplification of (71), we get

$$|\xi| = \frac{1}{9}(3 - 8c^2 + 2c^4 - 16s + 24sc^2 + 24s^2)^2. \quad (72)$$

For stability, we must have

$$\frac{1}{9}(3 - 8c^2 + 2c^4 - 16s + 24sc^2 + 24s^2)^2 \leq 1. \quad (73)$$

We consider (71) and for  $\omega_x \rightarrow 0$  and  $\omega_y \rightarrow 0$  we use the following approximations:

$$\begin{aligned} \cos(\omega_x) &\approx 1 - \frac{\omega_x^2}{2}, & \cos(\omega_y) &\approx 1 - \frac{\omega_y^2}{2}, \\ \cos(2\omega_x) &\approx 1 - 2\omega_x^2, & \cos(2\omega_y) &\approx 1 - 2\omega_y^2, \\ \sin(\omega_x) &\approx \omega_x, & \sin(\omega_y) &\approx \omega_y, \\ \sin(2\omega_x) &\approx 2\omega_x, & \sin(2\omega_y) &\approx 2\omega_y. \end{aligned} \quad (74)$$

We thus have

$$\begin{aligned} |\xi|^2 \approx & 1 - 2s(\omega_x^2 + \omega_y^2) + 4s^2\omega_x^2\omega_y^2 \\ & + \left(-2s^3\omega_y^2 + sc^2 + \frac{1}{4}c^4 - 2c^2s^2\omega_y^2 - \frac{1}{2}sc^4\omega_y^2 + s^2\right)\omega_x^4 \\ & + \left(s^4 + \frac{1}{16}c^8 + \frac{3}{2}s^2c^4 + \frac{1}{2}sc^6 + 2s^3c^2\right)\omega_x^4\omega_y^4 \\ & + \left(-\frac{1}{2}c^4s\omega_x^2 - 2c^2s^2\omega_x^2 + \frac{1}{4}c^4 + s^2 - 2s^3\omega_x^2 + c^2s\right)\omega_y^4. \end{aligned} \quad (75)$$

On neglecting higher order terms, we have

$$|\xi|^2 \approx 1 - 2s(\omega_x^2 + \omega_y^2). \quad (76)$$

Thus, the numerical method is stable if  $-2s \leq 0$ . Therefore, we have

$$s \geq 0. \quad (77)$$

When  $h = 0.025$ , we have  $c = 32k$  and  $s = 16k$ . Using (73) and (77), we get

$$\frac{1}{9}(2097152k^4 + 393216k^3 - 2048k^2 - 256k + 3)^2 \leq 1, \quad (78)$$

$$k \geq 0, \quad (79)$$

respectively. On combining (78) and (79), we get the stability region when  $h = 0.025$  for the LOD (1, 5) procedure as

$$0 \leq k \leq 0.026288. \quad (80)$$

When  $h = 0.05$ , we have  $c = 16k$  and  $s = 4k$  and the modulus of the amplification factor is given by

$$|\xi| = \frac{1}{9}(131072k^4 + 24576k^3 - 1664k^2 - 64k + 3)^2. \quad (81)$$

From (77) and (81), we obtain the stability region for the LOD (1, 5) procedure when  $h = 0.05$  as

$$0 \leq k \leq 0.073865. \quad (82)$$

We analyse the spectral analysis; for  $h = 0.025$ , we choose  $k = 0.005, 0.01, 0.02, 0.025$  and for  $h = 0.05$ , we choose  $k = 0.01, 0.02, 0.03$  and  $0.05$ .

3D plots of the modulus of the amplification factor versus phase angle in  $x$ -direction versus phase angle in  $y$ -direction at two values of  $h$ , namely, 0.025 and 0.05, at some different values of  $k$  are shown in Figures 7 and 8. 2D plots of the modulus of the amplification factor versus  $\omega_x$  when  $\omega_y = 0$  are illustrated in Figure 9. The scheme is in general less dissipative at  $h = 0.05$  as compared to  $h = 0.025$ . Out of the eight combinations of  $h$  and  $k$  values, the scheme is least dissipative when  $h = 0.05$  and  $k = 0.01$ .

Figures 10 and 11 show the 3D plots of the relative phase error versus  $\omega_x$  versus  $\omega_y$  for some different values of  $h$  and  $k$ . Figure 12 shows the 2D plots of the relative phase error versus  $\omega_x$ , for the case  $\omega_y = 0$  at  $h = 0.025$  and  $h = 0.05$ , respectively.

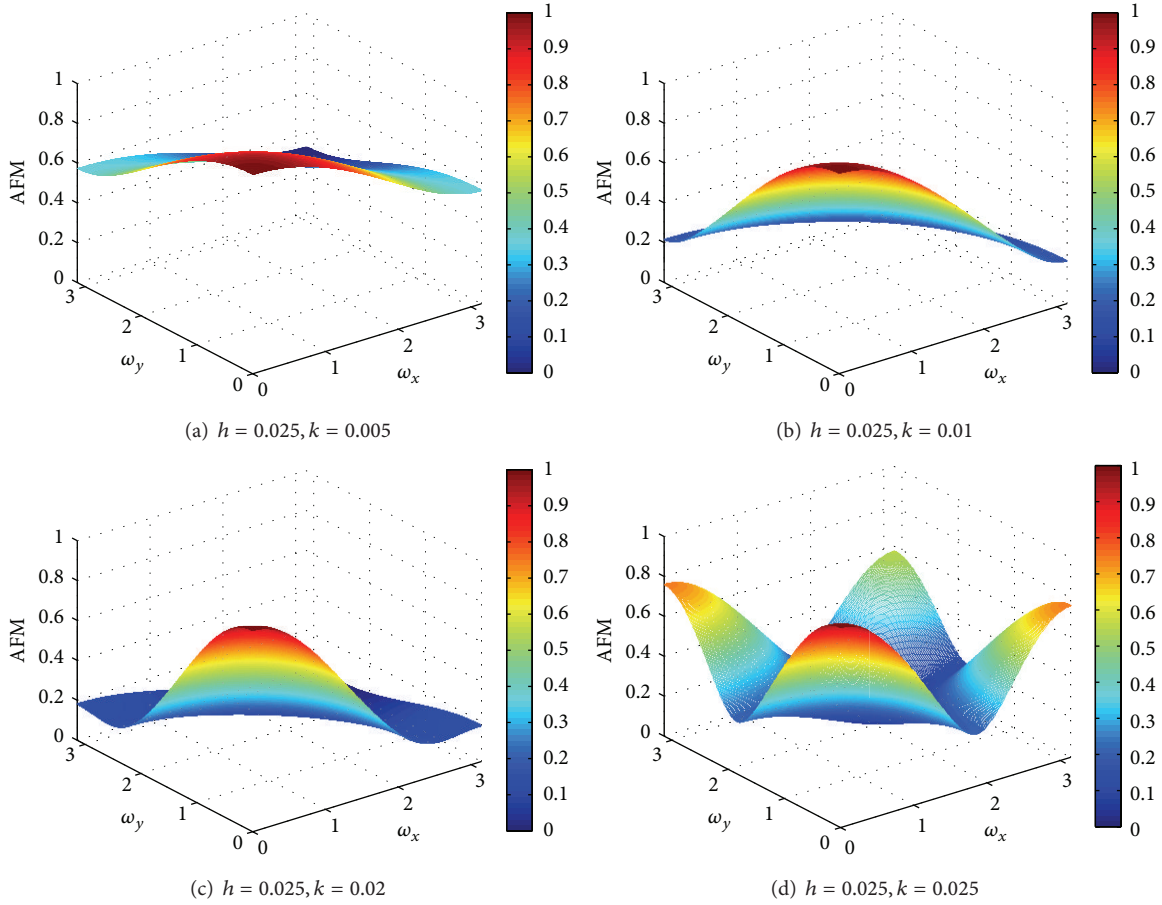


FIGURE 7: Plots of modulus of amplification factor versus phase angle in  $x$ -direction ( $\omega_x$ ) versus phase angle in  $y$ -direction ( $\omega_y$ ), at  $h = 0.025$  for some different values of  $k$  for the LOD (1, 5) procedure.

We observe that the scheme is least dispersive when  $h = 0.05$  and  $k = 0.05$  and most dispersive when  $h = 0.025$  and  $k = 0.025$ . We have phase lead when  $h = 0.05$  and  $k = 0.05$  and there is phase lag for the other seven combinations of  $h$  and  $k$ . In the following section, we present the results of the numerical experiment described in Section 3.2.

## 6. Numerical Results

**6.1. LOD Lax-Wendroff Procedure.** The results of the numerical experiment at some values of  $k$  using the LOD Lax-Wendroff procedure at  $T = 0.3$  at  $h = 0.025$  and  $h = 0.05$  are shown in Tables 1 and 2, respectively. We observe that the dispersion error is significantly greater than the dissipation error. Out of the five combinations of values of  $k$  and  $h$ , we observe that the dispersion error and total mean square error are both least when  $h = 0.05$  and  $k = 0.03$  and are both greatest when  $h = 0.05$  and  $k = 0.0025$ .

**6.2. LOD (1, 5) Procedure.** The results of the numerical experiment using the LOD (1, 5) procedure at  $T = 0.3$  for  $h = 0.025$  and  $h = 0.05$  are shown in Tables 3 and 4, respectively. Out of the 12 combinations of values of  $k$  and  $h$ , we observe that the dissipation, dispersion error, and error rate are all

least when  $h = 0.05$  and  $k = 0.05$ . Also, the dissipation and dispersion errors and error rate are greatest when  $h = 0.05$  and  $k = 0.0625$ . We observe that at  $h = 0.025$  the total mean square error, dispersion error, and dissipation error are not much affected by the values of  $k$ . Also, the dispersion error is greater than the at all values of  $h$  and  $k$  considered.

## 7. Optimization

In this section, we obtain the optimal value of  $k$  at  $h = 0.025$  that minimizes the dispersion error for the two time-splitting procedures.

Since the partial differential equation we consider is slightly dissipative and also we observe from the numerical experiments carried out that the dissipative errors are much less than the dispersive errors, we choose to minimize the square of the dispersion error of the two splitting schemes.

**7.1. Proposed Techniques of Optimization.** Tam and Webb [18], Bogey and Bailly [19], and Hixon [20] among others have implemented techniques which enable coefficients to be determined in numerical schemes specifically designed for computational aeroacoustics. We now describe briefly how Tam and Webb [18] and Bogey and Bailly [19] define their

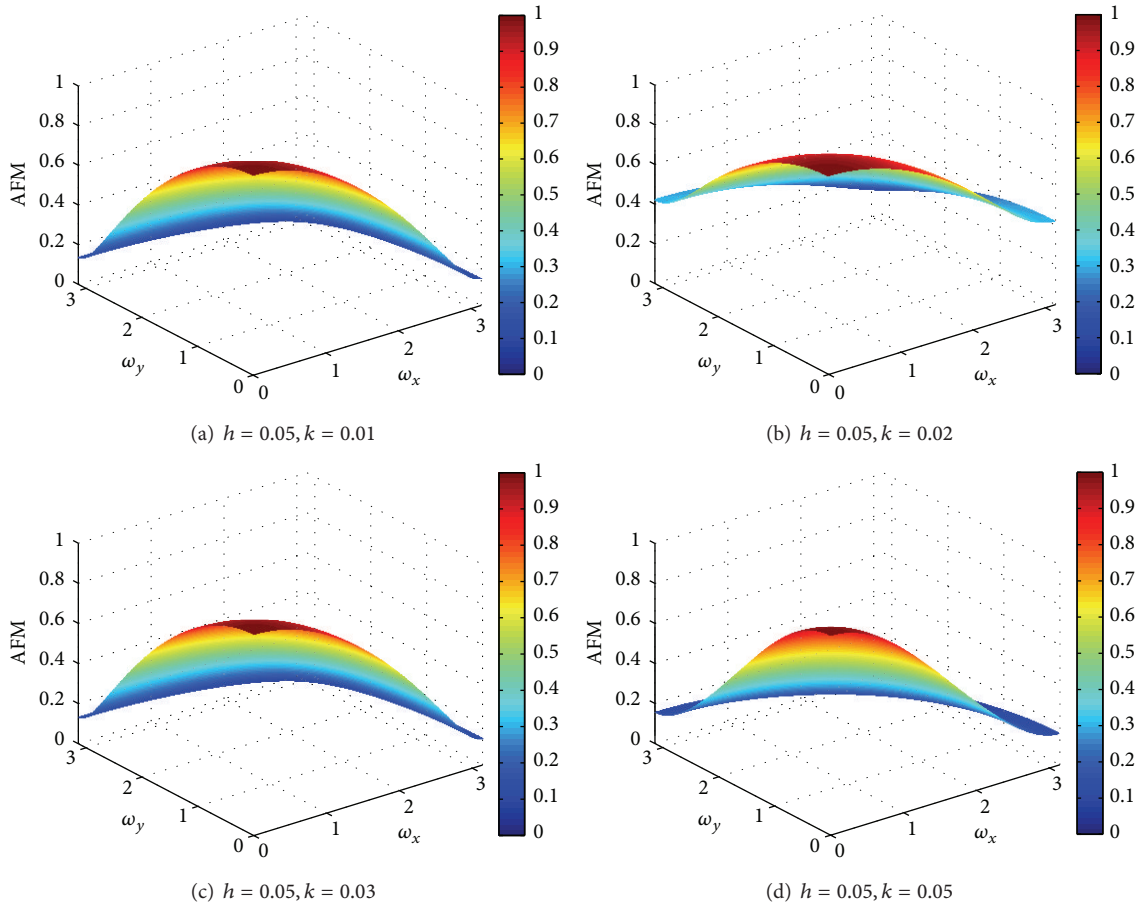


FIGURE 8: Plots of modulus of amplification factor versus phase angle in  $x$ -direction ( $\omega_x$ ) versus phase angle in  $y$ -direction ( $\omega_y$ ) at  $h = 0.05$  for some different values of  $k$  for the LOD (1, 5) procedure.

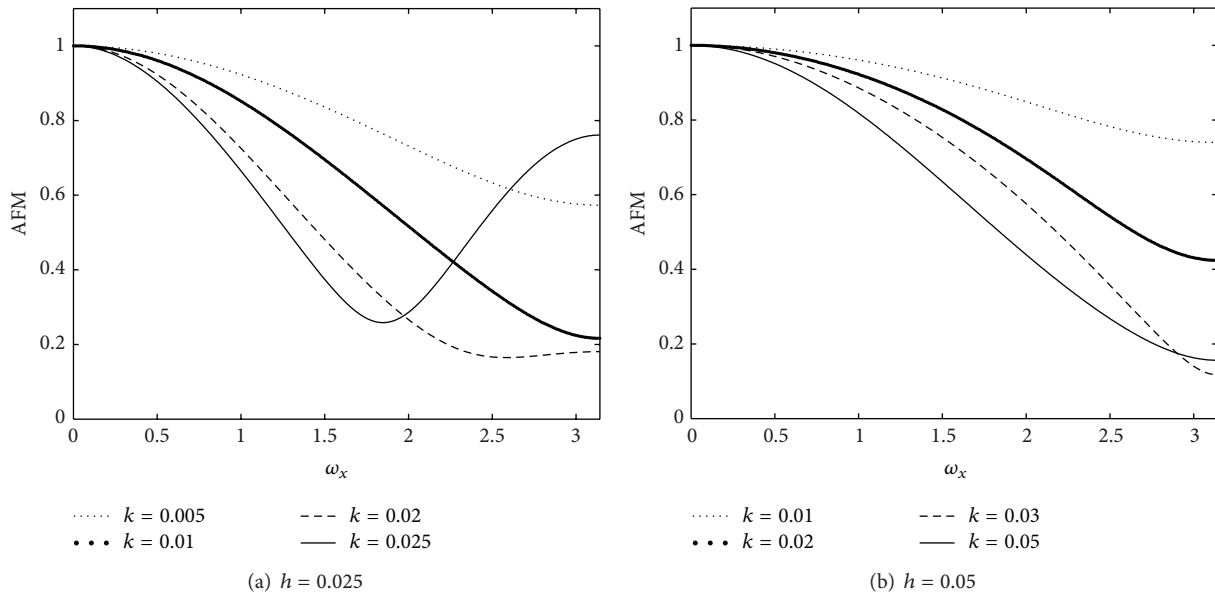


FIGURE 9: Plots of modulus of amplification factor versus  $\omega_x$  when  $\omega_y = 0$  at  $h = 0.025$  and  $h = 0.05$  with some different values of  $k$  for the LOD (1, 5) procedure.

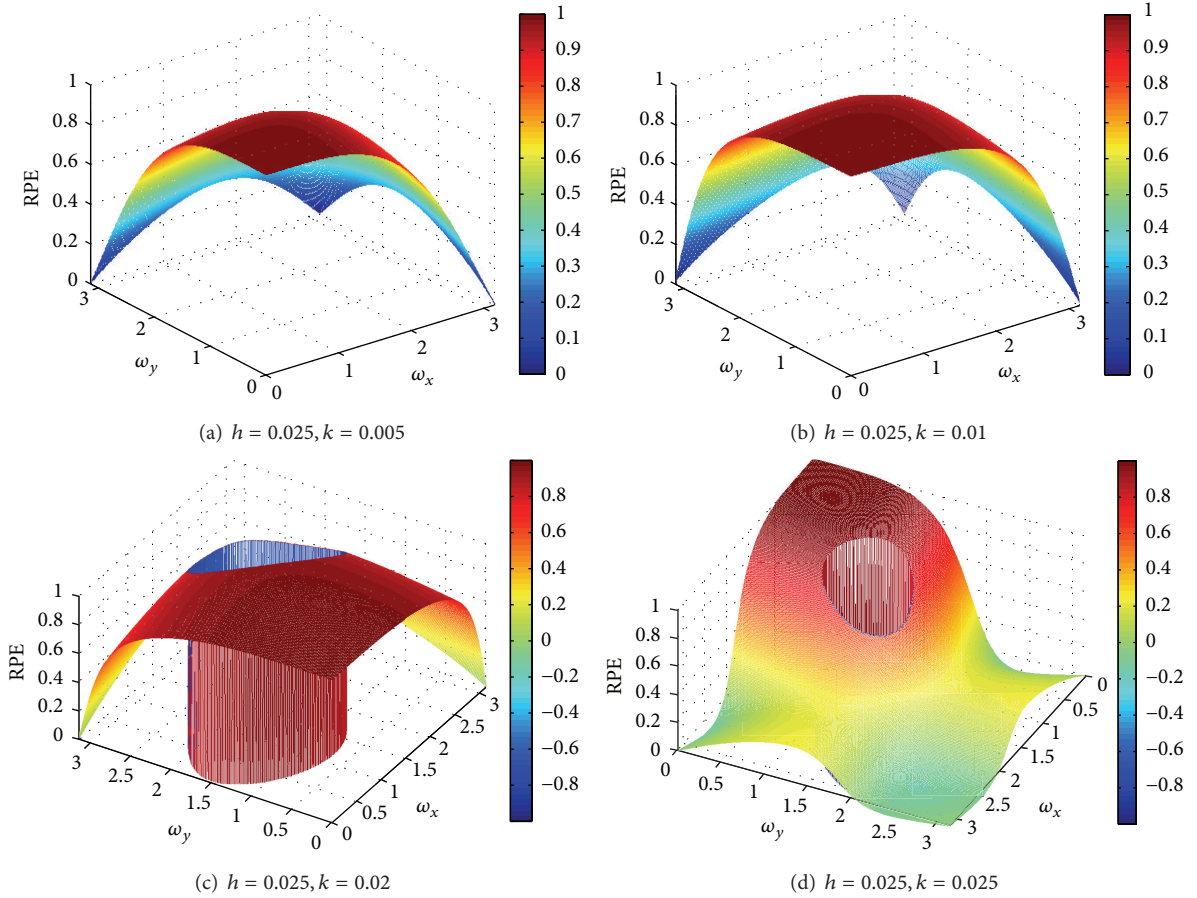


FIGURE 10: 3D plots of relative phase error versus  $\omega_x$  versus  $\omega_y$  at  $h = 0.025$  at some different values of  $k$  for the LOD (1, 5) procedure.

TABLE 1: Errors obtained from LOD Lax-Wendroff at  $h = 0.025$ .

$k$	CFL	$E_{\text{num}}$	Total mean square error	DISP. ERROR	DISS. ERROR
0.0025	0.08	$1.2043 \times 10^{-3}$	$1.0930 \times 10^{-5}$	$1.0602 \times 10^{-5}$	$2.5787 \times 10^{-7}$
0.005	0.16	$9.4236 \times 10^{-4}$	$7.4519 \times 10^{-6}$	$7.2355 \times 10^{-6}$	$2.4370 \times 10^{-7}$
0.01	0.32	$4.1557 \times 10^{-4}$	$4.1970 \times 10^{-6}$	$4.0222 \times 10^{-6}$	$1.6465 \times 10^{-7}$
3/160	0.6	$1.7126 \times 10^{-3}$	$2.0913 \times 10^{-5}$	$2.0819 \times 10^{-5}$	$5.5626 \times 10^{-8}$
1/60	8/15	$1.3626 \times 10^{-3}$	$1.3761 \times 10^{-5}$	$1.3675 \times 10^{-5}$	$8.3438 \times 10^{-8}$

TABLE 2: Errors obtained from LOD Lax-Wendroff at  $h = 0.05$ .

$k$	CFL	$E_{\text{num}}$	Total mean square error	DISP. ERROR	DISS. ERROR
0.0025	0.04	$1.3398 \times 10^{-3}$	$4.1073 \times 10^{-5}$	$4.1056 \times 10^{-5}$	$2.1203 \times 10^{-8}$
0.005	0.08	$1.2483 \times 10^{-3}$	$3.5560 \times 10^{-5}$	$3.5562 \times 10^{-5}$	$3.5412 \times 10^{-9}$
0.01	0.16	$1.0547 \times 10^{-3}$	$2.5261 \times 10^{-5}$	$2.5255 \times 10^{-5}$	$8.1665 \times 10^{-9}$
1/60	4/15	$7.7546 \times 10^{-4}$	$1.3488 \times 10^{-5}$	$1.3433 \times 10^{-5}$	$5.4469 \times 10^{-8}$
3/160	0.3	$6.8350 \times 10^{-4}$	$1.0388 \times 10^{-5}$	$1.0323 \times 10^{-5}$	$6.9368 \times 10^{-8}$
0.02	0.32	$6.2698 \times 10^{-4}$	$8.6851 \times 10^{-6}$	$8.6112 \times 10^{-6}$	$7.7093 \times 10^{-8}$
0.025	0.4	$3.9085 \times 10^{-4}$	$3.2351 \times 10^{-6}$	$3.1467 \times 10^{-6}$	$9.3072 \times 10^{-8}$
1/34	8/17	$4.5965 \times 10^{-4}$	$5.2537 \times 10^{-6}$	$5.2510 \times 10^{-6}$	$3.708 \times 10^{-9}$
0.03	0.48	$1.4596 \times 10^{-4}$	$4.6945 \times 10^{-7}$	$3.9599 \times 10^{-7}$	$7.7350 \times 10^{-8}$
0.04	0.64	$1.1718 \times 10^{-3}$	$2.4062 \times 10^{-5}$	$2.3462 \times 10^{-5}$	$6.0153 \times 10^{-7}$

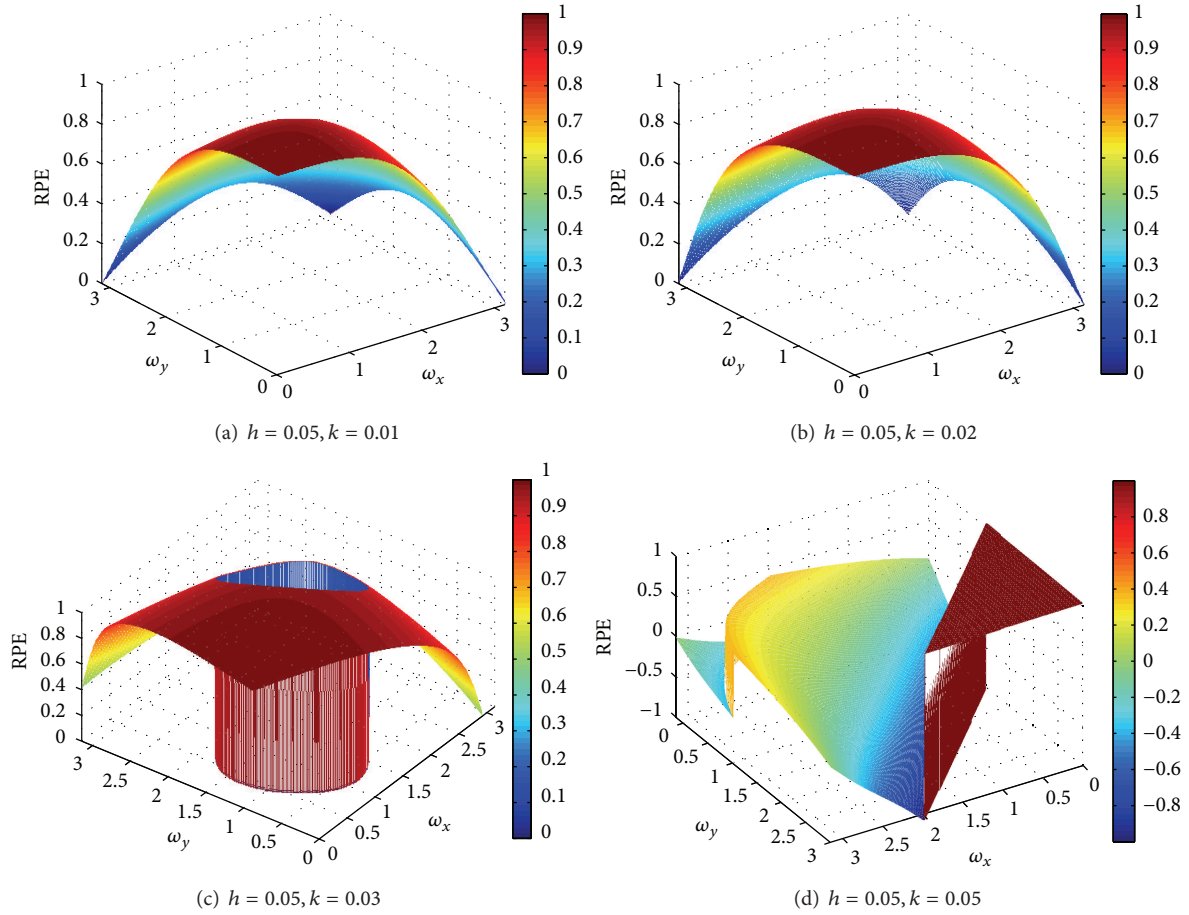


FIGURE 11: 3D plots of relative phase error versus  $\omega_x$  versus  $\omega_y$ , at  $h = 0.05$  at some different values of  $k$  for the LOD (1, 5) procedure.

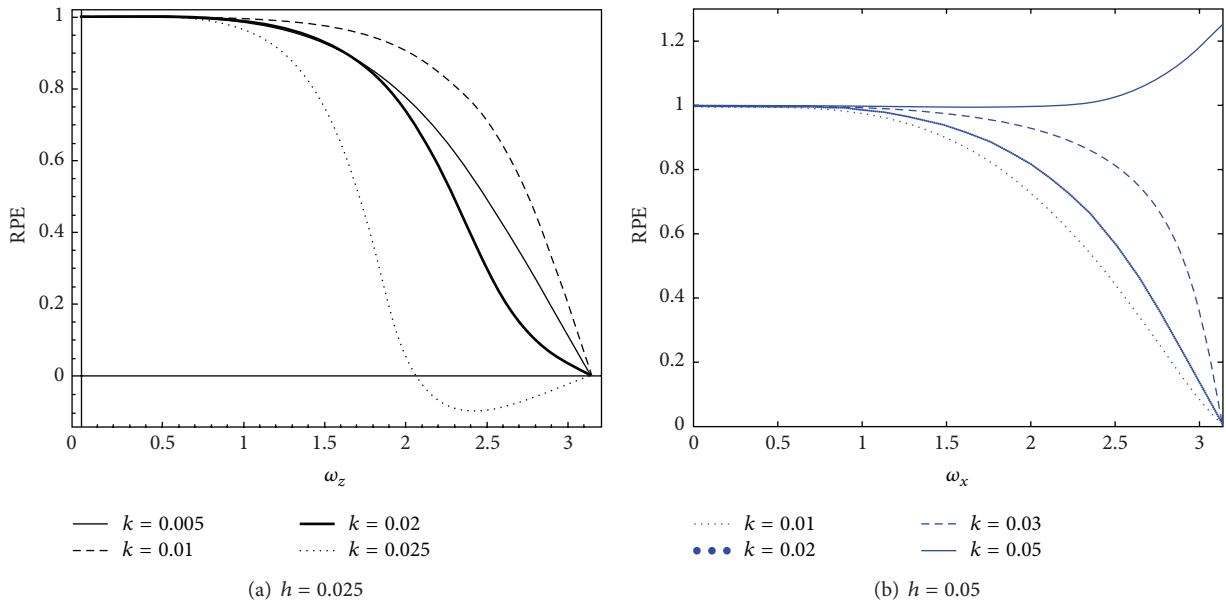
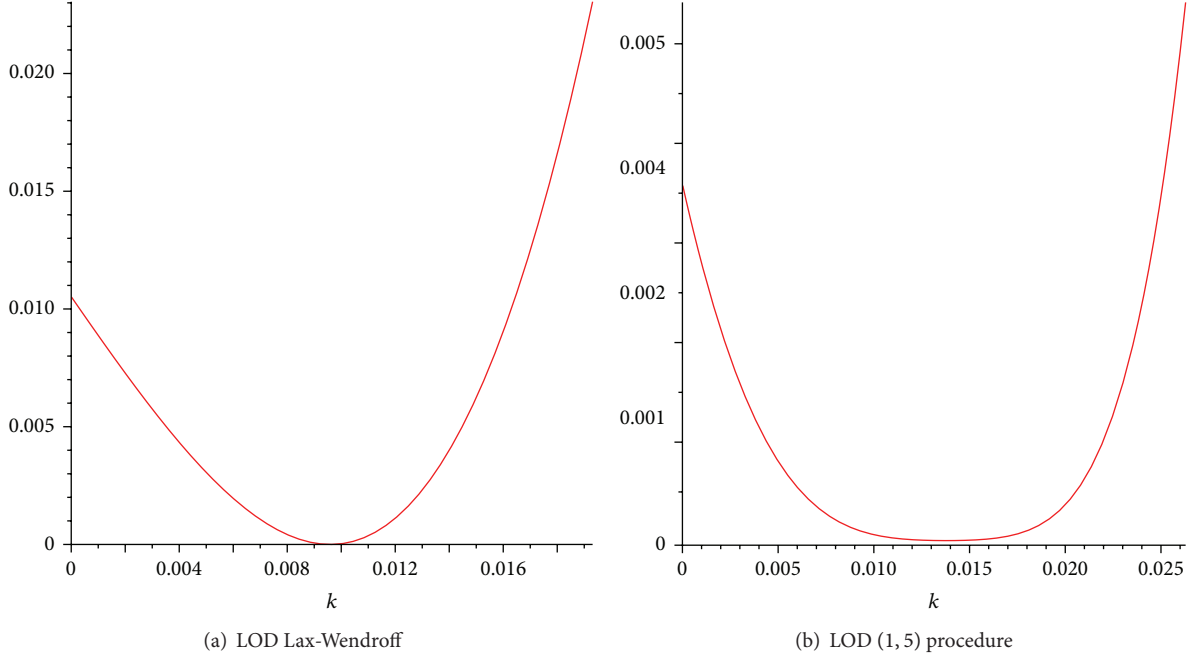


FIGURE 12: Plots of relative phase error versus  $\omega_x$  when  $\omega_y = 0$  at  $h = 0.025$  and  $h = 0.05$  with some different values of  $k$  for the LOD (1, 5) procedure.

FIGURE 13: Plots of integrated errors versus  $k$  at  $h = 0.025$  for the two time-splitting schemes.TABLE 3: Errors obtained from the LOD (1, 5) procedure at  $h = 0.025$ .

$k$	CFL	$E_{\text{num}}$	Total mean square error	DISP. ERROR	DISS. ERROR
0.005	0.16	$4.0539 \times 10^{-4}$	$4.1593 \times 10^{-6}$	$4.0009 \times 10^{-6}$	$1.6455 \times 10^{-7}$
0.01	0.32	$4.0072 \times 10^{-4}$	$4.1573 \times 10^{-6}$	$3.9874 \times 10^{-6}$	$1.6540 \times 10^{-7}$
1/60	8/15	$4.0565 \times 10^{-4}$	$4.1577 \times 10^{-6}$	$3.9797 \times 10^{-6}$	$1.6390 \times 10^{-7}$
3/160	0.60	$3.9839 \times 10^{-4}$	$4.1494 \times 10^{-6}$	$3.9782 \times 10^{-6}$	$1.6268 \times 10^{-7}$
0.02	0.64	$3.9878 \times 10^{-4}$	$4.1481 \times 10^{-6}$	$3.9768 \times 10^{-6}$	$1.6174 \times 10^{-7}$
0.025	0.80	$4.0890 \times 10^{-4}$	$4.1640 \times 10^{-6}$	$4.0430 \times 10^{-6}$	$1.5618 \times 10^{-7}$

measures and consequently their technique of optimization in computational aeroacoustics.

The dispersion-relation-preserving (DRP) scheme was designed so that the dispersion relation of the finite difference scheme is formally the same as that of the original partial differential equations. The integrated error is defined as

$$E = \int_{-\eta}^{\eta} |\theta^* h - \theta h|^2 d(\theta h), \quad (83)$$

where the quantities  $\theta^* h$  and  $\theta h$  represent the numerical and exact wavenumbers, respectively. The dispersion error and dissipation error are calculated as  $|\Re(\theta^* h) - \theta h|$  and  $|\Im(\theta^* h)|$ , respectively.

Tam and Shen [21] set  $\eta$  as 1.1 and optimize the coefficients in the numerical scheme such that the integrated error is minimized.

Bogey and Bailly minimize the relative difference between the exact wavenumber  $\theta h$  and the effective/numerical wavenumber  $\theta^* h$  and define their integrated errors as

$$E = \int_{(\theta h)_l}^{(\theta h)_h} \frac{|\theta^* h - \theta h|}{\theta h} d(\theta h) \quad (84)$$

or

$$E = \int_{\ln(\theta h)_l}^{\ln(\theta h)_h} |\theta^* h - \theta h| d(\ln(\theta h)). \quad (85)$$

In computational fluid dynamics for a particular method under consideration, the dispersion error is calculated as

$$|1 - \text{RPE}|. \quad (86)$$

We have modified the measures used by Tam and Webb and Bogey and Bailly in a computational aeroacoustics framework to suit them in a computational fluid dynamics framework [22] such that the optimal parameter can be obtained. We have defined the following integrated errors integrated error from Tam and Webb (IETAM) integrated error from Bogey and Bailly (IEBOGEY) [22] as follows:

$$\begin{aligned} \text{IETAM} &= \int_0^{w_1} |1 - \text{RPE}|^2 dw, \\ \text{IEBOGEY} &= \int_0^{w_1} |1 - \text{RPE}| dw. \end{aligned} \quad (87)$$

TABLE 4: Errors obtained from the LOD (1, 5) procedure at  $h = 0.05$ .

$k$	CFL	$E_{\text{num}}$	Total mean square error	DISP. ERROR	DISS. ERROR
0.01	0.16	$2.0000 \times 10^{-4}$	$7.8149 \times 10^{-7}$	$7.7377 \times 10^{-7}$	$1.1297 \times 10^{-8}$
0.02	0.32	$1.3905 \times 10^{-4}$	$3.9277 \times 10^{-7}$	$3.8065 \times 10^{-7}$	$1.4712 \times 10^{-8}$
1/34	8/17	$4.1603 \times 10^{-4}$	$4.0763 \times 10^{-6}$	$4.0663 \times 10^{-6}$	$1.1482 \times 10^{-8}$
0.03	0.48	$9.5979 \times 10^{-5}$	$2.1598 \times 10^{-7}$	$2.0584 \times 10^{-7}$	$1.4193 \times 10^{-8}$
0.05	0.8	$7.9301 \times 10^{-5}$	$1.7934 \times 10^{-7}$	$1.7059 \times 10^{-7}$	$1.0449 \times 10^{-8}$
0.0625	1	$8.5551 \times 10^{-4}$	$1.4674 \times 10^{-5}$	$1.4310 \times 10^{-5}$	$3.6790 \times 10^{-7}$

In [8], the integrated error for a scheme discretising the 1D advection-diffusion equation

$$\frac{\partial u}{\partial t} + \frac{\partial u}{\partial x} = 0.01 \frac{\partial^2 u}{\partial x^2} \quad (88)$$

is obtained as

$$\int_0^{1.1} (\text{RPE} - 1)^2 d\omega. \quad (89)$$

The value of  $h$  was fixed as 0.02 and the range of values of  $k$ , was determined. Then the integrated error, which is a function of  $k$ , was minimized and the optimal value of  $k$  is determined using NLPsolve function in maple.

We extend the work on optimization of parameters in [8] which is for the 1D advection-diffusion equation for the case of the 2D advection-diffusion equation. We define the integrated error as

$$\int_0^{1.1} \int_0^{1.1} (\text{RPE} - 1)^2 d\omega_x d\omega_y. \quad (90)$$

We first obtain an expression for the RPE of the LOD Lax-Wendroff when discretizing the equation

$$\frac{\partial u}{\partial t} + 0.8 \frac{\partial u}{\partial x} + 0.8 \frac{\partial u}{\partial y} = 0.01 \frac{\partial^2 u}{\partial x^2} + 0.01 \frac{\partial^2 u}{\partial y^2}. \quad (91)$$

Since  $c = 0.8k/h$  and  $s = 0.8k/h^2$  and we choose  $h = 0.025$ , we have  $c = 32k$  and  $s = 16k$ . Hence, the RPE is a function of  $k$ ,  $\omega_x$ , and  $\omega_y$ . Since we can have phase wrapping, we make use of Taylor's expansion to obtain an approximation for the RPE up to the terms

$$(\omega_x)^3 (\omega_y)^2, (\omega_x)^5, (\omega_x)^2 (\omega_y)^3, (\omega_y)^5, \omega_x (\omega_y)^4, (\omega_x)^4 \omega_y. \quad (92)$$

The integrated error  $\int_0^{1.1} \int_0^{1.1} (\text{RPE} - 1)^2 d\omega_x d\omega_y$  is obtained by using Simpson's method and it is a function of  $k$  only. A plot of the integrated error versus  $k$  is shown in Figure 13(a) for  $k \in [0, 0.0193]$ . Using the NLPsolve function in maple, this optimal value of  $k$  is found to be 0.009593 and the minimum value of the integrated error is  $1.883960 \times 10^{-7}$ .

To validate our results, we perform the same numerical experiment described in Section 3.2 at  $h = 0.025$  and use the

optimal value of  $k$  or a value of  $k$  close to this optimal value, in that case,  $k = 3/310 \approx 0.0096$ , and compute the errors. The error rate, total mean square error, and dispersion error are  $3.9967 \times 10^{-4}$ ,  $4.1603 \times 10^{-6}$ ,  $3.9878 \times 10^{-6}$ . These three errors are all least as compared to when other values of  $k$  are used as shown in Table 1.

We adopt the same procedure to compute the optimal value of  $k$  for the LOD (1, 5) scheme when  $h = 0.025$ . We obtain an approximate expression for the RPE of the LOD (1, 5) when  $c = 32k$  and  $s = 16k$ . We use Simpson's rule to approximate the integral given by (90) which is a function of  $k$ . A plot of the integrated error versus  $k$  for  $k \in [0, 0.026288]$  is shown in Figure 13(b) and using NLPsolve function in maple the optimal value of  $k$  is 0.013782 and also the minimum value of the integral is  $1.139313 \times 10^{-6}$ .

We perform the numerical experiment described in Section 3.2 with  $k = 3/220$  which is close to the optimal value of  $k$  we have obtained with  $h = 0.025$ . The error rate, total mean square error, dispersion error, and dissipation error are  $3.9948 \times 10^{-4}$ ,  $4.1504 \times 10^{-6}$ ,  $3.9459 \times 10^{-6}$ , and  $1.6501 \times 10^{-7}$ , respectively. The total mean square error and dispersion error are both least when  $k = 3/220 \approx 0.01378$ .

## 8. Conclusion

In this paper, two time-splitting procedures are used to solve a 2D advection-diffusion equation with constant coefficients when the advection velocity in both  $x$ - and  $y$ -directions is 0.8 and also when the coefficient of diffusivity in both  $x$ - and  $y$ -directions is 0.01. We perform a stability analysis and spectral analysis of the dispersion and dissipation properties of the two schemes at some values of  $h$  and  $k$ . Numerical experiments are carried out and various errors are computed. These errors are dependent on the values of  $h$  and  $k$ . It is observed that in general the dispersion error is more affected by the values of  $k$  and  $h$  for the LOD Lax-Wendroff scheme as compared to that of the LOD (1, 5) scheme at a given value of  $h$ . We then use an optimization technique based on minimisation of the square of the dispersion error to find the optimal value of  $k$  when  $h$  is chosen as 0.025 and this is validated by numerical experiments.

Future extension of this work to consider other types of advection-diffusion equations when dissipation dominates and to find out which optimization techniques are suitable in these cases. Also, the work can be extended to 2D nonlinear convection-diffusion problems.

## Nomenclature

$I$ :	$\sqrt{(-1)}$
$h$ :	Spatial step
$k$ :	Time step
$R_\Delta$ :	Reynolds number
RPE:	Relative phase error per unit time step
AFM:	Modulus of amplification factor
$\beta_x$ :	Advection velocity in $x$ -direction
$\beta_y$ :	Advection velocity in $y$ -direction
$\beta_z$ :	Advection velocity in $z$ -direction
$\alpha_x$ :	Coefficient of diffusivity in $x$ -direction
$\alpha_y$ :	Coefficient of diffusivity in $y$ -direction
$\alpha_z$ :	Coefficient of diffusivity in $z$ -direction
$\theta_1$ :	Wavenumber in $x$ -direction
$\theta_2$ :	Wavenumber in $y$ -direction
$\omega_x$ :	Phase angle in $x$ -direction
$\omega_y$ :	Phase angle in $y$ -direction
$\omega_x$ :	$\Delta x \theta_1$
$\omega_y$ :	$\Delta y \theta_2$
$c_x$ :	$\beta_x k / h$
$c_y$ :	$\beta_y k / h$
$s_x$ :	$\alpha_x k / h^2$
$s_y$ :	$\alpha_y k / h^2$
DISP. ERROR:	Dispersion error
DISS. ERROR:	Dissipation error.

## Acknowledgments

The work of Dr A. R. Appadu was funded through the Research Development Programme of the University of Pretoria and the period of funding is from January 2013 to January 2014. Mr Hagos is grateful to the African Institute for Mathematical Sciences (AIMS), South Africa, for a full bursary for the structured Master's program from August 2012 to July 2013. The authors are grateful to the two anonymous reviewers for their comments which were useful in clarifying and focusing the presentation.

## References

- [1] A. Shukla, A. K. Singh, and P. Singh, "A recent development of numerical methods for solving convection-diffusion problems," *Applied Mathematics*, vol. 1, pp. 1-12, 2011.
- [2] M. Dehghan, "On the numerical solution of the one-dimensional convection-diffusion equation," *Mathematical Problems in Engineering*, vol. 2005, no. 1, pp. 61-74, 2005.
- [3] M. Dehghan, "Time-splitting procedures for the solution of the two-dimensional transport equation," *Kybernetes*, vol. 36, no. 5-6, pp. 791-805, 2007.
- [4] C. B. Laney, *Computational Gasdynamics*, Cambridge University Press, Cambridge, UK, 1998.
- [5] J. E. Fromm, "A method for reducing dispersion in convective difference schemes," *Journal of Computational Physics*, vol. 3, no. 2, pp. 176-189, 1968.
- [6] R. J. Babarsky and R. Sharpley, "Expanded stability through higher temporal accuracy for time-centered advection schemes," *Monthly Weather Review*, vol. 125, no. 6, pp. 1277-1295, 1997.
- [7] K. W. Morton and D. F. Mayers, *Numerical Solution of Partial Differential Equations*, Cambridge University Press, Cambridge, UK, 1994.
- [8] A. R. Appadu, "Numerical solution of the 1D advection-diffusion equation using standard and nonstandard finite difference schemes," *Journal of Applied Mathematics*, vol. 2013, Article ID 734374, 14 pages, 2013.
- [9] R. Smith and Y. Tang, "Optimal and near-optimal advection-diffusion finite-difference schemes. V. Error propagation," *Proceedings of the Royal Society of London A*, vol. 457, no. 2008, pp. 803-816, 2001.
- [10] C. Hirsch, *Numerical Computation of Internal and External Flows*, vol. 1, John Wiley & Sons, New York, NY, USA, 1988.
- [11] R. W. MacCormack and A. J. Paullay, "Computational efficiency achieved by time splitting of finite difference operators," Tech. Rep. AIAA Paper 72-154, 1972.
- [12] M. Dehghan, "Weighted finite difference techniques for the one-dimensional advection-diffusion equation," *Applied Mathematics and Computation*, vol. 147, no. 2, pp. 307-319, 2004.
- [13] L. L. Takacs, "A two-step scheme for the advection equation with minimized dissipation and dispersion errors," *Monthly Weather Review*, vol. 113, no. 6, pp. 1050-1065, 1985.
- [14] A. R. Appadu and M. Z. Dauhoo, "The concept of minimized integrated exponential error for low dispersion and low dissipation schemes," *International Journal for Numerical Methods in Fluids*, vol. 65, no. 5, pp. 578-601, 2011.
- [15] A. R. Appadu, "Some applications of the concept of minimized integrated exponential error for low dispersion and low dissipation," *International Journal for Numerical Methods in Fluids*, vol. 68, no. 2, pp. 244-268, 2012.
- [16] A. C. Hindmarsh, P. M. Gresho, and D. F. Griffiths, "The stability of explicit Euler time-integration for certain finite difference approximations of the multi-dimensional advection-diffusion equation," *International Journal for Numerical Methods in Fluids*, vol. 4, no. 9, pp. 853-897, 1984.
- [17] E. Sousa, "The controversial stability analysis," *Applied Mathematics and Computation*, vol. 145, no. 2-3, pp. 777-794, 2003.
- [18] C. K. W. Tam and J. C. Webb, "Dispersion-relation-preserving finite difference schemes for computational acoustics," *Journal of Computational Physics*, vol. 107, no. 2, pp. 262-281, 1993.
- [19] C. Bogey and C. Bailly, "A family of low dispersive and low dissipative explicit schemes for flow and noise computations," *Journal of Computational Physics*, vol. 194, no. 1, pp. 194-214, 2004.
- [20] R. Hixon, "On increasing the accuracy of MacCormack schemes for aeroacoustic applications," Tech. Rep. AIAA Paper 10.2514/6.1997-1586, 1997.
- [21] C. K. W. Tam and H. Shen, "Direct computation of nonlinear acoustic pulses using high-order finite differences schemes," Tech. Rep. AIAA Paper 93-4325, 1993.
- [22] A. R. Appadu, "Comparison of some optimisation techniques for numerical schemes discretising equations with advection terms," *International Journal of Innovative Computing and Applications*, vol. 4, no. 1, pp. 12-27, 2012.

## Research Article

# Model of Infiltration of Spent Automotive Catalysts by Molten Metal in Process of Platinum Metals Recovery

**Agnieszka Fornalczyk, Slawomir Golak, and Mariola Saternus**

*Faculty of Materials Engineering and Metallurgy, Silesian University of Technology, Krasinskiego 8, 40-019 Katowice, Poland*

Correspondence should be addressed to Slawomir Golak; [slawomir.golak@polsl.pl](mailto:slawomir.golak@polsl.pl)

Received 30 July 2013; Revised 30 September 2013; Accepted 30 September 2013

Academic Editor: Waqar Khan

Copyright © 2013 Agnieszka Fornalczyk et al. This is an open access article distributed under the Creative Commons Attribution License, which permits unrestricted use, distribution, and reproduction in any medium, provided the original work is properly cited.

This paper presents the model for the washing-out process of precious metals from spent catalysts by the use of molten lead in which the metal flow is caused by the rotating electromagnetic field and the Lorentz force. The model includes the coupling of the electromagnetic field with the hydrodynamic field, the flow of metal through anisotropic and porous structure of the catalyst, and the movement of the phase boundary (air-metal) during infiltration of the catalyst carrier by the molten metal. The developed model enabled analysis of the impact of spacing between the catalysts and the supply current on the degree of catalyst infiltration by the molten metal. The results of calculations carried out on the basis of the model were verified experimentally.

## 1. Introduction

Spent catalysts containing precious metals are very attractive for recycling [1–6]. However, this process faces two major obstacles. First of all, a single catalyst carrier contains, at best, a few grams of platinum metals and secondly, the metals are trapped in the capillary structure of the ceramic carrier of a catalyst. That is why, the condition for economic viability of such a process is to minimise the cost of processing a single carrier. The authors have proposed and patented a new technology based on leaching PGMs from the catalyst structure by means of liquid metals [7]. This technique does not require a grinding of a catalyst carrier, thereby helping to reduce costs. Since the use of a mechanical pump in case of aggressive molten metal, in terms of large-scale recycling of catalysts, is practically impossible, the authors proposed a method based on a noncontact action of the electromagnetic field and magnetohydrodynamic phenomena [8, 9]. Unfortunately, this method of propelling the metal is further complicated by the fact that the electromagnetic field acts on the metal outside of the catalyst carrier, which is the area where we would like to obtain the flow. The key for the success is to produce a pressure difference on both sides of the catalyst that is sufficient to overcome the resistance of the capillary structure of the catalyst carrier.

The technological process analyzed in the paper is quite a big challenge for modeling by means of computational fluid dynamics. So far only the flow of gases through a working automotive catalyst was modeled [10, 11]. The modeling of the proposed recycling process of catalysts is much more complex. In the case of the considered process a multiphysical model taking into account coupling of the electromagnetic field with the hydrodynamic field has to be developed. Such models were previously developed for many industrial processes [12–15] but without a porous medium limiting the impact of electromagnetic field on the molten metal. Only paper [16] describes such a simple one-dimensional model of the Lorentz force infiltration of the porous structure.

At the initial state of the described process, there is a two-phase flow of molten metal and air in the area of the catalyst carrier and during its infiltration the phase boundary moves. There are similar phenomena in the process of manufacturing metal matrix composites reinforced with a preform [17, 18]. Created models of this process take into account the two-phase flow and resistance of the preform to the penetration of the molten melt [19, 20]. However, these models cannot be directly applied for the process of catalysts recycling because of the ultra-anisotropic, capillary structure of the catalyst carrier and nonuniform distribution of pressure on both sides of the carrier. In contrast to the process of the composite

fabrication, the model of the analyzed recycling process must include not only the area of the porous carrier but also the whole device used in this process.

The multiphysical model presented in the paper was created on the basis of commercial software packages the Cedrat Flux (electromagnetic model) and the Ansys Fluent (hydrodynamic model). However, the coupling between the electromagnetic field and the hydrodynamic field was implemented, with the use of software developed by the authors. The package Fluent has been extended with a new model allowing the analysis of two-phase flow through anisotropic, capillary structure taking into account the flow resistance and capillary pressure.

The paper contains description of the model of the catalyst carriers infiltration by molten metal, analysis of the influence of chosen parameters on efficiency of the process, and results of the experimental verification of the developed model.

## 2. Model of Process

The model of the analyzed process requires the coupling of the electromagnetic field with hydrodynamic field. It is possible to apply the commonly used one-way coupling of these fields [12–15] due to the fact that in the modeled process the magnetic Reynolds number is low; the moving (during the infiltration of catalyst carrier) phase boundary is present only in the area of the ceramic carrier and does not influence the distribution of the electromagnetic field because of zero macroscopic conductivity of the carrier capillary structure (independent of the presence of metal). This made it possible to divide simulation into two separate stages—the quasi-static simulation of the electromagnetic field giving the distribution of Lorentz force acting on liquid metal and the unsteady hydrodynamic simulation (Figure 1).

The research was conducted on the basis of two-dimensional electromagnetic and hydrodynamic models. This allowed reduction of simulation time (to tens hours) with maintaining the representativeness of the model. It was possible because of the channel depth similar to the height of the catalyst carrier. It means that there was no flow under and above the carrier. At the same time the coil considerably higher than the channel allowed the assumption that the electromagnetic field is uniform in the direction parallel to the electromagnetic stirrer axis.

The periodicity of the electromagnetic field as well as the hydrodynamic field was assumed in the model (Figure 2). The size of the calculation domain expressed by  $\beta$  angle depends on the number of catalyst carriers placed in the channel.

**2.1. Channel Area outside Catalysts Carriers.** The electromagnetic field was modeled using the equation, commonly used for quasistatic electromagnetic problems, based on the magnetic vector potential [15, 21, 22]. In the case of the two-dimensional model the potential is a scalar which significantly simplifies the calculations. Consider

$$\nabla \times \left( \frac{1}{\mu} \nabla \times \mathbf{A} \right) + j\omega\sigma\mathbf{A} = \mathbf{J}_s, \quad (1)$$

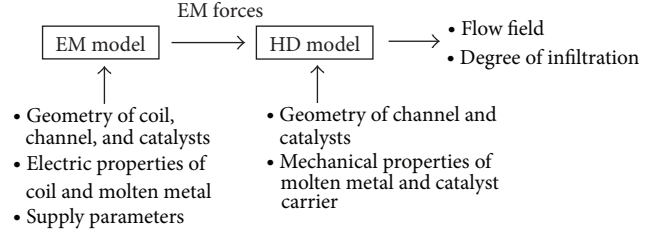


FIGURE 1: Schematic diagram of simulation.

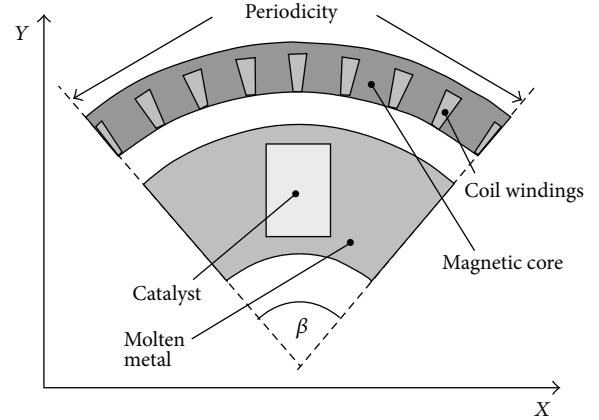


FIGURE 2: Schematic diagram of model geometry.

where  $\mu$ ,  $\sigma$  are magnetic permeability and conductivity of the molten metal,  $\omega$  is angular frequency,  $\mathbf{J}_s$  is source current density.

After calculation of the potential distribution, it is possible to determine the Eddy current density  $\mathbf{J}$  and the magnetic induction  $\mathbf{B}$ . Consider

$$\begin{aligned} \mathbf{B} &= \nabla \times \mathbf{A}, \\ \mathbf{J} &= j\omega\sigma\mathbf{A}. \end{aligned} \quad (2)$$

On this basis, the distribution of the time-averaged Lorentz force acting on the molten metal was determined. Consider

$$\mathbf{f}_e = \frac{1}{2} \operatorname{Re}(\mathbf{J} \times \mathbf{B}^*). \quad (3)$$

The electromagnetic model was implemented by use of the commercial software Cedrat Flux complemented by the module which enables the calculation of the time-averaged Lorentz force.

The model of metal flow in the channel outside catalysts carriers was based on the solution of continuity and Navier-Stokes equations for the incompressible fluid. The electromagnetic force density  $\mathbf{f}_e$  was added as the source term in the momentum equation (5). Consider

$$\nabla \cdot \mathbf{v} = 0 \quad (4)$$

$$\rho_f \left( \frac{\partial \mathbf{v}}{\partial t} + \mathbf{v} \cdot \nabla \mathbf{v} \right) = -\nabla p + \eta_e \nabla^2 \mathbf{v} + \mathbf{f}_e, \quad (5)$$

where  $\mathbf{v}$  is velocity;  $\eta_e$  is effective viscosity taking into account turbulent viscosity determined for the commonly used  $k - \varepsilon$  model [23, 24],  $\rho$  is density;  $p$  is pressure.

Due to the fact that the air squeezed out from the catalyst carrier is almost immediately removed from the molten metal as a result of the buoyancy force, only one phase in this area—the molten metal—was assumed.

The hydrodynamic model was created with the use of the Ansys Fluent complemented by User-Defined Functions enabling import of the electromagnetic force distribution from the Cedrat Flux.

**2.2. Catalyst Carrier Area.** The capillary structure of the carrier requires substantial modification of the model describing the channel zone outside the catalyst carriers. First of all, because the macroscopic electrical conductivity of the ceramic carrier area is zero (in the direction of the eddy current flow), the Lorentz force does not act on the metal in this area. Therefore, the source term representing the electromagnetic force can be neglected in (5). The capillary structure of the catalyst forces the unidirectional flow in the direction of the capillaries. The orientation of the catalyst according to the coordinate system (Figure 2) allowed reducing calculation to only the horizontal component of the velocity, assuming the vertical component  $v_y$  is equal to zero.

After immersion of the catalyst into the molten metal, the infiltration of its capillary structure by the metal begins. This is why, in the area of the catalyst carrier, a two-phase flow was modeled using the modified volume of fluid (VOF) method which allowed tracking of the interface between air and molten metal during the infiltration of the carrier porous structure. The authors' modification of the VOF method enables modeling the two-phase flow through ultra-anisotropic, capillary structure of the catalyst, taking into account the flow resistance and capillary pressure.

The catalyst capillary structure inhibits the flow of molten metal. The pressure drop across the length of the capillary can be determined on the basis of Hagen-Poiseuille equation [10]:

$$\frac{\Delta p}{L} = \frac{28.5}{d^2} \eta v, \quad (6)$$

where  $\Delta p$  is pressure drop,  $L$  is unit length,  $d$  is hydraulic diameter of the capillary,  $\eta$  is viscosity of metal, and  $v$  is velocity.

At the same time the presence of channel walls separating different fluid streams results in the lack of the term directly expressing the internal friction of fluid in the momentum equation (8). This friction was taken into account indirectly in the term derived from the Hagen-Poiseuille equation (6).

The metal, which is infiltrating the ceramic structure of the catalyst, also meets the additional resistance in the form of the capillary pressure due to the wetting angle for the system of ceramics and metal greater than 90 degrees. Consider

$$p_c = \frac{4\sigma \cos \theta}{d}, \quad (7)$$

where  $p_c$  is capillary pressure,  $\sigma$  is surface tension, and  $d$  is capillary diameter.

TABLE 1: Geometry and material properties.

External radius of channel	0.139 m
Internal radius of channel	0.61 m
Internal radius of coil	0.149 m
Frequency of coil	50 Hz
Lead density	10540 kg·m <sup>-3</sup>
Lead viscosity	0.002154 Pa·s
Width of carrier	40 mm
Height of carrier	60 mm
Hydraulic diameter of capillary	0.00085 m
Wetting angle of carrier ceramics (Al <sub>2</sub> O <sub>3</sub> ) by molten lead	120°
Surface tension of lead	0.439 N·m <sup>-1</sup>

The capillary pressure and flow resistance resulting from the Hagen-Poiseuille relationship were included in the Navier-Stokes equation

$$\rho_m \frac{dv_x}{dt} = -\frac{dp}{dx} - \frac{28.5}{d^2} \eta_m v_x - \frac{4\sigma \cos \theta}{d} \frac{d\alpha}{dx}, \quad (8)$$

where  $\alpha$  expresses the volume fraction of metal and  $\rho_m$  and  $\eta_m$  are the effective density and viscosity expressed by formulas:

$$\begin{aligned} \rho_m &= \alpha \rho_{\text{lead}} + (1 - \alpha) \rho_{\text{air}}, \\ \eta_m &= \alpha \eta_{\text{lead}} + (1 - \alpha) \eta_{\text{air}}. \end{aligned} \quad (9)$$

Tracing the metal phase distribution by the use of VOF method required adding to the model another continuity equation for the volume fraction of the metal:

$$\frac{\partial \alpha}{\partial t} + \frac{\partial (\alpha v_x)}{\partial x} = 0. \quad (10)$$

This multiphase model for the capillary medium was implemented as an additional module of the Fluent by the use of User-Defined Functions.

### 3. Numerical Simulation

Computer simulations (based on the developed model of the process) helped to evaluate the effectiveness of rinsing the catalyst structure by the liquid metal. The calculations also allowed the assessment of the impact of inductor current, the number of catalysts in the channel (distance between them) on the efficiency of the process. The study was conducted using liquid lead as a rinsing medium, for the process parameters shown in Table 1.

The research began with the two catalysts in the channel. The liquid metal was treated by a rotating electromagnetic field generated by a coil energized with a three-phase current of 40 A. The distribution of the obtained electromagnetic force density is shown in Figure 3.

Electromagnetic forces reach the maximum value at the outer wall of the channel and vanish exponentially as the distance from the wall increases. This means that the effective

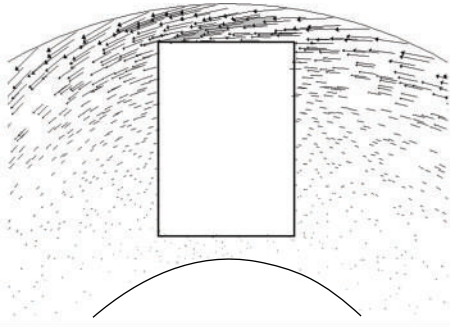


FIGURE 3: Distribution of electromagnetic force density.

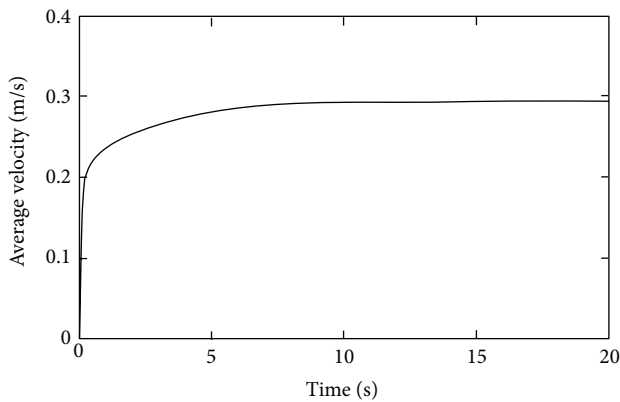


FIGURE 4: Average velocity as a function of time for two catalysts in the channel and current of 40 A.

acceleration of metal occurs only in the outer metal layers. In the catalyst area, the Lorentz force does not act on the molten metal due to zero macroscopic conductivity of the carrier in the directions orthogonal to the direction of capillaries.

The distribution geometry of the electromagnetic force does not vary with changes in the supply current. The current only affects the values of this force.

About 20 seconds after power turn-on, the average velocity of the metal (Figure 4) reaches its maximum and thus the final flow structure and degree of the catalyst infiltration are obtained.

Only half of the carrier was infiltrated by metal, as shown in Figure 5. The main reason is insufficient, differential pressure between the inlet and outlet of capillaries which is not able to overcome the capillary pressure (7). As a result, precious metals are leached only from the half of the carrier. It dramatically worsens the efficiency and economy of the process.

Placing only one catalyst in the channel expands the area where the metal can be effectively accelerated, thereby increasing the pressure difference obtained on both sides of the catalyst. This results in a significant improvement of the catalyst structure infiltration (Figure 6). However, in the case of only one catalyst in the channel and approximately the same supply power, the efficiency of the process is reduced by half.

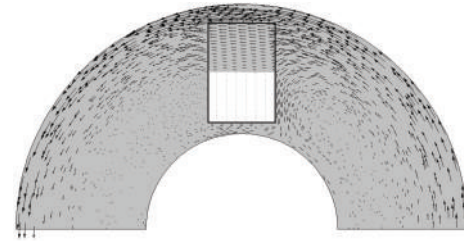


FIGURE 5: Distribution of velocity and degree of catalyst infiltration by liquid metal after stabilizing the flow field in the case of two catalysts in the channel and current of 40 A.

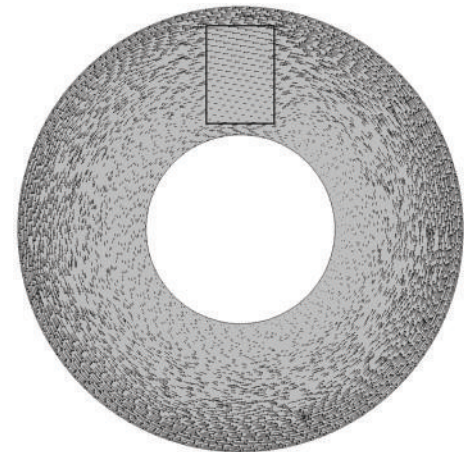


FIGURE 6: Distribution of velocity and degree of catalyst infiltration by liquid metal after stabilizing the velocity in the case of one catalyst in the channel and current of 40 A.

For comparison, simulations for four and eight catalysts in the channel were carried out. However, in these cases there was almost no infiltration of the catalysts by liquid metal, which means the complete failure of the recycling process. All the energy was consumed for producing vortices in the spaces between the catalysts.

Increasing the supply current to 57 A and thus doubling the electromagnetic forces acting on the molten metal without changing the geometry of their distribution increased the average velocity that the liquid lead reaches in the channel (approximately 0.5 m/s). Increasing the difference of pressure between the inlet and outlet of the catalyst significantly improved the degree of infiltration of the carrier structure (Figure 8(a)).

However, the increase of the current causes a double increase in the power consumed by the device. That electrical efficiency of the process is halved. Comparison of the results obtained for one catalyst in the channel and the input current 40 A with the results for the two catalysts and supply current 57 A shows that better results can be obtained by increasing the spacing between the catalysts than by increasing the supply current (and consumed power). Increasing the supply current allowed a certain degree of infiltration of the carrier for case four (Figure 8(b)) and eight (Figure 8(c)) catalysts in the channel, but it should be considered as insufficient.

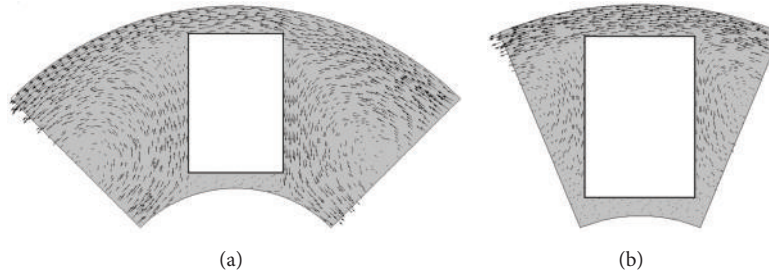


FIGURE 7: Distribution of velocity and degree of catalyst infiltration by liquid metal after stabilizing the velocity in the case of four (a) and eight (b) catalysts in the channel and current of 40 A.

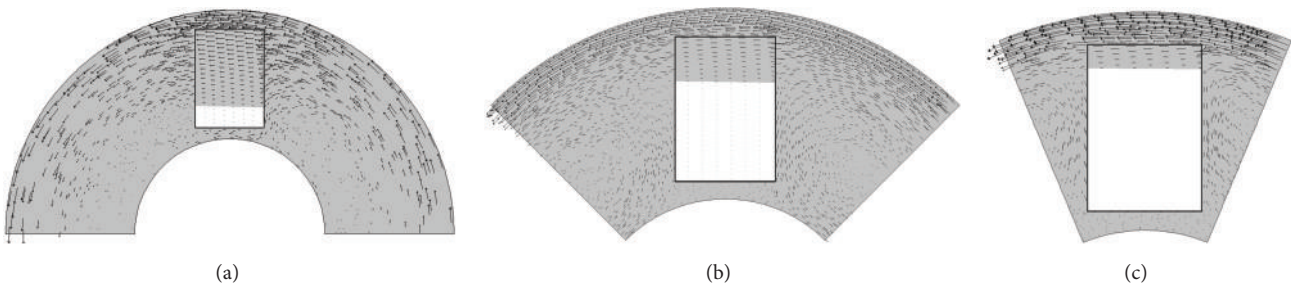


FIGURE 8: Distribution of velocity and degree of catalyst infiltration by liquid metal after stabilizing the velocity in the case of two (a), four (b), and eight (c) catalysts in channel and current of 57 A.

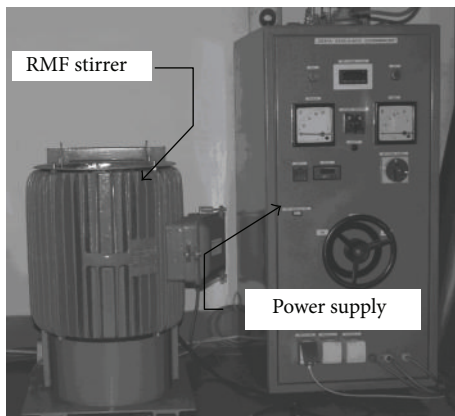


FIGURE 9: Experimental facility of automotive catalysts recycling.

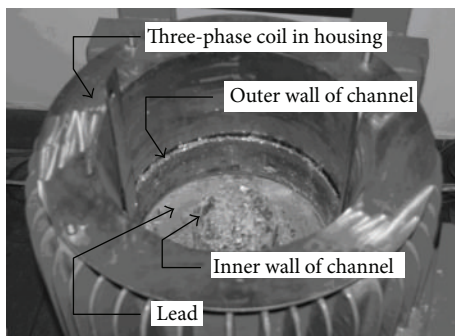


FIGURE 10: RMF stirrer.

#### 4. Experimental Verification

The making of measurements of molten metal flow is not an easy task. A number of measurement methods were developed [25], but none of them is suitable for measuring the flow of metal through the porous structure of the catalyst. The only way to check the reliability of the presented model of infiltration is placing the catalysts in a stream of liquid metal, removing them after infiltration, and checking which capillaries were filled by the molten metal. The problem is that after the removal of the catalyst from the channel still liquid metal flows out from capillaries due to the action of the gravity and capillary pressure. For this reason, the only evidence of the presence of molten lead in a capillary during the process is the small amount of the solidified metal at its outlet.

Experimental verification of the described numerical model was carried with the use of the facility shown in Figure 9.

The facility consists of the rotating magnetic field stirrer (adapted a three-phase asynchronous motor) and the power supply (inverter). In the annular channel of the RMF stirrer (Figure 10) there was molten lead with a depth of 60 millimeters.

Three experiments were performed: for one, two, and four catalysts immersed in the molten lead. The three phase inductor of the stirrer was supplied with current of 40 A and frequency of 50 Hz.

Front surfaces of the catalysts with remains of lead are presented in Figure 11 (the right wall of the catalyst is one close to the outer wall of the channel). The obtained experimental

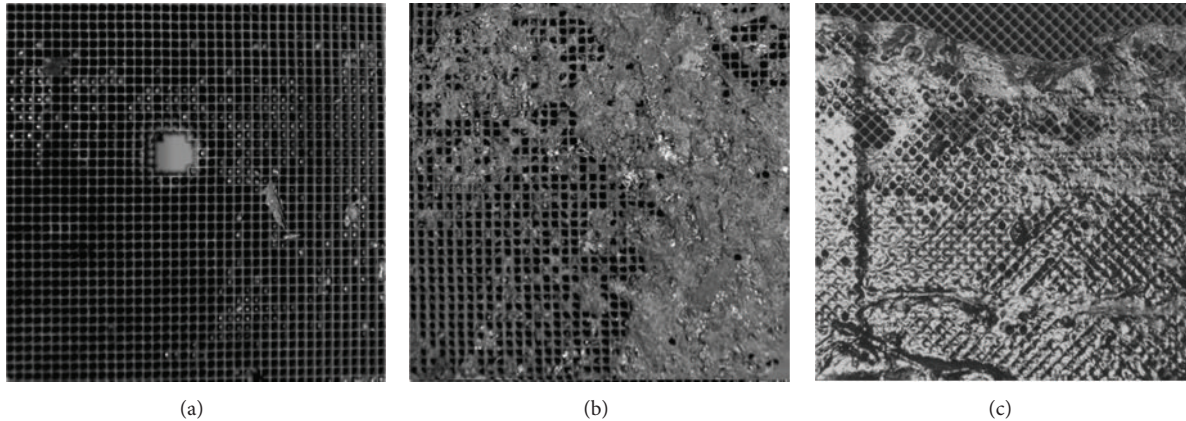


FIGURE 11: Front surface of catalyst carrier with remains of metal at outlets of capillaries: (a) four catalysts in channel, (b) two catalysts in channel, (c) one catalyst in channel.

results are consistent with the results of the numerical model presented in Figures 5–7. Vertical nonuniformity of metal distribution is the result of the three-dimensional character of the real process (that is not taken into account by the presented two-dimensional model), and imperfection of the used measurement method.

## 5. Conclusions

The experimentally verified numerical model of the catalyst infiltration by molten metal takes into account the most important phenomena present in the process—the magneto-hydrodynamic flow, the two-phase flow, and the flow through porous medium. The developed model enables the analysis of the process, impossible to realize using only experimental methods.

The research indicated that in case of too high number of catalysts in the channel (too small distances between them) the molten metal did not have enough momentum to overcome the capillary pressure and the flow resistance in the catalyst carrier. If the current of coil increased, the situation would be better but at the cost of increased energy consumption on a single catalyst. Caulking spaces between a catalyst and channel walls could increase the pressure difference between the inlet and outlet of capillaries, but in case of a real technological process of recycling catalysts of random geometry, such a method is very difficult to implement.

The numerical simulations and experimental verification were conducted on a small laboratory scale. However, in case of industrial scale and higher diameters of the stirrer channel, the influence of the distance between catalysts and the supply current on the degree of carriers infiltration by the molten metal will be the same.

## References

- [1] M. Benson, C. R. Bennett, J. E. Harry, M. K. Patel, and M. Cross, “The recovery mechanism of platinum group metals from catalytic converters in spent automotive exhaust systems,” *Resources, Conservation and Recycling*, vol. 31, no. 1, pp. 1–7, 2000.
- [2] T. N. Angelidis, “Development of a laboratory scale hydrometallurgical procedure for the recovery of Pt and Rh from spent automotive catalysts,” *Topics in Catalysis*, vol. 16-17, no. 1-4, pp. 419–423, 2001.
- [3] B.-S. Kim, J.-C. Lee, S.-P. Seo, Y.-K. Park, and H. Y. Sohn, “A process for extracting precious metals from spent printed circuit boards and automobile catalysts,” *JOM*, vol. 56, no. 12, pp. 55–58, 2004.
- [4] Y. Kayanuma, T. H. Okabe, and M. Maeda, “Metal vapor treatment for enhancing the dissolution of platinum group metals from automotive catalyst scrap,” *Metallurgical and Materials Transactions B*, vol. 35, no. 5, pp. 817–824, 2004.
- [5] A. Fornalczyk and M. Saternus, “Removal of platinum group metals from the used auto catalytic converter,” *Metallurgija*, vol. 48, no. 2, pp. 133–136, 2009.
- [6] A. Fornalczyk and M. Saternus, “Vapour treatment method against other pyro- and hydrometallurgical processes applied to recover platinum from used auto catalytic converters,” *Acta Metallurgica Sinica*, vol. 26, no. 3, pp. 247–256, 2013.
- [7] A. Fornalczyk and M. Saternus, “Removal of platinum group metals from the used auto catalytic converter,” *Metallurgija*, vol. 48, no. 2, pp. 133–136, 2009.
- [8] A. Fornalczyk, R. Przyłucki, M. Saternus, and S. Golak, “Analysis of using magneto-hydrodynamic pump for the platinum recovery from spent auto catalytic converters,” *Archives of Materials Science and Engineering*, vol. 58, no. 2, pp. 199–204, 2012.
- [9] A. Fornalczyk, S. Golak, and R. Przyłucki, “Analysis of electromagnetic and flow fields in the channel of a device used for precious metals leaching from auto catalytic converters,” *Przegląd Elektrotechniczny*, vol. 89, no. 3, pp. 57–60, 2013.
- [10] D. N. Tsinoglou, G. C. Koltsakis, D. K. Missirlis, and K. J. Yakinthos, “Transient modelling of flow distribution in automotive catalytic converters,” *Applied Mathematical Modelling*, vol. 28, no. 9, pp. 775–794, 2004.
- [11] Q. Su, L. Xie, S. Shuai, J. Wang, J. Song, and Z. Li, “Optimization of automotive catalytic converter by numerical modeling and simulation with detailed mechanism,” *Catalysis Today*, vol. 216, pp. 292–298, 2013.

- [12] C. Sajdak, S. Golak, and A. Kurek, "Electromagnetic stirring of liquid ingot core in the process of continuous casting of steel," *Przegląd Elektrotechniczny*, vol. 83, no. 3, pp. 67–71, 2007.
- [13] J. Barglik, D. Dołęga, and A. Smagór, "Coupled temperature electromagnetic flow fields in the electromagnetic stirrer with a rotating magnetic field," *Magneto hydrodynamics*, no. 4, pp. 387–392, 2010.
- [14] M. Ščepanskis, A. Jakovičs, and E. Baake, "Statistical analysis of the influence of forces on particles in EM driven recirculated turbulent flows," *Journal of Physics: Conference Series*, vol. 333, no. 1, Article ID 012015, 2011.
- [15] S. Golak and R. Przulucki, "Homogenization of electromagnetic force field during casting of functionally graded composites," *IEEE Transactions on Magnetics*, vol. 47, no. 12, pp. 4701–4706, 2011.
- [16] R. M. Andrews and A. Mortensen, "Lorentz force infiltration of fibrous preforms," *Metallurgical Transactions A*, vol. 22, no. 12, pp. 2903–2915, 1991.
- [17] M. Dyzia, A. J. Dolata, and J. Sleziona, "Preliminary analysis of aluminum matrix compositions for composites reinforcement with carbon fibers," *Steel Research International*, vol. 83, no. 10, pp. 981–987, 2012.
- [18] A. Boczkowska, P. Chabera, A. J. Dolata, M. Dyzia, and A. Ozieblo, "Porous ceramic-metal composites obtained by infiltration methods," *Metallurgija*, vol. 52, no. 3, pp. 345–348, 2013.
- [19] J. Xie, R. S. Amano, P. M. Mohan Das, and P. K. Rohatgi, "Transit simulation analysis for the pressure infiltration of aluminum melts into metal matrix components," in *ASME Summer Heat Transfer Conference*, pp. 213–220, July 2005.
- [20] B. Wang and K. M. Pillai, "Numerical simulation of pressure infiltration process for making metal matrix composites using dual-scale fabrics," *Metallurgical and Materials Transactions A*, 2013.
- [21] P. Karban, V. Kotlan, and I. Dolezel, "Numerical model of induction shrink fits in monolithic formulation," *IEEE Transactions on Magnetics*, vol. 48, no. 2, pp. 315–318, 2012.
- [22] S. Golak and R. Zagorski, "Model and optimization of electromagnetic filtration of metals," *Metallurgija*, vol. 52, no. 2, pp. 215–218, 2013.
- [23] B. E. Launder and D. B. Spalding, "The numerical computation of turbulent flows," *Computer Methods in Applied Mechanics and Engineering*, vol. 3, no. 2, pp. 269–289, 1974.
- [24] T. Merder, "Effect of casting flow rate on steel flow phenomena in tundish," *Metallurgija*, vol. 52, no. 2, pp. 161–164, 2013.
- [25] S. Eckert, A. Cramer, and G. Gerbeth, "Velocity measurement techniques for liquid metal flows," in *Magneto hydrodynamics*, vol. 80 of *Fluid Mechanics and Its Applications*, pp. 275–294, Springer, Dordrecht, The Netherlands, 2007.

## Research Article

# A Fractal Model for the Maximum Droplet Diameter in Gas-Liquid Mist Flow

Xiao-Hua Tan, Jian-Yi Liu, Xiao-Ping Li, Guang-Dong Zhang, and Chuan Tang

State Key Laboratory of Oil and Gas Reservoir Geology and Exploitation, Southwest Petroleum University, Chengdu 610500, China

Correspondence should be addressed to Xiao-Hua Tan; xiaohua-tan@163.com

Received 17 June 2013; Revised 18 September 2013; Accepted 22 September 2013

Academic Editor: Tirivanhu Chinyoka

Copyright © 2013 Xiao-Hua Tan et al. This is an open access article distributed under the Creative Commons Attribution License, which permits unrestricted use, distribution, and reproduction in any medium, provided the original work is properly cited.

Distribution characteristics of liquid droplet size are described using the fractal theory for liquid droplet size distribution in gas-liquid mist flow. Thereby, the fractal expression of the maximum droplet diameter is derived. The fractal model for maximum droplet diameter is obtained based on the internal relationship between maximum droplet diameter and the droplet fractal dimension, which is obtained by analyzing the balance between total droplet surface energy and total gas turbulent kinetic energy. Fractal model predictions of maximum droplet diameter agree with the experimental data. Maximum droplet diameter and droplet fractal dimension are both found to be related to the superficial velocity of gas and liquid. Maximum droplet diameter decreases with an increase in gas superficial velocity but increases with an increase in liquid superficial velocity. Droplet fractal dimension increases with an increase in gas superficial velocity but decreases with an increase in liquid superficial velocity. These are all consistent with the physical facts.

## 1. Introduction

Since the 1960s, coalescence and breakup phenomena of droplets in gas-liquid mist flow have obtained extensive attention in many physical and chemical process applications [1–3], such as distillation, gas absorption, and multiphase reactions. In nature, the tendency toward droplet coalescence or breakup depends on droplet size [4]. Numerous studies have shown that the main parameters influencing these phenomena are droplet size, system physical properties, and flow properties [5].

Numerous semiempirical models that predict droplet size in gas-liquid mist flow have been developed. According to Woodmansee and Hanratty [6], removal of microwaves on top of liquid film flow surges leads to atomization. Based on Woodmansee and Hanratty's [6] droplet generation assumptions, Tatterson et al. [7] derived a prediction model for droplet size. Then, an empirical binomial equation was introduced by Andreussi et al. [8] based on their own data, with the first term proportional to gas superficial velocity and the second term linked to the square root of film thickness. Ueda [9] measured size and droplet removal flow rate in

upward annular gas-liquid flow. He derived the rate of droplet movement between the liquid film and the gas core by considered droplet transference rates between the gas core and the liquid film. Lastly, Ueda proposed a mean diameter model for droplets under interface tension in gas flow by assuming a gamma-like size distribution for the gas core droplets. The empirical equation contained a single term, and droplet size was proportional to the gas velocity to the power of  $-0.34$ , which contrasted to most other equations having a power of  $-1.0$ . Sevik and Park [10] studied the assumption that the natural oscillation frequency of the liquid package is equal to the characteristic frequency of the disturbance. Under these conditions, droplets will break when resonance occurs. According to their results, Azzopardi et al. [11] derived an equation linking droplet size to the rupture of liquid packages in gas flow. Using a similar methodology, Lopes and Dukler [12] and Kocamustafaogullari et al. [13] used their own data to optimize this equation. Azzopardi et al. [14] developed a new laser optical technique to study annular flow where droplet size and axial and radial velocity are simultaneously measured and the flow conditions that droplet size distributions depend on are analyzed. Their equation, based on Tatterson et al.

[7] and Azzopardi et al. [11], deals with the influence of coalescence by defining a mean free path between collisions. This processing method is similar to the gas kinetic theory.

Shavit and Chigier [15] were the first to observe the existence of fractal characteristics during droplet separation and jet. This observation provided the basis for using fractal theory to describe droplet size distribution. Weixing et al. [16] studied the fractal characteristics associated with the distribution of droplet sizes in the atomization process. They measured the fractal dimensions using droplet-splitting simulations. The results of this experiment led to the creation of a droplet splitting model, which uses a uniformly distributed probability function. Based on Weixing et al. [16], Zhou and Yu [17] measured droplet size distribution data using a dual particle dynamic analyzer and proposed a multifractal model to describe droplet dissolution characteristics. Kolmogorov described the breakup of solid particles as a discrete random process. Apte et al. [18] adopted Kolmogorov's concept and established a stochastic subgrid model for large-eddy simulation of atomizing spray. Apte et al. showed that the atomization of droplets at high relative liquid-to-gas velocity was not affected by the initial droplet size in the framework of uncorrelated breakup events. According to the description of the droplet dissolution process proposed by Kolmogorov Gorokhovski and Saveliev [19] developed a droplet distribution model in the phase space of droplet position velocity by studying the breakup of droplets at the large Weber number. This numerical method can be used to stochastically model droplet production. According to the self-similarity of droplet breakup, Liu et al. [20] introduced a finite stochastic breakup model for air-blast atomizers, which is used to simulate the process of secondary atomization. Jiang et al. [21] researched the atomization process of the coaxial air-blast atomizer on the basis of the self-similarity of droplet breakup during secondary atomization. According to the breakup time study and the motion features of droplets in gas flow, they observed the factors that affect the Sauter mean diameter (SMD), which are the liquid/gas mass flux ratio, gas jet velocity, liquid jet velocity, and liquid droplet diameter.

In this paper, the distribution characteristics of mist flow droplet size are studied using a fractal mechanism. The fractal model of maximum droplet diameter is obtained by combining the analysis of the droplets total surface energy with that of gas flow total turbulent kinetic energy balance.

## 2. Model

**2.1. Distribution Characteristics of Liquid Droplet Size in Gas-Liquid Mist Flow.** Many researchers study the distribution characteristics of liquid droplet size using statistical methods. Results show that cross-sectional distribution characteristics of liquid droplet size have fractal features [15–17]. According to fractal geometry, distribution of the fractal accumulative droplet number,  $N$ , and droplet diameter submit to the following scale relationship [22, 23]:

$$N(L \geq \lambda) = \left( \frac{\lambda_{\max}}{\lambda} \right)^{D_f}, \quad (1)$$

where  $\lambda_{\max}$  is the maximum droplet diameter.  $D_f$  is the droplet fractal dimension,  $0 < D_f < 2$  in two-dimensional space, and  $0 < D_f < 3$  in three-dimensional space [24].

Solving the differential of (1), the liquid droplet number between  $\lambda$  to  $\lambda + d\lambda$  can be obtained [25]:

$$-dN = D_f \lambda_{\max}^{D_f} \lambda^{-(D_f+1)} d\lambda. \quad (2)$$

The negative variable in (2) indicates that liquid droplet number increases along with a decrease in droplet size [26, 27] and  $-dN > 0$ .

The cross-sectional area of gas-liquid mist flow,  $A$ , is expressed as

$$A = \frac{\pi D^2}{4}, \quad (3)$$

where  $D$  is the diameter of the cross-section.

In cross-section  $A$ , the area occupied by the droplets is

$$A_1 = - \int_{\lambda_{\min}}^{\lambda_{\max}} \frac{\pi \lambda^2}{4} dN = \frac{\pi D_f \lambda_{\max}^2}{4(2 - D_f)} \left[ 1 - \left( \frac{\lambda_{\min}}{\lambda_{\max}} \right)^{2-D_f} \right]. \quad (4)$$

Generally,  $0 < D_f < 2$  in two-dimensional space. In gas-liquid mist flow real situation,  $\lambda_{\min}/\lambda_{\max} < 10^{-6}$ , and  $D_f$  is greater than 0.5, so  $(\lambda_{\min}/\lambda_{\max})^{2-D_f} < 10^{-3}$ ; (4) can be simplified as

$$A_1 = \frac{\pi D_f \lambda_{\max}^2}{4(2 - D_f)}. \quad (5)$$

In cross-section  $A$ , the area occupied by gas is

$$A_g = A - A_1 = \frac{\pi D^2}{4} \left[ 1 - \frac{D_f \lambda_{\max}^2}{(2 - D_f) D^2} \right]. \quad (6)$$

In gas-liquid mist flow, the relationship between liquid velocity,  $v_l$ , and liquid superficial velocity,  $v_{sl}$ , is

$$v_{sl} = \frac{A_l}{A} v_l. \quad (7)$$

Substituting (3) and (5) into (7), liquid superficial velocity can be expressed as

$$v_{sl} = \frac{D_f v_l \lambda_{\max}^2}{(2 - D_f) D^2}. \quad (8)$$

It can be observed from (8) that  $D_f$  is proportional to cross-sectional droplet number. An increase in  $D_f$  indicates that the liquid carried by gas flow disperses into smaller liquid droplets (i.e., liquid coalesces into smaller liquid droplets). This conforms to the physical fact that  $\lambda_{\max}$  decreases along with an increase in  $D_f$ .

Liquid droplet velocity can be synchronously measured by phase Doppler anemometry (Azzopardi and Teixeira [28]) or Ronchi grating technology (Fore and Dukler [29]).

The results of these two methodologies are similar: when gas and liquid mix sufficiently, liquid velocity approximately equals that of gas in gas-liquid mist flow:

$$v_l = v_g. \quad (9)$$

According to the definition of velocity and superficial velocity of gas and liquid, the relationship between gas and liquid superficial velocity can be obtained from (9):

$$v_{sg} = \frac{A_g}{A_l} v_{sl}. \quad (10)$$

Substituting (5) and (6) into (10), the maximum droplet diameter on the basis of mist flow characteristics can be solved:

$$\lambda_{\max} = \left[ \frac{(2 - D_f) D^2 v_{sl}}{D_f (v_{sg} + v_{sl})} \right]^{1/2}. \quad (11)$$

As the maximum droplet diameter,  $\lambda_{\max}$ , and the droplet fractal dimension,  $D_f$ , in (11) are both unknown variables, they cannot be directly solved by gas superficial velocity,  $v_{sg}$ , and liquid superficial velocity,  $v_{sl}$ . The internal relationship between the maximum droplet diameter,  $\lambda_{\max}$ , and the droplet fractal dimension,  $D_f$ , can be found by analyzing the balance relationship between the surface energy of the dispersed phase and the turbulent kinetic energy of the continuous phase. Therefore, the subsidiary condition for solving (11) is obtained.

**2.2. Droplet Total Surface Energy and Total Gas Turbulent Kinetic Energy Balance Analysis.** The droplet breakup model is applied to describe the cause of mist flow formation. According to the balance relationship between the surface energy of the dispersed phase and the turbulent kinetic energy of the continuous phase, Hinze [30] theoretically derived the maximum stability diameter of the dispersed phase in continuous fluid. Similar phenomenon also exists in gas-liquid mist flow. The maximum stability diameter of a droplet can be derived with the aid of the droplet dispersion model.

According to Adamson [31], free surface energy per unit area equals the interfacial tension per unit area in the gas-liquid phase; that is,

$$e_s = \sigma. \quad (12)$$

The total free surface energy of dispersed droplets in continuous gas flow is

$$E_S = -v_l \sigma \int_{\lambda_{\min}}^{\lambda_{\max}} \pi \lambda dN = \frac{\pi D_f v_l \sigma \lambda_{\max}}{(1 - D_f)}. \quad (13)$$

It can be seen that the value of the droplet fractal dimension is  $0 < D_f < 1$ ; when the total free surface energy of the dispersed droplets is greater than 0,  $E_S > 0$ . An increase in  $D_f$  indicates that cross-sectional droplet distribution, contact area between the gas and liquid phase,

and the value of  $E_S$  are large. In limiting cases, when  $D_f$  equals 0, cross-sectional droplets aggregate which leads to an extremely small contact area and  $E_S$  tends towards 0; when  $D_f$  equals 1, tiny liquid droplets dispersed on the cross-section,  $E_S$ , tend toward infinity. An increase in the maximum droplet diameter,  $\lambda_{\max}$ , indicates an increase in the contact area between the gas and liquid phases. Therefore, the rule that  $E_S$  increases with an increase in  $\lambda_{\max}$  and  $D_f$  conforms to the physical definition of free surface energy.

By substituting (8) into (13), the relationship between total free surface energy of the dispersed droplets and liquid superficial velocity can be obtained:

$$E_S = \frac{\pi \sigma (2 - D_f) D^2}{(1 - D_f) \lambda_{\max}} v_{sl}. \quad (14)$$

According to White [32] and Zhang et al. [33], gas flow's turbulent kinetic energy per unit volume can be expressed as

$$e_T = \frac{3}{2} \rho_g \overline{v_r'^2}, \quad (15)$$

where  $\rho_g$  is gas density and  $v_r'$  is the radial velocity of gas.

Thus, the total turbulent kinetic energy of the continuous gas phase can be obtained:

$$E_T = \frac{3}{2} \rho_g \overline{v_r'^2} A v_{sg}. \quad (16)$$

According to Taitel et al. [34] and Chen et al. [35], gas radial velocity; approximately equals friction velocity; that is,

$$\overline{v_r'^2}^{1/2} = v_{sg} \left( \frac{f_{sg}}{2} \right)^{1/2}. \quad (17)$$

The friction factor  $f_{sg}$  caused by gas flow is expressed as

$$\frac{1}{\sqrt{f_{sg}}} = 1.14 - 2 \lg \left( \frac{e}{D} + \frac{21.25}{\text{Re}^{0.9}} \right), \quad (18)$$

where  $e$  is the absolute roughness,  $e = 1.6 \times 10^{-6}$  m. Re is the Reynolds number.

Substituting (17) into (16), the total turbulent kinetic energy of gas-liquid mist flow can be expressed as

$$E_T = \frac{3}{4} f_{sg} \rho_g A v_{sg}^3. \quad (19)$$

In high-speed gas flow, total droplet surface energy is equal to the total turbulent kinetic energy of the gas phase [36]:

$$E_S = E_T. \quad (20)$$

Substituting (14) and (19) into (20), maximum droplet diameter based on the droplet dispersion model can be obtained:

$$\lambda_{\max} = \frac{16 \sigma (2 - D_f) v_{sl}}{3 f_{sg} \rho_g (1 - D_f) v_{sg}^3}. \quad (21)$$

It can be seen from (21) that the maximum droplet diameter increases with a decrease in gas superficial velocity and an increase in liquid superficial velocity. This rule is consistent with physical reality.

**2.3. Fractal Model of Maximum Liquid Droplet Diameter.** The droplet size distribution rule describes droplet distribution in gas-liquid mist flow. Droplet distribution is controlled by the balance relationship between total droplet surface energy and total gas turbulent kinetic energy. Therefore, the droplet fractal dimension under gas-liquid mist flow conditions can be calculated by substituting (21) into (11):

$$AD_f^2 + BD_f + C = 0, \quad (22)$$

where

$$\begin{aligned} A &= (3Df_{sg}\rho_g v_{sg}^3)^2 + 256v_{sg}v_{sl}\sigma^2 + 256(v_{sl}\sigma)^2, \\ B &= -2 \left[ (3Df_{sg}\rho_g v_{sg}^3)^2 + 256v_{sg}v_{sl}\sigma^2 + 256(v_{sl}\sigma)^2 \right], \\ C &= (3Df_{sg}\rho_g v_{sg}^3)^2. \end{aligned} \quad (23)$$

Equation (22) has one solution between 0 and 1. Therefore, the liquid droplet fractal dimension in gas-liquid mist flow can be expressed as

$$D_f = \frac{-B - \sqrt{B^2 - 4AC}}{2A}. \quad (24)$$

By combining (11) with (24), the fractal expression of maximum droplet diameter under gas-liquid mist flow conditions can be obtained:

$$\begin{aligned} \lambda_{\max} &= \left[ \frac{(2 - D_f) D^2 v_{sl}}{D_f (v_{sg} + v_{sl})} \right]^{1/2}, \\ D_f &= \frac{-B - \sqrt{B^2 - 4AC}}{2A}. \end{aligned} \quad (25)$$

Equation (25) is the analytical solution of the fractal model of maximum droplet diameter in gas-liquid mist flow. The maximum droplet diameter,  $\lambda_{\max}$ , and the droplet fractal dimension,  $D_f$ , can be simultaneously solved using gas superficial velocity,  $v_{sg}$ , and liquid superficial velocity,  $v_{sl}$ . The model proposed in this paper contains no empirical constants, and every parameter has clear physical meaning. However, other parameters are required to identify  $\lambda_{\max}$  and  $D_f$ , such as the cross-sectional diameter of gas-liquid mist flow,  $D$ , gas density,  $\rho_g$ , and interface tension,  $\sigma$ .

### 3. Results and Discussion

Figure 1 shows a comparison between the proposed model's predictions and experimental results measured by Fore and Dukler [29]. Agreement between the fractal model predictions and the experimental results of Fore and Dukler in different liquid viscosity and superficial velocity conditions is obtained. Results suggest that the proposed gas-liquid mist flow maximum liquid droplet diameter model is reliable.

Figure 2 shows the relationships between maximum droplet diameter,  $\lambda_{\max}$ , droplet fractal dimension,  $D_f$ , and

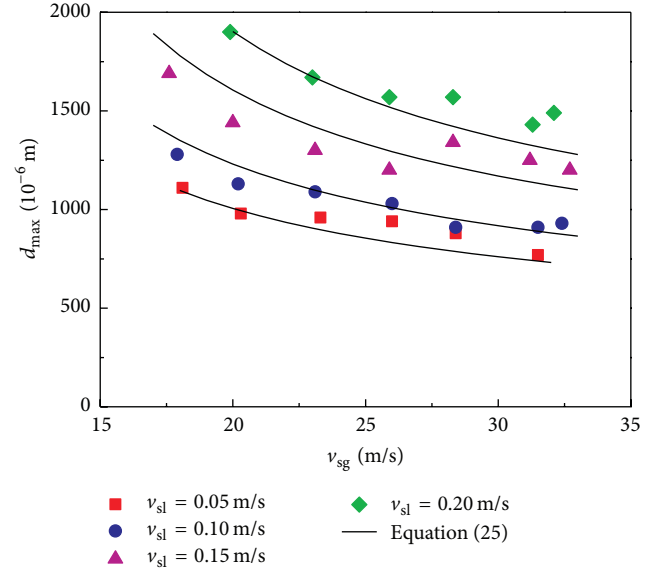


FIGURE 1: Comparison between the proposed model predictions and experimental results ( $D = 0.15$  m,  $\sigma = 0.072$  N/m, and  $\mu_l = 1.05 \times 10^{-3}$  Pa·s).

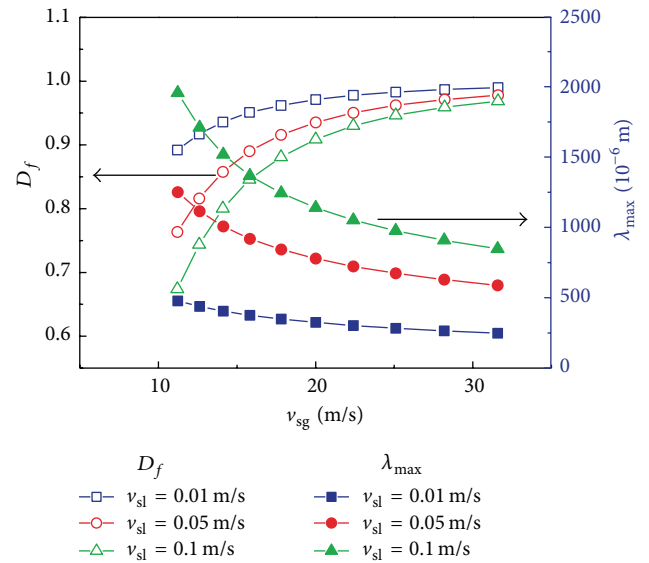


FIGURE 2: Maximum droplet diameter and droplet fractal dimension versus  $v_{sl}$  at different  $v_{sg}$  for gas-liquid mist flow.

gas superficial velocity,  $v_{sg}$ , calculated by the present model. It can be seen that  $\lambda_{\max}$  decreases with an increase in  $v_{sg}$ . Inversely,  $D_f$  increases with an increase in  $v_{sg}$ . As  $v_{sg}$  increases, the turbulent kinetic energy of the gas in the gas-liquid mist flow increases, which forces the original droplets to disperse into smaller droplets, making  $\lambda_{\max}$  decrease and  $D_f$  increase. These all conform to the physical facts.

Figure 3 shows the relationships between maximum droplet diameter,  $\lambda_{\max}$ , droplet fractal dimension,  $D_f$ , and liquid superficial velocity,  $v_{sl}$ , calculated by the present model.  $\lambda_{\max}$  increases with an increase in  $v_{sl}$ . Inversely,  $D_f$  decreases

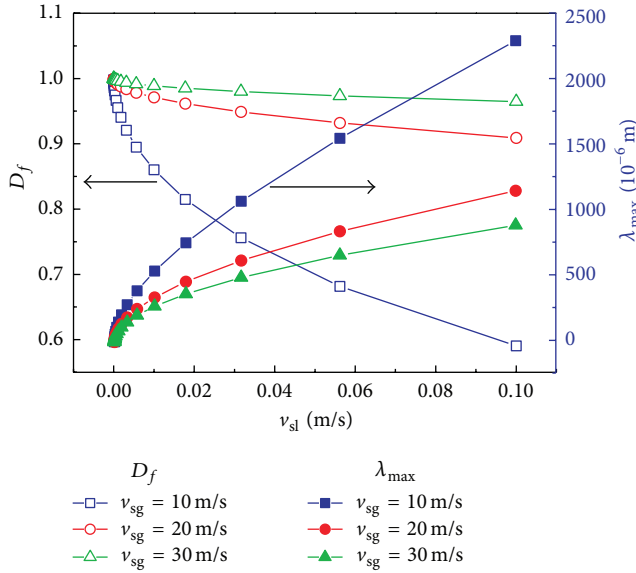


FIGURE 3: Maximum droplet diameter and droplet fractal dimension versus  $v_{sl}$  at different  $v_{sl}$  for gas-liquid flow.

with an increase in  $v_{sl}$ . As  $v_{sl}$  increases, surface energy of the liquid in the gas-liquid mist flow increases, which forces the original droplets to coalesce into smaller droplets, making  $\lambda_{max}$  increase and  $D_f$  decrease. These all conform to the physical facts.

#### 4. Conclusion

- (1) Based on liquid droplet fractal size distribution properties in gas-liquid mist flow, we describe the characteristics of droplet distribution under mist flow conditions. The fractal expression of maximum droplet diameter is derived and the internal relationship between maximum droplet diameter and droplet fractal dimension is confirmed by analyzing the balance relationship between total droplet surface energy and total gas turbulent kinetic energy. Therefore, the fractal model of the maximum droplet diameter in gas-liquid mist flow is derived. Fractal expressions of cross-sectional area occupied by gas or liquid and the superficial velocity of gas and liquid are obtained. Every parameter proposed in this paper has clear physical meaning.
- (2) Agreement between predictions of the proposed fractal model and experimental measurements is obtained. Results verify the reliability of the proposed model.
- (3) The influence of gas and liquid superficial velocity on maximum liquid droplet diameter,  $\lambda_{max}$ , and liquid droplet fractal dimension,  $D_f$ , is analyzed.  $\lambda_{max}$  increases with a decrease in  $v_{sg}$  and with an increase in  $v_{sl}$ .  $D_f$  increases with an increase in  $v_{sg}$  and with a decrease in  $v_{sl}$ . These coincide with the physical facts.

#### Nomenclature

$A$ :	Cross-sectional area of a conduit, $m^2$
$A_g$ :	Cross-sectional area occupied by gas, $m^2$
$A_l$ :	Cross-sectional area occupied by liquid, $m^2$
$D$ :	Conduit diameter, m
$D_f$ :	Droplet fractal dimensions
$E_s$ :	Total surface free energy, W
$E_T$ :	Total turbulent kinetic energy, W
$e$ :	Absolute pipe wall roughness, m
$e_s$ :	Surface free energy per unit volume, $J/m^2$
$e_T$ :	Turbulent kinetic energy per unit area, $J/m^3$
$f_{sg}$ :	Friction factor at gas superficial velocity
$N$ :	Fractal accumulative droplet number
Re:	Reynolds number
$v_g$ :	Gas velocity, m/s
$v_l$ :	Liquid velocity, m/s
$v_{sg}$ :	Gas superficial velocity, m/s
$v_{sl}$ :	Liquid superficial velocity, m/s
$v'_r$ :	Radial velocity, m/s
$\lambda$ :	Droplet diameter, m
$\lambda_{max}$ :	Maximum droplet diameter, m
$\lambda_{min}$ :	Minimum droplet diameter, m
$\rho_g$ :	Gas density, $kg/m^3$
$\rho_l$ :	Liquid density, $kg/m^3$
$\sigma$ :	Interfacial tension, N/m.

#### Subscripts

$g$ :	Gas phase
$l$ :	Liquid phase
$s$ :	Superficial
$T$ :	Turbulent.

#### Acknowledgments

The authors are grateful for financial support from the National Science Fund for Distinguished Young Scholars of China (Grant no. 51125019) and Science and Technology Innovation Fund of Southwest Petroleum University (Grant no. GIFSB0701).

#### References

- [1] G. T. Vladislavjević, I. Kobayashi, and M. Nakajima, "Effect of dispersed phase viscosity on maximum droplet generation frequency in microchannel emulsification using asymmetric straight-through channels," *Microfluidics and Nanofluidics*, vol. 10, no. 6, pp. 1199–1209, 2011.
- [2] T. S. H. Leong, T. J. Wooster, S. E. Kentish, and M. Ashokkumar, "Minimising oil droplet size using ultrasonic emulsification," *Ultrasonics Sonochemistry*, vol. 16, no. 6, pp. 721–727, 2009.
- [3] N. Vankova, S. Tcholakova, N. D. Denkov, I. B. Ivanov, V. D. Vulchev, and T. Danner, "Emulsification in turbulent flow. I. Mean and maximum drop diameters in inertial and viscous regimes," *Journal of Colloid and Interface Science*, vol. 312, no. 2, pp. 363–380, 2007.

- [4] J.-L. Liu, R. Xia, B.-W. Li, and X.-Q. Feng, "Directional motion of droplets in a conical tube or on a conical fibre," *Chinese Physics Letters*, vol. 24, no. 11, pp. 3210–3213, 2007.
- [5] X.-Y. Peng, J. Zhang, T.-J. Liang et al., "Double jet emission of hot electrons from a micro-droplet spray," *Chinese Physics Letters*, vol. 21, no. 4, pp. 693–696, 2004.
- [6] D. E. Woodmansee and T. J. Hanratty, "Mechanism for the removal of droplets from a liquid surface by a parallel air flow," *Chemical Engineering Science*, vol. 24, no. 2, pp. 299–307, 1969.
- [7] D. F. Tatterson, J. C. Dallman, and T. J. Hanratty, "Drop sizes in annular gas-liquid flows," *AIChE Journal*, vol. 23, no. 1, pp. 68–76, 1977.
- [8] P. Andreussi, G. Romano, and S. Zanelli, "Drop size distribution in annular mist flow," in *Proceedings of the 1st Conference on Liquid Atomisation and Spray Systems*, Tokyo, Japan, 1978.
- [9] T. Ueda, "Entrainment rate and size of entrained droplets in annular two-phase flow," *Bulletin of the JSME*, vol. 22, no. 171, pp. 1258–1265, 1979.
- [10] M. Sevik and S. H. Park, "The splitting of drops and bubbles by turbulent fluid flow," *Journal of Fluids Engineering*, vol. 95, no. 1, pp. 53–60, 1973.
- [11] B. Azzopardi, G. Freeman, and D. King, "Drop sizes and deposition in annular two-phase flow," UKAEA Report AERE-R9634, 1980.
- [12] J. C. B. Lopes and A. E. Dukler, *Droplet Sizes, Dynamics and Deposition in Vertical Annular Flow*, 1985.
- [13] G. Kocamustafaogullari, S. Smits, J. Razi, and W. Huang, "Droplet size modelling in annular flow," in *Proceedings of the 6th International Topical Meeting on Nuclear Reactor Thermal Hydraulics*, 1993.
- [14] B. J. Azzopardi, A. Pearcey, and D. M. Jepson, "Drop size measurements for annular two-phase flow in a 20 mm diameter vertical tube," *Experiments in Fluids*, vol. 11, no. 2-3, pp. 191–197, 1991.
- [15] U. Shavit and N. Chigier, "fractal dimensions of liquid jet interface under breakup," *Atomization and Sprays*, vol. 5, no. 6, pp. 525–543, 1995.
- [16] Z. Weixing, Z. Tiejun, W. Tao, and Y. Zunhong, "Application of fractal geometry to atomization process," *Chemical Engineering Journal*, vol. 78, no. 2-3, pp. 193–197, 2000.
- [17] W.-X. Zhou and Z.-H. Yu, "Multifractality of drop breakup in the air-blast nozzle atomization process," *Physical Review E*, vol. 63, no. 1, Article ID 016302, 6 pages, 2001.
- [18] S. V. Apte, M. Gorokhovski, and P. Moin, "LES of atomizing spray with stochastic modeling of secondary breakup," *International Journal of Multiphase Flow*, vol. 29, no. 9, pp. 1503–1522, 2003.
- [19] M. A. Gorokhovski and V. L. Saveliev, "Analyses of Kolmogorov's model of breakup and its application into Lagrangian computation of liquid sprays under air-blast atomization," *Physics of Fluids*, vol. 15, no. 1, pp. 184–192, 2003.
- [20] H.-F. Liu, X. Gong, W.-F. Li, F.-C. Wang, and Z.-H. Yu, "Prediction of droplet size distribution in sprays of prefilming air-blast atomizers," *Chemical Engineering Science*, vol. 61, no. 6, pp. 1741–1747, 2006.
- [21] D.-J. Jiang, H.-F. Liu, W.-F. Li, J.-L. Xu, F.-C. Wang, and X. Gong, "Modeling atomization of a round water jet by a high-speed annular air jet based on the self-similarity of droplet breakup," *Chemical Engineering Research and Design*, vol. 90, no. 2, pp. 185–192, 2012.
- [22] M.-J. Yun, B.-M. Yu, P. Xu, and J.-C. Cai, "Fractal analysis of power-law fluid in a single capillary," *Chinese Physics Letters*, vol. 25, no. 2, pp. 616–619, 2008.
- [23] Y. Mei-Juan and Z. Wei, "Fractal analysis of Robertson-Stiff fluid flow in porous media," *Chinese Physics Letters*, vol. 29, no. 6, Article ID 064706, 2012.
- [24] M. Yun, B. Yu, and J. Cai, "Analysis of seepage characters in fractal porous media," *International Journal of Heat and Mass Transfer*, vol. 52, no. 13-14, pp. 3272–3278, 2009.
- [25] Y. Mei-Juan, Z. Wei, L. Yun-Bao, and L. Yu, "Fractal analysis of Herschel-Bulkley fluid flow in a capillary," *Acta Physica Sinica*, vol. 61, no. 16, Article ID 164701, 2012.
- [26] M. Yun, B. Yu, and J. Cai, "A fractal model for the starting pressure gradient for Bingham fluids in porous media," *International Journal of Heat and Mass Transfer*, vol. 51, no. 5-6, pp. 1402–1408, 2008.
- [27] M.-J. Yuan, B.-M. Yu, W. Zheng, and J. Yuan, "Fractal analysis of Casson fluid flow in porous media," *Acta Physica Sinica*, vol. 60, no. 2, Article ID 024703, 2011.
- [28] B. J. Azzopardi and J. C. F. Teixeira, "Detailed measurements of vertical annular two-phase flow—part I: drop velocities and sizes," *Journal of Fluids Engineering*, vol. 116, no. 4, pp. 792–795, 1994.
- [29] L. B. Fore and A. E. Dukler, "The distribution of drop size and velocity in gas-liquid annular flow," *International Journal of Multiphase Flow*, vol. 21, no. 2, pp. 137–149, 1995.
- [30] J. O. Hinze, "Fundamentals of the hydrodynamic mechanism of splitting in dispersion processes," *AIChE Journal*, vol. 1, no. 3, pp. 289–295, 1955.
- [31] A. W. Adamson, *Physical Chemistry of Surfaces*, John Wiley & Sons, New York, NY, USA, 5th edition, 1990.
- [32] F. M. White, *Viscous Fluid Flow*, McGraw-Hill, New York, NY, USA, 2nd edition, 1991.
- [33] H.-Q. Zhang, W. Qian, C. Sarica, and J. P. Brill, "A unified mechanistic model for slug liquid holdup and transition between slug and dispersed bubble flows," *International Journal of Multiphase Flow*, vol. 29, no. 1, pp. 97–107, 2003.
- [34] Y. Taitel, D. Bornea, and A. E. Dukler, "Modelling flow pattern transitions for steady upward gas-liquid flow in vertical tubes," *AIChE Journal*, vol. 26, no. 3, pp. 345–354, 1980.
- [35] X. T. Chen, X. D. Cai, and J. P. Brill, "A general model for transition to dispersed bubble flow," *Chemical Engineering Science*, vol. 52, no. 23, pp. 4373–4380, 1997.
- [36] X.-H. Tan, X.-P. Li, and J.-Y. Liu, "Model of continuous liquid removal from gas wells by droplet diameter estimation," *Journal of Natural Gas Science and Engineering*, vol. 15, pp. 8–13, 2013.

## Research Article

# Framework for the Shape Optimization of Aerodynamic Profiles Using Genetic Algorithms

**D. López, C. Angulo, I. Fernández de Bustos, and V. García**

*Department of Mechanical Engineering, University of the Basque Country, UPV/EHU, Alameda Urquijo s/n, 48013 Bilbao, Spain*

Correspondence should be addressed to C. Angulo; [carlos.angulo@ehu.es](mailto:carlos.angulo@ehu.es)

Received 26 July 2013; Revised 9 September 2013; Accepted 10 September 2013

Academic Editor: Waqar Khan

Copyright © 2013 D. López et al. This is an open access article distributed under the Creative Commons Attribution License, which permits unrestricted use, distribution, and reproduction in any medium, provided the original work is properly cited.

This study developed a framework for the shape optimization of aerodynamics profiles using computational fluid dynamics (CFD) and genetic algorithms. A genetic algorithm code and a commercial CFD code were integrated to develop a CFD shape optimization tool. The results obtained demonstrated the effectiveness of the developed tool. The shape optimization of airfoils was studied using different strategies to demonstrate the capacity of this tool with different GA parameter combinations.

## 1. Introduction

Most optimization techniques developed for computational fluid dynamics (CFD) analysis in the last two decades have focused on design problems in aerospace, aeronautic, and automotive applications. Developments in the fields of optimization techniques and turbulence models have facilitated the solution of more realistic aerodynamic design problems by computer simulation.

In recent decades, advances in hardware have allowed a considerable progress in flow prediction using Direct Numerical Simulation (DNS) and Large Eddy Simulation (LES) methods, which are mainly used in research. This constitutes a platform for understanding the physics of flow and the development of better Reynolds Averaged Navier-Stokes (RANS) turbulence models. Recently, some insight has been gained in the understanding of the physical mechanisms of transition from laminar to turbulent flow [1, 2], this enables important advance in transition prediction in the field of RANS models [3–6]. However, there is still an inability to accurately predict flow separation, which also depends on appropriate transition prediction.

The progress in flow prediction has permitted the development of aerodynamic shape optimization towards a practical and realistic design tool [7, 8]. Optimization methods can be classified into two categories: global search methods, which are generally stochastic, for example, genetic algorithms (GA) that explore the entire search space; and local

search methods, which are generally deterministic, including those based on gradient calculations or their approximations.

Global methods must perform a vast number of evaluations, whereas local methods are less expensive but they tend to become trapped in local extrema. GAs have demonstrated their robustness to avoid local extrema and numerical noise in aerodynamic optimization [9–12], as well as their validity in problems with constraints [13, 14]. Although GAs do not guarantee obtaining the global optimum, they constitute reliable tools to find a better design [15]. GAs are explorative methods; that is, they analyze many possible profile shapes. This is not a problem because every shape with a bad verification according to the evaluation function will be assigned a low aptitude value.

A shape optimization system was developed for fluid dynamic problems, which used the genetic code known as Oriented to Mechanical Engineering Genetic Algorithm (OMEGA), which is based on David Levine's PGA Pack Library [16]. This method has been applied to the optimization of bidimensional aerodynamic profiles with geometric constraints. The evaluation function analyzes the flow using the Fluent commercial code. A study was carried out to obtain efficient combinations of the basic GA parameters.

## 2. Problem Definition

A high Reynolds number subsonic flow optimization problem is considered. Two different fitness functions are used

to optimize two different aerodynamic features for a two-dimensional airfoil, which is subjected to constraints on its geometry to guarantee a threshold structural strength. The first function to maximize is  $c_l/c_d$ , the second is to minimize  $c_d$  for a given  $c_l$  value.

Advances in transition prediction [3, 4] have condensed empirical models such as the empirical model of Menter et al. [5] or the phenomenological model of Walters and Cokljat [6]. These models are designed to switch the turbulence, depending only on local variables, that is, those defined at each point, which reduces the computational cost and facilitates the implementation of CFD codes, while the effects of the models on the flow are constrained to the transition region. In this study, the transition model of Walters and Cokljat [6] was used because it has proven its ability to predict transitional flow behavior in flows around airfoils versus current generation RANS-based turbulence models. This model is based on a simple two-equation  $k-\omega$  turbulence model [17] and a third equation is added to account for the physical effects of natural [18] and bypass [2] mechanisms of transition. Natural transition occurs for values of freestream turbulence intensity below 1%, while bypass transition happens above this value.

**2.1. Governing Equations.** The mathematical model used in this study is based on the RANS system of differential equations for incompressible flow. The governing equations for the steady mean flow are expressed as follows.

Conservation of mass, consider

$$\frac{\partial U_i}{\partial x_i} = 0, \quad (1)$$

where the vectors  $U_i$  and  $x_i$  are the average velocity and position, respectively.

Conservation of momentum, consider

$$\rho U_j \frac{\partial U_i}{\partial x_j} = \frac{\partial}{\partial x_j} (-P\delta_{ij} + 2\mu S_{ij} - \overline{\rho u_i u_j}), \quad (2)$$

where  $\rho$  is air density,  $P$  is the average pressure,  $S_{ij}$  is the mean flow strain rate tensor,  $\mu$  is the molecular viscosity, and  $\delta_{ij} = 1$  for  $i = j$ ; otherwise,  $\delta_{ij} = 0$ . Here,  $u_i$  is the velocity fluctuation, and the term  $-\overline{\rho u_i u_j}$  is the Reynolds stress tensor, where the overline denotes average.

The  $k-k_j-\omega$  turbulence model [6] was used in this study. It introduces the anisotropic component of the Reynolds stress tensor through the Boussinesq modeling hypothesis as follows:

$$-\overline{\rho u_i u_j} + \frac{1}{3} \overline{\rho u_k u_k} \delta_{ij} = 2\mu_t S_{ij}, \quad (3)$$

where  $\mu_t$  is the turbulent viscosity. The effects of transition to turbulence and turbulence itself are approximated by three additional transport equations and influence the mean flow through the value of the turbulent viscosity. This is a carefully defined function that considers those effects.

**2.2. Simulation.** All the simulations in the optimization runs presented in this paper were performed using the Fluent

solver based on finite volume method. A second order upwind discretization scheme was used. The boundary conditions applied on the computational fluid domain can be seen in Figure 2. A constant velocity profile for the inlet semicircumference along with a turbulence intensity of 0.93%, and a constant pressure condition for the outlet semicircumference were imposed. The no slip boundary condition was imposed at the airfoil wall. All the meshes were constructed with a first cell  $y+$  value around the unity. The same type of meshes were used for known NACA airfoils yielding errors around 25% and 5%, respectively, for the drag and lift efforts. The authors have checked that a higher density in the normal direction to the wall in the boundary layer can halve the error in both efforts, although this increases the CPU time per calculation.

**2.2.1. Parameterization.** To ensure a successful optimization process, the search space must incorporate as much geometric flexibility as possible with as few design variables as possible. In this sense, Bezier curves provide soft and flexible shapes if the design variable intervals are defined appropriately. The upper and lower airfoil curves, extrados and intrados, are each defined by a Bezier polygon with five vertices. The design variables used are the vertical positions of the three intermediate Bezier polygon vertices, as shown in Figure 1, and their ranges of definition are shown on the right.

**2.2.2. Meshing Method.** During aerodynamic shape optimization in search spaces with high geometric flexibility, the design variables are allowed to vary in wide ranges, but when GAs are used, the geometries vary drastically from one evaluation to the next, so the reliability of the meshing method is a key issue. A suitable meshing method for CFD analysis in GA optimizations must be robust and accurate. The capability to mesh every geometry in the search space is necessary, but the meshes also have to be well shaped in the critical flow zones to provide accurate results. By contrast, GAs evaluate massive populations among a large number of generations, thereby incurring a huge overall cost per execution. Thus, the meshing method used in this study was designed to accomplish three objectives: the robustness of the mesh generation process, the accuracy of the meshes, and an affordable mesh cost.

Using this framework, a reliable meshing procedure for GA optimization problems was developed [19]. Instead of deforming the previous grid, a new mesh is reconstructed by dividing the domain into mesh blocks, which vary according to the geometry of the profile. However, since the advent of more precise RANS turbulence models, several modifications have been included in this procedure to obtain meshes that are capable of predicting flows more realistically. It is important for the CFD analysis to calculate the transition points at the extrados and intrados of the airfoil where the boundary layer turns from laminar to turbulent. If a completely turbulent boundary layer is calculated (like  $k-\epsilon$  turbulence models) certain flow characteristics never occur in the simulation. Laminar separation bubble and the

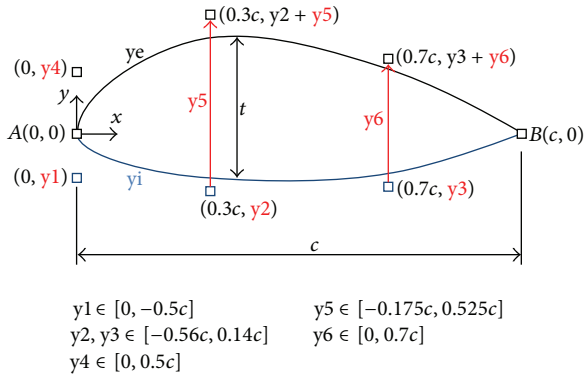


FIGURE 1: Design variables used to define the profile and their ranges.

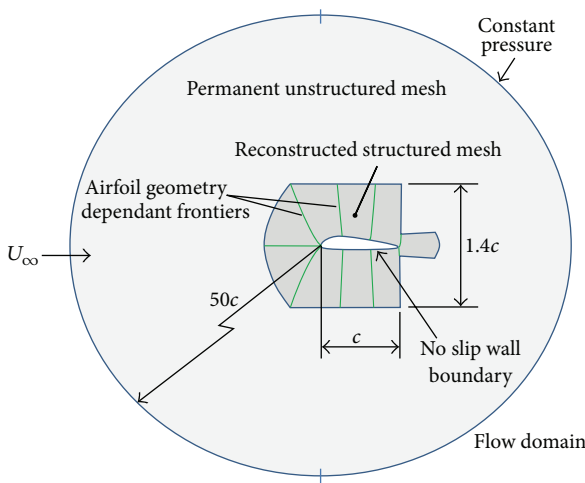


FIGURE 2: Flow domain for CFD analysis, type of boundary conditions and the structure of the mesh blocks.

associated change in pressure distribution are suppressed, and also predicted skin friction distribution and lift and drag values differ significantly. Moreover, the overall separation behavior is different.

As noted above, the new RANS transition models have facilitated the inclusion of transition predictions in CFD analysis in shape optimization. The correct use of these models requires very fine meshes in the wall region inside the boundary layer, with  $y^+$  values around the unity, so the number of cells across the boundary layer height and along the wall has increased greatly. As a secondary effect, this has generated an excessive number of transverse (to the flow) mesh lines in the outer region of the boundary layer, which is reduced by applying several layers of special-shaped cells that join two mesh lines in the transverse direction within the nearby boundary layer edge.

To minimize the shape distortion of nearby wall cells, the mesh block surrounding each wall was divided into three parts by tracing two new transverse block frontiers that emerge from the wall in a direction approximately perpendicular to it, as shown in Figure 2. In this manner, the direction of the surrounding transverse mesh lines is more constrained in the same way.

Given that the leading part of the airfoil is where the maximum slope variations are allowed (see Figure 1), cell shape control is increased in this region. Thus, the division of the wall surrounding mesh block is not divided in three equal ranges along the  $x$  direction, but instead by cutting at distances  $0.2c$  and  $0.66c$  from the leading edge. Here,  $c$  denotes the chord length of the airfoil.

Three transition cell layers were used in the second and third blocks, which reduced the mesh line density by eight. However, the flexibility of the geometry in the first part of the airfoil led to the possibility of excessively distorted cells in the third transition layer, the most exterior layer of the leading mesh block. To avoid this problem, a transition cell layer was eliminated in this block, which caused a relative increase in the mesh density in the outer area, as shown in Figure 3.

Unstructured meshes were used to reduce the mesh cost in the mesh blocks situated farther from the wall, where the flow variations are very small. This type of mesh permits a faster increase in the cell size in an outward direction. Thus, the overall mesh cost was reduced greatly while maintaining the accuracy (see Figures 2 and 3).

Structured mesh blocks were used in the airfoil surrounding the mesh blocks to guarantee the robustness of the grid generation process. These mesh blocks were regenerated for each new airfoil using the transfinite interpolation technique [20], which is a reliable technique whenever the curvilinear polygon defining the block is traced correctly and the cell length distribution along these curve-edges is adequate. Furthermore, transfinite interpolation permits highly anisotropic cell shapes (large aspect ratios) in the wall region of the boundary layer. These shapes facilitate a large reduction in the number of cells along the wall compared with isotropic shapes, because the flow gradients are several orders of magnitude smaller in the parallel direction than in the normal direction to the wall.

The block boundaries starting from the wall were designed according to the slope of the wall in the same way as a previous study [19], but the boundaries opposite to the wall are now straight and independent of the airfoil. As the family of the mesh lines “parallel” to the flow direction is calculated by linear interpolation between the wall and its opposite straight frontier, these mesh lines become more similar to the wall as one moves towards it. Now also all of the mesh blocks not adjacent to the airfoil become independent of its shape, and so they do not need to be reconstructed for each new airfoil.

These mesh blocks (except the wake region that had anisotropic cell shapes) were meshed with unstructured meshes using a mobile front technique [20], which can fail at the final stage of the meshing process. Then, to ensure robustness, the outer blocks of the domain were meshed before the start of the optimization process and they were kept permanent for each airfoil to avoid the possibility of failure when meshing an airfoil. This measure reduced the overall meshing time dramatically.

The meshes comprise approximately 12000 finite volumes or cells (see Figure 3). To confirm the grid-independence of the results, a second mesh was constructed with twice the

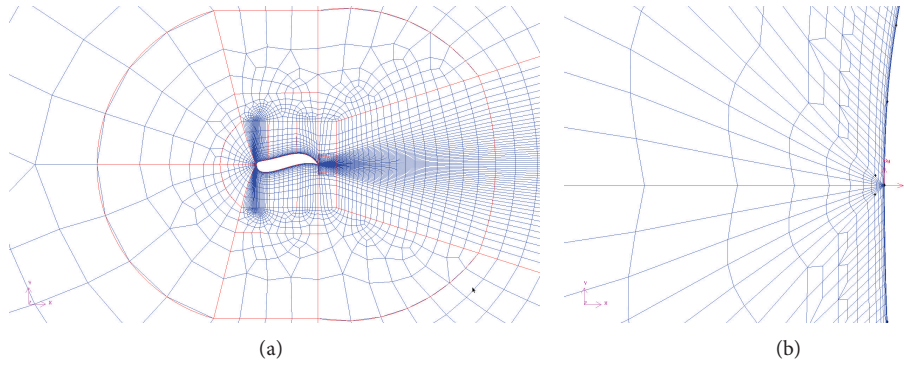


FIGURE 3: (a) Mesh around an aerodynamic profile and (b) detail near its leading edge.

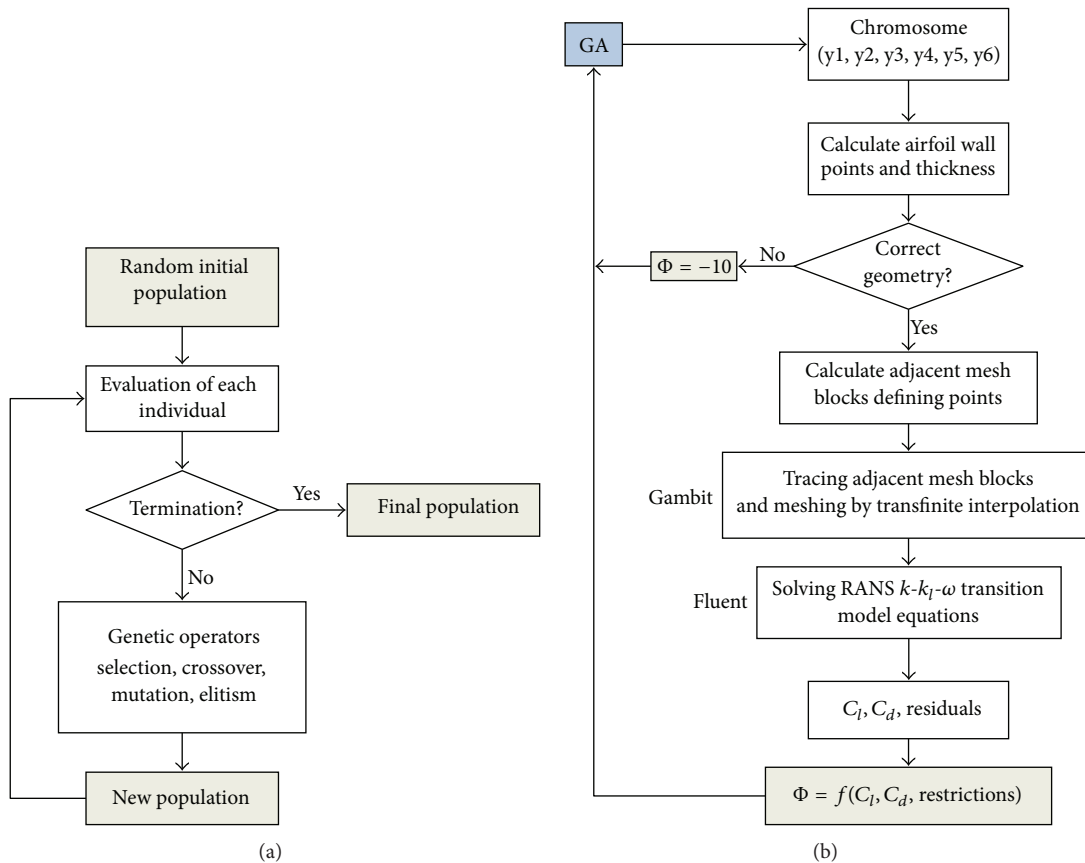


FIGURE 4: (a) Optimization scheme and (b) details of evaluation procedure used for each airfoil.

resolution in the streamwise and wall-normal directions, and the results were compared to those using the original mesh. In all cases, the results had negligible differences so were judged to be mesh-independent.

The validity of the meshing method was checked by numerous runs. Moreover, the method could be adapted to other problems and different domains.

The sequence used to mesh the domain around an airfoil is showed in the flowchart in Figure 4. Each airfoil shape is generated using NURBS curves (Not Uniform Rational B-Splines) by creating the files containing discrete data points

on the airfoil surface, which were defined as a Bezier curve (Figure 1). These files are imported into Gambit, a general purpose preprocessor for CFD analysis, which creates the mesh of the outer flow domain. Next, the blocks immediately surrounding the airfoil are designed and meshed, before the whole mesh is exported.

**2.3. Optimization.** Optimization was performed using a simple GA that follows the sequence shown in Figure 4(a). First, a seed number  $s$  is provided by the user, which is used to generate a univocal sequence of random numbers that form

the genes of the  $p$  chromosomes in the initial generation population. This is denoted as  $P(t = 0)$ , where  $P$  means population and  $t = 0$  is the number of the generation. The seed number could also be generated randomly, but the former option was preferred because it facilitated the performance of different experiments starting with the same initial population to investigate the separate effects of different combinations of GA parameters on exploratory and exploitative behaviors during search. The aim was to tune them to obtain the best results for a given objective function.

After generating the initial population  $P(0)$ , each individual was evaluated (as explained in paragraph 3, see Figure 4(b)), before selection, crossover, and mutation operators are applied to this population to obtain the next generation of individuals  $P(1)$ .

The sequence used to obtain  $P(1)$  is as follows. First, a new population  $P'(1)$  is generated after  $p$  tournaments. Next, with a crossover rate  $c$ , approximately  $pc/2$  pairs of individuals are crossed, each of which yielded two offsprings that substituted their parents and joined with the noncrossed individuals to form population  $P''(1)$ . The two-point crossover type was used. Next, a percentage  $m \cdot 100$  of the genes were mutated in this population. Finally, the duplicated individuals in the current population were mutated repeatedly until no identical individuals remained. This operation increases the exploration of the search space. After the first generation  $P(1)$  has been obtained, the same process is repeated until the termination criterion is satisfied. The criterion used in this study was 100 generations.

When elitism is applied, the most fit individual in a generation  $P(i)$  is automatically introduced into the next one  $P(i + 1)$ . This option increases the exploitative pressure and accelerates convergence, although it reduces the diversity in populations throughout evolution. Thus, the search is prone to becoming trapped in local extrema if small populations are used.

When elitism is not used, the algorithm tends to converge if a good individual is found, but this does not reduce the exploration of other possibilities in the search space. A more precise definition of the other parameters was required to achieve this behavior. This is the antagonism between the principal aspects of GAs: search and tuning. It is not possible to tune a solution if there is a tendency to search the entire space, and vice versa. Thus, the user has to find an adequate balance in each actual case.

### 3. Framework

In this study, the optimization by means of GAs of expensive nonanalytical objective functions is tackled. Each individual is an airfoil and its fitness value is a point in the search space. The fitness functions used in aerodynamic shape optimization problems aim to represent certain aspects of the airfoil's aerodynamic performance that need to be improved. Thus, the direct problem was tackled and several fitness functions were used, which were defined as functions of the aerodynamic loads imposed by the flow on the airfoil, that is, the aerodynamic coefficients  $c_l$  and  $c_d$ . Restrictions

on the airfoil thickness were also included to guarantee a threshold structural strength. An expensive CFD analysis has to be performed to evaluate an airfoil. This required the laborious implementation of a sequence of tasks using different techniques to generate an automatic process. This framework is shown in the flowchart in Figure 4. The most expensive and complex tasks are meshing and solving the flow model, which are achieved using two commercial codes, that is, the preprocessor Gambit and the CFD solver Fluent, respectively.

As shown in Figure 4, the GA optimizer sets the pace of the optimization process, which included each individual evaluation and assignment of a fitness value. This comprises the concatenation of calls to the different tools and codes that perform each task. The user entered the relevant parameters for the GA and these codes were controlled automatically using script files after the optimization commenced.

The airfoil evaluation process is governed by the GA, which operates as follows. Two sets of points are calculated using the set of Bezier vertices provided by the GA. The first set consists of two rows of 50 points, which are interpolated to define, respectively, the upper and lower curves of the airfoil. If these curves intersected with each other, the airfoil geometry is incorrect and it is assigned a negative fitness value, so it is omitted from the CFD analysis. The second set of points is used to define the boundaries of the mesh blocks adjacent to the airfoil. Next, both sets of point coordinates are written to the text journal file of Gambit, which also includes the commands used to build the mesh blocks next to the airfoil and to fill them with structured meshes. Finally, Gambit exports the whole mesh to the Fluent code.

Fluent conducts the processing and postprocessing tasks specified in its journal file. A second order discretization scheme is used. The airfoil characteristics  $c_l$  and  $c_d$  are obtained and the corresponding fitness value  $\Phi$  is calculated as a function of these data and a constraint on its thickness (see Figure 4).

### 4. Results

A preliminary experiment was performed to identify efficient combinations of parameters for the basic GA. The aim was to optimize the shape of the bidimensional aerodynamic profiles for incompressible flow with a Reynolds number of  $6 \times 10^6$  based on the chord length.

Two optimization criteria were used. The first is to maximize the ratio of the lift relative to the drag force, and the second consists on minimizing  $c_d$  for a given value of  $c_l$ . In both cases, the angle of attack is zero and the airfoil's thickness  $t$  is constrained to be above  $0.12c$ , where now  $c$  is the chord length and  $t$  is the maximum vertical distance between the intrados and the extrados along the chord.

These functions are defined in the following form:

$$\Phi = f(c_l, c_d) \cdot p_t \cdot p_a \cdot p_s, \quad (4)$$

where  $f$  is the aerodynamic function that needs to be optimized, and the variables  $p$  are penalty functions that

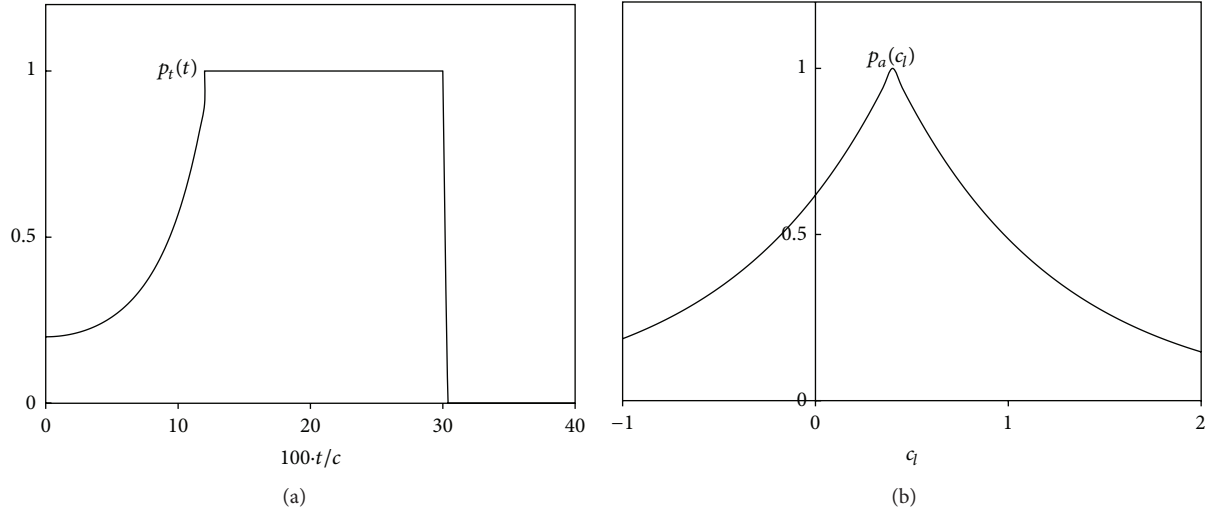


FIGURE 5: Penalty factors for the thickness (a) and lift (b) constraints.

include nonlinear constraints of different type. Their values are defined in the range  $[0, 1]$  and they were assigned 1 if the constraint was satisfied, but reduced from this value according to the degree to which the constraint was exceeded, where 0 was the minimum value. The penalty function  $p_t$  introduces the airfoil thickness constraint,  $p_a$  is the necessary condition for the aerodynamic loads, and  $p_s$  penalizes the airfoils where the flows are suspected to be solved incorrectly.

**4.1. Optimization of  $c_l/c_d$  with a Constraint on the Airfoil Thickness.** The first objective was to find airfoil shapes with a maximum lift per drag ratio and a thickness above  $0.12c$ . Thus, the objective function was defined in the following form:

$$\Phi = \left( \frac{c_l}{c_d} \right) \cdot p_t(t) \cdot p_s(r_k), \quad (5)$$

where

$$p_t(t) = \begin{cases} 0.2 \exp[0.01045t^2] & \text{if } 0 < t < 0.12c, \\ 1 & \text{if } 0.12c < t \leq 0.3c, \\ 0 & \text{if } t > 0.3, \end{cases} \quad (6)$$

$$p_s(r_k) = \begin{cases} 1 & \text{if } r_k \leq 5 \cdot 10^{-4}, \\ 0 & \text{if } r_k > 5 \cdot 10^{-4}, \end{cases} \quad (7)$$

where the two penalty factors  $p_t(t)$  and  $p_s(r_k)$  were defined carefully with respect to the constraint on the airfoil (maximum) thickness and to eliminate incorrectly calculated airfoils. The parameter  $r_k$  denotes the value of the residual of the turbulent kinetic energy equation obtained during the last iteration of the simulation.

In search spaces with constraints, the optimum solution may be found in the boundaries where the constraint conditions are satisfied. For this problem in particular, given a certain camber and an airfoil thickness distribution, the ratio of  $c_l/c_d$  is increased as the maximum thickness  $t$  is reduced.

This can be seen for example, by comparing the experimental data of decreasing thickness airfoils naca2424, naca2412, and naca2408 [21]. This fact was considered to define  $p_t(t)$  in (6), which is shown in Figure 5. The aim of this term was to direct the evolution towards airfoils with a thickness value over  $t = 0.12c$ , but also to conserve some useful genetic information from slightly thinner airfoils.

A severe penalty was used for excessively thin profiles, which was motivated by structural requirements and the relative increase in the ratio  $c_l/c_d$  as the thickness declined. The function  $p_t$  increases with the thickness to direct the population towards thicker airfoils, but without completely eliminating thinner ones with a good ratio  $c_l/c_d$  because they could add useful genetic information to the new generation. Moreover, a 10% amplitude jump was included at the thickness value  $t = 0.12c$  to highlight this boundary. Thicknesses above  $0.3c$  are considered excessive.

The factor  $p_s(r_k)$  was used to qualify the reliability of the solution to eliminate airfoils from the evolution process in the cases the flow was not calculated correctly. When the errors overestimate the aerodynamic performance they are very detrimental to the search process.

After performing CFD analysis using many airfoils with the  $k-k_l-\omega$  transition turbulence model, it was observed that simulations rarely produced great errors in the aerodynamic loads. And this usually occurred in simulations that gave flows with large separated regions. It was found that in contrast with the correct simulations, all of the incorrect ones had final values for the residual in the  $k_t$  equation that exceeded  $5 \times 10^{-4}$ . Therefore, correct flags were given when the residuals in the  $k_t$  equation fell below this value. This prevented the contamination of the genetic search with fake "superindividuals" which would have produced bad results.

The GA used a tournament selection operator and a generational replacement model. Tests were performed using different combinations of population sizes, crossover rates, and mutation rates, as shown in Table 1. Two-point-type

TABLE 1: Results for each combination of GA parameters.

Population size	40				100	
Mutation rate	0.0025		0.025		0.01	0.025
Crossover rate	0.5	0.65	0.5	0.65	0.65	0.65
Best individual found	(a) 75.53	(a) 82.30	(a) 82.64	(a) 68.84**	(e) 89.04	(e) 87.72
	(b) 81.72	(b) 77.32	(b) 88.02	(b) 86.60		
	(c) 82.07	(c) 76.27	(c) 87.95	(c) 88.11		
	(a)* 88.98	(a)* 81.91	(a)* 89.51	(a)* 90.77		
Best individual average	79.64	79.28 (a, c)	86.20	82.74	87.38 (b, c, d)	

( ) Initial population. \*Elitism. \*\* Anomalous evolution.

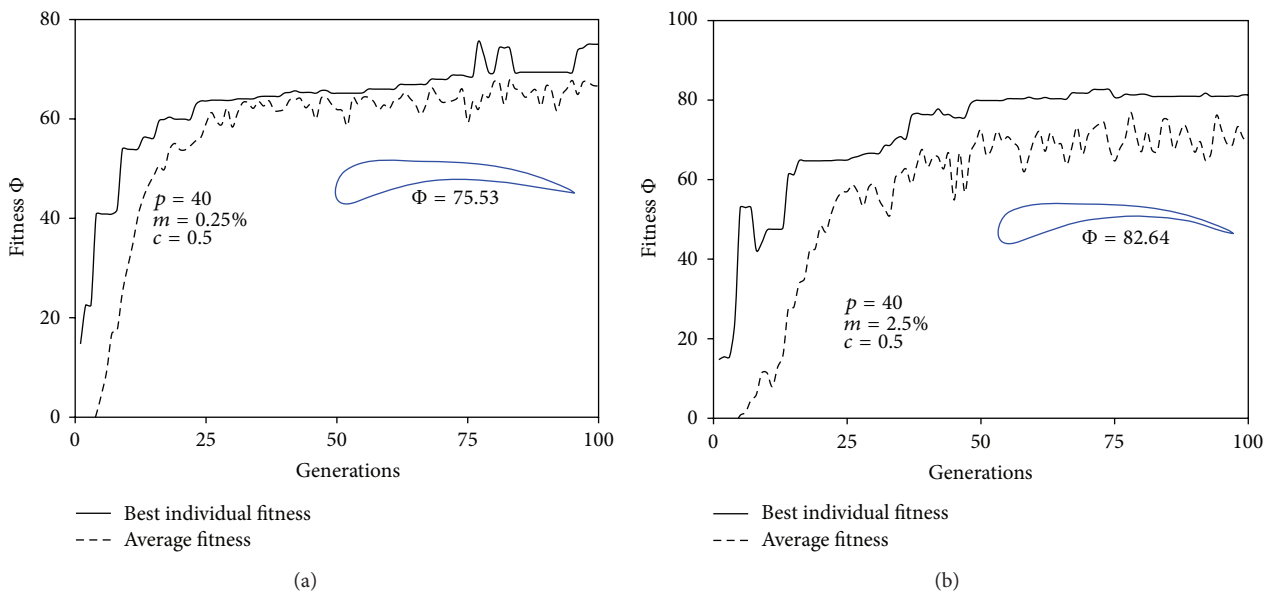


FIGURE 6: Typical evolution pattern for low and high mutation rates on the same initial population (a) for a population size of 40 individuals and a crossover rate  $c = 0.5$ .

crossover was used, and a simple mutation operator that flips bits at random positions along the chromosome was applied. At least three runs were performed for each combination. The termination criterion was established based on the number of generations, which was 100 in this case.

It was noted that the best solutions in populations with 40 chromosomes were obtained using a mutation rate of 2.5%, and that slightly better aptitude values could be obtained using populations of 100 individuals. However, moderate crossover rates did not appear to affect the maximum fitness significantly.

Figure 6 shows two particular runs starting from the same initial population for two different mutation rates. Both runs are representative of their respective typical evolution patterns.

When low mutation rates ( $m = 0.25\%$ ) are used (see Figure 6(a)), the average fitness in each generation keeps near the best individual fitness. There is little difference among the

individuals in the population and so the risk to get trapped in local maxima is relatively high. This is consistent with the results collected in Table 1.

When a higher mutation rate  $m = 2.5\%$  is used, also an (nonmonotonical) increase in both the average and the maximum fitness occurs. This feature indicates that although this mutation rate is relatively high, the GA does not yet behave as a random search and that constructive blocks remain. There is a wider diversity in the population and the average fitness evolves at a bigger distance below the maximum individual fitness. The former curve has now a more rugous aspect, these bigger variations from one generation to the next being consistent with a higher frequency of the random changes imposed to the genes.

High mutation rates reduce the risk of deceptive search of the GA but do not completely avoid it. In this sense the run marked with (\*\*) in Table 1 experimented an atypical evolution shown in Figure 7. The premature appearance

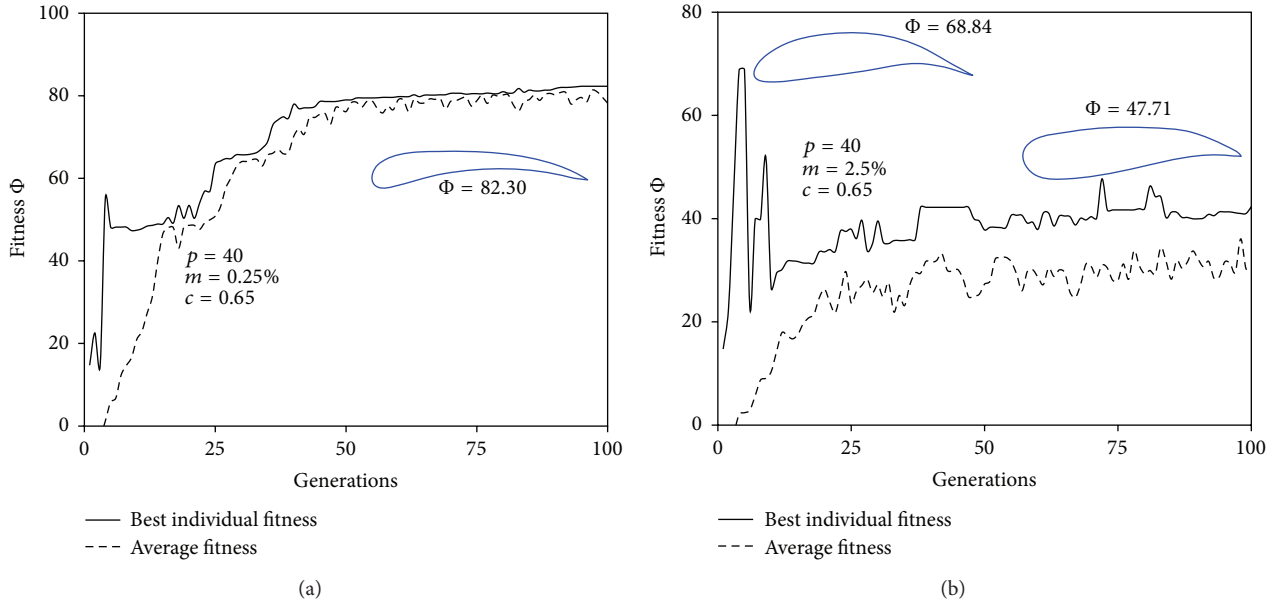


FIGURE 7: Search evolution for two runs performed on the same initial population for different mutation rates, (a) low and (b) high. The population size is 40 and the crossover rate is  $c = 0.65$ . The last run showed an anomalous behavior.

of a high fitness individual in the third generation (that lasted for two generations) guided the population towards nonprosperous regions where they got trapped.

The computing platform used in the analysis is a PC with 12 CPUs with 3 GHz speed and 96 Gb of RAM. In an optimization run using a population of 40 individuals along 100 generations, the number of function evaluations needed is usually in the range between 1600 and 2500 because some individuals are repeated in the next generation.

The use of elitism accelerated the convergence towards a high maximum in the landscape, as shown in the run selected in Figure 8. The populations become nearly converged around a third of the maximum number of generations. Consistent with the related reduction in the exploration, the results in Table 1 show that the use of elitism does not guarantee the achievement of the global maximum. However, in three among four runs it outperformed the best individual fitness obtained in the corresponding runs without elitism but with the same GA parameters and initial population.

**4.2. Drag Minimization for a Given Value of  $c_l$ , and Minimum Airfoil Thickness.** To minimize the  $c_d$ , the maximization of  $1/c_d$  is tackled. The objective function was defined in the following form:

$$\Phi = \left(\frac{1}{c_d}\right) \cdot p_t(t) \cdot p_a(c_l) \cdot p_s(r_k), \quad (8)$$

where

$$p_a(c_l) = \begin{cases} \exp[1.2(c_l - 0.4)] & \text{if } c_l < 0.4, \\ \exp[-1.2(c_l - 0.4)] & \text{if } c_l \geq 0.4, \end{cases} \quad (9)$$

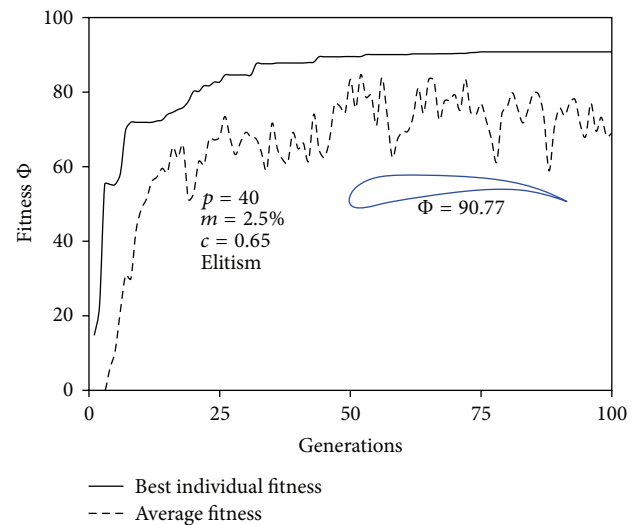


FIGURE 8: Typical convergence pattern with elitism. Search evolution for the best fitness value in Table 1.

$p_a(c_l)$  is the constraint in the lift value used to get airfoils that approximately satisfy the condition  $c_l = 0.4$ . For the calculations, two different initial populations of 40 individuals were used along with the same combinations of GA parameters used above. Two clear differences can be distinguished in the evolutionary behavior of these runs compared with those of the previous criterion. First, the convergence is slower (as seen in the run collected in Figure 9(b), which has a typical evolution pattern) and there is a bigger tendency to get trapped in local maxima. An expression of this is the thickness of the best airfoil in the run represented in Figure 9(a).

TABLE 2: Results for each combination of GA parameters.

Population size	40				100
Mutation rate	0.0025		0.025		0.025
Crossover rate	0.5	0.65	0.5	0.65	0.65
Best individual found	(f) 70.57	(f) 105.88	(f) 117.37	(f) 111.78	(g) 122.32
	(a) 89.31	(a) 85.68	(a) 123.18	(a) 111.63	
Best individual average	79.94	95.78	120.28	111.70	122.32

( ) Initial population.

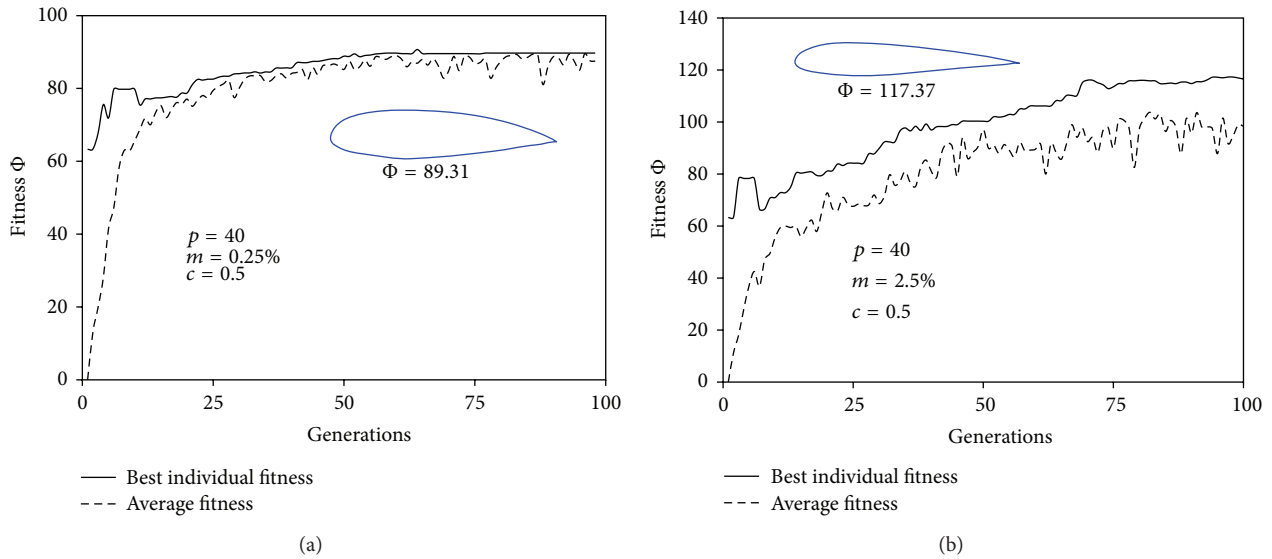


FIGURE 9: Search evolution for two runs performed on the same initial population for different mutation rates. The population size is 40 and the crossover rate is  $c = 0.5$ .

However, the effects of the different combinations of the GA parameters in the search appear to be qualitatively similar to the ones observed with the previous objective function. In this sense, the results of the few runs collected in Table 2 suggest that high-mutation rates give the best results, and also that bigger populations could improve the best individual fitness (see Figure 10(a)). The search evolution for the best fitness value in Table 2 is shown in Figure 10(b).

The increased tendency observed in the GA to get trapped in local maxima is consistent with the current more abrupt six-dimensional landscape. The introduction of the lift constraint in the objective function as the multiplying factor  $p_a(c_l)$  defined in  $[0, 1]$  (see Figure 5) excavates valleys in the six-dimensional landscape corresponding to the six design variables that define the profile. Now, there are more local maxima, and so the difficulty for the GA to get the highest peak is increased. The authors opine that a less steep definition of the factor  $p_a$  (see Figure 5) could substantially improve the results.

Finally, the use of metamodels can reduce the CFD runs as in the case of artificial neural networks, utilized to create surrogate models. In this way, the total computational time

of optimization can be reduced. However, it is important to assess the effectiveness of the metamodel using validation.

### 5. Conclusions

A CFD shape optimization tool was developed by integrating the genetic code known as OMEGA, which is based on David Levine’s PGA Pack Library, and a commercial CFD code known as Fluent. This tool facilitated shape optimization for aerodynamic profiles. A current generation RANS turbulence model that predicts transition from laminar to turbulent flow in the boundary layer was employed in order to achieve accurate results. A fast and reliable meshing procedure was developed that generates low-cost meshes with small heights and little distortion in the boundary layer. The system robustness was verified for the specific optimization problem of an aerodynamic profile.

In addition, a preliminary experiment was performed to identify efficient parameters for the optimization algorithm with respect to this problem. Two different objective functions with nonlinear constraints were defined to find improved airfoils for two aerodynamic goals. Different

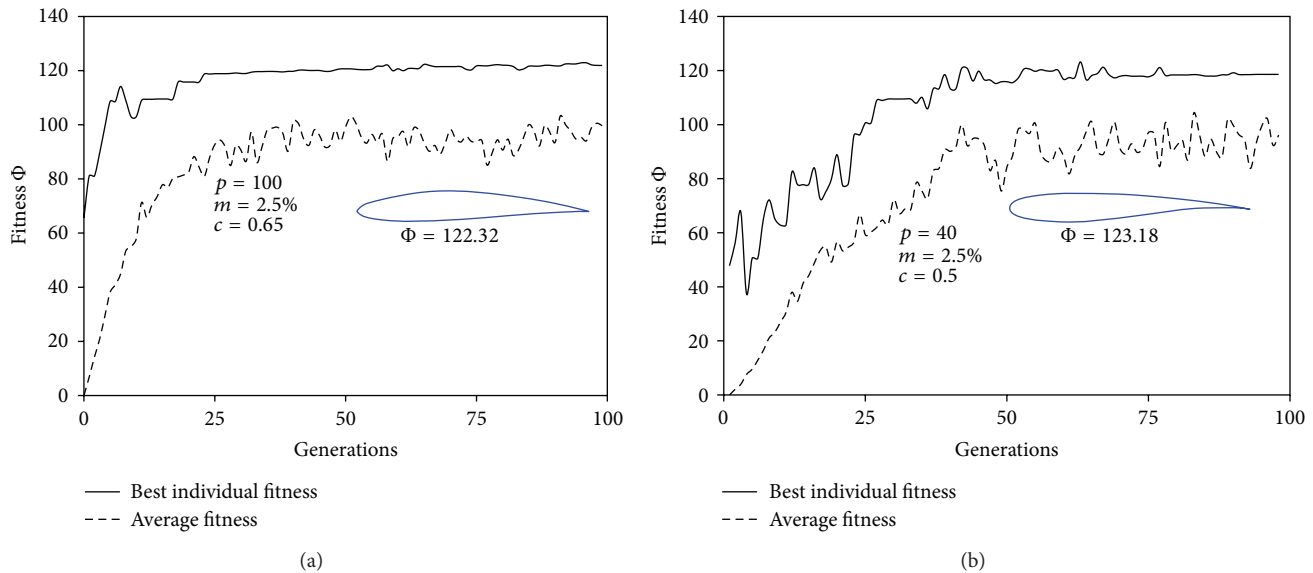


FIGURE 10: (a) Search evolution for a run with a population of 100 individuals and a crossover rate  $c = 0.65$  and mutation rate  $m = 2.5\%$ . (b) Search evolution for the best fitness value in Table 2.

penalty functions were included in their definition to improve the convergence to optimum solutions. In both cases, the use of populations of 40 individuals along with a high mutation rate and a moderate crossover rate showed a good behavior.

The future application of this type of technique to the multiobjective optimization of airfoils with different angles of attack was considered.

## Acknowledgments

The authors wish to acknowledge the financial support provided by the Department of Research, the Universities of the Basque Government, the Ministry of Science and Innovation in Spain through the research Project DPI2009-07900, and the UPV/EHU under Program no. UFI 11/29.

## References

- [1] G. Kalitzin, X. Wu, and P. A. Durbin, "DNS of fully turbulent flow in a LPT passage," *International Journal of Heat and Fluid Flow*, vol. 24, no. 4, pp. 636–644, 2003.
- [2] T. A. Zaki and P. A. Durbin, "Mode interaction and the bypass route to transition," *Journal of Fluid Mechanics*, vol. 531, pp. 85–111, 2005.
- [3] D. K. Walters and J. H. Leylek, "A new model for boundary layer transition using a single-point RANS approach," *Journal of Turbomachinery*, vol. 126, no. 1, pp. 193–202, 2004.
- [4] Y. B. Suzen, P. G. Huang, L. S. Hultgren, and D. E. Ashpis, "Predictions of separated and transitional boundary layers under low-pressure turbine airfoil conditions using an intermittency transport equation," *Journal of Turbomachinery*, vol. 125, no. 3, pp. 455–464, 2003.
- [5] F. R. Menter, R. Langtry, and S. Vlker, "Transition modelling for general purpose CFD codes," *Flow, Turbulence and Combustion*, vol. 77, no. 1–4, pp. 277–303, 2006.
- [6] D. K. Walters and D. Cokljat, "A three-equation eddy-viscosity model for reynolds-averaged navier-stokes simulations of transitional flow," *Journal of Fluids Engineering*, vol. 130, no. 12, Article ID 121401, 14 pages, 2008.
- [7] A. Shahrokhi and A. Jahangirian, "Airfoil shape parameterization for optimum Navier-Stokes design with genetic algorithm," *Aerospace Science and Technology*, vol. 11, no. 6, pp. 443–450, 2007.
- [8] J. D. Lee and A. Jameson, "Natural-laminar-flow airfoil and wing design by adjoint method and automatic transition prediction," in *Proceedings of the 47th AIAA Aerospace Sciences Meeting*, pp. 1–25, Orlando, Fla, USA, January 2009.
- [9] S. Obayashi and T. Tsukahara, "Comparison of optimization algorithms for aerodynamic shape design," *AIAA Journal*, vol. 35, no. 8, pp. 1413–1415, 1997.
- [10] R. A. E. Makinen, J. Periaux, and J. Tovainen, "Multidisciplinary shape optimization in aerodynamics and electromagnetics using genetic algorithms," *International Journal for Numerical Methods in Fluids*, vol. 30, no. 2, pp. 149–159, 1999.
- [11] J. Burman and B. R. Gebart, "Influence from numerical noise in the objective function for flow design optimization," *International Journal of Numerical Methods for Heat and Fluid Flow*, vol. 11, no. 1, pp. 6–19, 2001.
- [12] D. Quagliarella and A. Vicini, "Viscous single and multicomponent airfoil design with genetic algorithms," *Finite Elements in Analysis and Design*, vol. 37, no. 5, pp. 365–380, 2001.
- [13] F. Schmid, K. Hirschen, S. Meynen, and M. Schäfer, "An enhanced approach for shape optimization using an adaptive algorithm," *Finite Elements in Analysis and Design*, vol. 41, no. 5, pp. 521–543, 2005.
- [14] S. Peigin and B. Epstein, "Robust optimization of 2D airfoils driven by full Navier-Stokes computations," *Computers and Fluids*, vol. 33, no. 9, pp. 1175–1200, 2004.
- [15] J. H. Holland, *Adaptation in Natural and Artificial Systems*, University of Michigan Press, Ann Arbor, Mich, USA, 1975.
- [16] V. Gomez, I. Fernandez de Bustos, J. Aguirrebeitia, C. Angulo, and R. Aviles, "A modified genetic algorithm suitable for

nonstationary environments,” in *Proceedings of the 4th World Congress of Structural and Multidisciplinary Optimization (WCSMO-4)*, pp. 1–6, Dalian, China, 2001.

- [17] D. C. Wilcox, *Turbulence Modelling for CFD*, DCW Industries Inc., 1998.
- [18] H. Schlichting and K. Gersten, *Boundary Layer Theory*, Springer, Berlin, Germany, 2000.
- [19] D. López, C. Angulo, and L. Macareno, “An improved meshing method for shape optimization of aerodynamic profiles using genetic algorithms,” *International Journal for Numerical Methods in Fluids*, vol. 56, no. 8, pp. 1383–1389, 2008.
- [20] J. F. Thompson, B. K. Soni, and N. P. Weatherill, *Handbook of Grid Generation*, CRC Press, Boca Raton, Fla, USA, 1999.
- [21] I. H. Abbott and A. E. von Doenhoff, *Theory of Wing Sections: Including a Summary of Airfoil Data*, Dover, New York, NY, USA, 1959.

## Research Article

# Nonlinear Characteristics of Helicopter Rotor Blade Airfoils: An Analytical Evaluation

**Constantin Rotaru**

*Department of Aviation Integrated Systems, Military Technical Academy, 39-49 George Cosbuc Avenue, 050141 Bucharest, Romania*

Correspondence should be addressed to Constantin Rotaru; [rotaruconstantin@yahoo.com](mailto:rotaruconstantin@yahoo.com)

Received 27 June 2013; Revised 4 September 2013; Accepted 6 September 2013

Academic Editor: Tirivanhu Chinyoka

Copyright © 2013 Constantin Rotaru. This is an open access article distributed under the Creative Commons Attribution License, which permits unrestricted use, distribution, and reproduction in any medium, provided the original work is properly cited.

Some results are presented about the study of airloads of the helicopter rotor blades, the aerodynamic characteristics of airfoil sections, the physical features, and the techniques for modeling the unsteady effects found on airfoil operating under nominally attached flow conditions away from stall. The unsteady problem was approached on the basis of Theodorsen's theory, where the aerodynamic response (lift and pitching moment) is considered as a sum of noncirculatory and circulatory parts. The noncirculatory or apparent mass accounts for the pressure forces required to accelerate the fluid in the vicinity of the airfoil. The apparent mass contributions to the forces and pitching moments, which are proportional to the instantaneous motion, are included as part of the quasi-steady result.

## 1. Introduction

The most important component of the helicopter is the main rotor for which there is a great deal of activity in developing new and improved mathematical models that predict the flow physics. A high tip speed gives the rotor a high level of stored rotational kinetic energy and reduces the rotor torque required for a given power, but there are two important factors that work against the use of a high tip speed: compressibility effects and noise.

The additional effects of compressibility on the overall rotor profile power requirements, when the tip of the advancing blade approaches and exceeds the drag divergence Mach number, were estimated using blade element theory combined with the airfoil section characteristics [1]. A more detailed analysis of compressibility effects on the rotor must represent the actual nonlinear airfoil characteristics as functions of Mach number through stall at each blade element followed by numerical integration.

The classical unsteady aerodynamic theories describing the observed behavior have formed the basis for many types of rotor analysis. The tools for the analysis of 2D, incompressible, and unsteady aerodynamic problems were extended to compressible flows, being a basis for developing linearized

unsteady aerodynamic models applicable to compressible flows [2]. But, while the classical theories assume linearity in the airloads, the assumption of linearity can probably be justified for many of the problems encountered on the rotor, in practice. The advent of nonlinear methods based on CFD solutions to the Euler and Navier-Stokes equations has provided new results that justify and define the limits of the linear models and may give guidance in developing improved and more practical unsteady aerodynamic models for future use in helicopter rotor blade airloads prediction, aeroelastic analysis, and rotor design [3]. At the blade element level, the various sources of unsteady effects can be decomposed into perturbations to the local angle of attack and velocity field. At low angle of attack with fully attached flow, the various sources of unsteady effects manifest as moderate amplitude and phase variations relative to the quasi-steady airloads. At higher angles of attack when time-dependent flow separation from the airfoil may be involved, a phenomenon characterized by large overshoots in the values of the lift, drag, and pitching moments relative to the quasi-steady stall values may occur [4].

The helicopter rotor airfoil must assure a high maximum lift coefficient, a high drag divergence Mach number, a good lift-to-drag ratio over a wide range of Mach number, and a

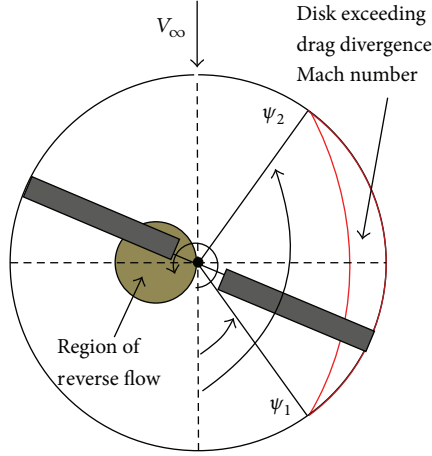


FIGURE 1: Helicopter rotor blade in forward flight.

low pitching moment. At high angles of attack, the adverse pressure gradients produced on the upper surface of the airfoil result in a progressive increase in the thickness of the boundary layer and cause some deviation from the linear lift versus angle of attack behavior. On many airfoils, the onset of flow separation and stall occurs gradually with increasing angle of attack, but on some airfoils (those with sharp leading edges) the flow separation may occur suddenly.

## 2. Helicopter Rotor Blade Aerodynamics

The region of the rotor disk affected by compressibility effects is shown in Figure 1 and is defined on the surface where the incident Mach number of the flow that is normal to the leading edge of the blade exceeds the drag divergence Mach number,  $M_{dd}$ . If  $M_{\Omega R}$  is the hover tip Mach number, then the region of the disk affected by compressibility effects is defined by

$$M_{r,\psi} = M_{\Omega R} (r + \mu \sin \psi) \geq M_{dd}. \quad (1)$$

The angular or rotational speed of the rotor is denoted by  $\Omega$ , the rotor radius by  $R$ , the advanced ratio by  $\mu$  and the radial distance from the rotational axis by  $y$ . In the above equation the nondimensional quantities are  $r = y/R$  and  $\mu = V_{\infty} \cos \alpha / \Omega R$ , where  $\alpha$  is the angle between the forward velocity  $V_{\infty}$  and the plane of the rotor [1, 2]. The azimuth angle for the onset drag divergence,  $\psi_1$ , can be obtained by setting  $r = 1$ , so that

$$\psi_1 = \arcsin \left( \left[ \frac{1}{\mu} \left( \frac{M_{dd}}{M_{\Omega R}} - 1 \right) \right] \right) \quad (2)$$

and  $\psi_2 = 180 - \psi_1$ .

The increment in profile power  $\Delta C_P$  associated with this region on the disk is

$$\frac{\Delta C_P}{\sigma} = \frac{1}{4\pi} \int_{\psi_1}^{\psi_2} \int_{r_{dd}}^1 (r + \mu \sin \psi)^3 \Delta C_d r dr d\psi, \quad (3)$$

where  $\Delta C_d$  is the extra drag on the blade section when it exceeds the drag divergence Mach number,  $M_{dd}$ , and  $\sigma$  is

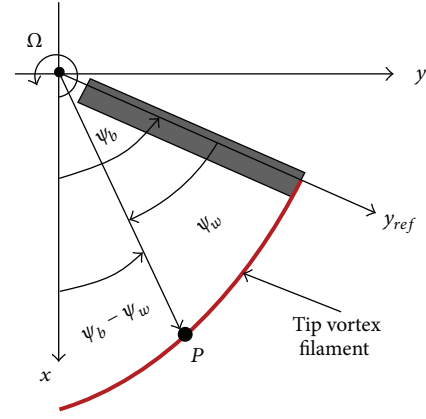


FIGURE 2: Tip vortex trajectory.

rotor solidity coefficient which represents the ratio of the blades area to the rotor disk area. For the NACA 0012 airfoil, Prouty [4] suggests that this can be approximated by

$$\Delta C_d(M) = \begin{cases} 12.5(M - 0.74)^3 & \text{for } M \geq 0.74, \\ 0 & \text{otherwise.} \end{cases} \quad (4)$$

The rotor limits may be determined by two conditions, one condition given by advancing blade compressibility effects and the other condition given by retreating blade stall. In either case the advancing blade operates at low angle of attack (AoA) but at high subsonic or transonic conditions, whereas the retreating blade operates at low Mach numbers and high lift coefficients.

The aerodynamic behavior of airfoils in the high AoA regime is important for predicting the adverse effects produced in the reverse flow regime on the rotor. In the reverse flow region, the direction of the relative flow vector changes from the trailing edge toward the leading edge of the airfoil. While the fundamental process of the blade wake and tip vortex formation is similar to that found with a fixed wing, one difference with helicopter tip vortices is that they are curved, and so they experience a self-induced effect. Another complication with helicopter rotors is that the wakes and tip vortices from other blades can lie close to each other and to the plane of blade rotation, and so they have large induced effects on the blade lift distribution.

If the wake is assumed to be undistorted in the tip path plane and no wake contraction occurs in the radial direction (Figure 2), then the tip vortex trajectories are described by the equations

$$\begin{aligned} x &= R \cos(\psi_b - \psi_w) + R\mu\psi_w, \\ y &= R \sin(\psi_b - \psi_w), \end{aligned} \quad (5)$$

where  $\psi_b$  is the position of the blade when the vortex was formed and  $\psi_w$  is the position of the vortex element relative to the blade.

One important parameter used in the description of unsteady aerodynamics and unsteady airfoil behavior is the reduced frequency,  $k$ , defined as  $k = \omega \cdot c / (2V)$ , where  $\omega$  is

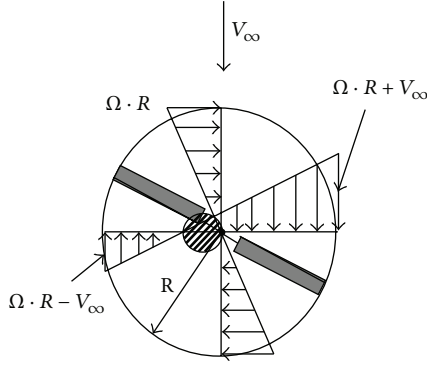


FIGURE 3: Helicopter main rotor.

the angular frequency,  $c$  is the chord of the airfoil, and  $V$  is the flow velocity [3]. According to the dimensional analysis, the resultant force,  $F$ , on the airfoil chord  $c$  can be written in functional form as  $F/(\rho V^2 c^2) = f(\text{Re}, M, k)$ . For  $k = 0$ , the flow is steady, and for  $0 \leq k \leq 0.05$ , the flow can be considered quasi-steady; that is, unsteady effects are generally small. Flows with characteristic reduced frequencies above 0.05 are considered unsteady [5, 6]. For a helicopter rotor in forward flight (Figure 3), the local sectional velocity, which appears in the denominator of the reduced frequency expression, is constantly changing.

The approach to modeling of unsteady aerodynamic effects through an extension of steady, 2D thin airfoil theory gives a good level of analysis of the problem and provides considerable insight into the physics responsible for the underlying unsteady behavior. The Laplace's equation for incompressible flow is elliptic; therefore, the unsteady aerodynamic theories cannot be obtained in a corresponding analytical form.

### 3. The Apparent Mass Tensor

The rate of change of the impulse vector, in general, is not in the direction of the acceleration of the body. The external force  $F_e$  applied to the body to translate it through the fluid has to be applied in a direction different from that of the acceleration of the body through the fluid [7]. Physical conditions that should be satisfied on given boundaries of the fluid (boundary conditions) depend on the assumptions made with regard to the nature of the fluid, more specifically on the nature of the differential equations that are assumed to govern the motion of the fluid. For a solid-fluid boundary, at each point of the solid-fluid surface, at every instant, the component normal to the surface of the relative velocity between the fluid and the solid must be vanish,  $\vec{V} \cdot \vec{n} = 0$ , where  $\vec{V}$  represents the relative velocity and  $\vec{n}$  the normal to the surface (Figure 4).

If the surface is represented by a scalar function of position and time,  $F(\vec{r}, t) = 0$ , then the total time rate of change is zero:

$$\frac{D(F)}{Dt} = \frac{\partial(F)}{\partial t} + \vec{V} \cdot \text{grad}(F) = 0 \quad (6)$$

on  $F(\vec{r}, t) = 0$ .

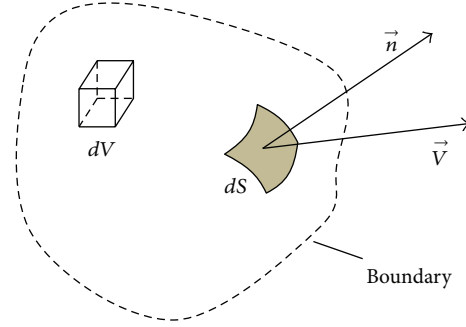


FIGURE 4: Solid-fluid surface.

The fluid force acting on a rigid body of arbitrary shape translating with a velocity  $\vec{U}(t)$  is given by

$$\vec{F} = - \iint_S p \vec{n} dS, \quad (7)$$

where  $S$  denotes the surface of the body and  $p$  is the pressure on the surface of the body. In general, the body may be translating, rotating, and deforming; consequently, the velocity  $U$  is a function of position on the surface and time. If the body is rigid and is in translatory motion, then  $U$  is a function of time but uniform over the surface of the body. The mathematical problem is to determine the external force  $\vec{F}_e$  applied to the body to translate it through the fluid. According to Newton's second law, we have

$$\frac{d}{dt} (m\vec{U}) = \vec{F}_e + \vec{F}, \quad (8)$$

where  $m$  is the mass of the body. The above equation may be rewritten as

$$\vec{F}_e = \frac{d}{dt} (m\vec{U}) - \vec{F} \quad (9)$$

or

$$\vec{F}_e = \frac{d}{dt} (m\vec{U} + \vec{I}), \quad (10)$$

where  $\vec{I}$  is the impulse applied on the fluid and  $-d\vec{I}/dt = \vec{F}$ . The fluid force acting on the body is

$$\vec{F} = \frac{\partial}{\partial t} \iint_S \rho \phi \vec{n} dS - \rho \vec{U} \times \iint_S \vec{n} \times \text{grad}(\phi) dS. \quad (11)$$

The integral

$$\vec{I}_C = \iint_S \vec{n} \times \text{grad}(\phi) dS \quad (12)$$

is related to the circulation  $C$  around the body, and  $\phi$  is the velocity potential.

The unit vector  $\vec{e}$  is normal to the cutting planes, the unit vector  $\vec{e}_1$  is tangent to the curve of intersection between the blade element surface and the cutting plane, and the unit vector  $\vec{e}_2$  is tangent to the blade element surface.

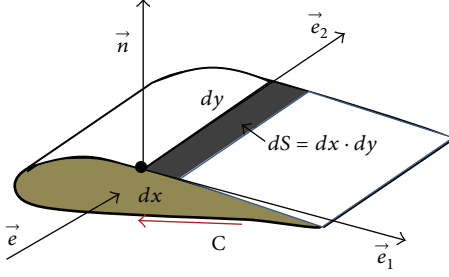


FIGURE 5: Rotor blade element.

The component of the vector  $\vec{I}_C$  in the direction  $\vec{e}$  is

$$\vec{e} \cdot \vec{I}_C = \iint_S \vec{e} \cdot \vec{n} \times \vec{q} dS, \quad (13)$$

and the vector  $\vec{n} dS$  corresponding to the surface element  $dS = dx \cdot dy$  may be written as  $\vec{n} dS = d\vec{x} \times d\vec{y}$ , where  $d\vec{x} = dx\vec{e}_1$ ,  $d\vec{y} = dy\vec{e}_2$ , and  $\vec{q} = \text{grad}(\phi)$ .

On the other hand,

$$\begin{aligned} \vec{n} dS \times \vec{q} &= (d\vec{x} \times d\vec{y}) \times \vec{q} = (\vec{q} \cdot d\vec{x}) d\vec{y} - (\vec{q} \cdot d\vec{y}) d\vec{x}, \\ \vec{e} \cdot \vec{n} \times \vec{q} dS &= \vec{e} \cdot (\vec{q} \cdot d\vec{x}) d\vec{y} - \vec{e} \cdot (\vec{q} \cdot d\vec{y}) d\vec{x}. \end{aligned} \quad (14)$$

Since the unit vectors  $\vec{e}$  and  $\vec{e}_1$  are normal, it follows that  $\vec{e} \cdot d\vec{x} = 0$  and

$$\vec{e} \cdot (\vec{n} \times \vec{q}) dS = (\vec{q} \cdot d\vec{x}) (\vec{e} \cdot d\vec{y}). \quad (15)$$

The scalar product  $\vec{e} \cdot d\vec{y}$ , is the normal distance between the cutting planes of the solid body (Figure 5). If we denote  $dh = \vec{e} \cdot d\vec{y}$ , it follows that

$$\vec{e} \cdot \iint_S \vec{n} \times \vec{q} dS = \int_{h_1}^{h_2} \left( \oint_C \vec{q} \cdot d\vec{x} \right) dh = \int_{h_1}^{h_2} \Gamma_e(h) dh. \quad (16)$$

Here,  $h$  is the distance measured along the fixed direction  $\vec{e}$ , and

$$\Gamma_e(h) = \oint_C \vec{q} \cdot d\vec{x} \quad (17)$$

is the circulation around the curve of intersection between the body surface and the cutting plane. The limits  $h_1$  and  $h_2$  denote the extremities of the body measured along the direction  $\vec{e}$ . It follows that for motions without circulation the force on the body is given by

$$\vec{F} = \frac{\partial}{\partial t} \left( \iint_S \rho \phi \vec{n} dS \right), \quad (18)$$

where the velocity potential  $\phi$  is the solution of the system

$$\begin{aligned} \nabla^2 \phi &= 0, \\ \text{grad } \phi \cdot \vec{n} &= \frac{\partial \phi}{\partial n} = U(t) n \quad \text{on } S. \end{aligned} \quad (19)$$

Since the equation and boundary condition for  $\phi$  are linear, the solution could have the form

$$\phi = \phi_1 + \phi_2 + \phi_3, \quad (20)$$

where each of the functions  $\phi_1$ ,  $\phi_2$ , and  $\phi_3$  is a solution of the equations

$$\begin{aligned} \nabla^2 \phi_i &= 0, \\ \text{grad}(\phi_i) \cdot \vec{n} &= \frac{\partial \phi_i}{\partial n} = u_i n_i \quad \text{on } S, \end{aligned} \quad (21)$$

where  $i = 1, 2$ , or  $3$ .

In the Cartesian coordinate system, the vectors  $\vec{U}$  and  $\vec{n}$  have the expressions

$$\begin{aligned} \vec{U} &= u_1 \vec{i} + u_2 \vec{j} + u_3 \vec{k}, \\ \vec{n} &= n_1 \vec{i} + n_2 \vec{j} + n_3 \vec{k}. \end{aligned} \quad (22)$$

Because time enters through  $u_i$ , it is convenient to set  $\phi_i = u_i \varphi_i$ , so the system (21) takes the form

$$\begin{aligned} \nabla^2 \varphi_i &= 0, \\ \text{grad}(\varphi_i) \cdot \vec{n} &= \frac{\partial \varphi_i}{\partial n} = n_i \quad \text{on } S. \end{aligned} \quad (23)$$

With these considerations the impulse  $\vec{I}$  becomes

$$\begin{aligned} -\vec{I} &= \iint_S \rho \phi \vec{n} dS = \iint_S \rho \left( \sum_{k=1}^3 u_k \varphi_k \right) \vec{n} dS \\ &= \sum_{k=1}^3 \left( \iint_S \rho \varphi_k \vec{n} dS \right) u_k. \end{aligned} \quad (24)$$

The components of the impulse  $\vec{I} = I_1 \vec{i} + I_2 \vec{j} + I_3 \vec{k}$  are

$$\begin{aligned} I_1 &= \vec{j} \cdot \vec{I} = \sum_{k=1}^3 \left( -\iint_S \rho \varphi_k n_1 dS \right) u_k, \\ I_2 &= \vec{j} \cdot \vec{I} = \sum_{k=1}^3 \left( -\iint_S \rho \varphi_k n_2 dS \right) u_k, \\ I_3 &= \vec{k} \cdot \vec{I} = \sum_{k=1}^3 \left( -\iint_S \rho \varphi_k n_3 dS \right) u_k. \end{aligned} \quad (25)$$

The surface integral in above equations may be written as follows:

$$\iint_S \rho \varphi_k n_i dS = \iint_S \rho \varphi_k \frac{\partial \varphi_i}{\partial n} dS. \quad (26)$$

According to Green's theorem, if  $f_1$  and  $f_2$  are two harmonic functions, then

$$\iint_S f_1 \frac{\partial f_2}{\partial n} dS = \iint_S f_2 \frac{\partial f_1}{\partial n} dS. \quad (27)$$

Introducing the symbol  $m_{ki}$ ,

$$m_{ki} = -\iint_S \rho \varphi_k \frac{\partial \varphi_i}{\partial n} dS \quad (28)$$

with  $m_{ki} = m_{ik}$ ; the components of the impulse  $\vec{I}$  are therefore given by

$$I_i = \sum_{k=1}^3 m_{ik} u_k, \quad i = 1, 2, 3, \quad (29)$$

and the force applied externally to the body is

$$\begin{aligned} \vec{F}_e &= \frac{d}{dt} m (u_1 \vec{i} + u_2 \vec{j} + u_3 \vec{k}) \\ &+ \frac{d}{dt} (m_{11} u_1 + m_{12} u_2 + m_{13} u_3) \vec{i} \\ &+ \frac{d}{dt} (m_{21} u_1 + m_{22} u_2 + m_{23} u_3) \vec{j} \\ &+ \frac{d}{dt} (m_{31} u_1 + m_{32} u_2 + m_{33} u_3) \vec{k} \end{aligned} \quad (30)$$

or

$$\begin{aligned} \vec{F}_e &= \left[ (m + m_{11}) \frac{du_1}{dt} + m_{12} \frac{du_2}{dt} + m_{13} \frac{du_3}{dt} \right] \vec{i} \\ &+ \left[ m_{21} \frac{du_1}{dt} + (m + m_{22}) \frac{du_2}{dt} + m_{23} \frac{du_3}{dt} \right] \vec{j} \\ &+ \left[ m_{31} \frac{du_1}{dt} + m_{32} \frac{du_2}{dt} + (m + m_{33}) \frac{du_3}{dt} \right] \vec{k}. \end{aligned} \quad (31)$$

The coefficients  $m_{ik}$  form a set of nine numbers which may be displayed as an array

$$\begin{pmatrix} m_{11} & m_{12} & m_{13} \\ m_{21} & m_{22} & m_{23} \\ m_{31} & m_{32} & m_{33} \end{pmatrix} \quad (32)$$

and may be referred to as a virtual mass tensor or virtual masses that need to be added to the mass of the body in order to find the force that must be applied to translate it through the fluid. Introducing the symbol  $\delta_{ik}$  defined by  $\delta_{ik} = 0$  if  $i \neq k$  and  $\delta_{ik} = 1$  for  $i = k$ , (30) may be rewritten as

$$(F_e)_i = \sum_{k=1}^3 (m \delta_{ik} + m_{ik}) \frac{du_k}{dt}. \quad (33)$$

For any body, there are three perpendicular directions such that  $m_{ik} = 0$  for  $i \neq k$ , so with respect to such axes, (33) becomes

$$(F_e)_i = (m + m_{ii}) \frac{du_i}{dt}, \quad i = 1, 2, 3. \quad (34)$$

The sum  $(m + m_{ii})$  represents the apparent mass for translation in the  $i$ -direction, and the corresponding  $m_{ii}$  is the additional apparent mass.

#### 4. The Airloads on an Oscillating Airfoil

The oscillatory motion of the airfoil can be decomposed into contributions associated with angle of attack which is equivalent to a pure plunging motion (Figure 6) and contributions associated with pitching (Figure 7).

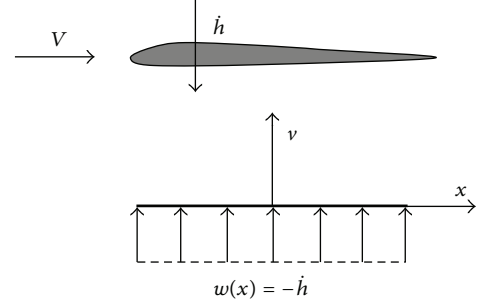


FIGURE 6: Plunge velocity.

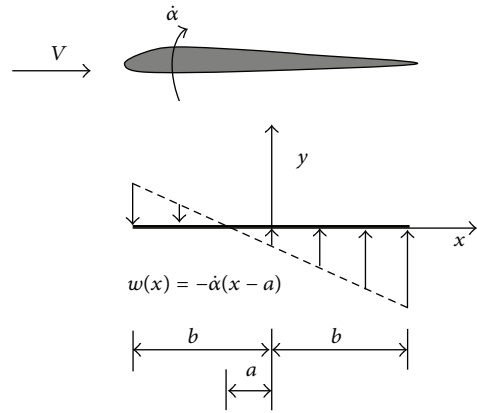


FIGURE 7: Pitch rate.

A plunge velocity  $\dot{h}$  produces a uniform velocity perturbation  $w$  that is normal to the chord,  $w(x) = -\dot{h}$ , and the pitch-rate term produces a linear variation in normal perturbation velocity.

For a pitch rate imposed about an axis at “ $a$ ” semichords from the midchord, then  $w(x) = -\dot{\alpha}(x - a)$ , so that the induced chamber is a parabolic arc.

The problem of finding the airloads on an oscillating airfoil was solved by Theodorsen, who gave a solution to the unsteady airloads on a 2D harmonically oscillated airfoil in inviscid, incompressible flow, with the assumption of small disturbances [6]. Both the airfoil and its shed wake were represented by a vortex sheet with the shed wake extending as a planar surface from the trailing edge downstream to infinity. The assumption of planar wake is justified if the angle of attack disturbances remain relatively small. As with the standard quasi-steady thin airfoil theory, the bound vorticity,  $\gamma_b$ , can sustain a pressure difference and, therefore, a lift force. The wake vorticity,  $\gamma_w$ , must be force-free with zero net pressure jump over the sheet. According to the Theodorsen’s theory, the solution for the loading  $\gamma_b$  on the airfoil surface under harmonic forcing conditions is obtained from integral equation

$$w(x, t) = \frac{1}{2\pi} \int_0^c \frac{\gamma_b(x, t)}{x - x_0} dx + \frac{1}{2\pi} \int_c^\infty \frac{\gamma_w(x, t)}{x - x_0} dx, \quad (35)$$

where  $w$  is the downwash on the airfoil surface. At the trailing edge,  $\gamma_b(c, t) = 0$ , and the airfoil circulation  $\Gamma(t)$  is given by

$$\Gamma(t) = \int_0^c \gamma_b(x, t) dx. \quad (36)$$

So long as the circulation about the airfoil is changing with respect to time, the circulation is continuously shed into the wake and will continuously affect the aerodynamic loads on the airfoil.

For a general motion, where an airfoil of chord  $c = 2b$  is undergoing a combination of pitching ( $\alpha, \dot{\alpha}$ ) and plunging ( $h$ ) motion in a flow of steady velocity  $V$ , Theodorsen's solution [8–10] for the lift coefficient and pitching moment coefficient corresponding to midchord,  $M_{1/2}$ , is

$$\begin{aligned} c_l &= \pi b \left[ \frac{\ddot{h}}{V^2} + \frac{\dot{\alpha}}{V} - \frac{b}{V^2} a \ddot{\alpha} \right] \\ &\quad + 2\pi \left[ \frac{\dot{h}}{V} + \alpha + \frac{b\dot{\alpha}}{V} \left( \frac{1}{2} - a \right) \right] C(k), \\ c_{m1/2} &= \frac{\pi}{2} \left[ \frac{ba\ddot{h}}{V^2} - \frac{b^2}{V^2} \left( \frac{1}{8} + a^2 \right) \ddot{\alpha} \right] \\ &\quad + \pi \left( a + \frac{1}{2} \right) \left[ \frac{\dot{h}}{V} + \alpha + b \left( \frac{1}{2} - a \right) \frac{\dot{\alpha}}{V} \right] C(k) \\ &\quad - \frac{\pi}{2} \left[ \left( \frac{1}{2} - a \right) \frac{b\dot{\alpha}}{V} \right], \end{aligned} \quad (37)$$

where  $a$  is the pitch axis location relative to the midchord of the airfoil, measured in terms of semichord and  $C(k) = F(k) + iG(k)$  is the complex transfer function (known as Theodorsen's function) which accounts for the effects of the shed wake on the unsteady airloads:

$$\begin{aligned} C(k) &= \frac{H_1^{(2)}(k)}{H_1^{(2)}(k) + i \cdot H_0^{(2)}(k)} \\ &= \frac{J_1(J_1 + J_0) + Y_1(Y_1 - J_0)}{(J_1 + Y_0)^2 + (Y_0 - J_1)^2} \\ &\quad + i \frac{Y_1 Y_0 + J_1 J_0}{(J_1 + Y_0)^2 + (Y_0 - J_1)^2} \end{aligned} \quad (38)$$

with  $J_0, J_1, Y_0,$  and  $Y_1$  being Bessel functions of the first and second kinds, respectively (Figure 8).

The Hankel functions in above expression are

$$\begin{aligned} H_0^{(2)} &= J_0 - i \cdot Y_0, \\ H_1^{(2)} &= J_1 - i \cdot Y_1. \end{aligned} \quad (39)$$

The real and imaginary parts of  $C(k)$  function are plotted in Figure 9.

It could be appreciated that  $C(k)$  function serves to introduce an amplitude reduction and phase lag effect on the circulatory part of the lift response compared to the result obtained under quasi-steady conditions [11].

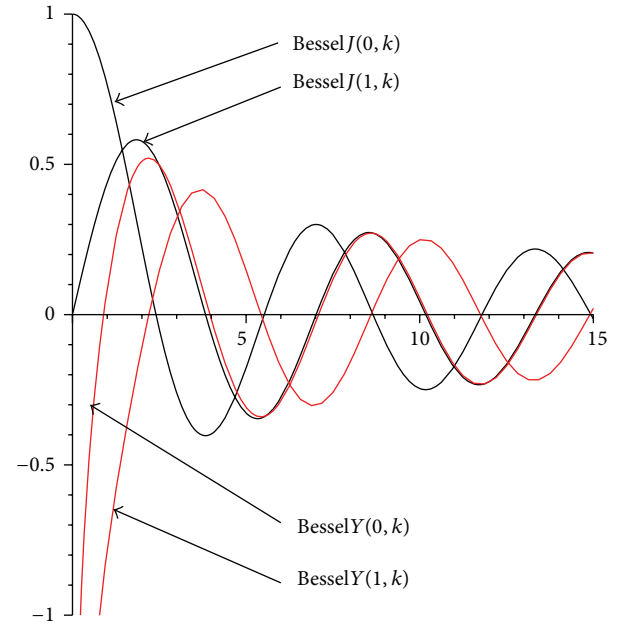


FIGURE 8: Bessel functions.

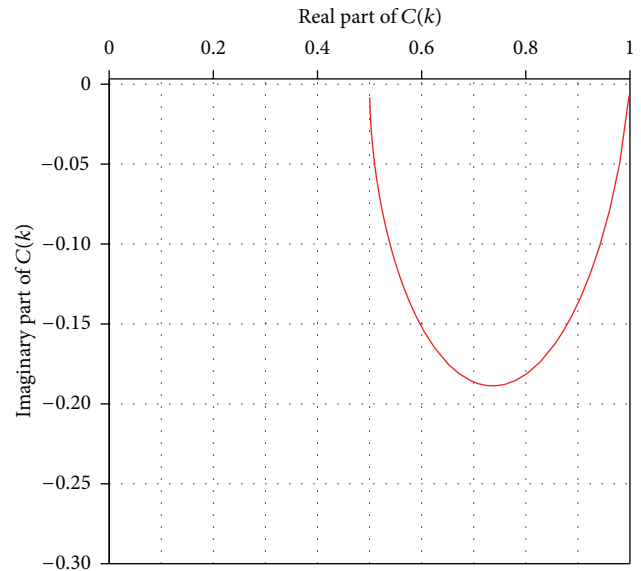


FIGURE 9: Theodorsen's function.

This effect can be seen if a pure oscillatory variation in angle of attack is considered, that is,  $\alpha = \bar{\alpha} e^{i\omega t}$ , so the circulatory part of the airfoil lift coefficient is given by

$$c_l = 2\pi \bar{\alpha} C(k) = 2\pi \bar{\alpha} [F(k) + iG(k)]. \quad (40)$$

For  $k = 0$ , the steady-state lift behavior is obtained; that is,  $c_l$  is linearly proportional to  $\alpha$ . As  $k$  is increased, the lift plots develop into hysteresis loops, and these loops rotate such that the amplitude of the lift response (half of the peak-to-peak value) decreases with increasing reduced frequency.

These loops are circumvented in a counterclockwise direction such that the lift is lower than the steady value, when

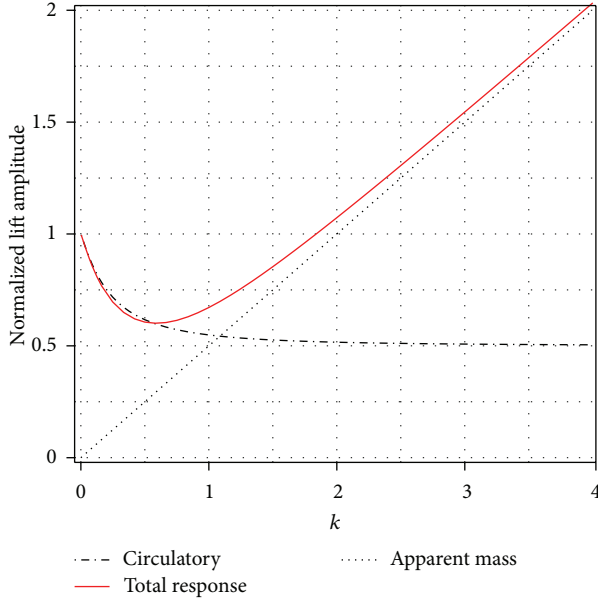


FIGURE 10: Normalized lift amplitude.

$\alpha$  is decreasing with time (i.e., there is a phase lag). For infinite reduced frequency, the circulatory part of the lift amplitude is half that at  $k = 0$ , and there is no phase lag angle.

## 5. Pure Angle of Attack Oscillations

For a harmonic variation in  $\alpha$ , that is,  $\alpha = \bar{\alpha}e^{i\omega t}$ , the lift is

$$L = 2\pi\rho V^2 b \left[ C(k) + \frac{1}{2}i\frac{\omega b}{V} \right] \bar{\alpha}e^{i\omega t} \quad (41)$$

or, in terms of the lift coefficient, the result is

$$c_l = \frac{L}{\rho V^2 b} = [2\pi(F + iG) + i\pi k] \bar{\alpha}e^{i\omega t}. \quad (42)$$

The term inside the square brackets can be considered the lift transfer function, which accounts for the difference between the unsteady and quasi-steady airloads.

The first term inside the brackets is the circulatory term, and the second term is the apparent mass contribution, which is proportional to the reduced frequency and leads the forcing by a phase angle of  $\pi/2$ . The noncirculatory or apparent mass terms arise from the nonsteady term of the velocity potential and account for the pressure forces required to accelerate the fluid in the vicinity of the airfoil.

The normalized lift amplitude is

$$\frac{c_l}{2\pi\alpha} = (F + iG) + i\frac{k}{2}. \quad (43)$$

The normalized lift amplitude and phase of lift for pure angle of attack oscillations are presented in Figures 10 and 11, where the significance of the apparent mass contribution to both the amplitude and phase can be appreciated.

At lower values of reduced frequency, the circulatory terms dominate the solution. At higher values of reduced frequency, the apparent mass forces dominate.

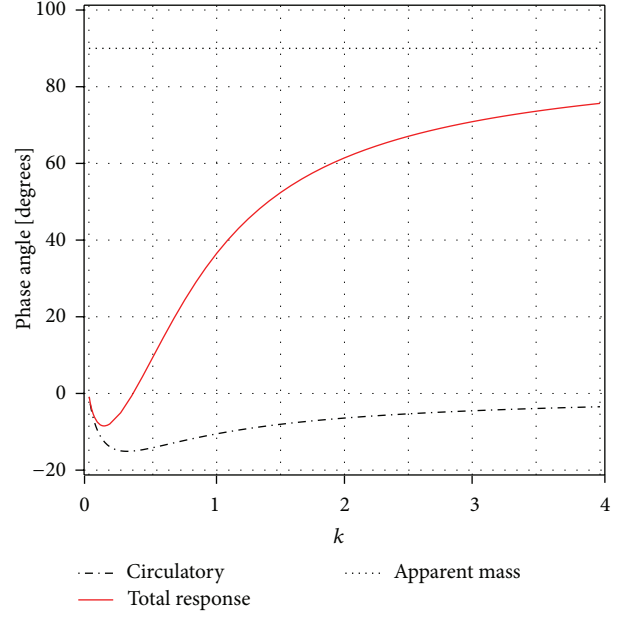


FIGURE 11: Phase angle.

## 6. Pure Plunging Oscillations

For a harmonic plunging motion such as that contributed by blade flapping, the forcing is  $h = \bar{h}e^{i\omega t}$  so that  $\dot{h} = i\omega\bar{h}e^{i\omega t}$  and  $\ddot{h} = -\omega^2\bar{h}e^{i\omega t}$ . Substituting into the expression for the lift and solving for the lift coefficient, it gives

$$c_l = [2\pi k(iF - G) - \pi k^2] \frac{\bar{h}}{b} e^{i\omega t}. \quad (44)$$

The complete term inside the square brackets can be considered as the lift transfer function [12]. The circulatory part of the lift response leads the forcing displacement  $h$  by a phase angle of  $\pi/2$ . Also, the apparent mass force leads the circulatory part of the response by a phase angle of  $\pi/2$  or the forcing by a phase angle of  $\pi$ . The corresponding pitching moment about midchord for this case is

$$c_{m1/2} = \left(\frac{\pi}{4}\right) k^2 \frac{\bar{h}}{b} e^{i\omega t}. \quad (45)$$

## 7. Pitching Oscillations

For harmonic pitch oscillations, additional terms involving pitch rate  $\dot{\alpha}$  appear in the equations for the aerodynamic response. The forcing is given by  $\alpha = \bar{\alpha}e^{i\omega t}$  and the pitch rate by  $\dot{\alpha} = i\omega\bar{\alpha}e^{i\omega t}$ . In this case, the lift coefficient is

$$c_l = 2\pi [F(1 + ik) + G(i - k)] \bar{\alpha}e^{i\omega t} + \pi k \left(i - \frac{k}{2}\right) \bar{\alpha}e^{i\omega t}. \quad (46)$$

The lift amplitude initially decreases with increasing  $k$  because of the effects of the shed wake; and then, for  $k > 0.5$ , it begins to increase, as the apparent mass forces begin to

dominate the airloads. This is also shown by the phase angle, which exhibits an increasing lead for  $k > 0.3$ .

Von Karman and Sear analyzed the problem of a thin airfoil moving through a sinusoidal vertical gust field, where the gust can be considered as an upwash velocity that is uniformly convected by the free stream. The forcing function in this case is

$$w_g(x, t) = \sin\left(\omega_g t - \frac{\omega_g x}{V}\right), \quad (47)$$

where  $\omega_g$  is the gust frequency. If the gust is referenced to the airfoil leading edge, then  $x = 0$  and  $w_g(x, t)$  becomes  $w_g(x, t) = \sin(\omega_g t)$ , and if the gust is referenced to the midchord, then  $x = b = c/2$  and

$$\frac{\omega_g x}{V} = \frac{\omega_g (c/2)}{V} = \frac{\omega_g c}{2V} = k_g. \quad (48)$$

Therefore,  $w_g(t) = \sin(\omega_g t) \cdot \cos(k_g) - \sin(k_g) \cdot \cos(\omega_g t)$ , which is equivalent to a phase shift. In this case, the lift coefficient can be written as

$$c_l = 2\pi \left(\frac{w_0}{V}\right) S(k_g), \quad (49)$$

where  $S(k_g)$  is known as Sears function and the gust encounter frequency,  $k_g$ , is given by

$$k_g = \frac{2\pi V}{\lambda_g}, \quad (50)$$

and  $\lambda_g$  is the wavelength of the gust.

In terms of Bessel functions, Sears's function is given by

$$S(k_g) = [J_0(k_g) - iJ_1(k_g)] C(k_g) + iJ_1(k_g). \quad (51)$$

The terms of real and imaginary parts are

$$\begin{aligned} \text{Real } S(k_g) &= F(k_g) \cdot J_0(k_g) + G(k_g) \cdot J_1(k_g), \\ \text{Im } S(k_g) &= G(k_g) \cdot J_0(k_g) - F(k_g) \cdot J_1(k_g) + J_1(k_g). \end{aligned} \quad (52)$$

If the gust is referenced to the leading edge of the airfoil, the function will be called  $S'$  and can be written as

$$\begin{aligned} \text{Real } S'(k_g) &= \text{Real } S(k_g) \cdot \cos(k_g) \\ &\quad + \text{Im } S(k_g) \cdot \sin(k_g), \\ \text{Im } S'(k_g) &= -\text{Real } S(k_g) \cdot \sin(k_g) \\ &\quad + \text{Im } S(k_g) \cdot \cos(k_g). \end{aligned} \quad (53)$$

The two results are plotted in Figure 12. The peculiar spiral shape of the  $S$  transfer function arises only when the gust front is referenced to the midchord of the airfoil.

The kinematics of the pitching and plunging airfoil of a typical blade element is the resultant of a combination of forcing from collective and cyclic blade pitch, twist angle,

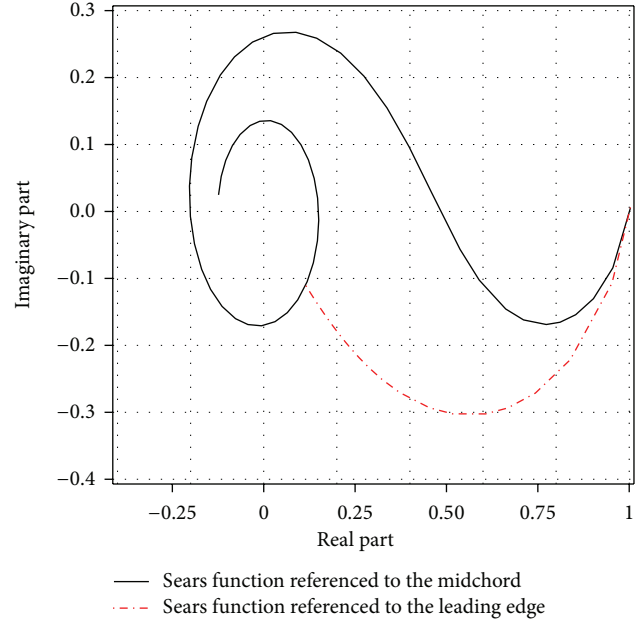


FIGURE 12: Sears function.

elastic torsion, blade flapping velocity, and elastic bending. At low angles of attack with fully attached flow, the various sources of unsteady effects manifest primarily as moderate amplitude and phase variations relative to the quasi-steady airloads. At higher angles of attack when time-dependent flow separation from the airfoil may be involved, the dynamic stall may occur. The amplitude and phase effects produced by the stalled airloads can lead to various aeroelastic problems on the helicopter rotor that may limit its performance. The need to control the aerodynamic forces on the rotor requires that the pitch of each blade be changed individually as the blades rotate about the shaft.

## 8. Summary

The first flap frequency of a helicopter rigid blade is about  $1.05 \Omega$ , then the reduced frequency at the 75% radius location is  $k = 0.7c/R$ . For a blade aspect ratio  $R/c > 10$ , the reduced frequency is in excess of 0.07, which is in the unsteady range. In the case of the first elastic torsion mode, which is typically about  $3 \div 4\Omega$  at the blade tip, the reduced frequency is in excess of 0.2. At these reduced frequencies, there is a significant amplitude and phasing introduced into the airloads by the effects of the unsteady aerodynamics.

When a wing's angle of attack is increased rapidly, it can momentarily generate a higher maximum lift coefficient than it could if the angle of attack was increased slowly. This overshoot can be related to the change in angle of attack during the time required for the air to travel one chord length. The dynamic overshoot is attributed to two effects (for the airfoils that stall first at the leading edge): the delay in the separation of the boundary layer and the momentary existence of a vortex shed at the leading edge after the boundary layer does separate. The delay in separation corresponds to the finite

time required for the aft edge of the separation bubble to move forward to its bursting position. On the other hands, the airfoil can generate high lift as a result of a vortex that is shed at the leading edge at the instant of stall. The vortex travels back over the top of the airfoil carrying with it a low pressure wave that accounts for the very large lift coefficient. Airfoils that stall first at the trailing edge also exhibit a dynamic overshoot but considerably less than those airfoils that have leading edge stall.

## References

- [1] J. G. Leishman, *Principles of Helicopter Aerodynamics*, Cambridge University Press, 2007.
- [2] J. Seddon and S. Newman, *Basic Helicopter Aerodynamics*, AIAA Education Series, 2001.
- [3] M. A. Ashraf, J. Young, and I. C. S. Lai, "Oscillation frequency and amplitude effects on plunging airfoil propulsion and flow periodicity," *The American Institute of Aeronautics and Astronautics Journal*, pp. 2308–2324, 2012.
- [4] R. Prouty, *Helicopter Performance, Stability and Control*, Krieger, Gainesville, Fla, USA, 2002.
- [5] P. D. Gareth, *Helicopter Flight Dynamics*, AIAA Education Series, 2007.
- [6] B. J. Lee and M. S. Liou, "Unsteady adjoint approach for design optimization of flapping airfoils," *The American Institute of Aeronautics and Astronautics Journal*, pp. 2460–2491, 2012.
- [7] K. Karamcheti, *Principles of Ideal-Fluid Aerodynamics*, Krieger, Gainesville, Fla, USA, 1966.
- [8] T. Theodorsen, "General theory of aerodynamic instability and the mechanism of flutter," Tech. Rep. 496, NACA, 1934.
- [9] I. E. Garrick, "On some reciprocal relations in the theory of non-stationary flows," NACA Report 629, 1938.
- [10] J. Katz and A. Plotkin, *Low Speed Aerodynamics*, Cambridge University Press, 2010.
- [11] C. Rotaru, I. Circiu, and M. Boscoianu, "Computational methods for the aerodynamic design," *Review of the Air Force Academy*, vol. 2, no. 17, pp. 43–48, 2010.
- [12] C. Rotaru and V. Jaulin, "Numerical simulations of Helicopter rotor blade airloads," *MTA Review*, vol. 22, no. 2, pp. 81–90, 2012.

## Research Article

# The Use of Fractional Order Derivative to Predict the Groundwater Flow

Abdon Atangana<sup>1</sup> and Necdet Bildik<sup>2</sup>

<sup>1</sup> *Institute for Groundwater Studies, Faculty of Natural and Agricultural Sciences, University of the Free State, P.O. Box 9300, Bloemfontein, South Africa*

<sup>2</sup> *Department of Mathematics, Faculty of Art & Sciences, Celal Bayar University, Muradiye Campus, 45047 Manisa, Turkey*

Correspondence should be addressed to Abdon Atangana; [abdonatangana@yahoo.fr](mailto:abdonatangana@yahoo.fr)

Received 2 July 2013; Revised 27 August 2013; Accepted 3 September 2013

Academic Editor: Tirivanhu Chinyoka

Copyright © 2013 A. Atangana and N. Bildik. This is an open access article distributed under the Creative Commons Attribution License, which permits unrestricted use, distribution, and reproduction in any medium, provided the original work is properly cited.

The aim of this work was to convert the Thiem and the Theis groundwater flow equation to the time-fractional groundwater flow model. We first derived the analytical solution of the Theim time-fractional groundwater flow equation in terms of the generalized Wright function. We presented some properties of the Laplace-Carson transform. We derived the analytical solution of the Theis-time-fractional groundwater flow equation (TFGFE) via the Laplace-Carson transform method. We introduced the generalized exponential integral, as solution of the TFGFE. This solution is in perfect agreement with the data observed from the pumping test performed by the Institute for Groundwater Study on one of its borehole settled on the test site of the University of the Free State. The test consisted of the pumping of the borehole at the constant discharge rate  $Q$  and monitoring the piezometric head for 350 minutes.

## 1. Introduction

Groundwater problem is perhaps one of the most difficult real-world problems to be modelled into mathematical formulation. To model this problem accurately, one must know precisely the behavior of the medium through which the water is moving. However, this medium through which the flow occurs can change from one point to another, also from one period to another. For example, the hydraulic conductivity of an aquifer can differ from one direction to another. Several scholars have intensively tried to propose a better model that can be used to predict the movement of water through the aquifer. However, their results still present some lacks. Recently, It was revealed that real problems modelled via fractional order derivative present better results when matching their mathematical representation with experimental data. To test this, Botha and Cloot [1] presented some good results by generalizing the groundwater flow equation to the concept of fractional order derivatives. In the same line of ideas, Atangana [2] examined an approximate solution of the generalized groundwater flow equation via

the Frobenius method. The results obtained from his investigation showed better prediction. Recently, Atangana and Botha further extended the fractional groundwater equation to the concept of the fractional-variation order groundwater [3]. They presented the stability and the convergence of the numerical scheme via Crank-Nicolson method. Up to now, there is no approximate or exact analytical mathematical expression that can be used to describe the solution of the fractional groundwater flow equation. Therefore, one of the purposes of this work is to present some analytical mathematical expression than can be used as approximate solution of the time-fractional groundwater flow equation.

An aquifer test (or a pumping test) is conducted to evaluate an aquifer by “stimulating” the aquifer through constant pumping and observing the aquifer’s “response” (drawdown) in observation wells. Aquifer testing is a common tool that hydrogeologists use to characterize a system of aquifers, aquitards, and flow system boundaries. Aquifer tests are typically interpreted by using an analytical model of aquifer flow (the most fundamental being the Theis solution) to

match the data observed in the real-world then assuming that the parameters from the idealized model apply to the real-world aquifer. In more complex cases, a numerical model may be used to analyze the results of an aquifer test, but adding complexity does not ensure better results. For the most part frequently, an aquifer assessment is carried out by propelling water out from one borehole at a fixed speed and for as a minimum of 24 hours at the same time as cautiously evaluating the water levels in the observed borehole. When water is pumped from the pumping well, the pressure in the aquifer that feeds that well declines. This decline in pressure will show up as drawdown (change in hydraulic head) in an observation well. Drawdown decreases with radial distance from the pumping well and drawdown increases with the length of time that the pumping continues. The aquifer characteristics which are evaluated by most aquifer tests are [4, 5] as follows.

- (i) The hydraulic conductivity is the rate of flow of water through a unit cross sectional area of an aquifer at a unit hydraulic gradient. In English units the rate of flow is in gallons per day per square foot of cross sectional area.
- (ii) Specific storage or storativity being a measure of the amount of water a confined aquifer will give up for a certain change in head.
- (iii) The transmissivity is the rate at which water is transmitted through a unit thickness of an aquifer under a unit hydraulic gradient. It is equal to the hydraulic conductivity times the thickness of an aquifer.

The rest of this paper has been presented as follows. In Section 1, we presented the background of the fractional order derivative. We derived the analytical solution of the Thiem fractional groundwater flow equation in Section 3. In Section 4, we presented the derivation of the Theis fractional groundwater flow via the Laplace-Carson transform method. We presented an alternative analytical solution of the Theis fractional groundwater flow equation in terms of the generalized exponential integral in Section 5. The numerical comparisons with experimental data are presented in Section 6 and the conclusion is in Section 7. We will start with the background of the fractional derivative.

## 2. Background of the Fractional Order Derivative

There exists the vast literature on different definitions of fractional derivatives. The most popular ones are the Riemann-Liouville and the Caputo derivatives [6–11]. Caputo's definition has the form of

$$D_x^\alpha (f(x)) = \frac{1}{\Gamma(n-\alpha)} \frac{d^n}{dx^n} \times \int_0^x (x-t)^{n-\alpha-1} f(t) dt, \quad n-1 \leq \alpha \leq n. \quad (1)$$

For the case of the Caputo fractional order derivative, we have the following definition:

$$D_x^\alpha (f(x)) = \frac{1}{\Gamma(n-\alpha)} \times \int_0^x (x-t)^{n-\alpha-1} \frac{d^n}{dx^n} f(t) dt, \quad n-1 \leq \alpha \leq n. \quad (2)$$

Each of the previous fractional order derivatives presents some advantages and disadvantages [6–10]. The Riemann-Liouville derivative of a constant is not zero while Caputo derivative of a constant is zero but demands higher conditions of regularity for differentiability [6–10]: to compute the fractional derivative of a function in the Caputo sense, we must first calculate its derivative [11]. Caputo derivatives are defined only for differentiable functions while functions that have no first-order derivative might have fractional derivatives of all orders less than one in the Riemann-Liouville sense [12, 13]. Guy Jumarie has recently modified the Riemann-Liouville derivative (see [14])

$$D_x^\alpha (f(x)) = \frac{1}{\Gamma(n-\alpha)} \frac{d^n}{dx^n} \times \int_0^x (x-t)^{n-\alpha-1} \{f(t) - f(0)\} dt. \quad (3)$$

The Caputo fractional derivative will be considered in this work due to the applicability of the Caputo derivative in real-world problems [15].

## 3. Thiem' Groundwater Flow Equation

The Thiem fractional groundwater flow equation is an ordinary differential equation given in the following. The equation describes the change in level of water as function of distance during the pumping test [5]:

$$D_{rr}^\alpha \Phi(r) + \frac{1}{r} \Phi(r) = 0, \quad 1 < \alpha \leq 2. \quad (4)$$

Subject to the initial condition,  $Q = 2\pi T D_r(\Phi(r_b))$ .

We will make use of the Laplace transform to derive analytical solution of (4). Thus, multiplying on both sides of (4) by  $r$  and secondly applying the Laplace transform, we obtain the following expression:

$$\frac{d[L(\Phi)(s)]}{ds} + \left(\frac{\alpha}{s} + \frac{1}{s^\alpha}\right) (L(\Phi)(s)) = \sum_{m=2}^l d_m (m-1) s^{m-2-\alpha}, \quad (5)$$

where  $d_m = D_{0^+}^{\alpha-m} \Phi(0^+)$  ( $m = 2, \dots, l$ ). Now, one can derive the solution of the ordinary order differential equation with respect to the Laplace transform of  $\Theta(s) = L(\Phi(r))$ :

$$\Theta(s) = s^{-\alpha} \exp\left[-\frac{s^{1-\alpha}}{1-\alpha}\right] \times \left[ a_1 + \sum_{m=2}^l d_m (m-1) \int s^{m-2} \exp\left[-\frac{s^{1-\alpha}}{1-\alpha}\right] ds \right], \quad (6)$$

with  $a_1$  an arbitrary real constant that will be obtained via the initial condition. We next expand the exponential function in the integrand in a series, and using term-by-term integration, we arrive at the following expression:

$$\Theta(s) = c\Theta_1(s) + \sum_{m=2}^l d_m(m-1)\Theta_m^*(s) \quad (7)$$

with, of course,

$$\Theta_1(s) = s^{-\alpha} \exp\left[-\frac{s^{1-\alpha}}{1-\alpha}\right],$$

$$\Theta_m^*(s) = s^{-\alpha} \exp\left[\frac{s^{1-\alpha}}{\alpha-1}\right] \sum_{j=0}^{\infty} \left(\frac{1}{1-\alpha}\right)^j \frac{s^{(1-\alpha)j+m-1}}{[(1-\alpha)j+m-1]j!}. \quad (8)$$

Now, applying the inverse Laplace transform on  $\Theta_1(s)$  and using the fact that

$$s^{-[\alpha+(\alpha-1)j]} = L\left[\frac{r^{\alpha+(\alpha-1)j-1}}{\Gamma(\alpha+(\alpha-1)j)}\right] \quad (9)$$

we obtain

$$\Phi_1(r) = r^{\alpha-1} {}_0\Psi_1\left[\left(\alpha, \alpha-1\right) \mid \frac{r^{\alpha-1}}{\alpha-1}\right] \quad (10)$$

with  ${}_0\Psi_1[\cdot]$  the generalized Wright function [16] for  $p = 1$  and  $q = 2$ . We next expand the exponential function  $\exp[-s^{1-\alpha}/(1-\alpha)]$  in power series; multiplying the resulting two series; in addition of this if we consider the number  $b_k(\alpha, m)$  defined for  $\alpha > 0, m = 2, \dots, l, (\alpha \neq (p+m-1)/p, p \notin \mathbb{N})$  and  $k \in \mathbb{N}_0$ ,

$$b_k(\alpha, m) = \sum_{p,j=0,\dots,k, p+j=k}^l \frac{(-1)^q}{p!j!(1-\alpha)q+m-1}. \quad (11)$$

The previous family of number possesses satisfies the following recursive formula:

$$\frac{b_k(\alpha, m)}{b_{k+1}(\alpha, m)} = \frac{\alpha-m}{\alpha-1} + k, \quad (12)$$

which produces the explicit expression for  $b_k(\alpha, m)$  in the form of

$$b_k(\alpha, m) = \frac{\Gamma[(\alpha-m)/(\alpha-1)]}{(m-1)\Gamma[(\alpha-m)/(\alpha-1)+k]}, \quad k \in \mathbb{N}_0. \quad (13)$$

Now, having the previous expression on hand, we can derive that

$$\begin{aligned} \Theta_m^*(s) &= s^{m-\alpha-1} \left( \sum_{j=0}^{\infty} \left(\frac{1}{1-\alpha}\right)^j \frac{s^{(1-\alpha)j}}{j!} \right) \\ &\times \left( \sum_{p=0}^{\infty} \left(\frac{1}{1-\alpha}\right)^p \frac{(-1)^p}{[(1-\alpha)p+m-1]p!} s^{(1-\alpha)p} \right) \\ &= \sum_{k=0}^{\infty} b_k(\alpha, m) \left(\frac{1}{1-\alpha}\right)^k s^{(1-\alpha)k+m-\alpha-1} \quad (m=2, \dots, l). \end{aligned} \quad (14)$$

However, remembering (9) with  $\beta = (\alpha-1)k + \alpha + 1 - m$ , we can further derive the following expression for  $\Phi_m^*(r)$  as

$$\begin{aligned} \Phi_m^*(r) &= \sum_{k=0}^{\infty} b_k(\alpha, m) \left(\frac{1}{1-\alpha}\right)^k \\ &\times \frac{\Gamma(k+1)}{\Gamma[\alpha+1-m+(\alpha-1)k]} \frac{r^{(\alpha-1)k+\alpha-m}}{k!} \end{aligned} \quad (15)$$

or in the simplified version we have

$$\Phi_m^*(r) = \frac{\Gamma[(\alpha-m)/(\alpha-1)]}{(m-1)} \Phi_m(r), \quad (16)$$

where

$$\begin{aligned} \Phi_m(r) &= r^{\alpha-m} {}_1\Psi_2 \\ &\times \left[ \begin{matrix} (1, 1) \\ (\alpha+1-m, \alpha-1), \left(\frac{\alpha-m}{\alpha-1}, 1\right) \end{matrix} \mid \frac{r^{\alpha-1}}{\alpha-1} \right]. \end{aligned} \quad (17)$$

It follows that the solution of the fractional-Thiem groundwater flow equation is in the form of

$$\begin{aligned} \Phi(r) &= a_1 r^{\alpha-1} {}_0\Psi_1\left[\left(\alpha, \alpha-1\right) \mid \frac{r^{\alpha-1}}{\alpha-1}\right] \\ &+ a_2 \sum_{m=2}^l b_m(m-1) \frac{\Gamma[(\alpha-m)/(\alpha-1)]}{(m-1)} r^{\alpha-m} \\ &\times {}_1\Psi_2\left[\begin{matrix} (1, 1) \\ (\alpha+1-m, \alpha-1), \left(\frac{\alpha-m}{\alpha-1}, 1\right) \end{matrix} \mid \frac{r^{\alpha-1}}{\alpha-1}\right]. \end{aligned} \quad (18)$$

In our case  $l = 2$ .

### 4. Time-Fractional Theis Groundwater Flow Equation

The easiest sweeping statement of subsurface water flow equation, which while we are on the subject is in addition in harmony in the midst of the real physics of the observed fact, is to presume that water level is not in a balanced state but momentary state. Theis (1935) [17] was the first to develop a formula for unsteady-state flow that introduces the time factor and the storativity. He noted that when a well-penetrating extensive confined aquifer is pumped at a constant rate, the influence of the discharge extends outward with time. The rate of decline of head, multiplied by the storativity and summed over the area of influence, equals the discharge. The unsteady-state (or Theis) equation, which was derived from the analogy between the flow of groundwater and the conduction of heat, is perhaps the most widely used partial differential equation in groundwater investigations:

$$SD_t \Phi(r, t) = TD_{rr} \Phi(r, t) + \frac{1}{r} D_r \Phi(r, t). \quad (19)$$

The aforementioned equation is classified under parabolic equation. To include explicitly the variability of the medium through which the flow takes place, the standard version of the partial derivative respect to time is replaced here with time-fractional order derivative to obtain

$$SD_t^\alpha \Phi(r, t) = TD_{rr} \Phi(r, t) + \frac{1}{r} D_r \Phi(r, t), \quad 0 < \alpha \leq 1 \quad (20)$$

with initial condition  $\Phi(r, 0) = 0$  and boundary condition  $\lim_{r \rightarrow \infty} \Phi(r, t) = 0$ ,  $Q = 2\pi T \partial r \Phi(r_b, t)$ , here  $T$  is the transmissivity of the aquifer,  $r_b$  is the ratio of the borehole, and  $Q$  is the discharge rate, or the rate at which the water is being taken out of the aquifer.

Some few integral transform operators have been intensively used to solve some kind of ordinary and partial differential equations. See, for instance, the Fourier transform, the Laplace transform, the Mellin transform [18], and the Sumudu transform [19–22]. Beside these integral operators, there exists a similar operators called the Laplace-Carson transform [23]; this operator has been neglected. However, this operator has some properties that can be used to solve a kind of ODE, PDE, FODE, and FPDE. The aim of this section is therefore devoted to the discussion underpinning the definition, properties of the Laplace-Carson transform, and its application to the fractional groundwater flow equation. We shall start with the definition and properties.

*Definition 1.* Let  $f(x)$  be a continuous function over an open interval  $(0, \infty)$  such that its Laplace transform is  $n$  time differentiable; then the Laplace-Carson transform  $f$  is defined as follows:

$$L_c(s) = L_c[f(x)](s) = \int_0^\infty x e^{-xs} f(x) dx \quad (21)$$

and the inverse Laplace-Carson transform is defined as

$$f(x) = L_c^{-1}[L_c[f(x)]] \\ = \frac{-1}{2\pi i} \int_{\alpha-i\infty}^{\alpha+i\infty} e^{sx} \left[ -1 \left[ \int_0^s L_c(t) + F(0) \right] \right] ds, \quad (22)$$

where  $F(s)$  is the Laplace transform of  $f(x)$ . Before we continue, we shall prove that the previous definition is indeed the inverse inverse Laplace-Carson. In fact, from the definition of inverse Laplace-Carson of a function  $f(x)$ , we have that

$$L_c(s) = L_c[f(x)](s) = \int_0^\infty x e^{-xs} f(x) dx = -\frac{dF(s)}{ds}; \quad (23)$$

thus,

$$\int_0^s L_c(t) dt = -[F(s) - F(0)]. \quad (24)$$

It follows that

$$\begin{aligned} & \frac{-1}{2\pi i} \int_{\alpha-i\infty}^{\alpha+i\infty} e^{sx} \left[ -1 \left[ \int_0^s L_c(t) dt + F(0) \right] \right] ds \\ &= \frac{-1}{2\pi i} \int_{\alpha-i\infty}^{\alpha+i\infty} e^{sx} [-F(s)] ds, \\ L_c^{-1}[L_c[f(x)]] &= \frac{(-1)^2}{2\pi i} \int_{\alpha-i\infty}^{\alpha+i\infty} e^{sx} [[F(s)]] ds = f(x). \end{aligned} \quad (25)$$

Therefore, the inverse inverse Laplace-Carson is well defined.

## 5. Some Properties of Laplace-Carson Transform

In this part of the section, we consider some of the properties of the inverse Laplace-Carson that will enable us to find further transform pairs  $\{f(x), L_c(s)\}$  without having to compute and consider the following:

$$(I) L_c[s + c] = M_n[e^{-cx} f(x)] \quad (26)$$

$$(II) L_c[f(ax)](s) = \frac{1}{a} L_c\left[\frac{s}{a}\right] \quad (27)$$

$$(III) \int_{\alpha-i\infty}^{\alpha+i\infty} e^{sx} L_c(s) ds = xf(x) \quad (28)$$

$$(IV) L_c[af(x) + bg(x)](s) \\ = [aL_c(f(x)) + bL_c(g(x))](s) \quad (29)$$

$$(V) L_c\left[\frac{f(x)}{x}\right](s) = L[f(x)](s) \quad (30)$$

$$(VI) L_c[f(x) * h(x)](s) \\ = -\left[ \frac{dF(s)}{ds} G(s) + \frac{dG(s)}{ds} F(s) \right] \quad (31)$$

$$(VII) L_c\left[\frac{d^n f(x)}{dx^n}\right](s) \\ = -\left[ ns^{n-1} F(s) + s^n \frac{dF(s)}{ds} \right. \\ \left. - \sum_{k=0}^{n-2} (n-k-1) s^{n-k-2} \frac{d^k f(0)}{dx^k} \right]. \quad (32)$$

Let us verify the previous properties. We shall start with (I), by definition, we have the following:

$$\begin{aligned} L_c[e^{-cx} f(x)] &= \int_0^\infty [x e^{-cx} e^{-sx} f(x)] dx \\ &= \int_0^\infty [x e^{-(c+s)x} f(x)] dx = L_c[s + c] \end{aligned} \quad (33)$$

and then the first property is verified.

For (II) we have the following by definition:

$$L_c [f(ax)](s) = \int_0^\infty [xe^{-xs} f(ax)] dx = -\frac{d}{ds} [L[f(ax)](s)]. \quad (34)$$

Now, using the property of the Laplace transform  $L[f(ax)](s) = (1/a)F(s/a)$ , we can further obtain

$$L_c [f(ax)](s) = -\frac{d}{ds} \left[ \frac{1}{a} F\left(\frac{s}{a}\right) \right] = \frac{1}{a} (-1) \frac{d}{ds} \left[ F\left(\frac{s}{a}\right) \right] = \frac{1}{a} L_c \left[ \frac{s}{a} \right] \quad (35)$$

and then, the property number (II) is verified.

For number (III), we have the following: Let  $g(x) = xf(x)$ ; then

$$\int_{\alpha-i\infty}^{\alpha+i\infty} e^{sx} L_c(s) ds = \int_{\alpha-i\infty}^{\alpha+i\infty} e^{sx} \left[ \int_0^\infty e^{-xs} xf(x) dx \right] ds = \int_{\alpha-i\infty}^{\alpha+i\infty} e^{sx} \left[ \int_0^\infty e^{-xs} g(x) dx \right] ds. \quad (36)$$

By the theorem of inverse Laplace transform, we obtain

$$\int_{\alpha-i\infty}^{\alpha+i\infty} e^{sx} M_n(s) ds = g(x) = xf(x). \quad (37)$$

Number (IV) and (V) are obvious to be verified. For number (VI), we have the following by definition:

$$L_c [f(x) * h(x)](s) = \int_0^\infty [xe^{-sx} f(x) * h(x)] = -\frac{d}{ds} [L(f(x) * h(x))](s). \quad (38)$$

Now, using the property of Laplace transform of the convolution, we obtain the following:

$$L(f(x) * h(x))(s) = F(s) \cdot G(s) \quad (39)$$

and then, using the property of the derivative for the product of two functions, we obtain

$$L_c [f(x) * h(x)](s) = -\frac{d}{ds} [F(s) \cdot G(s)] = -\left[ \frac{dF(s)}{ds} G(s) + \frac{dG(s)}{ds} F(s) \right]. \quad (40)$$

And then, the property number (VI) is verified.

For number (VII), by definition, we have the following:

$$L_c \left[ \frac{d^n f(x)}{dx^n} \right](s) = \int_0^\infty \left[ xe^{-sx} \frac{d^n f(x)}{dx^n} \right] dx = -\frac{d}{ds} \left[ L \left( \frac{d^n f(x)}{dx^n} \right) (s) \right]. \quad (41)$$

Now, using the property of the Laplace transform,

$$L \left( \frac{d^n f(x)}{dx^n} \right) (s) = s^n F(s) - \sum_{k=0}^{n-1} s^{n-k-1} \frac{d^k f(0)}{dx^k}. \quad (42)$$

Now, deriving the previous expression  $n$ -time, we obtain the following expression:

$$-\frac{d}{ds} \left[ s^n F(s) - \sum_{k=0}^{n-1} s^{n-k-1} \frac{d^k f(0)}{dx^k} \right] = -\left[ ns^{n-1} F(s) + s^n \frac{dF(s)}{ds} - \sum_{k=0}^{n-2} (n-k-1) s^{n-k-2} \frac{d^k f(0)}{dx^k} \right]. \quad (43)$$

This completes the proof of number (VI). We shall now use some properties of the Laplace-Carson transform to solve the fractional groundwater flow equation. To achieve this, we shall start by assuming that the solution of the main equation can be separated as follows:

$$\Phi(r, t) = \Phi_1(t) \Phi_2(r); \quad (44)$$

then, the separated equations become

$${}_0^C D_t^\alpha \Phi_1(t) + \lambda^2 \Phi_1(t) = 0, \quad (45)$$

$$D_{rr} \Phi_2(r) + \frac{1}{r} D_r \Phi_2(r) + \lambda^2 \Phi_2(r) = 0, \quad (46)$$

where  $\lambda$  is the separation constant.

The first equation (45) can be solve directly by applying on both sides the Laplace transform to obtain

$$L(\Phi_1(t)) = \Theta_1(s) = \frac{s^{\alpha-1}}{s^\alpha + \lambda^2}. \quad (47)$$

Using the inverse formula of Laplace transform of two-parameter Mittag-Leffler function, we get

$$\Phi_1(t) = cE_{\alpha,1} \left( -\frac{S}{T} \lambda^2 t^\alpha \right), \quad (48)$$

where the Mittag-Leffler function is defined as follows:

$$E_{\alpha,1}(t) = \sum_{n=0}^{\infty} \frac{t^{\alpha n}}{\Gamma[\alpha n + 1]}. \quad (49)$$

To solve the second equation, we make use of the Laplace-Carson presented earlier, to obtain

$$-D_s \left[ s^2 \Theta_2(s) - s \Phi_2(0) - \frac{d\Phi_2(0)}{dr} \right] + s \Theta_2(s) - \Phi_2(0) - D_s \Theta_2(s) = 0. \quad (50)$$

Deriving, we obtain the following ordinary differential equation:

$$D_s \Theta_2(s) [s^2 + \lambda^2] = -s \Theta_2(s) \quad (51)$$

for which the exact solution is given as

$$\Theta_2(s) = \frac{1}{\sqrt{s^2 + \lambda^2}}. \quad (52)$$

Now applying the inverse Laplace transform operator on both sides in the previous equation, we obtain the following in terms of the Bessel function first kind [24]:

$$\Phi_1(r) = J_0(\lambda r), \quad (53)$$

where the Bessel function first kind is defined as

$$J_0(r) = \sum_{k=0}^{\infty} \frac{(-1)^k}{k!} \frac{1}{\Gamma(k+1)} \left(\frac{r}{2}\right)^{2k}. \quad (54)$$

Therefore, the solution of the fractional groundwater flow equation is given as

$$\Phi(r, t) = c \sum_{n=0}^{\infty} E_{\alpha,1} \left( -\frac{S}{T} \lambda_n^2 t^\alpha \right) J_0(\lambda_n r). \quad (55)$$

Making use of the initial and boundary conditions, we obtain the constant  $c$  to be

$$c = \frac{Q}{4\pi T}. \quad (56)$$

Then,

$$\Phi(r, t) = \frac{Q}{4\pi T} \sum_{n=0}^{\infty} E_{\alpha,1} \left( -\frac{S}{T} \lambda_n^2 t^\alpha \right) J_0(\lambda_n r). \quad (57)$$

We shall present an alternative solution in the next section via the Boltzmann variable method. By using the boundary condition, we can determine the Eigen value of (55).

## 6. An Alternative Derivation of the Time-Fractional Groundwater Equation

In this section, we present an alternative approximate solution of the groundwater flow equation. A method frequently used to derive some kind of parabolic partial differential equations is the so-called Boltzmann transformation [5], defined for an arbitrary  $t_0 < t$  by equation.

$$u_0 = \frac{Sr^2}{4T(t-t_0)}. \quad (58)$$

Let us consider now the following function:

$$\Phi(r, t) = \frac{c}{(t-t_0)} E_{\alpha,1}[-u_0] \quad (59)$$

with  $c$  an arbitrary constant. If we assume that  $r_b$  is the ratio of the borehole from which the water is taken out of the aquifer, then the total volume of the water withdrawn from the aquifer is given by

$$Q_0 \Delta t_0 = 4\pi c T. \quad (60)$$

Hence,

$$\Phi(r, t) = \frac{Q_0 \Delta t_0}{4\pi T(t-t_0)} E_{\alpha,1}[-u_0] \quad (61)$$

is the drawdown that will be observed at a distance,  $r$ , from the pumped borehole after the period  $\Delta t_0$ .

Now suppose that the a previous procedure is repeated  $n$  times; that is, water is withdrawn for a short period of time,  $\Delta t_k$ , at a consecutive times,  $t_{k+1} = t_k + \Delta t_k$ , ( $k = 0, 1, \dots, n$ ). Now, since the fractional groundwater flow equation is linear differential equation, the total drawdown at any time  $t > t_n$  will be given by

$$\Phi(r, t) = \frac{1}{4\pi T} \sum_{k=0}^n \frac{Q_k \Delta t_k}{4\pi T(t-t_k)} E_{\alpha,1}[-u_k]. \quad (62)$$

Therefore, if  $\Delta t \rightarrow 0$ , the definition of the defined integral can be invoked to write

$$\Phi(r, t) = \frac{1}{4\pi T} \int_{t_0}^t \frac{Q(\tau) d\tau}{(t-\tau)} E_{\alpha,1} \left[ -\frac{Sr^2}{4T(t-\tau)} \right] d\tau. \quad (63)$$

However, using the Boltzman variable, we arrive at the following expression:

$$y = \frac{Sr^2}{4T(t-\tau)}, \quad (64)$$

$$\Phi(r, t) = \frac{1}{4\pi T} \int_{t_0}^{\infty} \frac{Q(y)}{y} E_{\alpha,1}[-y] dy.$$

The previous solution will be called the most generalized general solution of fractional groundwater equation. However, this solution can be simplified somewhat under certain conditions. A particularly important solution which arises when  $t_0$  is taken at zero and  $Q(t)$  is a constant independent of time, and then we arrive at

$$\Phi(r, t) = \frac{Q}{4\pi T} \int_u^{\infty} \frac{1}{y} E_{\alpha,1}[-y] dy = \frac{Q}{4\pi T} W_\alpha(u). \quad (65)$$

Here

$$W_\alpha(u) = \int_u^{\infty} \frac{1}{y} E_{\alpha,1}[-y] dy \quad (66)$$

will be called the generalized exponential integral. It is worth pointing out that if alpha is equal to 1, we recover the exact analytical solution of the groundwater flow equation proposed by Theis. Alternative iterations method [8, 11, 20] can be used to derive approximate solutions of these problems.

## 7. Numerical Simulations

In this section, we investigate the behavior of the analytical solutions of the Theim fractional and the Theis fractional groundwater flow equation. We compare the analytical

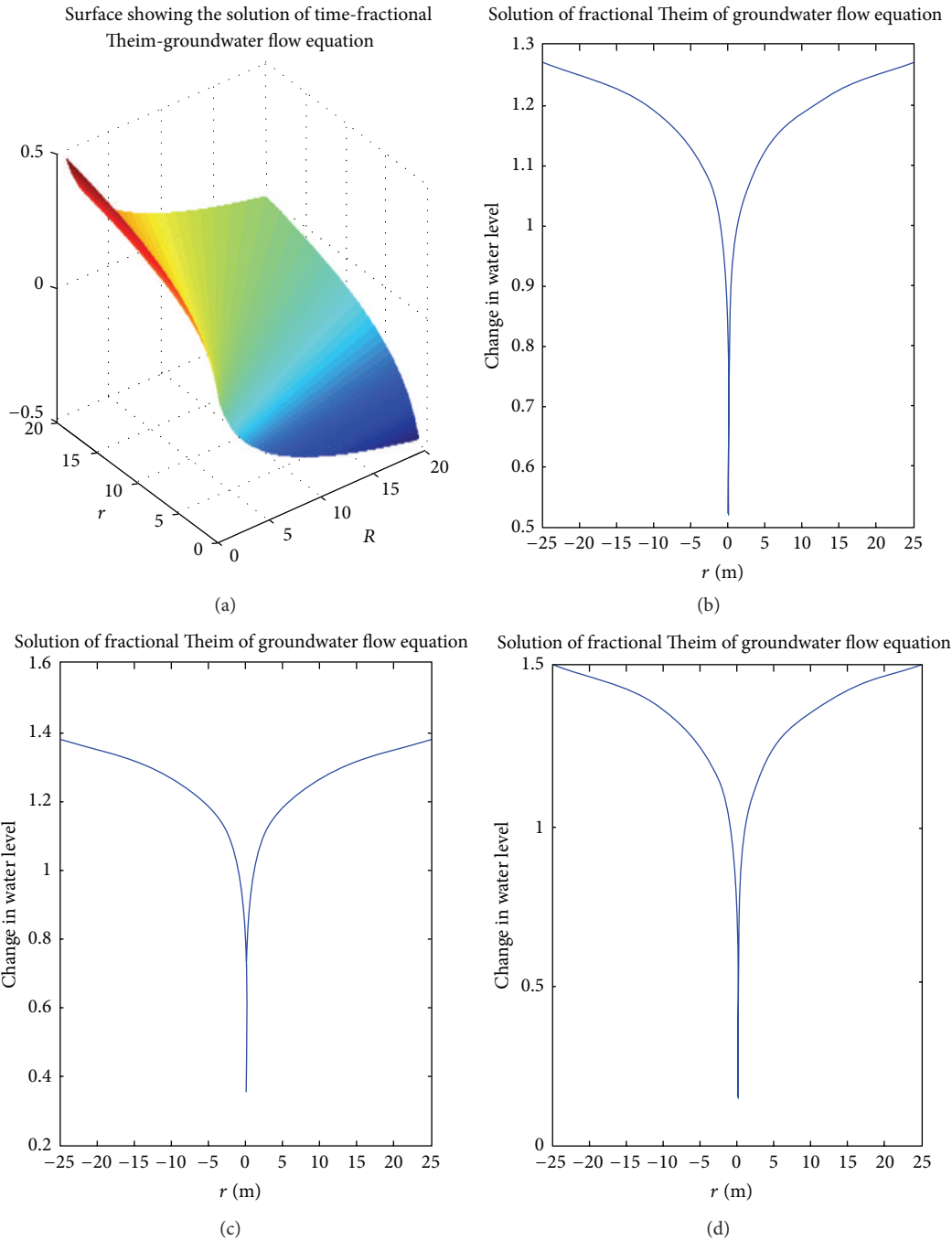


FIGURE 1: Numerical simulation of the Theim-time-fractional order groundwater flow equation, ((a) showing the surface for  $\alpha = 0.95$ ); ((b)  $\alpha = 0.75$ ); ((c)  $\alpha = 0.65$ ) and ((d)  $\alpha = 0.55$ ).

solution with the experimental data from the pumping test obtained from the experimental site of the Institute for Groundwater Studies, the University of the Free State, Bloemfontein Campus, South Africa. We shall start with the simulation of Theim fractional groundwater flow equation. The analytical solution of the main problem was depicted in Figures 1(a), 1(b), 1(c), and 1(d). It is worth to mention from the figures that the order of the derivative plays an important role in the simulation.

We shall present the numerical solution for the Theis-time-fractional groundwater flow equation for a fixed distance. The analytical solution of the main problem was depicted in Figures 2(a), 2(b), 2(c), and 2(d).

We shall present in Figure 3 the comparison of the analytical solution of the Theis-time-fractional groundwater flow equation, with the experimental data from the pumping test performed by the Institute for Groundwater Study on one of its borehole settled on the test site of the University of the

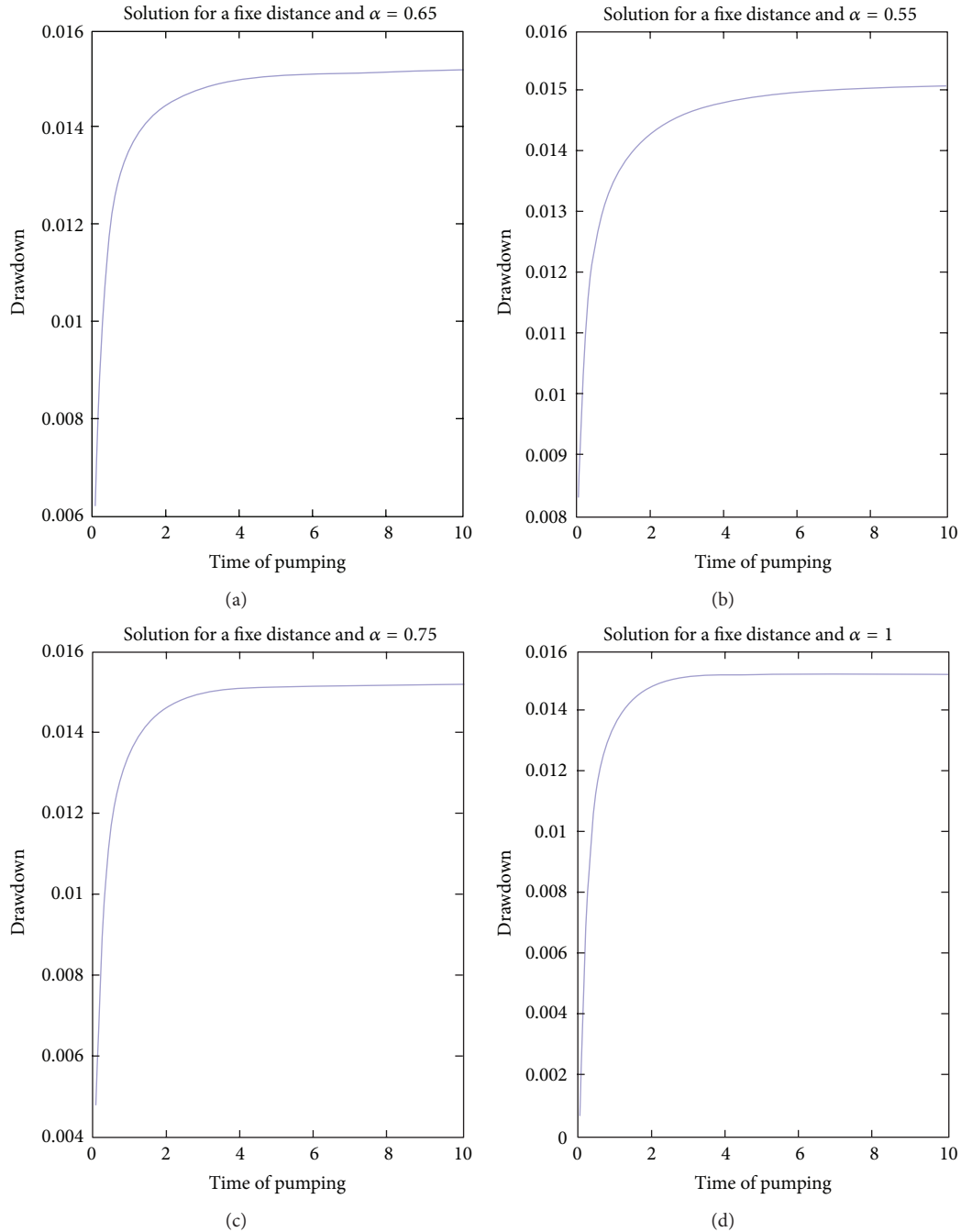


FIGURE 2: Numerical representation of (66) for different values of alpha.

Free State. The test consisted of the pumping of the borehole at the constant discharge rate  $Q = 4.5$  and monitoring the piezometric head for 350 minutes, at the distance of  $r = 31.54$  m.

A Chinese proverb says, I quote “An image is equivalent to ten thousand words.” With any reservation we can conclude that the fractional order derivative plays an important role while modeling real-world problem into mathematical equation. This solution is in perfect agreement with the data observed from the pumping test performed by the institute

for groundwater study on one of their borehole settled on the test site of the University of the Free State.

## 8. Conclusion

We have generalized to Theim and Theis groundwater flow equation to the concept of fractional order derivatives. The resulting equations were solved analytically via several techniques, including the Laplace transform method, the Fourier transform method, the Laplace-Carson transform

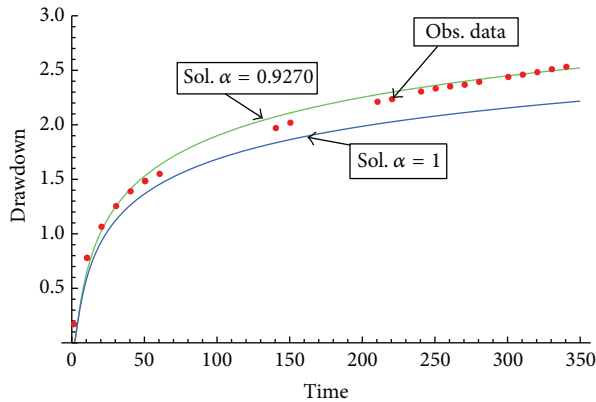


FIGURE 3: Comparison of Theis-time-fractional groundwater flow equation with experimental data from real observation.

method, and the Boltzmann variable method. The numerical simulations show that the fractional order derivative plays an important role in the simulation process. In addition, we compare the analytical solution with experimental data to access the accuracy of the fractional groundwater model. The analytical solution was in perfect agreement with experimental data.

## References

- [1] J. F. Botha and A. H. Cloot, "A generalised groundwater flow equation using the concept of non-integer order derivatives," *Water SA*, vol. 32, no. 1, pp. 1–7, 2006.
- [2] A. Atangana, "Numerical solution of space-time fractional order derivative of groundwater flow equation," in *Proceedings of the International Conference of Algebra and Applied Analysis*, p. 20, Istanbul, Turkey, June 2012.
- [3] A. Atangana and J. F. Botha, "Generalized groundwater flow equation using the concept of variable order derivative," *Boundary Value Problems*, vol. 2013, article 53, 2013.
- [4] J. Boonstra and R. A. L. Kselik, *SATEM 2002: Software for Aquifer Test Evaluation*, International Institute for Land Reclamation and Improvement, Wageningen, The Netherlands, 2002.
- [5] G. P. Kruseman and N. A. de Ridder, *Analysis and Evaluation of Pumping Test Data*, International Institute for Land Reclamation and Improvement, Wageningen, The Netherlands, 2nd edition, 1990.
- [6] H. Jafari and C. M. Khalique, "Homotopy perturbation and variational iteration methods for solving fuzzy differential equations," *Communications in Fractional Calculus*, vol. 3, no. 1, pp. 38–48, 2012.
- [7] S. Duan, R. Rach, D. Baleanu, and A. M. Wazwaz, "A review of the Adomian decomposition method and its applications to fractional differential equations," *Communications in Fractional Calculus*, vol. 3, no. 2, pp. 73–99, 2012.
- [8] A. Atangana and E. Alabaraoye, "Solving system of fractional partial differential equations arisen in the model of HIV infection of CD4+ cells and attractor one-dimensional Keller-Segel equation," *Advances in Difference Equations*, vol. 2013, article 94, 2013.
- [9] D. Baleanu, K. Diethelm, E. Scalas, and J. J. Trujillo, *Fractional Calculus Models and Numerical Methods*, Series on Complexity, Nonlinearity and Chaos, World Scientific, Singapore, 2012.
- [10] A. Atangana and A. Secer, "A note on fractional order derivatives and table of fractional derivatives of some special functions," *Abstract and Applied Analysis*, vol. 2013, Article ID 279681, 8 pages, 2013.
- [11] G. C. Wu, "New trends in the variational iteration method," *Communications in Fractional Calculus*, vol. 2, pp. 59–75, 2011.
- [12] G. Jumarie, "On the representation of fractional Brownian motion as an integral with respect to  $(dt)^{\alpha}$ ," *Applied Mathematics Letters*, vol. 18, no. 7, pp. 739–748, 2005.
- [13] G. Jumarie, "Modified Riemann-Liouville derivative and fractional Taylor series of nondifferentiable functions further results," *Computers and Mathematics with Applications*, vol. 51, no. 9-10, pp. 1367–1376, 2006.
- [14] G. Jumarie, "Table of some basic fractional calculus formulae derived from a modified Riemann-Liouville derivative for non-differentiable functions," *Applied Mathematics Letters*, vol. 22, no. 3, pp. 378–385, 2009.
- [15] A. Atangana, "New class of boundary value problems," *Information Sciences Letters*, vol. 1, no. 2, pp. 67–76, 2012.
- [16] S. G. Samko, A. A. Kilbas, and O. I. Marichev, *Fractional Integrals and Derivatives, Translated from the 1987 Russian Original*, Gordon and Breach, Yverdon, Switzerland, 1993.
- [17] C. V. Theis, "The relation between the lowering of the piezometric surface and the rate and duration of discharge of a well using ground-water storage," *Transactions, American Geophysical Union*, vol. 16, no. 2, pp. 519–524, 1935.
- [18] P. Flajolet, X. Gourdon, and P. Dumas, "Meilin transforms and asymptotics: harmonic sums," *Theoretical Computer Science*, vol. 144, no. 1-2, pp. 3–58, 1995.
- [19] G. K. Watugala, "Sumudu transform: a new integral transform to solve differential equations and control engineering problems," *International Journal of Mathematical Education in Science and Technology*, vol. 24, pp. 35–43, 1993.
- [20] A. Atangana and A. Kılıçman, "The use of Sumudu transform for solving certain nonlinear fractional heat-like equations," *Abstract and Applied Analysis*, vol. 2013, Article ID 737481, 12 pages, 2013.
- [21] M. G. M. Hussain and F. B. M. Belgacem, "Transient solutions of Maxwell's equations based on sumudu transform," *Progress in Electromagnetics Research*, vol. 74, pp. 273–289, 2007.
- [22] S. Weerakoon, "The 'Sumudu transform' and the Laplace transform—reply," *International Journal of Mathematical Education in Science and Technology*, vol. 28, no. 1, pp. 159–160, 1997.
- [23] F. Oberhettinger and L. Badii, *Tables of Laplace Transforms*, Springer, Berlin, Germany, 1973.
- [24] I. Podlubny, *Fractional Differential Equations*, Academic Press, New York, NY, USA, 1999.

## Research Article

# Unsteady Analyses of a Control Valve due to Fluid-Structure Coupling

Yudong Xie,<sup>1,2</sup> Yong Wang,<sup>1,2</sup> Yanjun Liu,<sup>1,2</sup> Fang Cao,<sup>1,2</sup> and Yongcheng Pan<sup>1,2</sup>

<sup>1</sup> School of Mechanical Engineering, Shandong University, Jingshi Road 17923, Jinan, Shandong 250061, China

<sup>2</sup> Key Laboratory of High-Efficiency and Clean Mechanical Manufacture, Shandong University, Ministry of Education, Jinan, Shandong 250061, China

Correspondence should be addressed to Yudong Xie; [yudong\\_2177@163.com](mailto:yudong_2177@163.com)

Received 11 July 2013; Revised 27 August 2013; Accepted 27 August 2013

Academic Editor: Waqar Khan

Copyright © 2013 Yudong Xie et al. This is an open access article distributed under the Creative Commons Attribution License, which permits unrestricted use, distribution, and reproduction in any medium, provided the original work is properly cited.

Control valves play important roles in the control of the mixed-gas pressure in the combined cycle power plants (CCPP). In order to clarify the influence of coupling between the structure and the fluid system at the control valve, the coupling mechanism was presented, and the numerical investigations were carried out. At the same operating condition in which the pressure oscillation amplitude is greater when considering the coupling, the low-order natural frequencies of the plug assembly of the valve decrease obviously when considering the fluid-structure coupling action. The low-order natural frequencies at 25% valve opening, 50% valve opening, and 75% valve opening are reduced by 11.1%, 7.0%, and 3.8%, respectively. The results help understand the processes that occur in the valve flow path leading to the pressure control instability observed in the control valve in the CCPP.

## 1. Introduction

The steel mills generate vast amounts of blast furnace gas (BFG) and coke-oven gas (COG) in the production. In order to reduce the environmental pollution, some steel mills mix BFG with COG and build combined cycle power plants (CCPP) to make use of the gas [1]. For the normal operation of CCPP, the pressure of mixed gas delivered to the gas turbine should be kept in a steady range.

In CCPP, control valves play important roles in the control of the mixed-gas pressure. The signal of mixed-gas pressure measured using the pressure meter is compared to the signal of the desired pressure by the controller. The controller output accordingly adjusts the opening/closing actuator of the control valve in order to maintain the actual pressure close to the desired pressure. The opening of the control valve depends on the flow forces and the driving forces of the control-valve actuator, while the flow forces and the driving forces are affected by the valve opening. Therefore, there is strong coupling interaction between the fluid and the control valve structure.

According to Morita et al. (2007) and Yonezawa et al. (2008), the typical flow pattern around the control valve is

transonic [2, 3]. When pressure fluctuations occur, large static and dynamic fluid forces will act on the valves. Consequently, problematic phenomena, such as valve vibrations and loud noises, can occur, with the worst cases resulting in damage of the valve plug and seal [4]. In order to understand the underlying physics of flow-induced vibrations in a steam control valve head, experimental investigations described by Yonezawa et al. (2012) are carried out. Misra et al. (2002) reported that the self-excited vibration of a piping system occurs due to the coincidence of water hammer, acoustic feedback in the downstream water piping, high acoustic resistance at the control valve, and negative hydraulic stiffness at the control valve [5]. Araki et al. (1981) reported that the steam control-valve head oscillation mechanism was forced vibration, while self-excited vibration was not observed [6].

Those studies cited previously are mainly aimed at the modeling of the self-excited vibration, the analysis of vibration parameters stability, and so on [7–11]. Whereas, the studies on the influence of nonlinear fluid-structure coupling of control valve on the valve control characteristics, such as the pressure regulation feature, are still very limited [12–17]. In the CCPP, the valve control characteristics affected by the fluid-structure coupling are particularly important for

the stability of the mixed-gas pressure control. It has not been uncommon to see that the instability of the mixed-gas pressure causes a severe disturbance or even an emergency shutdown of the whole plant, and the handling of such an emergency often becomes a source of new problems and confusion. In this paper, numerical investigations are carried out to clarify the influence of fluid-structure coupling of control valve on not only the flow field but also the gas pressure regulation and the natural frequency changes of the control valve. This study helps understand the processes that occur in the valve flow path leading to the mixed-gas pressure pulsations, which is valuable for the pressure stability control of the mixed gas in the CCP.

## 2. Fluid-Structure Coupling Mechanism of Control Valve

When the mixed gas passes through the control valve, the gas pressure and flow rate change with the valve opening, as shown in Figure 1.  $p_1$  and  $p_2$  express the inlet pressure and outlet pressure of mixed gas, respectively.  $\hat{v}_1$  and  $\hat{v}_2$  denote the inlet flow rate and outlet flow rate of mixed gas, respectively.

The flow infinitesimal of mixed gas is shown in Figure 2. According to the law of conservation of mass, we can get

$$\begin{aligned} \frac{\partial \rho}{\partial t} + \frac{\rho}{A_{ax}} \frac{\partial A_{ax}}{\partial t} + u \frac{\partial \rho}{\partial x} + \frac{\rho u}{A_{ax}} \frac{\partial A_{ax}}{\partial x} + \rho \frac{\partial u}{\partial x} &= 0, \\ \frac{\partial \rho}{\partial t} + \frac{\rho}{A_{ay}} \frac{\partial A_{ay}}{\partial t} + v \frac{\partial \rho}{\partial y} + \frac{\rho v}{A_{ay}} \frac{\partial A_{ay}}{\partial y} + \rho \frac{\partial v}{\partial y} &= 0, \quad (1) \\ \frac{\partial \rho}{\partial t} + \frac{\rho}{A_{az}} \frac{\partial A_{az}}{\partial t} + w \frac{\partial \rho}{\partial z} + \frac{\rho w}{A_{az}} \frac{\partial A_{az}}{\partial z} + \rho \frac{\partial w}{\partial z} &= 0, \end{aligned}$$

where  $A_{ax}$ ,  $A_{ay}$ , and  $A_{az}$  represent the  $x$ -direction cross-sectional area,  $y$ -direction cross-sectional area, and  $z$ -direction cross-sectional area of the flow infinitesimal, respectively.  $\rho$  expresses the mixed-gas density.  $u$ ,  $v$ , and  $w$  denote  $x$ -direction velocity component,  $y$ -direction velocity component, and  $z$ -direction velocity component, respectively.

According to the balance equation of dynamic flow, we can obtain

$$\begin{aligned} \frac{\partial p}{\partial x} + \rho \left[ \frac{\partial u}{\partial t} + u \frac{\partial u}{\partial x} + v \frac{\partial u}{\partial y} + w \frac{\partial u}{\partial z} \right] &= 0, \\ \frac{\partial p}{\partial y} + \rho \left[ \frac{\partial v}{\partial t} + u \frac{\partial v}{\partial x} + v \frac{\partial v}{\partial y} + w \frac{\partial v}{\partial z} \right] &= 0, \quad (2) \\ \frac{\partial p}{\partial z} + \rho g + \rho \left[ \frac{\partial w}{\partial t} + u \frac{\partial w}{\partial x} + v \frac{\partial w}{\partial y} + w \frac{\partial w}{\partial z} \right] &= 0. \end{aligned}$$

According to the equation of flow continuity, we have

$$\frac{\partial u}{\partial x} + \frac{\partial v}{\partial y} + \frac{\partial w}{\partial z} + \frac{1}{K} \frac{\partial p}{\partial t} = 0. \quad (3)$$

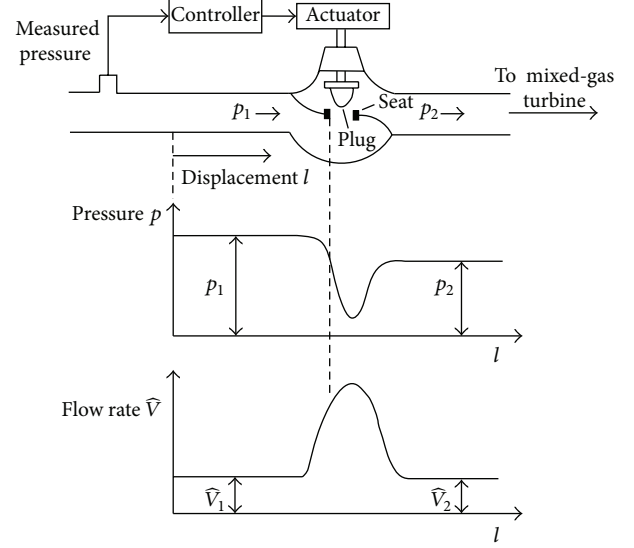


FIGURE 1: Pressure and flow rate change when the fluid passes through the control valve.

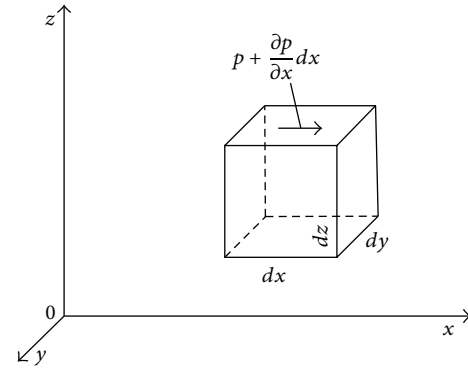


FIGURE 2: Flow infinitesimal.

Based on (1)~(3), the flow equation of mixed gas in control valve can be described as

$$\frac{\partial^2 p}{\partial x^2} + \frac{\partial^2 p}{\partial y^2} + \frac{\partial^2 p}{\partial z^2} - \frac{\rho}{K} \frac{\partial^2 p}{\partial t^2} = 0, \quad (4)$$

where  $K$  is the bulk modulus of elasticity of the flow.

The discrete pressure distribution of mixed-gas flow field, using Galerkin method, can be expressed as follows:

$$\Psi(x, y, z, t) = Y^T(x, y, z) \vec{p}(t) = \sum_{m=1}^M r_m(x, y, z) p_m(t), \quad (5)$$

where  $Y(x, y, z)$  is the shape function matrix and  $\vec{p}(t)$  is the pressure vector.  $Y(x, y, z)$  can be written as

$$Y(x, y, z) = \begin{bmatrix} r_1(x, y, z) \\ r_2(x, y, z) \\ \vdots \\ r_m(x, y, z) \end{bmatrix}. \quad (6)$$

$\vec{p}(t)$  can be described as

$$\vec{p}(t) = \begin{bmatrix} p_1(t) \\ p_2(t) \\ \vdots \\ p_m(t) \end{bmatrix}. \quad (7)$$

Then

$$\frac{\partial^2 \Psi}{\partial x^2} + \frac{\partial^2 \Psi}{\partial y^2} + \frac{\partial^2 \Psi}{\partial z^2} - \frac{\rho}{K} \ddot{\Psi} = R, \quad (8)$$

where  $R$  is the residual part. The value choice of  $\Psi$  should make the value of  $R$  get the minimum. Using Galerkin method,  $\Psi$  can be calculated as

$$\begin{aligned} \iiint_{\Omega} \Upsilon \left( \frac{\partial^2 \Psi}{\partial x^2} + \frac{\partial^2 \Psi}{\partial y^2} + \frac{\partial^2 \Psi}{\partial z^2} \right) d\Omega \\ - \frac{\rho}{K} \iiint_{\Omega} \Upsilon \Psi d\Omega = 0. \end{aligned} \quad (9)$$

The discrete flow equation of mixed gas can be described as

$$\begin{aligned} \left( \frac{\rho}{K} \iiint_{\Omega} \Upsilon \Upsilon^T d\Omega \right) \frac{\partial^2 \vec{p}}{\partial t^2} + \left( \frac{1}{\sqrt{K/\rho}} \iint_{S_r} \Upsilon \Upsilon^T dS_r \right) \frac{\partial \vec{p}}{\partial t} \\ + \left( \iiint_{\Omega} \nabla \Upsilon \cdot \nabla \Upsilon^T d\Omega \right) \vec{p} + \rho \left( \iint_{S_i} \Upsilon \Upsilon_s^T dS_i \right) \Lambda \frac{\partial^2 \Gamma}{\partial t^2} \\ = F_i, \end{aligned} \quad (10)$$

where  $\Gamma$  is the displacement vector,  $\Lambda$  represents the coordinate transformation matrix,  $F_i$  denotes the input exciting vector,  $\Omega$  expresses the flow domain volume,  $\Upsilon_s$  is the insertion function vector of structure system,  $S_i$  is the surface area of the fluid-structure edge, and  $S_r$  denotes the surface area of the boundary of flange interface of control valve.

The motion equation of structure domain can be written as

$$M \frac{\partial^2 \Gamma}{\partial t^2} + C \frac{\partial \Gamma}{\partial t} + K_F \Gamma + F_e = F_s, \quad (11)$$

where  $M$  is the mass matrix of structure,  $C$  denotes the damping matrix,  $K_F$  is the structure stiffness matrix,  $F_e$  expresses the flow-nodal force vector of the fluid-structure edge, and  $F_s$  is the external exciting vector.

In the fluid-structure edge, the generalized normal force vector of the flow infinitesimal is as follows:

$$F_e^* = -\Lambda^T \left( \iint_{S_{ie}} \Upsilon_{en} \Upsilon_{sen}^T dS_{ie} \right) \vec{p}_{en}, \quad (12)$$

where  $\Upsilon_{en}$  is the shape function vector of the structure infinitesimal,  $S_{ie}$  is the surface area of the fluid-structure edge of the infinitesimal,  $\Upsilon_{sen}$  denotes the shape function vector of the flow infinitesimal, and  $\vec{p}_{en}$  is the pressure vector of the flow infinitesimal.

From (11) and (12), we can get

$$\begin{aligned} M \frac{\partial^2 \Gamma}{\partial t^2} + C \frac{\partial \Gamma}{\partial t} + K_F \Gamma \\ - \sum_{n=1}^N \Lambda^T \left( \iint_{S_{ie}} \Upsilon_{en} \Upsilon_{sen}^T dS_{ie} \right) \vec{p}_{en} = F_s. \end{aligned} \quad (13)$$

Based on (10) and (13), the fluid-structure coupling model of control valve can be described as

$$\begin{aligned} \begin{bmatrix} \rho \xi & \delta \\ M & 0 \end{bmatrix} \begin{bmatrix} \frac{\partial^2 \Gamma}{\partial t^2} \\ \frac{\partial^2 \vec{p}}{\partial t^2} \end{bmatrix} \\ + \begin{bmatrix} 0 & \varphi \\ C & 0 \end{bmatrix} \begin{bmatrix} \frac{\partial \Gamma}{\partial t} \\ \frac{\partial \vec{p}}{\partial t} \end{bmatrix} \\ + \begin{bmatrix} 0 & \phi \\ K_F & -\xi^T \end{bmatrix} \begin{bmatrix} \Gamma \\ \vec{p} \end{bmatrix} = \begin{bmatrix} F_i \\ F_s \end{bmatrix}, \end{aligned} \quad (14)$$

with

$$\begin{aligned} \delta &= \frac{\rho}{K} \iiint_{\Omega} \Upsilon \Upsilon^T d\Omega, \\ \xi &= \left( \iint_{S_i} \Upsilon \Upsilon_s^T dS_i \right) \Lambda, \\ \phi &= \iiint_{\Omega} \nabla \Upsilon \cdot \nabla \Upsilon^T d\Omega, \\ \varphi &= \frac{1}{\sqrt{K/\rho}} \iint_{S_r} \Upsilon \Upsilon^T dS_r. \end{aligned} \quad (15)$$

### 3. Influence Analyses of the Fluid-Structure Coupling

In this section, numerical simulations utilizing ANSYS, CFX, and Workbench were performed. In the analysis, a time step of 0.0005 s was used. A compressible, ideal gas flow was assumed for simulations. Inflow boundary conditions based on an inlet total pressure of 2 MPa and a temperature of 240°C were specified at the inlet plane of the control valve. At the outflow plane of the control valve, a flow rate of 20 kg/s was maintained. The reference pressure of the model environment was normal atmospheric pressure. The initial velocity vector was zero. And the mean residual of the convergence of the solution was less than 0.001.

Figure 3 shows the general structure of the flow field through the control valve, which depicts the streamlines without fluid-structure coupling. For the time period of the simulation, about 32 cycles of data were collected. The progression of the simulation at intervals of  $T/4$  is shown in Figure 3. When taking the fluid-structure coupling into account, the general structure of the flow field is shown in Figure 4. As it is seen from Figures 3 and 4, after considering

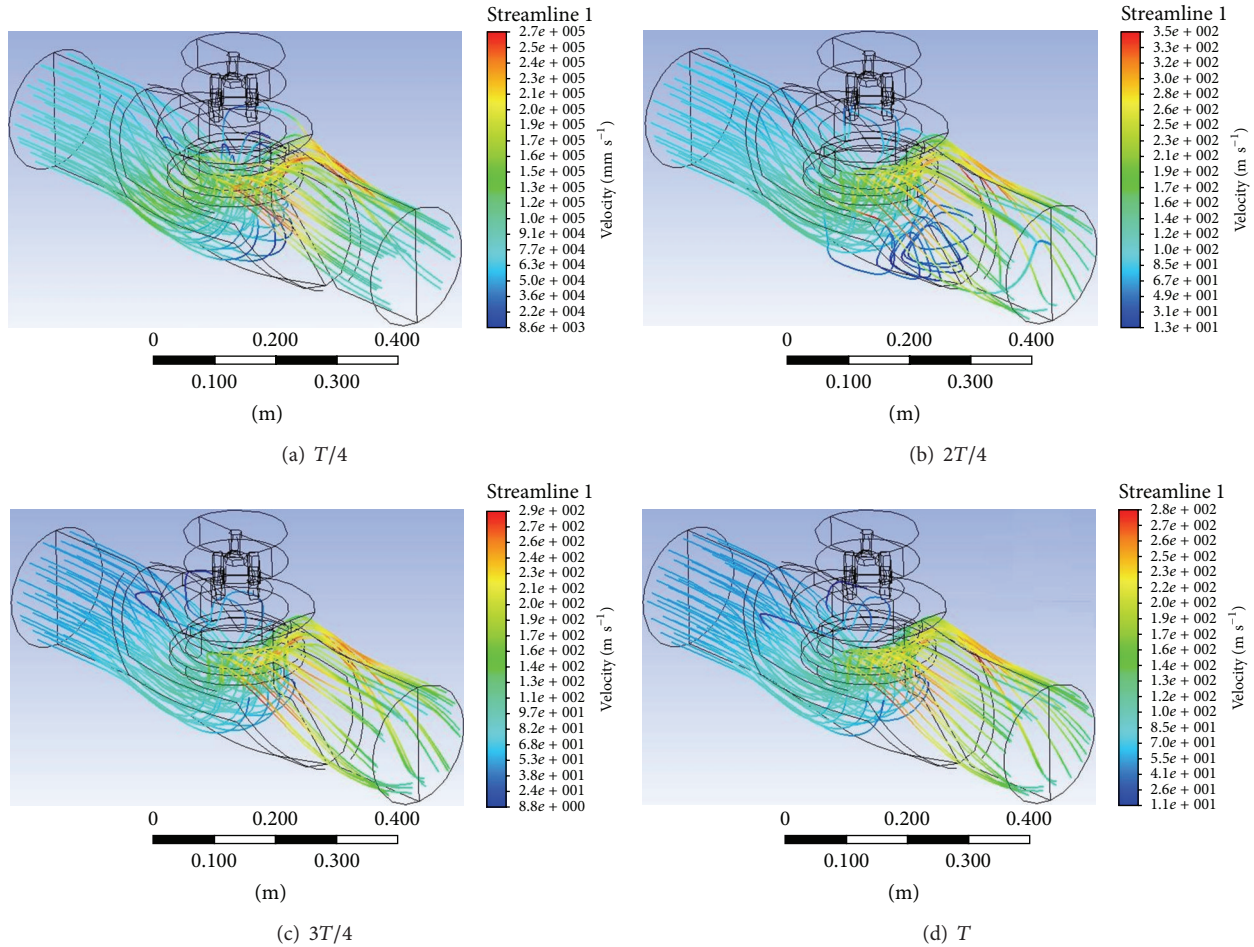


FIGURE 3: Streamlines without fluid-structure coupling.

the fluid-structure coupling, some of the secondary flow structures present in the corner regions of the valve housing, and the large recirculation develops in the bottom and upper portion of the valve body as the flow negotiates the transition from the valve assembly to the valve outlet. The flow sharply accelerates around the valve seat region.

The unsteady flow, as stated in Figure 4, causes pressure fluctuations with random and impulsive wave forms. The pressure distributions of the flow field through the control valve, considering and not considering the fluid-structure coupling, are shown in Figure 5. The peak pressure presented in Figure 5(a) is 1.9 MPa, while the peak pressure that appeared in Figure 5(b) is 2.3 MPa. Furthermore, the maximum pressure position shown in Figure 5(b) is different from that shown in Figure 5(a). In order to verify the influence of fluid-structure coupling on the gas pressure regulation of the control valve, a sine pressure with an amplitude of 1 MPa and an initial value of 1 MPa was specified at the inlet of the control valve. Figure 6 gives time-history plots of outlet pressure changes of control valve as compared to the inlet pressure changes without considering fluid-structure coupling. The outlet pressure can follow the inlet pressure

signal well, which does not have obvious oscillations. When taking the fluid-structure coupling into account, the time-history plots of outlet pressure changes of control valve as compared to the inlet pressure changes are shown in Figure 7. The simulation process with fluid-structure coupling has obvious pressure oscillations that are far greater than those obtained from the simulation process without fluid-structure coupling. As a result, the coupled oscillations of the flow in the control valve are maintained at certain operating conditions, and the fluid force acting on the valve plug becomes a random and pulse-like wave form, as shown in Figure 8. This fluid force is added to the driving force of the control valve, which brings about the result that the resultant force may be greater or less than the control force used to adjust the valve opening, and consequently, the control precision of the control valve is reduced.

Table 1 shows the natural frequencies obtained by the simulation at different valve opening positions. When taking the fluid-structure coupling into account, the low-order natural frequencies of the plug assembly of the control valve decrease. The first-order natural frequencies at 25% valve opening, 50% valve opening, and 75% valve opening are reduced by

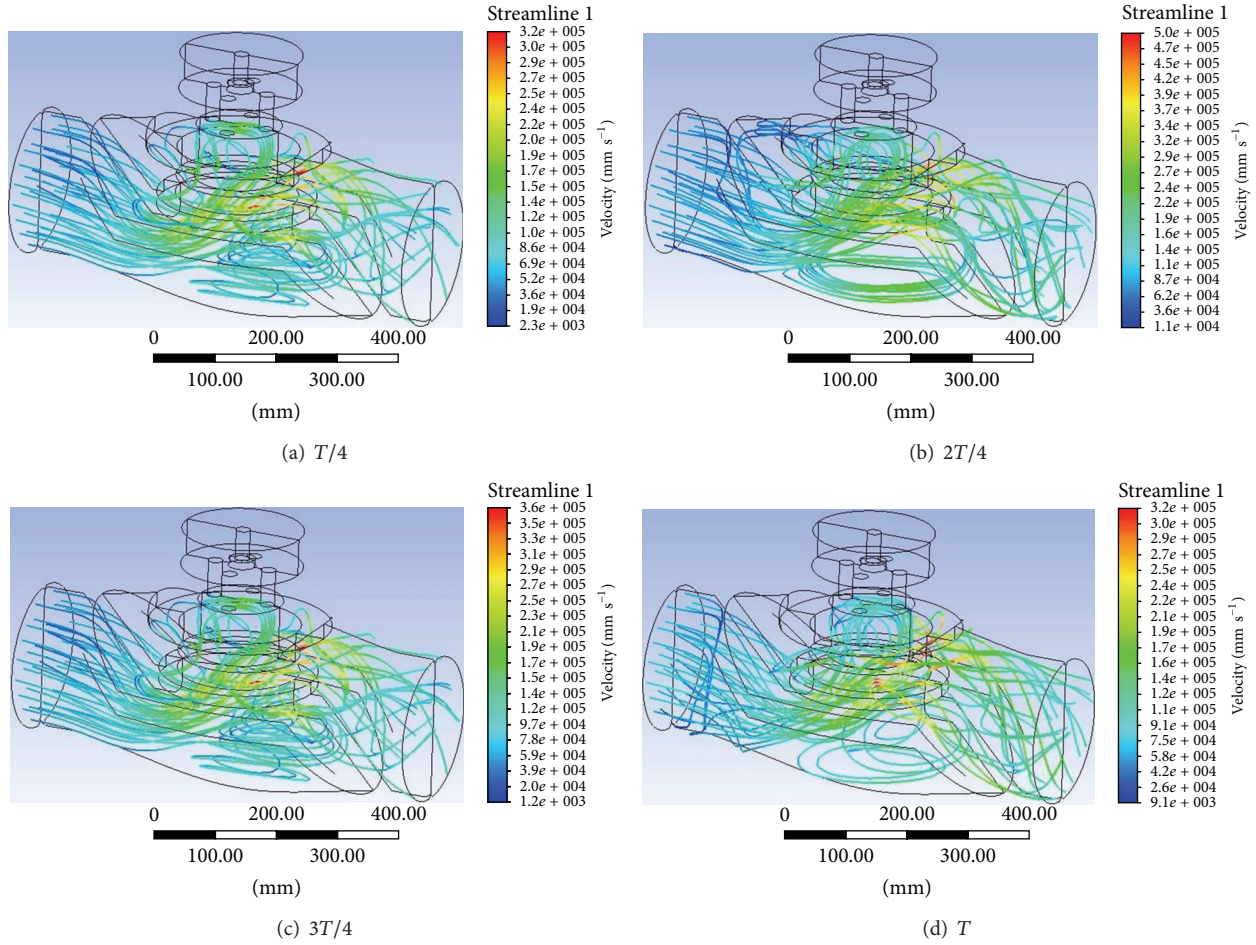


FIGURE 4: Streamlines with fluid-structure coupling.

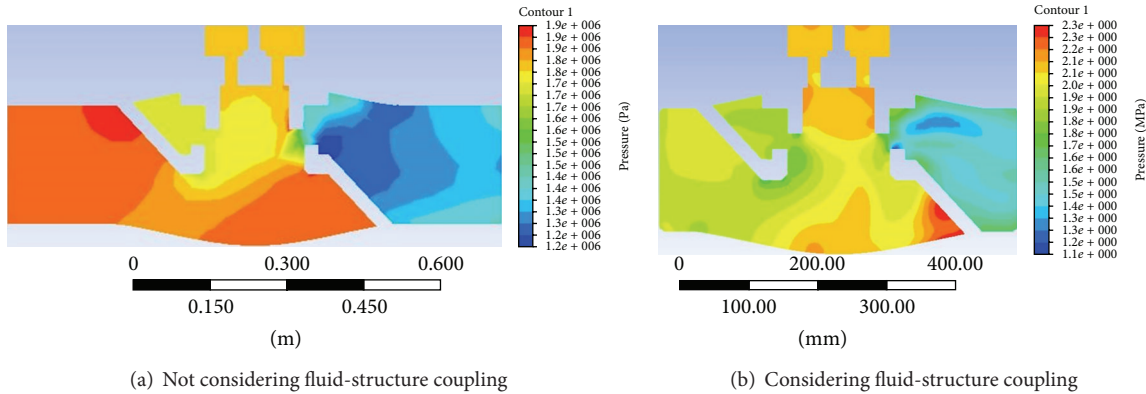


FIGURE 5: Pressure distributions.

11.1%, 7.0%, and 3.8%, respectively. As a result, the vibrations become easy to excite due to the pressure fluctuations caused by the fluid-structure coupling. At the same time, the valve plug vibration affects the pressure fluctuation. The pressure fluctuation increases when the valve plug vibration increases, and in some cases with very small valve opening ratios, the valve plug hits the valve seat.

#### 4. Conclusions

Fluid-structure interaction between the structure and the fluid system at the control valve has to be taken into account for the analysis of the control valve characteristics. This is extremely useful in a better understanding of the detailed flow physics that occur in control valves. The general

TABLE 1: Natural frequencies of the plug assembly of the control valve.

Valve opening	Order	Natural frequency without coupling $f$ (Hz)	Natural frequency with coupling $f_s$ (Hz)	Ratio $(f_s - f)/f$ (%)
25%	1	89.822	79.901	-11.1
	2	1158.6	1158.4	0.0
	3	3387.1	3387.3	0.0
	4	3388.0	3388.3	0.0
	5	6221.6	6221.3	0.0
50%	1	107.84	100.32	-7.0
	2	1347.5	1347.8	0.0
	3	3979.9	3980.1	0.0
	4	3981.7	3982.5	0.0
	5	8549.4	8552.3	0.0
75%	1	145.56	140.10	-3.8
	2	1668.3	1669.0	0.0
	3	4375.8	4376.0	0.0
	4	4376.7	4376.5	0.0
	5	9899.1	9899.3	0.0

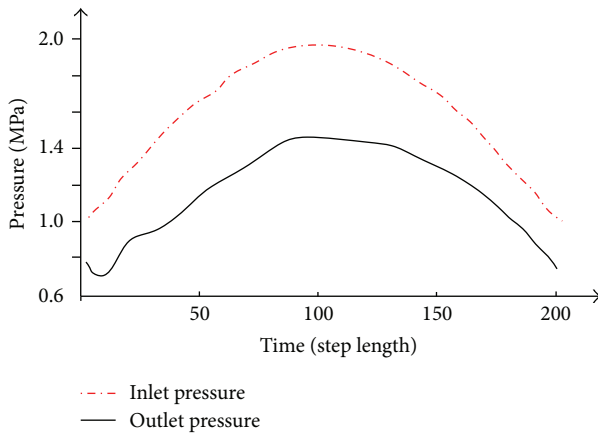


FIGURE 6: Pressure response plots (without considering fluid-structure coupling).

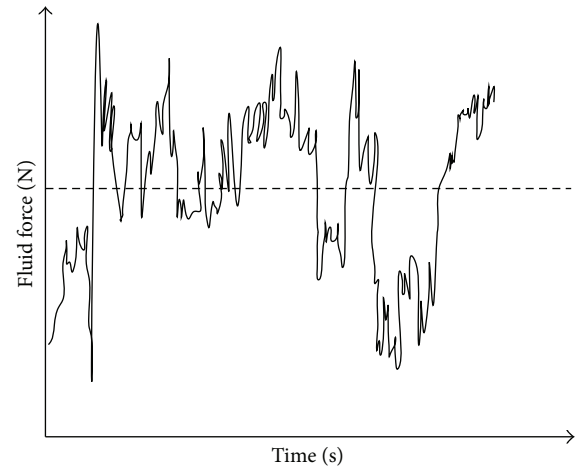


FIGURE 8: Time history of the fluid force on the valve plug.

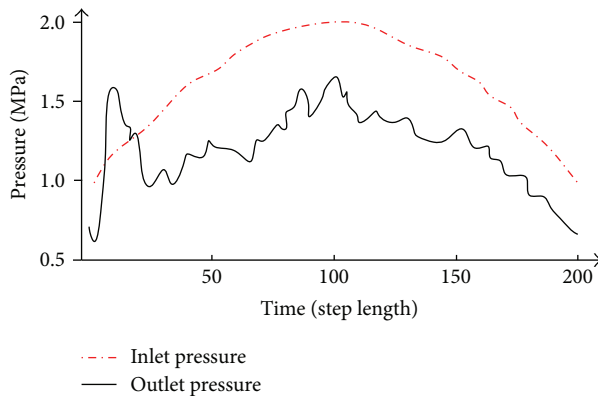


FIGURE 7: Pressure response plots (considering fluid-structure coupling).

structure of the flow field through the control valve, the valve plug vibration, and the pressure regulation performance are affected by the fluid-structure coupling. The unsteady fluid force due to the coupled oscillations of the flow in the control valve is added to the driving force of the control valve, which brings about the result that the resultant force may be greater or less than the control force used to adjust the valve opening, and consequently, the control precision of the control valve is reduced.

## Acknowledgments

This work is supported by the National Natural Science Foundation of China (Grant no. 51305234), Special Funds for Postdoctoral Innovative Projects of Shandong Province (no.

201103033), Independent Innovation Foundation of Shandong University (IIFSDU no. 2011GN045), and Key Laboratory of High-Efficiency and Clean Mechanical Manufacture at Shandong University of Education Ministry.

## References

- [1] Y.-D. Xie, Y.-J. Liu, and Y. Wang, "Design of cascade-smith hybrid control structure for pressure control," *Key Engineering Materials*, vol. 419-420, pp. 797–800, 2010.
- [2] K. Yonezawa, Y. Toyohira, T. Nagashima et al., "An experimental study of unsteady transonic flow in a steam control valve with simple model," *Transactions of the Japan Society of Mechanical Engineers B*, vol. 74, no. 2, pp. 303–309, 2008.
- [3] R. Morita, F. Inada, M. Mori, K. Tezuka, and Y. Tsujimoto, "CFD simulations and experiments of flow fluctuations around a steam control valve," *Journal of Fluids Engineering, Transactions of the ASME*, vol. 129, no. 1, pp. 48–54, 2007.
- [4] K. Yonezawa, R. Ogawa, K. Ogi et al., "Flow-induced vibration of a steam control valve," *Journal of Fluid and Structures*, vol. 35, pp. 76–88, 2012.
- [5] A. Misra, K. Behdinin, and W. L. Cleghorn, "Self-excited vibration of a control valve due to fluid-structure interaction," *Journal of Fluids and Structures*, vol. 16, no. 5, pp. 649–665, 2002.
- [6] T. Araki, Y. Okamoto, and F. Otomo, "Fluid-induced vibration of steam control valves," *Toshiba Review*, vol. 36, no. 7, pp. 648–656, 1981.
- [7] K. Yonezawa, Y. Toyohira, T. Nagashima et al., "An experimental study of unsteady transonic flow in a steam control valve with simple model," *Journal of Environment and Engineering*, vol. 5, no. 1, pp. 134–143, 2010.
- [8] N. S. Akbar and S. Nadeem, "Numerical and analytical simulation of the peristaltic flow of Jeffrey fluid with Reynold's model of viscosity," *International Journal of Numerical Methods for Heat and Fluid Flow*, vol. 22, no. 4, pp. 458–472, 2012.
- [9] N. S. Akbar and S. Nadeem, "Mixed convective magnetohydrodynamic peristaltic flow of a Jeffrey nanofluid with newtonian heating," *Zeitschrift Für Naturforschung A*, vol. 68, pp. 433–441, 2013.
- [10] N. S. Akbar and S. Nadeem, "Characteristics of heating scheme and mass transfer on the peristaltic flow for an Eyring-Powell fluid in an endoscope," *International Journal of Heat and Mass Transfer*, vol. 55, no. 1–3, pp. 375–383, 2012.
- [11] N. S. Akbar and S. Nadeem, "Simulation of heat transfer on the peristaltic flow of a Jeffrey-six constant fluid in a diverging tube," *International Communications in Heat and Mass Transfer*, vol. 38, no. 2, pp. 154–159, 2011.
- [12] N. S. Akbar and S. Nadeem, "An analytical and numerical study of peristaltic transport of a Johnson—Segalman fluid in an endoscope," *Chinese Physics B*, vol. 22, no. 1, pp. 1–9, 2013.
- [13] J. Deng, X.-M. Shao, X. Fu, and Y. Zheng, "Evaluation of the viscous heating induced jam fault of valve spool by fluid-structure coupled simulations," *Energy Conversion and Management*, vol. 50, no. 4, pp. 947–954, 2009.
- [14] D. Zhang, A. Engeda, J. R. Hardin, and R. H. Aungier, "Experimental study of steam turbine control valves," *Proceedings of the Institution of Mechanical Engineers C*, vol. 218, no. 5, pp. 493–508, 2004.
- [15] K.-J. Bathe, H. Zhang, and S. Ji, "Finite element analysis of fluid flows fully coupled with structural interactions," *Computers and Structures*, vol. 72, no. 1, pp. 1–16, 1999.
- [16] H. Kohno and K.-J. Bathe, "A nine-node quadrilateral FCBI element for incompressible fluid flows," *Communications in Numerical Methods in Engineering*, vol. 22, no. 8, pp. 917–931, 2006.
- [17] K.-J. Bathe and H. Zhang, "Finite element developments for general fluid flows with structural interactions," *International Journal for Numerical Methods in Engineering*, vol. 60, no. 1, pp. 213–232, 2004.

## Research Article

# The Flow of a Variable Viscosity Fluid down an Inclined Plane with a Free Surface

**M. S. Tshehla**

*Department of Mathematics, Faculty of Military Science, University of Stellenbosch, Private Bag X2, Saldanha 7395, South Africa*

Correspondence should be addressed to M. S. Tshehla; [samuel@ma2.sun.ac.za](mailto:samuel@ma2.sun.ac.za)

Received 17 June 2013; Accepted 14 August 2013

Academic Editor: Oluwole Daniel Makinde

Copyright © 2013 M. S. Tshehla. This is an open access article distributed under the Creative Commons Attribution License, which permits unrestricted use, distribution, and reproduction in any medium, provided the original work is properly cited.

The effect of a temperature dependent variable viscosity fluid flow down an inclined plane with a free surface is investigated. The fluid film is thin, so that lubrication approximation may be applied. Convective heating effects are included, and the fluid viscosity decreases exponentially with temperature. In general, the flow equations resulting from the variable viscosity model must be solved numerically. However, when the viscosity variation is small, then an asymptotic approximation is possible. The full solutions for the temperature and velocity profiles are derived using the Runge-Kutta numerical method. The flow controlling parameters such as the nondimensional viscosity variation parameter, the Biot and the Brinkman numbers, are found to have a profound effect on the resulting flow profiles.

## 1. Introduction

The study of the flow of a viscous fluid with temperature dependent properties is of great importance in industries such as food processing, coating, and polymer processing, see Macosko and Oron et al. [1, 2]. In industrial systems fluids can be subjected to extreme conditions such as high temperature, pressure, and shear rates. External heating such as the ambient temperature and high shear rates can lead to a high temperature being generated within the fluid. This may have a significant effect on the fluid properties. It is a well-known fact in fluid dynamics studies that the property which is most sensitive to temperature rise is viscosity, see Myers et al. [3]. Fluids used in industries such as polymer fluids have a viscosity that varies rapidly with temperature and this may give rise to strong feedback effects, which can lead to significant changes in the flow structure of the fluid, see Wyle and Huang [4]. Due to the strong coupling effect between the Navier-Stokes and energy equations, viscous heating also plays an important role in fluids with strong temperature dependence, see Costa and Macedonio [5]. In this paper we focus on the effect of temperature on the viscosity. In particular, we investigate the viscosity variation by Reynolds law [5] or Nahme's law [3], which assumes that the viscosity varies exponentially with temperature. Myers et al. [3] studied the flow of variable

viscosity between parallel plates with shear heating. Costa and Macedonio [5] applied the temperature dependent viscosity model to study magma flows. Elbashbeshy and Bazid [6] investigated the effect of temperature dependent viscosity on heat transfer over a moving surface. In their investigation, the fluid viscosity model varies as an inverse linear function of temperature. The work in [6] was extended in [7] to include variable internal heat generation. The solution was obtained using the Runge-Kutta numerical method, and results presented show that when the coefficient of viscosity variation parameter increases, the temperature of the fluid (water) increases slightly, whilst the opposite is true for the velocity profiles. Elbarbary and Elgazery [8] investigated the effects of variable viscosity and variable thermal conductivity on heat transfer from moving surfaces with radiation. In their work the fluid viscosity also varies as an inverse linear function of temperature, and the thermal conductivity varies as a linear function of temperature. The effect of convective heat transfer is extremely important in understanding the flow structure of many fluids used in industrial and natural applications. The present paper is aimed at investigating the effect of convective heat transfer on the flow of a viscous fluid with exponential temperature dependent viscosity, down an inclined plane with a free surface.

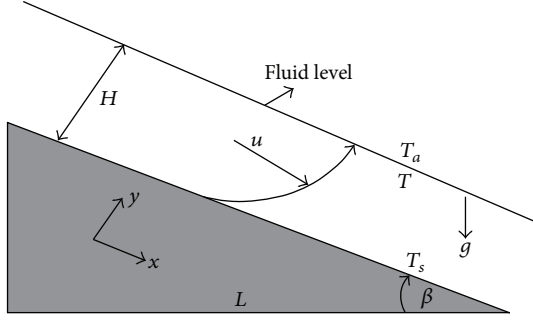


FIGURE 1: The geometry of the problem.

## 2. Problem Formulation

Figure 1 represents a two-dimensional laminar flow with a free surface. The figure depicts an infinitely wide channel of typical length scale  $L$  in the  $x$  direction and height  $H$  in the  $y$  direction. The fluid flows down a plane inclined at an angle  $\beta$ , and the dominant driving force for the flow is gravity, denoted  $g$ . The ambient temperature is denoted  $T_a$ , the fluid temperature is denoted  $T$ , and the temperature at the bottom surface is denoted  $T_s$ . The fluid viscosity  $\mu$  will not be specified, but the viscosity of the fluid will vary exponentially with temperature.

In developing the mathematical model for the fluid flow, the following assumptions will be made:

- (i) the fluid is incompressible, but the viscosity,  $\mu(T)$ , is temperature dependent;
- (ii) the governing equations are derived for a thin film flow such that lubrication theory may be applied;
- (iii) the film height  $T$  is considered to be constant;
- (iv) the flow regime is laminar.

Taking into account these assumptions, the continuity, Navier-Stokes, and energy equations are written as follows:

$$\begin{aligned} \frac{\partial u}{\partial x} + \frac{\partial v}{\partial y} &= 0, \\ \rho \left( \frac{\partial u}{\partial t} + u \frac{\partial u}{\partial x} + v \frac{\partial u}{\partial y} \right) &= -\frac{\partial p}{\partial x} + \rho g \sin \beta + 2 \frac{\partial}{\partial x} \left( \mu \frac{\partial u}{\partial x} \right) \\ &\quad + \frac{\partial}{\partial y} \left[ \mu \left( \frac{\partial u}{\partial y} + \frac{\partial v}{\partial x} \right) \right], \\ \rho \left( \frac{\partial u}{\partial t} + u \frac{\partial v}{\partial x} + v \frac{\partial v}{\partial y} \right) &= -\frac{\partial p}{\partial y} + \rho g \cos \beta + 2 \frac{\partial}{\partial y} \left( \mu \frac{\partial v}{\partial y} \right) \\ &\quad + \frac{\partial}{\partial x} \left[ \mu \left( \frac{\partial u}{\partial y} + \frac{\partial v}{\partial x} \right) \right], \end{aligned}$$

$$\begin{aligned} \rho c_p \left( \frac{\partial T}{\partial t} + u \frac{\partial T}{\partial x} + v \frac{\partial T}{\partial y} \right) &= k \left( \frac{\partial^2 T}{\partial x^2} + \frac{\partial^2 T}{\partial y^2} \right) + \left[ \frac{\partial p}{\partial t} + u \frac{\partial p}{\partial x} + v \frac{\partial p}{\partial y} \right] \\ &\quad + \mu \left[ 2 \left( \frac{\partial u}{\partial x} \right)^2 + \left( \frac{\partial u}{\partial x} + \frac{\partial v}{\partial y} \right)^2 + 2 \left( \frac{\partial v}{\partial y} \right)^2 \right], \end{aligned} \quad (1)$$

where the notation is defined in the nomenclature showed at the end of the paper. These governing equations are nondimensionalised using the following scales:

$$\begin{aligned} x &= Lx', & y &= Hy', & u &= Uu', \\ v &= \frac{HU}{L}v', & t &= \frac{L}{U}t', \\ \mu &= \mu_0 \mu' p = Pp' = \frac{\mu_0 UL}{H^2} p', \end{aligned} \quad (2)$$

$$T = T_0 + (T_a - T_0) T' = T_0 + \Delta T T',$$

where all quantities with prime denote nondimensional parameters. The pressure scale  $P = \mu_0 UL/H^2$  is standard for lubrication theory. The reference viscosity and the temperature difference are denoted by  $\mu_0$  and  $\Delta T$ , respectively. To simplify notation, the primes are omitted from now on. Since the film is thin, the aspect ratio  $\varepsilon = H/L \ll 1$ . Using the scaled parameters, (1) now becomes

$$\begin{aligned} \frac{\partial u}{\partial x} + \frac{\partial v}{\partial y} &= 0, \\ \varepsilon^2 \text{Re} \left( \frac{\partial u}{\partial t} + u \frac{\partial u}{\partial x} + v \frac{\partial u}{\partial y} \right) &= -\frac{\partial p}{\partial x} + 1 + 2\varepsilon^2 \frac{\partial}{\partial x} \left( \mu \frac{\partial u}{\partial x} \right) \\ &\quad + \frac{\partial}{\partial y} \left[ \mu \left( \frac{\partial u}{\partial y} + \varepsilon^2 \frac{\partial v}{\partial x} \right) \right], \\ \varepsilon^2 \text{Re}^4 \left( \frac{\partial u}{\partial t} + u \frac{\partial v}{\partial x} + v \frac{\partial v}{\partial y} \right) &= -\frac{\partial p}{\partial y} + \varepsilon \cot \beta \\ &\quad + 2\varepsilon^2 \frac{\partial}{\partial y} \left( \mu \frac{\partial v}{\partial y} \right) \\ &\quad + \varepsilon^2 \frac{\partial}{\partial x} \left[ \mu \left( \frac{\partial u}{\partial y} + \varepsilon^2 \frac{\partial v}{\partial x} \right) \right], \\ \varepsilon^2 \text{Pe} \left( \frac{\partial T}{\partial t} + u \frac{\partial T}{\partial x} + v \frac{\partial T}{\partial y} \right) &= \varepsilon^2 \frac{\partial^2 T}{\partial x^2} + \frac{\partial^2 T}{\partial y^2} \\ &\quad + \text{Pr Ec} \left[ \frac{\partial p}{\partial t} + u \frac{\partial p}{\partial x} + v \frac{\partial p}{\partial y} \right] \\ &\quad + \Phi, \end{aligned} \quad (3)$$

where

$$\Phi = \text{Br} \mu \left[ 2\varepsilon^2 \left( \frac{\partial u}{\partial x} \right)^2 + 2\varepsilon^2 \left( \frac{\partial v}{\partial y} \right)^2 + \left( \frac{\partial u}{\partial y} + \varepsilon^2 \frac{\partial v}{\partial x} \right)^2 \right]. \quad (4)$$

The Péclet number  $Pe = \rho c_p UL/k$  represents the ratio of convective heat transport to the conductive heat transport, and the Brinkman number  $Br = \mu_0 U^2/k\Delta T$  represents the ratio of heat dissipation to fluid conduction. The Prandtl number  $Pr = \mu_0 c_p/k$  denotes the ratio of diffusivity for momentum to thermal diffusivity. The Eckert number  $Ec = U^2/c_p T_0$  denotes the ratio of kinetic energy to thermal mass. The velocity scale is given by  $U = \rho g H^2 \sin \beta / \mu_0$ , which denotes the ratio of gravitational forces to the dynamic viscosity. The parameter values may vary widely depending on the particular industrial application or the models under investigation. The parameter values for a lubricant are

$$\begin{aligned} \mu_0 &\sim 10^{-3} \text{--} 0.5 \text{ kg/ms}, & c_p &\sim 2000 \text{ J/kgK}, \\ H &\sim 10^{-3} \text{ m}, & k &\sim 0.13 \text{ W/mK}, \\ K_c &\sim 10^3, & L &\sim 0.005, \\ \varepsilon &\sim 10^{-4}, & \rho &\sim 880\text{--}940 \text{ kg/m}^3. \end{aligned} \quad (5)$$

The experimental values listed above are taken from several references, [9, page 4], and [10–13]. Using these values listed above, we obtain

$$\begin{aligned} Br &= \frac{\mu_0 U^2}{k\Delta T} \sim 0.01\text{--}0.5, & Pe &= \frac{\rho c_p UL}{k} \sim 10^5, \\ PrEc &= \frac{\mu_0 U^2}{kT_0} \sim 5 \times 10^{-4}, \\ Re &= \frac{\rho UL}{\mu_0} \sim 40\text{--}2000, \\ U &= \frac{\rho g H^2 \sin 30}{\mu_0} \sim 0.4 \text{ m/s}. \end{aligned} \quad (6)$$

Despite the fact that the Péclet number is large, the reduced Péclet number  $\varepsilon^2 Pe \approx 10^{-3}$  is small and may be neglected in the governing equations. The reduced Reynolds number  $\varepsilon^2 Re \approx 1.8 \times 10^{-5}$  may also be neglected. The reduced quantity  $PrEc$  is also assumed to be small, so it will be neglected from the governing equations. The Brinkman number may be close to unity and so must be retained. Using the above approximations, (3) may now be reduced to their final form:

$$\frac{\partial u}{\partial x} + \frac{\partial v}{\partial y} = 0, \quad (7)$$

$$-\frac{\partial p}{\partial x} + \frac{\partial}{\partial y} \left[ \mu \left( \frac{\partial u}{\partial y} \right) \right] + 1 = 0 + \mathcal{O}(\varepsilon^2, \varepsilon^2 Re), \quad (8)$$

$$-\frac{\partial p}{\partial y} + \varepsilon \cot \beta = 0 + \mathcal{O}(\varepsilon^2, \varepsilon^4 Re), \quad (9)$$

$$\frac{\partial^2 T}{\partial y^2} + \mu Br \left( \frac{\partial u}{\partial y} \right)^2 = 0 + \mathcal{O}(\varepsilon^2, \varepsilon^2 Pe). \quad (10)$$

The velocity and the temperature profiles may be determined after the boundary conditions associated with (7)–(10) are stated.

### 3. Boundary Conditions

- (i) At  $y = 0$ , a no slip boundary condition is applied, and the temperature at the bottom surface is constant:

$$u(0) = v(0) = 0, \quad T(0) = 0. \quad (11)$$

- (ii) At the free surface, the shear stress is zero and the fluid temperature is imposed by the air and substrate, respectively:

$$\left( \frac{\partial u}{\partial y} \right) \Big|_{y=h} = 0, \quad \left( \frac{\partial T}{\partial y} \right) \Big|_{y=h} = Bi(T - 1), \quad (12)$$

where  $Bi = HK_c/k$  is the Biot number and denotes the ratio of heat transfer to thermal conductivity, Alhama and Zueco [14] and Makinde [15]. The parameters  $k$  and  $K_c$  denote the thermal conductivity and heat transfer coefficient, respectively. The fluid at the free surface is exposed to the ambient temperature. Hence, a cooling condition is applied.

In the following section the variable viscosity model is introduced, and the equations governing the flow are coupled to this model and solved using both analytical and numerical methods.

### 4. Variable Viscosity Analysis

We now focus on the fluid with an exponential variation of the form:

$$\mu = \mu_0 e^{-\theta(T-T_0)}, \quad (13)$$

where  $\mu_0$  is the reference viscosity at the reference temperature  $T_0$  and  $\theta$  is the coefficient of viscosity variation with temperature Costa and Macedonio [5]. Equation (13) can be written in nondimensional form,

$$\mu = e^{\alpha T}, \quad (14)$$

where  $\alpha = \theta\Delta T$ . Equation (14) is commonly known as Nahme's exponential law [5] or Reynolds law, see Myers et al. [3]. Combining (8) and (14), integrating with respect to  $y$ , and applying the boundary conditions (12) give the velocity gradient,

$$\frac{\partial u}{\partial y} = (1 - y) e^{\alpha T}, \quad (15)$$

where we have used the fact that  $\partial p/\partial x = 0$  to write (15) as a result from (9). Equation (15) cannot be integrated further to determine  $u$ , since it involves the temperature  $T$  which is unknown, so it must be solved numerically using the Runge-Kutta method. Substituting (14) and (15) into the reduced energy (10) gives

$$\frac{\partial^2 T}{\partial y^2} = Br(1 - y)^2 e^{\alpha T}. \quad (16)$$

Equations (15) and (16) form a coupled system of nonlinear partial differential equations which require a numerical technique to obtain a full solution. However, when the viscosity variation is gradual, that is,  $\alpha \ll 1$  and  $T \sim \mathcal{O}(1)$ , an asymptotic analysis is possible. The main reason for using an asymptotic analysis is that we can clearly illustrate how the parameters affect the flow by looking into the dominant terms from the governing equations. This approach can be used to validate numerics. The question is how small must the parameter  $\alpha$  be? Therefore, the key factor in determining the stage at which  $\alpha$  is small is the magnitude of  $\Delta T$ , since  $\theta$  is the fluid property. In certain industrial applications for lubricating oil, the experimental values for the temperature may be confined in the region  $50^\circ\text{C} \leq T \leq 300^\circ\text{C}$ ; see [12, 13, 16], for example. Our interest is on large values  $\Delta T$ , since  $\alpha \sim \theta \Delta T$ , and usually the fluid property  $\theta$  for lubricant is small. Now taking the temperature difference  $\Delta T \sim 200^\circ\text{C}$  and  $\theta \sim 0.00242$  (see [17, page 31]), it can easily be shown that  $\alpha \sim 0.5$  for a lubricating oil. It is important to note that for different values of  $\theta$  and  $\Delta T$ , the results will obviously yield a different value of  $\alpha$ , depending on the fluid under investigation. The velocity and temperature may then be expanded in a series form,

$$u = u_0 + \alpha u_1, \quad (17)$$

$$T = T_0 + \alpha T_1, \quad (18)$$

where  $u_0$ ,  $T_0$ ,  $u_1$ , and  $T_1$  represent the leading-order terms and the first-order perturbation terms in  $\alpha$ . Substituting for  $T$  into (16) yields

$$\frac{\partial^2 T_0}{\partial y^2} + \alpha \frac{\partial^2 T_1}{\partial y^2} = -\text{Br}(1-y)^2 - \alpha T_0(1-y)^2. \quad (19)$$

The leading order and  $\mathcal{O}(\alpha)$  terms from (19) are

$$\frac{\partial^2 T_0}{\partial y^2} = -\text{Br}(1-y)^2, \quad (20)$$

$$\frac{\partial^2 T_1}{\partial y^2} = -\text{Br}(1-y)^2. \quad (21)$$

Equations (20) and (21) are solved subject to

$$\begin{aligned} T_0 = T_1 = 0 \quad \text{at } y = 0, \quad \left. \left( \frac{\partial T_0}{\partial y} \right) \right|_{y=1} &= -\text{Bi} (T_0 - 1), \\ \left. \left( \frac{\partial T_1}{\partial y} \right) \right|_{y=1} &= \text{Bi} T_1. \end{aligned} \quad (22)$$

Integrating (21) with respect to  $y$  and applying the boundary conditions in (22) yield

$$T_0 = -\frac{\text{Br}}{12} \left[ (1-y)^4 - \left( 1 - \frac{\text{Bi}}{\text{Bi}-1} \right) \right] + \left( \frac{\text{Bi}}{\text{Bi}-1} \right) y. \quad (23)$$

Integrating Equation (21) and applying the boundary conditions (22), we obtain

$$\begin{aligned} T_1 = \frac{\text{Br}^2}{12} & \left[ \frac{1}{56} (1-y)^2 \right. \\ & \left. - \frac{1}{60} \left( 5(1-y)^4 \right. \right. \\ & \left. \left. + \frac{\text{Bi}}{(\text{Bi}-1)} (10y^3 - 10y^4 + 3y^5) \right) \right] \\ & + \frac{\text{Br}^2}{12} \left[ \frac{\text{Bi}}{(\text{Bi}-1)} \left( \frac{1}{12(\text{Bi}-1)} - \frac{\text{Bi}}{20(\text{Bi}-1)} \right) y \right. \\ & \left. + \frac{11}{168} \right] + \frac{\text{Bi}}{(\text{Bi}-1)} (10y^3 - 10y^4 + 3y^5) \\ & + \frac{\text{Bi}}{(\text{Bi}-1)^2} \left( \frac{1}{12} - \frac{\text{Bi}}{20} \right) y. \end{aligned} \quad (24)$$

The final temperature profile is obtained by combining both (23) and (24) as  $T = T_0 + \alpha T_1$ . Similarly, a solution for the velocity profile can be derived. Combining (15) and (17) gives

$$\frac{\partial u_0}{\partial y} + \alpha \frac{\partial u_1}{\partial y} = (1-y) + \alpha T_a (1-y). \quad (25)$$

The leading order and  $\mathcal{O}(\alpha)$  terms are therefore

$$\frac{\partial u_0}{\partial y} = (1-y), \quad (26)$$

$$\frac{\partial u_1}{\partial y} = T_0 (1-y). \quad (27)$$

Equations (26) and (27) are solved subject to

$$u_0 = u_1 = 0 \quad \text{at } y = 0. \quad (28)$$

Equation (26) gives the Newtonian velocity profile as

$$u_0 = \frac{y}{2} (2-y). \quad (29)$$

A similar expression for (29) may be obtained in Myers et al. [3]. To obtain  $u_1$ , (23) and (27) are combined and integrated subject to (28),

$$\begin{aligned} u_1 = -\frac{\text{Br}}{72} & \left[ (1-y)^6 \right. \\ & \left. - 6 \left( \left( \frac{y}{2} (2-y) \right) - \frac{\text{Bi} y^2}{6(\text{Bi}-1)} (3-2y) \right) - 1 \right] \\ & + \frac{\text{Bi} y^2}{6(\text{Bi}-1)} (3-2y). \end{aligned} \quad (30)$$

The final velocity profile is given by (29) and (32) as  $u = u_0 + \alpha u_1$ . The numerical solution is discussed in the following section.

### 5. Numerical Solution

The coupled nonlinear partial differential equations (15) and (16) for the velocity and the temperature profiles are solved numerically using the fourth-order Runge-Kutta integration scheme. The solution for the temperature profile must be calculated first and then substituted into the velocity equation to obtain the solution for the velocity profile. Setting  $t_1 = T$  and  $t_2 = \partial T / \partial y$ , (16) can be written as a system of two first-order equations in  $t_1$  and  $t_2$  of the form,

$$\frac{\partial}{\partial y} \begin{bmatrix} t_1 \\ t_2 \end{bmatrix} = \begin{bmatrix} t_2 \\ -Br(1-y)^2 e^{\alpha t_1} \end{bmatrix}. \tag{31}$$

This system can be written in vector form,

$$\frac{\partial \mathbf{t}}{\partial y} = F(\mathbf{t}, y), \tag{32}$$

where  $\mathbf{t} = (t_1, t_2)$ . The solutions for this system of differential equations are solved subject to the boundary conditions (11) and (12). The Runge-Kutta method requires an initial value, and the initial value for the temperature  $t_1$  is taken as the boundary condition at  $y = 0$ . The corresponding initial value for  $t_2$  is randomly chosen. It is important to note that the best numerical results largely depend on a good guess for the initial condition; see [6, 7]. Once this initial value is chosen, we employ the Runge-Kutta method to solve for the temperature. When the solution of the iterative process for the Runge-Kutta scheme terminates, then the derivative for the temperature  $t_2$  at the free surface is eventually corrected using the given boundary conditions (12). The set of parameters  $\alpha$ , Bi, and Br are coupled to the system of differential equations, and we solve our equations using a small step size for  $\Delta y$ . The velocity gradient is given by

$$\frac{\partial u}{\partial y} = (1-y) e^{\alpha t_1}. \tag{33}$$

Once the temperature profile is calculated, the velocity profile is computed from (32) using the finite difference scheme,

$$u_{n+1} = u_n + \Delta u_y \cdot \left( \frac{\partial u}{\partial y} \right) \Big|_{(y_i, t_i)}. \tag{34}$$

In Section 6, we will discuss the results for the asymptotic and numerical methods. We will give account of the findings in this paper. We proceed our analysis for comparison of the asymptotic and numerical solutions.

### 6. Results and Discussion

Figure 2 depicts a typical application of the temperature dependent model in (16). This illustrates the relations between temperatures of the fluid with the Brinkman number. This also is widely studied by several references, such as Myers et al. [3] who studied the application in a closed channel and Makinde [15, 18, 19] who investigated the application with a free surface flow. In this case, the critical point for the temperature is depicted at 0.53 after which the two solution

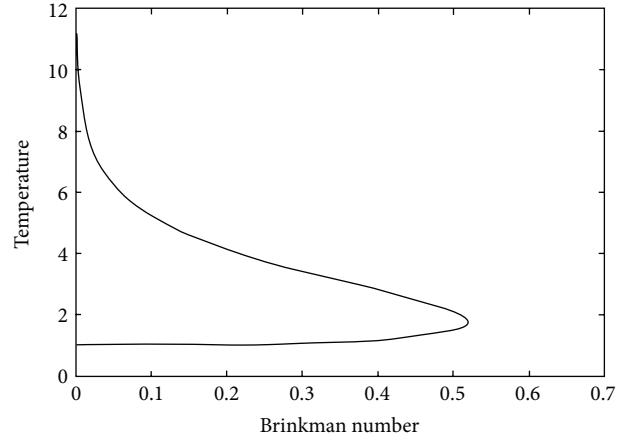


FIGURE 2: The channel temperature.

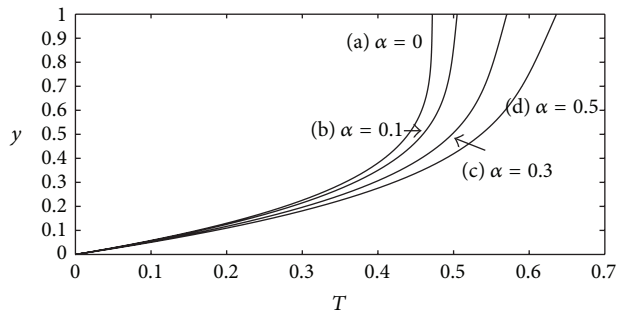


FIGURE 3: The temperature profiles for (18) and numerical solution.

branches are shown. When the temperature is greater than 0.53, the system has no real solution which is indicative of thermal runaway.

Figure 3 shows the temperature profiles corresponding to (18) where  $T_0$  and  $T_1$  are given by (23) and (24) and the numerical solution. In this figure the dotted lines represent the profiles from the asymptotic solution and solid lines for the numerical solution. The results are calculated for the case  $Bi = Br = 0.3$ , so that the Biot and the Brinkman numbers are of the same magnitude. Different values of  $\alpha$  were considered in order to investigate its effect on resulting flow profiles. We start our investigation with a simple case where  $\alpha = 0$  for a Newtonian fluid to a maximum of  $\alpha = 0.5$  typically, for a lubricating oil. Curves (a), (b), (c), and (d) display four different values of  $\alpha$ , namely,  $\alpha = 0, 0.1, 0.3$ , and  $0.5$ . It is important to note that when  $\alpha$  increases, the viscosity of the fluid decreases. The temperature of the fluid in all four curves increases to their maximum temperatures at the free surface. When  $\alpha$  increases, the temperature of the fluid increases due to heat generation by the internal friction caused by the collision of the fluid particles. The Newtonian case is retrieved in curve (a) with  $\alpha$ . The numerical results are in good agreement with the asymptotic as shown in curves (a) through to (d). In Figure 4, four curves representing the velocity profiles for (17) where  $u_0$  and  $u_1$  are given by (29) and (32) are plotted together with the numerical solution.

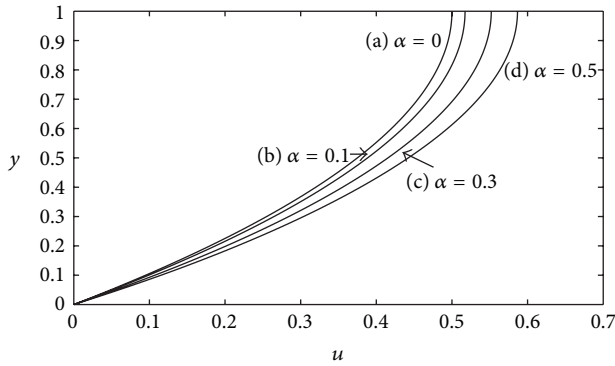


FIGURE 4: The velocity profile for (17) and numerical solution.

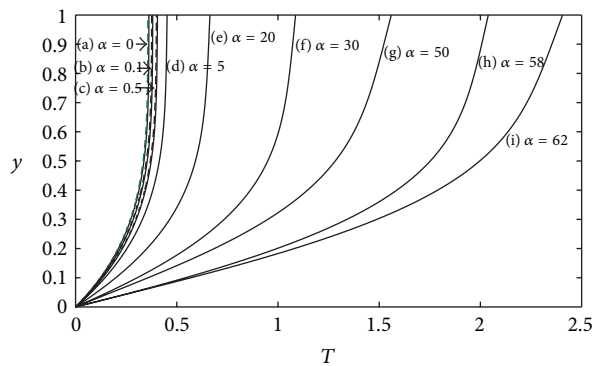


FIGURE 5: The temperature profiles for varying  $\alpha$ .

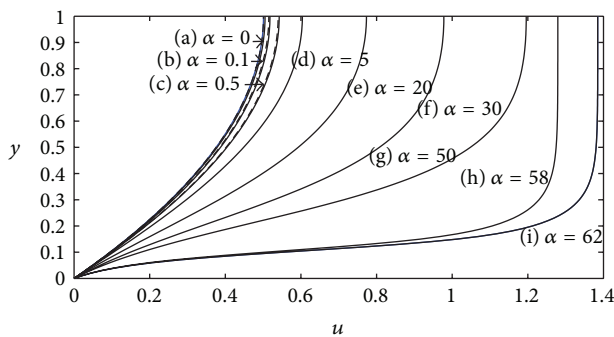


FIGURE 6: The velocity profiles for varying  $\alpha$ .

These profiles correspond to different values of  $\alpha$  as shown in Figure 3. The figure shows that the velocity of the fluid increases when  $\alpha$  increases. This is a result of the resistance force to the flow which decreases as  $\alpha$  increases. Curve (a) displays a Newtonian velocity profile with  $\alpha = 0$ , and this curve increases across the fluid layer to the maximum point at the top due to the effect of the gravitational forces and lack of resistance force to the flow. As shown in the figure, the numerical and asymptotic velocity profiles are in good agreement, particularly for the set of curves (c) and (d).

In Figures 5 and 6 the temperature and the velocity profiles for a numerical solution are displayed. The profiles are plotted to include large values for  $\alpha$  as shown in curves (c) through to (h) from  $\alpha = 10$  to 62 for the temperature profiles

in Figure 5. The velocity gradient in (11) increases exponentially with temperature, which eventually feeds back into (12) through the viscous heating term. The Newtonian temperature profile is shown in curve (a) with  $\alpha = 0$ , and curve (b) is plotted with  $\alpha = 0.5$ ; these curves are the same as the ones which are shown in Figure 3 curves (a) and (b). It is important to note that the large values of  $\alpha$  were randomly chosen to test the reliability of the numerical scheme. The resulting temperature profiles show that the temperature of the fluid increases significantly when  $\alpha$  increases. The velocity profiles are displayed in Figure 6. Curves (a) through to (f) correspond to different values of  $\alpha$  as displayed in the figure, and other flow controlling parameters are the same as those which are given in Figure 5. The velocity of the fluid for all these curves increases to the maximum velocity occurring at the free surface. In this case, when  $\alpha$  increases, the velocity of the fluid increases due to less resistance force to the flow. Curves (a) with  $\alpha = 0$  and (b) with  $\alpha = 0.5$  are similar to the ones shown in Figure 4. The resulting velocity profiles show that for values of  $\alpha > 50$ , a change in the flow structure is observed.

In Figure 6, curves (g) and (h) show different flow behaviour as compared to curves (a) through to (f). Since the viscosity of the fluid decreases exponentially when  $\alpha$  increases, this therefore causes the fluid to behave like a Newtonian fluid when  $\alpha = 58$  and 62. Elbashbeshy and Bazid [6] analysed the effect of temperature dependent viscosity on heat transfer over a continuous moving surface. The full solutions for the velocity and temperature profiles were obtained using the fourth-order Runge-Kutta numerical scheme. Their results indicate that when the viscosity variation parameter increases for water, the temperature of the fluid increases slightly, which is in agreement with our results. However, in their investigation the velocity of the fluid decreases when the viscosity variation parameter increases.

The effect of the Biot number on the resulting temperature and velocity profiles is investigated. The importance of the Biot number is that it helps understand the influence of the ambient temperature on the flow system. When the Biot number tends to infinity ( $k \rightarrow \infty$ ), then both the ambient temperature and the fluid temperature reach equilibrium and  $\sim 0$ . However, when the Biot number decreases ( $k \rightarrow 0$ ), the fluid loses its temperature to the surrounding atmosphere, and this process will have a major influence on the temperature variation of the fluid. An increase in the Biot number indicates that more heat is lost from the fluid to the surrounding atmosphere (hence cooling the fluid). When the Biot number decreases, a reduction in heat transferred to the surrounding atmosphere occurs, and the fluid gets hotter [11]. Because of the strong feedback between the Navier-Stokes and the energy equations, the Biot number will have a major influence on the resulting velocity and temperature profiles. Using the parameters listed in the previous section, we can easily show that  $Bi = 7.692 \sim 8$ . We again begin with a simple analysis for  $Bi = 0$  to a maximum of  $Bi = 8$  calculated for lubricating oil. The curves for the temperature profiles are shown in Figure 7 with different values of the Biot numbers, namely,  $Bi = 0, 0.01, 1, 4$ , and 8. The fluid temperature increases across the fluid layer to its maximum temperatures at the free surface as  $Bi$  decreases due to reduction in the heat

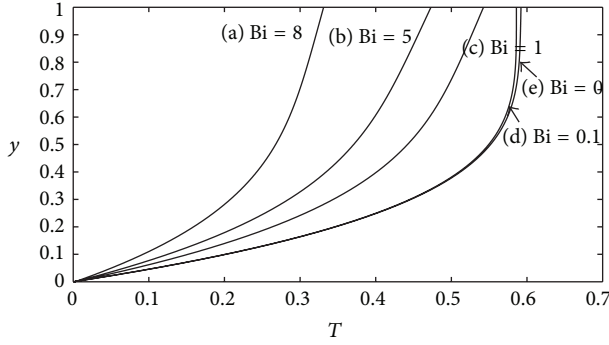


FIGURE 7: The temperature profiles for varying Bi.

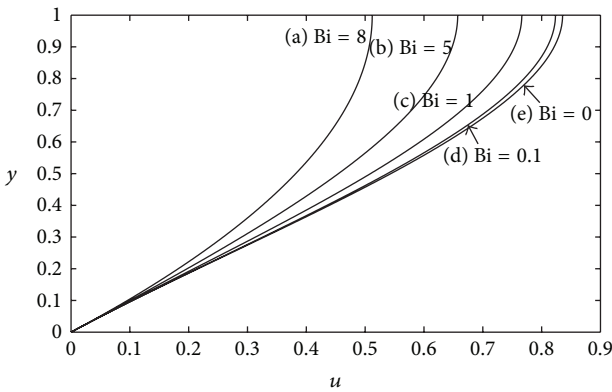


FIGURE 8: The velocity profiles for varying Bi.

transferred to the surrounding atmosphere. The figure clearly demonstrates that the fluid temperature rises with decreasing values of the Biot number, and the temperature profiles flatten out at the free surface as  $Bi$  decreases, and when  $Bi = 0$ , the temperature profile shows that the temperature gradient at the free surface is zero. Khaled [11] investigated the rate of heat and entropy transfer to the slab wall, and the results showed that the dimensionless temperature in the slab wall increases as  $Bi$  decreases, which is in agreement with our findings. The corresponding velocity profiles are shown in Figure 8 with different values of the Biot numbers. The fluid velocity increases across the layer to its maximum at the free surface as the Biot number decreases. This is a result of the resistance force to the flow which decreases as  $Bi$  decreases.

The effect of the Brinkman number is displayed in Figures 9 and 10 for the temperature and velocity profiles. Other parameters are given by  $\alpha = 0.3$  and  $Bi = 0.3$ . Using the values listed in the previous section, the Brinkman numbers are given by  $Br = 0$  for the Newtonian case to 0.5 as shown in Figure 9. We have the Newtonian case displayed in curves (a) in each figure with a constant viscosity. Increasing  $Br$  results in increased viscous heat dissipation effect. The temperature of the fluid increases significantly when  $Br$  increases. In Figure 9, when  $Br$  increases, the fluid heats up quickly, the viscosity of the fluid drops, and the flow is faster. As a result, the fluid velocity increases significantly in the direction of the flow.

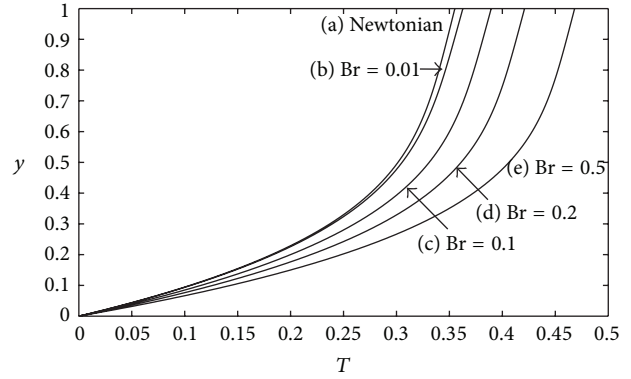


FIGURE 9: The effect of the Brinkman number on temperature profiles.

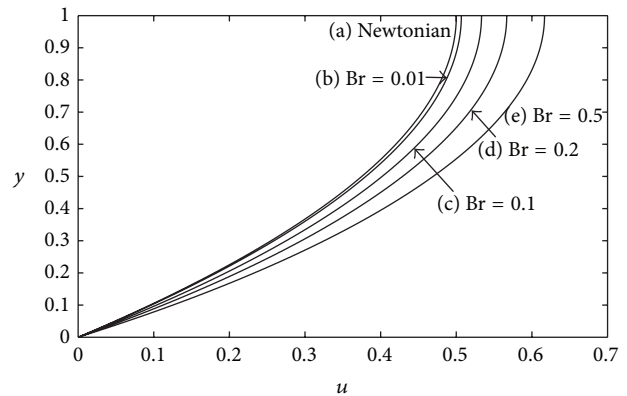


FIGURE 10: The effect of the Brinkman number on the velocity profiles.

## 7. Conclusion

A steady gravity driven flow of a temperature dependent variable viscosity model was investigated. The results were obtained using an asymptotic technique and the fourth-order Runge-Kutta integration scheme. We used experimental values for lubricating oil to determine the value of  $\alpha$  for the asymptotic approximation terms. The numerical results were compared with the asymptotics. The Newtonian cases for both the temperature and velocity of the fluid are retrieved when  $\alpha$  is zero, and the results showed good agreement in all the curves for the temperature and velocity profiles. The effects of large values of  $\alpha$  on the resulting velocity and temperature profiles were further investigated. When  $\alpha$  increase, the temperature and the velocity of the fluid increase significantly. However, when  $\alpha = 58$ , a change in the flow structure is observed from the velocity profiles. Since the viscosity of the fluid decreases exponentially when  $\alpha$  increases, the prediction of the velocity profiles shows a different flow structure. This therefore causes the fluid to behave like a Newtonian fluid, in particular when  $\alpha \geq 58$ . Furthermore, the effect of the flow controlling parameters such as the Biot and the Brinkman numbers was investigated. In the case of the Biot number, the temperature of the fluid increases significantly when the Biot number decreases due

to heat lost from the fluid to the surrounding atmosphere, and as a result, the fluid temperature flattens out at the free surface. The velocity of the fluid increases as the Biot number decreases, due to less resistance force to the flow. The Brinkman number  $Br$  was also investigated, and the results showed that as  $Br$  increases, the temperature of the fluid increases due to heat dissipation, and the velocity of the fluid increased significantly due to the resistance force to the flow, which decreases when the  $Br$  increases.

## Nomenclature

$Bi = HK_c/k$ :	Biot number
$Br = \mu_0 U^2/k\Delta T$ :	Brinkman number
$C_p$ :	Heat capacity ( $J\cdot Kg^{-1}\cdot K^{-1}$ )
$Ec = U^2/c_p T_0$ :	Eckert number
$g$ :	Acceleration due to gravity ( $m\ s^{-2}$ )
$H$ :	Channel height (m)
$k$ :	Thermal conductivity ( $W\cdot m^{-1}\cdot K^{-1}$ )
$K_c$ :	Heat transfer coefficient ( $W\cdot m^{-2}\cdot K^{-1}$ )
$L$ :	Channel length (m)
$P$ :	Pressure scale (Pa)
$p$ :	Pressure (Pa)
$Pe = \rho c_p LU/k$ :	Péclet number
$Pr = \mu_0 c_p/k$ :	Prandtl number
$Re = \rho UL/\mu_0$ :	Reynolds number
$t$ :	Time (s)
$T$ :	Temperature ( $^{\circ}C$ )
$T_a$ :	Ambient temperature ( $^{\circ}C$ )
$T_s$ :	Bottom surface temperature ( $^{\circ}C$ )
$\Delta T$ :	Temperature drop ( $^{\circ}C$ )
$U = \rho g H^2 \sin \beta/\mu_0$ :	Velocity scale ( $m\ s^{-1}$ )
$(u, v)$ :	Cartesian velocity ( $m\ s^{-1}$ )
$(x, y)$ :	Cartesian coordinates (m)
$\varepsilon$ :	Aspect ratio of the flow
$\mu$ :	Dynamic viscosity ( $kg\cdot m^{-1}\cdot s^{-1}$ )
$\mu_0$ :	Dynamic viscosity reference ( $kg\cdot m^{-1}\cdot s^{-1}$ )
$\Phi$ :	Viscous dissipation function
$\rho$ :	Fluid density ( $Kg\cdot m^{-3}$ )
$\theta$ :	Coefficient of viscosity variation ( $K^{-1}$ ).

## References

- [1] C. W. Macosko, *Rheology, Principles, Measurements, and Applications*, Wiley-VCH, Poughkeepsie, NY, USA, 1994.
- [2] A. Oron, S. H. Davis, and S. G. Bankoff, "Long-scale evolution of thin liquid films," *Reviews of Modern Physics*, vol. 69, no. 3, pp. 931–980, 1997.
- [3] T. G. Myers, J. P. F. Charpin, and M. S. Tshehla, "The flow of a variable viscosity fluid between parallel plates with shear heating," *Applied Mathematical Modelling*, vol. 30, no. 9, pp. 799–815, 2006.
- [4] J. J. Wyle and H. Huang, "Extensional flows with viscous heating," *Journal of Fluid Mechanics*, vol. 571, pp. 359–370, 2007.
- [5] A. Costa and G. Macedonio, "Viscous heating in fluids with temperature-dependent viscosity: implications for magma flows," *Nonlinear Processes in Geophysics*, vol. 10, no. 6, pp. 545–555, 2003.
- [6] E. M. A. Elbashbeshy and M. A. A. Bazid, "The effect of temperature-dependent viscosity on heat transfer over a continuous moving surface," *Journal of Physics D*, vol. 33, no. 21, pp. 2716–2721, 2000.
- [7] E. M. A. Elbashbeshy and M. A. A. Bazid, "The effect of temperature-dependent viscosity on heat transfer over a continuous moving surface with variable internal heat generation," *Applied Mathematics and Computation*, vol. 153, no. 3, pp. 721–731, 2004.
- [8] E. M. E. Elbarbary and N. S. Elgazery, "Chebyshev finite difference method for the effects of variable viscosity and variable thermal conductivity on heat transfer from moving surfaces with radiation," *International Journal of Thermal Sciences*, vol. 43, no. 9, pp. 889–899, 2004.
- [9] V. N. Constantinescu, *Laminar Viscous Flow*, Mechanical Engineering Series, Springer, New York, NY, USA, 1995.
- [10] J. P. Holman, *Heat Transfer*, McGraw-Hill, New York, NY, USA, 6th edition, 1990.
- [11] A.-R. A. Khaled, "Conduction heat and entropy transfer in a semi-infinite medium and wall with a combined periodic heat flux and convective boundary condition," *International Journal of Thermal Sciences*, vol. 47, no. 1, pp. 76–83, 2008.
- [12] J. A. Schetz and A. E. Fuhs, *Fundamentals of Fluid Mechanics*, John Wiley & Sons, New York, NY, USA, 1999.
- [13] F. M. White, *Fluid Mechanics*, McGraw-Hill, New York, NY, USA, 3rd edition, 1994.
- [14] F. Alhama and J. Zueco, "Application of a lumped model to solids with linearly temperature-dependent thermal conductivity," *Applied Mathematical Modelling*, vol. 31, no. 2, pp. 302–310, 2007.
- [15] O. D. Makinde, "Laminar falling liquid film with variable viscosity along an inclined heated plate," *Applied Mathematics and Computation*, vol. 175, no. 1, pp. 80–88, 2006.
- [16] H. A. Barnes, J. F. Hutton, and K. Walters, *An Introduction to Rheology*, Elsevier, 1989.
- [17] D. Knezevic and V. Savic, "Mathematical modelling of dynamic viscosity, as a function of temperature and pressure, of mineral oil for hydraulic systems," *Mechanical Engineering*, vol. 4, no. 1, pp. 27–34, 2006.
- [18] O. D. Makinde, "Hermite-Padé approximation approach to steady flow of a liquid film with adiabatic free surface along an inclined heat plate," *Physica A*, vol. 381, no. 1-2, pp. 1–7, 2007.
- [19] O. D. Makinde, "Thermal criticality for a reactive gravity driven thin film flow of a third-grade fluid with adiabatic free surface down an inclined plane," *Applied Mathematics and Mechanics*, vol. 30, no. 3, pp. 373–380, 2009.

## Research Article

# A New Numerical Approach of MHD Flow with Heat and Mass Transfer for the UCM Fluid over a Stretching Surface in the Presence of Thermal Radiation

S. Shateyi<sup>1</sup> and G. T. Marewo<sup>2</sup>

<sup>1</sup> Department of Mathematics, University of Venda, Private Bag X5050, Thohoyandou 0950, South Africa

<sup>2</sup> Department of Mathematics, University of Swaziland, Private Bag 4, Kwaluseni, Swaziland

Correspondence should be addressed to S. Shateyi; stanford.shateyi@univen.ac.za

Received 18 March 2013; Accepted 13 August 2013

Academic Editor: Tirivanhu Chinyoka

Copyright © 2013 S. Shateyi and G. T. Marewo. This is an open access article distributed under the Creative Commons Attribution License, which permits unrestricted use, distribution, and reproduction in any medium, provided the original work is properly cited.

This paper numerically investigates the magnetohydrodynamic boundary layer flow with heat and mass transfer of an incompressible upper-convected Maxwell fluid over a stretching sheet in the presence of viscous dissipation and thermal radiation as well as chemical reaction. The governing partial differential equations are transformed into a system of ordinary differential equations by using suitable similarity transformations. The resultant highly nonlinear ordinary differential equations are then solved using spectral relaxation method. The results are obtained for velocity, temperature, concentration, skin friction, and Nusselt number. The effects of various material parameters on the flow with heat and mass transfer and the dimensionless variables are illustrated graphically and briefly discussed.

## 1. Introduction

In the past few decades, the studies of boundary layer flows of Newtonian and non-Newtonian fluids of stretching surfaces have received great attention by virtue of their numerous applications in the fields of metallurgy, chemical engineering, and biological systems. These applications include geothermal reservoirs, wire and fiber coating, food stuff processing, reactor fluidization, transpiration cooling, enhanced oil recovery, packed bed catalytic reactors, and cooling of nuclear reactors. The prime aim in extrusion is to keep the surface quality of the extricate. Coating processes demand a smooth glossy surface to meet the requirements for the best appearance and optimum properties. Sakiadis [1, 2] did pioneering work on boundary layer flow on a continuously moving surface. After that many investigators discussed various aspects of the stretching flow problem (see, e.g., Chiam [3], Crane [4], Liao and Pop [5], Khan and Sanjayanand [6], Abel and Mahesha [7], and Fang et al. [8], among others).

A number of industrial fluids such as molten plastics, artificial fibers, blood, polymeric liquids, and food stuff exhibit non-Newtonian fluid behaviour. In many industrial processes, cooling continuous strips or filaments is done by drawing them through a quiescent fluid. It must be noted that during these processes, the strips are sometimes stretched or shrunk. Therefore the properties of the final product depend to a great extent on the rate of cooling. The rate of cooling can be controlled and the desired characteristics of the final product can be obtained by drawing the strips in electrically conducting fluids subjected to uniform magnetic fields.

In recent years, MHD flows of viscoelastic fluids above stretching sheets have also been studied by various researchers (Liu [9], Cortell [10], among others). This is the simplest subclass of viscoelastic fluid known as the second grade fluid. However, a non-Newtonian second grade fluid does not give meaningful industrial results for highly elastic fluids such as polymer melts, which occur at high Deborah number (Hayat et al. [11]). For theoretical results to become

of any industrial use, more realistic viscoelastic fluid models such as upper-convected Maxwell model should be used in the analysis.

Alizadeh-Pahlavan et al. [12] investigated using a two-auxiliary-parameter homotopy analysis method for the problem of laminar MHD flow of an upper-convected Maxwell fluid above a porous isothermal stretching sheet. Aliakbar et al. [13] analyzed the influence of Maxwell fluids above stretching sheets. Abel et al. [14] performed an analysis to investigate the influence of MHD and thermal radiation on the two-dimensional steady flow of an incompressible, upper-convected Maxwell fluid. Motsa et al. [15] investigated the MHD boundary layer flow of an incompressible upper-convected Maxwell fluid over a porous stretching surface. Hayat et al. [16] investigated MHD flow of a more realistic viscoelastic fluid model above a porous stretching sheet. Sadeghy et al. [17] also studied MHD flows of upper-convected Maxwell model fluids above porous stretching sheet using homotopy analysis method. Raftari and Yildirim [18] approximated an analytical solution of the magneto-hydrodynamic boundary layer flow of an upper-convected Maxwell fluid over a porous stretching sheet. More recently, Alinejad and Samarbakhsh [19] numerically investigated the flow and heat transfer characteristics of the incompressible viscous flow over a nonlinear stretching sheet with viscous dissipation.

Hayat et al. [20] proposed the modified decomposition method and the Padé approximants for the MHD flow over a nonlinear sheet. In recent years, scientists and engineers have endeavored to develop more accurate and fast converging numerical and/or analytical techniques. Methods such as homotopy and their hybrid techniques have been extensively applied to solve nonlinear equations (Liao [21], He [22], Domairry and Nadim [23], Shateyi and Motsa [24], Sheikholeslami et al. [25], and Ganji [26], among others). Recently, successive linearization method has been reported and successfully utilized in solving boundary value problems (see, e.g., Motsa and Shateyi [27], Motsa et al. [28], and Shateyi and Motsa [29]).

The aim of this study is to investigate the effects of thermal radiation and viscous dissipation on steady MHD flow with heat and mass transfer of an upper-convected Maxwell fluid past a stretching sheet in the presence of a chemical reaction. Secondly, we aim to use a recently developed iterative method known as spectral relaxation method (SRM), and details of this method can be found in [30–32].

## 2. Mathematical Formulation

We consider the steady and incompressible MHD boundary layer flow with heat and mass transfer of an electrically conducting fluid obeying UCM model over a stretching sheet in the presence of thermal radiation. The flow is generating by the stretching of the sheet by applying two equal and opposite forces along the  $x$ -axis, keeping the origin fixed and considering the flow to be confined to the region  $y > 0$ . We assume that the continuous stretching sheet has a linear velocity,  $u = bx$ , with  $b$  as the stretching rate and  $x$  being the distance from the slit. We impose a uniform magnetic field of

strength  $B_0$  along the  $y$ -axis, and the induced magnetic field is negligible. This assumption is valid on a laboratory scale under the assumption of small magnetic Reynolds number, and the external electric field is zero. We also assume that the boundary layer approximations are applicable to all momentum, energy, and mass equations. Although this theory is incomplete for viscoelastic fluids, but it is more plausible for Maxwell fluids as compared to other viscoelastic fluid models (Renardy [33]). Following Sadeghy et al. [17] among others, in a two-dimensional flow, the equation of continuity, the equation of motion, and the diffusion equations can be written as

$$\frac{\partial u}{\partial x} + \frac{\partial v}{\partial y} = 0, \quad (1)$$

$$\begin{aligned} u \frac{\partial u}{\partial x} + v \frac{\partial u}{\partial y} + \lambda_1 \left[ u^2 \frac{\partial^2 u}{\partial x^2} + v^2 \frac{\partial^2 u}{\partial y^2} + 2uv \frac{\partial^2 u}{\partial x \partial y} \right] \\ = \nu \frac{\partial^2 u}{\partial y^2} - \frac{\sigma B_0^2}{\rho} u, \end{aligned} \quad (2)$$

$$u \frac{\partial T}{\partial x} + v \frac{\partial T}{\partial y} = \frac{k}{\rho c_p} \frac{\partial^2 T}{\partial y^2} + \frac{\mu}{\rho c_p} \left( \frac{\partial u}{\partial y} \right)^2 - \frac{1}{\rho c_p} \frac{\partial q_r}{\partial y}, \quad (3)$$

$$u \frac{\partial C}{\partial x} + v \frac{\partial C}{\partial y} = D \frac{\partial^2 C}{\partial y^2} - K_n (C - C_\infty)^n, \quad (4)$$

where  $u$  and  $v$  are velocity components in the  $x$ - and  $y$ -directions, respectively,  $\rho$  is the fluid density,  $\sigma$  is the electrical conductivity,  $B_0$  is the uniform magnetic field,  $T$  is the temperature,  $c_p$  is the specific heat at constant pressure,  $k$  is the thermal conductivity,  $C$  is the concentration of the species diffusion,  $D$  is the diffusion coefficient of the diffusion species,  $\nu$  is the kinematic viscosity,  $\lambda$  is the relaxation time, and  $K_n$  denotes the reaction rate constant of the  $n$ th-order homogeneous and irreversible reaction. The appropriate boundary conditions are

$$\begin{aligned} u(x, 0) &= U_w(x) = bx, \\ v(x, 0) &= 0, \\ T(x, 0) &= T_\infty + T_s \left( \frac{x}{l} \right)^2, \\ C(x, 0) &= C_\infty + C_s \left( \frac{x}{l} \right)^2, \end{aligned} \quad (5)$$

$$u(x, \infty) = 0,$$

$$T(x, \infty) = T_\infty,$$

$$C(x, \infty) = C_\infty.$$

By using the Rosseland diffusion approximation (Hossain et al. 1999, among other researchers), the radiative heat flux,  $q_r$ , is given by

$$q_r = -\frac{4\sigma^*}{3K_s} \frac{\partial T^4}{\partial y}, \quad (6)$$

where  $\sigma^*$  and  $K_s$  are the Stefan-Boltzmann constant and the Rosseland mean absorption coefficient, respectively. We assume that the temperature differences within the flow are sufficiently small such that

$$T^4 \approx 4T_\infty^3 T - 3T_\infty^4. \quad (7)$$

Using (6) and (7) in the last term of (3) we obtain

$$\frac{\partial q_r}{\partial y} = -\frac{16\sigma^* T_\infty^3}{3K_s} \frac{\partial^2 T}{\partial y^2}. \quad (8)$$

**2.1. Similarity Transformation.** To make the problem amenable we introduce the following nondimensional quantities:

$$\begin{aligned} \eta &= \sqrt{\frac{b}{\nu}} y, & \psi &= \sqrt{b\nu x} f(\eta), \\ \theta(\eta) &= \frac{T - T_\infty}{T_w - T_\infty}, \\ \phi(\eta) &= \frac{C - C_\infty}{C_w - C_\infty}, \end{aligned} \quad (9)$$

where  $f(\eta)$  is the dimensionless stream function and  $\eta$  is the similarity variable,  $\theta$  is the dimensionless temperature, and  $\phi$  is the mass concentration. The continuity equation is automatically satisfied through the variables. Then introducing the relations (9) into (2)-(3), we obtain the following nonlinear system of ordinary differential equations:

$$f''' + ff'' - f'^2 - M^2 f' + \beta(2ff'f'' - f^2 f''') = 0, \quad (10)$$

$$\left(1 + \frac{4}{3}R\right)\theta'' + \text{Pr}(f\theta' - 2f'\theta) + \text{Pr Ec} f''^2 = 0, \quad (11)$$

$$\phi'' + \text{Sc}[f\phi' - 2f'\phi - \gamma\phi^n] = 0. \quad (12)$$

Here  $M^2 = \sigma B_0^2 / \rho b$  and  $\beta = \lambda b$  are magnetic and elastic parameters, respectively,  $\text{Pr} = \mu c_p / k$  is the Prandtl number,  $\text{Ec} = bl^2 / c_p T_s$  is the Eckert number,  $R = 4\sigma^* T_\infty^3 / kK_s$  is the thermal radiation parameter,  $\gamma = K_n C_0^{n-1} b^{n-2} x^n / l^2$  is the chemical reaction parameter, and  $\text{Sc} = D/\nu$  is the Schmidt number. The boundary conditions are

$$\begin{aligned} f(0) &= 0, & f'(0) &= 1, & \theta(0) &= 1, & \phi(0) &= 1, \\ f' &\rightarrow 0, & \theta &\rightarrow 0, & \phi &\rightarrow 0, & \text{as } \eta &\rightarrow \infty. \end{aligned} \quad (13)$$

### 3. Method of Solution

The Successive Relaxation Method (SRM) begins by letting

$$p = f' \quad (14)$$

so that  $p' = f''$  and  $p'' = f'''$ . Consequently, (10) through (12) become

$$p'' + fp' - p^2 - M^2 p + \beta(2fpp' - f^2 p'') = 0, \quad (15)$$

$$\left(1 + \frac{4}{3}R\right)\theta'' + \text{Pr}(f\theta' - 2p\theta) + \text{Pr Ec} p'^2 = 0, \quad (16)$$

$$\phi'' + \text{Sc}[f\phi' - 2p\phi - \gamma\phi^n] = 0. \quad (17)$$

Proceeding in a manner similar to the Gauss-Seidel method, (14) and (15) through (16) are replaced by the following recursive formulae:

$$f'_{r+1} = p_r, \quad f_{r+1}(0) = 0, \quad (18)$$

$$\begin{aligned} p''_{r+1} + f_{r+1} p'_r - p_r^2 - M^2 p_{r+1} \\ + \beta(2f_{r+1} p_r p'_r - f_{r+1}^2 p_r'') = 0, \end{aligned} \quad (19)$$

$$\begin{aligned} p_{r+1}(0) &= 1, & p_{r+1}(\infty) &= 0, \\ \frac{1}{\text{Pr}} \left(1 + \frac{4R}{3}\right) \theta''_{r+1} + f_{r+1} \theta'_{r+1} \\ - 2p_{r+1} \theta_{r+1} + \text{Ec} p_{r+1}^2 &= 0, \end{aligned} \quad (20)$$

$$\begin{aligned} \theta_{r+1}(0) &= 1, & \theta_{r+1}(\infty) &= 0, \\ \phi''_{r+1} + \text{Sc}[f\phi'_{r+1} - 2p_{r+1}\phi_{r+1} - \gamma\phi_{r+1}^n] &= 0, \end{aligned} \quad (21)$$

The Chebyshev spectral collocation method will be used to solve (18) through (21). First, we replace the semi-infinite interval  $[0, \infty)$  with the closed interval  $[0, L]$ , where  $L$  is sufficiently large. It is convenient to use the change of variable

$$\eta(\xi) = \frac{1 + \xi}{2} L \quad (22)$$

to map the interval  $[0, L]$  on the  $\eta$ -axis onto the interval  $[-1, 1]$  on the  $\xi$ -axis. On  $[-1, 1]$  we form a computational grid  $-1 = \xi_N < \xi_{N-1} < \dots < \xi_0 = 1$ , where

$$\xi_j = \cos\left(\frac{\pi p}{N}\right), \quad j = 0, 1, \dots, N, \quad (23)$$

are the Chebyshev collocation points. The derivative  $h'(\xi_j)$  at each collocation point is evaluated using formula

$$\begin{aligned} h'(\xi_j) &= \sum_{k=0}^N D_{jk} h(\xi_k) \\ \implies \mathbf{h}' &= D\mathbf{h}, \end{aligned} \quad (24)$$

where  $D$  is the Chebyshev differentiation matrix. Successive application of Chebyshev differentiation reveals the more general formula

$$\frac{d^q}{d\xi^q} \mathbf{h} = D^q \mathbf{h}. \quad (25)$$

Chebyshev differentiation transforms (18) through (21) to discrete form:

$$\begin{aligned}
A_1 \mathbf{f}_{r+1} &= B_1, & f_{r+1}(\xi_N) &= 0, \\
A_2 \mathbf{p}_{r+1} &= B_2, & p_{r+1}(\xi_N) &= 1, & p_{r+1}(\xi_0) &= 0, \\
A_3 \mathbf{\Theta}_{r+1} &= B_3, & \theta_{r+1}(\xi_N) &= 1, & \theta_{r+1}(\xi_0) &= 0, \\
A_4 \mathbf{\Phi}_{r+1} &= B_4, & \phi_{r+1}(\xi_N) &= 1, & \phi_{r+1}(\xi_0) &= 0,
\end{aligned} \tag{26}$$

where

$$\begin{aligned}
A_1 &= D, & B_1 &= \mathbf{p}_r, \\
A_2 &= D^2 + \text{diag}[\mathbf{f}_{r+1}]D - M^2 I, \\
B_2 &= \mathbf{p}_r^2 - \beta (2\mathbf{f}_{r+1}\mathbf{p}_r\mathbf{p}_r' - \mathbf{f}_{r+1}^2\mathbf{p}_r''), \\
A_3 &= \left(1 + \frac{4}{3}R\right)D^2 + \text{Pr}(\text{diag}[\mathbf{f}_{r+1}]D - 2\text{diag}[\mathbf{p}_{r+1}]), \\
B_3 &= -\text{Pr Ec}\mathbf{p}_{r+1}^{\prime 2}, \\
A_4 &= D^2 + \text{Sc}(\text{diag}[\mathbf{f}_{r+1}]D - 2\text{diag}[\mathbf{p}_{r+1}]), \\
B_4 &= \text{Sc}\gamma\mathbf{\Phi}_r^n.
\end{aligned} \tag{27}$$

Initial approximations needed to drive this iterative scheme must satisfy boundary conditions (13). Suitable choices are

$$\begin{aligned}
f_0(\eta) &= 1 - e^{-\eta}, & p_0(\eta) &= e^{-\eta}, \\
\theta_0(\eta) &= e^{-\eta}, & \phi_0(\eta) &= e^{-\eta}.
\end{aligned} \tag{28}$$

## 4. Results and Discussion

In this section we give the SRM results for the main parameters that have significant effects on the fluid flow velocity and temperature. We remark that all the SRM results presented in this work were obtained using  $N = 50$  collocation points, and also convergence was achieved after as few as five iterations. Also the infinity value ( $\eta_\infty$ ) was taken to be 50. It is also important to note that the magnetic field is taken quite strong by assigning large values of  $M$  to ensure the occurrence of steady flow near the sheet. Unless otherwise stated, the default values for the parameters are taken as  $M = 1$ ,  $\beta = 0.1$ ,  $R = 1$ ,  $\text{Pr} = 0.71$ ,  $\text{Ec} = 0.1$ ,  $\text{Sc} = 0.2$ ,  $\gamma = 0.2$ , and  $n = 2$ . In order to validate the numerical method, it was compared with the MATLAB routine *bvp4c* which is an adaptive Lobatto quadrature iterative scheme. Table 1 presents a comparison between SRM approximate results and the *bvp4c* results for selected default values of the magnetic parameter  $M$ . It can be seen from this table that there is an excellent agreement between the results from the two methods. Analyzing Table 1 shows that an increase in the magnetic field strength leads to an increase in the skin-friction but a decrease to the Nusselt number. This is physically expected as application of a transverse magnetic field produces a drag force which then reduces the flow velocity but generates heat within the fluid.

TABLE 1: Comparison of the SRM results of  $-f''(0)$ ,  $-\theta'(0)$  with those obtained by *bvp4c* for different values of the magnetic parameter.

$M$	$-f''(0)$		$-\theta'(0)$	
	<i>bvp4c</i>	SRM	<i>bvp4c</i>	SRM
0.0	1.42811186	1.42811186	0.57932373	0.57932373
1.0	1.87763199	1.87763199	0.40978550	0.40978550
2.0	2.71897650	2.71897650	0.27809236	0.27809236

TABLE 2: Comparison of the SRM results of  $-f''(0)$ ,  $-\theta'(0)$  with those obtained by *bvp4c* for different values of the elastic parameter.

$\beta$	$-f''(0)$		$-\theta'(0)$	
	<i>bvp4c</i>	SRM	<i>bvp4c</i>	SRM
0.0	1.39382112	1.39382112	3.22830067	3.22830067
0.2	1.46105462	1.46105462	3.20679682	3.20679682
0.4	1.52344386	1.52344386	3.18653107	3.18653107

Table 2 gives a comparison of the SRM results to those obtained by the *bvp4c* for different values of the elasticity parameter  $\beta$ . We again observe that the results from the two methods agree very well giving confidence to the current proposed method. Increasing the fluid elasticity parameter leads to the increase in the skin friction coefficient but a decrease in the heat transfer coefficient. Figures 1 and 2 show the influence of the elasticity parameter  $\beta$  on the  $u$ -velocity and  $v$ -velocity profiles, respectively. From both these figures, we observe that an increase in the elasticity parameter results in the decrease in both velocity components and a decrease in the thickness of the momentum boundary layer.

Figures 3 and 4 depict the effects of the magnetic field parameter  $M$  on the  $u$ -velocity and  $v$ -velocity profiles, respectively. From these figures we clearly observe that increasing magnetism significantly reduces the thickness of the boundary layer, thereby reducing the velocity components. Physically, the application of the transverse magnetic field presents a damping effect on the flow velocity by producing a drag force that opposes the fluid motion.

Figure 5 depicts the effect of increasing the elasticity parameter  $\beta$  on the temperature distribution. A decrease in the streamwise velocity component,  $u$ , can result in a decrease in the amount of heat transferred on the surface sheet. Similarly, a decrease in the transverse velocity component,  $v$ , means that the amount of fresh fluid which is extended from the lower-temperature region outside the boundary layer and directed towards the sheet is reduced, thereby reducing the rate of heat transfer. These two effects on the velocity components in the same direction reinforce each other. Thus, an increase in the elastic number increases the temperature distribution in the fluid as depicted in Figure 5.

Figure 6 represents the dimensionless temperature for different values of the magnetic field parameter  $M$ . From this figure we clearly see that the temperature profiles increase with the increase of the magnetic field parameter. Thus the applied magnetic field tends to heat the fluid and thus reduces

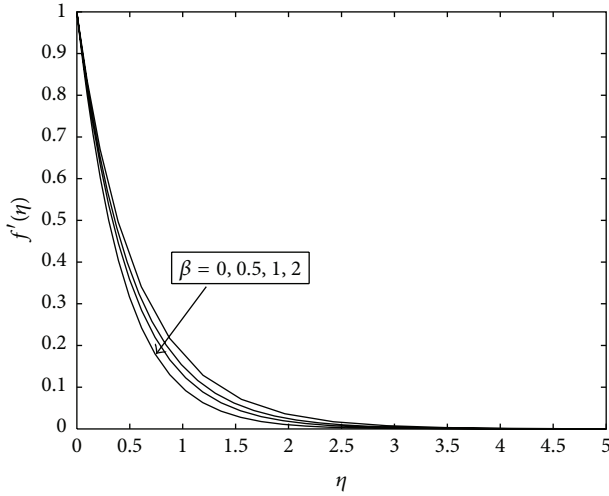


FIGURE 1: Graph of the SRM solutions of the  $u$ -velocity for different values of  $\beta$ .

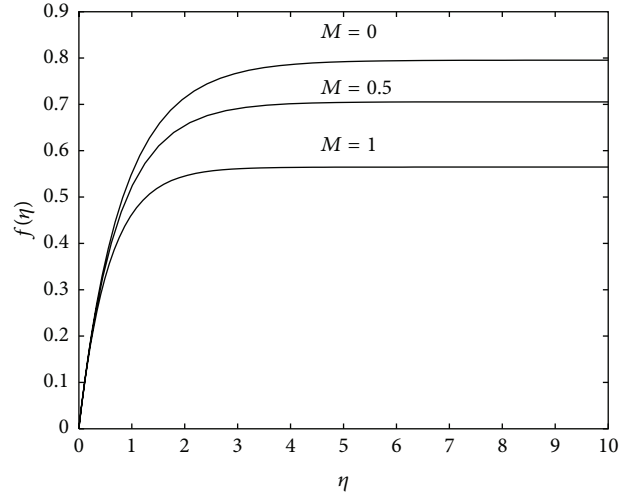


FIGURE 4: The variation of the  $v$ -velocity component for different values of  $M$ .

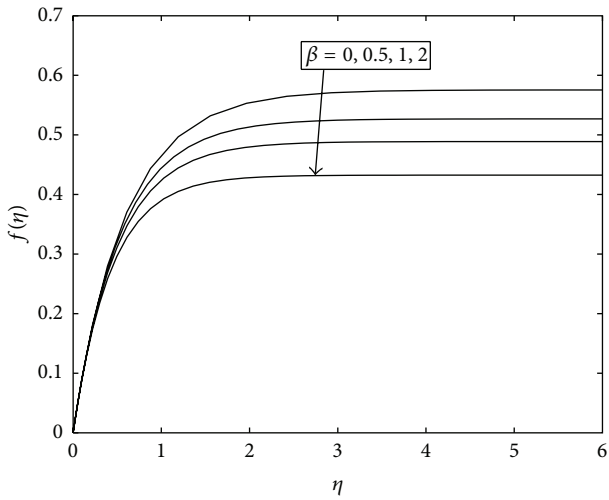


FIGURE 2: Effect of the  $\beta$  on the  $v$ -velocity profile.

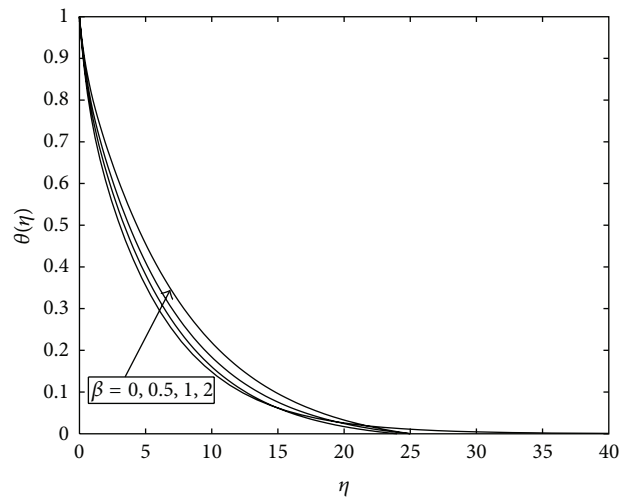


FIGURE 5: Graph of the SRM solutions of the temperature distribution for different values of  $\beta$ .

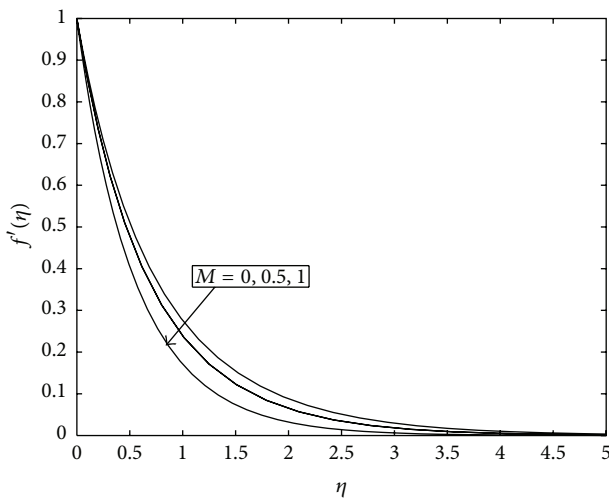


FIGURE 3: Influence of the magnetic parameter  $M$  on the  $u$ -velocity profile.

the heat transfer from the wall which in turn enlarges the thermal boundary layer thickness.

In Figure 7 we display the effect of the Eckert number on the temperature profiles. An increase in the values of the Eckert number is seen to increase the temperature of the fluid at any point above the sheet. Increasing the Eckert number allows energy to be stored in the fluid region as a consequence of dissipation due to viscosity and elastic deformation.

The influence of thermal radiation on the temperature profiles is shown in Figure 8. It can be seen that the thermal boundary layer thickness increases as  $R$  increases. This induces the decrease in the absolute value of the temperature gradient at the surface. Thus, the heat transfer rate at the surface decreases with increasing  $R$ , thereby causing the temperature profiles to increase.

Figure 9 depicts the effect of increasing the Prandtl number on the fluid temperature distribution. An increase in

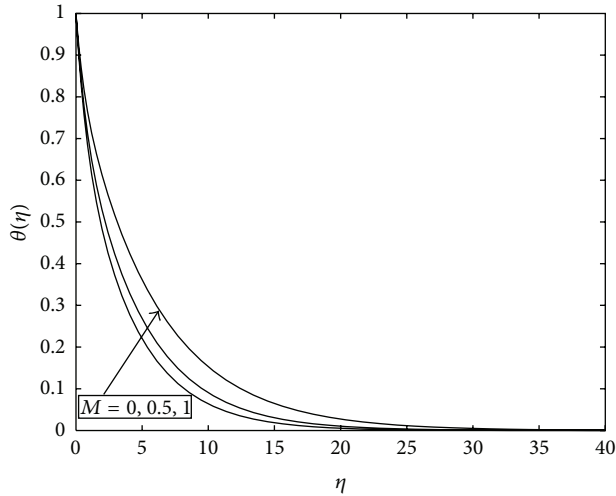


FIGURE 6: Variation of the temperature distribution for different values of  $M$ .

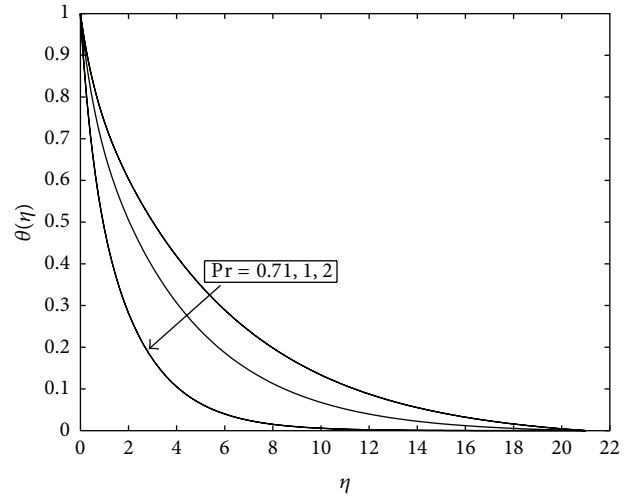


FIGURE 9: The effect of the Prandtl number on the temperature distribution.

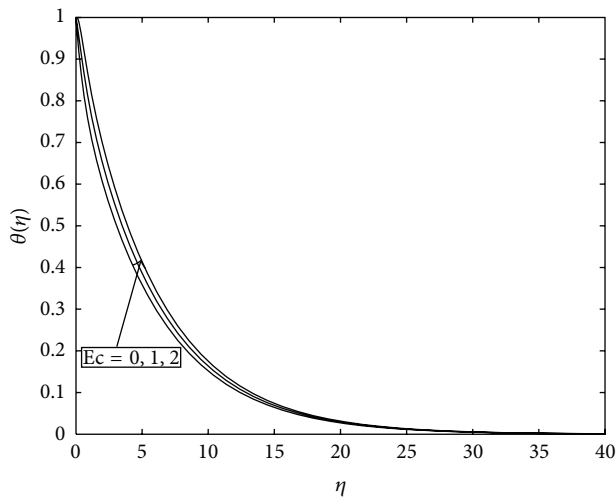


FIGURE 7: Graph of the SRM solutions of the temperature profile for different values of  $Ec$ .

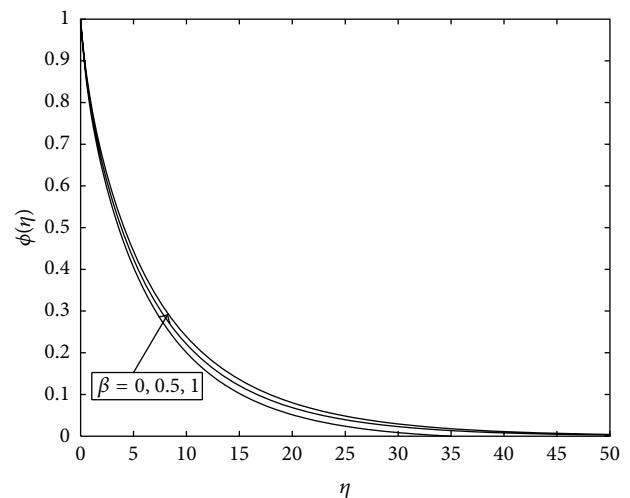


FIGURE 10: Graph of the SRM solutions of the concentration profile for different values of  $\beta$ .

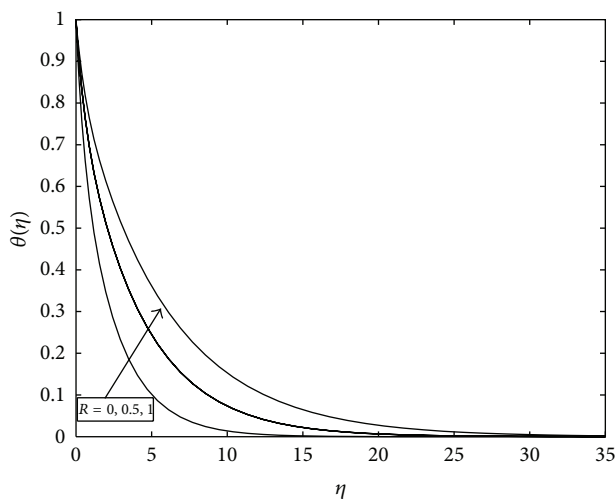


FIGURE 8: Influence of thermal radiation of the fluid temperature.

the Prandtl number as expected is seen to reduce the fluid temperature above the sheet. This is because as the Prandtl number increases, the thermal boundary layer becomes thinner. Thus the rate of thermal diffusion drops, resulting in the fluid temperature dropping as well.

Figure 10 shows how the elastic parameter  $\beta$  affects the concentration profiles. As the elasticity parameter reduces the flow velocity, it means that less fluid is taken away at any given point resulting in the concentration profiles increasing. The same phenomenon happens when the values of the magnetic parameter increase as can be clearly seen in Figure 11. The reduction of flow velocity as the result of increasing the strength of the magnetic field causes the fluid concentration to increase as less fluid is taken downstream at any given point.

Figure 12 presents the profiles of the concentration for selected default values of the chemical reaction parameter

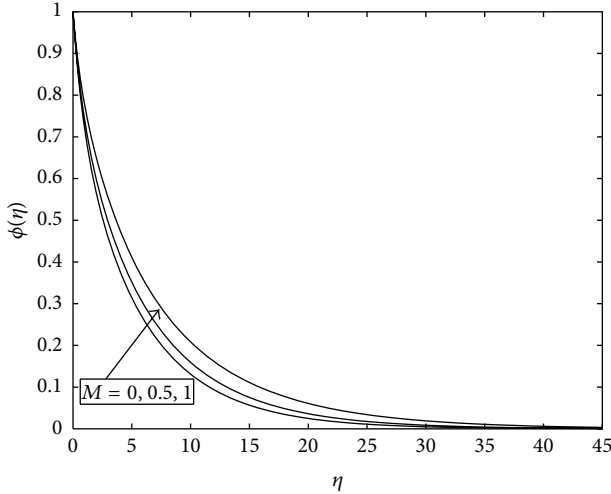


FIGURE 11: Graph of how the magnetic parameter affects the concentration distribution.

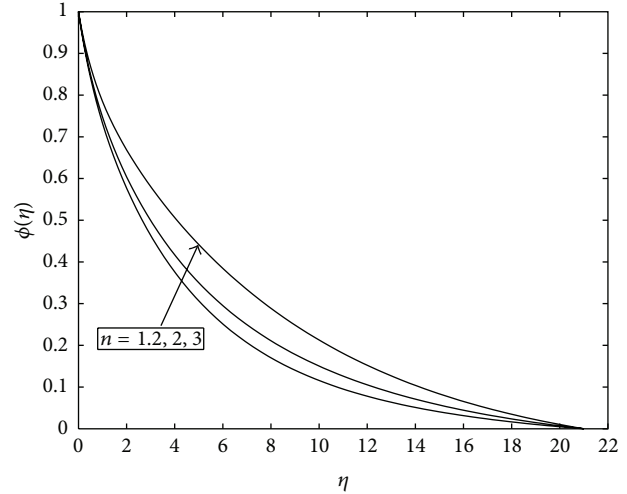


FIGURE 13: Graph of the SRM solutions of the concentration for different orders of the homogeneous reaction.

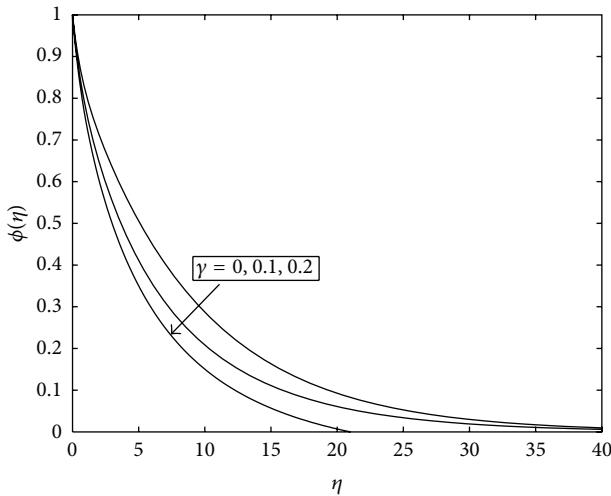


FIGURE 12: Influence of the chemical reaction on the concentration distribution.

$\gamma \geq 0$ . It is observed from this figure that an increase in the values of chemical reaction parameter leads to a decrease in the concentration profiles. The concentration boundary layer becomes thin as the reaction parameter increases.

Figure 13 shows graphically the effect of increasing the reaction-order parameter  $n$ . The effect of  $n$  is seen as to increase the fluid concentration.

### 5. Conclusion

The present work analyzed the MHD flow with heat and mass transfer within a boundary layer of an upper-convected Maxwell fluid above a stretching sheet in the presence of viscous dissipation, thermal radiation, and chemical reaction. Numerical results are presented in tabular/graphical form to elucidate the details of flow with heat and mass transfer characteristics and their dependence on the various physical

parameters. The accuracy of the SRM is validated against the MATLAB in-built *bvp4c* routine for solving boundary value problems.

- (1) We observe that the flow velocity is decreased when the magnetic parameter increases. Also an increase in the elasticity parameter results in velocity decrements. However, both the temperature and concentration profiles are enhanced by increasing the values of the magnetic parameter as well as the elasticity parameter.
- (2) The dimensionless temperature  $\theta$  increases with increase in the thermal radiation but decreases with increasing Prandtl number.
- (3) The effect of the chemical reaction  $\gamma$  is to decrease the fluid concentration while the concentration profiles are increased as the order of reaction  $n$  is increased.
- (4) It is shown that the skin-friction increases with an increase of the magnetic parameter and elasticity parameter, but the Nusselt number and Sherwood number (not shown for brief) are found to be decreased as these parameters are increased.
- (5) Finally the Nusselt number increases with increasing values of the Prandtl number but decreases as thermal radiation increases.

### Acknowledgments

The authors wish to acknowledge financial support from the University of Venda and NRF.

### References

[1] B. C. Sakiadis, "Boundary-layer behaviour on continuous solid surfaces: I. Boundary-layer equations for two-dimensional and axisymmetric flow," *AIChE Journal*, vol. 7, no. 1, pp. 26–28, 1961.

- [2] B. C. Sakiadis, "Boundary-layer behaviour on continuous solid surfaces: II. Boundary-layer equations for two-dimensional and axisymmetric flow," *AIChE Journal*, vol. 7, no. 2, pp. 221–225, 1961.
- [3] T. C. Chiam, "Hydromagnetic flow over a surface stretching with a power-law velocity," *International Journal of Engineering Science*, vol. 33, no. 3, pp. 429–435, 1995.
- [4] L. J. Crane, "Flow past a stretching plate," *Zeitschrift für Angewandte Mathematik und Physik*, vol. 21, no. 4, pp. 645–647, 1970.
- [5] S. Liao and I. Pop, "Explicit analytic solution for similarity boundary layer equations," *International Journal of Heat and Mass Transfer*, vol. 47, no. 1, pp. 75–85, 2004.
- [6] S. K. Khan and E. Sanjayanand, "Viscoelastic boundary layer flow and heat transfer over an exponential stretching sheet," *International Journal of Heat and Mass Transfer*, vol. 48, no. 8, pp. 1534–1542, 2005.
- [7] M. S. Abel and N. Mahesha, "Heat transfer in MHD viscoelastic fluid flow over a stretching sheet with variable thermal conductivity, non-uniform heat source and radiation," *Applied Mathematical Modelling*, vol. 32, no. 10, pp. 1965–1983, 2008.
- [8] T. G. Fang, C. F. F. Lee, and J. Zhang, "The boundary layers of an unsteady incompressible stagnation-point flow with mass transfer," *International Journal of Non-Linear Mechanics*, vol. 46, no. 7, pp. 942–948, 2011.
- [9] I. C. Liu, "Flow and heat transfer of an electrically conducting fluid of second grade in a porous medium over a stretching sheet subject to a transverse magnetic field," *International Journal of Non-Linear Mechanics*, vol. 40, no. 4, pp. 465–474, 2005.
- [10] R. Cortell, "Flow and heat transfer of an electrically conducting fluid of second grade over a stretching sheet subject to suction and to a transverse magnetic field," *International Journal of Heat and Mass Transfer*, vol. 49, no. 11–12, pp. 1851–1856, 2006.
- [11] T. Hayat, Z. Abbas, and M. Sajid, "Series solution for the upper-convected Maxwell fluid over a porous stretching plate," *Physics Letters A*, vol. 358, no. 5–6, pp. 396–403, 2006.
- [12] A. Alizadeh-Pahlavan, V. Aliakbar, F. Vakili-Farahani, and K. Sadeghy, "MHD flows of UCM fluids above porous stretching sheets using two-auxiliary-parameter homotopy analysis method," *Communications in Nonlinear Science and Numerical Simulation*, vol. 14, no. 2, pp. 473–488, 2009.
- [13] V. Aliakbar, A. Alizadeh-Pahlavan, and K. Sadeghy, "The influence of thermal radiation on MHD flow of Maxwellian fluids above stretching sheets," *Communications in Nonlinear Science and Numerical Simulation*, vol. 14, no. 3, pp. 779–794, 2009.
- [14] M. S. Abel, J. V. Tawade, and J. N. Shinde, "The effects of MHD flow and heat transfer for the UCM fluid over a stretching surface in presence of thermal radiation," *Advances in Mathematical Physics*, vol. 2012, Article ID 702681, 21 pages, 2012.
- [15] S. S. Motsa, T. Hayat, and O. M. Aldossary, "MHD flow of upper-convected Maxwell fluid over porous stretching sheet using successive Taylor series linearization method," *Applied Mathematics and Mechanics*, vol. 33, no. 8, pp. 975–990, 2012.
- [16] T. Hayat, Z. Abbas, M. Sajid, and S. Asghar, "The influence of thermal radiation on MHD flow of a second grade fluid," *International Journal of Heat and Mass Transfer*, vol. 50, no. 5–6, pp. 931–941, 2007.
- [17] K. Sadeghy, H. Hajibeygi, and S. Taghavi, "Stagnation-point flow of upper-convected Maxwell fluids," *International Journal of Non-Linear Mechanics*, vol. 41, no. 10, pp. 1242–1247, 2006.
- [18] B. Raftari and A. Yildirim, "The application of homotopy perturbation method for MHD flows of UCM fluids above porous stretching sheets," *Computers and Mathematics with Applications*, vol. 59, no. 10, pp. 3328–3337, 2010.
- [19] J. Alinejad and S. Samarbakhsh, "Viscous flow over nonlinearly stretching sheet with effects of viscous dissipation," *Journal of Applied Mathematics*, vol. 2012, Article ID 587834, 10 pages, 2012.
- [20] T. Hayat, Q. Hussain, and T. Javed, "The modified decomposition method and Padé approximants for the MHD flow over a non-linear stretching sheet," *Nonlinear Analysis: Real World Applications*, vol. 10, no. 2, pp. 966–973, 2009.
- [21] S. J. Liao, *Beyond Perturbation: Introduction to Homotopy Analysis Method*, CRC Series: Modern Mechanics and Mathematics, Chapman & Hall/CRC Press, Boca Raton, Fla, USA, 2003.
- [22] J. H. He, "Homotopy perturbation technique," *Computer Methods in Applied Mechanics and Engineering*, vol. 178, no. 3–4, pp. 257–262, 1999.
- [23] G. Domairry and N. Nadim, "Assessment of homotopy analysis method and homotopy perturbation method in non-linear heat transfer equation," *International Communications in Heat and Mass Transfer*, vol. 35, no. 1, pp. 93–102, 2008.
- [24] S. Shateyi and S. S. Motsa, "A new approach for the solution of three-dimensional magnetohydrodynamic rotating flow over a shrinking sheet," *Mathematical Problems in Engineering*, vol. 2010, Article ID 586340, 15 pages, 2010.
- [25] M. Sheikholeslami, H. R. Ashorynejada, D. D. Ganji, and A. Yildirim, "Homotopy perturbation method for three-dimensional problem of condensation film on inclined rotating disk," *Scientia Iranica*, vol. 19, no. 3, pp. 437–442, 2012.
- [26] D. D. Ganji, "A semi-analytical technique for non-linear settling particle equation of motion," *Journal of Hydro-Environment Research*, vol. 6, no. 4, pp. 323–327, 2012.
- [27] S. S. Motsa and S. Shateyi, "Successive linearisation solution of free convection non-darcy flow with heat and mass transfer," in *Advanced Topics in Mass Transfer*, M. El-Amin, Ed., pp. 425–438, InTech, Rijeka, Croatia, 2011.
- [28] S. S. Motsa, Y. Khan, and S. Shateyi, "Application of piecewise successive linearization method for the solutions of the Chen chaotic system," *Journal of Applied Mathematics*, vol. 2012, Article ID 258948, 12 pages, 2012.
- [29] S. Shateyi and S. S. Motsa, "Variable viscosity on magnetohydrodynamic fluid flow and heat transfer over an unsteady stretching surface with Hall effect," *Boundary Value Problems*, vol. 2010, Article ID 257568, 20 pages, 2010.
- [30] S. S. Motsa, P. G. Dlamini, and M. Khumalo, "Solving hyperchaotic systems using the spectral relaxation method," *Abstract and Applied Analysis*, vol. 2012, Article ID 203461, 18 pages, 2012.
- [31] S. S. Motsa, P. Dlamini, and M. Khumalo, "A new multistage spectral relaxation method for solving chaotic initial value systems," *Nonlinear Dynamics*, vol. 72, no. 1–2, pp. 265–283, 2013.
- [32] S. S. Motsa and Z. G. Makukula, "On spectral relaxation method approach for steady von Kármán flow of a Reiner-Rivlin fluid with Joule heating, viscous dissipation and suction/injection," *Central European Journal of Physics*, vol. 11, no. 3, pp. 363–374, 2013.
- [33] M. Renardy, "High Weissenberg number boundary layers for the upper converted Maxwell fluid," *Journal of Non-Newtonian Fluid Mechanics*, vol. 68, no. 1, pp. 125–132, 1997.

## Research Article

# Analytical Solution of Flow and Heat Transfer over a Permeable Stretching Wall in a Porous Medium

M. Dayyan,<sup>1</sup> S. M. Seyyedi,<sup>2</sup> G. G. Domairry,<sup>2</sup> and M. Gorji Bandpy<sup>2</sup>

<sup>1</sup> Department of Mechanical and Aerospace Engineering, Science and Research Branch, Islamic Azad University, Tehran, Iran

<sup>2</sup> Department of Mechanical Engineering, Babol University of Technology, Babol, Iran

Correspondence should be addressed to M. Dayyan; [morteza.dayyan@gmail.com](mailto:morteza.dayyan@gmail.com)

Received 6 April 2013; Revised 18 July 2013; Accepted 18 July 2013

Academic Editor: Waqar Khan

Copyright © 2013 M. Dayyan et al. This is an open access article distributed under the Creative Commons Attribution License, which permits unrestricted use, distribution, and reproduction in any medium, provided the original work is properly cited.

Boundary layer flow through a porous medium over a stretching porous wall has been solved with analytical solution. It has been considered two wall boundary conditions which are power-law distribution of either wall temperature or heat flux. These are general enough to cover the isothermal and isoflux cases. In addition to momentum, both first and second laws of thermodynamics analyses of the problem are investigated. The governing equations are transformed into a system of ordinary differential equations. The transformed ordinary equations are solved analytically using homotopy analysis method. A comprehensive parametric study is presented, and it is shown that the rate of heat transfer increases with Reynolds number, Prandtl number, and suction to the surface.

## 1. Introduction

Boundary layer flows over a stretching surface have application in engineering processes such as liquid composite molding, extrusion of plastic sheets, paper production, glass blowing, metal spinning, wire drawing, and hot rolling [1–3]. More importantly, the quality of the products, in the abovementioned processes, depends on the kinematics of stretching and the simultaneous heat and mass transfer rates during the fabrication process. Sakiadis [4, 5] and Crane [6] were the pioneers in the investigations of boundary layer flow over continuously moving surfaces that are quite different from the free stream flow over stationary flat plates. Pop and Na [7] studied free convection heat transfer of non-Newtonian fluids along a vertical wavy surface in a porous medium.

The flow field of a stretching surface with a power-law velocity variation was discussed by Banks [8]. Elbashbeshy [9] investigated heat transfer over a stretching surface with variable surface heat flux. Elbashbeshy and Bazid [10] analyzed heat transfer in a porous medium over a stretching surface with internal heat generation and suction or injection. This work was extended by Cortell [11] to include power-law temperature distribution. Steady flow and heat transfer of

a viscous incompressible fluid flow through porous medium over a stretching sheet were studied by Sriramalu et al. [12]. Ali [13] investigated thermal boundary layer on a power-law stretched surface with suction or injection for uniform and variable surface temperatures. Recently, Pantokratoras [14] published analytical solution for velocity distribution inside a Darcy-Brinkman porous medium with a stretching boundary. Elbashbeshy [15] included thermal radiation effects in a stretching surface problem. Tamayol and Bahrami [16] understood that porous materials can be used to enhance the heat transfer rate from stretching surfaces to improve processes such as hot rolling and composite fabrication.

In view of the above, an analytical solution is developed in the present study to solve fluid flow, heat transfer in a porous medium over a porous plate with linear velocity, subjected to different power-law thermal boundary conditions. The analytical solution is successfully validated in comparison with numerical analysis. There are many effective methods for obtaining the solutions of nonlinear equation such as variational iteration method [17], Adomian method [18], and homotopy perturbation method [19, 20], and we use one of a powerful technique, namely, the homotopy analysis method (HAM) which was expressed by Liao [21–24]. This method has been successfully applied to solve many types

of nonlinear problems [25–29] and provides us with great freedom to express solutions of a given nonlinear problem by means of different base functions. Secondly, unlike all previous analytic techniques, the homotopy analysis method always provides us with a family of solution expressions in the auxiliary parameter  $\hbar$ , even if a nonlinear problem has a unique solution. Thirdly, unlike perturbation techniques, the homotopy analysis method is independent of any small or large quantities. So, the homotopy analysis method can be applied no matter if governing equations and boundary/initial conditions of a given nonlinear problem contain small or large quantities or not.

Above all, there are no rigorous theories to direct us to choose the initial approximations, auxiliary linear operators, auxiliary functions, and auxiliary parameter  $\hbar$ . From the practical viewpoints, there are some fundamental rules such as the rule of solution expression, the rule of coefficient ergodicity, and the rule of solution existence, which play important roles within the homotopy analysis method. Unfortunately, the rule of solution expression implies such an assumption that we should have, more or less, some knowledge about a given nonlinear problem a priori. So, theoretically, this assumption impairs the homotopy analysis method, although we can always attempt some base functions even if a given nonlinear problem is completely new for us.

## 2. Governing Equation

Consider a steady, constant property, two-dimensional flow through a homogenous porous medium of permeability  $K$ , over a stretching surface with linear velocity distribution; that is,  $u_w = u_0 x/L$  (Figure 1). The transport properties of the medium can be assumed independent of temperature when the difference between wall and ambient temperatures is not significant [4]. The origin is kept fixed, while the wall is stretching, and the  $y$ -axis is perpendicular to the surface. The governing equations are [4, 5]

$$\begin{aligned} \frac{\partial u}{\partial x} + \frac{\partial v}{\partial y} &= 0, \\ \rho \left( u \frac{\partial u}{\partial x} + v \frac{\partial u}{\partial y} \right) &= \mu_{\text{eff}} \frac{\partial^2 u}{\partial y^2} - \frac{\mu}{K'} u, \\ u \frac{\partial T}{\partial x} + v \frac{\partial T}{\partial y} &= \alpha_{\text{eff}} \frac{\partial^2 T}{\partial y^2}, \end{aligned} \quad (1)$$

where  $u$  and  $v$  are velocity components in the  $x$  and  $y$  directions, respectively.  $\mu_{\text{eff}}$  is the effective viscosity which for simplicity in the present study is considered to be identical to the dynamic viscosity,  $\mu$ . The transport properties of the porous medium such as permeability depend on their microstructure and can be calculated either using existing correlations in the literature or through experimental measurements.  $\alpha_{\text{eff}}$  is the effective thermal diffusivity of the medium. The hydrodynamic boundary conditions are

$$u(x^*, 0) = u_0 x^*, \quad v(x^*, 0) = v_w, \quad u(x^*, \infty) = 0, \quad (2)$$

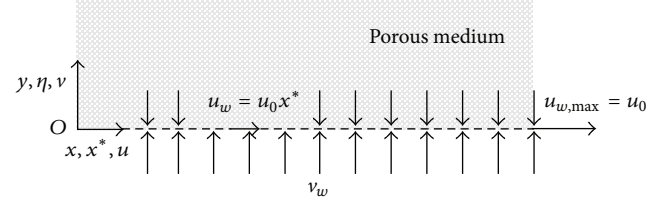


FIGURE 1: Schematic diagram of problem.

where  $x^* = x/L$  is the nondimensional  $x$ -coordinate and  $L$  is the length of the porous plate. The following thermal boundary conditions are considered:

$$\begin{aligned} T(x^*, 0) &= T_\infty + T_0(x^*)^n, & T(x^*, \infty) &= T_\infty, \\ -\kappa \frac{\partial T}{\partial y} \Big|_{(x^*, 0)} &= q_0(x^*)^n, & T(x^*, \infty) &= T_\infty, \end{aligned} \quad (3)$$

where  $\kappa$  is the effective thermal conductivity of the medium and is a function of thermal conductivities of the fluid and solid phases and the porous medium microstructure.

Using dimensionless parameters,

$$\begin{aligned} \eta &= \frac{y}{\sqrt{K}}, \\ u &= u_0 x^* f'(\eta), \\ v &= -\frac{u_0}{L} \sqrt{K} f(\eta), \\ \psi &= u_0 x^* \sqrt{K} f(\eta), \end{aligned} \quad (4)$$

where  $f'$  is  $df/d\eta$ .

The transformed nonlinear ordinary differential equations are

$$\begin{aligned} f''' + \text{Re}(ff'' - f'^2) - f' &= 0, \\ \theta'' + \text{Re} \cdot \text{Pr}(f\theta') - n \cdot \text{Re} \cdot \text{Pr}(f'\theta) &= 0, \end{aligned} \quad (5)$$

where  $\text{Re} = \rho u_0 K / L \mu$  is the Reynolds number. Equation (5) should be solved subject to the following boundary conditions:

$$f'(0) = 1, \quad f(0) = -\frac{v_w L}{u_0 \sqrt{K}} = f_w, \quad f'(\infty) = 0, \quad (6)$$

$$\theta(0) = 1, \quad \theta(\infty) = 0 \quad \text{Power-law temperature}, \quad (7a)$$

$$\theta'(0) = -1, \quad \theta'(\infty) = 0 \quad \text{Power-law heat flux}, \quad (7b)$$

where  $f_w$  is the injection parameter. Positive/negative values of  $f_w$  show suction/injection into/from the porous surface, respectively. The wall shear stress term can be calculated as

$$\tau_L = \frac{-\mu u_0 L f''(0)}{2\sqrt{K}}. \quad (8)$$

For power-law fluid with constant temperature and heat flux boundary conditions, respectively. Employing the definition of convective heat transfer coefficient, the local Nusselt numbers become

$$\text{Nu}_x = \frac{hx}{k} = \begin{cases} -\frac{\theta'(0)x}{\sqrt{K}}, & \text{Power-law temperature,} \\ \frac{q_w x}{k(T_w - T_\infty)} = \frac{x}{\theta(0)\sqrt{K}}, & \text{Power-law heat flux.} \end{cases} \quad (9)$$

### 3. Solution of Problem by Homotopy Analysis Method (HAM)

As mentioned by Liao, a solution may be expressed with different base functions, among which some converge to the exact solution of the problem faster than others. Such base functions are obviously better suited for the final solution to be expressed in terms of. Noting these facts, we have decided to express  $g(\eta)$  by a set of base functions of the following form:

$$\begin{aligned} f(\eta) &= \sum_{m=0}^{\infty} \sum_{n=0}^{\infty} \sum_{k=0}^{\infty} b_{m,n}^k \eta^k \exp(-n\eta), \\ \theta(\eta) &= \sum_{m=0}^{\infty} \sum_{n=0}^{\infty} \sum_{k=0}^{\infty} b_{m,n}^k \eta^k \exp(-n\eta). \end{aligned} \quad (10)$$

The rule of solution expression provides us with a starting point. It is under the rule of solution expression that initial approximations, auxiliary linear operators, and the auxiliary functions are determined. So, according to the rule of solution expression, we choose the initial guess and auxiliary linear operator in the following form:

$$f_0(\eta) = f_w + 1 - \exp(-\eta), \quad \theta_0(\eta) = \exp(-\eta). \quad (11)$$

We choose linear operator as follows:

$$\begin{aligned} \mathcal{L}_1(f) &= f''' + f'', & \mathcal{L}_2(\theta) &= \theta'' + \theta', \\ \mathcal{L}_1(c_1 + c_2\eta + c_3 \exp(-\eta)) &= 0, & \mathcal{L}_2(c_4 + c_5 \exp(-\eta)) &= 0, \end{aligned} \quad (12)$$

where  $c_i$  ( $i = 1-5$ ) are constants. Let  $P \in [0, 1]$  denote the embedding parameter, and let  $\hbar$  indicate nonzero auxiliary parameters. Then, we construct the following equations.

#### 3.1. Consider Zeroth-Order Deformation Equations.

$$\begin{aligned} (1-P)\mathcal{L}_1[f(\eta; p) - f_0(\eta)] &= p\hbar_1 H(\eta) N_1[f(\eta; p)], \\ f(0; p) &= f_w, \\ f'(0; p) &= 1, \quad f'(\infty; p) = 0, \end{aligned}$$

$$\begin{aligned} (1-P)\mathcal{L}_2[\theta(\eta; p) - \theta_0(\eta)] &= p\hbar_2 H(\eta) N_2[\theta(\eta; p)], \\ \theta(0; p) &= 1, \quad \theta(\infty; p) = 0 \quad \text{Power-law temperature,} \\ \theta'(0; p) &= -1, \quad \theta(\infty; p) = 0 \quad \text{Power-law heat flux,} \\ N_1[f(\eta; p), \theta(\eta; p)] &= \frac{\partial^3 f(\eta; p)}{\partial \eta^3} \\ &+ \text{Re} \left( f(\eta; p) \frac{\partial^2 f(\eta; p)}{\partial \eta^2} - \left( \frac{\partial f(\eta; p)}{\partial \eta} \right)^2 \right) \\ &- \frac{\partial f(\eta; p)}{\partial \eta}, \\ N_2[f(\eta; p), \theta(\eta; p)] &= \frac{\partial^2 \theta(\eta; p)}{\partial \eta^2} + \text{Re} \cdot \text{Pr} \left( f(\eta; p) \frac{\partial \theta(\eta; p)}{\partial \eta} \right) \\ &- n \cdot \text{Re} \cdot \text{Pr} \left( \theta(\eta; p) \frac{\partial f(\eta; p)}{\partial \eta} \right). \end{aligned} \quad (13)$$

For  $p = 0$  and  $p = 1$ , we have

$$\begin{aligned} f(\eta; 0) &= f_0(\eta), & f(\eta; 1) &= f(\eta), \\ \theta(\eta; 0) &= \theta_0(\eta), & \theta(\eta; 1) &= \theta(\eta). \end{aligned} \quad (14)$$

When  $p$  increases from 0 to 1, then  $f(\eta; p)$  and  $\theta(\eta; p)$  vary from  $f_0(\eta)$  and  $\theta_0(\eta)$  to  $f(\eta)$  and  $\theta(\eta)$ . By Taylor's theorem and using (14), we can write the following:

$$\begin{aligned} f(\eta; p) &= f_0(\eta) + \sum_{m=1}^{\infty} f_m(\eta) p^m, \\ f_m(\eta) &= \frac{1}{m!} \frac{\partial^m (f(\eta; p))}{\partial p^m}, \end{aligned} \quad (15)$$

$$\begin{aligned} \theta(\eta; p) &= \theta_0(\eta) + \sum_{m=1}^{\infty} \theta_m(\eta) p^m, \\ \theta_m(\eta) &= \frac{1}{m!} \frac{\partial^m (\theta(\eta; p))}{\partial p^m}. \end{aligned}$$

In which  $\hbar_1$  and  $\hbar_2$  are chosen in such a way that these two series are convergent at  $p = 1$ ; therefore we have the following through (15):

$$f(\eta) = f_0(\eta) + \sum_{m=1}^{\infty} f_m(\eta), \quad (16)$$

$$\theta(\eta) = \theta_0(\eta) + \sum_{m=1}^{\infty} \theta_m(\eta).$$

#### 3.2. Consider Mth-Order Deformation Equations.

$$\mathcal{L}_1[f_m(\eta) - \chi_m f_{m-1}(\eta)] = \hbar_1 H(\eta) R_m^f(\eta), \quad (17)$$

$$f_m(0) = 0, \quad f'_m(0) = 0, \quad f'_m(\infty) = 0, \quad (18)$$

$$R_m^f(\eta) = f_{m-1}''' + \sum_{k=0}^{m-1} f_k f_{m-1-k}'' - \sum_{k=0}^{m-1} f'_k f'_{m-1-k} - K f'_{m-1}, \quad (19)$$

$$\mathcal{L}_2[\theta_m(\eta) - \chi_m \theta_{m-1}(\eta)] = \hbar_2 H(\eta) R_m^\theta(\eta), \quad (20)$$

$$\theta_m(0) = 0, \quad \theta_m(\infty) = 0, \quad (21)$$

$$\theta'_m(0) = 0, \quad \theta'_m(\infty) = 0, \quad (22)$$

$$R_m^\theta(\eta) = \theta_{m-1}'' + \text{Re} \cdot \text{Pr} \left( \sum_{k=0}^{m-1} f_k \theta'_{m-1-k} \right) - n \cdot \text{Re} \cdot \text{Pr} \left( \sum_{k=0}^{m-1} \theta_k f'_{m-1-k} \right), \quad (23)$$

$$\chi_m = \begin{cases} 0, & m \leq 1, \\ 1, & m > 1. \end{cases} \quad (24)$$

The general solutions of (17)–(23) are

$$\begin{aligned} f_m(\eta) - \chi_m f_{m-1}(\eta) &= f_m^*(\eta) + C_1^m + C_2^m \eta + C_3^m \exp(-\eta), \\ \theta_m(\eta) - \chi_m \theta_{m-1}(\eta) &= \theta_m^*(\eta) + C_4^m + C_5^m \exp(-\eta), \end{aligned} \quad (25)$$

where  $C_1^m$  to  $C_5^m$  are constants that can be obtained by applying the boundary condition in (18), (21), and (22).

As discussed by Liao, the rule of coefficient ergodicity and the rule of solution existence play important roles in determining the auxiliary function and ensuring that the high-order deformation equations are closed and have solutions. In many cases, by means of the rule of solution expression and the rule of coefficient ergodicity, auxiliary functions can be uniquely determined. So we define the auxiliary function  $H(\eta)$  in the following form:

$$H(\eta) = \exp(-\eta). \quad (26)$$

### 4. Convergence of the HAM Solution

As was mentioned in introduction, the convergence and the rate of approximation of the HAM solution strongly depend on the values of auxiliary parameter  $\hbar$ . By means of the so-called  $\hbar$  curves, it is easy to find out the so-called valid regions of  $\hbar$  to gain a convergent solution series. According to Figures 2 and 3, the acceptable range of auxiliary parameter for  $\text{Pr} = 1, n = 0, \text{Re} = 1,$  and  $f_w = 0$  is  $-0.3 < \hbar_1 < -0.1$  and  $-1.8 < \hbar_2 < -0.3$ .

Figures 4 and 5 show how auxiliary parameters  $\hbar_1$  and  $\hbar_2$  vary with changing  $f_w$ . If  $f_w$  increases, the range of convergence of solution is restricted and then decreased.

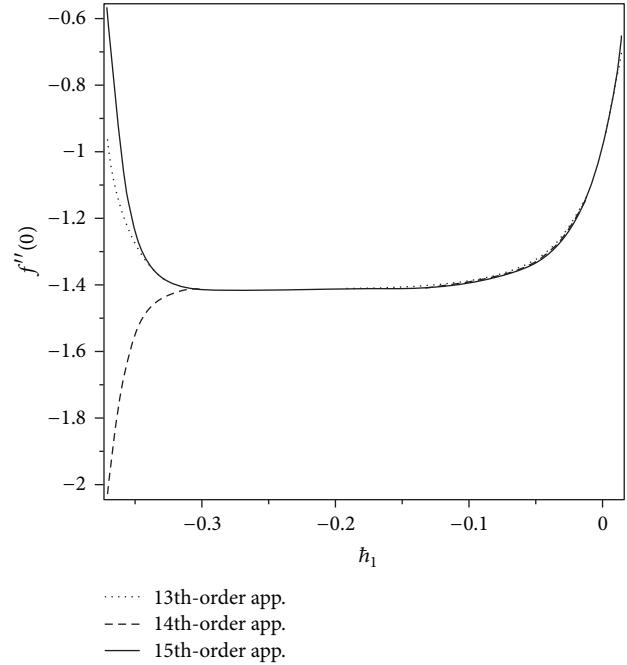


FIGURE 2: The  $\hbar_1$  validity for  $\text{Pr} = 1, n = 0, \text{Re} = 1,$  and  $f_w = 0$ .

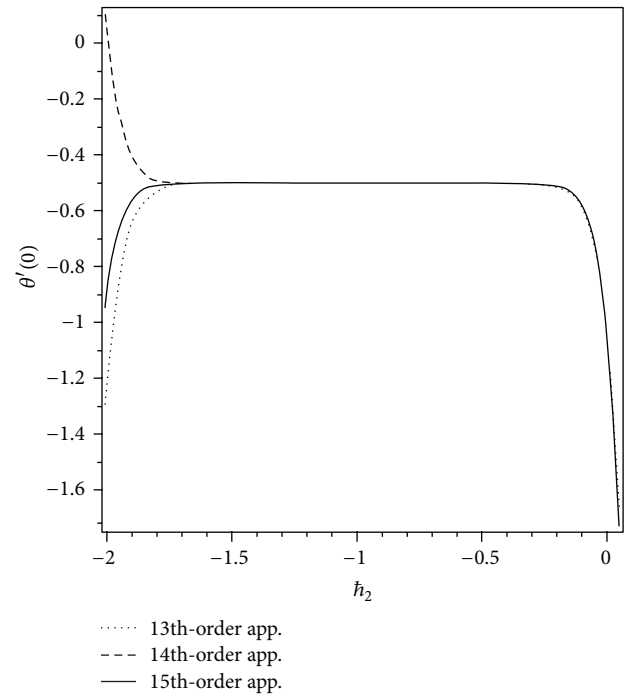


FIGURE 3: The  $\hbar_2$  validity for  $\text{Pr} = 1, n = 0, \text{Re} = 1,$  and  $f_w = 0$ .

### 5. Results and Discussion

In the present study, the Homotopy analysis method has been used to solve the nonlinear equations of heat transfer and fluid flow over a permeable stretching wall in a porous medium. The nondimensional numbers introduced in the present analysis are Reynolds number (Re), Prandtl number

TABLE 1: The results of HAM and NS for  $f(\eta)$ ,  $f'(\eta)$ , and  $\theta(\eta)$  when  $f_w = 0$ ,  $Pr = 1$ ,  $n = 0$ , and  $Re = 1$ .

$\eta$	$f(\eta)$		$f'(\eta)$		$\theta(\eta)$ (temperature)		$\theta(\eta)$ (heat flux)	
	HAM	NS	HAM	NS	HAM	NS	HAM	NS
0.0	0.00000	0.00000	0.99999	1.00000	0.999999	1.00000	1.9565	1.9615
0.2	0.17042	0.17420	0.75376	0.75363	0.89633	0.89996	1.7677	1.7627
0.4	0.30564	0.30549	0.56813	0.75363	0.80205	0.80327	1.5658	1.5706
0.6	0.40571	0.40443	0.42820	0.42804	0.71301	0.71225	1.3856	1.3898
0.8	0.47505	0.47900	0.32272	0.32259	0.62792	0.62826	1.2210	1.2229
1.0	0.53802	0.53519	0.24322	0.24311	0.55226	0.55191	1.0690	1.0712
1.2	0.58010	0.57754	0.18330	0.18322	0.48134	0.48329	0.9313	0.9340
1.4	0.61161	0.60946	0.13814	0.13808	0.42056	0.42214	0.8094	0.8134
1.6	0.64096	0.63352	0.10410	0.10406	0.36595	0.36800	0.6943	0.7058
1.8	0.65374	0.65165	0.07845	0.07842	0.31817	0.32029	0.6095	0.6110
2.0	0.66952	0.66531	0.05912	0.05910	0.27657	0.27841	0.5193	0.5278
2.2	0.67812	0.67560	0.04455	0.04454	0.23934	0.24175	0.4480	0.4549
2.4	0.68567	0.68336	0.03357	0.03357	0.20813	0.20971	0.3861	0.3913
2.6	0.69054	0.68921	0.02530	0.02529	0.17972	0.18177	0.3323	0.3358
2.8	0.69675	0.69362	0.01907	0.01906	0.15519	0.15743	0.2858	0.2874
3.0	0.69842	0.69694	0.01437	0.01436	0.13407	0.13623	0.2456	0.2453

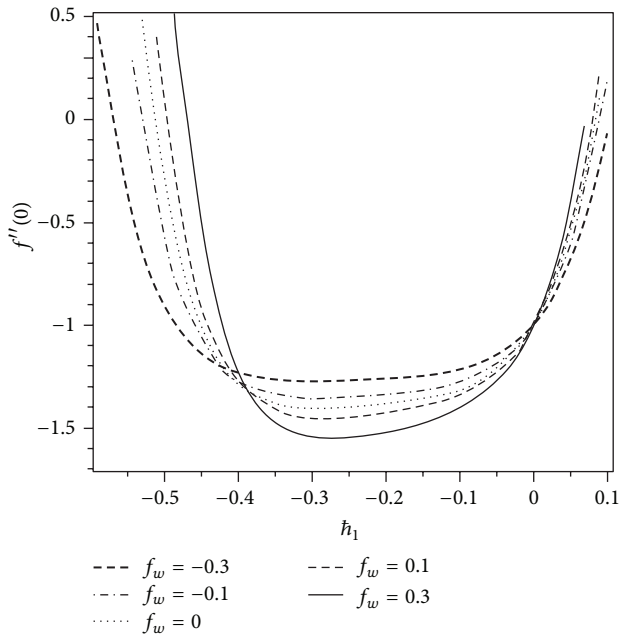


FIGURE 4: The  $\tilde{h}_1$  validity for various  $f_w$ ,  $Pr = 1$ ,  $n = 0$ , and  $Re = 1$ .

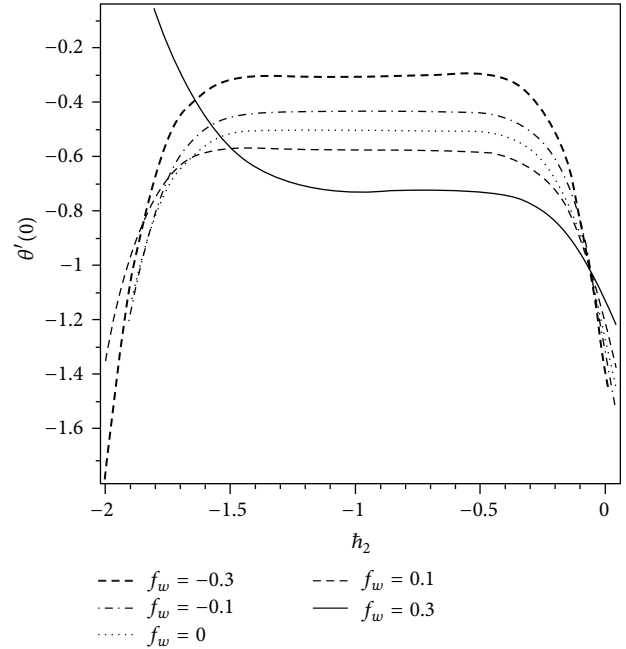


FIGURE 5: The  $\tilde{h}_2$  validity for various  $f_w$ ,  $Pr = 1$ ,  $n = 0$ ,  $Re = 1$ , and  $f_w = 0$ .

( $Pr$ ), and the injection number ( $f_w$ ). Another important parameter is the power of the surface temperature/heat flux distribution ( $n$ ), which is considered in the present study.

In order to ensure the convergence of the solution series, the variation of  $f$  has been plotted at different orders of approximation in Figure 6. The comparison between results of HAM and numerical solution (Runge-Kutta) has been displayed in Table 1. It can be observed that there is a good agreement between HAM method and numerical solution. Figures 7, 8, and 9 illustrate effect of variation of wall injection/suction parameter ( $f_w$ ) on velocity and

temperature distribution. It can be observed that all boundary layer thickness decreased by increasing  $f_w$  from negative to positive (from injection to suction). Figures 10, 11, and 12 show the effect of Reynolds number on the velocity profile when  $Pr = 1$ ,  $n = 0$ , and  $f_w = 0$ . This figure shows that the boundary layer thickness and thermal boundary layer thickness are quite opposite to that of Reynolds number. The influence of  $n$  on temperature field for both types of the thermal boundary conditions considered has been studied in Figures 13 and 14. We notice that increasing  $n$  reduces

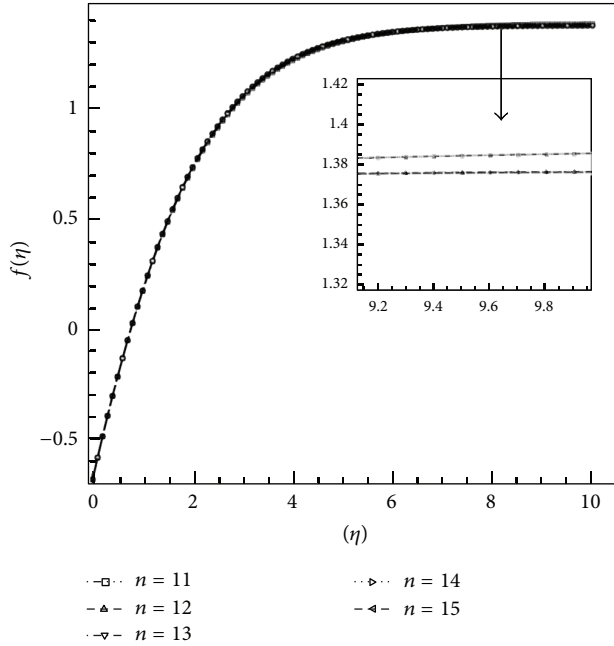


FIGURE 6: The variation of  $f$  at different orders of approximations,  $Pr = 1, n = 0, Re = 1,$  and  $f_w = 0.$

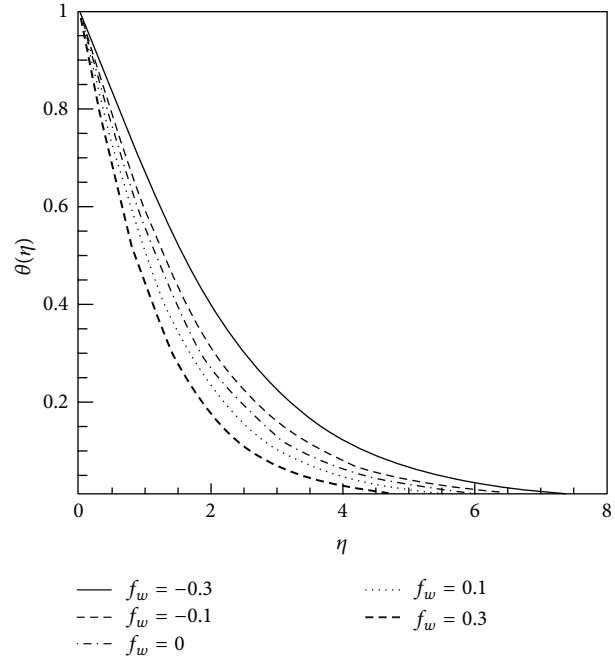


FIGURE 8: Temperature profile (isothermal)  $\theta$  for various  $f_w$  when  $Pr = 1, n = 0,$  and  $Re = 1.$

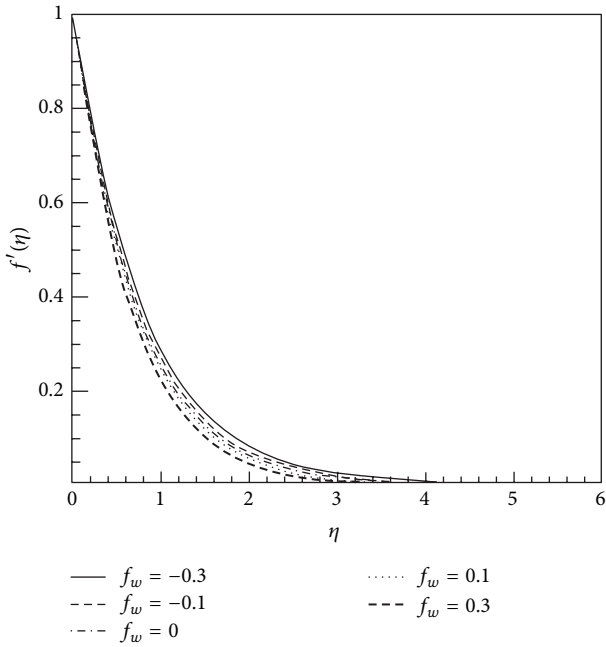


FIGURE 7: Velocity profile  $f'$  for various  $f_w$  when  $Pr = 1, n = 0,$  and  $Re = 1.$

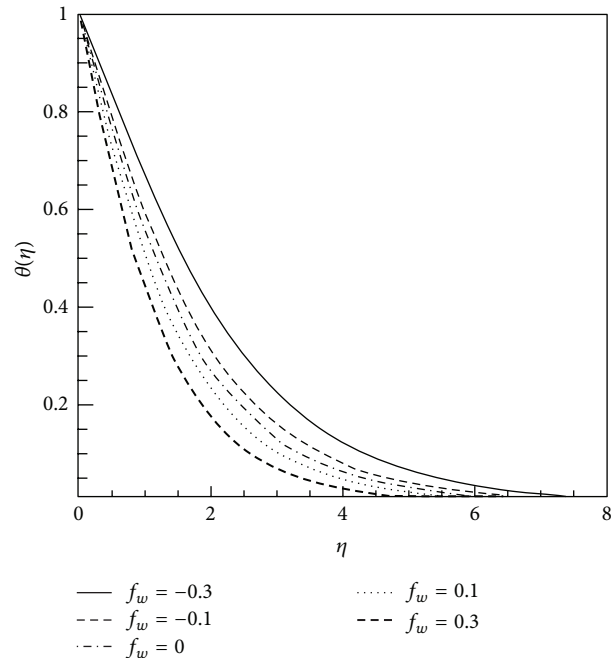


FIGURE 9: Temperature profile (isoflux)  $\theta$  for various  $f_w$  when  $Pr = 1, n = 0,$  and  $Re = 1.$

the thermal boundary layer thickness regardless of the boundary condition type leading to a heat transfer augmentation. Effect of Prandtl number (isothermal) on the temperature field is plotted in Figure 15. This figure shows that thermal boundary layer thickness directly depends on Prandtl number.

Tables 2 and 3 compare the results of HAM and numerical solution when the Reynolds number varies for  $f_w = 0,$

$Pr = 1,$  and  $n = 0$  for isothermal and heat flux boundary conditions, respectively. It can be seen that for isothermal boundary condition with increasing Reynolds number, the wall shear stress for both boundary conditions considered here (isothermal and heat flux) and Nusselt number increase with Reynolds number for isothermal state and independent of Reynolds number for heat flux boundary condition.

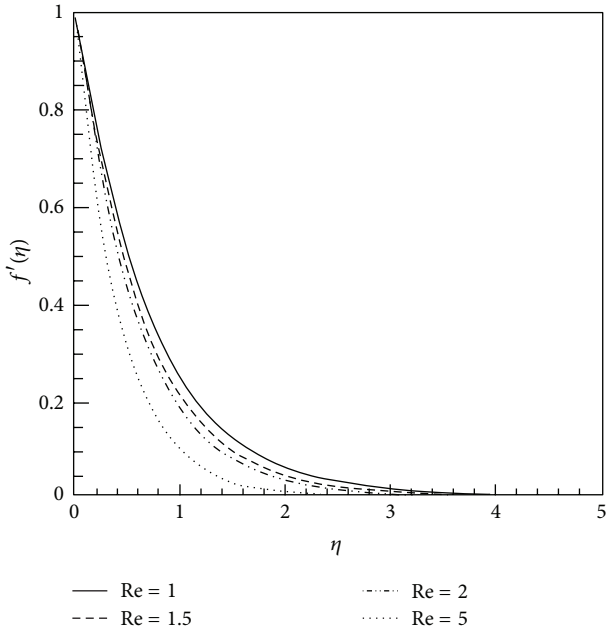


FIGURE 10: Velocity profile  $f'$  for various Re when  $Pr = 1, n = 0,$  and  $f_w = 0.$

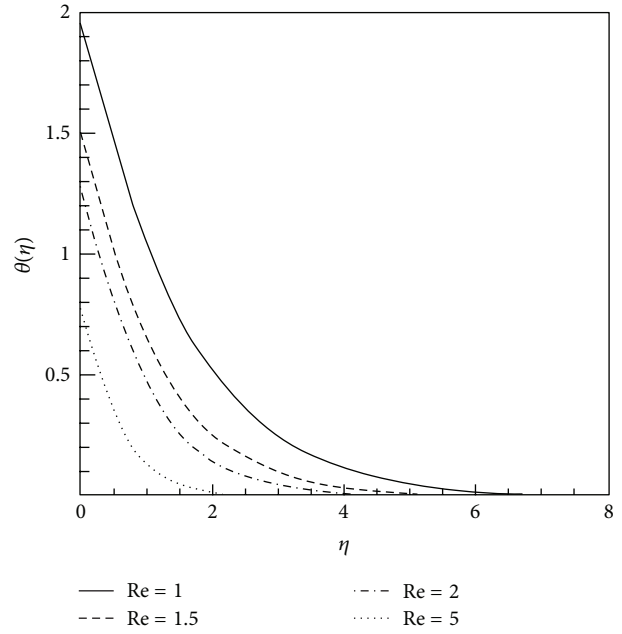


FIGURE 12: Temperature profile (isoflux)  $\theta$  for various Re when  $Pr = 1, n = 0,$  and  $f_w = 0.$

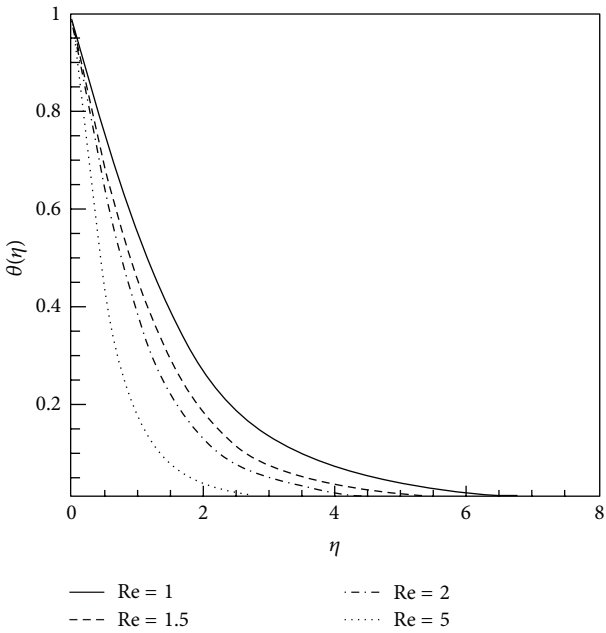


FIGURE 11: Temperature profile (isothermal)  $\theta$  for various Re when  $Pr = 1, n = 0,$  and  $f_w = 0.$

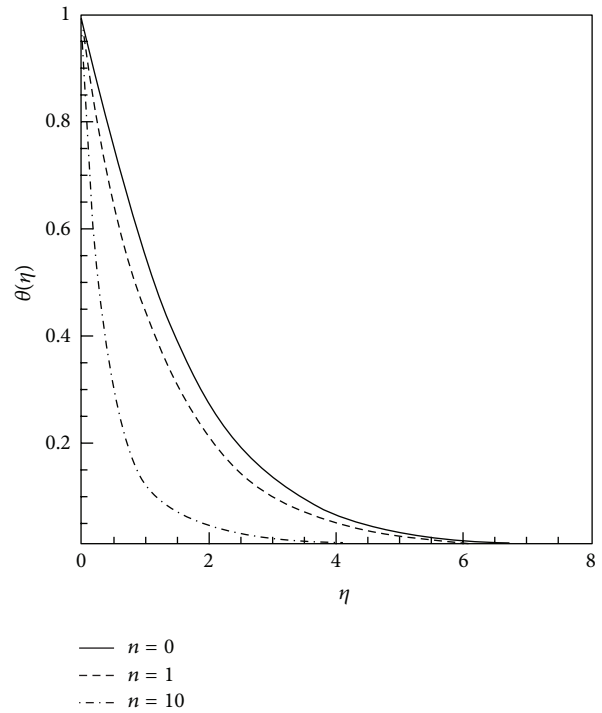


FIGURE 13: Temperature profile (isothermal)  $\theta$  for various  $n$  when  $Pr = 1, n = 0,$  and  $f_w = 0.$

Comparison of the results of HAM and numerical solution has been shown in Tables 4 and 5 for various Prandtl numbers when  $Re = 1, n = 0$  and  $f_w = -0.3, f_w = 0.3,$  respectively. It can be observed that the Prandtl number has no effect on the wall shear stress for both boundary conditions and Nusselt number for heat flux boundary condition.

### 6. Summary and Conclusions

Homotopy analysis method (HAM) is applied to compute wall driven flow through a porous medium over a stretching permeable surface subjected to power-law temperature and heat flux boundary conditions. The proper range of

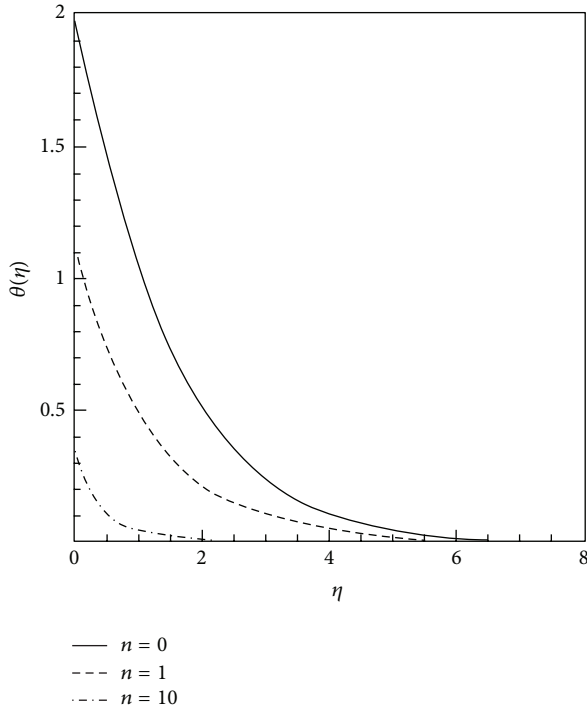


FIGURE 14: Temperature profile (isoflux)  $\theta$  for various  $n$  when  $Pr = 1$ ,  $n = 0$ , and  $f_w = 0$ .

TABLE 2: The results of HAM and NS for  $f''(0), \theta'(0)$  when  $f_w = 0$ ,  $Pr = 1$ , and  $n = 0$  for temperature.

Re	$\tilde{h}_1$	$\tilde{h}_2$	$-f''(0)$		$-\theta'(0)$	
			HAM	NS	HAM	NS
1	-0.2	-0.4	1.4198	1.4242	0.5030	0.5033
1.5	-0.25	-0.4	1.5799	1.5811	0.6456	0.6422
2	-0.2	-0.2	1.7234	1.7320	0.7518	0.7592
5	-0.1	-0.1	2.4394	2.4494	1.2636	1.2576

TABLE 3: The results of HAM and NS for  $f''(0), \theta'(0)$  when  $f_w = 0$ ,  $Pr = 1$ , and  $n = 0$  for heat flux.

Re	$\tilde{h}_1$	$\tilde{h}_2$	$-f''(0)$		$-\theta'(0)$	
			HAM	NS	HAM	NS
1	-0.25	-0.2	1.4191	1.4242	0.9997	1
1.5	-0.2	-0.4	1.5791	1.5811	1.0000	1
2	-0.15	-0.3	1.7298	1.7320	0.9985	1
2.5	-0.1	-0.1	2.4445	2.4494	0.9939	1

the auxiliary parameter  $\tilde{h}$  to ensure the convergency of the solution series was obtained through the so-called  $\tilde{h}$  curves. When compared with other analytical methods, it is clear that HAM provides highly accurate analytical solutions for non-linear problems. Moreover, second-law (of thermodynamics) aspects of the problem are investigated. The highlights of this study are the following.

- (i) The nondimensional viscous boundary layer thickness has a direct relationship with Reynolds number; thus Nusselt number rate increases with Re.

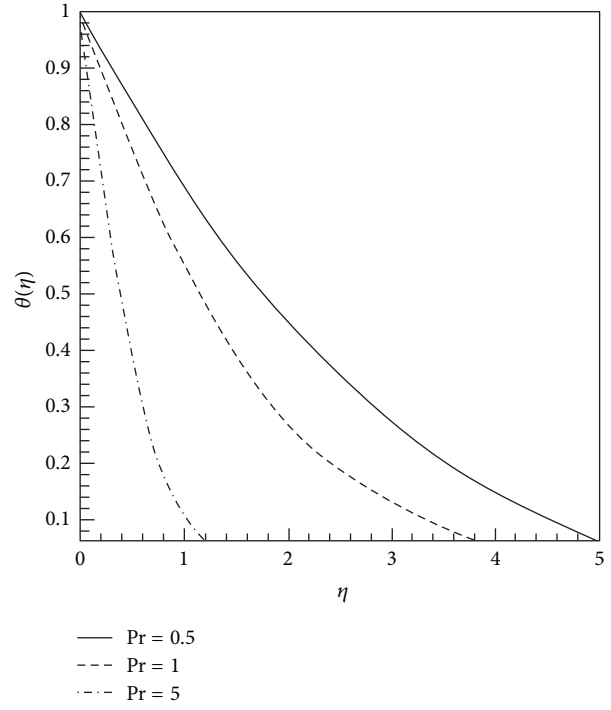


FIGURE 15: Temperature profile  $\theta$  (isothermal) for various  $Pr$  when  $Pr = 1$ ,  $n = 0$ , and  $f_w = 0$ .

TABLE 4: The results of HAM and NS for  $f''(0), \theta'(0)$  for various  $Pr$  when,  $Re = 1$ ,  $n = 0$ , and  $f_w = -0.3$ .

Pr	$-f''(0)$				$-\theta'(0)$			
	$f_w = -0.3$				$f_w = -0.3$			
	Temperature		Heat flux		Temperature		Heat flux	
	HAM	NS	HAM	NS	HAM	NS	HAM	NS
0.5	1.2699	1.2721	1.2711	1.2721	0.216	0.219	1.000	0.999
1	1.2699	1.2721	1.2711	1.2721	0.3128	0.313	1.000	1.000
5	1.2699	1.2721	1.2711	1.2721	0.636	0.623	1.000	0.999

TABLE 5: The results of HAM and NS for  $f''(0), \theta'(0)$  for various  $Pr$  when,  $Re = 1$ ,  $n = 0$ , and  $f_w = 0.3$ .

Pr	$-f''(0)$				$-\theta'(0)$			
	$f_w = 0.3$				$f_w = 0.3$			
	Temperature		Heat flux		Temperature		Heat flux	
	HAM	NS	HAM	NS	HAM	NS	HAM	NS
0.5	1.5699	1.5721	1.5695	1.5721	0.4145	0.4100	1.0002	1.0000
1	1.5699	1.5721	1.5695	1.5721	0.7258	0.7216	1.0002	1.0000
5	1.5699	1.5721	1.5695	1.5721	2.5821	2.5826	1.0002	1.0000

- (ii) Nusselt number, wall shear stress have a reverse relationship with and mass transfer from the wall,  $f_w$ .
- (iii) Increasing the Prandtl number results in reduction of thermal boundary layer thickness.

Consequently, Nusselt number increase with  $Pr$ .

## Nomenclature

$f$ :	Similarity function for velocity
$f_w$ :	Injection parameter, $f_w = -v_w L / u_0 \sqrt{K}$
$\tilde{h}$ :	Auxiliary parameter
HAM:	Homotopy analysis method
$H$ :	Auxiliary function
$\mathcal{L}$ :	Linear operator of HAM
$K$ :	Permeability of the porous medium, $m^2$
$N$ :	Non-linear operator
$n$ :	Power of temperature/heat flux distribution
Nu:	Local Nusselt number
$Nu_L$ :	Averaged Nusselt number
Pr:	Prandtl number, $Pr = \nu / \alpha_{\text{eff}}$
$q_0$ :	Wall heat flux coefficient, $W/m^2$
Re:	Reynolds number, $Re = \rho u_0 K / L$
$T$ :	Temperature
$T_0$ :	Wall temperature coefficient, $K$
$u$ :	Velocity in $x$ direction
$u_0$ :	Wall velocity coefficient, $m/s$
$v$ :	Velocity in $y$ direction
$v_w$ :	Injection velocity, $m/s$
$B$ :	Positive constant
$\theta$ :	Similarity function for temperature
$x$ :	Coordinate system, $m$
$y$ :	Coordinate system, $m$
$Q$ :	Volumetric rate of heat generation
$\lambda$ :	Heat generation
$N$ :	Radiation parameter
$\rho$ :	Density of the fluid
$\Psi$ :	Stream function
$\mu$ :	Dynamic viscosity
$\sigma_1$ :	Effective viscosity
$\kappa_1$ :	Absorption coefficient
$\eta$ :	Dimensionless similarity variable
$\nu$ :	Kinematic viscosity.

## References

- [1] M. Q. Al-Odat, R. A. Damesh, and T. A. Al-Azab, "Thermal boundary layer on an exponentially stretching continuous surface in the presence of magnetic field effect," *International Journal of Applied Mechanics and Engineering*, vol. 11, pp. 289–299, 2006.
- [2] B. Yu, H. T. Chiu, Z. Ding, and L. J. Lee, "Analysis of flow and heat transfer in liquid composite molding," *International Polymer Processing*, vol. 15, no. 3, pp. 273–283, 2000.
- [3] R. Nazar, A. Ishak, and I. Pop, "Unsteady boundary layer flow over a stretching sheet in a micropolar fluid," *International Journal of Mathematical, Physical and Engineering Sciences*, vol. 2, pp. 161–165, 2008.
- [4] B. C. Sakiadis, "Boundary layer behaviour on continuous solid surfaces. I: boundary layer equations for two-dimensional and axisymmetric flow," *AIChE Journal*, vol. 7, no. 1, pp. 26–28, 1961.
- [5] B. C. Sakiadis, "Boundary layer behaviour on continuous solid surfaces. II: boundary layer behaviour on continuous flat surfaces," *AIChE Journal*, vol. 7, no. 2, pp. 221–225, 1961.
- [6] L. J. Crane, "Flow past a stretching plate," *Journal of Applied Mathematics and Physics*, vol. 21, no. 4, pp. 645–647, 1970.
- [7] I. Pop and T. Y. Na, "Free convection heat transfer of non-Newtonian fluids along a vertical wavy surface in a porous medium," in *Proceedings of the 4th International Symposium on Heat Transfer (ISHT '96)*, pp. 452–457, Beijing, China, October 1996.
- [8] W. H. H. Banks, "Similarity solutions of the boundary layer equations for a stretching wall," *Journal de Mecanique Theorique et Appliquee*, vol. 2, no. 3, pp. 375–392, 1983.
- [9] E. M. A. Elbashbeshy, "Heat transfer over a stretching surface with variable surface heat flux," *Journal of Physics D*, vol. 31, no. 16, pp. 1951–1954, 1998.
- [10] E. M. A. Elbashbeshy and M. A. A. Bazid, "Heat transfer over a stretching surface with internal heat generation," *Canadian Journal of Physics*, vol. 81, no. 4, pp. 699–703, 2003.
- [11] R. Cortell, "Flow and heat transfer of a fluid through a porous medium over a stretching surface with internal heat generation/absorption and suction/blowing," *Fluid Dynamics Research*, vol. 37, no. 4, pp. 231–245, 2005.
- [12] A. Sriramalu, N. Kishan, and R. J. Anand, "Steady flow and heat transfer of a viscous incompressible fluid flow through porous medium over a stretching sheet," *Journal of Energy Heat and Mass Transfer*, vol. 23, pp. 483–495, 2001.
- [13] M. E. Ali, "On thermal boundary layer on a power-law stretched surface with suction or injection," *International Journal of Heat and Fluid Flow*, vol. 16, no. 4, pp. 280–290, 1995.
- [14] A. Pantokratoras, "Flow adjacent to a stretching permeable sheet in a Darcy-Brinkman porous medium," *Transport in Porous Media*, vol. 80, no. 2, pp. 223–227, 2009.
- [15] E. M. A. Elbashbeshy, "Radiation effect on heat transfer over a stretching surface," *Canadian Journal of Physics*, vol. 78, no. 12, pp. 1107–1112, 2000.
- [16] A. Tamayol and M. Bahrami, "Analytical determination of viscous permeability of fibrous porous media," *International Journal of Heat and Mass Transfer*, vol. 52, no. 9–10, pp. 2407–2414, 2009.
- [17] J. H. He, "Variational iteration method—a kind of non-linear analytical technique: some examples," *International Journal of Non-Linear Mechanics*, vol. 34, no. 4, pp. 699–708, 1999.
- [18] G. Adomian, "A review of the decomposition method and some recent results for nonlinear equations," *Mathematical and Computer Modelling*, vol. 13, no. 7, pp. 17–43, 1990.
- [19] A. H. Nayfeh, *Perturbation Methods*, Wiley, New York, NY, USA, 2000.
- [20] D. D. Ganji, "The application of He's homotopy perturbation method to nonlinear equations arising in heat transfer," *Physics Letters A*, vol. 355, no. 4–5, pp. 337–341, 2006.
- [21] S. J. Liao, *The proposed homotopy analysis technique for the solution of nonlinear problems [Ph.D. thesis]*, Shanghai Jiao Tong University, 1992.
- [22] S. J. Liao, "Boundary element method for general nonlinear differential operators," *Engineering Analysis with Boundary Elements*, vol. 202, pp. 91–99, 1997.
- [23] S. J. Liao, "An approximate solution technique not depending on small parameters: a special example," *International Journal of Non-Linear Mechanics*, vol. 30, no. 3, pp. 371–380, 1995.
- [24] S. Liao, *Beyond Perturbation: Introduction to the Homotopy Analysis Method*, Chapman & Hall/CRC, Boca Raton, Fla, USA, 2003.
- [25] T. Hayat and M. Khan, "Homotopy solutions for a generalized second-grade fluid past a porous plate," *Nonlinear Dynamics*, vol. 42, no. 4, pp. 395–405, 2005.

- [26] A. Fakhari, G. Domairry, and E. Ebrahimpour, "Approximate explicit solutions of nonlinear BBMB equations by homotopy analysis method and comparison with the exact solution," *Physics Letters A*, vol. 368, no. 1-2, pp. 64–68, 2007.
- [27] M. Dayyan, D. D. Ganji, and S. M. Seyyedi, "Application of homotopy analysis method for velocity and temperature distribution of viscose stagnation point," *International Journal of Nonlinear Dynamics in Engineering and Sciences*, vol. 2, no. 2, pp. 189–205, 2010.
- [28] G. Domairry and M. Fazeli, "Homotopy analysis method to determine the fin efficiency of convective straight fins with temperature-dependent thermal conductivity," *Communications in Nonlinear Science and Numerical Simulation*, vol. 14, no. 2, pp. 489–499, 2009.
- [29] M. Dayyan, D. D. Ganji, A. Imam, and S. M. Seyyedi, "Analytical solution of heat transfer over a flat plate with radiation for bingham non-newtonian fluid," *International Journal of Nonlinear Dynamics in Engineering and Sciences*, vol. 4, no. 1, pp. 155–167, 2012.

## Research Article

# Calculation Analysis of Pressure Wave Velocity in Gas and Drilling Mud Two-Phase Fluid in Annulus during Drilling Operations

Yuanhua Lin,<sup>1</sup> Xiangwei Kong,<sup>2</sup> Yijie Qiu,<sup>2</sup> and Qiji Yuan<sup>1</sup>

<sup>1</sup> State Key Laboratory of Oil and Gas Reservoir Geology and Exploitation, Southwest Petroleum University, Chengdu, Sichuan 610500, China

<sup>2</sup> School of Petroleum Engineering, Southwest Petroleum University, Chengdu, Sichuan 610500, China

Correspondence should be addressed to Xiangwei Kong; [m13880214723@163.com](mailto:m13880214723@163.com)

Received 4 June 2013; Revised 6 July 2013; Accepted 7 July 2013

Academic Editor: Waqar Khan

Copyright © 2013 Yuanhua Lin et al. This is an open access article distributed under the Creative Commons Attribution License, which permits unrestricted use, distribution, and reproduction in any medium, provided the original work is properly cited.

Investigation of propagation characteristics of a pressure wave is of great significance to the solution of the transient pressure problem caused by unsteady operations during management pressure drilling operations. With consideration of the important factors such as virtual mass force, drag force, angular frequency, gas influx rate, pressure, temperature, and well depth, a united wave velocity model has been proposed based on pressure gradient equations in drilling operations, gas-liquid two-fluid model, the gas-drilling mud equations of state, and small perturbation theory. Solved by adopting the Runge-Kutta method, calculation results indicate that the wave velocity and void fraction have different values with respect to well depth. In the annulus, the drop of pressure causes an increase in void fraction along the flow direction. The void fraction increases first slightly and then sharply; correspondingly the wave velocity first gradually decreases and then slightly increases. In general, the wave velocity tends to increase with the increase in back pressure and the decrease of gas influx rate and angular frequency, significantly in low range. Taking the virtual mass force into account, the dispersion characteristic of the pressure wave weakens obviously, especially at the position close to the wellhead.

## 1. Introduction

One of the future trends of the petroleum industry is the exploration and development of high pressure, low permeability reservoirs [1]. Drilling-related issues such as excessive mud cost, wellbore ballooning/breathing, kick-detection limitations, difficulty in avoiding gross overbalance conditions, differentially stuck pipe, and resulting well-control issues together contribute to the application of managed pressure drilling (MPD) technology [2]. MPD technology has the ability to quickly react to the expected drilling problems and formations pressures uncertainties, reduce nonproductive time and mitigating drilling hazards, and offer a considerable amount of tangible benefits while drilling in extremely narrow fracture/pore pressure windows [3]. It allows drilling operations to proceed where conventional drilling is easy to cause formation damage or considered uneconomical,

of high risk, or even impossible [4]. Although drilling operators try to avoid the risk of influxes, occasionally there are influxes for various reasons. Gas influx occurs whenever the pressure of a gas-bearing formation exceeds the pressure at the bottom of a wellbore. Since the subsequent intrusion of gas displaces drilling mud, it decreases the pressure in the wellbore and makes gas enter even faster [5, 6]. If it is not counteracted in time, the unstable effect can escalate into a blowout creating severe financial losses, environmental contamination, and potential loss of human lives. The basic principle of MPD well control is to keep the bottomhole pressure (BHP) as constant as possible at a value that is at least equal to the formation pressure [7]. MPD is a class of techniques that allow precise management of BHP under both static and dynamic conditions through a combination of controlling the flow rate, mud density, and back pressure (or wellhead pressure) on the fluid returns (choke manifold) of

the enclosed and pressurized fluid system [8, 9]. As a result of the ability to manipulate the back pressure, MPD offers the capability to improve safety and well control through early detection of influxes and losses in a microflux level, reduces the risk of influx and thus the chance of blowouts, and controls an influx dynamically without conventionally shutting-in [10].

During the managed pressure drilling process, all the unsteady operations such as adjustment of choke, wellhead back pressure controls [11], tripping in/out [12], shutting-in [13], and mud pump rate changes [14] will cause generation and propagation of pressure waves, which would threaten the whole drilling system from the wellhead facilities to the bottomhole drilling equipment and the formation [15]. In the analysis of an influx well and formulation of well control scheme, the dynamic effects of these operations, appeared as pressure fluctuations, should be accounted for [16]. As a basic parameter of pressure fluctuation, the pressure wave velocity has close relevance with the determination of transient pressure and safe operating parameters for well control. However, the gas influx is more troublesome for the higher compressibility and lower density of influx gas than the single phase drilling mud [17]. The works of Bacon et al. [18] had demonstrated that compressibility effects of a gas influx can be significant during an applied-back-pressure, dynamic, MPD well control response and can impact the well control process. Hence, this paper considered the propagation behavior of pressure wave in gas-drilling mud two-phase flow in the annulus to provide reference for the MPD operations.

Well control includes not only the handling but also early detection of a gas influx. Besides the transient pressure problem mentioned previously, investigation of the propagation characteristics of pressure wave is of great significance to the early detection of gas influx [19]. Many scholars believe that the pressure fluctuations procedure contains a wealth of information about the flow. Thus, characteristics of pressure wave can be easily used to measure some important parameters in the two-phase flow [20]. In the late 1970s, the former Soviet All-Union Drilling Technology Research Institute began to study characteristics of pressure wave propagation velocity in gas-liquid two-phase flow to detect early gas influx and achieved some important results [21]. According to the functional relationship between the pressure wave propagation velocity in gas-liquid two-phase flow and the gas void fraction, Li et al. [22] presented a method of detecting the gas influxes rate and the height of gas migration early after gas influxes into the wellbore. Furthermore, mud pulse telemetry is the most common method of data transmission used by measurement-while-drilling, and the transmission velocity of the pulse is a basic parameter for this kind of data transmission mode [23].

The pressure wave discussed in this paper can be transmitted as a pressure perturbation along the direction of flow in wellbore, which propagates with the speed of sound in the mud and gas two-phase drilling fluid. Due to the compressibility of the gas phase, the changes in interface between the gas and drilling mud, and the momentum and energy transfer between two phases, it is complicated to

predict the pressure wave velocity in gas and drilling mud two-phase flow. Since the 1940s, many experimental and theoretical studies have been performed. Experimental tests were conducted to inspect the contributions of fluctuation and flow characteristics on pressure wave. Ruggles et al. [24] firstly performed the experimental investigation on the dispersion property of pressure wave propagation in air-water bubbly flow. It was demonstrated that the propagation speed of pressure wave varies over a range of values for the given state, depending on the angular frequency of the pressure wave. Legius et al. [25] tested the propagation of pressure waves in bubbly and slug flow. The experimental result is similar to the calculation result of the Nguyen model and simulation result of the Sophy-2 package. Concluded from Miyazaki and Nakajima experiments [26] in Nitrogen-Mercury two-phase system, the slip between the phases plays a very important role in the mechanism of pressure wave propagation. From experimental investigation, Bai [27] found that the fractal dimension, correlation dimension, and the Kolmogorov entropy have close relationship with flow regime, and the fractal dimension will be greater than 1.5 when the flow is annular with high gas velocity. The characteristics of pressure wave propagation in bubbly and slug flow in a vertical pipe were investigated experimentally by Huang et al. in detail [28]. It confirmed that the propagation velocity is greatly affected by the gas void fraction and angular frequency of the pressure disturbance, and the superficial velocity of flowing medium has almost no effect on the propagation velocity. Also, there are some widely accepted models including elasticity model, homogeneous mixture model, and continuum model for pressure wave propagation in gas-liquid two-phase flow. Tangren et al. [29] took the two-phase media as a homogeneous fluid and presented the solution model concerning the problem of pressure wave velocity in two-phase flow at low gas void fraction. Wallis [30] studied the propagation mechanism of pressure waves and derived the propagation velocity in a bubbly flow and separated flow using the homogeneous model, in which the two-phase mixture is treated as a compressible fluid with suitably averaged properties. Nguyen et al. [31] applied the elastic theory to predict the propagation velocity of pressure waves in several different flow regimes. The comparison between the calculation results and available experimental data suggests its success at low void fraction. Mecredy and Hamilton [32] derived a detailed continuum model for sound wave propagation in gas-liquid flow by using six separate conservation equations to describe the flow of the vapor and liquid phases. This so-called two-fluid representation allows for nonequilibrium mass, heat, and momentum transfer between the phases. Results indicated that in a bubbly flow, high angular frequency waves travelled an order of magnitude faster than low angular frequency waves. With the development of hydrodynamics, the two-fluid model is widely used to determine the propagation velocity of the pressure wave in two-phase flow as it can provide a general dispersion relation valid for arbitrary flow regimes including effects of the interphase mass, heat, and momentum transfer. Ardron and Duffey [33] developed a model for sound-wave propagation in nonequilibrium vapor-liquid flows which

predicts sound speeds and wave attenuations dependent only on measurable flow properties on the basis of two-fluid conservation equations. Ruggles et al. [24], Xu and Chen [34], Chung et al. [35], Huang et al. [28], and Bai et al. [27] investigated the propagation velocity behavior of pressure wave via two-fluid model and small perturbation theory, and the predicted results show good agreement with the experimental data. In recent years, some new researches and models that are especially important in this area were developed. Xu and Gong [36] proposed a united model to predict wave velocity for different flow patterns. In this united model, the effect of a virtual mass coefficient was taken into consideration. The propagation of pressure wave during the condensation of R404A and R134a refrigerants in pipe mini-channels that undergo periodic hydrodynamic disturbances was given by Kuczynski [37, 38]. Li et al. [39] simulated the condensation of gas oxygen in subcooled liquid oxygen and the corresponding mixing process in pump pipeline with the application of thermal phase change model in Computational Fluid Dynamics code CFX and investigated the pressure wave propagation characteristics in two-phase flow pipeline for liquid-propellant rocket based on a proposed pressure wave propagation model and the predicted flow parameters. Based on the unified theory of Kanagawa et al. [40], the nonlinear wave equation for pressure wave propagation in liquids containing gas bubbles is rederived. On the basis of numerical simulation of the gaseous oxygen and liquid oxygen condensation process with the thermal phase model in ANSYS CFX, Chen et al. [41] solved the pressure wave propagation velocity in pump pipeline via the dispersion equation derived from ensemble average two-fluid model. Li and He [42] developed an improved slug flow tracking model and analyzed the variation rule of the pressure wave along the pipeline and influence of the variation of initial inlet liquid flow rate and gas flow rate in horizontal air-water slug flow with transient air flow rate. Meanwhile, the compressibility effects of gas had been noticed in the research field of propagation of pressure waves in the drilling industry, and some efforts have been made. Li et al. [22] established the relationship between wave velocity and gas void fraction according to the empirical formula of the homogeneous mixture model presented by Martin and Padmanatbhan [43] and frequency response model presented by Henry [44]. By applying the unsteady flow dynamic theory, Liu et al. [45] derived the pressure wave velocity calculation formula for gas-drilling mud-solid three-phase flow based on the continuity equation. Wang and Zhang [46] studied the pressure pulsation in mud and set up a model for calculating the amplitude of pressure pulsation when pressure wave is transmitted in drilling-fluid channel especially drilling hose with different inside diameters. However some efforts have been made; the pressure wave velocity is usually determined by empirical formula. In the past researches, the influencing factors for pressure wave propagation were simulated and analyzed with the mathematical model; however, the variation of wave velocity and gas void at different depth of wellbore was not considered. In addition, the current researches are limited in their assumption and neglect the flow pattern translation and interphase forces along the annulus. Up to now, no complete

mathematical model of pressure wave in an annulus with variations of gas void, flow pattern, temperature, and back pressure during MPD operations has been derived.

The object of the present work is to study the velocity for the transmission of pressure disturbance in the two-phase drilling fluid in the form of a pressure wave in annulus during MPD operations. In this paper, in addition to the pressure, temperature, and the void fraction in the annulus, the compressibility of the gas phase, the virtual mass force, and the changes of interface in two phases are also taken into consideration. By introducing the pressure gradient equations in MPD operations, gas-liquid two-fluid model, the gas-drilling mud equations of state (EOS), and small perturbation theory, a united model for predicting pressure wave velocity in gas and drilling mud in an annulus is developed. The model can be used to predict the wave velocity of various annulus positions at different influx rates, applied back pressures, and angular frequencies with a full consideration of drilling mud compressibility and interphase forces.

## 2. The Mathematical Model

*2.1. The Basic Equation.* In this paper, the two-fluid model and the pressure gradient equation along the flow direction in the annulus are combined to study the pressure wave velocity in MPD operations. Drilling fluid contains clay, cuttings, barite, other solids, and so forth. The solid particles are small and uniformly distributed; therefore, drilling fluid is considered to be a pseudohomogeneous liquid, and the influx natural gas is considered to be the gas phase. The following assumptions are made:

- (i) the two-phase flow is treated as one dimension;
- (ii) no mass transfers between the gas and drilling mud;
- (iii) the flow pattern in an annulus is either bubbly or slug flow.

As shown in Figure 1, the gas and drilling mud two-phase fluid travels along the annulus in the drilling process. The fluid flows along the annulus in “-z” direction, and the annulus is formed by the casing and drill string.

The momentum conservation equation for gas and liquid two-phase flow is

$$\sum F_z = \rho_m A dz \frac{dv_m}{dt}. \quad (1)$$

The mass conservation equations are

$$\begin{aligned} \frac{\partial}{\partial t} (\phi_G \rho_G) + \frac{\partial}{\partial z} (\phi_G \rho_G v_G) &= 0, \\ \frac{\partial}{\partial t} (\phi_L \rho_L) + \frac{\partial}{\partial z} (\phi_L \rho_L v_L) &= 0. \end{aligned} \quad (2)$$

The momentum conservation equations for gas are

$$\begin{aligned} \frac{\partial}{\partial t} (\phi_G \rho_G v_G) + \frac{\partial}{\partial z} (\phi_G \rho_G v_G^2) + \frac{\partial}{\partial z} (\phi_G \rho_G) \\ - \frac{\partial}{\partial z} \left[ \phi_G (\tau_G^{fr} + \tau_G^{Re}) + M_{Gi} - 4 \frac{\tau_G}{D} \right] &= 0. \end{aligned} \quad (3)$$

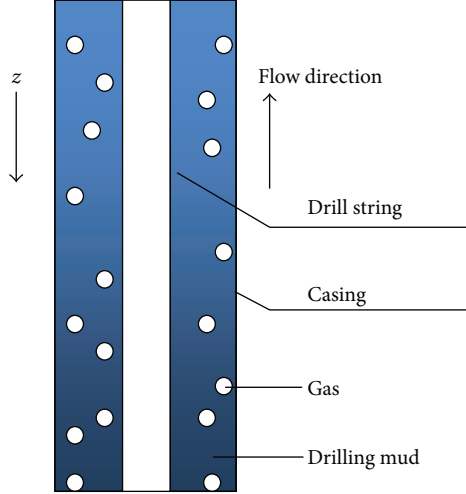


FIGURE 1: The schematic of gas and drilling mud two-phase flow in annulus.

The momentum conservation equations for liquid are

$$\begin{aligned} \frac{\partial}{\partial t} (\phi_L \rho_L v_L) + \frac{\partial}{\partial z} (\phi_L \rho_L v_L^2) + \frac{\partial}{\partial z} (\phi_L \rho_L) \\ - \frac{\partial}{\partial z} \left[ \phi_L (\tau_L^{fr} + \tau_L^{Re}) + M_{Li} - 4 \frac{\tau_L}{D} \right] = 0. \end{aligned} \quad (4)$$

The interphase forces include virtual mass force, drag force, and the wall shear stress. The transfer of momentum between the gas and drilling mud phases  $M_{Gi}$  and  $M_{Li}$  can be written as follows:

$$\begin{aligned} M_{Gi} = -M_{Li}^{nd} - M_{Li}^d + (\tau_{Li}^{fr} + \tau_{Li}^{Re}) \frac{\partial \phi_L}{\partial z} \\ + \frac{\partial (\phi_G \sigma_s)}{\partial z} + \frac{\partial (\phi_G p_{Gi})}{\partial z} - \phi_G \frac{\partial (p_{Li})}{\partial z}, \end{aligned} \quad (5)$$

$$M_{Li} = M_{Li}^{nd} + M_{Li}^d + p_{Li} \frac{\partial (\phi_L)}{\partial z} - (\tau_{Li}^{fr} + \tau_{Li}^{Re}) \frac{\partial \phi_L}{\partial z}.$$

The momentum transfer term caused by the gas-liquid interfacial relative acceleration motion (i.e., the virtual mass force) can be expressed as

$$M_{Li}^{nd} = c_{VM} \phi_G \rho_L \alpha_{VM} - 0.1 \phi_G \rho_L v_s \frac{\partial v_s}{\partial z} - c_{m1} \rho_L v_s^2 \frac{\partial \phi_G}{\partial z}, \quad (6)$$

where  $c_{m1} = 0.1$  and  $v_s$  is the slip velocity;  $v_s = v_G - v_L$ .

The momentum transfer term caused by the drag force provided by Park et al. [47] can be described as

$$M_{Li}^d = \frac{3}{8} \frac{C_D}{r} \rho_L R_G v_s^2. \quad (7)$$

The pressure difference between the liquid interface and liquid is defined by the following formula presented by Park et al.:

$$p_{Li} - p_L = -c_p \rho_L v_s^2, \quad (8)$$

where  $c_p = 0.25$ .

The proportion of gas phase in the interface between the gas and drilling mud is rather small in that the pressure difference between the gas interface and gas is not very high. Omitting the pressure difference, the gas interface pressure  $p_{Gi}$  can be written as

$$p_{Gi} - p_G \approx 0. \quad (9)$$

According to the equations of Arnold [48], the pressure of the drilling mud is described as follows:

$$p_L = p - 0.25 \rho_L \phi_G v_s^2. \quad (10)$$

In fact, the shear stress and the interphase shear stress are very small relative to the Reynolds stress. Also, the Reynolds stress in gas phase can be omitted relative to the interphase force. Hence, it can be described as

$$\tau_G^{fr} \approx \tau_{Li}^{fr} \approx \tau_L^{fr} \approx \tau_G \approx \tau_G^{Re} \approx 0. \quad (11)$$

The Reynolds stress and interfacial average Reynolds stress can be obtained by

$$\tau_L^{Re} = -c_r \rho_L v_s^2 \frac{\phi_G}{\phi_L}, \quad (12)$$

$$\tau_{Li}^{Re} = -c_r \rho_L v_s^2,$$

where  $c_r = 0.2$ .

The wall shear stress of liquid phase is given by Wallis in the following form [30]:

$$\tau_L = 0.5 f_L \rho_L v_L^2. \quad (13)$$

## 2.2. Physical Equations

2.2.1. Equations of State for Gas. The equation of state (EOS) for gas can be expressed as follows:

$$\rho_G = \frac{P}{(Z_G \cdot R \cdot T)}, \quad (14)$$

where  $Z_G$  is the compression factor of gas.

The formula presented by Dranchuk and Abou-Kassem has been used to solve the gas deviation factor under the condition of low and medium pressure ( $p < 35$  MPa) [49]:

$$\begin{aligned} Z_G = 1 + \left( 0.3051 - \frac{1.0467}{T_r} - \frac{0.5783}{T_r^3} \right) \rho_r \\ + \left( 0.5353 - \frac{0.26123}{T_r} - \frac{0.6816}{T_r^3} \right) \rho_r^2, \end{aligned} \quad (15)$$

where  $T_r = T/T_c$ ,  $p_r = p/p_c$ , and  $\rho_r = 0.27 p_r / Z_G T_r$ .

The formula presented by Yarborough and Hall has been adopted to solve the gas deviation factor under the condition of high pressure ( $p \geq 35$  MPa) [50]:

$$Z_G = \frac{0.06125 P_r T_r^{-1} \exp(-1.2(1 - T_r^{-1})2)}{Y}, \quad (16)$$

where  $Y$  is given by

$$\begin{aligned} & -0.06125p_r T_r^{-1} \exp\left(-1.2(1 - T_r^{-1})^2\right) + \frac{Y + Y^2 + Y^3 + Y^4}{(1 - Y)^3} \\ & = (14.76T_r^{-1} - 9.76T_r^{-2} + 4.58T_r^{-3})Y^2 \\ & \quad - (90.7T_r^{-1} - 242.2T_r^{-2} + 42.4T_r^{-3})Y^{(2.18+2.82T_r^{-1})}. \end{aligned} \quad (17)$$

**2.2.2. Equations of State for Liquid.** Under different temperatures and pressures, the density of drilling mud can be obtained by the empirical formulas.

If  $T < 130^\circ\text{C}$ , the density of drilling mud can be obtained by the following equation:

$$\rho_L = \rho_0 \left(1 + 4 \times 10^{-10} p_L - 4 \times 10^{-5} T - 3 \times 10^{-6} T^2\right). \quad (18)$$

If  $T \geq 130^\circ\text{C}$ , the density of drilling mud is

$$\begin{aligned} \rho_L = \rho_0 \left(1 + 4 \times 10^{-10} P_L - 4 \times 10^{-5} T \right. \\ \left. - 3 \times 10^{-6} T^2 + 0.4 \left(\frac{T - 130}{T}\right)^2\right). \end{aligned} \quad (19)$$

**2.2.3. Correlation of Temperature Distribution.** The temperature of the drilling mud at different depths of the annulus can be determined by the relationship presented by Hasan and Kabir [51]:

$$\begin{aligned} T = T_{ei} + F \left[1 - e^{(z_{bh}-z)/A}\right] \left(-\frac{g \sin \theta}{g_c J c_{pm}} + N + g_T \sin \theta\right) \\ + e^{(z_{bh}-z)/A} (T_{fbh} - T_{ebh}). \end{aligned} \quad (20)$$

**2.3. Flow Pattern Analysis.** Based on the analysis of flow characteristics in the enclosed drilling system, it can be safely assumed that the flow pattern in an annulus is either bubbly or slug flow [52]. The pattern transition criteria for bubbly flow and slug flow given by Orkiszewski are used to judge the flow pattern in the gas-drilling mud two-phase flow [53].

For bubbly flow,

$$\frac{q_G}{q_m} < L_B. \quad (21)$$

For slug flow,

$$\frac{q_G}{q_m} > L_B, \quad N_{GV} < L_S, \quad (22)$$

where  $q_m$  is the volumetric flow rate of two-phase flow,  $q_m = q_G + q_L$ .

The dimensionless numbers  $L_S$  and  $L_B$  are defined as

$$\begin{aligned} L_S &= 50 + 36 N_{GV} \frac{q_L}{q_G}, \\ L_B &= 1.071 - \frac{0.7277 v_m^2}{D}, \end{aligned} \quad (23)$$

where

$$N_{GV} = v_s \left(\frac{\rho_L}{g \sigma_s}\right)^{0.25}. \quad (24)$$

Flow parameters such as void fraction, mixture density, and virtual mass force coefficient are discussed for a specific flow pattern.

The correlation between void fraction and liquid holdup is expressed as

$$\phi_G + \phi_L = 1. \quad (25)$$

**2.3.1. Bubbly Flow.** As for bubbly flow, the density of gas and drilling mud mixture is described as the following formula:

$$\rho_m = \phi_L \rho_L + \phi_G \rho_G. \quad (26)$$

The void fraction is determined by the following formula:

$$\phi_G = \frac{1}{2} \left[1 + \frac{q_m}{v_s A} - \sqrt{\left(1 + \frac{q_m}{v_s A}\right)^2 - \frac{4q_G}{v_s A}}\right]. \quad (27)$$

The coefficient of virtual mass force  $C_{vm}$  for bubbly flow can be expressed as follows [54]:

$$C_{vm} = 0.5 \frac{1 + 2\phi_G}{1 - \phi_G}. \quad (28)$$

The coefficient of resistance coefficient  $C_D$  for bubbly flow can be expressed as

$$C_D = \frac{4R_b}{3} \sqrt{\frac{g(\rho_L - \rho_G)}{\sigma_s}} \left[ \frac{1 + 17.67(1 - \phi_G)^{9/7}}{18.67(1 - \phi_G)^{1.5}} \right]^2. \quad (29)$$

The friction pressure gradient for bubbly flow can be obtained from the following equation:

$$\tau_f = f \frac{\rho_L v_L^2}{2D}. \quad (30)$$

**2.3.2. Slug Flow.** As for slug flow, distribution coefficient of gas in the liquid phase is

$$C_0 = \frac{0.00252 \lg(10^3 \mu_L)}{A^{1.38}} - 0.782 + 0.232 \lg v_m - 0.428 \lg A. \quad (31)$$

The average density of the mixture for slug flow is determined by

$$\rho_m = \frac{W_m + \rho_L v_s A}{q_m + v_s A} + C_0 \rho_L. \quad (32)$$

The void fraction for slug flow is determined by the following formula:

$$\phi_G = \frac{q_G}{q_G + q_L}. \quad (33)$$

The coefficient of virtual mass force  $C_{vm}$  for slug flow can be expressed as follows:

$$C_{vm} = 3.3 + 1.7 \frac{3L_q - 3R_q}{3L_q - R_q}. \quad (34)$$

The coefficient of resistance coefficient  $C_D$  for slug flow can be expressed as

$$C_D = 110\phi_L^3 R_b. \quad (35)$$

The friction pressure gradient of bubbly flow can be obtained from the following equation:

$$\tau_f = f \frac{\rho_L v_m^2}{2D} \left( \frac{q_L + v_s A}{q_m + v_s A} + C_0 \right). \quad (36)$$

**2.4. Annulus Characteristic Analysis.** The annulus effective diameter proposed by Sanchez [55] is used in the hydraulic calculation of annulus

$$D = \frac{\pi(D_o^2 - D_i^2)/4}{\pi(D_o + D_i)/4} = D_o - D_i. \quad (37)$$

The effective roughness of the annulus can be expressed as

$$k_e = k_o \frac{D_o}{D_o + D_i} + k_i \frac{D_i}{D_o + D_i}, \quad (38)$$

where the  $D_i$  and  $D_o$  are the diameters of inner pipe and outer pipe, respectively; the  $k_o$  and  $k_i$  are the roughnesses of outer pipe and the inner pipe, respectively.

### 3. The United Model Developed

The total pressure drop gradient is the sum of pressure drop gradients due to potential energy change and kinetic energy and frictional loss. From (1), the equation used to calculate the pressure gradient of gas and drilling mud flow within the annulus can be written as

$$\frac{dp}{dz} = \rho_m g \sin \theta - \frac{\tau_w \pi D}{A} - \rho_m v_m \frac{dv_m}{dz}. \quad (39)$$

Assuming the compressibility of the gas is only related to the pressure in the annulus, the kinetic energy or acceleration term in the previous equation can be simplified to

$$\rho_m v_m \frac{dv_m}{dz} = -\frac{\rho_m v_m v_{sg}}{p} \frac{dp}{dz} = -\frac{W_m q_g}{A^2 p} \frac{dp}{dz}. \quad (40)$$

Substituting (39) into (40), the total pressure drop gradient along the flow direction within the annulus can be expressed as

$$\frac{dp}{dz} = \frac{\rho_m g + \tau_f}{1 - W_m q_g / (A^2 p)}. \quad (41)$$

It is assumed that the gas obeys to the EOS (14), and the compressibility of drilling mud can be obtained by adopting

the simplified EOS ((18) and (19)) which neglects the thermal expansion of liquid. The sonic speed of gas phase  $c_G$  and that of liquid phase  $c_L$  can be presented in the following form:

$$\begin{aligned} \frac{dp_L}{d\rho_L} &= c_L^2, \\ \frac{dp_G}{d\rho_G} &= c_G^2. \end{aligned} \quad (42)$$

By introducing (42), the hydrodynamic equations of two-fluid model ((2)–(4)) can be written in the matrix form

$$A \frac{\partial \xi}{\partial t} + B \frac{\partial \xi}{\partial z} = C \xi, \quad (43)$$

where  $A$  is the matrix of parameters considered in relation to time,  $B$  is the matrix of parameters considered in relation to the spatial coordinate, and  $C$  is the vector of extractions.

By introducing the small disturbance theory, the disturbance of the state variable  $\xi(\phi_G, p, v_G, v_L)^T$  can be written as

$$\xi = \xi_0 + \delta \xi \exp [i(\omega t - kt)]. \quad (44)$$

In (44),  $k$  is the wave number, and  $\omega$  is the angular frequency of the disturbances. Substituting (44) into (43) gives homogenous linear equations concerning the expression  $(\delta \phi_G, \delta p, \delta v_G, \delta v_L)^T$ . According to the solvable condition of the homogenous linear equations that the determinant of the equations is zero, dispersion equation of pressure wave can be expressed in the following form:

$$\begin{vmatrix} M_1 & M_2 & M_3 & M_4 \\ -\rho_L \omega & \frac{1 - \phi_G}{c_L^2} \omega & 0 & -k(1 - \phi_G) \rho_L \\ M_5 & M_6 & M_7 & M_8 \\ M_9 & M_{10} & M_8 & M_{11} \end{vmatrix} = 0, \quad (45)$$

where  $M_1 - M_{11}$  can be illustrated by

$$\begin{aligned} M_1 &= \left( \rho_G + c_p \phi_G \rho_L \frac{v_s^2}{c_G^2} \right) \omega, \\ M_2 &= \frac{\phi_G}{c_G^2} \left[ 1 - c_p \phi_L \right] \frac{v_s^2}{c_L^2} \omega, \\ M_3 &= - \left[ \phi_G \rho_G k + 2c_p \phi_G \phi_L \rho_L \frac{v_s}{c_L^2} \omega \right], \\ M_4 &= 22c_p \phi_G \phi_L \rho_L \frac{v_s}{c_L^2} \omega, \\ M_5 &= \rho_L v_r^2 k \left( -\phi_G c_p + c_r - c_i + c_{m2} \right), \\ M_6 &= -\phi_G k \left[ 1 - \phi_L \frac{c_p v_s^2}{c_L^2} + c_i \frac{v_s^2}{c_L^2} \right], \end{aligned}$$

$$\begin{aligned}
M_7 &= \phi_G (\rho_G + c_{vm}\rho_L) w - i \left( \frac{3}{4} \frac{c_D}{r} \rho_L \phi_G v_s + \frac{4}{D} f_{Gw} \rho_G v_G \right), \\
M_8 &= -c_{vm} \phi_G \rho_L w + i \left( \frac{3}{4} \frac{c_D}{r} \rho_L \phi_G v_s \right), \\
M_9 &= \rho_L v_s^2 k (\phi_L c_p - 2c_r - c_{m2}), \\
M_{10} &= -k \left( \phi_L + c_r \phi_G \frac{v_s^2}{c_L^2} \right), \\
M_{11} &= \rho_L [\phi_L + \phi_G c_{vm}] w - i \left( \frac{3}{4} \frac{c_D}{r} \rho_L \phi_G v_s + \frac{4}{D} f_{L\rho_L} v_L \right),
\end{aligned} \tag{46}$$

where  $c_{m2} = 0.1$ ,  $c_p = 0.25$ ,  $c_i = 0.3$ , and  $c_r = 0.2$ .

By solving the dispersion equation indicated previously, four roots can be obtained. Because the wavelengths associated with two of the roots are too short to allow the two-fluid medium to be treated as a continuum, the two roots should be omitted. As for the two remaining roots, one of them represents a pressure wave that transmitted along the axis  $z$ , and the other represents a pressure wave transmits in the opposite direction in accordance with the direction of the flow along the annulus. The real value of wave number can be used to determine the wave velocity  $c$ . The wave velocity in the two-phase fluid can be determined by the following model:

$$c = \frac{|(w/R^+(k)) - (w/R^-(k))|}{2}. \tag{47}$$

#### 4. Solution of the United Model

Obtaining the analytical solution of the mathematical models concerned with flow pattern, void fraction, characteristic parameters, and pressure drop gradient is generally impossible for two-phase flow. In this paper, the Runge-Kutta method (R-K4) is used to discretize the theoretical model.

We can obtain pressure, temperature, gas velocity, drilling mud velocity, and void fraction at different annulus depths by R-K4. The solution of pressure drop gradient equation (41) can be seen as an initial-value problem of the ordinary differential equation:

$$\begin{aligned}
\frac{dp}{dz} &= F(z, p), \\
p(z_0) &= P_0.
\end{aligned} \tag{48}$$

With the initial value  $(z_0, p_0)$  and the function  $F(z, p)$ , (50)–(53) can be obtained by

$$k_1 = F(z_0, p_0), \tag{49}$$

$$k_2 = F\left(z_0 + \frac{h}{2}, p_0 + \frac{h}{2}k_1\right), \tag{50}$$

$$k_3 = F\left(z_0 + \frac{h}{2}, p_0 + \frac{h}{2}k_2\right), \tag{51}$$

$$k_4 = F(z_0 + h, p_0 + hk_3), \tag{52}$$

where  $h$  is the step of depth. The pressure on the nod  $i = i + 1$  can be obtained by

$$p_1 = p_0 + \Delta p = p_0 + \frac{h}{6} (k_1 + 2k_2 + 2k_3 + k_4). \tag{53}$$

In the present work, the mathematical model and pressure wave velocity calculation model are solved by a personally compiled code on VB.NET (Version 2010). The solution procedure for the wave velocity in the annulus is shown in Figure 1. At initial time, the wellhead back pressure, wellhead temperature, wellbore structure, well depth, gas and drilling mud properties, and so forth, are known. On the node  $i$ , the pressure gradient, temperature, and the void fraction can be obtained by adopting R-K4. Then, the determinant (45) is calculated based on the calculated parameters. Omitting the two unreasonable roots, the pressure wave velocity at different depths of the annulus in MPD operations can be solved by (47). The process is repeated until the pressure wave velocity of every position in the wellbore is obtained as shown in Figure 2.

The developed model takes full consideration of the interfacial interaction and the virtual mass force. Owing to the complex conditions of the annulus in MPD operations, measurement of wave velocity in the actual drilling process is very difficult. In order to verify the united model, the predicted pressure waves are compared with the results of previous simulated experimental investigations presented for gas and drilling mud by Liu et al. [45] in Figure 3(a) and by Li et al. [22] in Figure 3(b). The lines represent the calculation results, and the points represent the experimental data.

The comparisons reveal that the developed united model fits well with the experimental data. Thus, the united model can be used to accurately predict wave velocity at different wellhead back pressures and gas influx rates (the influx rate of gas in the bottomhole) in MPD operations.

#### 5. Analysis and Discussion

The drilling system described is an enclosed system. The schematic diagram of the gas influx process is illustrated in Figure 4. The drilling mud is pumped from surface storage down the drill pipe. Returns from the wellbore annulus travel back through surface processing, where drilling solids are removed, to surface storage. The key equipments include the following.

- (i) *The Rotating Control Device (RCD)*. The rotating control device provides the seal between atmosphere and wellbore, while allowing pipe movement and diverting returns flow. In conjunction with the flow control choke, the RCD provides the ability to apply back pressure on the annulus during an MPD operation.
- (ii) *Choke*. The MPD choke manifold provides an adjustable choke system which is used to dynamically control the required BHP by means of applying surface BP.
- (iii) *Coriolis Meter*. A Coriolis meter is used to accurately measure the mass flow rate of fluid exiting

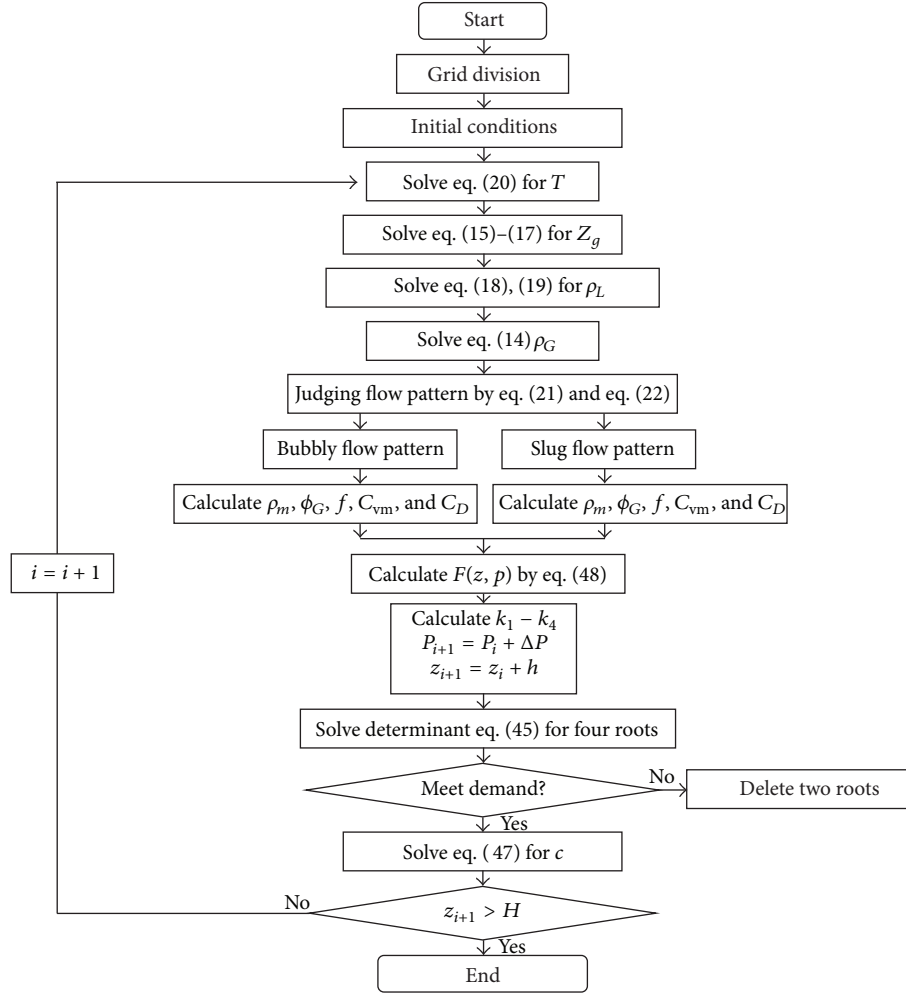


FIGURE 2: Solution procedure for wave velocity in MPD operations.

the annulus. The ability to measure return flow accurately is essential for the applied back pressure.

- (iv) *Pressure Sensor*. A pressure sensor is used to measure surface back pressure on the wellhead.

The gas and drilling mud flow rate measured by the Coriolis meter and the back pressure measured by the pressure sensor are the initial data for annulus pressure calculation. The well used for calculation is a gas well in Xinjiang Uygur Autonomous Region, Northwest China. The wellbore structure, well design parameters (depths and diameters), gas and drilling mud properties (density and viscosity), and operational conditions of calculation well are displayed in Table 1.

The drilling mud mixed with gas is taken as a two-phase flow medium. The propagation velocity of pressure wave in the gas-drilling mud flow is calculated and discussed by using the established model and well parameters.

*5.1. Effect of Back Pressure on Wave Velocity*. Increase in applied back pressure is the most common approach for dynamic well control. The wellbore can be seen as an enclosed

TABLE 1: Parameters of calculation well.

Type	Property	Value
Mud	Dynamic viscosity (Pa · s)	0.056
	Density (kg/cm <sup>3</sup> )	1460
Gas	Relative density	0.65
	Viscosity (Pa · s)	$1.14 \times 10^{-5}$
String	Elastic modulus of string (Pa)	$2.07 \times 10^{11}$
	Poisson ratio of string	0.3
	Roughness (m)	$1.54 \times 10^{-7}$
Surface condition	Surface temperature (K)	298
	Atmosphere pressure (MPa)	0.101

pressurized system. The pressure at different depths of the annulus varied with the change of back pressure. According to the EOS of gas and drilling mud, the influence of pressure on gas volume is much greater than that of drilling mud for the greater compressibility of gas. So, the gas void fraction changes with the variation of gas volume at the nearly constant flow rate of drilling mud at different annular pressures. Meanwhile, the pressure wave velocity is sensitive

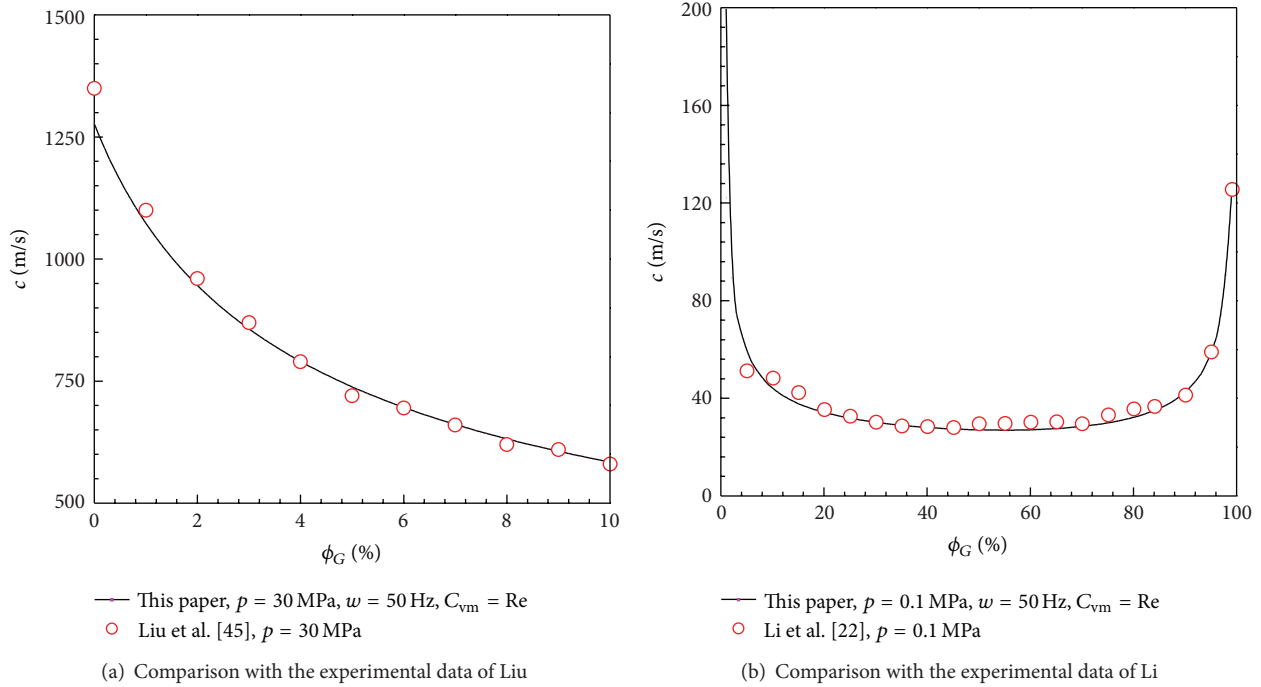


FIGURE 3: Experimental verification by comparison with previous experimental data.

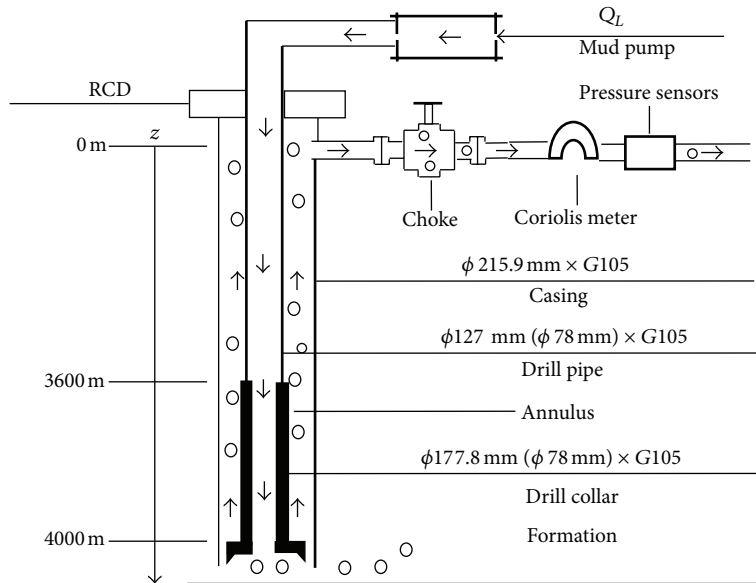


FIGURE 4: Schematic diagram of the gas influx process.

to the gas void fraction. As a result, when the back pressure at the wellhead is changed by adjusting the choke, the wave velocity in the two-phase drilling fluid and the distribution of void fraction at different depth of the annulus will diverge. The calculation results affected by the back pressure are presented.

Figures 5 and 6 show the distributions of void fraction and variations of wave velocity along the flow direction in the annulus when the back pressure at the wellhead is 0.1 MPa, 0.8 MPa, 1.5 MPa, 2.5 MPa, 5.0 MPa, and 6.5 MPa,

respectively. It can be seen that the void fraction significantly increases along the flow direction in the annulus. Conversely, the wave velocity shows a remarkable decrease tendency. For instance, BP = 1.5 MPa, at the wellhead, the wave velocity is 90.12 m/s, and the void fraction is 0.611, while in the bottomhole, the wave velocity reaches 731.42 m/s, and void fraction is reduced to 0.059. However, a sudden increase in wave velocity is observed in Figure 5 when the back pressure is 0.1 MPa at the position close to wellhead as the void fraction is further increased. Moreover, the influence of back pressure

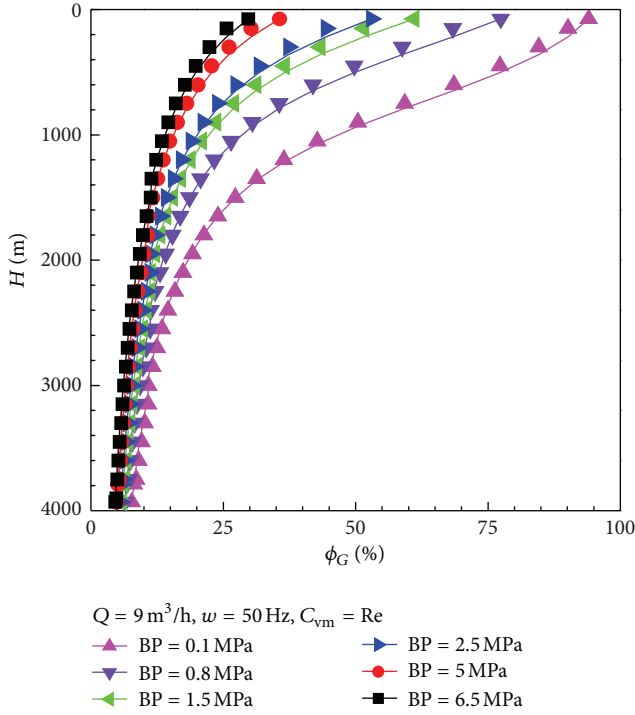


FIGURE 5: Void fraction distribution at different back pressures.

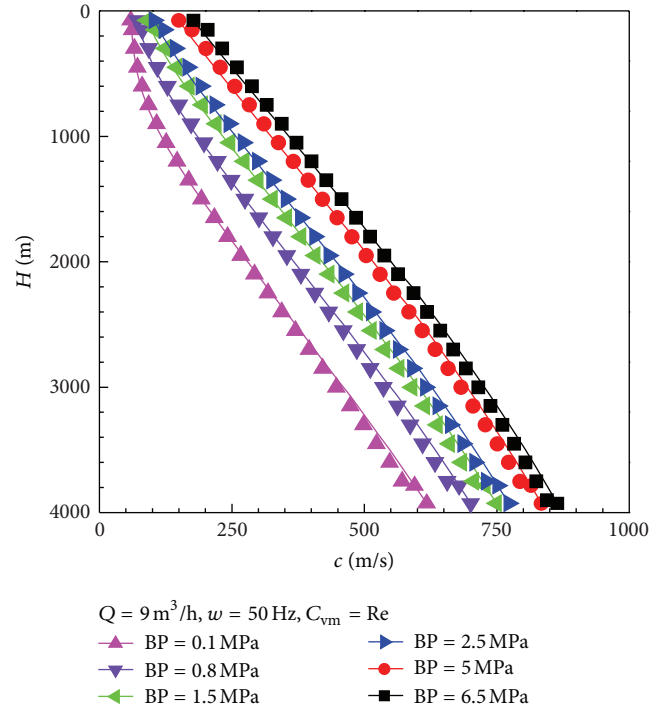


FIGURE 6: Wave velocity variations at different back pressures.

on the void fraction is larger at the position close to the wellhead than that in the bottomhole.

This can be explained from the viewpoints of mixture density and compressibility of two-phase fluid and the pressure drop along the flow direction in the wellbore. In the low void fraction range, the gas phase is dispersed in the liquid as bubble, so the wave velocity is influenced greatly by the added gas phase. According to the EOS, if gas invades into the wellbore with a small amount in the bottomhole, the density of the drilling mud has little variation while the compressibility increases obviously, which makes the wave velocity decreased. Then, the two-phase drilling mud flow from the bottomhole to the wellhead along the annulus with a drop of pressure caused by, potential energy change, kinetic energy and frictional loss, which leads to an increase in void fraction. When the void fraction is increased, both the density and the compressibility of the two-phase fluid change slightly, resulting in a flat decrease in wave velocity along the flow direction. With the further increasing in void fraction, the bubbly flow turns into slug flow according to the flow pattern transient criteria of Orkiszewski which shows that the flow pattern is dependent on the void fraction. Generally speaking, the gas-drilling mud slug flow is composed of liquid and gas slugs. In the preliminary slug flow, the liquid slugs are much longer than the gas slugs, so the wave velocity is determined primarily by the wave velocities in the liquid slugs which are hardly affected by the void fraction. At the position close to the wellhead, the pressure of two-phase flow fluid can be reduced to a low value which approaches the back pressure. The compressibility of gas will be improved at the low pressure. It results in significant increase in void

fraction. As the void fraction increases greatly at the position close to the wellhead, gas slugs become much longer than the liquid slugs. It is assumed that the actual wave velocity in slug flow happens to play a leading role when the void fraction increases to some extent. For the decrease in liquid holdup in the gas slug with the increasing in void fraction, the wave velocity in the gas slug is infinitely close to that in pure gas, which is equivalent to an increase in wave velocity in the gas slug. Meanwhile, the gas content in liquid slug also increases and results in a lower wave velocity in the liquid slug. As a result, a slight increase in wave velocity appears.

Figures 7 and 8 present the influence of back pressure on the void fraction and wave velocity with respect to the parameters of well depth. As the back pressure increases, the void fraction at different depth of the annulus is reduced gradually, while the wave velocity in the two-phase flow tends to increase. Analytical results show that the increased back pressure is equivalent to be applied to the entire enclosed drilling fluid cyclical system. The pressure transmits from the wellhead to the bottomhole; therefore, the annular pressure in the entire wellbore is increased. According to the EOS, the density of gas increases and the compressibility of gas decreases with the increasing of gas pressure. So, the loss of interphase momentum and energy exchange is reduced and the interphase momentum exchange is promoted. It contributes to the increase in wave velocity with the increase in gas pressure. In addition, due to lower compressibility of two-phase flow medium under high pressure, the increase tendency of pressure wave velocity and the decrease tendency of void fraction are slowed down in the high back pressure range.

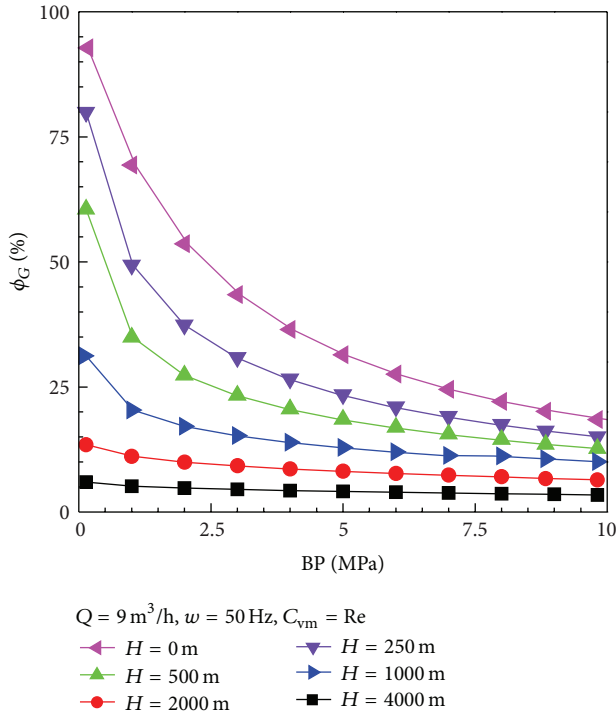


FIGURE 7: Effect of back pressure on the void fraction.

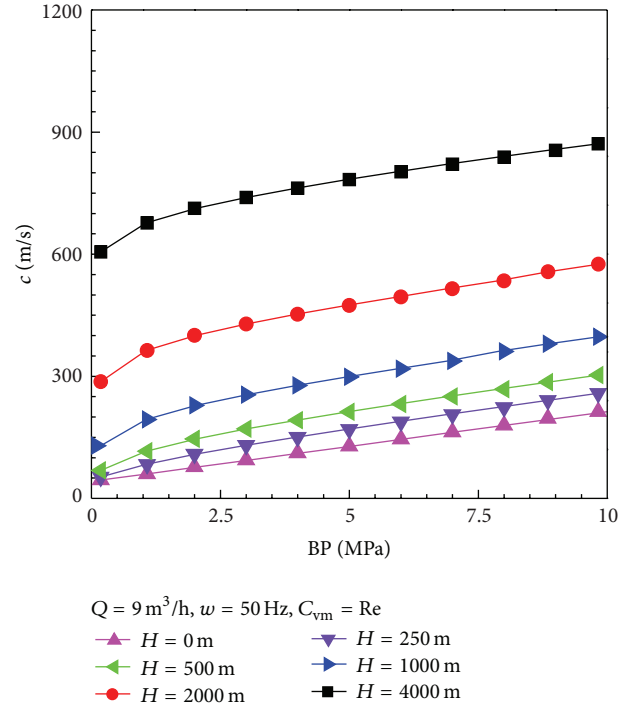


FIGURE 8: Effect of back pressure on the pressure wave velocity.

5.2. *Effect of Gas Influx Rate on Wave Velocity.* Figures 9 and 10 graphically interpret the distributions of void fraction and variations of wave velocity along the flow direction in the annulus. When gas influx occurs in the bottomhole, gas invades into the wellbore and migrates from the bottomhole to the wellhead along the flow direction. At a low gas influx rate, it is extremely obvious that the void fraction and wave velocity first slightly change in a comparatively smooth value then change sharply. It is because of the rapid expansion of gas volume with the decreasing in pressure near the wellhead that the void fraction increases sharply, and the wave velocity decreases obviously at the same time. But under the high bottomhole pressure (up to 50 MPa), the compressibility of the gas is low. This results in a slight change in void fraction and wave velocity at the position far away from the wellhead. Since the compressible component increases with the increase in the gas influx rate, the compressibility of the gas and drilling mud two-phase fluid is improved. So the variations of void fraction and wave velocity become more prominent. Also, the void fraction still shows an increase tendency that is steady first and then sharp. It acts in accordance with the variation of void fraction at a low gas influx rate. At a low gas influx rate, if the void fraction at the position close to the wellhead can not increase to a high extent, the wave velocity always shows a decrease tendency. At a high gas influx rate, such as the  $Q = 8.312 \text{ m}^3/\text{h}$ , the wave velocity tends to increase because the void fraction in the wellhead is increased to a high extent. In conclusion, the wave pressure is sensitive to the void fraction, and the void fraction is dominated by influx rate and pressure in the annulus, especially the influx rate.

With the influx of gas, the mixing of gas and drilling mud occurs in the annulus and the corresponding interfacial transfer of momentum and mass causes an increase in gas phase void fraction and a decrease in pressure wave velocity, as shown in Figures 11 and 12. Within the range of low gas influx rate, the wave velocity decreases significantly. It is because of this that the compressibility of the gas increases remarkably, and the medium appears to be of high elasticity, though the density of gas-drilling mud two-phase flow changes slightly. With the increase in the gas influx rate and corresponding increase in the void fraction in the annulus, the compressibility of the two-phase unceasingly increases, which promotes the momentum and energy exchange in the interface. So, the pressure wave continuously decreases. When the void fraction increases to some extent following the increase in the gas influx rate, the decrease in wave velocity in the liquid slug is gradually less than the increase in wave velocity in the gas slug; thus, the decrease of wave velocity is slowed down for the growth of gas slug. Especially in the wellhead, a slight increase in wave velocity is observed.

5.3. *Effect of Virtual Mass Force on Wave Velocity.* Figure 13 illustrates the effect of virtual mass force on the wave velocity with the parameter of gas influx rate. As shown in Figure 15, under the same gas influx rate ( $0.594 \text{ m}^3/\text{h}$ ,  $1.098 \text{ m}^3/\text{h}$ , and  $1.768 \text{ m}^3/\text{h}$ , resp.) the wave velocity curve of  $C_{vm} = Re$  diverges from the curve of  $C_{vm} = 0$  at the position close to the wellhead, whereas the wave velocity curve of the two types is almost coincided below the position of  $H = 500 \text{ m}$ . This divergence between the two types of curves is connected with the fact that significance of influence of interphase virtual

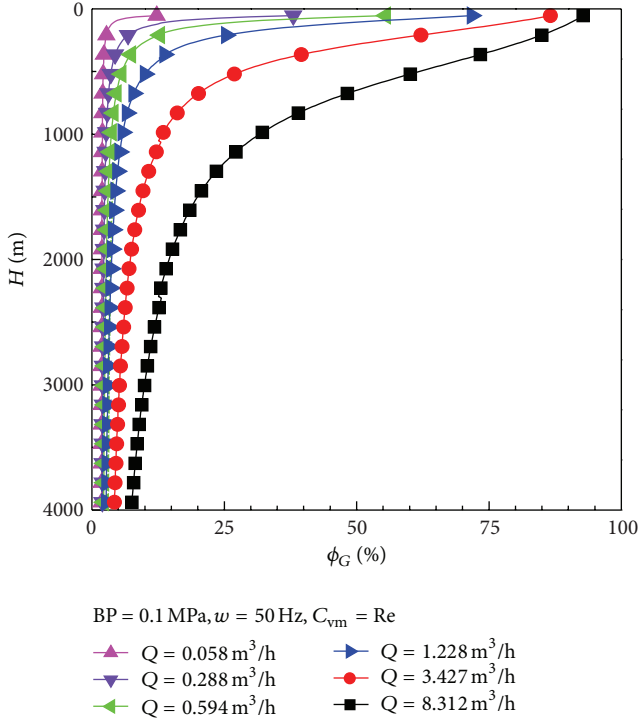


FIGURE 9: Void fraction distribution at different gas influx rates.

mass forces increases together with the increase of the relative motion in the interphase. It is evident that the bottomhole pressure is hundreds of times higher than the wellhead pressure. As a result, the void fraction at the position close to the wellhead increases sharply, meanwhile the interphase momentum and energy exchanges are promoted. The virtual mass force can be described as the transfer of momentum between the gas phase and drilling mud phase caused by the relative motion in the interphase. If the relative motion in the interphase is quite weak, the value of virtual mass force will intend to approach 0, and the influence on the wave velocity can be ignored. However, if the relative motion is rather intense, the effect of virtual mass force on the wave velocity should not be ignored. Furthermore, taking the virtual mass force into account, the dispersion characteristic of the pressure wave weakens obviously. Compared with the pressure wave velocity calculated by ignoring the effect of virtual mass force, the calculated pressure wave velocity with a consideration of the virtual mass force is lower. Therefore, it is necessary to analyze the effect of the virtual mass force on the wave velocity at the position close to the wellhead in MPD operations.

5.4. Effect of Disturbance Angular Frequency on Wave Velocity.

Figure 14 presents the pressure wave velocity in the annulus at different angular frequencies. According to Figures 5 and 9, the void fraction first slightly increases in the bottomhole and then sharply increases along the flow direction at the position close to the wellhead. At a fixed angular frequency, this phenomenon results in an overall decrease in the pressure wave velocity except for the section near the wellhead. At the

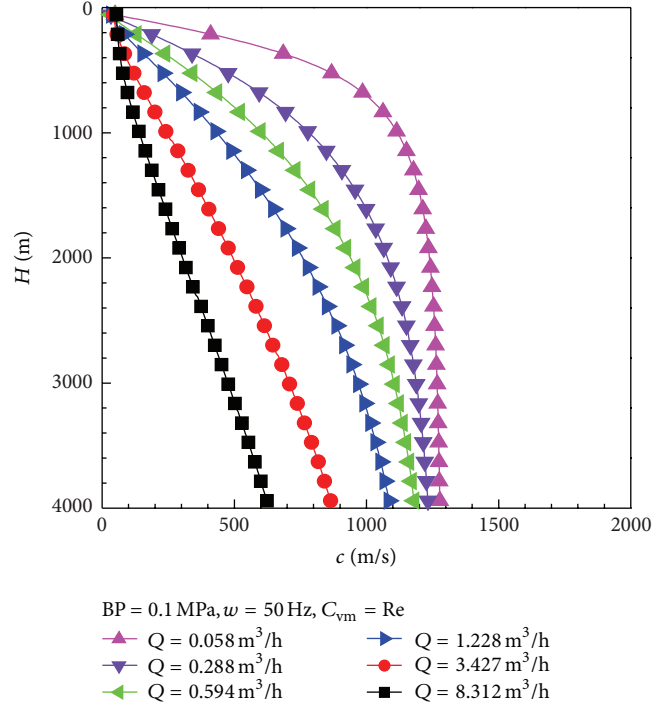


FIGURE 10: Wave velocity variations at different gas influx rates.

section close to the wellhead, an opposite change trend of pressure wave velocity is observed for the transition of flow pattern from bubbly flow to slug flow due to the continuous increase in void fraction along the flow direction. In addition, it can be clearly seen from the curves that the wave velocity increases accompanying with the increase in the angular frequency above the position of  $H = 500$  m. This property is not very distinct at the position below  $H = 500$  m for the low void fraction.

Figure 15 shows the effect of frequency on the wave velocity in the gas-drilling mud flow ( $C_{vm} = 0$ ). The curves of the wave velocity of different positions reveal that the propagation velocity of pressure disturbances increases together with the growth of the angular frequency ( $0 < \omega < 500$  Hz). It proves that the pressure wave has an obvious dispersion characteristic in the two-phase flow. As the angular frequency increases in the range of less than 500 Hz, there is sufficient time to carry out the exchange of energy and momentum between two phases. It achieves a state of mechanical and thermodynamic equilibrium between the two phases. So the wave velocity increases gradually with the increase in the angular frequency at different depths of the annulus. It is considered that the wave velocity is mainly affected by the interphase mechanical and thermodynamic equilibrium at low angular frequencies. When the angular frequency reaches the value of  $\omega = 500$  Hz, the pressure wave velocity achieves a constant value and remains on this level regardless of the further growth in angular frequency  $\omega$ . With the increase in angular frequency, there is not enough time for energy and momentum exchange between the gas-drilling mud two phases to reach the mechanical and thermodynamic

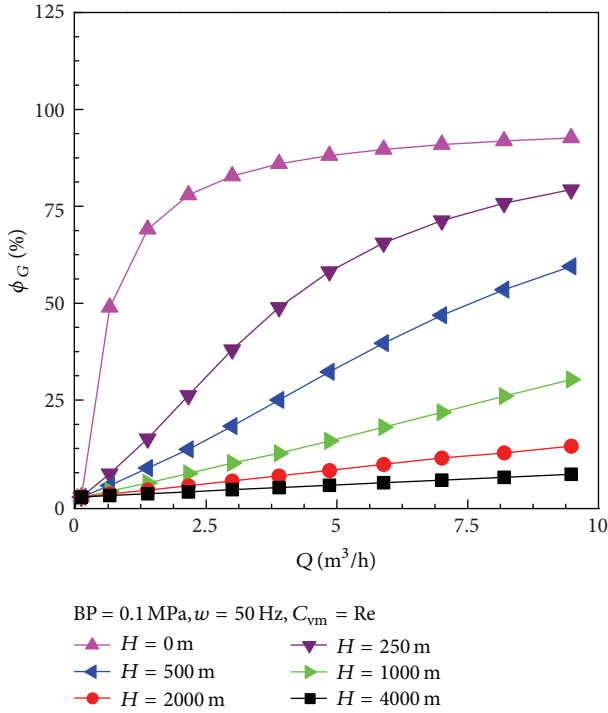


FIGURE 11: Effect of gas influx rate on the void fraction.

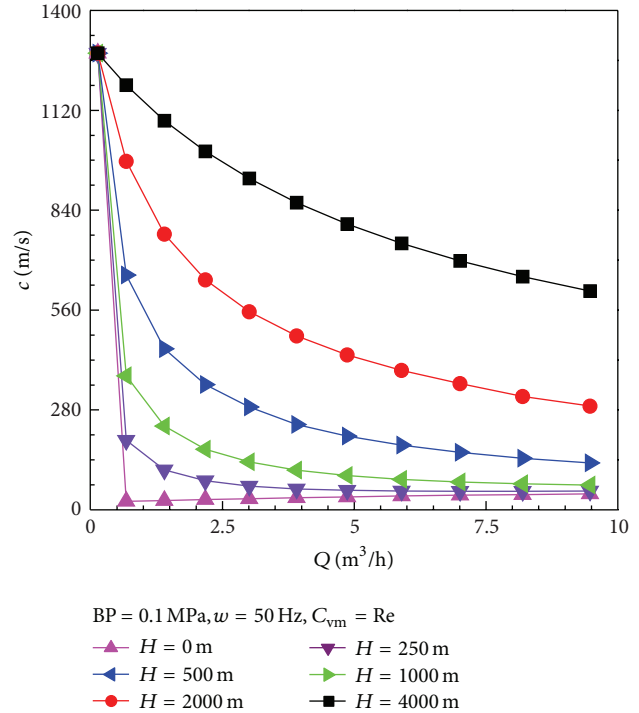


FIGURE 12: Effect of gas influx rate on the pressure wave velocity.

equilibrium state, and thus the wave dispersion does not exist. At a high angular frequency, the wave velocity is mainly dominated by the mechanical and thermal nonequilibrium in the flow and keeps almost unchanged when the angular frequency is further increased. This is consistent with the influences of the angular frequency in the horizontal pipe [28]. Moreover, the effect of virtual mass force is also shown in this figure ( $C_{vm} = Re$ ). It is observed that the wave velocity is significantly reduced when the virtual mass force is taken into consideration in the calculation of the wave velocity at the position close to the wellhead such as  $H = 0$  m. It can be explained by the reduction of dispersion characteristic of a pressure wave. Along the wellbore from the wellhead to the bottomhole, the distinction gradually decreases.

### 6. Conclusions

With full consideration of the important factors such as virtual mass force, drag force, gas void fraction, pressure, temperature, and angular frequency, a united wave velocity model has been proposed based on pressure drop gradient equations in MPD operations, gas-liquid two-fluid model, the gas-drilling mud equations of state, and small perturbation theory. Solved by the fourth-order explicit Runge-Kutta method, the model is used to predict wave velocity for different back pressures and gas influx rates in MPD operations. The main conclusions can be summarized as follows.

- (1) With the introduction of virtual mass force and drag force, the united model agrees well with the previous experimental data. The united model can be used to

accurately calculate the wave velocity in the annulus. The application of the model will be beneficial to further study the wave velocity at different gas influx rates and back pressures in MPD operations, reduce nonproductive times, and provide a reference for the drilling operations in extremely narrow pore/fracture windows existing conditions.

- (2) The wave velocity and void fraction have different values with respect to well depth. In the annulus, the drop of pressure causes an increase in the void fraction along the flow direction. The void fraction increases first slightly and then sharply. Correspondingly, the wave velocity first gradually decreases in the bubbly flow and preliminary slug flow, and then the wave velocity slightly increases accompanying with the increase in the relative length ratio of gas slug to the liquid slug for the continuous increase in void fraction at the position close to the wellhead. The minimum wave velocity appears in the long gas slug flow.
- (3) When the back pressure in the MPD operations increases, the void fraction at different depths of the annulus is reduced gradually, while the wave velocity in the two-phase flow tends to increase. Moreover, the influence of back pressure on the void fraction is greater at a position close to the wellhead than that in the bottomhole because of the great decrease in the pressure from the bottomhole to the wellhead. Also, the effect of back pressure on void fraction and wave velocity is decreased in the high back pressure range.

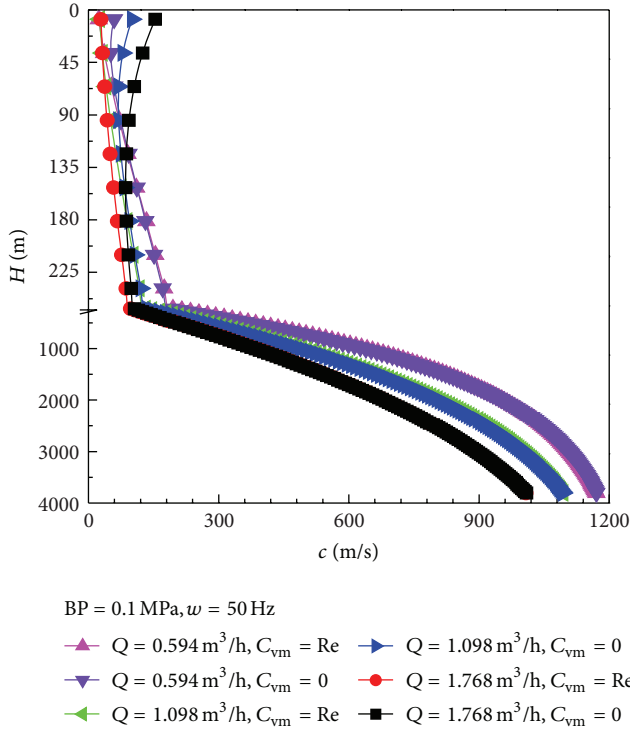


FIGURE 13: Effect of virtual mass force on the pressure wave velocity.

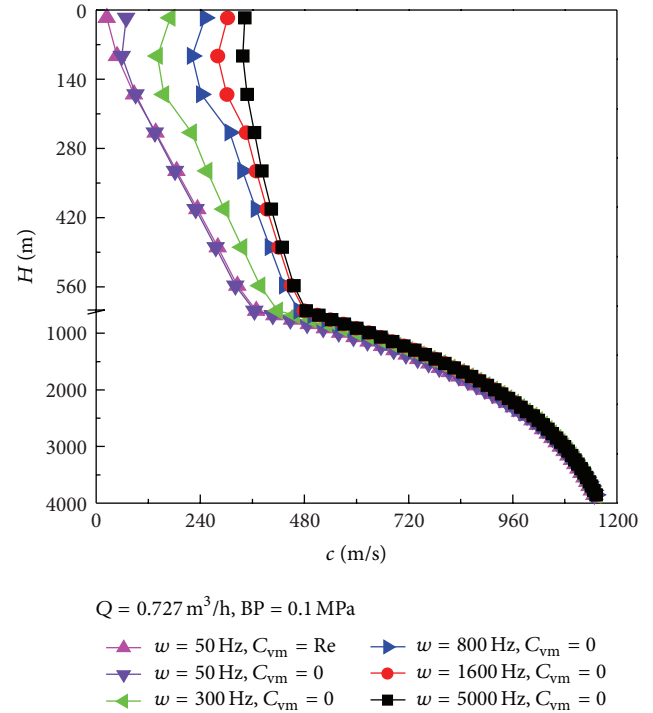


FIGURE 14: Wave velocity variations at different angular frequencies.

- (4) The wave velocity is sensitive to the void fraction, but the void fraction is dominated by gas influx rate and pressure in the annulus, especially the gas influx rate. Since the compressibility of the gas and drilling mud two-phase fluid is improved with the increase in the influx rate, the void fraction increases greatly, and the wave velocity decreases significantly within the low gas influx rate range. When the void fraction is increased to some extent following the increase in the gas influx rate, the decrease of wave velocity is slowed for the growth of gas slug. Especially at the wellhead, a slight increase in wave velocity is observed at a high gas influx rate for the sharp increase in void fraction.
- (5) It is necessary to analyze the effect of the virtual mass force on the wave velocity in MPD operations. Especially, at the position close to the wellhead the effect of virtual mass force is more prominent for the intense phase interactions. Taking the virtual mass force into account, the dispersion characteristic of the pressure wave weakens obviously. Compared with the results calculated by ignoring the effect of virtual mass force, the calculated pressure wave velocity with a consideration of the virtual mass force is lower.
- (6) The effect of angular frequency on the propagation velocity of pressure wave appears at a low angular frequency. The propagation velocity of pressure disturbances increases together with the growth of the angular frequency ( $0 < \omega < 500$  Hz). When the angular frequency reaches the value of  $\omega = 500$  Hz, the pressure wave velocity achieves a constant value

and remains on this level regardless of the further growth in angular frequency  $\omega$ .

## Nomenclature

- $A$ : Annulus effective cross area ( $\text{m}^2$ )
- $c_G$ : Wave velocity in gas ( $\text{m/s}$ )
- $c_L$ : Wave velocity in Drilling mud ( $\text{m/s}$ )
- $C_D$ : The coefficient of drag force
- $D$ : Annulus effective diameter (m)
- $D_i$ : Diameter of the inner pipe (m)
- $D_o$ : Diameter of the outer pipe (m)
- $f_G$ : Shear stresses coefficient of gas interface
- $f_L$ : Shear stresses coefficient of drilling mud interface
- $F_z$ : Pressure applied to the two-phase flow (N)
- $g$ : Acceleration due to gravity ( $\text{m}^2/\text{s}$ )
- $g_c$ : Conversion factor
- $g_T$ : Geothermal temperature gradient (K/m)
- $h$ : One discrete length of annulus (m)
- $k_e$ : Annulus effective roughness (m)
- $k_o$ : Roughness of outer pipe (m)
- $k_i$ : Roughness of inner pipe (m)
- $H$ : The depth of annulus (m)
- $L_q$ : Air bubbles length of slug (m)
- $M_{Gi}$ : Momentum transfer in gas interface ( $\text{N}/\text{m}^3$ )
- $M_{Li}$ : Momentum transfer in liquid interface ( $\text{N}/\text{m}^3$ )
- $M_{Li}^{nd}$ : The none-drag-force (virtual mass force) ( $\text{N}/\text{m}^3$ )
- $M_{Li}^d$ : The momentum transfer term caused by the drag force ( $\text{N}/\text{m}^3$ )

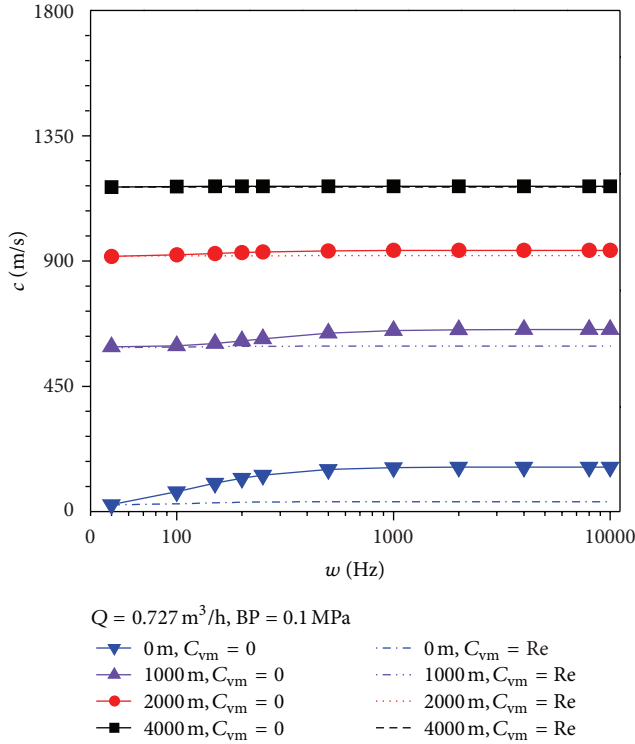


FIGURE 15: Effect of angular frequency on wave velocity.

- N: Parameter combining Thompson energy effects
- $p_{Gi}$ : Gas interface pressure (MPa)
- $p_{Li}$ : Liquid interface pressure (MPa)
- $p$ : Pressure (MPa)
- $p_0$ : Initial pressure of annulus (MPa)
- $p_c$ : Critical pressure (kPa)
- $p_L$ : Pressure of drilling mud (MPa)
- $p_r$ : Reduced pressure
- $q_m$ : Volumetric flow rate of gas and drilling mud (m<sup>3</sup>/s)
- $q_G$ : Velocity of the gas (m<sup>3</sup>/s)
- $q_L$ : Velocity of the drilling mud (m<sup>3</sup>/s)
- $Q_L$ : Drilling mud rate within the annulus (m<sup>3</sup>/h)
- $r$ : Average diameter of the bubble (m)
- $R$ : Constant of EOS (J/KgK)
- $R_q$ : Air bubbles radius of slug (m)
- $R_b$ : The bubble diameter (m)
- $T$ : Temperature (K)
- $T_c$ : Critical temperature (K)
- $T_r$ : Reduced temperature
- $T_{ei}$ : Undisturbed formation temperature at a depth (K)
- $T_{ebh}$ : Undisturbed formation temperature of wellhead (K)
- $T_{fbh}$ : Undisturbed formation temperature at the bottomhole (K)
- $v_m$ : Gas and drilling mud flow velocity (m/s)

- $v_G$ : Gas flow velocity (m/s)
- $v_s$ : Slip velocity (m/s)
- $v_{sg}$ : Superficial gas velocity (m/s)
- $v_L$ : Drilling mud flow velocity (m/s)
- $W_m$ : Mass flow velocity (kg/m<sup>3</sup>)
- $Z_G$ : Gas deviation factor
- $z_0$ : Initial calculation height of annulus (m)
- $z_{bh}$ : Total well depth from surface (m)
- $z$ : Variable of distance from surface (m).

Greek Letters

- $\rho_G$ : Gas density (kg/m<sup>3</sup>)
- $\tau_{Li}^{fr}$ : Shear stresses of drilling mud noninterfacial (N/m<sup>2</sup>)
- $\tau_L^{fr}$ : Shear stresses of drilling mud interface (N/m<sup>2</sup>)
- $\tau_L^{Re}$ : Reynolds stress of drilling mud (N/m<sup>2</sup>)
- $\tau_L^{Re}$ : Reynolds stress of drilling mud interface (N/m<sup>2</sup>)
- $\tau_G^{Re}$ : Reynolds stress of gas interface (N/m<sup>2</sup>)
- $\tau_G^{fr}$ : Shear stresses of gas interface (N/m<sup>2</sup>)
- $\alpha_{VM}$ : Acceleration due to virtual mass force coefficient (m/s<sup>2</sup>)
- $\tau_L$ : Shear stresses of drilling mud along wall (N/m<sup>2</sup>)
- $\tau_G$ : Shear stresses of gas along wall (N/m<sup>2</sup>)
- $\tau_G^{Re}$ : Reynolds stress of gas (N/m<sup>2</sup>)
- $\tau_f$ : Frictional pressure gradient (Pa/m)
- $\tau_w$ : Frictional pressure coefficient
- $\rho_m$ : Gas and drilling density (kg/m<sup>3</sup>)
- $\rho_0$ : Density under standard atmospheric pressure (kg/m<sup>3</sup>)
- $\rho_L$ : Drilling mud density (kg/m<sup>3</sup>)
- $\sigma_s$ : Surface tension (N/m<sup>2</sup>)
- $\Phi_G$ : Gas void fraction
- $\Phi_L$ : Drilling mud holdup
- $\rho_r$ : Reduced density
- $\mu_L$ : Viscosity of drilling mud (Pa · s).

Subscripts

- BHP: Bottomhole pressure
- BP: Back pressure
- EOS: Equations of state
- MPD: Managed pressure drilling
- RCD: The rotating control device
- R-K4: The fourth-order explicit Runge-Kutta.

Subscripts of Graph

- BP: Back pressure (MPa)
- c: Wave velocity in gas and drilling mud two-phase flow (m/s)
- C<sub>vm</sub>: The coefficient of virtual mass force

$H$ : Depth of annulus (m)  
 $Q$ : Gas influx rate at the bottomhole ( $\text{m}^3/\text{h}$ )  
 $Re$ : The value of virtual mass force coefficient according to (28) or (34)  
 $w$ : Angle frequency (Hz)  
 $\Phi_G$ : Void fraction (%).

## Acknowledgment

Research work was cofinanced by the National Natural Science Foundation of China (nos. 51074135 and 51274170). Without their support, this work would not have been possible.

## References

- [1] Y. Bu, F. Li, Z. Wang, and J. Li, "Preliminary study of air injection in annuli to manage pressure during cementing," *Procedia Engineering*, vol. 18, pp. 329–334, 2011.
- [2] P. Vieira, F. Torres, R. A. Qamar, and G. E. Marin, "Downhole pressure uncertainties related to deep wells drilling are safely and precisely ascertained using automated MPD technology," in *Proceedings of the North Africa Technical Conference and Exhibition*, Cairo, Egypt, February 2012.
- [3] S. Saeed and R. Lovorn, "Automated drilling systems for MPD—the reality," in *Proceedings of the IADC/SPE Drilling conference and Exhibition*, San Diego, Calif, USA, March 2012.
- [4] W. A. Bacon, *Consideration of compressibility effects for applied-back-pressure dynamic well control response to a gas kick in managed pressure drilling operations [M.S. thesis]*, University of Texas, Arlington, Tex, USA, 2011.
- [5] J. Choe, C. Hans, and J. Wold, "A modified two-phase well-control model and its computer applications as a training and educational tool," *SPE Computer Applications*, vol. 2, pp. 14–20, 1997.
- [6] J. A. Tarvin, I. Walton, and P. Wand, "Analysis of a gas kick taken in a deep well drilled with oil-based mud," in *Proceedings of the Annual Technical Conference and Exhibition of the Society of Petroleum Engineers*, pp. 255–264, Dallas, Tex, USA, 1991.
- [7] W. Guo, F. Honghai, and L. Gang, "Design and calculation of a MPD model with constant bottom hole pressure," *Petroleum Exploration and Development*, vol. 38, no. 1, pp. 103–108, 2011.
- [8] J. Zhou and G. Nygaard, "Automatic model-based control scheme for stabilizing pressure during dual-gradient drilling," *Journal of Process Control*, vol. 21, no. 8, pp. 1138–1147, 2011.
- [9] A. Ochoa, O. Acevedo, L. Nieto, J. E. Lambarria, and H. Pérez, "Successful application of MPD (Managed Pressure Drilling) for prevention, control, and detection of borehole ballooning in tight gas reservoir in Cuervito Field, Mexico," in *Proceedings of the Canadian Unconventional Resources Conference (CURC '11)*, pp. 172–185, November 2011.
- [10] P. Vieira, F. Torres, R. A. Qamar, and G. E. Marin, "Downhole pressure uncertainties related to deep wells drilling are safely and precisely ascertained using automated MPD technology," in *Proceedings of the North Africa Technical Conference and Exhibition*, Cairo, Egypt, February 2012.
- [11] R. Ashena and J. Moghadasi, "Bottom hole pressure estimation using evolved neural networks by real coded ant colony optimization and genetic algorithm," *Journal of Petroleum Science and Engineering*, vol. 77, no. 3–4, pp. 375–385, 2011.
- [12] S. Wang, C. Qiang, and K. Bo, "Fluctuating pressure calculation during the progress of trip in managed pressure drilling," *Advanced Materials Research*, vol. 468–471, pp. 1736–1742, 2012.
- [13] I. Zubizarreta, "Pore pressure evolution, core damage and tripping out schedules: a computational fluid dynamics approach," in *Proceedings of the SPE/IADC Drilling Conference and Exhibition*, Amsterdam, The Netherlands, March 2013.
- [14] C. H. Whitson, "Cyclic shut-in eliminates liquid-loading in gas wells," in *Proceedings of the SPE/EAGE European Unconventional Resources Conference and Exhibition*, Vienna, Austria, March 2012.
- [15] G. M. de Oliveira, A. T. Franco, C. O. R. Negrao, A. L. Martins, and R. A. Silva, "Modeling and validation of pressure propagation in drilling fluids pumped into a closed well," *Journal of Petroleum Science and Engineering*, vol. 103, pp. 61–71, 2012.
- [16] Y. Sato and H. Kanki, "Formulas for compression wave and oscillating flow in circular pipe," *Applied Acoustics*, vol. 69, no. 1, pp. 1–11, 2008.
- [17] J. Xie, B. Yu, X. Zhang, Q. Shao, and X. Song, "Numerical simulation of gas-liquid-solid three-phase flow in deep wells," *Advances in Mechanical Engineering*, vol. 2013, Article ID 951298, 10 pages, 2013.
- [18] W. Bacon, A. Tong, O. Gabaldon, C. Sugden, and P. V. Suryanarayana, "An improved dynamic well control response to a gas influx in managed pressure drilling operations," in *Proceedings of the IADC/SPE Drilling Conference and Exhibition*, San Diego, California, USA, March 2012.
- [19] J. I. Hage and D. ter Avest, "Borehole acoustics applied to kick detection," *Journal of Petroleum Science and Engineering*, vol. 12, no. 2, pp. 157–166, 1994.
- [20] A. M. R. Hopkins, *Fluid dynamics and surface pressure fluctuations of two-dimensional turbulent boundary layers over densely distributed surface roughness [Ph.D. thesis]*, Virginia Polytechnic Institute and State University, Blacksburg, Va, USA, 2010.
- [21] Z. S. Fu, "The gas cut detect technology during drilling in Soviet Union," *Petroleum Drilling Techniques*, vol. 18, no. 1, pp. 19–21, 1990.
- [22] X. F. Li, C. X. Guan, and X. X. Sui, "The theory of gas influx detection of pressure wave and its application," *Acta Petrolei Sinica*, vol. 18, no. 3, pp. 128–133, 1997.
- [23] H. Li, Y. Meng, G. Li et al., "Propagation of measurement-while-drilling mud pulse during high temperature deep well drilling operations," *Mathematical Problems in Engineering*, vol. 2013, Article ID 243670, 12 pages, 2013.
- [24] A. E. Ruggles, R. T. Lahey Jr., D. A. Drew, and H. A. Scarton, "Investigation of the propagation of pressure perturbations in bubbly air/water flows," *Journal of Heat Transfer*, vol. 110, no. 2, pp. 494–499, 1988.
- [25] H. J. W. M. Legius, H. E. A. Van Den Akker, and T. Narumo, "Measurements on wave propagation and bubble and slug velocities in cocurrent upward two-phase flow," *Experimental Thermal and Fluid Science*, vol. 15, no. 3, pp. 267–278, 1997.
- [26] K. Miyazaki and I. Nakajima, "Propagation of pressure wave in Nitrogen-Mercury two-phase system," *Journal of Nuclear Science and Technology*, vol. 9, no. 5, pp. 315–318, 1972.
- [27] B. Bai, L. Guo, and X. Chen, "Pressure fluctuation for air-water two-phase flow," *Journal of Hydrodynamics*, vol. 18, no. 4, pp. 476–482, 2003.
- [28] F. Huang, M. Takahashi, and L. Guo, "Pressure wave propagation in air-water bubbly and slug flow," *Progress in Nuclear Energy*, vol. 47, no. 1–4, pp. 648–655, 2005.

- [29] R. F. Tangren, C. H. Dodge, and H. S. Seifert, "Compressibility effects in two-phase flow," *Journal of Applied Physics*, vol. 20, no. 7, pp. 637–645, 1949.
- [30] G. B. Wallis, *One Dimensional Two Phase Flow*, McGraw Hill, New York, NY, USA, 1969.
- [31] D. L. Nguyen, E. R. F. Winter, and M. Greiner, "Sonic velocity in two-phase systems," *International Journal of Multiphase Flow*, vol. 7, no. 3, pp. 311–320, 1981.
- [32] R. C. Mecredy and L. J. Hamilton, "The effects of nonequilibrium heat, mass and momentum transfer on two-phase sound speed," *International Journal of Heat and Mass Transfer*, vol. 15, no. 1, pp. 61–72, 1972.
- [33] K. H. Ardron and R. B. Duffey, "Acoustic wave propagation in a flowing liquid-vapour mixture," *International Journal of Multiphase Flow*, vol. 4, no. 3, pp. 303–322, 1978.
- [34] J. Xu and T. Chen, "Acoustic wave prediction in flowing steam-water two-phase mixture," *International Journal of Heat and Mass Transfer*, vol. 43, no. 7, pp. 1079–1088, 2000.
- [35] N. Chung, W. Lin, B. Pei, and Y. Hsu, "Model for sound velocity in a two-phase air-water bubbly flow," *Nuclear Technology*, vol. 99, no. 1, pp. 80–89, 1992.
- [36] X. Xu and J. Gong, "A united model for predicting pressure wave speeds in oil and gas two-phase pipeflows," *Journal of Petroleum Science and Engineering*, vol. 60, no. 3-4, pp. 150–160, 2008.
- [37] W. Kuczynski, "Characterization of pressure-wave propagation during the condensation of R404A and R134a refrigerants in pipe mini-channels that undergo periodic hydrodynamic disturbance," *International Journal of Heat and Fluid Flow*, vol. 40, pp. 135–150, 2013.
- [38] W. Kuczynski, "Modeling of the propagation of a pressure wave during the condensation process of R134a refrigerant in a pipe minichannel under the periodic conditions of hydrodynamic disturbances," *International Journal of Heat and Mass Transfer*, vol. 56, pp. 715–723, 2013.
- [39] Y. Li, C. Li, E. Chen, and Y. Ying, "Pressure wave propagation characteristics in a two-phase flow pipeline for liquid-propellant rocket," *Aerospace Science and Technology*, vol. 15, no. 6, pp. 453–464, 2011.
- [40] T. Kanagawa, M. Watanabe, T. Yano, and S. Fujikawa, "Non-linear wave equations for pressure wave propagation in liquids containing gas bubbles (comparison between two-fluid model and mixture model)," *Journal of Fluid Science and Technology*, vol. 6, no. 6, pp. 836–849, 2011.
- [41] E. Chen, Y. Li, and Y. Ying, "Numerical investigation on pressure wave propagation speed of gas-liquid two-phase flow in pump pipeline," *Journal of Aerospace Power*, vol. 25, no. 4, pp. 754–760, 2010.
- [42] F. Li and L. He, "Investigation on pressure wave propagation characteristics in slug flow field with increasing gas flow rate," *Petroleum Geology and Recovery Efficiency*, vol. 11, no. 5, pp. 78–80, 2004.
- [43] C. S. Martin and M. Padmanabhan, "Pressure pulse propagation in two-component slug flow," *Journal of Fluids Engineering*, vol. 101, no. 1, pp. 44–52, 1979.
- [44] R. E. Henry, "Pressure wave propagation in two-phase mixtures," *Chemical Engineering Progress*, vol. 66, no. 1, pp. 1–10, 1969.
- [45] X. Liu, B. Li, and Y. Yue, "Transmission behavior of mud-pressure pulse along well bore," *Journal of Hydrodynamics B*, vol. 19, no. 2, pp. 236–240, 2007.
- [46] X. Wang and J. Zhang, "The research of pressure wave Pulsation in mud pulse transmitting," *Journal of Chongqing University of Science and Technology*, vol. 14, no. 2, pp. 55–58, 2012.
- [47] J.-W. Park, D. A. Drew, and R. T. Lahey Jr., "The analysis of void wave propagation in adiabatic monodispersed bubbly two-phase flows using an ensemble-averaged two-fluid model," *International Journal of Multiphase Flow*, vol. 24, no. 7, pp. 1205–1244, 1998.
- [48] G. Arnold, *Entropy and objectivity as constraints upon constitutive equations for two-fluid modeling of multiphase flow [Ph.D. thesis]*, Rensselaer Polytechnic Institute, New York, NY, USA, 1998.
- [49] P. M. Dranchuk and J. H. Abou-Kassem, "Calculation of Z factors natural gases using equitation of state," *Journal of Canadian Petroleum Technology*, vol. 14, no. 3, pp. 34–36, 1975.
- [50] L. Yarborough and K. R. Hall, "How to solve equation of state for z-factors," *Oil and Gas Journal*, vol. 72, no. 7, pp. 86–88, 1974.
- [51] A. R. Hasan and C. S. Kabir, "Wellbore heat-transfer modeling and applications," *Journal of Petroleum Science and Engineering*, vol. 86, pp. 127–136, 2012.
- [52] H. Zhu, Y. Lin, D. Zeng, D. Zhang, and F. Wang, "Calculation analysis of sustained casing pressure in gas wells," *Petroleum Science*, vol. 9, no. 1, pp. 66–74, 2012.
- [53] J. Orkiszewski, "Predicting two-phase pressure drops in vertical pipe," *Journal of Petroleum Technology*, vol. 6, no. 6, pp. 829–838, 1967.
- [54] M. Ishii and K. Mishima, "Two-fluid model and hydrodynamic constitutive relations," *Nuclear Engineering and Design*, vol. 82, no. 2-3, pp. 107–126, 1984.
- [55] M. J. Sanchez, *Comparison of correlations for predicting pressure losses in vertical multiphase annular flow [M.S. thesis]*, University of Tulsa, Tulsa, Okla, USA, 1972.

## Research Article

# Spectral Local Linearisation Approach for Natural Convection Boundary Layer Flow

S. S. Motsa,<sup>1</sup> Z. G. Makukula,<sup>1</sup> and S. Shateyi<sup>2</sup>

<sup>1</sup> School of Mathematics, Statistics and Computer Sciences, University of KwaZulu-Natal, Private Bag X01, Scottsville, Pietermaritzburg 3209, South Africa

<sup>2</sup> Department of Mathematics, University of Venda, Private Bag X5050, Thohoyandou 0950, South Africa

Correspondence should be addressed to S. S. Motsa; sandilemotsa@gmail.com

Received 27 March 2013; Accepted 3 August 2013

Academic Editor: Waqar Khan

Copyright © 2013 S. S. Motsa et al. This is an open access article distributed under the Creative Commons Attribution License, which permits unrestricted use, distribution, and reproduction in any medium, provided the original work is properly cited.

The present work introduces a spectral local linearisation method (SLLM) to solve a natural convection boundary layer flow problem with domain transformation. It is customary to find solutions of semi-infinite interval problems by first truncating the interval and subsequently applying a suitable numerical method. However, this gives rise to increased error terms in the numerical solution. Carrying out a transformation of the semi-infinite interval problems into singular problems posed on a finite interval can avoid the domain truncation error and enables the efficient application of collocation methods. The SLLM is based on linearising and decoupling nonlinear systems of equations into a sequence or subsystems of differential equations which are then solved using spectral collocation methods. A comparative study between the SLLM and existing results in the literature was carried out to validate the results. The method has shown to be a promising efficient tool for nonlinear boundary value problems as it gives converging results after very few iterations.

## 1. Introduction

Boundary layer problems involve a rapid change in the value of a physical variable over a limited region of time or space and therefore are governed by highly nonlinear equations. They are very common in physics and have numerous applications in extrusion, melt spinning, food processing, mechanical forming processes, and many other fields.

In recent years, a host of different methods have been developed with the aim of finding the most efficient method for solving the often complex nonlinear equation systems governing the fluid flows. Boundary layer problems are very difficult to solve because besides having very thin regions where there is rapid change of the fluid properties they are defined on unbounded domains. Analytical methods are being used to solve boundary layer problems but converge very slowly for some boundary layer problems, particularly those with very large parameters. Traditional numerical techniques such as finite differences, finite element methods, Keller-Box method [1], Runge-Kutta with shooting methods

[2–4], and spectral collocation methods [5–7] are still being used in solving nonlinear BVPs arising in fluid mechanics and other engineering applications. However, numerical approaches also encounter problems in resolving the solution of the governing equations in the very thin regions and in cases where there are singularities or multiple solutions hence the need for the search for ways of improving numerical methods.

In this paper we present a new numerical technique based on linearising and decoupling nonlinear systems of equations into a sequence of or subsystems of differential equations which are then solved using spectral collocation methods. The spectral local linearisation method (SLLM) is used here to solve the problem of natural convection boundary layer flow that arises in glass-fibre production process. Free convection boundary layer problems arise in many applications including buoyancy-induced motions in the atmosphere, oceans, and quasi-solid bodies such as earth. The problem under study was earlier considered in the works of Kuiken [8, 9], Liao [10], and Motsa et al. [11]. In this work, however,

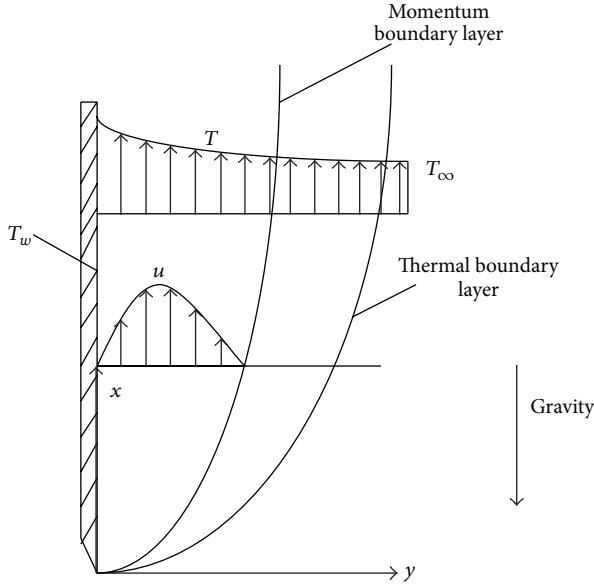


FIGURE 1: Free convection flow over a vertical plate.

the problem is first transformed from the semi-infinite domain  $[0, \infty)$  into the finite interval  $[0, 1]$  to avoid using a scaling parameter to invoke the boundary condition at infinity. The skin friction and Nusselt number are generated by the SLLM and validated by comparing them with those of Kuiken [8].

## 2. Problem Statement

Consider the laminar free-convection flow of an incompressible viscous fluid about a flat plate parallel to the direction of the generating body force. Figure 1 presents the physical model of the flow. The basic governing boundary layer equations, following Kuiken [9], Ghotbi et al. [12], and Ali et al. [13], are as follows:

$$\frac{\partial u}{\partial x} + \frac{\partial v}{\partial y} = 0, \quad (1)$$

$$u \frac{\partial u}{\partial x} + v \frac{\partial u}{\partial y} = \nu \frac{\partial^2 u}{\partial y^2} + g\beta(T - T_\infty), \quad (2)$$

$$u \frac{\partial T}{\partial x} + v \frac{\partial T}{\partial y} = \alpha \frac{\partial^2 T}{\partial y^2}, \quad (3)$$

with boundary conditions

$$\begin{aligned} \text{at } y = 0; \quad u = v = 0, \quad T = T_0, \\ \text{as } y \rightarrow \infty; \quad u \rightarrow 0, \quad T \rightarrow T_\infty, \end{aligned} \quad (4)$$

where  $u$  and  $v$  are the velocity components along the  $x$  and  $y$ -axes, respectively,  $\nu$  is the kinematic viscosity of the fluid,  $g$  is the acceleration due to gravity,  $\beta$  is the coefficient of thermal expansion,  $T$  is the fluid temperature,  $T_\infty$  is the temperature of the surrounding fluid, and  $\alpha$  is the thermal diffusivity.

Applying the transformations below following [9, 12, 13]

$$\begin{aligned} \psi &= [g\beta(T_w - T_\infty)\nu^2 x_0^2]^{1/4} f(\eta), \\ T &= T_\infty + (T_w - T_\infty) \left[ \frac{x}{x_0 - x} \right]^3 \theta(\eta), \\ \eta &= \left[ \frac{g\beta(T_w - T_\infty)x_0^3}{\nu^2} \right] \frac{y}{(x_0 - x)}, \end{aligned} \quad (5)$$

where  $\psi$  is the stream function defined as

$$u = \frac{\partial \psi}{\partial y}, \quad v = -\frac{\partial \psi}{\partial x}, \quad (6)$$

$f(\eta)$  and  $\theta(\eta)$  are similarity functions, (2) and (3) become

$$\begin{aligned} f'''(\eta) - f'^2(\eta) + \theta(\eta) &= 0, \\ \theta''(\eta) - 3\text{Pr}f'(\eta)\theta(\eta) &= 0, \end{aligned} \quad (7)$$

along with the boundary conditions

$$f(0) = f'(0) = 0, \quad \theta(0) = 1, \quad f'(\infty) = \theta(\infty) = 0. \quad (8)$$

Prime denotes differentiation with respect to the similarity variable  $\eta$  and  $\text{Pr}$  is the Prandtl number. It was reported in [9] that both  $f(\eta)$  and  $\theta(\eta)$  decay algebraically as  $\eta \rightarrow +\infty$ . Equations (7) can be simplified by using the following transformations [10]:

$$\xi = 1 + \lambda\eta, \quad F(\xi) = f'(\eta), \quad G(\xi) = \theta(\eta), \quad (9)$$

where  $\lambda$  is a spatial scale parameter. Substituting (9) in (7) and (8) results in

$$\begin{aligned} \lambda^2 F''(\xi) - F^2(\xi) + G(\xi) &= 0, \\ \lambda^2 G''(\xi) - 3\text{Pr}F(\xi)G(\xi) &= 0, \end{aligned} \quad (10)$$

with boundary conditions

$$F(1) = 0, \quad G(1) = 1, \quad F(\infty) = G(\infty) = 0, \quad (11)$$

where the prime now denotes differentiation with respect to  $\xi$ .

## 3. Domain Transformation

In this section we transform the problem from the semi-infinite domain into the finite domain  $[0, 1]$ . The transformation procedure proposed by Hammerling et al. [14] transforms a general BVP of the form

$$f(x, u, u', u'', \dots, u^{(n)}) = 0, \quad x \in [1, \infty), \quad (12)$$

into the domain  $[0, 1]$  by change of the independent variable. A transformation of the form  $x \rightarrow 1/x$  transforms the semi-infinite interval into  $[0, 1]$ . For the general case, the function and its derivatives are then expressed as

$$\begin{aligned} u\left(\frac{1}{x}\right) &= U(x) \\ u'\left(\frac{1}{x}\right) &= -x^2 U'(x) \\ u''\left(\frac{1}{x}\right) &= -x^2(-x^2 U'(x))' \\ u'''\left(\frac{1}{x}\right) &= -x^2(-x^2(-x^2 U'(x))')' \\ &\vdots \\ u^{(n)}\left(\frac{1}{x}\right) &= -x^2 \underbrace{\left[-x^2(-x^2(\dots(-x^2 U'(x))')')'\right]'}_{(n-1)\text{-products}} \end{aligned} \quad (13)$$

The boundary conditions are transformed in a similar manner with an exception of a problem with Neumann boundary conditions at the free end. In that case the problem has to be reduced to have admissible boundary conditions [14]. Previous studies carried out by Budd et al. [15] and Kitchofer et al. [16] showed that transforming a problem into a finite domain before it is being solved facilitates the efficient use of collocation methods, and classical convergence orders can be observed.

Using (13), (10) together with boundary conditions (11) is transformed into

$$\lambda^2 (\xi^4 F_1'' + 2\xi^3 F_1') - F_1^2 + G_1 = 0, \quad (14)$$

$$\lambda^2 (\xi^4 G_1'' + 2\xi^3 G_1') - 3PrF_1 G_1 = 0,$$

$$F_1(1) = 0, \quad G_1(1) = 1, \quad F_1(0) = 0, \quad G_1(0) = 0. \quad (15)$$

#### 4. Spectral Local Linearisation Method (SLLM)

The transformed system of (14) and (15) is solved in this section using the spectral local linearisation method. The SLLM is based on developing a decoupled iterative scheme that is then chronologically solved using spectral methods. Local linearisation is applied to the equations before generating the iterative scheme in a manner similar to the Gauss-Seidel approach of decoupling linear algebraic systems. Consider a system of  $n$  nonlinear ordinary differential equations in  $n$  unknown functions  $F_i(\eta)$ ,  $i = 1, 2, \dots, n$  written as a sum of its linear and nonlinear terms as follows:

$$L_i [F_1, F_2, \dots, F_n] + N_i [F_1, F_2, \dots, F_n] = 0, \quad i = 1, 2, \dots, n. \quad (16)$$

Let the subscripts  $r$  and  $r + 1$  represent the previous and current iteration, respectively. Local linearisation of  $N_i$  at the previous iteration about  $F_i$  is then carried out as follows:

$$\begin{aligned} N_i [F_1, F_2, \dots, F_n] &= N_i [F_{1,r}, F_{2,r}, \dots, F_{n,r}] \\ &\quad + \frac{\partial N_i}{\partial F_i} [F_{1,r}, F_{2,r}, \dots, F_{n,r}] (F_i - F_{i,r}), \end{aligned} \quad (17)$$

so that, at the current iteration, (16) becomes

$$\begin{aligned} L_i [F_{1,r+1}, F_{2,r+1}, \dots, F_{n,r+1}] &+ \frac{\partial N_i}{\partial F_i} [\dots] F_{i,r+1} \\ &= \frac{\partial N_i}{\partial F_i} [\dots] F_{i,r} - N_i [F_{1,r}, F_{2,r}, \dots, F_{n,r}], \end{aligned} \quad (18)$$

where  $[\dots]$  represents  $[F_{1,r}, F_{2,r}, \dots, F_{n,r}]$ . Using the Gauss-Seidel approach, whereby the updated solutions  $F_j$  ( $j < i$ ), obtained at previous equations, are used to find a solution  $F_i$  at the current iteration level  $F_{i,r+1}$ , the local linearisation iteration scheme can be generated as follows:

$$\begin{aligned} L_1 [F_{1,r+1}, F_{2,r}, \dots, F_{n,r}] &+ \frac{\partial N_1}{\partial F_1} [\dots] F_{1,r+1} \\ &= \frac{\partial N_1}{\partial F_1} [\dots] F_{1,r} - N_1 [F_{1,r}, \dots, F_{n,r}], \\ L_1 [F_{1,r+1}, F_{2,r+1}, F_{3,r}, \dots, F_{n,r}] &+ \frac{\partial N_2}{\partial F_2} [\dots] F_{2,r+1} \\ &= \frac{\partial N_2}{\partial F_2} [\dots] F_{2,r} - N_2 [F_{1,r+1}, F_{2,r}, \dots, F_{n,r}], \\ &\vdots \\ L_n [F_{1,r+1}, F_{2,r+1}, \dots, F_{n,r+1}] &+ \frac{\partial N_n}{\partial F_n} [\dots] F_{n,r+1} \\ &= \frac{\partial N_n}{\partial F_n} [\dots] F_{n,r} - N_n [F_{1,r+1}, \dots, F_{n-1,r+1}, F_{n,r}], \end{aligned} \quad (19)$$

where  $[\dots]$  at the  $i$ th iteration represents  $[F_{1,r+1}, F_{2,r+1}, \dots, F_{i-1,r+1}, F_{i,r}, \dots, F_{n,r}]$ . Hence, starting from an initial approximation  $F_{1,0}, F_{2,0}, \dots, F_{n,0}$ , the iterative scheme (19) is solved until convergence is reached for all unknowns.

Following the guidelines above, we generate the iterative scheme for (14) with the corresponding boundary conditions as follows:

$$\begin{aligned} \lambda^2 (\xi^4 F_{1,r+1}'' + 2\xi^3 F_{1,r+1}') - 2F_{1,r} F_{1,r+1} &= -F_{1,r}^2 - G_{1,r}, \\ F_{1,r+1}(0) = 0, \quad F_{1,r+1}(1) = 0, \\ \lambda^2 (\xi^4 G_{1,r+1}'' + 2\xi^3 G_{1,r+1}') - 3PrF_{1,r+1} G_{1,r+1} &= 0, \\ G_{1,r+1}(0) = 0, \quad G_{1,r+1}(1) = 1. \end{aligned} \quad (20)$$

Since the coefficient parameters and the right hand side of (20) are known (from previous iterations), the equation

system (20) can easily be solved using any numerical method such as finite differences, finite elements, Runge-Kutta-based shooting methods, or collocation methods. In this work, the equations are solved using the Chebyshev spectral collocation method. This method is based on approximating the unknown functions by the Chebyshev interpolating polynomials in such a way that they are collocated at the Gauss-Lobatto points defined as

$$X_j = \cos \frac{\pi j}{N}, \quad j = 0, 1, \dots, N, \quad (21)$$

where  $N$  is the number of collocation points used (see, e.g., [17, 18]). In order to implement the method, the physical region  $[0, 1]$  is transformed into the region  $[-1, 1]$  using the following mapping:

$$\xi = \frac{X + 1}{2}, \quad -1 \leq X \leq 1. \quad (22)$$

The unknown functions  $F_{1,r+1}$  and  $G_{1,r+1}$  are approximated at the collocation points by

$$\begin{aligned} F_{1,r+1}(X) &\approx \sum_{k=0}^N F_{1,r+1}(X_k) T_k(X_j), \\ G_{1,r+1}(X) &\approx \sum_{k=0}^N G_{1,r+1}(X_k) T_k(X_j), \end{aligned} \quad (23)$$

$$j = 0, 1, \dots, N,$$

where  $N$  is the number of collocation points and  $T_k$  is the  $k$ th Chebyshev polynomial defined as

$$T_k(X) = \cos[k \cos^{-1}(X)]. \quad (24)$$

The derivatives of the variables at the collocation points are represented as

$$\begin{aligned} \frac{d^2 F_{1,r+1}}{d\xi^2} &= \sum_{k=0}^N \mathbf{D}_{kj}^2 F_{1,r+1}(X_k), \\ \frac{d^2 G_{1,r+1}}{d\xi^2} &= \sum_{k=0}^N \mathbf{D}_{kj}^2 G_{1,r+1}(X_k), \end{aligned} \quad (25)$$

$$j = 0, 1, \dots, N,$$

where  $\mathbf{D} = 2\mathcal{D}$  with  $\mathcal{D}$  being the Chebyshev spectral differentiation matrix (see, e.g., [17, 18]). Substituting (22)–(25) in (20) we obtain the following system:

$$\begin{aligned} A_1 \mathbf{F}_{1,r+1} &= B_1, \quad F_{1,r+1}(X_N) = 0, \quad F_{1,r+1}(X_0) = 0, \\ A_2 \mathbf{G}_{1,r+1} &= B_2, \quad G_{1,r+1}(X_N) = 0, \quad G_{1,r+1}(X_0) = 1, \end{aligned} \quad (26)$$

where

$$\begin{aligned} A_1 &= \lambda^2 \text{diag}(\xi^4) D^2 + 2\lambda^2 \text{diag}(\xi^3) D \\ &\quad - 2 \text{diag}(F_{1,r}), \quad B_1 = -F_{1,r}^2 - G_{1,r}, \\ A_2 &= \lambda^2 \text{diag}(\xi^4) D^2 + 2\lambda^2 \text{diag}(\xi^3) D \\ &\quad - 3\text{Pr} \text{diag}(F_{1,r+1}), \quad B_2 = \mathbf{0}. \end{aligned} \quad (27)$$

In the above equations  $\mathbf{F}_{1,r+1}$  and  $\mathbf{G}_{1,r+1}$  are the values of functions  $F_{1,r+1}$  and  $G_{1,r+1}$ , respectively, and  $\mathbf{0}$  is a  $(N+1) \times 1$  zero vector.

Equations (26) are then solved chronologically starting from the initial approximate solutions

$$F_{1,0}(\xi) = \gamma(\xi^2 - \xi^3), \quad G_{1,0}(\xi) = \xi^4, \quad (28)$$

which are chosen to satisfy the boundary conditions (15). These initial guesses were suggested in [10] and are presented here after being transformed into the finite interval. The parameter  $\gamma$  appearing in (28) is the so-called auxiliary parameter which is used to control convergence of the solution.

The convergence rate of the SLLM algorithm can be significantly improved by applying the successive overrelaxation (SOR) technique on (20). Under the SOR framework, a convergence controlling relaxation parameter  $\omega$  is introduced and the SLLM scheme for finding, say  $Y$ , is modified to

$$A_1 Y_{r+1} = (1 - \omega) A_1 Y_r + \omega B_1. \quad (29)$$

The results in the following section show that, for  $\omega < 1$ , applying the SOR method improves the efficiency and accuracy of the SLLM.

## 5. Results and Discussion

Numerical computations for the solution of the governing equations (14) and (15) were carried out using the spectral local linearization method. Values of the skin friction and the Nusselt number were generated at different Prandtl numbers. Results for the typical velocity and temperature profiles were also presented. In order to measure the accuracy and convergence of the SLLM, the present results were verified by comparing them with those obtained by Kuiken [8]. The plots were generated using 50 collocation points unless specified.

As pointed out in Section 4 that  $\gamma$  is a convergence controlling parameter, a proper selection of  $\gamma$  is necessary. To choose proper values of  $\gamma$  we use the norm of residual function of  $F_1(\xi)$  ( $\text{Res}F$ ) and that of  $G_1(\xi)$  ( $\text{Res}G$ ) where  $\text{Res}F$  and  $\text{Res}G$  are plotted as functions of  $\gamma$ :

$$\begin{aligned} \text{Res}F &= \left\| \lambda^2 (\xi^4 \mathbf{F}_{1,r+1}'' + 2\xi^3 \mathbf{F}_{1,r+1}') - \mathbf{F}_{1,r+1}^2 + \mathbf{G}_{1,r+1} \right\|_{\infty}, \\ \text{Res}G &= \left\| \lambda^2 (\xi^4 \mathbf{G}_{1,r+1}'' + 2\xi^3 \mathbf{G}_{1,r+1}') - 3\text{Pr} \mathbf{F}_{1,r+1} \mathbf{G}_{1,r+1} \right\|_{\infty}. \end{aligned} \quad (30)$$

The valid region of  $\gamma$  where the solution converges becomes the horizontal part of the residual curve. Numerical iterations are carried out until a representative solution residual falls below a set tolerance. In this work the tolerance level was set to be  $10^{-10}$ . Illustrative residual curves are shown in Figures 2 and 3. For example, in Figure 2, the valid values of  $\gamma$  that will give converging results for  $\lambda = 2$  are  $\lambda \geq 30$  and about  $\lambda \geq 12$  for  $\lambda = 1$ .

Figures 4 and 5 show the velocity and temperature profiles, respectively, when the Prandtl number  $\text{Pr}$  is varied. The dimensionless velocity profiles are observed to decrease with increase in  $\text{Pr}$  in Figure 4. Because of the nature of

TABLE 1: Comparison of SLLM solutions for  $f''(0)$  against those of Kuiken [8] for different values of Pr when  $N = 50$ .

Pr	$\gamma$	$\lambda$	Basic SLLM		$\omega$	SLLM with SOR ( $\omega$ )		Reference [8]
			Iter.	$f''(0)$		Iter.	$f''(0)$	
0.001	40	0.1	39	1.12313813	0.85	19	1.12313813	1.12313813
0.01	50	0.1	43	1.06338086	0.90	19	1.06338086	1.06338086
0.1	30	0.1	37	0.92408304	0.85	19	0.92408304	0.92408304
1	10	0.1	25	0.69321163	0.90	13	0.69321163	0.69321163
10	5	1	36	0.44711652	0.85	13	0.44711652	0.44711652
100	5	1	46	0.26452354	0.85	14	0.26452354	0.26452354
1000	5	1	49	0.15129020	0.85	15	0.15129020	0.15129020
10000	5	1	50	0.08554085	0.85	16	0.08554085	0.08554085

TABLE 2: Comparison of the values of the SLLM solutions for  $-\theta'(0)$  with those of Kuiken [8] for different values of Pr generated using  $N = 50$ .

Pr	$\gamma$	$\lambda$	Basic SLLM		$\omega$	SLLM with SOR ( $\omega$ )		Reference [8]
			Iter.	$-\theta'(0)$		Iter.	$-\theta'(0)$	
0.001	30	0.1	36	0.04680746	0.85	24	0.04680746	0.04680746
0.01	30	0.1	41	0.13576074	0.85	19	0.13576074	0.13576074
0.1	30	0.5	37	0.35005967	0.90	18	0.35005967	0.35005967
1	5	1	27	0.76986120	0.90	13	0.76986119	0.76986120
10	5	1	36	1.49709921	0.85	13	1.49709921	1.49709921
100	5	1	46	2.74688550	0.85	14	2.74688549	2.74688550
1000	5	1	49	4.93494763	0.85	15	4.93494756	4.93494763
10000	5	1	50	8.80444927	0.85	16	8.80444960	8.80444927

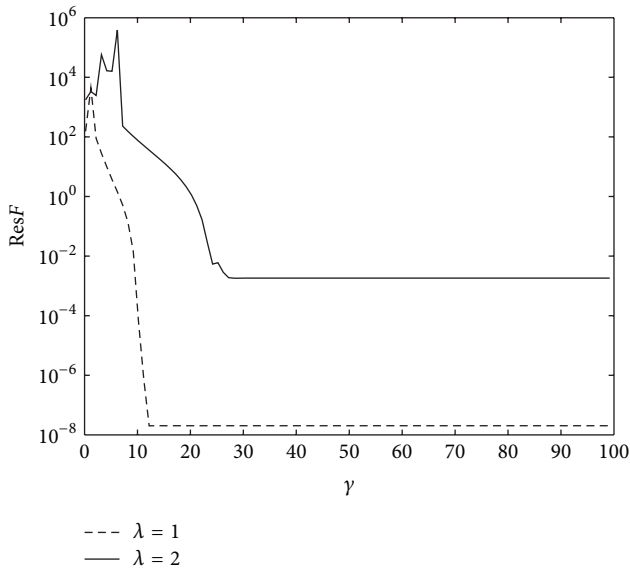


FIGURE 2: The residual of  $F_1(\xi)$  at different values of  $\lambda$  for Pr = 0.1 when  $N = 50$ .

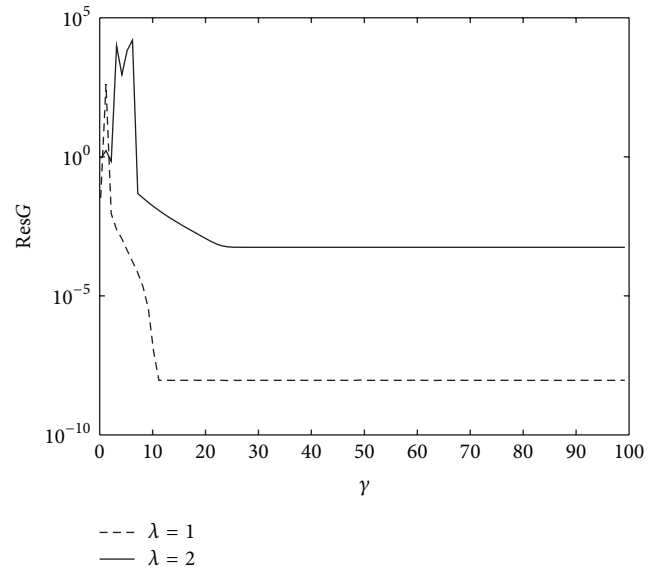


FIGURE 3: The residual of  $G_1(\xi)$  at different values of  $\lambda$  for Pr = 0.1 when  $N = 50$ .

the boundary conditions (slip boundary condition not considered), the velocity profile is seen to increase to reach a particular maximum point and then reduces to zero as  $\eta \rightarrow \infty$ . Similarly, as Pr increases, the temperature profiles also decrease as can be seen from Figure 5. For larger values of the Prandtl number, the thermal boundary layer thickness tends to be shorter because it is when the effective thermal

diffusivity is low for a fixed kinematic viscosity. The results are consistent with results in the literature (see, e.g., [10, 12]).

Tables 1 and 2 present a comparison of the SLLM solutions of the skin friction and the Nusselt number for the flow at different values of the Prandtl number against those of Kuiken [8]. The effect of the Prandtl number on the skin friction coefficient and the Nusselt number is further shown in

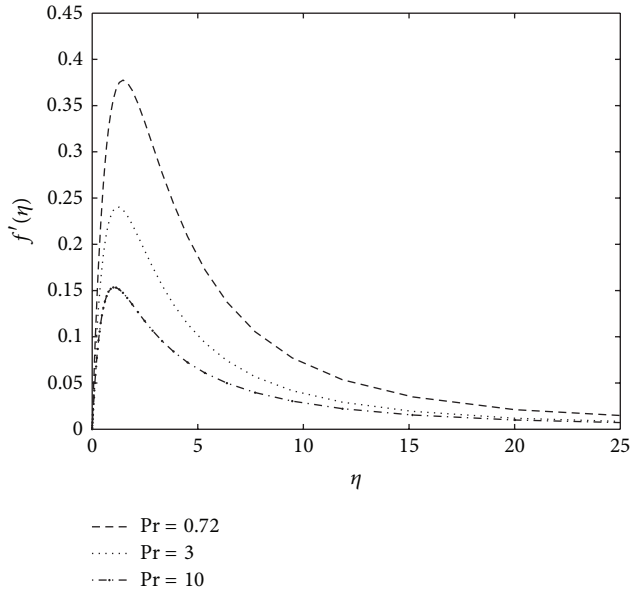


FIGURE 4: The effect of the Prandtl number on the velocity profile.

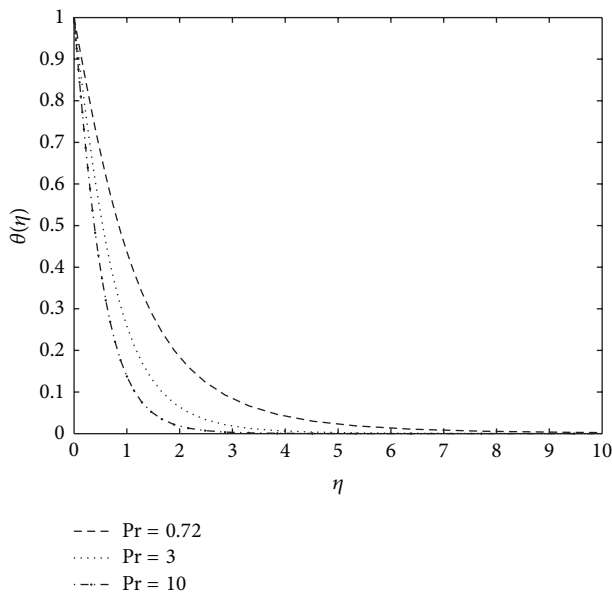


FIGURE 5: The effect of the Prandtl number on the temperature profile.

Figures 6 and 7. Convergence to the numerical solutions obtained by Kuiken [8] is achieved for up to eight decimal places. Values of the skin friction are accurate for all values of  $Pr$  while the Nusselt number is accurate for up to six decimal places in some cases. The skin friction decreased with increase in the Prandtl numbers while the heat transfer rates increased with increased Prandtl numbers. The tables also reveal the advantage of relaxation on the method. Convergence rates are improved remarkably for each case. Worth noting also is the advantage of transforming the domain into the finite interval. There was no need to search

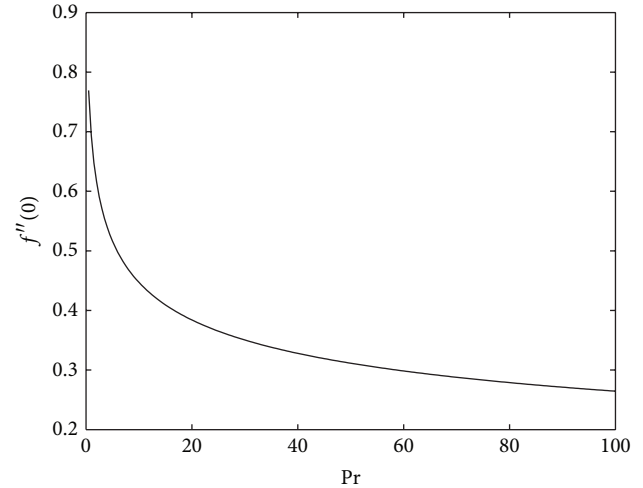


FIGURE 6: Variation of the skin friction with  $Pr$  when  $\lambda = 1$  and  $\gamma = 5$ .

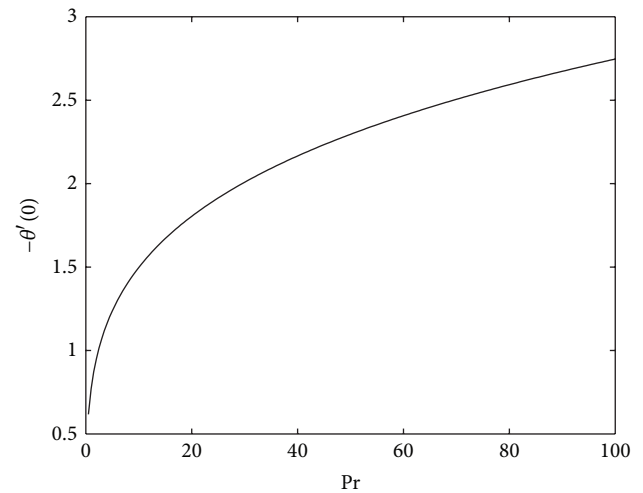


FIGURE 7: Variation of the heat transfer rate with  $Pr$  when  $\lambda = 1$  and  $\gamma = 5$ .

for a suitable scaling parameter to invoke the boundary conditions at infinity while a minimal number of collocation points were used to generate the results.

## 6. Conclusion

The problem of natural convection boundary layer flow with heat transfer has been considered in the current study. The coupled nonlinear system of differential equations was transformed into a finite domain and solved using the spectral local linearisation method (SLLM). The convergence rate of the SLLM algorithm was improved by applying the successive overrelaxation (SOR) technique. Solving the problem in a finite domain avoided the errors that come with approximating the scaling parameter for the boundary conditions at infinity leading to more accurate results. In this work the efficiency of domain transformation on spectral methods was

revealed as accurate results were achieved while using relatively small numbers of collocation points. The flow velocity, temperature profiles, skin friction, and rate of surface heat transfer were successfully computed. Both the velocity and temperature of the flow were seen to be reduced by increased Prandtl numbers. The effect of the Prandtl number was seen to reduce the skin friction while increasing the rate of heat transfer. The SLLM results were also found to be consistent with results available in the literature. The method gave converging results for very large Prandtl numbers. While quite simple and easy to implement, the method has produced accurate results at quite remarkable convergence rates, thus displaying its potential as an improved numerical method for solving nonlinear boundary value problems.

## References

- [1] T. Cebeci and P. Bradshaw, *Physical and Computational Aspects of Convective Heat Transfer*, Springer, New York, NY, USA, 1984.
- [2] M. S. Alam, M. M. Rahman, and M. A. Sattar, "Similarity solutions for hydromagnetic free convective heat and mass transfer flow along a semi-infinite permeable inclined flat plate with heat generation and thermophoresis," *Nonlinear Analysis: Modelling and Control*, vol. 12, no. 4, pp. 433–445, 2007.
- [3] K. V. Prasad, M. S. Abel, and S. K. Khan, "Momentum and heat transfer in visco-elastic fluid flow in a porous medium over a non-isothermal stretching sheet," *International Journal of Numerical Methods for Heat and Fluid Flow*, vol. 10, no. 8, pp. 786–801, 2000.
- [4] M. Yürüsöy, "Similarity solutions of boundary layer equations for a special non-Newtonian fluid in a special coordinate system," *Applied Mathematics and Mechanics*, vol. 25, no. 5, pp. 587–594, 2004.
- [5] E. M. E. Elbarbary and N. S. Elgazery, "Chebyshev finite difference method for the effect of variable viscosity on magnetomicro-polar fluid flow with radiation," *International Communications in Heat and Mass Transfer*, vol. 31, no. 3, pp. 409–419, 2004.
- [6] E. M. E. Elbarbary and N. S. Elgazery, "Chebyshev finite difference method for the effects of variable viscosity and variable thermal conductivity on heat transfer from moving surfaces with radiation," *International Journal of Thermal Sciences*, vol. 43, no. 9, pp. 889–899, 2004.
- [7] N. S. Elgazery, "The effects of chemical reaction, Hall and ion-slip currents on MHD flow with temperature dependent viscosity and thermal diffusivity," *Communications in Nonlinear Science and Numerical Simulation*, vol. 14, no. 4, pp. 1267–1283, 2009.
- [8] H. K. Kuiken, "On boundary layers in fluid mechanics that decay algebraically along stretches of wall that are not vanishingly small," *IMA Journal of Applied Mathematics*, vol. 27, no. 4, pp. 387–405, 1981.
- [9] H. K. Kuiken, "A "backward" free-convective boundary layer," <http://qjmam.oxfordjournals.org/>.
- [10] S. Liao, *Beyond Perturbation: Introduction to Homotopy Analysis Method*, CRC Series: Modern Mechanics and Mathematics, Chapman & Hall/CRC Press, Boca Raton, Fla, USA, 2003.
- [11] S. S. Motsa, S. Shateyi, and Z. Makukula, "Homotopy analysis of free convection boundary layer flow with heat and mass transfer," *Chemical Engineering Communications*, vol. 198, no. 6, pp. 783–795, 2011.
- [12] A. R. Ghotbi, H. Bararnia, G. Domairry, and A. Barari, "Investigation of a powerful analytical method into natural convection boundary layer flow," *Communications in Nonlinear Science and Numerical Simulation*, vol. 14, no. 5, pp. 2222–2228, 2009.
- [13] F. M. Ali, R. Nazar, and N. M. Arifin, "Numerical investigation of free convective boundary layer in a viscous fluid," *The American Journal of Scientific Research*, no. 5, pp. 13–19, 2009.
- [14] R. Hammerling, O. Koch, Ch. Simon, and E. Weinmuller, "Numerical solution of singular eigenvalue problems for ODEs with a focus on problems posed on semi-infinite intervals," 2012, <http://www.math.tuwien.ac.at/>.
- [15] C. Budd, O. Koch, and E. Weinmuller, "Computation of self-similar solution profiles for the nonlinear Schrodinger equation," 2012, <http://www.math.tuwien.ac.at/>.
- [16] G. Kitzhofer, O. Koch, G. Pulverer, C. Simon, and E. B. Weinmüller, "BVPSUITE, a new MATLAB solver for singular implicit boundary value problems," ASC Report No. 35, 2009.
- [17] C. Canuto, M. Y. Hussaini, A. Quarteroni, and T. A. Zang, *Spectral Methods in Fluid Dynamics*, Springer Series in Computational Physics, Springer, New York, NY, USA, 1988.
- [18] L. N. Trefethen, *Spectral Methods in MATLAB*, vol. 10 of *Software, Environments, and Tools*, SIAM, Philadelphia, Pa, USA, 2000.

## Research Article

# Gel Characteristics of Urea-Formaldehyde Resin under Shear Flow Conditions

**Dang-liang Wang, Han-ying Bai, and Gao Yue**

*State Key Laboratory for Geomechanics and Deep Underground Engineering, China University of Mining and Technology, Xuzhou 221008, China*

Correspondence should be addressed to Dang-liang Wang; [dlw9800@163.com](mailto:dlw9800@163.com)

Received 18 March 2013; Revised 12 July 2013; Accepted 12 July 2013

Academic Editor: Waqar Khan

Copyright © 2013 Dang-liang Wang et al. This is an open access article distributed under the Creative Commons Attribution License, which permits unrestricted use, distribution, and reproduction in any medium, provided the original work is properly cited.

Urea-formaldehyde resin (UFR), one of chemical grouts in which the major ingredients are urea-formaldehyde and resin, is widely used in Chinese coal mines grouting. The gel characteristics of urea-formaldehyde resin (UFR) chemical grout under static conditions have been studied by many researchers. However, there is little research carried out on the gel characteristics under shear flow conditions. In fact, chemical grout like UFR keeps in shear flow conditions before gelling in the grouting process. In order to investigate the gel characteristics of UFR in shear flow conditions, an apparatus which consists of a magnetic stirrer and a viscometer was established. Magnetic stirrer was used to shear UFR at different velocity. Then the changes of UFR viscosity could be recorded by viscometer. As a result, the gel characteristics were summarized under different shear rates, and a formula of gelling is derived. The results show that the grouting flow rate influences the gelling time. Faster flow rates will cause longer gelling time, which means that the time for the grout to gel during the flowing process under shear flow conditions is longer than that under static conditions.

## 1. Introduction

Currently, chemical grout is widely used to control seepage and leakage, especially in the prevention and treatment of water and quicksand in coal mines. Urea-formaldehyde resin (UFR) has been used to address many difficulties as it has the advantages of low viscosity, good groutability, and good performance in terms of antiseepage and water plugging in a high pressure stratum. From 2002 to 2007, UFR resin chemical grout has been popularized and applied in the curing of shaft wall fractures and used in water and sand inrush disasters in the east of China. Aside from those advantages, UFR has provided remarkable economic benefits and social effects [1–4].

Typically, the gel time of grout under static conditions is set as a parameter that is used for reference when designing the grouting. However, the motion of grout has been overlooked. In reality, when underground water is in static conditions, the grout flow rate is lower, in which pressure is increased with time [5, 6]. When underground water is in motion, the grout flow rate is faster, in which pressure is lower

at first and increases after a lengthy amount of time [7, 8]. Regardless whether it is the grouting pressure in the pipeline or fractures and pore structures, it causes grout to remain in a flowing and shearing state. The gel time of grout under a flow state is the real gel time in real life practical situations, which has been neglected.

There is a national standard only for the testing of the gel time of epoxy resin grout. The method specified in this standard test the gel time of grout under static conditions. However, whether this standard can be employed for UFR still requires further studies [9]. Chen and Jiang analyzed a method to test the gel time of UFR in the early stages and argued that the inverted cup method is simple, practical, and convenient, which comprises the basis for recommendation in using the method [10]. However, this method lacks a set of full testing criteria. Furthermore, the method merely tests the gel time of grout under static conditions. In this paper, a set of equipment and techniques has been designed which can be applied to test the gelling of UFR under the state of shear and flow on the basis of the national standard that tests the gelling of epoxy resin. Moreover, this study aims to determine

the flowing characteristics of the UFR chemical grout so as to draw the attention of experts in the field to this problem.

## 2. Rheology of Chemical Grout

**2.1. Shear Thinning of Grout under Shear Flow Conditions.** The gel time of chemical grout is an important parameter in the designing of chemical grouting. Currently, the testing methods adopted mainly include apparatuses such as a spreading Tu-four-cup or viscometer to measure the variation of the grout viscosity or strength under static conditions and determine the results of their parameters. In grouting practices, the grout gels are kept in motion rather than in static conditions. As a result, the gel time for grout under static conditions is not its real gel time.

High-molecular polymer grout is in a gelling state while flowing in a porous medium, in which the viscosity of the grout under the state of shear and flow is lower than that of grout under static conditions [11, 12].

**2.2. Relationship between Shearing Rate and Grout Viscosity.** The viscosity of chemical grout has great variation between the impact of shearing motion and static conditions. As observed in previous research, most scholars have paid more attention to the grout viscosity or viscosity variation in gelling under static conditions. However, they have neglected the gel time of grout under a state of shear motion.

Research on the relationship between viscosity and shearing rate of normal fluids has involved three types of models: the Cross, Meter, and Karol models [13].

**(1) Cross Model.** The Cross model obtains the relation between viscosity and shearing rate through experiments that are conducted in an internal environment. The expression is given as follows:

$$\mu = \mu_{\infty} + \frac{\mu_0 - \mu_{\infty}}{1 + \alpha\gamma^{n_c}}, \quad (1)$$

where  $\mu_{\infty}$  refers to the fluid viscosity when the shearing rate is infinitely great,  $\mu_0$  refers to the fluid viscosity when the shearing rate is zero,  $\alpha$  is a constant,  $\gamma$  is the shearing rate, and  $n_c$  is the model index, 2/3.

**(2) Meter Model.** Consider

$$\mu = \mu_{\infty} + \frac{\mu_0 - \mu_{\infty}}{1 + (\gamma/\gamma_{1/2})^{p-1}}, \quad (2)$$

where  $p$  is the experience parameter and  $\gamma_{1/2}$  refers to the shearing rate when the viscosity is  $\mu_0/2$ .

**(3) Karol Model.** Consider

$$\mu = \mu_0 [1 + (\lambda\gamma)^2]^{(n-1)/2}, \quad (3)$$

where  $t$  is the time constant and  $n$  is the power law index or slope of the  $\mu(\gamma)$  curve.

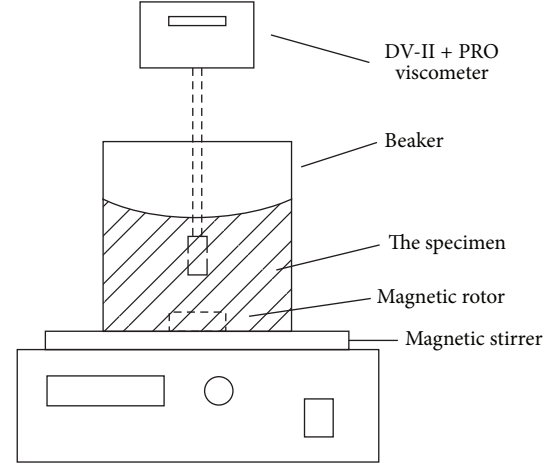


FIGURE 1: Testing device for gel characteristics.

TABLE 1: Gelling time for UFR in static conditions and motion (viscosity 100 mPa·s for motion).

	Ratios (A : B)*	Speed of rotor/rpm			
		0	987	1560	1980
Gel time/s	10 : 1	423	541	630	820
	10 : 2	190	350	460	542
	10 : 4	92	285	340	420

\*The concentration of B (acidity curing agent) is 8%.

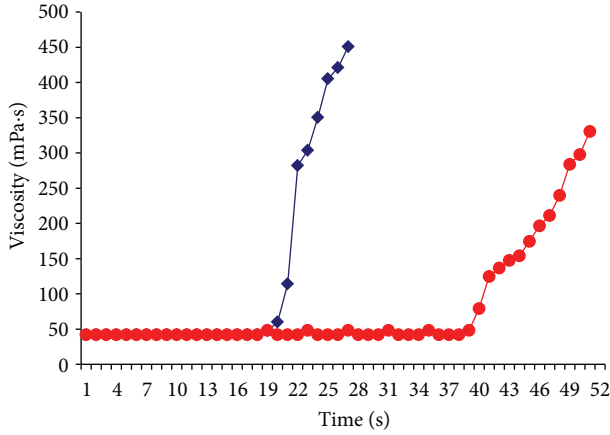
## 3. Gel Characteristics and Formula of UFR Grout in Motion

As grout flows under shearing conditions, it is relatively difficult to directly test the motion of grout gelling. In order to obtain the gelling properties of grout in motion, the experimental equipment shown in Figure 1 was designed for this purpose.

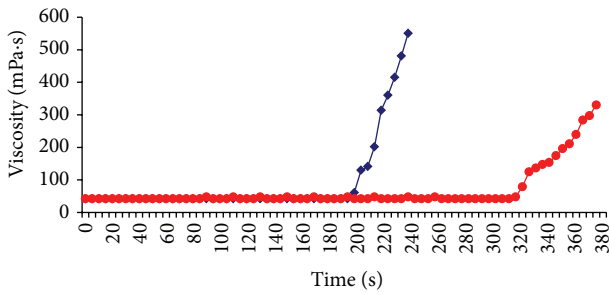
Testing device is composed of two components: a magnetic stirrer and a viscometer. The spinning of the rotor in the magnetic stirrer continuously moves the grout during the gelling process. Then, the variation of the grout viscosity in the gelling process is tested by using a DV-II+PRO on-line viscometer. At the same time, the spinning speed of the rotor in the magnetic stirrer has to be altered so as to change the speed of moving the grout.

**3.1. Gel Time of UFR under Different Shear Rates.** Experiments on grout gelling in static conditions and motion (rotor speed at 987 rounds per minute, rpm) were conducted, respectively, by using the experimental equipment as shown in Figure 1. The UFR that was used in this research comprises double liquids A and B. Liquid A is urea-formaldehyde and resin, while liquid B is the acidity curing agent. The ratios of the double liquids in the UFR (A : B) were 10 : 4, 10 : 2, and 10 : 1. The testing results are shown in Table 1.

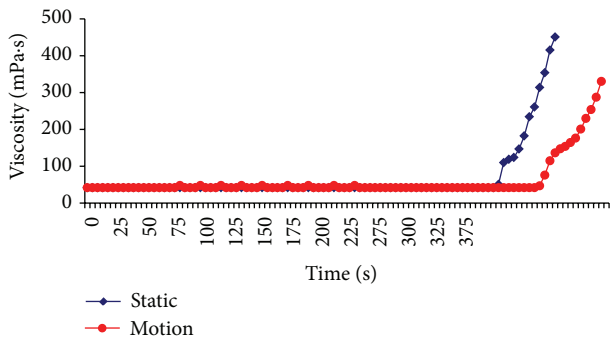
As shown in Figures 2(a) to 2(c), the gelling time of grout in motion is evidently lagging behind that of grout in static conditions. Furthermore, the less gelling time that the grout



(a) Time-viscosity curve (ratio A : B = 10 : 4)



(b) Time-viscosity curve (ratio A : B = 10 : 2)



(c) Time-viscosity curve (ratio A : B = 10 : 1)

FIGURE 2: Time-viscosity curves for different ratios of UFR.

experiences, the more obvious the lag effect of the grout gelling in motion. As the amount of curing agent B that is added increases, both in static and dynamic environments, the gelling time is reduced, but in a more dynamic environment, this is even more so significantly reduced. Thus, the variation of the gelling characteristics under a state of shear and flow needs to be taken into account when designing the grouting.

**3.2. Comparison of Gel Time of UFR under Different Rotational Speeds.** In order to study the impact of the rotational speed of grout on the gel time, a comparison for the variation in the gelation of grout with a ratio of 10 : 4 at 987, 1560, and 1980 rpm was made, as shown in Figure 3.

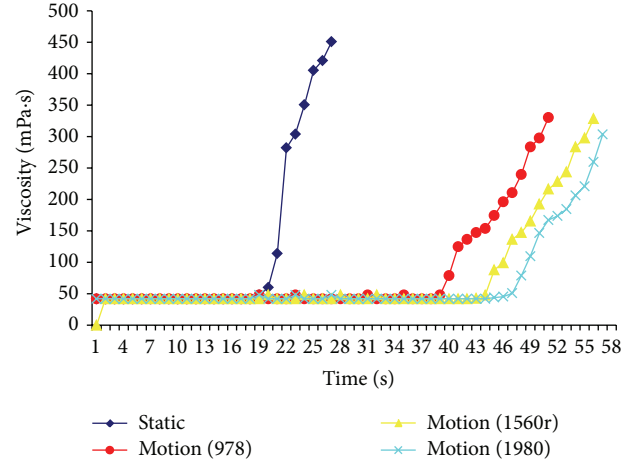


FIGURE 3: Time-viscosity curve for different rotational speeds (ratio: 10 : 4).

As shown in Figure 3, when grout is in a static condition, its gel time is about 100 s. When the grout is stirred at rotational speeds of 987, 1560, and 1980 rpm via a magnetic stirrer, its gel time is somewhere between 200 and 300 s. In other words, the time of gelling while in motion is two to three times that of gelling under a static state. The experimental results indicate that a higher rotational speed means a more obvious impact on the grout by the shearing motion and a longer gel time of the grout. Otherwise, a lower rotational speed means a less obvious impact on the grout, and a shorter gel time.

**3.3. Mathematical Formula for Gelling of UFR.** In view of  $\tau$  as the viscosity resistance of fluid, a high polymer chemical grout used as the viscous fluid is Bingham fluid, which has a viscosity that increases with time. Therefore, the velocity and acceleration at a fixed point are related to the location of the fluid. However, fluid needs a certain time  $t$  to flow from the grouting point to reach the fixed point. During period  $t$ , the grout fluid viscosity involves the following variations:

$$\mu(t) = \begin{cases} \mu_0, & (t = 0), \\ \mu(t), & (0 < t < T), \\ \infty, & (t \geq T). \end{cases} \quad (4)$$

The graphic in Figure 3 is similar to a tangent function. Thus, the relation between  $\mu(t) \sim t$  can be shown in the following equation:

$$\mu(t) = \mu_0 + \tan\left(\frac{t}{2T}\pi\right) \quad (0 < t < T), \quad (5)$$

where  $\mu_0$  refers to the viscosity of the grout fluid at the initial time and  $T$  refers to the standard time for the gelling of the fluid grout relevant to its properties.

If the lag effect of the gel time of the grout in motion is taken into consideration, namely, the shear thinning behavior of grout, then the viscosity variation curve of chemical grout under a state of shear is shown in Figure 4.

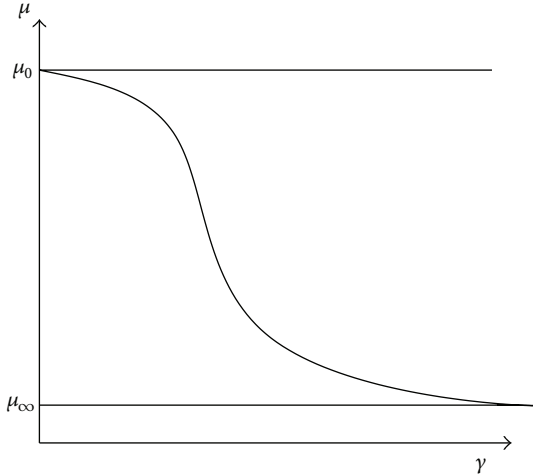


FIGURE 4: Typical viscosity-time curve of chemical grout in motion under shear flow conditions.

Based on the relation between the viscosity of the liquid grout and the shearing rate, it can be seen that the Cross model is a simple means and has a physically applicable format which not only describes the rheological behavior of the power law at high shearing rates, but also represents Newton rheological behavior that is close to a zero shearing rate. Consider

$$\mu(\gamma) = \begin{cases} \mu_0, & (\gamma = 0), \\ \mu(\gamma), & (0 < \gamma < \infty), \\ \mu_\infty, & (\gamma \rightarrow \infty), \end{cases} \quad (6)$$

$$\mu = \mu_\infty + \frac{\mu_0 - \mu_\infty}{1 + \alpha\gamma^{n_c}},$$

where  $\mu_0$  refers to the grout viscosity when the shearing rate is zero.  $\mu_\infty$  refers to the grout viscosity when the shearing rate is  $\infty$ .  $\alpha$  is a constant.  $\gamma$  is the shearing rate.  $n_c$  is the model index,  $2/3$ .

Therefore, viscosity of grout in motion versus change in time should satisfy the equation:

$$\mu(\gamma, t) = f(\gamma, t = 0) \lambda(t), \quad (7)$$

where  $f(\gamma, t = 0)$  refers to the function relationship between grout viscosity and shearing rate at the moment of zero;  $\lambda(t)$  refers to the time correction factor at the moment of  $t$ :

$$0 \leq t \leq T, \quad \lambda(t) = \frac{\mu(t)}{\mu_0}. \quad (8)$$

Thus, (8) is the mathematical equation for the gelling of UFR chemical grout.

The mathematical equation curve for the gelling of UFR chemical grout was calculated by applying MATLAB. As shown in Figure 5, as the shearing rate improves, the grout viscosity decreases and its frictional resistance also decreases, and the gel time is longer. Furthermore, the grout viscosity increases steadily and gradually becomes a gel with time.

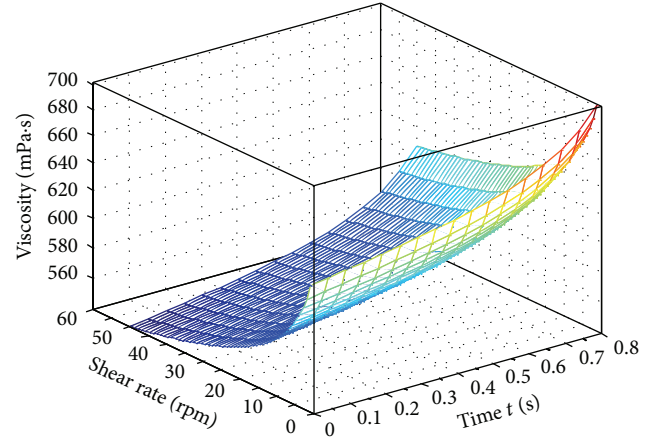


FIGURE 5: Mathematical curve for UFR gelling.

## 4. Conclusion

The variation laws of grout viscosity under different shearing rates by using a gel testing apparatus are examined in this paper by which a dynamic equation for the gelling of UFR grout in motion is established. The results of the equation calculations show that as the shearing rate improves grout viscosity decreases and its frictional resistance also decreases with a longer gel time. In other words, the gel time of grout in motion is longer than that of grout in a static state. This law should be taken into consideration in the designing of grouting.

## Acknowledgments

Financial supports from National Natural Science Foundation under Grant no. 40772192 and Jiangsu Provincial Preponderant Discipline Construction Project are gratefully acknowledged.

## References

- [1] W. H. Sui, Z. Q. Jiang, and D. L. Wang, "One kind of chemical grouting material in coal mines: China," 200810123239. 2[P], 2008.
- [2] D. L. Wang, W. H. Sui, and Z. Q. Jiang, "One kind of grouting material used in broken coal body solidification: China," 201110376459. 8[P], 2011.
- [3] X. H. Ni, W. H. Sui, Y. Z. Guan et al., *Study of Prevention Technology of Vertical Shaft Broken Borehole Wall in Coal Mines*, Press of China University of Mining and Technology, Xuzhou, China, 2005.
- [4] W. H. Sui, G. L. Zhang, Z. Q. Jiang, and D. L. Wang, "The state-of-the-art of chemical grouting treatment for quicksand hazards in coal mines and the prospect of several key problems," *Journal of Engineering Geology*, vol. 16, no. 1, pp. 73–77, 2008.
- [5] D. L. Wang and W. H. Sui, "Research on law of grouting pressure change in rock mass," *Metal Mine*, no. 1, pp. 53–55, 2008.
- [6] D. Wang and Y. Gao, "Empirical formula of chemical grouting pressure in porous media based on similarity theory," *Applied Mechanics and Materials*, vol. 71–78, pp. 3320–3324, 2011.

- [7] K. C. Ren, "Diffusing and grouting method of chemical grout with flowing water," *Water Resources and Hydropower Engineering*, no. 7, pp. 57–62, 1982.
- [8] D. L. Wang, X. F. Dong, and W. D. Du, "Comparison analysis on pre-grouting experiment plan of high pressurized ultra large aquifer for coal mining face in shaft mine," *Coal Engineering*, no. 11, pp. 25–28, 2010.
- [9] PRC Industrial Standard Editorial Group, *GB12007.7-89 Testing Method of Gelling Time of Epoxy Resin*, China Standards Press, Beijing, China, 1990.
- [10] L. H. Chen and Y. S. Jiang, "Determination of gel time of chemical grout," *Railway Construction Technology*, vol. 9, pp. 77–79, 2011.
- [11] M. M. Cross, "Relation between viscoelasticity and shear-thinning behaviour in liquids," *Rheologica Acta*, vol. 18, no. 5, pp. 609–614, 1979.
- [12] A. Chougnnet, A. Audibert, and M. Moan, "Linear and non-linear rheological behaviour of cement and silica suspensions. Effect of polymer addition," *Rheologica Acta*, vol. 46, no. 6, pp. 793–802, 2007.
- [13] T. Shi and D. F. Wu, *Polymer Rheology Principles*, Chemical Industry Press, Beijing, China, 2009.

## Research Article

# On the Comparison between Compact Finite Difference and Pseudospectral Approaches for Solving Similarity Boundary Layer Problems

P. G. Dlamini,<sup>1</sup> S. S. Motsa,<sup>2</sup> and M. Khumalo<sup>1</sup>

<sup>1</sup> Department of Mathematics, University of Johannesburg, P.O. Box 17011, Doornfontein 2028, South Africa

<sup>2</sup> School of Mathematical Sciences, University of KwaZulu-Natal, Private Bag X01, Pietermaritzburg, Scottsville 3209, South Africa

Correspondence should be addressed to P. G. Dlamini; [phgdlamini@gmail.com](mailto:phgdlamini@gmail.com)

Received 22 March 2013; Revised 15 July 2013; Accepted 26 July 2013

Academic Editor: Tirivanhu Chinyoka

Copyright © 2013 P. G. Dlamini et al. This is an open access article distributed under the Creative Commons Attribution License, which permits unrestricted use, distribution, and reproduction in any medium, provided the original work is properly cited.

We introduce two methods based on higher order compact finite differences for solving boundary layer problems. The methods called compact finite difference relaxation method (CFD-RM) and compact finite difference quasilinearization method (CFD-QLM) are an alternative form of the spectral relaxation method (SRM) and spectral quasilinearization method (SQLM). The SRM and SQLM are Chebyshev pseudospectral-based methods which have been successfully used to solve boundary layer problems. The main objective of this paper is to give a comparison of the compact finite difference approach against the pseudo-spectral approach in solving similarity boundary layer problems. In particular, we seek to identify the most accurate and computationally efficient method for solving systems of boundary layer equations in fluid mechanics. The results of the two approaches are comparable in terms of accuracy for small systems of equations. For larger systems of equations, the proposed compact finite difference approaches are more accurate than the spectral-method-based approaches.

## 1. Introduction

Low-order (second or lower) finite difference schemes are not accurate enough for solving many problems in fluid dynamics and other areas. Recently the focus has shifted to higher-order compact finite difference (CFD) schemes. Researchers have found significant improvement to the accuracy of numerical solutions by using fourth or sixth-order CFD schemes compared to the convectional second order finite central difference scheme [1]. Various CFD schemes used for applications such as interpolation, filtering, and evaluating high-order derivatives were discussed in detail by Lele [2]. CFD schemes have largely been applied to solve partial differential equations, for example, Burger's equation [3, 4], Navier-Stokes equation [5], Korteweg-de Vries equation [6], Black-Scholes equation [7], and many more [8–10]. A limited number of researchers have utilised the CFD schemes in ordinary differential equations. For example in [11], Zhao solved two-point boundary value problems. In [12], Zhao and Corless used the CFD schemes to solve integro-differential equations.

The advantage of the higher-order CFD schemes is that they give high accuracy on coarser grids with greater computational efficiency [13]. The difficulty that comes with the higher order CFD schemes especially near the boundaries makes many researchers shy away from using them in practical computations. To retain the accuracy of the schemes at the boundaries, the schemes are adjusted for the boundary points.

When compared to spectral methods, compact schemes are more flexible in terms of application to complex geometries and boundary conditions. Lele [2] pointed out that the use of spectral methods in turbulent fluid flows is limited to flows in simple domains and simple boundary conditions. Spectral methods become less accurate for problems with complex geometries. Rai [14] gave a comprehensive comparison between results obtained using finite differences and spectral methods for direct simulation of turbulent flows. They used high-order accurate upwind schemes. They concluded that the spectral method is extremely accurate but it has restrictions on the type of geometry and grids that

can be efficiently handled. They further state that unlike the spectral methods, the finite difference method can be used efficiently with curvilinear grids.

In recent years Motsa and his coworkers [15–18] have developed successful methods based on the spectral method to solve nonlinear similarity boundary layer problems. The methods include, among others, the spectral relaxation method (SRM) [15, 19, 20], the spectral successive linearisation method [21–23], spectral homotopy analysis method [24–27], and the spectral quasilinearisation method (SQLM) [16]. The SRM is based on simple decoupling and rearrangement of the governing equations and numerically integrating the resulting equations using the Chebyshev spectral collocation method. The SQLM combines the quasilinearization technique developed by Bellman and Kalaba [28] to linearize nonlinear differential equations and solve the resulting equations using the spectral method. In this work we present alternative approach to the implementation of the SRM and SQLM. Instead of using the spectral method in these methods, we use the higher order CFD schemes, and hence the resulting methods are the compact finite difference relaxation method (CFD-RM) and compact finite difference quasilinearization method (CFD-QLM), respectively.

The main objective of this work is to compare the spectral-method-based and the CFD-based methods discussed above. We compare the performance of the methods in terms of accuracy and computational speed when solving nonlinear boundary layer problems in one dimension and three dimensions. We first consider the flow of a viscous incompressible electrically conducting fluid over a continuously shrinking sheet which is governed by a third-order nonlinear differential equation. The known exact analytical solution [29, 30] of this problem is used as a benchmark to validate the accuracy of the proposed algorithm discussed in this work. We also consider a three-equation system that models the problem of unsteady free convective heat and mass transfer on a stretching surface in a porous medium in the presence of a chemical reaction [23, 31].

## 2. Description of the Methods of Solution

This section presents a brief description of how the proposed iterative methods of solution are developed for a general system of  $m$  nonlinear ordinary differential equations in  $m$  unknown functions.

**2.1. Spectral Relaxation Method.** The spectral relaxation method (SRM) is a new method that has been introduced recently by Motsa et al. [15, 19, 20] to solve initial and boundary value problems. The method is based on simple decoupling and rearrangement of the governing equations and numerically integrating the resulting equations using the Chebyshev spectral collocation method. The algorithm for the method is summarized as follows.

- (1) Arrange the governing nonlinear equations in a particular order, placing the equations with the least unknowns at the top of the equations list.

- (2) Assign the labels  $Z_1, Z_2, Z_3, \dots$  to the ordered equations obtained in the above step, where each  $Z_i$  ( $i = 1, 2, 3, \dots$ ) is an unknown function which, in the  $i$ th equation, is identified as the unknown function associated with the highest-order derivative.
- (3) In the equation for  $Z_1$  (1st equation), the iteration scheme is developed by assuming that only linear terms in  $Z_1$  are to be evaluated at the current iteration level (denoted by  $r + 1$ ) and all other terms (linear and nonlinear) in  $Z_2, Z_3, \dots$  are assumed to be known from the previous iteration (denoted by  $r$ ). In addition nonlinear terms in  $Z_1$  are also evaluated at the previous iteration. Furthermore, all derivative terms in  $Z_1$  are assumed to be known from the previous iteration.
- (4) Similarly, in developing the iteration scheme in the equation for  $Z_2$  (2nd equation), only linear terms in  $Z_2$  are evaluated at the current iteration level ( $r + 1$ ) with all other terms evaluated at the previous level, except  $Z_1$  which is now known from the solution of the first equation.
- (5) This process is repeated in the  $i$ th equation ( $i = 3, 4, \dots$ ) using the updated solutions for  $Z_{i-1}$  obtained from the previous  $i - 1$  equations.

The resulting iteration scheme is integrated using the Chebyshev spectral method. The region of integration is discretized using the Gauss-Lobatto points defined by

$$\tau_j = \cos\left(\frac{\pi j}{N}\right), \quad j = 1, 2, 3, \dots, N, \quad (1)$$

where  $N$  is the number of collocation points used. The Chebyshev spectral collocation method is based on the idea of introducing a differentiation matrix  $D$  which is used to approximate the derivatives of the unknown variables  $Z_i(x)$  ( $i = 1, 2, 3, \dots$ ) at the collocation points as the matrix vector product

$$\frac{dZ_i}{dx} = \sum_{k=0}^N D_{jk} Z_i = \mathbf{D}Z_i, \quad j = 1, 2, \dots, N, \quad (2)$$

where  $Z_i = [Z_i(\tau_0), Z_i(\tau_1), \dots, Z_i(\tau_N)]$  is the vector function at the collocation points  $\tau_j$ .

**2.2. Compact Finite Difference Relaxation Method.** The compact finite difference relaxation method (CFD-RM) uses the same procedure followed in the SRM. The difference is that instead of using spectral methods to solve the resulting iteration schemes, higher order compact finite difference schemes are used. In this work we use sixth-order CFD schemes.

In the derivation of the CFD schemes we consider a one-dimensional uniform mesh on the region  $[a, b]$  with nodes  $x_i$  ( $i = 1, 2, \dots, N$ ) where

$$a = x_1 < x_2 < \dots < x_N = b \quad (3)$$

and a corresponding function  $y_i = y(x_i)$  at the nodes. The distance between any two successive nodes is a constant  $h =$

$x_i - x_{i-1}$ . Sixth-order approximations of the first, second, and third derivatives at interior nodes can be obtained using the following schemes (see [2] for details):

$$\frac{1}{3}y'_{i-1} + y'_i + \frac{1}{3}y'_{i+1} \quad (4)$$

$$= \frac{14}{9} \frac{y_{i+1} - y_{i-1}}{2h} + \frac{1}{9} \frac{y_{i+2} - y_{i-2}}{4h},$$

$$\frac{2}{11}y''_{i-1} + y''_i + \frac{2}{11}y''_{i+1} \quad (5)$$

$$= \frac{12}{11} \frac{y_{i+1} - 2y_i + y_{i-1}}{h^2} + \frac{3}{11} \frac{y_{i+2} - 2y_i + y_{i-2}}{4h^2},$$

$$\frac{7}{16}y'''_{i-1} + y'''_i + \frac{7}{16}y'''_{i+1} \quad (6)$$

$$= 2 \frac{y_{i+2} - 2y_{i+1} - 2y_{i-1} - y_{i-2}}{2h^3} - \frac{1}{8} \frac{y_{i+3} - 3y_{i+1} - 3y_{i-1} - y_{i-3}}{8h^3}.$$

For illustrative purposes we describe the application of the CFD schemes to second-order differential equations for  $y(x)$  with known boundary conditions at  $y(a)$  and  $y(b)$ . Consider the nonlinear differential equations

$$y'' + p(x)y' + q(x)y(x) + f(x, y, y') = 0, \quad (7)$$

$$y(a) = y_a, \quad y(b) = y_b,$$

where  $f(x, y, y')$  is a nonlinear function,  $p(x)$  and  $q(x)$  are known functions of  $x$ , and  $y_a$  and  $y_b$  are known constants. In solving (7), we apply the CFD approximation for the first and second derivatives given by (4) and (5), respectively, at the interior nodes ( $i = 2, \dots, N-1$ ). Since we know boundary conditions at  $i = 1$  and  $i = N$ , the CFD schemes must be adjusted for the nodes near the boundary points. In order to maintain the order  $O(h^6)$  accuracy at the boundary points as in the interior points and to maintain the same tridiagonal format, we use the following one-sided scheme at  $i = 2$ :

$$y'_2 + \frac{1}{3}y'_3 = \frac{1}{h} (a_1y_1 + a_2y_2 + a_3y_3 + a_4y_4 + a_5y_5 + a_6y_6 + a_7y_7), \quad (8)$$

and when  $i = N-1$ , we use

$$\frac{1}{3}y'_{N-2} + y'_{N-1} = \frac{1}{h} (b_1y_N + b_2y_{N-1} + b_3y_{N-3} + b_4y_{N-4} + b_5y_{N-5} + b_6y_{N-6} + b_7y_{N-7}), \quad (9)$$

where  $a_i, b_i$  ( $i = 1, \dots, 7$ ) are constants to be determined. To obtain a sixth-order accurate scheme, we use Taylor series

expansion about  $x_1$  and  $x_N$  up to  $O(h^7)$ , in (8) and (9), respectively, and equate terms of order  $h$ . In each case, we obtain a system of seven linear algebraic equations in seven unknowns which are solved to give

$$a_1 = -\frac{7}{45}, \quad a_2 = -\frac{17}{12}, \quad a_3 = \frac{83}{36},$$

$$a_4 = -\frac{11}{9}, \quad a_5 = \frac{2}{3},$$

$$a_6 = -\frac{37}{180}, \quad a_7 = \frac{1}{36},$$

$$b_k = -a_k, \quad k = 1, 2, \dots, 7. \quad (10)$$

Similarly, for the second derivatives, we use

$$y''_2 + \frac{2}{11}y''_3 = \frac{1}{h^2} (c_1y_1 + c_2y_2 + c_3y_3 + c_4y_4 + c_5y_5 + c_6y_6 + c_7y_7 + c_8y_8), \quad (11)$$

at  $i = 2$  and

$$\frac{2}{11}y''_{N-2} + y''_{N-1} = \frac{1}{h^2} (d_1y_N + d_2y_{N-1} + d_3y_{N-3} + d_4y_{N-4} + d_5y_{N-5} + d_6y_{N-6} + d_7y_{N-7} + d_8y_{N-8}) \quad (12)$$

at  $i = N-1$ . The parameters  $c_i, d_i$  can be determined by expanding (11) and (12) using Taylor series and equating powers of  $h$  and subsequently solving the resulting equations. This gives

$$c_1 = \frac{31}{45}, \quad c_2 = -\frac{19}{110}, \quad c_3 = -\frac{339}{110},$$

$$c_4 = \frac{1933}{396}, \quad c_5 = -\frac{40}{11},$$

$$c_6 = \frac{96}{55}, \quad c_7 = -\frac{479}{990}, \quad c_8 = \frac{13}{220},$$

$$d_i = c_i, \quad i = 1, 2, \dots, 8. \quad (13)$$







**2.4. Compact Finite Difference Quasilinearization Method.** Using compact finite difference schemes to solve the QLM scheme (35) results in the compact finite difference quasilinearization method (CFD-QLM). We will use the sixth-order finite difference schemes the same way we used them for the CFD-RM.

### 3. Examples

In this section, two numerical examples are discussed to compare the CFD results against spectral method results. We consider one-dimensional and three-dimensional problems.

**3.1. MHD Boundary Layer Flow over a Shrinking Sheet.** We first consider a steady one-dimensional laminar flow of a viscous incompressible electrically conducting fluid over a continuously shrinking sheet. The governing equation is given (see, e.g., [29, 30]) in similarity form as

$$f''' + ff'' - f'^2 - M^2 f' = 0 \quad (36)$$

subject to

$$f(0) = 0, \quad f'(0) = -1, \quad f'(\infty) = 0, \quad (37)$$

where  $f = f(\eta)$  and  $M$  is the magnetic interaction parameter. The analytical solution for (36) is given by

$$f(\eta) = \frac{1}{\alpha} (e^{-\alpha\eta} - 1), \quad \alpha = \sqrt{M^2 - 1}. \quad (38)$$

We solve (36) using the SRM and CFD-RM and the SQLM and CFD-QLM. In the next subsections we explain the development of each of the methods for the solution of (36).

**3.1.1. SRM and CFD-RM.** To apply the SRM and CFD-RM on (36), we first set  $f'(\eta) = g(\eta)$  and write the equation as the following system of equations:

$$f' = g, \quad (39)$$

$$g'' + fg' - g^2 - M^2 g = 0$$

with the boundary conditions

$$f(0) = 0, \quad g(0) = -1, \quad g(\infty) = 0. \quad (40)$$

Applying the SRM and CFD-RM on (36), we obtain the following iteration scheme:

$$f'_{r+1} = g_r, \quad f_{r+1}(0) = 0, \quad (41)$$

$$g''_{r+1} + f_{r+1}g'_{r+1} - M^2 g_{r+1} = g_r^2, \quad (42)$$

$$g_{r+1}(0) = -1, \quad g_{r+1}(\infty) = 0.$$

The SRM and CFD-RM schemes that result from applying the spectral method and compact finite difference schemes on (41)-(42), respectively, are given by

$$\begin{aligned} X_1 f_{r+1} &= Y_1, & f_{r+1}(\tau_N) &= 0, \\ X_2 g_{r+1} &= Y_2, & g_{r+1}(\tau_N) &= -1, \\ & & g_{r+1}(\tau_0) &= 0, \end{aligned} \quad (43)$$

where for the SRM,

$$X_1 = \mathbf{D}, \quad Y_1 = g_r, \quad (44)$$

$$X_2 = \mathbf{D}^2 + \text{diag}[f_{r+1}] \mathbf{D} - M^2 \mathbf{I}, \quad Y_2 = g_r^2,$$

where  $\mathbf{I}$  is an  $(N+1) \times (N+1)$  identity matrix and  $\text{diag}$  is a function that places a vector  $[\ ]$  on the main diagonal of an  $(N+1) \times (N+1)$  matrix of zeros. For the CFD-RM, we obtain

$$\begin{aligned} X_1 &= E_1, & Y_1 &= g_r - A_1^{-1} K_1, \\ X_2 &= E_2 + \text{diag}[f_{r+1}] E_1 - M^2 I, \end{aligned} \quad (45)$$

$$Y_2 = g_r^2 - A_2^{-1} K_2 - A_1^{-1} K_1,$$

where  $E_1 = A_1^{-1} B_1$  and  $E_2 = A_2^{-1} B_2$ .  $I$  is an  $(N-1) \times (N-1)$  identity matrix.

**3.1.2. SQLM and CFD-QLM.** To solve (36) using the SQLM and CFD-QLM, we first linearize the equation using the quasilinearization method. We first reduce the order of the equation by setting  $f'(\eta) = g(\eta)$  and write it as the following system of equations:

$$f' = g, \quad (46)$$

$$g'' + fg' - g^2 - M^2 g = 0$$

with the boundary conditions

$$f(0) = 0, \quad g(0) = -1, \quad g(\infty) = 0. \quad (47)$$

Applying the quasilinearization method on (46), we obtain

$$f'_{r+1} - g_{r+1} = 0, \quad (48)$$

$$g'_r f_{r+1} + g''_{r+1} + f_r g'_{r+1} - (2g_r + M^2) g_{r+1} = f_r g'_r - g_r^2 \quad (49)$$

subject to

$$f_{r+1}(0) = 0, \quad g_{r+1}(0) = -1, \quad g_{r+1}(\infty) = 0. \quad (50)$$

The SQLM and CFD-QLM schemes that result from applying the spectral method and compact finite difference schemes on (48)-(49), respectively, are given by

$$\begin{bmatrix} \Delta_{1,1} & \Delta_{1,2} \\ \Delta_{2,1} & \Delta_{2,2} \end{bmatrix} \begin{bmatrix} f_{r+1} \\ g_{r+1} \end{bmatrix} = \begin{bmatrix} \Phi_{1,r} \\ \Phi_{2,r} \end{bmatrix}, \quad (51)$$

where in the framework of the SQLM,

$$\Delta_{1,1} = \mathbf{D},$$

$$\Delta_{1,2} = -\mathbf{I},$$

$$\Delta_{2,1} = \text{diag}[g'_r],$$

$$\Delta_{2,2} = \mathbf{D}^2 + \text{diag}[f_r] \mathbf{D} - \text{diag}[2g_r + M^2], \quad (52)$$

$$\Phi_{1,r} = \mathbf{O},$$

$$\Phi_{2,r} = f_r g'_r - g_r^2,$$

TABLE 1: Comparison of the SRM and CFD-RM results for the solution of  $f''(0)$  in Example 1.

$M$	Exact	SRM			CFD6-RM		
		$N$	$f''(0)$	CPU time	$N$	$f''(0)$	CPU time
2	1.732050808	40	1.732050808	0.04	270	1.732050808	0.23
5	4.898979486	40	4.898979486	0.01	550	4.898979486	1.11
10	9.949874371	40	9.949874371	0.01	700	9.949874371	2.19

where  $\mathbf{O}$  is an  $(N + 1) \times 1$  zero vector. For the CFD-QLM, we have

$$\begin{aligned}
\Delta_{1,1} &= E_1, \\
\Delta_{1,2} &= -I, \\
\Delta_{2,1} &= \text{diag} [g'_r], \\
\Delta_{2,2} &= E_2 + \text{diag} [f_r] E_1 - \text{diag} [2g_r + M^2], \\
\Phi_{1,r} &= -A_1^{-1} K_1, \\
\Phi_{2,r} &= f_r g'_r - g_r^2 - A_2^{-1} K_2 - \text{diag} [f_r] (A_1^{-1} K_1).
\end{aligned} \tag{53}$$

**3.2. Unsteady Free Convective Heat and Mass Transfer on a Stretching Surface in a Porous Medium with Suction/Injection.** In this section we consider a three-equation system that models the problem of unsteady free convective heat and mass transfer on a stretching surface in a porous medium in the presence of a chemical reaction. The governing equations [23, 31] for this problem are given as the following dimensionless system of equations and boundary conditions:

$$\begin{aligned}
f''' + ff'' - (f')^2 - Kf' - A \left( f' + \frac{\eta}{2} f'' \right) \\
+ Gr\theta + Gc\phi = 0, \\
\frac{1}{Pr} \theta'' - f'\theta + f\theta' - A \left( \theta + \frac{1}{2} \eta \theta' \right) = 0, \\
\frac{1}{Sc} \phi'' - f'\phi + f\phi' - A \left( \phi + \frac{1}{2} \eta \phi' \right) - \gamma\phi = 0
\end{aligned} \tag{54}$$

subject to

$$\begin{aligned}
f(0) = f_w, \quad f'(0) = 1, \\
\theta(0) = 1, \quad \phi(0) = 1, \\
f'(\infty) = 0, \quad \theta(\infty) = 0, \quad \phi(\infty) = 0,
\end{aligned} \tag{55}$$

where  $f(\eta)$ ,  $\theta(\eta)$ , and  $\phi(\eta)$  are, respectively, the dimensionless velocity, temperature, and concentration,  $f_w$  is the suction/injection parameter,  $\gamma$  is the chemical reaction constant,  $Pr$  is the Prandtl number,  $Sc$  is the Schmidt number,  $K$  is the permeability parameter, and  $Gr$  and  $Gc$  are the temperature- and concentration-dependent Grashof numbers, respectively.

**3.2.1. SRM and CFD-RM.** To apply the SRM and CFD-RM on (54), we set  $f'(\eta) = g(\eta)$  and obtain the following iteration scheme:

$$\begin{aligned}
f'_{r+1} &= g_r, \\
g''_{r+1} + f_{r+1} g'_{r+1} - (A + K) g_{r+1} + \frac{\eta}{2} g'_{r+1} \\
&= g_r^2 - G_r \theta_r - G_c \phi_r, \\
\frac{1}{Pr} \theta_{r+1} - g_{r+1} \theta_{r+1} + f_{r+1} \theta'_{r+1} - A \left( \theta_{r+1} + \frac{\eta}{2} \theta'_{r+1} \right) &= 0, \\
\frac{1}{Sc} \phi_{r+1} - g_{r+1} \phi_{r+1} + f_{r+1} \phi'_{r+1} \\
- (A + \gamma) \phi_{r+1} - A \frac{\eta}{2} \phi'_{r+1} &= 0
\end{aligned} \tag{56}$$

subject to

$$\begin{aligned}
f_{r+1}(0) = f_w, \quad g_{r+1}(0) = 1, \\
g_{r+1}(\infty) = 0, \quad \theta_{r+1}(0) = 1, \\
\theta_{r+1}(\infty) = 0, \quad \phi_{r+1}(0) = 1, \\
\phi_{r+1}(\infty) = 0.
\end{aligned} \tag{57}$$

Applying the Chebyshev pseudo-spectral method and finite difference schemes, we obtain

$$\begin{aligned}
X_1 f_{r+1} &= Y_1, \quad f_{r+1}(0) = f_w, \\
X_2 g_{r+1} &= Y_2, \quad g_{r+1}(\tau_0) = 1, \quad g_{r+1}(\tau_N) = 0, \\
X_3 \theta_{r+1} &= Y_3, \quad \theta_{r+1}(\tau_0) = 1, \quad \theta(\tau_N) = 0, \\
X_4 \phi_{r+1} &= Y_4, \quad \phi_{r+1}(\tau_0) = 1, \quad \phi(\tau_N) = 0.
\end{aligned} \tag{58}$$

For the SRM, we have

$$\begin{aligned}
X_1 &= \mathbf{D}, \quad Y_1 = g_r, \\
X_2 &= \mathbf{D}^2 + \text{diag} \left[ f_{r+1} - A \frac{\eta}{2} \right] \mathbf{D} - (K + A) \mathbf{I}, \\
Y_2 &= g_r^2 - G_r \theta_r - G_c \phi_r,
\end{aligned}$$

TABLE 2: Comparison of the SQLM and CFD-QLM results for the solution of  $f''(0)$  in Example 1.

M	Exact	SQLM			CFD6-QLM		
		N	$f''(0)$	CPU time	N	$f''(0)$	CPU time
2	1.732050808	40	1.732050808	0.06	270	1.732050808	0.31
5	4.898979486	40	4.898979486	0.03	550	4.898979486	1.87
10	9.949874371	40	9.949874371	0.01	700	9.949874371	2.84

TABLE 3: Comparison of the SRM and CFD-RM results for the solution of  $f''(0)$  in Example 2.

A	$f_w$	Gr	K	SRM			CFD-RM		
				N	$f''(0)$	CPU time	N	$f''(0)$	CPU time
0	0	1	1	40	-0.63371481	0.43	250	-0.63371481	0.86
2	0	1	1	40	-1.30748109	0.50	200	-1.30748109	0.26
4	0	1	1	40	-1.79277127	0.55	230	-1.79277127	0.26
1	1	1	1	40	-1.55880093	0.12	210	-1.55880093	0.34
1	2	1	1	40	-2.31812942	0.23	340	-2.31812942	0.88
1	4	1	1	40	-4.14430512	0.29	410	-4.14430512	1.02
1	0	0	1	40	-1.32052206	0.11	180	-1.32052206	0.19
1	0	5	1	40	0.17151463	0.28	280	0.17151463	1.09
1	0	10	1	40	1.49371495	0.52	500	1.49371495	8.47
1	0	1	2	40	-0.61644148	0.18	200	-0.61644148	0.44
1	0	1	4	40	-1.84589956	0.27	310	-1.84589956	0.74
1	0	1	8	40	-2.65350852	0.36	620	-2.65350852	6.12

$$\begin{aligned}
 X_3 &= \frac{1}{P_r} \mathbf{D}^2 + \text{diag} \left[ f_{r+1} - A \frac{\eta}{2} \right] \mathbf{D} - \text{diag} [g_{r+1}] - \mathbf{A} \mathbf{I}, & Y_3 &= -\frac{1}{P_r} \left( A_2^{-1} K_2 \right) - \text{diag} \left[ f_{r+1} - A \frac{\eta}{2} \right] \left( A_1^{-1} K_1 \right), \\
 Y_3 &= \mathbf{O}, & Y_4 &= -\frac{1}{S_c} \left( A_2^{-1} K_2 \right) - \text{diag} \left[ f_{r+1} - A \frac{\eta}{2} \right] \left( A_1^{-1} K_1 \right). \\
 X_4 &= \frac{1}{S_c} \mathbf{D}^2 + \text{diag} \left[ f_{r+1} - A \frac{\eta}{2} \right] \mathbf{D} - \text{diag} [g_{r+1}] - (A + \gamma) \mathbf{I}, & & \\
 Y_4 &= \mathbf{O}, & & \\
 \end{aligned} \tag{59}$$

where  $\mathbf{O}$  is an  $(N + 1) \times 1$  zero vector.  
 For the CFD-RM, we have

$$\begin{aligned}
 X_1 &= E_1, \\
 X_2 &= E_2 + \text{diag} \left[ f_{r+1} - A \frac{\eta}{2} \right] E_1 - (K + A) I, \\
 X_3 &= \frac{1}{P_r} E_2 + \text{diag} \left[ f_{r+1} - A \frac{\eta}{2} \right] E_1 - \text{diag} [g_{r+1}] - \mathbf{A} \mathbf{I}, \\
 X_4 &= \frac{1}{S_c} E_2 + \text{diag} \left[ f_{r+1} - A \frac{\eta}{2} \right] E_1 - \text{diag} [g_{r+1}] - (A + \gamma) I, \\
 Y_1 &= g_r - A_1^{-1} K_1, \\
 Y_2 &= g_r^2 - G_r \theta_r - G_c \phi_r - A_2^{-1} K_2 \\
 &\quad - \text{diag} \left[ f_{r+1} - A \frac{\eta}{2} \right] \left( A_1^{-1} K_1 \right),
 \end{aligned}$$

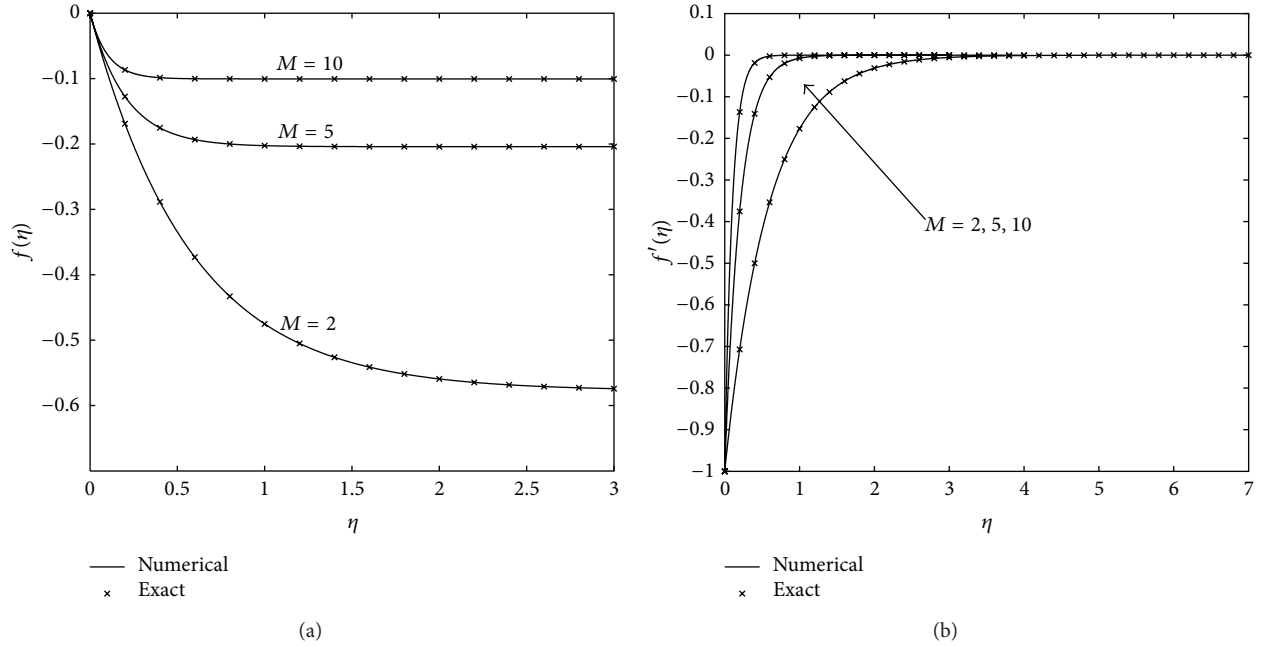
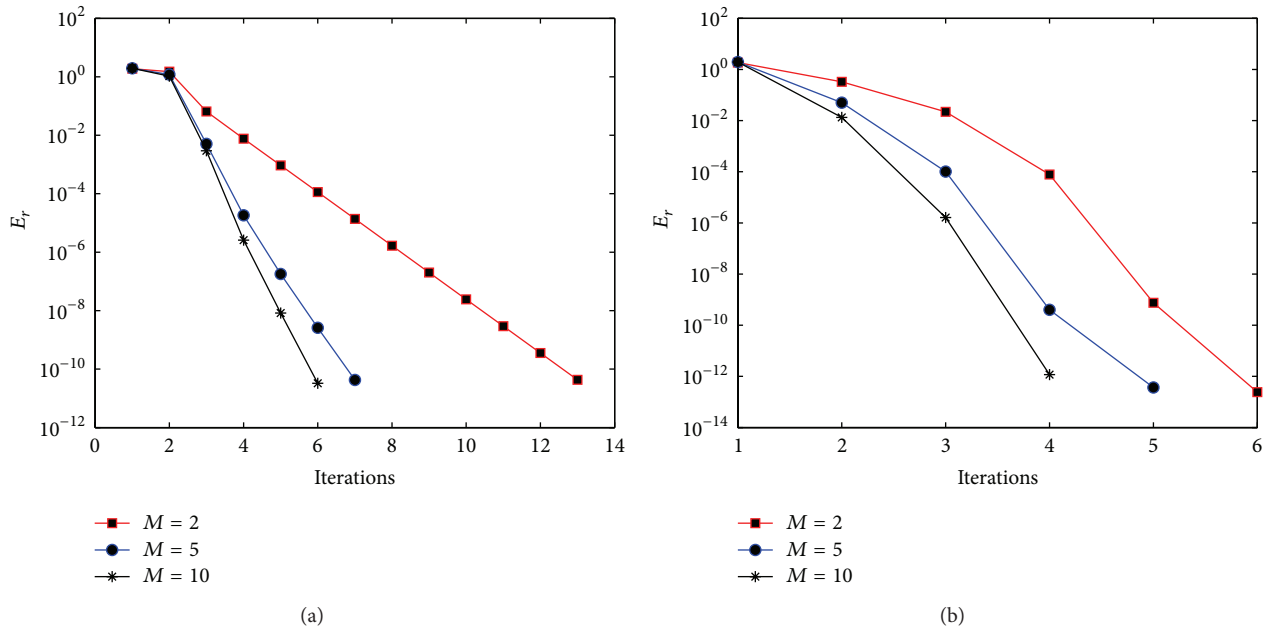
3.2.2. *SQLM and CFD-QLM.* To apply the SQLM and CFD-QLM on (54), we first apply the quasilinearization method and obtain the following iteration scheme:

$$\begin{aligned}
 f_{r+1}''' + \left( f_r - A \frac{\eta}{2} \right) f_{r+1}'' - (2f_r' + K + A) f_{r+1}' \\
 + f_r'' f_{r+1} + G_r \theta_{r+1} + G_c \phi_{r+1} = f_r f_r'' - f_r'^2, \\
 \frac{1}{P_r} \theta_{r+1}'' + \left( f_r - A \frac{\eta}{2} \right) \theta_{r+1}' - (f_r' + A) \theta_{r+1} - \theta_r f_{r+1}' \\
 + \theta_r' f_{r+1} = \theta_r' f_r - f_r' \theta_r,
 \end{aligned} \tag{61}$$

$$\begin{aligned}
 \frac{1}{S_c} \phi_{r+1}'' + \left( f_r - A \frac{\eta}{2} \right) \phi_{r+1}' - (f_r' + A + \gamma) \phi_{r+1} \\
 - \phi_r f_{r+1}' + \phi_r' f_{r+1} = \phi_r' f_r - f_r' \phi_r
 \end{aligned}$$

subject to

$$\begin{aligned}
 f_{r+1}(0) = f_w, \quad f_{r+1}'(0) = 1, \\
 \theta_{r+1}(0) = 1, \quad \phi_{r+1}(0) = 1, \\
 f_{r+1}'(\infty) = 0, \quad \theta_{r+1}(\infty) = 0, \quad \phi_{r+1}(\infty) = 0.
 \end{aligned} \tag{62}$$

FIGURE 1:  $f(\eta)$  and the velocity profile  $f'(\eta)$  for  $M = 2, 5, 10$ .FIGURE 2: Effect of varying  $M$  on the error for the CFD-RM and CFD-QLM.

Applying the spectral method and compact finite difference schemes, we obtain the SQLM and CFD-QLM iteration schemes, respectively. In matrix form, the SQLM and CFD-QLM schemes are given by

$$\begin{bmatrix} \Delta_{1,1} & \Delta_{1,2} & \Delta_{1,3} \\ \Delta_{2,1} & \Delta_{2,2} & \Delta_{2,3} \\ \Delta_{3,1} & \Delta_{3,2} & \Delta_{3,3} \end{bmatrix} \begin{bmatrix} f_{r+1} \\ \theta_{r+1} \\ \phi_{r+1} \end{bmatrix} = \begin{bmatrix} \Phi_{1,r} \\ \Phi_{2,r} \\ \Phi_{3,r} \end{bmatrix}. \quad (63)$$

For the SQLM, we have

$$\Delta_{1,1} = \mathbf{D}^3 - \text{diag} \left[ f_r - A \frac{\eta}{2} \right] \mathbf{D}^2 - \text{diag} \left[ 2f_r' + K + A \right] \mathbf{D} + \text{diag} \left[ f_r'' \right],$$

$$\Delta_{1,2} = G_r \mathbf{I},$$

$$\Delta_{1,3} = G_c \mathbf{I},$$

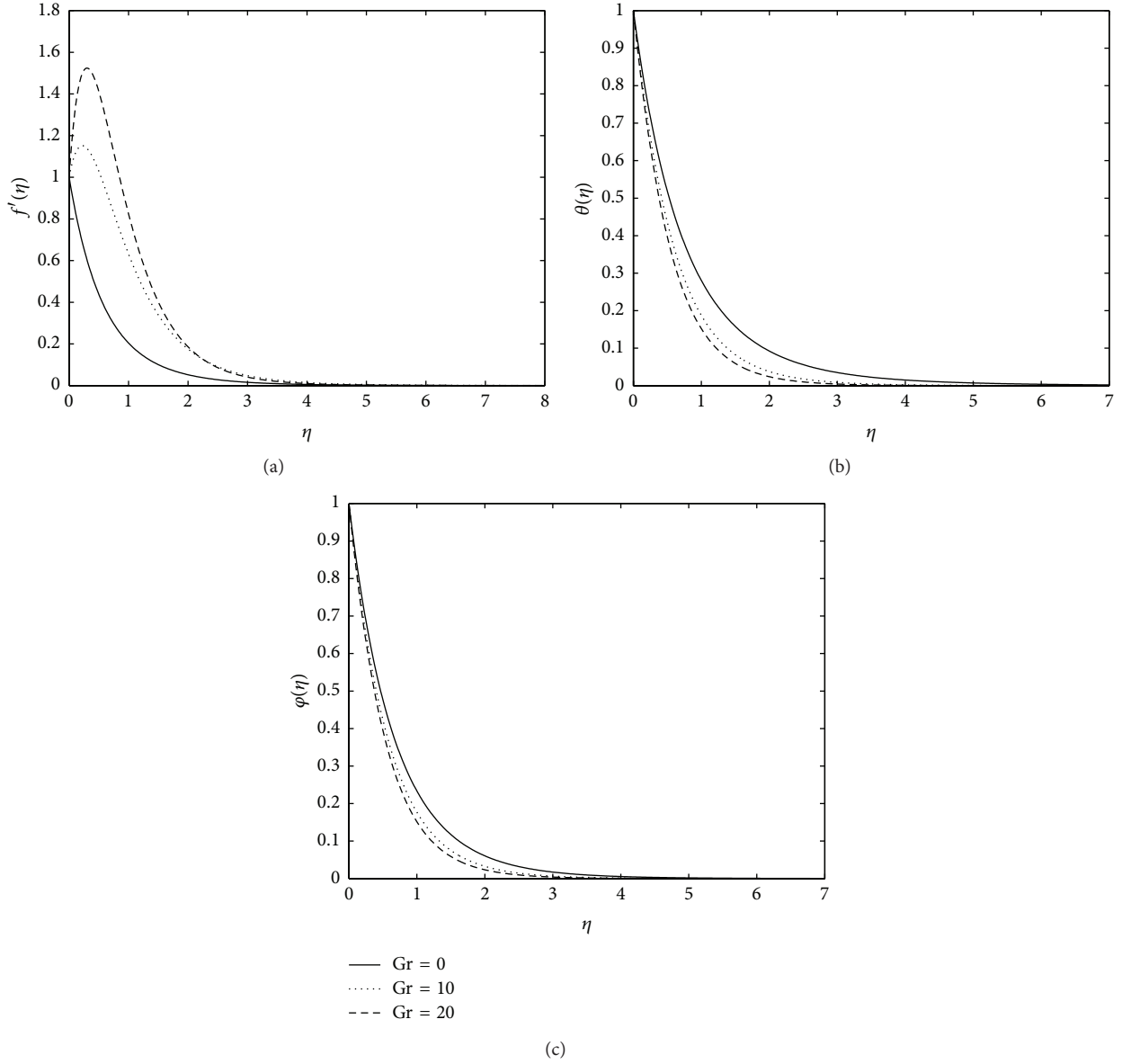


FIGURE 3: Velocity  $f(\eta)$ , temperature  $\theta(\eta)$ , and concentration  $\phi(\eta)$  profiles in Example 2 for various values of Gr (Gr = 0, 5, 20) when Pr = 0.72, Sc = 0.6, A = 0.5,  $\gamma = 1$ , Gc = 1,  $fw = 1$ , and K = 1.

$$\begin{aligned}
 \Delta_{2,1} &= -\text{diag}[\theta_r] \mathbf{D} + \text{diag}[\theta_r'], & \Phi_{2,r} &= f_r \theta_r' - f_r' \theta_r, \\
 \Delta_{2,2} &= \frac{1}{P_r} \mathbf{D}^2 + \text{diag}\left[f_r - A \frac{\eta}{2}\right] \mathbf{D} - A \mathbf{I} - \text{diag}[f_r'], & \Phi_{3,r} &= f_r \phi_r - f_r' \phi_r, \\
 \Delta_{2,3} &= \mathbf{O}, \\
 \Delta_{3,1} &= -\text{diag}[\phi_r] \mathbf{D} + \text{diag}[\phi_r'], & & \\
 \Delta_{3,2} &= \mathbf{O}, & & \\
 \Delta_{3,3} &= \frac{1}{S_c} \mathbf{D}^2 + \text{diag}\left[f_r - A \frac{\eta}{2}\right] \mathbf{D} - (A + \gamma) \mathbf{I} - \text{diag}[f_r'], & \Delta_{1,1} &= E_3 - \text{diag}\left[f_r - A \frac{\eta}{2}\right] E_2 - \text{diag}[2f_r' + K + A] E_1 \\
 & & & + \text{diag}[f_r''], \\
 \Phi_{1,r} &= f_r f_r'' - f_r'^2, & & 
 \end{aligned} \tag{64}$$

where  $\mathbf{O}$  is an  $(N + 1) \times (N + 1)$  zero matrix, and for the CFD-QLM, we have

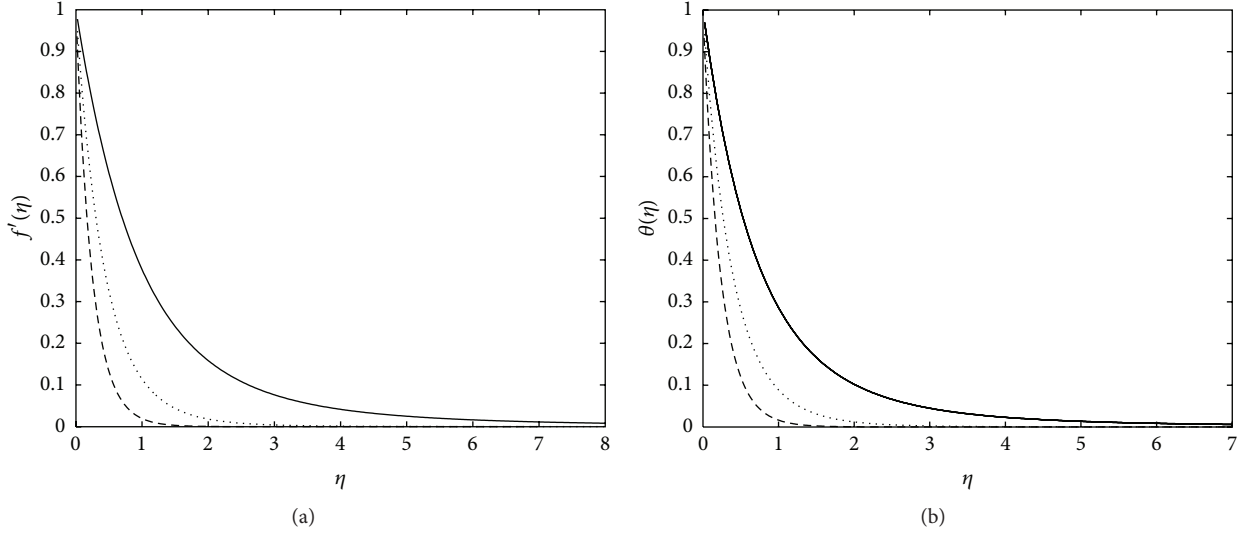


FIGURE 4: Velocity  $f(\eta)$ , temperature  $\theta(\eta)$ , and concentration  $\phi(\eta)$  profiles in Example 2 for various values of  $f_w$  ( $f_w = 0, 2, 4$ ) when  $Pr = 0.72$ ,  $Sc = 0.6$ ,  $A = 0.5$ ,  $\gamma = 1$ ,  $Gc = 1$ ,  $Gr = 1$ , and  $K = 1$ .

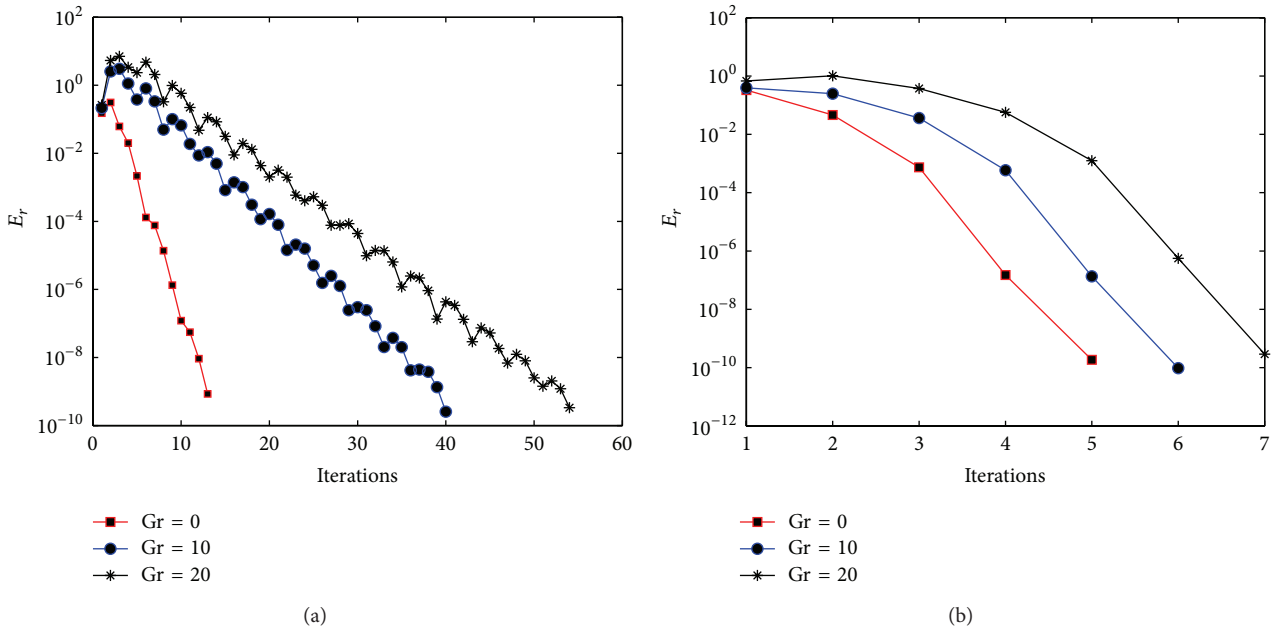


FIGURE 5: Effect of varying  $Gr$  on the errors for the CFD-RM and the CFD-QLM.

$$\begin{aligned} \Delta_{1,2} &= G_r I, \\ \Delta_{1,3} &= G_c I, \\ \Delta_{2,1} &= -\text{diag}[\theta_r] E_1 + \text{diag}[\theta'_r], \\ \Delta_{2,2} &= \frac{1}{Pr} E_2 + \text{diag}\left[f_r - A \frac{\eta}{2}\right] E_1 - A I - \text{diag}[f'_r], \\ \Delta_{2,3} &= O, \\ \Delta_{3,1} &= -\text{diag}[\phi_r] E_1 + \text{diag}[\phi'_r], \\ \Delta_{3,2} &= O, \end{aligned}$$

$$\begin{aligned} \Delta_{3,3} &= \frac{1}{Sc} E_2 + \text{diag}\left[f_r - A \frac{\eta}{2}\right] E_1 - (A + \gamma) I - \text{diag}[f'_r], \\ \Phi_{1,r} &= f_r f_r'' - f_r'^2 - A_3^{-1} K_3 - A_3^{-1} K'_r \\ &\quad - \text{diag}\left[f_r - A \frac{\eta}{2}\right] (A_2^{-1} K_2) \\ &\quad - \text{diag}\left[f_r - A \frac{\eta}{2}\right] (A_2^{-1} K'_2) \\ &\quad + \text{diag}[2f'_r] (A_1^{-1} K_1) - (A + K) (A_1^{-1} K_1) \\ &\quad + \text{diag}[2f'_r] (A_1^{-1} K'_1) - (A + K) (A_1^{-1} K'_1), \end{aligned}$$

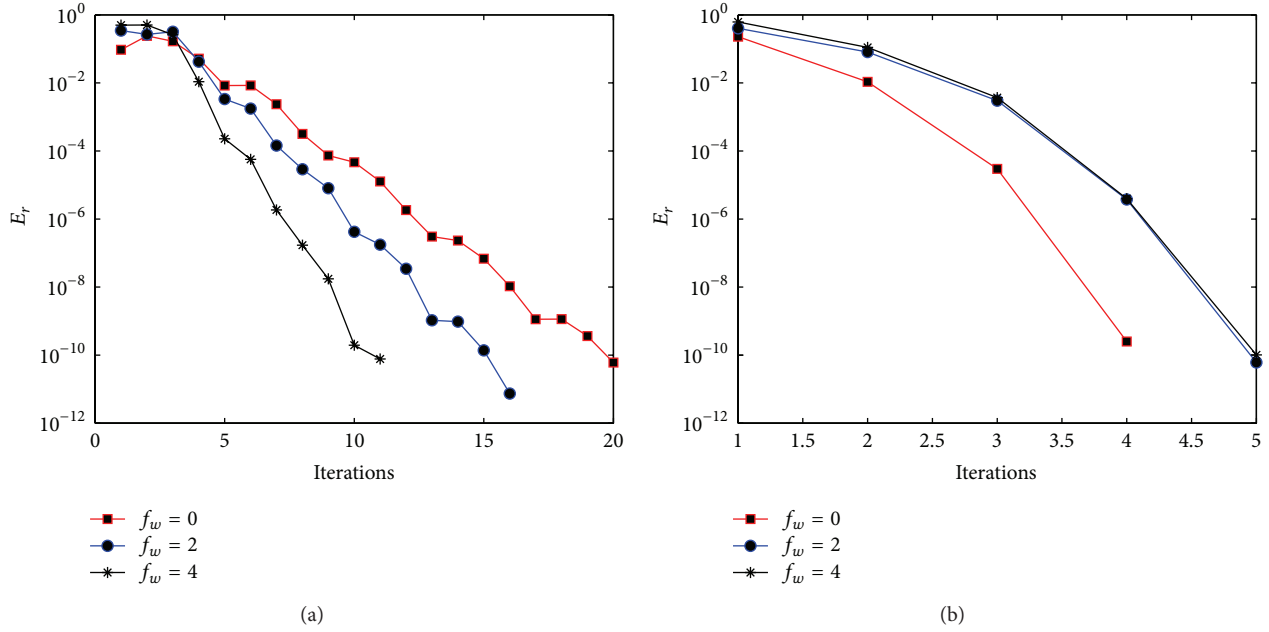


FIGURE 6: Effect of varying  $f_w$  on the errors for the CFD-RM and the CFD-QLM.

TABLE 4: Comparison of the SQLM and CFD-QLM results for the solution of  $f''(0)$  in Example 2.

A	$f_w$	Gr	K	N	SQLM		CFD-QLM		
					$f''(0)$	CPU time	N	$f''(0)$	CPU time
0	1	1	1	200	-0.63371481	64.49	210	-0.63371481	0.27
2	1	1	1	200	-1.44059181	23.20	490	-1.30748109	1.68
4	1	1	1	200	-3.62469942	20.89	650	-1.79277127	3.60
1	1	1	1	200	-1.55886443	64.09	230	-1.55880093	0.35
1	2	1	1	200	-2.31813091	85.57	310	-2.31812942	0.83
1	4	1	1	200	-4.14430509	105.76	440	-4.14430512	2.03
1	1	0	1	200	-1.32106621	26.51	300	-1.32052206	0.69
1	1	5	1	200	0.17105418	33.92	300	0.17151463	0.67
1	1	10	1	200	1.49345960	36.09	420	1.49371495	1.77
1	1	1	2	200	-0.61872790	31.20	360	-0.61644148	1.24
1	1	1	4	200	-2.07158002	33.19	380	-1.84589956	1.20
1	1	1	8	200	-2.98816061	27.64	450	-2.65350852	2.01

$$\begin{aligned}
 \Phi_{2,r} &= f_r \theta_r' - f_r' \theta_r - \frac{1}{P_r} (A_2^{-1} K_2) \\
 &\quad - \text{diag} \left[ f_r - A \frac{\eta}{2} \right] (A_1^{-1} K_1) + \text{diag} [\theta_r] (A_1^{-1} K_1) \\
 &\quad + \text{diag} [\theta_r] (A_1^{-1} K_1'), \\
 \Phi_{3,r} &= f_r \phi_r - f_r' \phi_r - \frac{1}{S_c} (A_2^{-1} K_2) \\
 &\quad - \text{diag} \left[ f_r - A \frac{\eta}{2} \right] (A_1^{-1} K_1) \\
 &\quad + \text{diag} [\phi_r] (A_1^{-1} K_1) + \text{diag} [\phi_r] (A_1^{-1} K_1'),
 \end{aligned} \tag{65}$$

where  $O$  is an  $(N - 1) \times (N - 1)$  zero matrix and  $E_3 = A_3^{-1} B_3$ .

### 4. Results and Discussion

In this section we present results for Examples 1 and 2 and give a comparison between the compact-finite-difference-based methods and the spectral-method-based methods, that is, the SRM and CFD-RM and the SQLM and CFD-QLM. The solution  $f(\eta)$  and the velocity profiles  $f'(\eta)$  for varying values of  $M$  for Example 1 are shown by Figure 1. The numerical results are compared against the exact analytical solution and good agreement is observed in all cases of varying parameter  $M$ . Tables 1 and 2 show the computed skin friction  $f''(0)$  to an accuracy of  $10^{-9}$  obtained using the four methods.

It can be seen from Table 1 that in terms of computational speed, the SRM is efficient compared to the CFD-RM. This is because quite a large number of grid points are needed for the CFD-RM to give an accuracy of  $10^{-9}$  as compared to the

SRM. From Table 2 we observe similar results with the SQLM being computationally faster than the CFD-QLM. Again the number of grid points is the main reason for the difference in speed. The spectral method based approaches only require few grid points to give highly accurate results.

Figure 2 shows the errors at different iterations for the CFD-RM, and CFD-QLM respectively. In all cases the error decreases with each iteration which shows convergence of the methods. Increasing the value of the magnetic interaction parameter,  $M$  increases the convergence of both the CFD-RM and CFD-QLM. This may be explained by the observation that when  $M$  is very large, the dominant terms in the equation from which the SRM scheme is derived are  $g'' - M^2 g$ . Solving this equation gives a solution of the form  $g = ce^{-M\eta}$  (where  $c$  is a constant). For large values of  $M$ , the  $M^2 - 1$  appearing in the given exact solution (38) is approximately equal to  $M^2$ . Consequently, the exact solution reduces to an exponential equation that has the same form as the approximate equation obtained from the SRM scheme at large  $M$ . The CFD-QLM shows a faster convergence than the CFD-RM as shown in Figure 2.

Figures 3 and 4 show the velocity  $f'(\eta)$ , temperature  $\theta(\eta)$ , and concentration  $\phi(\eta)$  for Example 2 for varying values of  $G$ , and  $f_w$ , respectively. We observe that the graphs are qualitatively similar to those reported in [23, 31]. The comparison of the performance of the methods is given by Tables 3 and 4. In Example 2 we compute the solution to an accuracy of  $10^{-8}$ . The SRM is computationally faster than the CFD-RM since it requires fewer grid points to give the required accuracy. We observe different results for the SQLM in Example 2 compared to Example 1. When comparing the results with the SRM, CFD-RM, and CFD-QLM, we observe that the SQLM fails to give results to the accuracy of  $10^{-8}$  as it can be seen in Table 4. In this case the CFD-QLM is much better than the SQLM in terms of accuracy. This is one instance where the advantage of using CFD over spectral approach to integrate linearised equations is highlighted. The spectral approach is less accurate than the CFD approach when large systems of equations are considered.

In terms of convergence between the CFD-RM and CFD-QLM, we observe a faster convergence with the CFD-QLM than the CFD-RM. This is depicted in Figures 5 and 6.

## 5. Conclusion

In this work we have introduced two new methods for solving systems of nonlinear boundary value equations. These methods called the compact finite difference relaxation method (CFD-RM) and compact finite difference quasilinearization method (CFD-QLM) are a modification of the spectral relaxation method (SRM) and the spectral quasilinearization method (SQLM), respectively. We compared the CFD schemes and spectral methods in solving nonlinear similarity boundary layer problems by comparing the CFD-based CFD-RM and CFD-QLM against the spectral-method-based SRM and SQLM. We did the comparison on one dimensional and three-dimensional problems. After comparing these methods we can conclude that they are all highly accurate with

the spectral method outperforming the CFD in terms of computational speed. The SQLM though was less accurate for the three-dimensional problems. The CFD-QLM was able to handle the three-dimensional problem. We also observed that the CFD-QLM converges faster than the CFD-RM. When solving nonlinear boundary value problems, we recommend that the spectral-method-based algorithms must be used in problems involving small systems of equations and when computational speed is of importance because they are easy to code and computationally faster. CFD-based algorithms are ideal for solving large systems of equations when high accuracy is required.

## References

- [1] S.-T. Yu, L. S. Hultgren, and N.-S. Liu, "Direct calculations of waves in fluid flows using high-order compact difference scheme," *AIAA Journal*, vol. 32, no. 9, pp. 1766–1773, 1994.
- [2] S. K. Lele, "Compact finite difference schemes with spectral-like resolution," *Journal of Computational Physics*, vol. 103, no. 1, pp. 16–42, 1992.
- [3] M. Sari and G. Gürarlan, "A sixth-order compact finite difference scheme to the numerical solutions of Burgers' equation," *Applied Mathematics and Computation*, vol. 208, no. 2, pp. 475–483, 2009.
- [4] P.-G. Zhang and J.-P. Wang, "A predictor-corrector compact finite difference scheme for Burgers' equation," *Applied Mathematics and Computation*, vol. 219, no. 3, pp. 892–898, 2012.
- [5] A. Shah, L. Yuan, and A. Khan, "Upwind compact finite difference scheme for time-accurate solution of the incompressible Navier-Stokes equations," *Applied Mathematics and Computation*, vol. 215, no. 9, pp. 3201–3213, 2010.
- [6] J. Li and M. R. Visbal, "High-order compact schemes for nonlinear dispersive waves," *Journal of Scientific Computing*, vol. 26, no. 1, pp. 1–23, 2006.
- [7] B. Düring, M. Fournié, and A. Jüngel, "High order compact finite difference schemes for a nonlinear Black-Scholes equation," *International Journal of Theoretical and Applied Finance*, vol. 6, no. 7, pp. 767–789, 2003.
- [8] M. Bastani and D. K. Salkuyeh, "A highly accurate method to solve Fisher's equation," *Journal of Physics*, vol. 78, no. 3, pp. 335–346, 2012.
- [9] M. Sari, "Solution of the porous media equation by a compact finite difference method," *Mathematical Problems in Engineering*, vol. 2009, Article ID 912541, 13 pages, 2009.
- [10] M. Sari and G. Gürarlan, "A sixth-order compact finite difference method for the one-dimensional sine-Gordon equation," *International Journal for Numerical Methods in Biomedical Engineering*, vol. 27, no. 7, pp. 1126–1138, 2011.
- [11] J. Zhao, "Highly accurate compact mixed methods for two point boundary value problems," *Applied Mathematics and Computation*, vol. 188, no. 2, pp. 1402–1418, 2007.
- [12] J. Zhao and R. M. Corless, "Compact finite difference method for integro-differential equations," *Applied Mathematics and Computation*, vol. 177, no. 1, pp. 271–288, 2006.
- [13] J. C. Kalita, D. C. Dalal, and A. K. Dass, "A class of higher order compact schemes for the unsteady two-dimensional convection-diffusion equation with variable convection coefficients," *International Journal for Numerical Methods in Fluids*, vol. 38, no. 12, pp. 1111–1131, 2002.

- [14] M. M. Rai, "Direct simulations of turbulent flow using finite-difference schemes," *Journal of Computational Physics*, vol. 96, no. 1, pp. 15–53, 1991.
- [15] S. S. Motsa, P. Dlamini, and M. Khumalo, "A new multistage spectral relaxation method for solving chaotic initial value systems," *Nonlinear Dynamics*, vol. 72, no. 1-2, pp. 265–283, 2013.
- [16] S. S. Motsa and P. Sibanda, "Some modifications of the quasilinearization method with higher-order convergence for solving nonlinear BVPs," *Numerical Algorithms*, vol. 63, no. 3, pp. 399–417, 2013.
- [17] S. S. Motsa and P. Sibanda, "On the solution of MHD flow over a nonlinear stretching sheet by an efficient semi-analytical technique," *International Journal for Numerical Methods in Fluids*, vol. 68, no. 12, pp. 1524–1537, 2012.
- [18] S. S. Motsa, "A new algorithm for solving nonlinear boundary value problems arising in heat transfer," *International Journal of Modeling, Simulation, and Scientific Computing*, vol. 2, no. 3, pp. 355–373, 2011.
- [19] S. S. Motsa, P. G. Dlamini, and M. Khumalo, "Solving hyperchaotic systems using the spectral relaxation method," *Abstract and Applied Analysis*, vol. 2012, Article ID 203461, 18 pages, 2012.
- [20] S. S. Motsa and Z. G. Makukula, "On spectral relaxation method approach for steady von Karman flow of a Reiner-Rivlin fluid with Joule heating, viscous dissipation and suction/injection," *Central European Journal of Physics*, vol. 11, pp. 363–374, 2013.
- [21] S. S. Motsa and S. Shateyi, "A successive linearization method approach to solve Lane-Emden type of equations," *Mathematical Problems in Engineering*, vol. 2012, Article ID 280702, 14 pages, 2012.
- [22] Z. G. Makukula, P. Sibanda, S. S. Motsa, and S. Shateyi, "On new numerical techniques for the MHD flow past a shrinking sheet with heat and mass transfer in the presence of a chemical reaction," *Mathematical Problems in Engineering*, vol. 2011, Article ID 489217, 19 pages, 2011.
- [23] S. S. Motsa and S. Shateyi, "Successive linearisation analysis of unsteady heat and mass transfer from a stretching surface embedded in a porous medium with suction/injection and thermal radiation effects," *The Canadian Journal of Chemical Engineering*, vol. 90, no. 5, pp. 1323–1335, 2012.
- [24] S. S. Motsa, P. Sibanda, and S. Shateyi, "A new spectral-homotopy analysis method for solving a nonlinear second order BVP," *Communications in Nonlinear Science and Numerical Simulation*, vol. 15, no. 9, pp. 2293–2302, 2010.
- [25] S. S. Motsa, P. Sibanda, F. G. Awad, and S. Shateyi, "A new spectral-homotopy analysis method for the MHD Jeffery-Hamel problem," *Computers and Fluids*, vol. 39, no. 7, pp. 1219–1225, 2010.
- [26] P. Sibanda, S. Motsa, and Z. Makukula, "A spectral-homotopy analysis method for heat transfer flow of a third grade fluid between parallel plates," *International Journal of Numerical Methods for Heat and Fluid Flow*, vol. 22, no. 1, pp. 4–23, 2012.
- [27] S. S. Motsa, "Application of the new spectral homotopy analysis method (SHAM) in the non-linear heat conduction and convective fin problem with variable thermal conductivity," *International Journal of Computational Methods*, vol. 9, no. 3, Article ID 1250039, 18 pages, 2012.
- [28] R. E. Bellman and R. E. Kalaba, *Quasilinearization and Nonlinear Boundary-Value Problems*, Modern Analytic and Computational Methods in Science and Mathematics, vol. 3, American Elsevier, New York, NY, USA, 1965.
- [29] C. Midya, "Exact solutions of chemically reactive solute distribution in MHD boundary layer flow over a shrinking surface," *Chinese Physics Letters*, vol. 29, no. 1, Article ID 014701, 2012.
- [30] C. Midya, G. C. Layek, A. S. Gupta, and T. R. Mahapatra, "Magnetohydrodynamic viscous flow separation in a channel with constrictions," *Journal of Fluids Engineering*, vol. 125, no. 6, pp. 952–962, 2003.
- [31] A. J. Chamkha, A. M. Aly, and M. A. Mansour, "Similarity solution for unsteady heat and mass transfer from a stretching surface embedded in a porous medium with suction/injection and chemical reaction effects," *Chemical Engineering Communications*, vol. 197, no. 6, pp. 846–858, 2010.

## Research Article

# Radiation and Magnetohydrodynamics Effects on Unsteady Free Convection Flow in a Porous Medium

**Sami Ulhaq, Ilyas Khan, Farhad Ali, and Sharidan Shafie**

*Department of Mathematical Sciences, Faculty of Science, Universiti Teknologi Malaysia, 81310 Skudai, Malaysia*

Correspondence should be addressed to Sharidan Shafie; [ridafie@yahoo.com](mailto:ridafie@yahoo.com)

Received 21 April 2013; Revised 7 July 2013; Accepted 7 July 2013

Academic Editor: Waqar Khan

Copyright © 2013 Sami Ulhaq et al. This is an open access article distributed under the Creative Commons Attribution License, which permits unrestricted use, distribution, and reproduction in any medium, provided the original work is properly cited.

The unsteady MHD free convection flow near an exponentially accelerated infinite vertical plate through porous medium with uniform heat flux in the presence of thermal radiation has been considered. The mathematical model, under the usual Boussinesq approximation, was reduced to a system of coupled linear partial differential equations for velocity and temperature. Exact solutions are obtained by the Laplace transform method. The influence of pertinent parameters such as the radiation parameter, Grashof number, Prandtl number, and time on velocity, temperature, and skin friction is shown by graphs.

## 1. Introduction

The study of natural convection heat transfer from a vertical plate has received much attention in the literature due to its industrial and technological applications. Stokes [1] first presented an exact solution to the Navier-Stokes equation for flow past an impulsively started infinite horizontal plate. But if an infinite isothermal vertical plate is provided with an impulsive motion, how free convection currents will influence the flow, which exists due to temperature difference between the plate and that of fluid away from the plate, was first studied by Soundalgekar [2]. Free convection effects on flow past an exponentially accelerated vertical plate were studied by Singh and Kumar [3]. MHD flow has applications in metrology, solar physics, aeronautics, chemical engineering, electronics, and motion of earth's core. MHD effects on impulsively started vertical infinite plate with variable temperature in the presence of transverse magnetic field were studied by Soundalgekar et al. [4]. The dimensionless governing equations were solved using Laplace transform technique. Gebhart et al. [5] pointed out that the interest in such flows arose in astrophysics, geophysics, and controlled nuclear physics. In the last two decades, problems of natural convection and heat transfer flows through porous media under the influence of a magnetic field have attracted the

attention of a number of researchers. Such flows have applications in heat removal from nuclear fuel debris, underground disposal of radioactive waste material, storage of food stuffs, and so forth. Theoretical studies in this area can be found in books by Nield and Bejan [6], Bejan and Kraus [7], Ingham et al. [8].

The effects of radiation are often more important when combined with free convection. Radiation can strongly modify free convection temperature profiles. Rajesh and Varma [9] considered the radiation effects on the free convection flow of a viscoelastic fluid past an impulsively started vertical plate. An interesting study of the effects of thermal radiation on the flow past an infinite vertical oscillating isothermal plate in the presence of a transversely applied magnetic field has been recently realized by Chandrakala and Bhaskar [10]. However, the free convection MHD flow with thermal radiation from an exponentially accelerated vertical infinite plate in the presence of porous media with uniform heat flux has not received the attention of any researcher. The objective of present investigations is to study the radiation and MHD effects on the free convection of an incompressible viscous fluid past an exponentially accelerated infinite vertical plate with uniform heat flux in a porous medium. Closed-form solutions are obtained by the Laplace transform method. A limiting case is considered for the absence of radiation effects.

The expression for the temperature reduces to those obtained by Chaudhary et al. [11, equation (15)] and Chandrakala and Bhaskar [12, equation (8)]. Again in the absence of radiation and  $a = 0$  (accelerating parameter), the solution obtained by Chaudhary et al. [11, equation (16)] is recovered for velocity.

## 2. Formulation of the Problem and Solution

We consider the unsteady free convection flow of an electrically conducting incompressible viscous fluid past an infinite vertical plate with uniform heat flux through porous medium in the presence of thermal radiation. A magnetic field of uniform strength  $B_0$  is transversely applied to the plate. The  $x$ -axis is along the plate in the vertically upward direction, and the  $y$ -axis is taken as normal to the plate. Initially, the plate and the adjacent fluid are at the same temperature  $T_\infty$ , in a stationary condition. At time  $t > 0$ , the plate is exponentially accelerated with a velocity  $u = U \exp(at)$  in its own plane according to

$$\mathbf{V} = U \exp(at) \mathbf{i}; \quad t > 0, \quad (1)$$

where the constant  $U$  is the amplitude of the motion,  $a$  is the accelerating parameter, and  $\mathbf{i}$  is the unit vector in the flow direction. Let us write the velocity of the fluid in a general form as

$$\mathbf{V} = \mathbf{V}(u, v, w). \quad (2)$$

This study is focused on a unidirectional flow; therefore, the only nonvanishing velocity component (in our case  $u$ ) remains (see [13]) whereas the other components  $v$  and  $w$  become zero. So the velocity vector reduces to the following form:

$$\mathbf{V} = u(x, y, t) \mathbf{i}. \quad (3)$$

It is clear from (3) that the flow is two-dimensional. As the plate is infinite in  $x$ -direction, therefore the flow is independent of the distance parallel to the plate and, hence, the physical variables depend on the space variable  $y$  and time coordinates  $t$  only (see [14–16]). So, (3) modifies to

$$\mathbf{V} = u(y, t) \mathbf{i}. \quad (4)$$

Then by the usual Boussinesq's approximation, the unsteady flow is governed by the following equations:

$$\frac{\partial u}{\partial t} = \nu \frac{\partial^2 u}{\partial y^2} - \frac{\sigma B_0^2}{\rho} u - \frac{\nu}{K} u + g\beta(T - T_\infty), \quad (5)$$

$$\frac{\partial T}{\partial t} = \frac{k}{\rho c_p} \frac{\partial^2 T}{\partial y^2} - \frac{1}{\rho c_p} \frac{\partial q_r}{\partial y}, \quad (6)$$

where  $u$  is the velocity in the  $x$ -direction,  $T$  is the temperature of the fluid,  $g$  is the acceleration due to gravity,  $\beta$  is the volumetric coefficient of thermal expansion,  $\nu$  is the kinematic viscosity,  $\rho$  is the density,  $\sigma$  is the electrical conductivity,  $K$  is the permeability of porous medium,  $k$  is the thermal conductivity,  $q_r$  is the radiative heat flux in the  $y$  direction, and  $c_p$  is the specific heat of the fluid at constant pressure.

The initial and boundary conditions are

$$\begin{aligned} u(y, 0) &= 0, \quad T(y, 0) = T_\infty \quad \text{for } y \geq 0, \\ u(0, t) &= U \exp(at), \quad \frac{\partial T(0, t)}{\partial y} = -\frac{q}{k} \quad \text{for } t > 0, \end{aligned} \quad (7)$$

$$u(y, t) \rightarrow 0, \quad T(y, t) \rightarrow T_\infty \quad \text{as } y \rightarrow \infty, \quad t > 0,$$

where  $q$  is the constant heat flux. The radiative heat flux in the case of an optically thick gray gas in one space coordinate  $y$  is expressed by

$$q_r = -\frac{4\sigma^* \partial T^4}{3\kappa^* \partial y}, \quad (8)$$

where  $\sigma^*$  is the Stefan-Boltzmann constant and  $\kappa^*$  is the mean absorption coefficient. Assuming small temperature difference between fluid temperature  $T$  and free stream temperature  $T_\infty$ ,  $T^4$  is expanded in Taylor series about the free stream temperature  $T_\infty$ . Neglecting second and higher order terms in  $(T - T_\infty)$ , we get

$$T^4 \cong 4T_\infty^3 T - 3T_\infty^4. \quad (9)$$

Using (9) and (8), (6) reduces to

$$\rho c_p \frac{\partial T}{\partial t} = k \frac{\partial^2 T}{\partial y^2} + \frac{16\sigma^* T_\infty^3}{3\kappa^*} \frac{\partial^2 T}{\partial y^2}. \quad (10)$$

Introducing the following non-dimensional quantities

$$\begin{aligned} u^* &= \frac{u}{U}, \quad y^* = \frac{y}{\nu}, \quad t^* = \frac{U^2}{\nu} t, \\ a^* &= \frac{\nu}{U^2} a, \quad \theta = \frac{Uk}{\nu k} (T - T_\infty), \end{aligned} \quad (11)$$

$$\begin{aligned} \text{Gr} &= \left(\frac{\nu}{U^2}\right)^2 \frac{g\beta q}{k}, \quad \text{Pr} = \frac{\mu c_p}{k}, \quad N = \frac{\kappa^* k}{4\sigma^* T_\infty^3}, \\ M^2 &= \frac{\sigma \nu B_0^2}{\rho U^2}, \quad K^* = \frac{U^2}{\nu^2} K \end{aligned} \quad (12)$$

and dropping out the star notation from  $u$ ,  $y$ ,  $t$ ,  $a$  and  $K$ , the governing equations (5) and (10) reduce to the simplified forms

$$\begin{aligned} \frac{\partial u(y, t)}{\partial t} &= \frac{\partial^2 u(y, t)}{\partial y^2} \\ &\quad - Hu(y, t) + \text{Gr}\theta(y, t); \quad y, t > 0, \end{aligned} \quad (13)$$

$$\frac{\partial \theta(y, t)}{\partial t} = \left(\frac{3N + 4}{3\text{Pr}N}\right) \frac{\partial^2 \theta(y, t)}{\partial y^2}; \quad y, t > 0,$$

where  $H = M^2 + 1/K$ ,  $\text{Pr}$  is the Prandtl number,  $\text{Gr}$  is the Grashof number, and  $N$  is the radiation parameter. In

dimensionless form, the initial and boundary conditions (7) become

$$\begin{aligned} u(y, t) = 0, \quad \theta(y, t) = 0 \quad \text{for } y \geq 0, \\ u(0, t) = \exp(at), \quad \frac{\partial \theta(0, t)}{\partial y} = -1 \quad \text{for } t > 0, \\ u(y, t) \rightarrow 0, \quad \theta(y, t) \rightarrow 0 \quad \text{as } y \rightarrow \infty, t > 0. \end{aligned} \quad (14)$$

Equation (13), subjected to the boundary conditions (14), is solved by the usual Laplace-transform technique and the solutions are derived as follows:

$$\theta(y, t) = \frac{1}{\sqrt{b}} \left[ 2\sqrt{\frac{t}{\pi}} \exp\left(-\frac{y^2 b}{4t}\right) - y\sqrt{b} \operatorname{erfc}\left(\frac{y\sqrt{b}}{2\sqrt{t}}\right) \right], \quad (15)$$

$$\begin{aligned} u(y, t) &= \frac{e^{at}}{2} \left[ e^{-y\sqrt{H+a}} \operatorname{erfc}\left(\frac{y}{2\sqrt{t}} - \sqrt{(H+a)t}\right) \right. \\ &\quad \left. + e^{y\sqrt{H+a}} \operatorname{erfc}\left(\frac{y}{2\sqrt{t}} + \sqrt{(H+a)t}\right) \right] \\ &\quad + \frac{\operatorname{Gr}}{H\sqrt{b}} \left[ -\frac{1}{\pi} \left[ \int_0^\infty \frac{\cos(y\sqrt{x})}{(x+H)^{3/2}} [1 - e^{-(x+H)t}] dx \right. \right. \\ &\quad \left. \left. + \int_0^H \frac{e^{-y\sqrt{x+H}}}{x^{3/2}} [1 - e^{-xt}] dx \right] \right. \\ &\quad \left. + \frac{e^{ct}}{\pi} \left[ \int_0^\infty \frac{\cos(y\sqrt{x})}{(x+H+c)\sqrt{x+H}} \right. \right. \\ &\quad \left. \left. \times [1 - e^{-(x+H+c)t}] dx \right. \right. \\ &\quad \left. \left. + \int_0^H \frac{e^{-y\sqrt{x+H}}}{(x+c)\sqrt{x}} [1 - e^{-(x+c)t}] dx \right] \right. \\ &\quad \left. + 2\sqrt{\frac{t}{\pi}} \exp\left(-\frac{y^2 b}{4t}\right) - y\sqrt{b} \operatorname{erfc}\left(\frac{y\sqrt{b}}{2\sqrt{t}}\right) \right. \\ &\quad \left. - \frac{e^{ct}}{2\sqrt{c}} \left[ e^{-y\sqrt{bc}} \operatorname{erfc}\left(\frac{y\sqrt{b}}{2\sqrt{t}} - \sqrt{ct}\right) \right. \right. \\ &\quad \left. \left. - e^{y\sqrt{bc}} \operatorname{erfc}\left(\frac{y\sqrt{b}}{2\sqrt{t}} + \sqrt{ct}\right) \right] \right], \quad (16) \end{aligned}$$

where  $b = 3\operatorname{Pr}N/(3N+4)$  and  $c = H/(b-1)$ . The temperature  $\theta(y, t)$  given by (15) is valid for all positive values of  $b$ , while the solution for velocity is not valid for  $b = 1$ . So, in this case,

the velocity  $u(y, t)$  has to be rederived starting from (13). The solution that is obtained for  $b = 1$  is

$$\begin{aligned} u(y, t) &= \frac{e^{at}}{2} \left[ e^{-y\sqrt{H+a}} \operatorname{erfc}\left(\frac{y}{2\sqrt{t}} - \sqrt{(H+a)t}\right) \right. \\ &\quad \left. + e^{y\sqrt{H+a}} \operatorname{erfc}\left(\frac{y}{2\sqrt{t}} + \sqrt{(H+a)t}\right) \right] \\ &\quad + \frac{\operatorname{Gr}}{H} \left[ -\frac{1}{\pi} \left[ \int_0^\infty \frac{\cos(y\sqrt{x})}{(x+H)^{3/2}} [1 - e^{-(x+H)t}] dx \right. \right. \\ &\quad \left. \left. + \int_0^H \frac{e^{-y\sqrt{x+H}}}{x^{3/2}} [1 - e^{-xt}] dx \right] \right. \\ &\quad \left. + 2\sqrt{\frac{t}{\pi}} \exp\left(-\frac{y^2}{4t}\right) - y \operatorname{erfc}\left(\frac{y}{2\sqrt{t}}\right) \right]. \end{aligned} \quad (17)$$

The corresponding skin friction, which is a measure of the shear stress at the plate, can be determined by considering (16) and (17) into

$$\tau = \tau(t) = -\left. \frac{\partial u(y, t)}{\partial y} \right|_{y=0}; \quad t > 0. \quad (18)$$

Its dimensionless expressions are

$$\begin{aligned} \tau &= \frac{e^{at}}{2} \left[ \frac{1}{\sqrt{t\pi}} e^{-(a+H)t} + \sqrt{H+a} \operatorname{erfc}\left(\sqrt{(H+a)t}\right) \right] \\ &\quad + \frac{\operatorname{Gr}}{H\sqrt{b}} \left[ \sqrt{b}(1 - e^{ct}) \right. \\ &\quad \left. - \frac{1}{\pi} \int_0^H \frac{\sqrt{H+x}}{x^{3/2}} [1 - e^{-tx}] dx \right. \\ &\quad \left. + \frac{e^{ct}}{\pi} \int_0^H \frac{\sqrt{H+x}}{(c+x)\sqrt{x}} [1 - e^{-(c+x)t}] dx \right] \end{aligned} \quad (19)$$

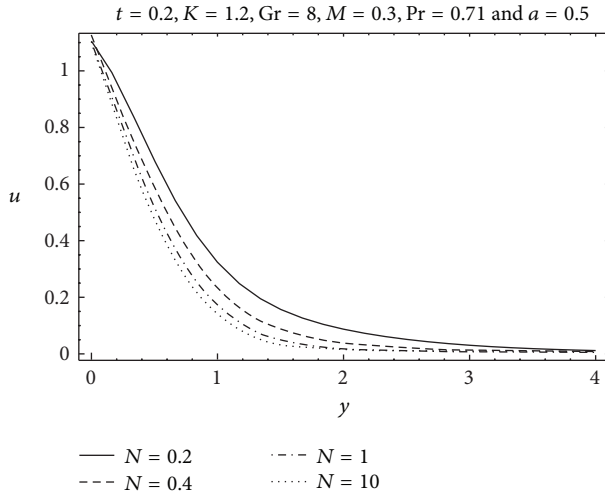
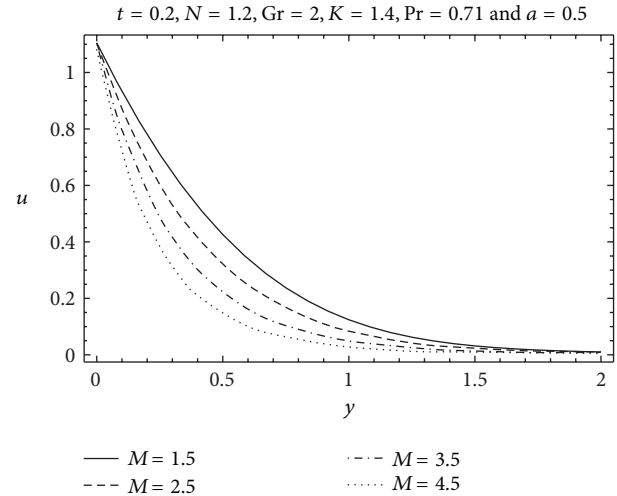
for  $b \neq 1$  and

$$\begin{aligned} \tau &= \frac{e^{at}}{2} \left[ \frac{1}{\sqrt{t\pi}} e^{-(a+H)t} + \sqrt{H+a} \operatorname{erfc}\left(\sqrt{(H+a)t}\right) \right] \\ &\quad + \frac{\operatorname{Gr}}{H} \left[ 1 - \frac{1}{\pi} \int_0^H \frac{\sqrt{H+x}}{x^{3/2}} [1 - e^{-tx}] dx \right] \end{aligned} \quad (20)$$

for  $b = 1$ .

### 3. Limiting Case $N \rightarrow \infty$ (in the Absence of Radiation)

Exact solutions for the fluid temperature and velocity are provided by (15)–(17). In order to highlight the effect of the corresponding parameters on the fluid flow, as well as for validation of the results, it is important to discuss some limiting cases of general solutions. In the absence of

FIGURE 1: Velocity profiles for different values of  $N$ .FIGURE 2: Velocity profiles for different values of  $M$ .

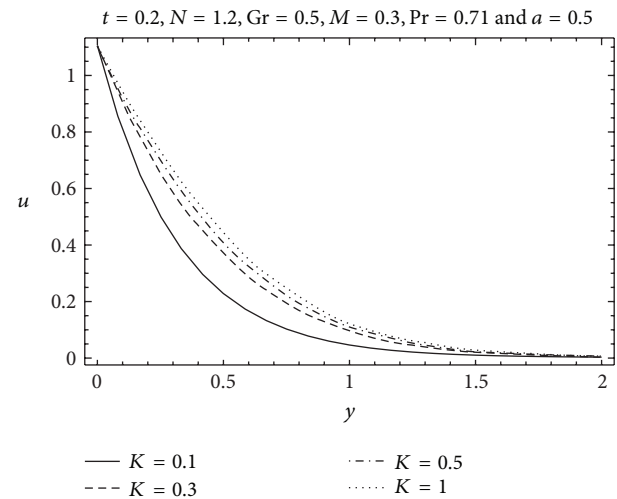
thermal radiation, that is, in the pure convection case which numerically corresponds to  $N \rightarrow \infty$ , the non-dimensional temperature  $\theta(y, t)$  takes the form

$$\theta(y, t) = \frac{1}{\sqrt{\text{Pr}}} \left[ 2\sqrt{\frac{t}{\pi}} \exp\left(-\frac{y^2 \text{Pr}}{4t}\right) - y\sqrt{\text{Pr}} \operatorname{erfc}\left(\frac{y\sqrt{\text{Pr}}}{2\sqrt{t}}\right) \right], \quad (21)$$

obtained in Chaudhary et al. [11, equation (15)]. Moreover, (16) and (17) for  $N \rightarrow \infty$  and  $a = 0$  reduce to the velocity profiles obtained in Chaudhary et al. [11, equations (16) and (17)].

#### 4. Numerical Results and Discussion

In order to get physical insight into the problem, the obtained solutions are numerically discussed to investigate the effects of different parameters such as radiation parameter  $N$ , magnetic parameter  $M$ , permeability parameter  $K$ , Prandtl number  $\text{Pr}$ , and Grashof number  $\text{Gr}$  on the velocity, temperature, and skin friction. The values of  $\text{Pr}$  are chosen 0.71, 1, and 7 which represent air, electrolytic solution, water at 20°C, respectively. Figure 1 elucidates the effect of radiation parameter  $N$  on the velocity profiles of air ( $\text{Pr} = 0.71$ ). It is observed that the fluid velocity decreases with increasing values of radiation parameter  $N$ . Figure 2 reveals velocity profiles due to the variations of the magnetic parameter  $M$ . The velocity of the fluid is decreasing with increasing values of  $M$ . It is physically justified due to the fact that increasing  $M$  increases frictional force which tends to resist the fluid flow and thus reducing its velocity. Figure 3 exhibits the velocity profiles for different values of the permeability parameter  $K$ . It is obvious from the figure that an increase in  $K$  decreases the resistance of the porous medium and so causes the velocity to increase. In Figure 4, the velocity profiles are shown for different values of Grashof number  $\text{Gr}$ . An increase in  $\text{Gr}$  gives rise to buoyancy effects which

FIGURE 3: Velocity profiles for different values of  $K$ .

results in more induced flows. So the velocity of the fluid increases with increasing values of  $\text{Gr}$ . Figure 5 represents the velocity profiles due to the variations of Prandtl number  $\text{Pr}$ . It is noted that the velocity for  $\text{Pr} = 0.71$  is higher than that for  $\text{Pr} = 1.0$  and  $\text{Pr} = 7.0$ , which is possible because fluids with high Prandtl number have high viscosity and hence move slowly. Figure 6 illustrates the variation of velocity profiles for different values of accelerating parameter  $a$ . It is found that the fluid velocity increases with increasing values of  $a$ . It is seen from Figure 7 that the velocity increases with an increase in time  $t$  near the plate and then decays to zero asymptotically.

The temperature profiles of air ( $\text{Pr} = 0.71$ ) are shown in Figures 8 and 9 for different values of  $N$  and  $t$ . It is depicted from Figure 8 that temperature decreases due to an increase in the radiation parameter  $N$ . This may be explained by the fact that radiation provides an additional means to diffuse energy. It is observed from Figure 9 that temperature increases with increasing time in the presence of radiation.

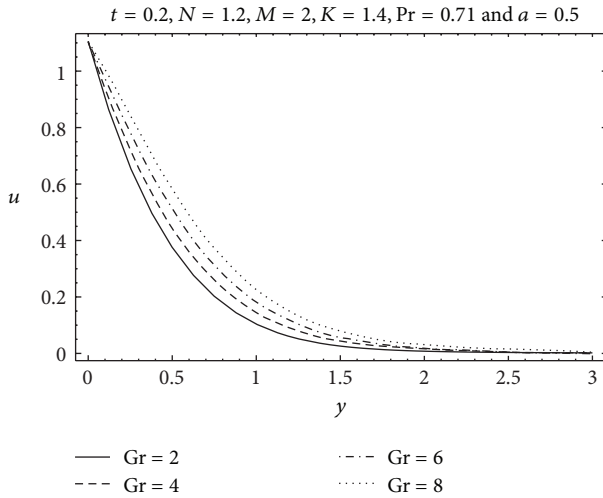


FIGURE 4: Velocity profiles for different values of Gr.

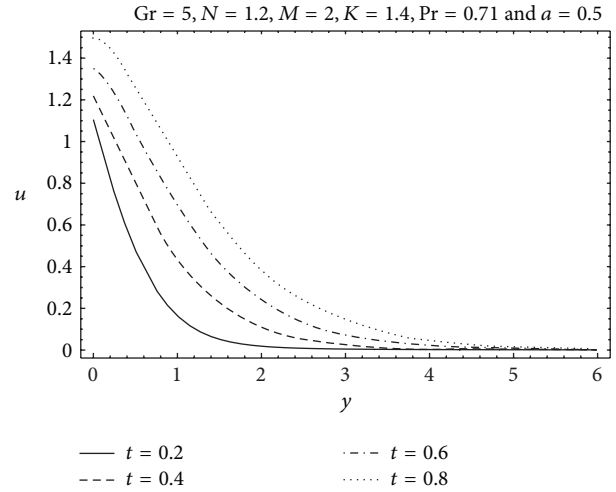


FIGURE 7: Velocity profiles for different values of  $t$ .

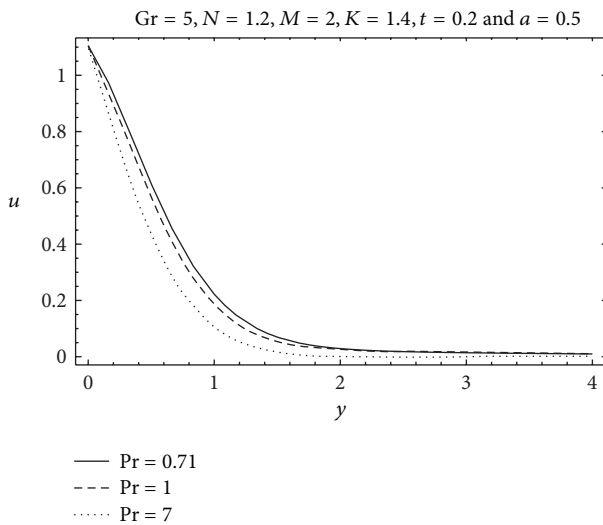


FIGURE 5: Velocity profiles for different values of Pr.

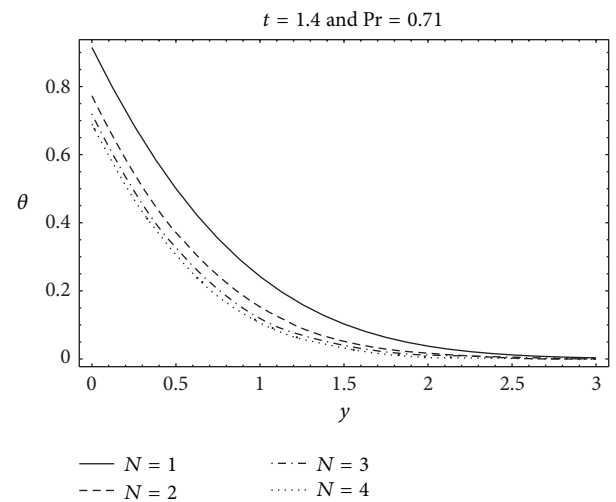


FIGURE 8: Temperature profiles for different values of  $N$ .

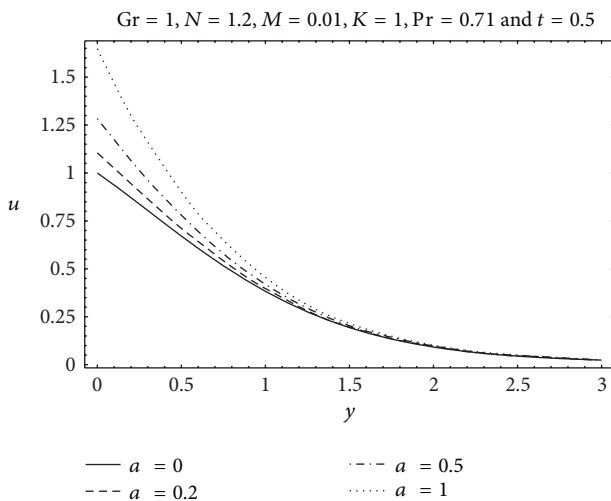


FIGURE 6: Velocity profiles for different values of  $a$ .

Figure 10 illustrates the variation of temperature profiles for different values of Prandtl number Pr. It reveals that the magnitude of the temperature for air is greater than those for electrolytic solution and water. It is due to the fact that thermal conductivity of fluid decreases with increasing Pr, which results a decrease in thermal boundary layer thickness.

The skin friction variation along time  $t$  is shown in Figures 11–13. Figures 11 and 12 elucidate the effects of  $N$  and  $M$  on the skin friction. It is clear that skin friction increases with increasing values of the radiation parameter  $N$  or magnetic parameter  $M$ . It is observed from Figure 13 that skin friction decreases with an increase in the permeability parameter  $K$ . It is justified as increasing values of  $K$  decreases the retarding effect of porous medium on the flow.

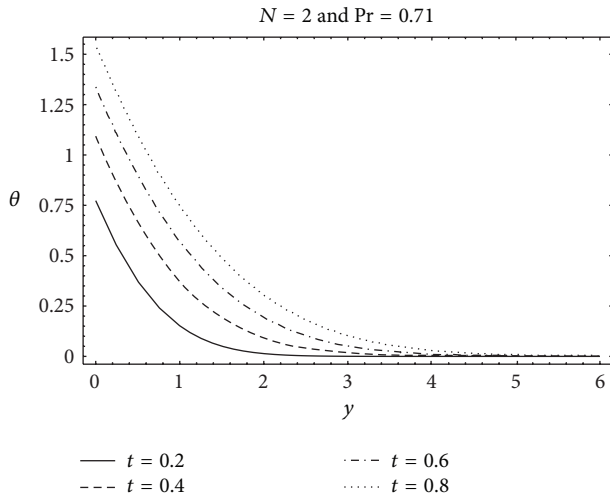


FIGURE 9: Temperature profiles for different values of  $t$ .

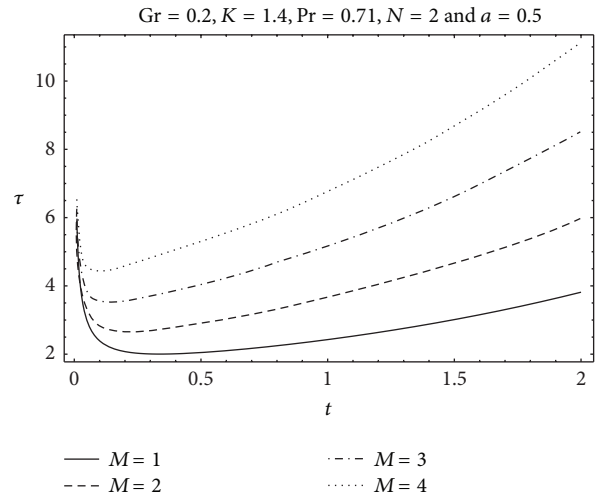


FIGURE 12: Skin friction profiles for different values of  $M$ .

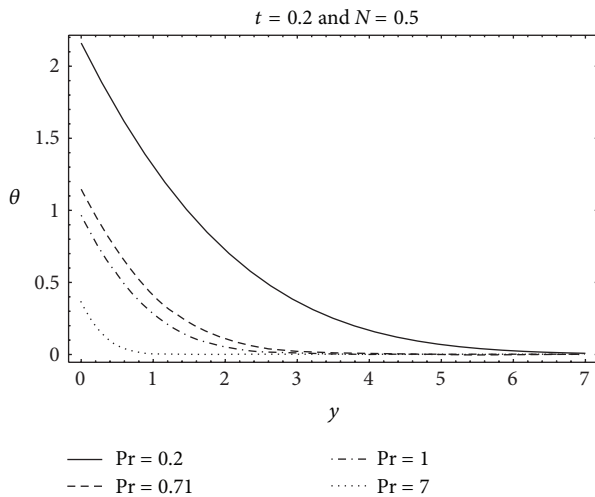


FIGURE 10: Temperature profiles for different values of  $Pr$ .

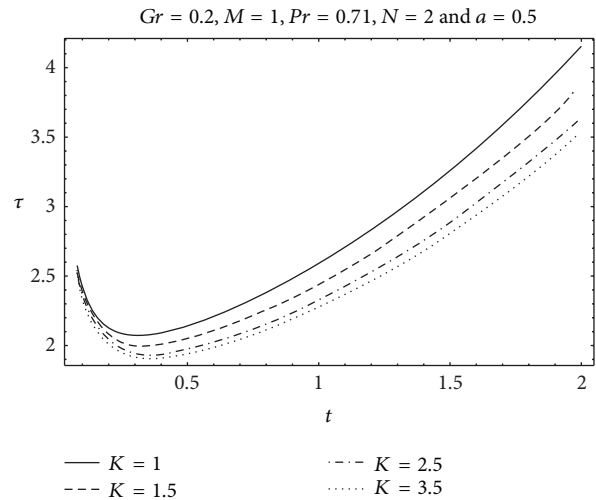


FIGURE 13: Skin friction profiles for different values of  $K$ .

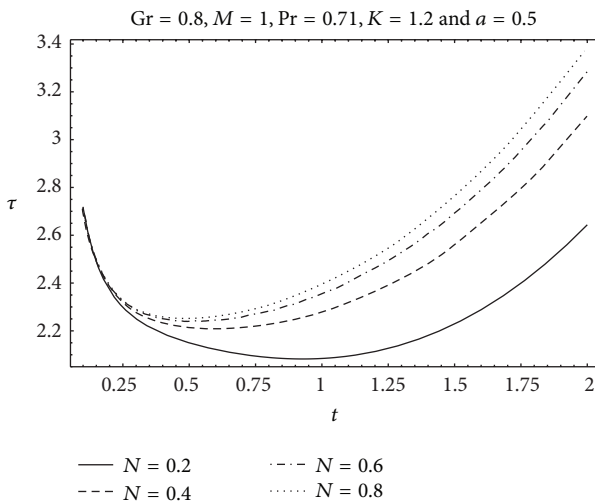


FIGURE 11: Skin friction profiles for different values of  $N$ .

### 5. Conclusions

We have studied the MHD free convection flow of an incompressible viscous fluid past an exponentially accelerated vertical plate embedded in porous medium with uniform heat flux in the presence of thermal radiation. The major findings of the study are summarized as follows.

- (1) The velocity of the fluid increases due to an increase in the permeability parameter  $K$ , Grashof number  $Gr$ , accelerating parameter  $a$ , and time  $t$ .
- (2) An increase in radiation parameter  $N$ , magnetic parameter  $M$ , and Prandtl number  $Pr$  retards the velocity of the fluid.
- (3) The growing values of  $N$  and  $Pr$  reduce the temperature of the fluid.
- (4) The temperature of the fluid increases with time  $t$ .

- (5) The skin friction  $\tau$  is enhanced due to an enhancement in  $N$  and  $M$ .
- (6) An increase in  $K$  reduces the skin friction.

## Acknowledgment

The authors would like to acknowledge the Research Management Centre, UTM, for the financial support through vote numbers 4F109, 04H27 and 02H80 for this research.

## References

- [1] G. G. Stokes, "On the effect of the internal friction of fluids on the motion of pendulums," *Cambridge Philosophical Society Transactions*, vol. 9, pp. 8–106, 1851.
- [2] V. M. Soundalgekar, "Free convection effects on the stokes problem for an infinite vertical plate," *Journal of Heat Transfer*, vol. 99, no. 3, pp. 499–501, 1977.
- [3] A. K. Singh and N. Kumar, "Free-convection flow past an exponentially accelerated vertical plate," *Astrophysics and Space Science*, vol. 98, no. 2, pp. 245–248, 1984.
- [4] V. M. Soundalgekar, S. K. Gupta, and R. N. Aranake, "Free convection effects on MHD Stokes problem for a vertical plate," *Nuclear Engineering and Design*, vol. 51, no. 3, pp. 403–407, 1979.
- [5] B. Gebhart, Y. Jaluria, R. L. Mahajan, and B. Sammakia, *Buoyancy Induced Flows and Transport*, Hemisphere Publishing Corporation, New York, NY, USA, 1988.
- [6] D. A. Nield and A. Bejan, *Convection in Porous Media*, Springer, New York, NY, USA, 2nd edition, 1999.
- [7] A. Bejan and A. D. Kraus, Eds., *Heat Transfer Handbook*, Wiley, New York, NY, USA, 2003.
- [8] D. B. Ingham, A. Bejan, E. Mamut, and I. Pop, Eds., *Emerging Technologies and Techniques in Porous Media*, Kluwer Academic Publishers, Dordrecht, The Netherlands, 2004.
- [9] V. Rajesh and S. V. K. Varma, "Radiation effects on MHD ow through a porous medium with variable temperature or variable mass diffusion," *Journal of Applied Mathematics and Mechanics*, vol. 6, no. 1, pp. 39–57, 2010.
- [10] P. Chandrakala and P. N. Bhaskar, "Thermal radiation effects on MHD flow past a vertical oscillating plate," *International Journal of Applied Mechanics and Engineering*, vol. 14, pp. 379–358, 2009.
- [11] R. C. Chaudhary, M. C. Goyal, and A. Jain, "Free convection effects on mhd flow past an infinite vertical accelerated plate embedded in porous media with constant heat flux," *Matemáticas*, vol. 17, no. 2, pp. 73–82, 2009.
- [12] P. Chandrakala and P. N. Bhaskar, "Effects of heat transfer on flow past an exponentially accelerated vertical plate with uniform heat flux," *International Journal of Dynamics of Fluids*, vol. 7, pp. 9–15, 2011.
- [13] J. H. Spurk, *Fluid Mechanics*, Springer, Berlin, Germany, 1997.
- [14] V. M. Soundalgekar, "Free convection effects on the oscillatory flow past an infinite, vertical, porous plate with constant suction—II," *Proceedings of the Royal Society of London*, vol. 333, no. 1592, pp. 37–50, 1973.
- [15] M. K. Chowdhury and M. N. Islam, "MHD free convection flow of visco-elastic fluid past an infinite vertical porous plate," *Heat and Mass Transfer/Waerme- und Stoffuebertragung*, vol. 36, no. 5, pp. 439–447, 2000.
- [16] C. J. Toki, "Unsteady free-convection flow on a vertical oscillating porous plate with constant heating," *Journal of Applied Mechanics, Transactions ASME*, vol. 76, no. 1, pp. 1–4, 2009.

## Research Article

# CFD Simulation of Heat Transfer and Friction Factor Augmentation in a Circular Tube Fitted with Elliptic-Cut Twisted Tape Inserts

Sami D. Salman,<sup>1,2</sup> Abdul Amir H. Kadhum,<sup>1</sup> Mohd S. Takriff,<sup>1</sup> and Abu Bakar Mohamad<sup>1</sup>

<sup>1</sup> Department of Chemical and Process Engineering, Faculty of Engineering and Built Environment, Universiti Kebangsaan Malaysia, 43600 Bangi, Selangor, Malaysia

<sup>2</sup> Biochemical Engineering Department, Al-Khwarizmi College of Engineering, University of Baghdad, Baghdad 47024, Iraq

Correspondence should be addressed to Sami D. Salman; [sami.albayati@gmail.com](mailto:sami.albayati@gmail.com)

Received 30 April 2013; Accepted 10 June 2013

Academic Editor: Tirivanhu Chinyoka

Copyright © 2013 Sami D. Salman et al. This is an open access article distributed under the Creative Commons Attribution License, which permits unrestricted use, distribution, and reproduction in any medium, provided the original work is properly cited.

This paper presents the application of a mathematical model for simulation of the swirling flow in a tube induced by elliptic-cut and classical twist tape inserts. Effects of the twist ratio ( $\gamma = 2.93, 3.91, \text{ and } 4.89$ ) and cut depth ( $w = 0.4, 0.8, \text{ and } 1.4 \text{ cm}$ ) on heat transfer enhancement (Nu) and friction factor ( $f$ ) in laminar flow are numerically investigated. The simulation is carried out using commercial CFD package (FLUENT-6.3.26) to grasp the physical behaviour of the thermal and fluid flows of a constant heat-fluxed tube fitted with elliptic-cut twist tape in the laminar flow regime for the Reynolds number ranging from 200 to 2100. The simulated results matched the literature correlations of plain tube for validation with 8% variation for Nusselt number and 10% for friction factor. The results show that the heat transfer rate and friction factor in the tube equipped with elliptic-cut twist tape (ECT) are significantly higher than those fitted with classical twist tape (CTT). Moreover the results also reveal that the Nusselt number and the friction factor in the tube with elliptic-cut twisted tape (ECT) increase with decreasing twist ratios ( $\gamma$ ) and cut depths ( $w$ ).

## 1. Introduction

The heat transfer augmentation techniques are widely utilized in many applications in the heating process to enable reduction in weight and size or increase the performance of heat exchangers. These techniques are classified as active and passive techniques. The active technique required external power such as surface vibration and electric or acoustic fields, whereas the passive techniques required fluid additives, special surface geometries, or swirl/vortex flow devices, that is, twisted tape inserts. The passive techniques are advantageous compared with the active techniques because the swirl inserts manufacturing process is simple and can be easily employed in an existing heat exchanger. Moreover the passive techniques can play an important role in the heat transfer augmentation if a proper configuration of the insert is being selected depending on working conditions that have been reported in the literature [1–9]. Due to advances in computer software, the Computational Fluid Dynamics (CFD)

modelling technique was developed as a powerful and effective tool for more understanding the hydrodynamics of heat transfer when using twist tape inserts.

Zhang et al. [10] investigated the heat transfer characteristics of a helically baffled heat exchanger combined with a finned tube using CFD modeling. Sivashanmugam et al. [11] reported the modeling of heat transfer augmentation in circular tube fitted with helical twist insert in a laminar and turbulent flows using CFD.

Eiamsa-ard et al. [12] have conducted a numerical study on a tube equipped with loose-fit twisted tapes using four turbulence models. The results showed that the prediction obtained by SST  $k$ - $\omega$  turbulence model has a better agreement with measurement results compared with other models.

Nagrajam and Sivashanmugam [13] conducted CFD simulations of heat transfer characteristics of  $\text{Al}_2\text{O}_3$  nanofluid in a circular tube fitted with helical twist inserts under constant heat flux using Fluent version 6.3.26. Different concentrations of  $\text{Al}_2\text{O}_3$  nanoparticles (0.5%, 1.0%, and 1.5%) and twist tape

TABLE 1: Thermophysical properties of materials at 298 K.

Materials	Density (Kg/m <sup>3</sup> )	Specific heat (J/kg K)	Thermal conductivity (W/m K)	Viscosity (Pa s)
Water	998.2	4182	0.6	0.001003
Steel	8030	502.48	16.27	—
Aluminium	2719	871	202.4	—



FIGURE 1: Elliptic-cut twisted insert.

inserts with different twist ratios ( $y = 2.93, 3.91, \text{ and } 4.89$ ) have been used for the simulation. The results showed that the Nusselt number and the friction factor are increased with increasing the nanofluid concentration and decreasing the twist ratios ( $y$ ).

Pathipakka and Sivashanmugam [14] proposed CFD simulation of heat transfer and friction factor behavior for the circular tube fitted with right-left helical twist insert with 100 mm spacer. The simulated Nusselt number and friction factor were compared with the experimental data and observed to have good agreement.

Shabaniyan et al. [15] have carried out an experimental and CFD modeling on heat transfer and friction factor characteristics in air cooled heat exchanger using butterfly twist tape insert. They found that the insert configuration has a main effect on the Nusselt number, friction factor, and thermal performance factor and the maximum thermal performance factor was obtained by the configuration of butterfly insert with an inclined angle of  $90^\circ$ . The results verified that there was a good agreement between the predicted and measured values of Nusselt number and friction factor values.

In the present study, a new configuration of twist tape inserts is presented using CFD simulation to predict the Nusselt number and friction factor in laminar flow regimes based on experimental data listed in [14]. This study can be used as guideline for experimental works.

## 2. Physical Model

The geometry of the elliptic-cut twisted tape (ECT) insert is illustrated in Figure 1. Twist tape with thickness ( $t$ ) of 0.08 cm and width ( $W$ ) of 2.45 cm and relative twisted ratios ( $y = 2.93, 3.91, \text{ and } 4.89$ ) fits in a tube with a diameter ( $D$ ) of 2.54 cm and length ( $L$ ) of 180 cm. Different cut depth ( $w = 0.4, 0.8, \text{ and } 1.4$  cm) is used for twisted tape with twist ratio  $y = 2.93$ . Steel and aluminium were selected as the material of construction of the tube and twisted tape. Water was selected as the working fluid, and the thermophysical properties were assumed to be temperature independent. The thermophysical properties of water and materials used for simulation are listed in Table 1.

The Reynolds number ( $Re$ ), the Nusselt number ( $Nu$ ), and the friction factor ( $f$ ) are defined by the following equations:

$$\begin{aligned} Re &= \frac{\rho u D}{\mu}, \\ Nu &= \frac{h D}{k}, \\ f &= \frac{16}{Re}, \end{aligned} \quad (1)$$

where  $\rho$  is the density,  $u$  is velocity,  $\mu$  is dynamic viscosity, and  $k$  is the thermal conductivity of the fluid.  $h$  is the heat transfer coefficient, and  $D$  is the inner diameter of the tube.

## 3. Numerical Simulations

Three-dimensional numerical simulation of the conjugate heat transfer was conducted using the CFD code FLUENT 6.3.26. The modeling was carried out in order to predict and explain the effect of elliptic-cut configuration on the Nusselt number and friction factor at steady-state laminar flow for constant heat-fluxed tube. The CFD modeling involves numerical solutions of the conservation equations for mass, momentum, and energy. These equations for incompressible flows can be written as follows.

3.1. *Continuity Equation for an Incompressible Fluid.* It is given as follows:

$$\frac{\partial \rho}{\partial t} + \nabla \cdot (\rho \vec{v}) = S_m. \quad (2)$$

3.2. *Conservation of Momentum.* It is given as follows:

$$\rho \frac{\partial \vec{v}}{\partial t} + \rho (\vec{v} \cdot \nabla) \vec{v} = -\nabla p + \rho \vec{g} + \nabla \cdot \tau_{ij} + \vec{F}. \quad (3)$$

3.3. *Conservation of Energy.* It is given as follows:

$$\begin{aligned} \frac{\partial}{\partial t} (\rho E) + \nabla \cdot \{ \vec{v} (\rho E + p) \} \\ = \nabla \cdot \left\{ K_{\text{eff}} \nabla T - \sum_j h_j (\vec{\tau}_{\text{eff}} \cdot \vec{v}) \right\} + S_h. \end{aligned} \quad (4)$$

## 4. Geometry and Grid Arrangement

The geometry and the grid of plain tube and elliptic-cut twisted tape were generated in GAMBIT and the CFD code

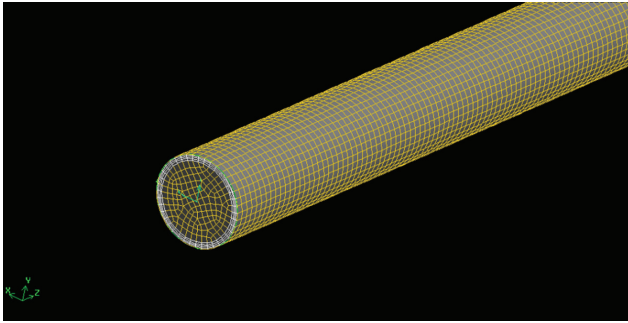


FIGURE 2: Grid for the plain tube.

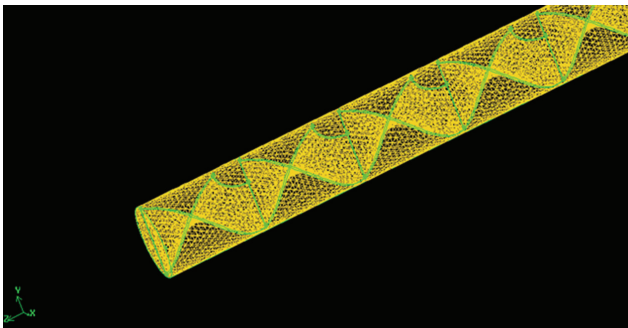


FIGURE 3: Grid for the plain tube with elliptic-cut twisted tape (ECT) insert.

FLUENT was used for simulation. The geometry consists of a cylindrical tube of diameter 25.54 cm and length of 180 cm. Figure 2 shows the grid for the plain tube configuration using a quadrilateral face mesh over the volume of the cylinder. Different types of meshing twisted tapes are available to mesh the volume but tetrahedral/hybrid and T grid type elements were the best mesh for irregular shapes. The grid generated in the tube fitted with ECT inserts is shown in Figure 3. The boundary conditions for the geometry were defined for inlet, outlet, wall of twist tape and cylinder wall, the continuum volume of fluid was defined as water. The mesh file is exported to FLUENT successfully.

### 5. Modeling Parameters

Numerical values of experimental data mentioned in [14] were used in a number of simulations that are given in Table 2.

### 6. Numerical Method

The commercial CFD package of Fluent 6.3.26 software was chosen as the CFD tool to solve the Navier-Stokes equation in common with energy equation accompanied with boundary conditions. Solution sequential algorithm (segregated solver algorithm) has been used with the following settings; implicit formulation, steady (time-independent) calculation, viscous laminar model, and energy equation.

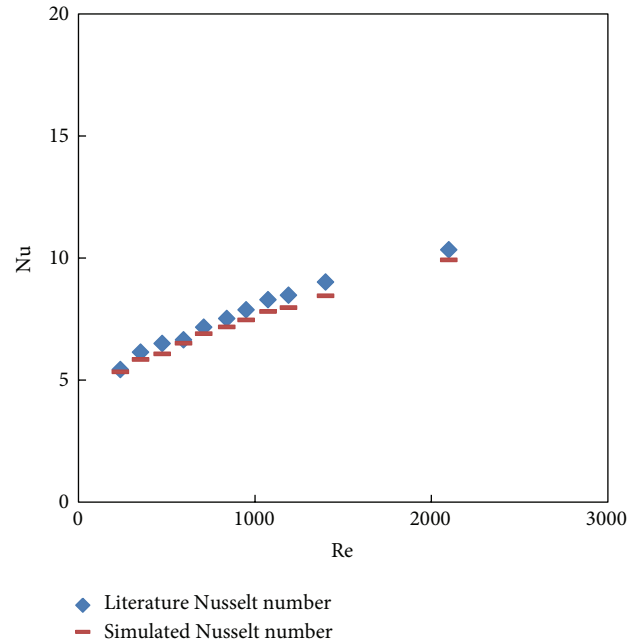


FIGURE 4: Plain tube simulated Nusselt number versus literature data.

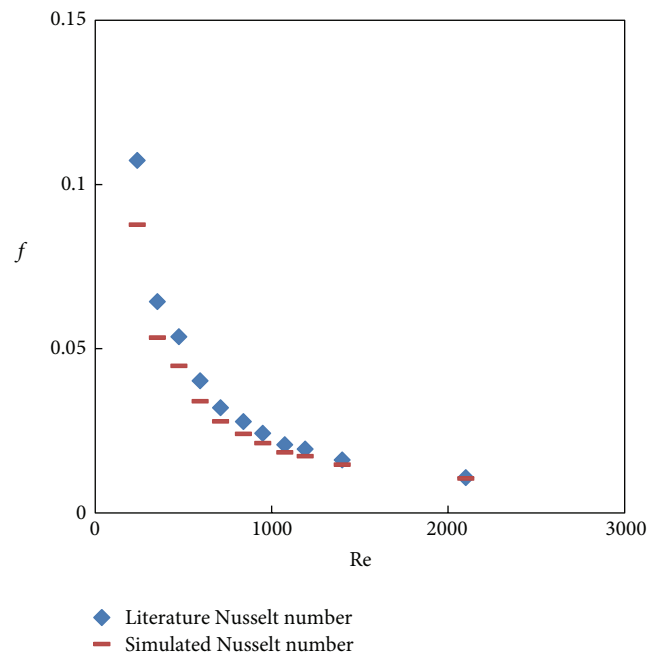


FIGURE 5: Plain tube simulated friction factor versus literature data.

## 7. Results and Discussion

7.1. Validation of Plain Tube Simulation Results. The simulated results of Nusselt number and friction factor for plain tube were compared with the correlations developed by Sieder and Tate [16] for validation. The predicted values of Nusselt number and friction factor are demonstrated in Figures 4 and 5; apparently, the present results reasonably

TABLE 2: Numerical values of the parameters used for simulations [14].

Flow rate (kg/sec)	0.003	0.005	0.006	0.008	0.01	0.116	0.0133	0.015	0.0166	0.02	0.03
Heat flux (w/m <sup>2</sup> )	240.03	340.77	459.15	563.38	749.85	1001.57	1363.26	1512.68	1893.56	2130.05	2445.25

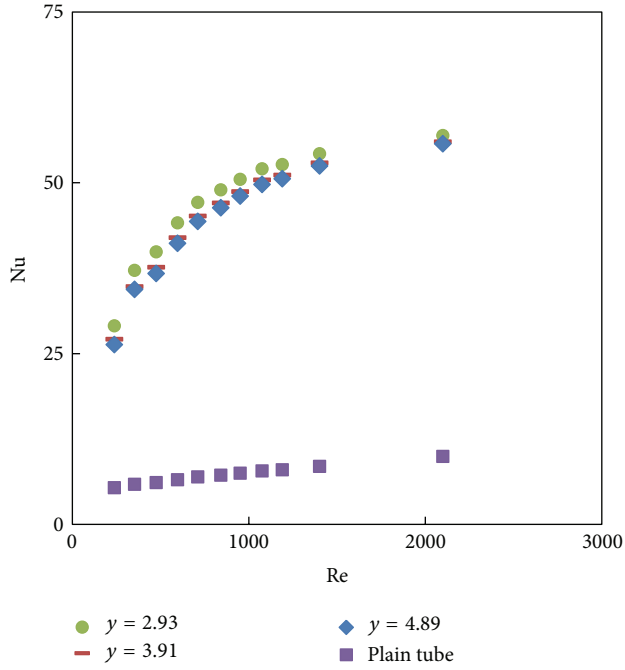


FIGURE 6: Simulated Nusselt number for plain tube and twisted tape with different twist ratios ( $\gamma$ ).

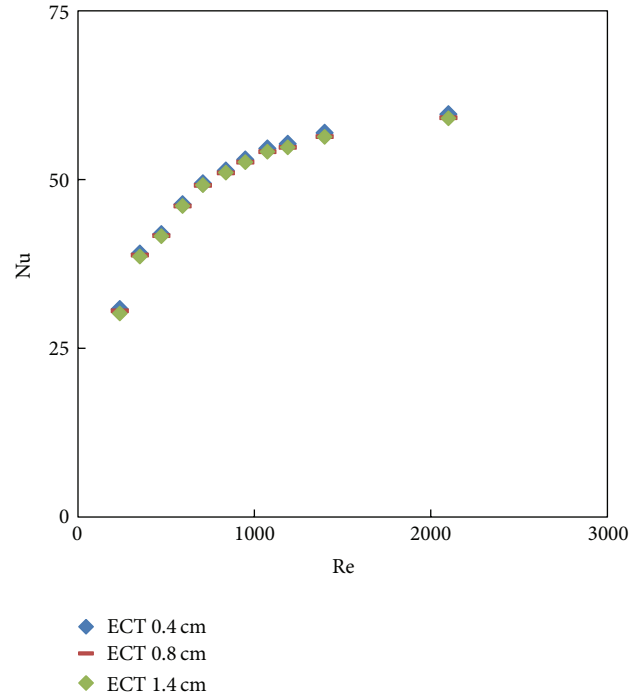


FIGURE 8: Simulated Nusselt number for elliptic-cut twisted tape with  $\gamma = 2.93$  and different cut depth ( $w$ ).

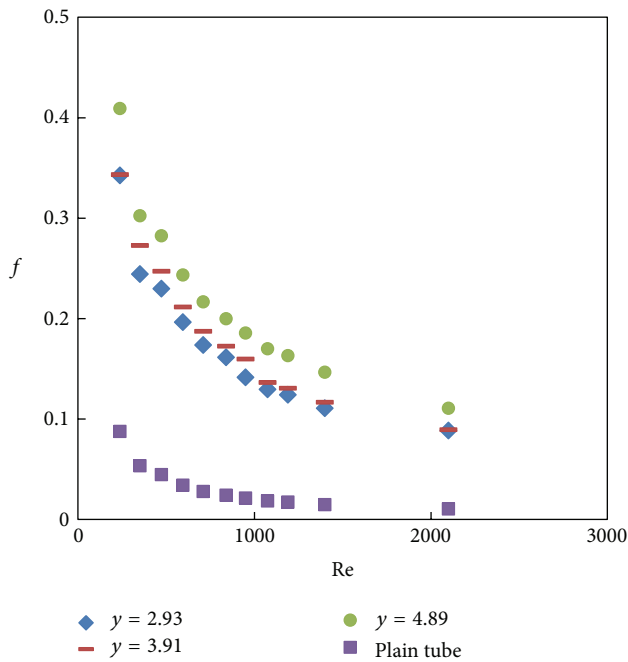


FIGURE 7: Simulated friction factor for plain tube twisted tape with different twist ratios ( $\gamma$ ).

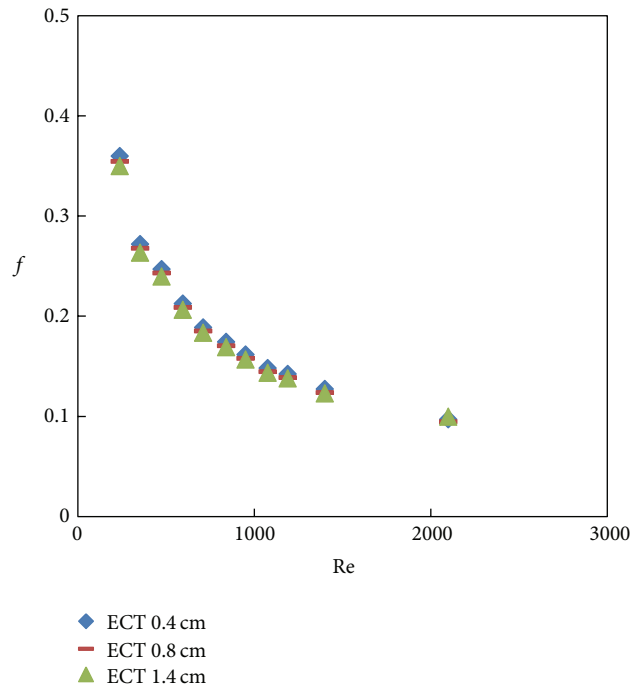


FIGURE 9: Simulated friction factor for elliptic-cut twisted tape with  $\gamma = 2.93$  and different cut depth ( $w$ ).

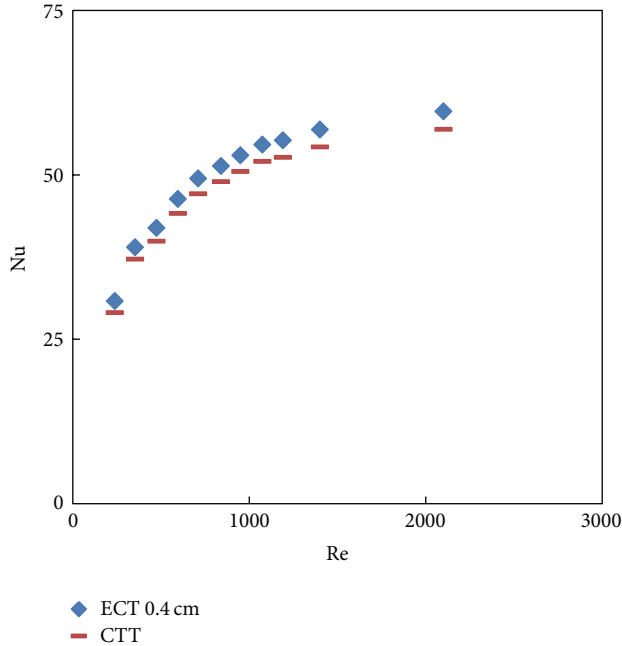


FIGURE 10: Simulated Nusselt number for elliptic-cut twisted tape (ECT) and classical twist tape (CTT).

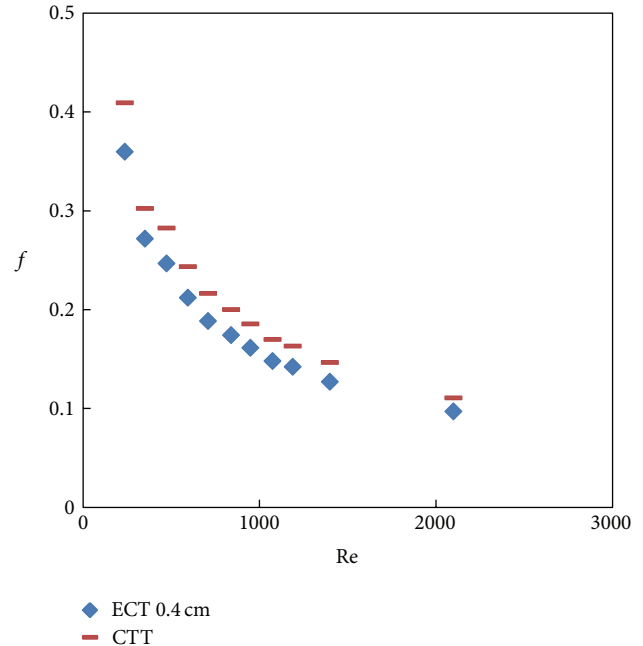


FIGURE 11: Simulated friction factor for elliptic-cut twisted tape (ECT) and classical twist tape (CTT).

agree well with the available correlations with 8% variation for Nusselt number and 20% for friction factor.

7.2. Effect of Twist Ratio on Heat Transfer and Friction Factor.

The simulated data of the Nusselt number and friction factor and their variation with a Reynolds number of cut twisted tape inserts with twist ratios ( $\gamma = 2.93, 3.91, \text{ and } 4.89$ ) are shown in Figures 6 and 7. Figure 6 indicates that the Nusselt number increases with Reynolds number increasing and the heat transfer rate is higher for the twist tape set than for the plain tube because of strong swirl flow in the presence of the twist tape. It is found that the heat transfer rate with the twist ratio ( $\gamma = 2.93$ ) is higher than those with other ratios ( $\gamma = 3.91$  and  $4.89$ ); this means that the turbulent intensity obtained from the lower twist ratio is higher than those from higher ratios ( $\gamma$ ). Figure 7 shows the variation of friction factor with a Reynolds number for different twist ratios ( $\gamma = 2.93, 3.91, \text{ and } 4.89$ ). The friction factor obtained from the tube with twisted tape insert is significantly higher than the plain tube. Moreover, the use of smaller twist ratio leads to higher tangential contact between the swirling flow and the tube surface. Therefore, the twisted tape with twist ratio ( $\gamma = 2.93$ ) has a maximum friction factor.

7.3. Effect of Cut Depth on Heat Transfer and Friction Factor.

The Nusselt number and friction factor and their variation with a Reynolds number of ECT inserts with twist ratio  $\gamma = 2.93$  and cut depth ( $w = 0.4, 0.8, \text{ and } 1.4$  cm) are shown in Figures 8, 9, 10, and 11. For a given Reynolds number, Nusselt number and friction factor are increased with decreasing the cut depth; this is mainly due to the combined effect of common swirling flow by the twisted tape and turbulence

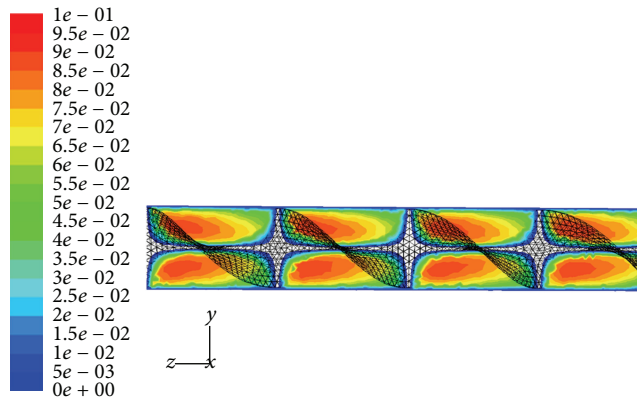


FIGURE 12: The velocity field of classical twist tape in an axial slice inside the tube.

generated by the alternative cuts along the edge of the twisted tape. Subsequently this leads to the destruction of the thermal boundary layer and creating better flow mixing between the fluids at the core and heating wall surface.

7.4. Velocity Field.

Figures 12 and 13 show the velocity field of classical and Elliptic-cut twisted tape inserts with a twisted ratio ( $\gamma = 2.93$ ) and cut depth ( $w = 0.4$ ) for  $Re = 2300$ . The figures illustrate that the predicted velocity in tube fitted with elliptic-cut twisted tape insert is higher than the classical twist tape insert and the vortices generated by the alternative cuts along the edge of the twisted tape are higher than those of classical twist tape. This can be the reason for more heat

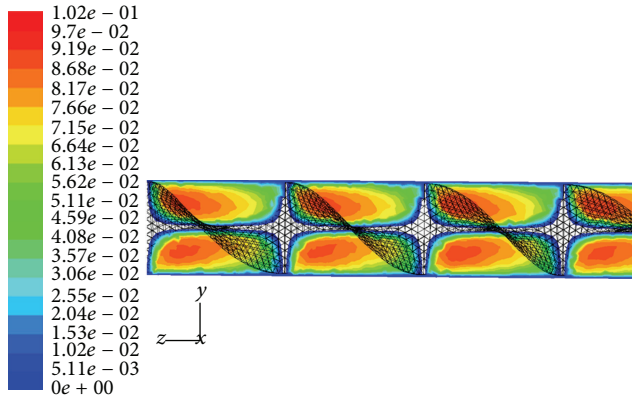


FIGURE 13: The velocity field of elliptic-cut twist tape in an axial slice inside the tube.

transfer rate obtained by the Elliptic-cut twisted tape as compared to classical twist tape insert.

## 8. Conclusion

In the present study, a circular tube inserted by Elliptic-cut twisted tape and classical twist tape insert with twisted ratios ( $y = 2.93, 3.91, \text{ and } 4.89$ ) and cut depths ( $w = 0.4, 0.8, \text{ and } 1.4 \text{ cm}$ ) in laminar flow conditions has been simulated using fluent version 6.23.26. The data obtained by simulation match the literature value for plain tube with a maximum discrepancy of 8% for Nusselt number and 10% for friction factor. The simulated results show that the elliptic-cut twisted tape with twist ratio ( $y = 2.93$ ) and cut depth ( $w = 0.4 \text{ cm}$ ) offered higher heat transfer rate and friction factor compared to the plain tube and other twisted tape. Furthermore, the influence of the cut depth ( $w = 0.4 \text{ cm}$ ) was more dominant than that of the cut depths ( $w = 0.8 \text{ and } 1.4 \text{ cm}$ ) for all the Reynolds number.

## Nomenclature

$E$ :	Energy component in energy equation
$F$ :	Force component in momentum equation, N
$f$ :	Fanning friction factor
$g$ :	Acceleration due to gravity, $\text{m/s}^2$
$k_{\text{eff}}$ :	Thermal conductivity in energy equation, $\text{W/m K}$
$m$ :	Mass flow rate of fluid, $\text{kg/s}$
Re:	Reynolds number based on internal diameter of the tube, dimensionless
Nu:	Nusselt number, dimensionless
$p$ :	Pressure component in momentum equation, $\text{N/m}^2$
$S_m$ :	Accumulation of mass, $\text{Kg}$
$S_h$ :	Accumulation of energy, $\text{J}$
$T$ :	Temperature, $^{\circ}\text{C}$
$v$ :	Velocity component in momentum equation, $\text{m/s}$
$y$ :	Twist ratio (length of one twist ( $360^{\circ}$ )/diameter of the twist), dimensionless.

## Greek Symbols

$\rho$ :	Density component in governing equations
$\vec{\tau}_{\text{eff}}$ :	Stress component in momentum equation, $\text{N/m}^2$ .

## Acknowledgments

The authors would like to thank Universiti Kebangsaan Malaysia and MOSTI of Grant Research (FRGS/1/2013/TK07/UKM/01/1) for financial support.

## References

- [1] L. Wang and B. Sundén, "Performance comparison of some tube inserts," *International Communications in Heat and Mass Transfer*, vol. 29, no. 1, pp. 45–56, 2002.
- [2] A. Ujhidy, J. Németh, and J. Szépvölgyi, "Fluid flow in tubes with helical elements," *Chemical Engineering and Processing*, vol. 42, no. 1, pp. 1–7, 2003.
- [3] S. Jaisankar, T. K. Radhakrishnan, and K. N. Sheeba, "Experimental studies on heat transfer and friction factor characteristics of thermosyphon solar water heater system fitted with spacer at the trailing edge of twisted tapes," *Applied Thermal Engineering*, vol. 29, no. 5-6, pp. 1224–1231, 2009.
- [4] J. Guo, A. Fan, X. Zhang, and W. Liu, "A numerical study on heat transfer and friction factor characteristics of laminar flow in a circular tube fitted with center-cleared twisted tape," *International Journal of Thermal Sciences*, vol. 50, no. 7, pp. 1263–1270, 2011.
- [5] K. Wongcharee and S. Eiamsa-ard, "Friction and heat transfer characteristics of laminar swirl flow through the round tubes inserted with alternate clockwise and counter-clockwise twisted-tapes," *International Communications in Heat and Mass Transfer*, vol. 38, no. 3, pp. 348–352, 2011.
- [6] E. Z. Ibrahim, "Augmentation of laminar flow and heat transfer in flat tubes by means of helical screw-tape inserts," *Energy Conversion and Management*, vol. 52, no. 1, pp. 250–257, 2011.
- [7] S. K. Saha, U. N. Gaitonde, and A. W. Date, "Heat transfer and pressure drop characteristics of turbulent flow in a circular tube fitted with regularly spaced twisted-tape elements," *Experimental Thermal and Fluid Science*, vol. 3, no. 6, pp. 632–640, 1990.
- [8] R. M. Manglik and A. E. Bergles, "Heat transfer and pressure drop correlations for twisted-tape inserts in isothermal tubes—part II: transition and turbulent flows," *Journal of Heat Transfer*, vol. 115, no. 4, pp. 890–896, 1993.
- [9] V. K. Naumov and N. N. Semashko, "Analytical model of estimating thermo-physical and strength parameters of cooled pipe with the twisted tape under asymmetric heating by a pulse of external heat flux," *Plasma Devices and Operations*, vol. 3, no. 4, pp. 267–280, 1994.
- [10] Z. Zhang, D. Ma, X. Fang, and X. Gao, "Experimental and numerical heat transfer in a helically baffled heat exchanger combined with one three-dimensional finned tube," *Chemical Engineering and Processing*, vol. 47, no. 9-10, pp. 1738–1743, 2008.
- [11] P. Sivashanmugam, P. K. Nagarajan, and S. Suresh, "Experimental studies on heat transfer and friction factor characteristics of turbulent flow through a circular tube fitted with right and left helical screw-tape insert," *Chemical Engineering Communications*, vol. 195, no. 8, pp. 977–987, 2008.

- [12] S. Eiamsa-ard, K. Wongcharee, and S. Sripattanapipat, "3-D numerical simulation of swirling flow and convective heat transfer in a circular tube induced by means of loose-fit twisted tapes," *International Communications in Heat and Mass Transfer*, vol. 36, no. 9, pp. 947–955, 2009.
- [13] P. K. Nagrajam and P. Sivashanmugam, "CFD Simulation of heat transfer augmentation in circular tube filled with right-left helical inserts with spacer," *International Journal of Chemical Engineering Research*, vol. 6, no. 1, pp. 1–11, 2009.
- [14] G. Pathipakka and P. Sivashanmugam, "Heat transfer behaviour of nanofluids in a uniformly heated circular tube fitted with helical inserts in laminar flow," *Superlattices and Microstructures*, vol. 47, no. 2, pp. 349–360, 2010.
- [15] S. R. Shabani, M. Rahimi, M. Shahhosseini, and A. A. Alsairafi, "CFD and experimental studies on heat transfer enhancement in an air cooler equipped with different tube inserts," *International Communications in Heat and Mass Transfer*, vol. 38, no. 3, pp. 383–390, 2011.
- [16] E. N. Sieder and C. E. Tate, "Heat transfer and pressure drop of liquids in tubes," *Industrial & Engineering Chemistry*, vol. 28, no. 12, pp. 1429–1435, 1936.

## Research Article

# Shock Wave Solutions for Some Nonlinear Flow Models Arising in the Study of a Non-Newtonian Third Grade Fluid

**Taha Aziz, R. J. Moitsheki, A. Fatima, and F. M. Mahomed**

*Centre for Differential Equations, Continuum Mechanics and Applications, School of Computational and Applied Mathematics, University of the Witwatersrand, Wits 2050, South Africa*

Correspondence should be addressed to R. J. Moitsheki; [raseelo.moitsheki@wits.ac.za](mailto:raseelo.moitsheki@wits.ac.za)

Received 28 February 2013; Revised 6 June 2013; Accepted 7 June 2013

Academic Editor: Waqar Khan

Copyright © 2013 Taha Aziz et al. This is an open access article distributed under the Creative Commons Attribution License, which permits unrestricted use, distribution, and reproduction in any medium, provided the original work is properly cited.

This study is based upon constructing a new class of closed-form shock wave solutions for some nonlinear problems arising in the study of a third grade fluid model. The Lie symmetry reduction technique has been employed to reduce the governing nonlinear partial differential equations into nonlinear ordinary differential equations. The reduced equations are then solved analytically, and the shock wave solutions are constructed. The conditions on the physical parameters of the flow problems also fall out naturally in the process of the derivation of the solutions.

## 1. Introduction

A shock wave is a disturbance that propagates through a media. Shock is yielded when a disturbance is made to move through a fluid faster than the speed of sound (the celerity) of the medium. This can occur when a solid object is forced through a fluid. It represents a sharp discontinuity of the parameters that delineate the media. Unlike solutions where the energy is a conserved quantity and thus remains constant during its propagation, shock wave dissipates energy relatively quickly with distance. One source of a shock wave is when the supersonic jets fly at a speed that is greater than the speed of sound. This results in the drag force on aircraft with shocks. These waves also appear in various interesting phenomena in real life situations. For example, solitons appear in the propagation of pulses through optical fibers. Another example is where cnoidal waves appear in shallow water waves, although this is an extremely scarce phenomena. Some interesting communications dealing with the shock wave solutions are found in [1–3].

During the past several decades, the study of the nonlinear problems dealing with the flow of non-Newtonian fluids has attracted considerable attention. This interest is due to several important applications in engineering and industry such as reactive polymer flows in heterogeneous porous media, electrochemical generation of elemental bromine

in porous electrode systems, manufacture of intumescent paints for fire safety applications, extraction of crude oil from the petroleum products, synthetic fibers, and paper production [4]. Due to the diverse physical nature of non-Newtonian fluids, there is no single constitutive expression which describe the physical behavior of all non-Newtonian fluid models. Because of this important issue, several models of non-Newtonian fluids have been proposed in the literature. Together with this factor, the mathematical modelling of non-Newtonian incompressible fluid flows gives rise to nonlinear and complicated differential equations. As a consequence of this nonlinearity factor, the exact (closed-form) solutions of these sort of problems are scarce in general. Several techniques and methods have been developed in the recent few years to construct the solutions of these non-Newtonian fluid flow problems. Some of these useful methods are variational iteration method, Adomian decomposition method, homotopy perturbation method, homotopy analysis method, and semi-inverse variational method. Literature survey witnesses that, despite all these methods, the exact (closed-form) solutions of the non-Newtonian fluid flow problems are still rare in the literature, and it is not surprising that new exact (closed-form) solutions are most welcome, provided they correspond to physically realistic situations. Some interesting and useful communications in this area are made in the studies [5–14].

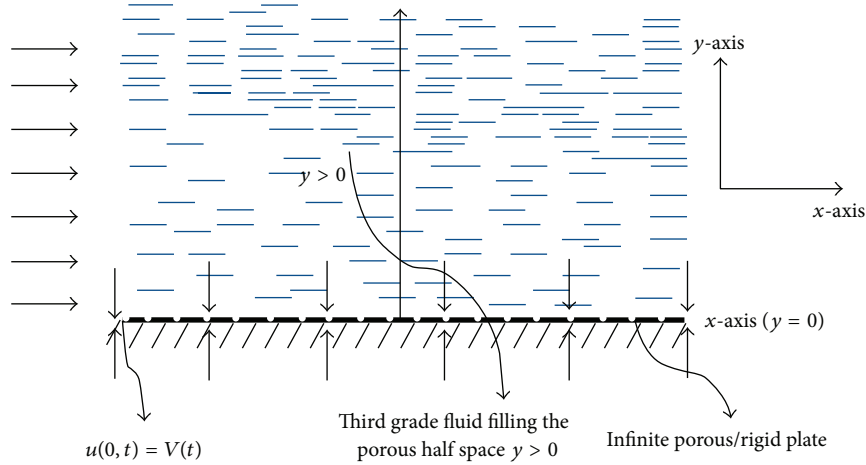


FIGURE 1: Geometry of the physical models and coordinate system.

One of the widely accepted models amongst non-Newtonian fluids is the class of Rivlin-Ericksen fluids of differential type [15]. Rivlin-Ericksen fluids of differential type have acquired the special status in order to describe the several nonstandard features such as normal stress effects, rod climbing, shear thinning, and shear thickening. In the literature much attention has been given to the flow of a second grade fluid [16–19]. A second grade fluid model is the simplest subclass of non-Newtonian fluids for which one can reasonably hope to obtain an analytical solution. In most of the flow situations, the governing equations for a second grade fluid are linear. Although a second grade fluid model is able to predict the normal stress differences, it does not take into account the shear thinning, and shear thickening phenomena that many fluids reveal. Therefore some experiments may be well described by third grade fluid [20–24]. The mathematical model of a third grade fluid represents a more realistic description of the behavior of non-Newtonian fluids. A third grade fluid model represents a further attempt towards the study of the flow properties of non-Newtonian fluids. Therefore, a third grade fluid model has been considered in this study. This model is known to capture the non-Newtonian effects such as shear thinning or shear thickening as well as normal stress.

In this particular study, we have constructed the shock wave solutions of some nonlinear PDEs arising in the study of third grade fluid flow in porous medium. We know that the flow of non-Newtonian fluids in a porous medium has wide range of engineering applications. These include enhanced oil recovery, ceramic processing, and geothermal engineering. Motivated by these facts, we have developed some shock wave solutions of three nonlinear problems dealing with the unsteady flow of third grade fluid in a porous half space.

## 2. Geometry of the Models

Consider a Cartesian coordinate frame of reference  $OXYZ$  with  $x$ -axis along the direction of the flow and  $y$ -axis pointing in the vertically upward direction. The third grade fluid

occupies the porous space  $y > 0$  and is in contact with an infinite plate at  $y = 0$ . Since the plate is infinite in the  $XZ$ -plane, therefore all the physical quantities except the pressure depend on  $y$  only. We have taken three different problems on the same flat plate geometry. The geometry of the problems is shown in Figure 1.

## 3. Problems to Be Investigated

**3.1. Unsteady Flow of a Third Grade Fluid over a Flat Rigid Plate with Porous Medium.** Following the methodology of [22, 23], the unsteady incompressible flow of a third grade fluid over the rigid plate with porous medium is governed by

$$\left(\rho + \alpha_1 \frac{\varphi}{\kappa}\right) \frac{\partial u}{\partial t} = \mu \frac{\partial^2 u}{\partial y^2} + \alpha_1 \frac{\partial^3 u}{\partial y^2 \partial t} + 6\beta_3 \left(\frac{\partial u}{\partial y}\right)^2 \frac{\partial^2 u}{\partial y^2} - 2\beta_3 \frac{\varphi}{\kappa} \left(\frac{\partial u}{\partial y}\right)^2 u - \frac{\varphi}{\kappa} \mu u, \quad (1)$$

where  $u$  is the velocity component in  $x$ -direction,  $t$  is time,  $y$  is spatial variable,  $\rho$  is the density,  $\mu$  is the coefficient of viscosity,  $\alpha_1$  and  $\beta_3$  are the material constants (for details on these material constants and the conditions that are satisfied by these constants, the reader is referred to [24]),  $\varphi$  is the porosity and  $\kappa$  is the permeability of the porous medium.

In order to solve (1), the relevant boundary and initial conditions are

$$u(0, t) = u_0 g(t), \quad t > 0, \quad (2)$$

$$u(\infty, t) = 0, \quad t > 0, \quad (3)$$

$$u(y, 0) = f(y), \quad y > 0, \quad (4)$$

where  $u_0$  is the reference velocity and  $g(t)$  and  $f(y)$  are yet functions to be determined. The first boundary condition (2) is the no-slip condition, and the second boundary condition (3) says that the main stream velocity is zero. This is not a restrictive assumption since we can always measure velocity

relative to the main stream. The initial condition (4) indicates initially that the fluid is moving with some nonuniform velocity  $f(y)$ .

**3.1.1. Reduction of the Governing Equation.** We know that from the principal of Lie symmetry methods [25, 26] that if a differential equation is explicitly independent of any dependent or independent variable, then this particular differential equation remains invariant under the translation symmetry corresponding to that particular variable. We noticed that (1) admits Lie point symmetry generators,  $\partial/\partial t$  (translation in  $t$ ) and  $\partial/\partial y$  (translation in  $y$ ). Let  $X_1$  and  $X_2$  be time-translation and space-translation symmetry generators, respectively. Then the solution corresponding to the generator

$$X = X_1 + mX_2 = \frac{\partial}{\partial t} + m\frac{\partial}{\partial y}, \quad (m > 0) \quad (5)$$

would represent travelling wave solution with constant wave speed  $m$ . Travelling wave solutions are characterized by the fact that the profiles of these solutions at different time instants are obtained from one another by appropriate shifts (translations) along the  $y$ -axis. Consequently, a Cartesian coordinate system moving with the constant speed can be introduced in which the profile of the derived quantity is stationary.  $m = 0$  represents the stationary or steady-state solutions.

The characteristic system corresponding to (5) is

$$\frac{dy}{m} = \frac{dt}{1} = \frac{du}{0}. \quad (6)$$

Solving (6), invariant solutions are given by

$$u(y, t) = F(\eta) \quad \text{with } \eta = y - mt, \quad (7)$$

where  $F(\eta)$  is an arbitrary function of the characteristic variable  $\eta = y - mt$ . Making use of (7) into (1) results in a third-order ordinary differential for  $F(\eta)$  as follows:

$$\begin{aligned} & \left(\rho + \alpha_1 \frac{\varphi}{\kappa}\right) m \frac{dF}{d\eta} + \mu \frac{d^2 F}{d\eta^2} - m\alpha_1 \frac{d^3 F}{d\eta^3} \\ & + 6\beta_3 \left(\frac{dF}{d\eta}\right)^2 \frac{d^2 F}{d\eta^2} - 2\beta_3 \frac{\varphi}{\kappa} F \left(\frac{dF}{d\eta}\right)^2 - \mu \frac{\varphi}{\kappa} F = 0. \end{aligned} \quad (8)$$

Thus the original third-order nonlinear PDE (1) is reduced to a third-order ODE (5) along certain curves in the  $y$ - $t$  plane. These curves are called *characteristic curves* or just the characteristic.

**3.1.2. Shock Wave Solution.** In this section, we show that the travelling wave solutions of (1) approach a shock wave solution. Now we construct the shock wave solution of the reduced equation (5). The starting hypothesis for shock wave solution is given by

$$F(\eta) = a \exp(b\eta), \quad (9)$$

where  $a$  and  $b$  are the free parameters to be determined. Substituting (9) into (8), we obtain

$$\begin{aligned} & \left[m \left(\rho + \alpha_1 \frac{\varphi}{\kappa}\right) b + \mu b^2 - m\alpha_1 b^3 - \mu \frac{\varphi}{\kappa}\right] \\ & + e^{2b\eta} \left[6\beta_3 a^2 b^4 - 2\beta_3 \frac{\varphi}{\kappa} a^2 b^2\right] = 0. \end{aligned} \quad (10)$$

Separating (10) in the powers of  $e^0$  and  $e^{2b\eta}$ , we find

$$e^0 : m \left(\rho + \alpha_1 \frac{\varphi}{\kappa}\right) b + \mu b^2 - m\alpha_1 b^3 - \mu \frac{\varphi}{\kappa} = 0, \quad (11)$$

$$e^{2B\eta} : \beta_3 a^2 \left[3b^4 - \frac{\varphi}{\kappa} b^2\right] = 0, \quad \text{with } \beta_3 a^2 \neq 0. \quad (12)$$

From (12), we deduce

$$b = \sqrt{\frac{\varphi}{3\kappa}}. \quad (13)$$

Using the value of  $b$  in (11), we obtain

$$m \left(\rho + \alpha_1 \frac{\varphi}{\kappa}\right) \sqrt{\frac{\varphi}{3\kappa}} + \mu \left(\frac{\varphi}{3\kappa}\right) - m\alpha_1 \left(\frac{\varphi}{3\kappa}\right) \sqrt{\frac{\varphi}{3\kappa}} - \mu \frac{\varphi}{\kappa} = 0. \quad (14)$$

Finally, the solution for  $F(\eta)$  (provided the condition (14) holds) is written as

$$F(\eta) = a \exp \left[ \sqrt{\frac{\varphi}{3\kappa}} \eta \right]. \quad (15)$$

So the solution  $u(y, t)$  which satisfies the condition (14) is written as

$$u(y, t) = a \exp \left[ \sqrt{\frac{\varphi}{3\kappa}} (y - mt) \right] \quad \text{with } m > 0. \quad (16)$$

*Remark 1.* Note that the solution (16) is the shock wave solution to the governing PDE (1). The previous solution is valid under the particular condition on the physical parameters of the flow given in (14) (which is some kind of dispersion relation in  $m$ ). This solution does show the hidden shock wave behavior of the flow problem with slope of the velocity field or the velocity gradient approaches to infinity such that

$$\frac{\partial u}{\partial y} \rightarrow \infty \quad \text{as } y \rightarrow \infty. \quad (17)$$

*Remark 2.* Note that the solution (16) also satisfies the particular initial and the boundary condition; that is,

$$u(0, t) = g(t) = \exp \left[ -\sqrt{\frac{\varphi}{3\kappa}} mt \right], \quad t > 0, \quad (18)$$

$$u(y, 0) = f(y) = \exp \left[ \sqrt{\frac{\varphi}{3\kappa}} y \right], \quad y > 0,$$

with

$$g(0) = f(0) = a = 1. \quad (19)$$

The functions  $g(t)$  and  $f(y)$  depend on the physical parameters of the flow.

*Remark 3.* We also observe that the physical significance of the imposing condition (14) is that it gives the speed of travelling shock wave. From (14), we deduce

$$m = \frac{2\mu(\varphi/3\kappa)^{1/2}}{(\rho + (2\alpha_1\varphi/3\kappa))} > 0. \quad (20)$$

**3.2. Unsteady Magnetohydrodynamic (MHD) Flow of Third Grade Fluid in a Porous Medium.** By employing the same geometry as we have explained in Section 2, in this problem we extend the previous model by considering the fluid to be electrically conducting under the influence of a uniform magnetic field applied transversely to the flow. We provide the closed-form solution of the problem by reducing the governing nonlinear PDE into an ODE with the help of Lie reduction technique.

The time-dependent magnetohydrodynamic flow of a third grade fluid in a porous half space in the absence of the modified pressure gradient takes the form

$$\begin{aligned} \left(\rho + \alpha_1 \frac{\varphi}{\kappa}\right) \frac{\partial v}{\partial t} &= \mu \frac{\partial^2 v}{\partial y^2} + \alpha_1 \frac{\partial^3 v}{\partial y^2 \partial t} + 6\beta_3 \left(\frac{\partial v}{\partial y}\right)^2 \frac{\partial^2 v}{\partial y^2} \\ &- 2\beta_3 \frac{\varphi}{\kappa} \left(\frac{\partial v}{\partial y}\right)^2 u - \frac{\varphi}{\kappa} \mu v - \sigma B_0^2 v, \end{aligned} \quad (21)$$

where  $v$  is the velocity component in  $x$ -direction,  $\sigma$  is the electrical conductivity, and  $B_0$  is the uniform applied magnetic field. In order to solve (21), the relevant time and space dependent velocity boundary conditions are

$$\begin{aligned} u(0, t) &= u_0 g(t), \quad t > 0, \\ u(\infty, t) &= 0, \quad t > 0, \\ u(y, 0) &= f(y), \quad y > 0. \end{aligned} \quad (22)$$

As it can be seen (21) also admits Lie point symmetry generators,  $\partial/\partial t$  (translation in  $t$ ) and  $\partial/\partial y$  (translation in  $y$ ). Let  $X_1$  and  $X_2$  be time-translation and space-translation symmetry generators, respectively. The invariant solution corresponding to the generator  $X = X_1 + mX_2$  is given by

$$v(y, t) = G(\xi) \quad \text{with } \xi = y - mt. \quad (23)$$

Using (23) into (21) yields

$$\begin{aligned} \left(\rho + \alpha_1 \frac{\varphi}{\kappa}\right) m \frac{dG}{d\xi} + \mu \frac{d^2 G}{d\xi^2} - m\alpha_1 \frac{d^3 G}{d\xi^3} + 6\beta_3 \left(\frac{dG}{d\xi}\right)^2 \frac{d^2 G}{d\xi^2} \\ - 2\beta_3 \frac{\varphi}{\kappa} G \left(\frac{dG}{d\xi}\right)^2 - \mu \frac{\varphi}{\kappa} G - \sigma B_0^2 G = 0. \end{aligned} \quad (24)$$

Following the same methodology adopted to solve the previous problem, the reduced ODE (24) admits an exact solution of the form

$$G(\xi) = a \exp \left[ \sqrt{\frac{\varphi}{3\kappa}} \xi \right], \quad (25)$$

provided that

$$\begin{aligned} m \left(\rho + \alpha_1 \frac{\varphi}{\kappa}\right) \sqrt{\frac{\varphi}{3\kappa}} + \mu \left(\frac{\varphi}{3\kappa}\right) \\ - m\alpha_1 \left(\frac{\varphi}{3\kappa}\right) \sqrt{\frac{\varphi}{3\kappa}} - \mu \frac{\varphi}{\kappa} - \sigma B_0^2 = 0. \end{aligned} \quad (26)$$

Thus the solution of the PDE (21) which satisfies the condition (26) is written as

$$v(y, t) = \exp \left[ \sqrt{\frac{\varphi}{3\kappa}} (y - mt) \right] \quad \text{with } m > 0. \quad (27)$$

*Remark 4.* Note that the previous solution (27) also satisfies the boundary and initial conditions given in (22). The imposing physical condition (26) gives the speed of travelling shock wave. From (26), we find

$$m = \frac{2\mu(\varphi/3\kappa) + \sigma B_0^2}{(\varphi/3\kappa)^{1/2} [\rho + (2\alpha_1\varphi/3\kappa)]} > 0. \quad (28)$$

If we set  $B_0 = 0$  (no magnetic field), we recover the condition given in (14).

**3.3. Unsteady Magnetohydrodynamic (MHD) Flow of Third Grade Fluid in a Porous Medium with Plate Suction/Injection.** This particular model is an extension of previous two problems with combined effects of plate suction/injection and MHD nature of the fluid. Thus, for flow under consideration, we seek a velocity of the form

$$\mathbf{V} = [w(y, t), -W, 0], \quad (29)$$

where  $w$  denotes the velocity of the fluid in  $x$ -direction and  $W > 0$  indicates suction velocity and  $W < 0$  blowing or injection velocity.

The unsteady MHD flow of a third grade fluid in a porous half space with plate suction/injection is governed by

$$\begin{aligned} \left(\rho + \alpha_1 \frac{\varphi}{\kappa}\right) \frac{\partial w}{\partial t} &= \left(\rho + \alpha_1 \frac{\varphi}{\kappa}\right) W \frac{\partial w}{\partial y} + \mu \frac{\partial^2 w}{\partial y^2} + \alpha_1 \frac{\partial^3 w}{\partial y^2 \partial t} \\ &+ 6\beta_3 \left(\frac{\partial w}{\partial y}\right)^2 \frac{\partial^2 w}{\partial y^2} - \alpha_1 W \frac{\partial^3 w}{\partial y^3} \\ &- 2\beta_3 \frac{\varphi}{\kappa} \left(\frac{\partial w}{\partial y}\right)^2 u - \frac{\varphi}{\kappa} \mu w - \sigma B_0^2 w. \end{aligned} \quad (30)$$

The PDE (30) is solved subject to the same boundary and initial conditions specified for the previous models. The invariant solution of the previous nonlinear PDE under the linear combination of time-translation and space-translation symmetry generators is given by

$$w(y, t) = H(\theta) \quad \text{with } \theta = y - mt. \quad (31)$$

Inserting (31) in (30), we get a third-order nonlinear ODE in  $H(\theta)$ , namely,

$$\begin{aligned} & \left(\rho + \alpha_1 \frac{\varphi}{\kappa}\right) m \frac{dH}{d\theta} + \left(\rho + \alpha_1 \frac{\varphi}{\kappa}\right) W \frac{dH}{d\theta} + \mu \frac{d^2 H}{d\theta^2} \\ & - m \alpha_1 \frac{d^3 H}{d\theta^3} + 6\beta_3 \left(\frac{dH}{d\theta}\right)^2 \frac{d^2 H}{d\theta^2} - \alpha_1 W \frac{\partial^3 H}{\partial \theta^3} \\ & - 2\beta_3 \frac{\varphi}{\kappa} H \left(\frac{dH}{d\theta}\right)^2 - \left(\mu \frac{\varphi}{\kappa} + \sigma B_0^2\right) H(\theta) = 0. \end{aligned} \quad (32)$$

Following the same procedure used to tackle the first problem, (32) admits the exact solution of the form

$$H(\theta) = a \exp \left[ \sqrt{\frac{\varphi}{3\kappa}} \theta \right], \quad (33)$$

provided

$$\begin{aligned} 0 = & m \left(\rho + \alpha_1 \frac{\varphi}{\kappa}\right) \sqrt{\frac{\varphi}{3\kappa}} + \left(\rho + \alpha_1 \frac{\varphi}{\kappa}\right) W \sqrt{\frac{\varphi}{3\kappa}} + \mu \left(\frac{\varphi}{3\kappa}\right) \\ & - (m + W) \alpha_1 \left(\frac{\varphi}{3\kappa}\right) \sqrt{\frac{\varphi}{3\kappa}} - \left(\mu \frac{\varphi}{\kappa} + \sigma B_0^2\right). \end{aligned} \quad (34)$$

The solution of  $w(y, t)$  is written as

$$w(y, t) = \exp \left[ \sqrt{\frac{\varphi}{3\kappa}} (y - mt) \right] \quad \text{with } m > 0. \quad (35)$$

*Remark 5.* The previous solution is valid only under the particular condition on the physical parameters given in (34). The condition (34) also gives the speed of shock wave. Thus from (34), we obtain

$$m = \frac{2\mu(\varphi/3\kappa) + \sigma B_0^2 - (\rho + (\alpha_1\varphi/3\kappa))\sqrt{\varphi/3\kappa}W}{\sqrt{\varphi/3\kappa}[\rho + (2\alpha_1\varphi/3\kappa) - (\alpha_1\varphi/3\kappa)W]} > 0. \quad (36)$$

Note that, if we set  $W = B_0 = 0$  (with no porosity and magnetic field), we recover the previous two conditions given in (14) and (26).

*Remark 6.* We note that the shock wave solutions (16), (27), and (35) are the same, but the imposing conditions on the physical parameters of the flow given in (14), (26), and (34) under which these solutions are valid are different. This means that in each case the speed of the travelling shock wave is different. Therefore, the graphical behavior of these solutions is the same which shows the shock wave behavior of the flow problems. However, the imposing conditions contain the magnetic field, suction/blowing, porosity, and second grade and the third grade parameters. Thus these closed-form shock wave solutions are valid for the particular values of these parameters.

#### 4. Shock Wave Behavior of the Solutions

Figures 2 and 3 show the shock wave behavior of the solutions (16), (27), and (35) in 2D and 3D, respectively. From the

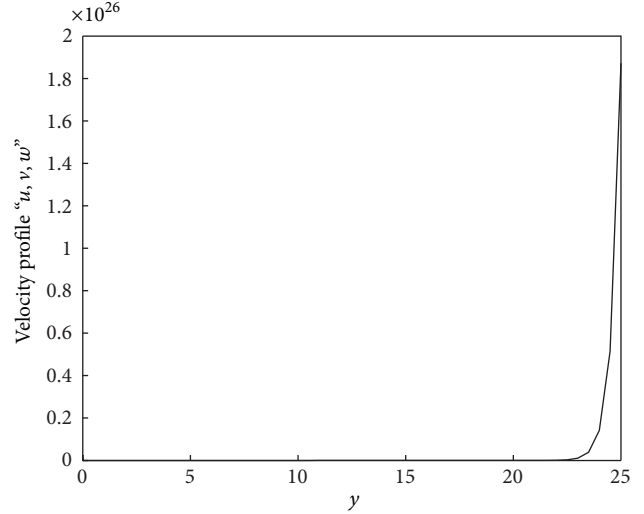


FIGURE 2: Profile of the shock wave solutions (16), (27), and (35) with  $\varphi = 4, \kappa = 0.2, m = 1$ , and  $t = \pi/2$ .

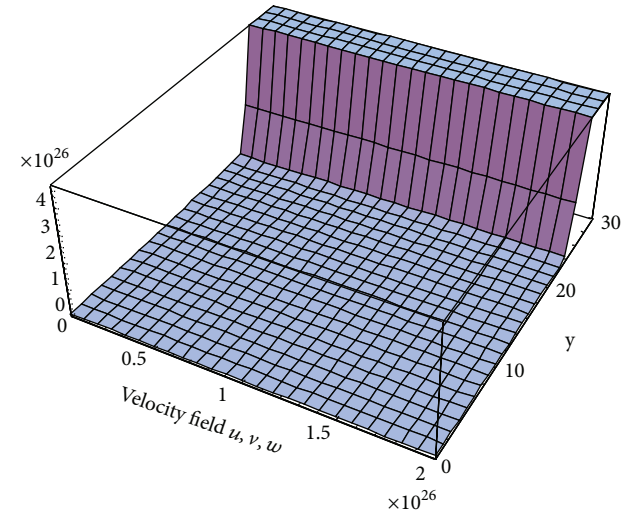


FIGURE 3: 3D profile of the shock wave solutions (16), (27), and (35) with  $\varphi = 4, \kappa = 0.2, m = 1$ , and  $t = \pi/2$ .

graphs it is quite clear that the slope of the velocity profile is approaching to infinity representing the sudden sharp discontinuity in the velocity field.

#### 5. Final Comments

In this paper, we have presented closed-form shock wave solutions for some nonlinear problems which describe the phenomena of third grade fluids. In each case the governing nonlinear PDEs are reduced to nonlinear ODEs by using the Lie point symmetry (which is translation) in the  $t$  and  $y$  directions. The reduced ODEs are then solved analytically. We observe that the shock wave solutions (16), (27), and (35) are the same, but the imposing conditions on the physical parameters of the flow models given in (14), (26), and (34) under which these solutions are valid are different. These solutions

do not directly contain the parameter which is responsible for showing the behavior of third grade fluid parameter on the flow. However, the imposing conditions under which these solutions are valid do contain the third grade parameter. To emphasize, we can say that these solutions are valid for the particular values of third grade fluid parameter. The results obtained describe the mathematical structure of the shock wave behavior of the flow problems. The models considered in this study are prototype, but the obtained solutions are going to be very helpful in carrying out further analysis of the shock wave characteristic associated with the non-Newtonian fluid flow models. The method that we have adopted is also prosperous for tackling wide range of nonlinear problems in non-Newtonian fluid mechanics.

## Acknowledgments

T. Aziz and A. Fatima would like to thank the School of Computational and Applied Mathematics and the Financial Aid and Scholarship office, University of the Witwatersrand, for financial support and scholarships.

## References

- [1] T. Aziz, A. Fatima, and F. M. Mahomed, "Shock wave solution for a nonlinear partial differential equation arising in the study of a non-Newtonian fourth grade fluid model," *Mathematical Problems in Engineering*, vol. 2013, Article ID 573170, 5 pages, 2013.
- [2] Y.-Z. Peng, "Exact solutions for some nonlinear partial differential equations," *Physics Letters A*, vol. 314, no. 5-6, pp. 401-408, 2003.
- [3] S. A. El-Wakil, A. Elgarayhi, and A. Elhanbaly, "Exact periodic wave solutions for some nonlinear partial differential equations," *Chaos, Solitons and Fractals*, vol. 29, no. 4, pp. 1037-1044, 2006.
- [4] W. R. Schowalter, "Mechanics of Non-Newtonian Fluids," Pergamon, New York, NY, USA, 1978.
- [5] G. Saccomandi, "Group properties and invariant solutions of plane micropolar flows," *International Journal of Engineering Science*, vol. 29, no. 5, pp. 645-648, 1991.
- [6] G. Saccomandi, "Some exact pseudo-plane solutions of the first kind for the Navier-Stokes equations," *Zeitschrift für Angewandte Mathematik und Physik*, vol. 45, no. 6, pp. 978-985, 1994.
- [7] A. Kacou, K. R. Rajagopal, and A. Z. Szeri, "Flow of a fluid of the differential type in a journal bearing," *Journal of Tribology*, vol. 109, no. 1, pp. 100-107, 1987.
- [8] C. Bridges, S. Karra, and K. R. Rajagopal, "On modeling the response of the synovial fluid: unsteady flow of a shear-thinning, chemically-reacting fluid mixture," *Computers & Mathematics with Applications*, vol. 60, no. 8, pp. 2333-2349, 2010.
- [9] A. Farina, A. Fasano, L. Fusi, and K. R. Rajagopal, "On the dynamics of an elastic-rigid material," *Advances in Mathematical Sciences and Applications*, vol. 20, no. 1, pp. 193-217, 2010.
- [10] A. Z. Szeri and K. R. Rajagopal, "Flow of a non-Newtonian fluid between heated parallel plates," *International Journal of Non-Linear Mechanics*, vol. 20, no. 2, pp. 91-101, 1985.
- [11] T. Aziz and F. M. Mahomed, "Closed-form solutions for a nonlinear partial differential equation arising in the study of a fourth grade fluid model," *Journal of Applied Mathematics*, vol. 2012, Article ID 931587, 16 pages, 2012.
- [12] T. Aziz, F. M. Mahomed, and A. Aziz, "Group invariant solutions for the unsteady MHD flow of a third grade fluid in a porous medium," *International Journal of Non-Linear Mechanics*, vol. 47, no. 7, pp. 792-798, 2012.
- [13] E. Momoniat, D. P. Mason, and F. M. Mahomed, "Non-linear diffusion of an axisymmetric thin liquid drop: group-invariant solution and conservation law," *International Journal of Non-Linear Mechanics*, vol. 36, no. 6, pp. 879-885, 2001.
- [14] V. Marinca, N. Herişanu, C. Bota, and B. Marinca, "An optimal homotopy asymptotic method applied to the steady flow of a fourth-grade fluid past a porous plate," *Applied Mathematics Letters*, vol. 22, no. 2, pp. 245-251, 2009.
- [15] R. S. Rivlin and J. L. Ericksen, "Stress-deformation relations for isotropic materials," *Journal of Rational Mechanics and Analysis*, vol. 4, pp. 323-425, 1955.
- [16] C. Fetecau, T. Hayat, C. Fetecau, and N. Ali, "Unsteady flow of a second grade fluid between two side walls perpendicular to a plate," *Nonlinear Analysis. Real World Applications. An International Multidisciplinary Journal*, vol. 9, no. 3, pp. 1236-1252, 2008.
- [17] C. Fetecau, C. Fetecau, and M. Rana, "General solutions for the unsteady flow of second-grade fluids over an infinite plate that applies arbitrary shear to the fluid," *Zeitschrift für Naturforschung A*, vol. 66, pp. 753-759, 2011.
- [18] M. Jamil, A. Rauf, C. Fetecau, and N. A. Khan, "Helical flows of second grade fluid due to constantly accelerated shear stresses," *Communications in Nonlinear Science and Numerical Simulation*, vol. 16, no. 4, pp. 1959-1969, 2011.
- [19] M. Nazar, C. Fetecau, D. Vieru, and C. Fetecau, "New exact solutions corresponding to the second problem of Stokes for second grade fluids," *Nonlinear Analysis. Real World Applications. An International Multidisciplinary Journal*, vol. 11, no. 1, pp. 584-591, 2010.
- [20] F. T. Akyildiz, H. Bellout, and K. Vajravelu, "Exact solutions of nonlinear differential equations arising in third grade fluid flows," *International Journal of Non-Linear Mechanics*, vol. 39, no. 10, pp. 1571-1578, 2004.
- [21] M. Yürüsoy and M. Pakdemirli, "Approximate analytical solutions for the flow of a third-grade fluid in a pipe," *International Journal of Non-Linear Mechanics*, vol. 37, no. 2, pp. 187-195, 2002.
- [22] A. Aziz and T. Aziz, "MHD flow of a third grade fluid in a porous half space with plate suction or injection: an analytical approach," *Applied Mathematics and Computation*, vol. 218, no. 21, pp. 10443-10453, 2012.
- [23] P. D. Ariel, "Flow of a third grade fluid through a porous flat channel," *International Journal of Engineering Science*, vol. 41, no. 11, pp. 1267-1285, 2003.
- [24] R. L. Fosdick and K. R. Rajagopal, "Thermodynamics and stability of fluids of third grade," *Proceedings of the Royal Society London A*, vol. 369, no. 1738, pp. 351-377, 1980.
- [25] G. W. Bluman and S. Kumei, *Symmetries and Differential Equations*, Springer, New York, NY, USA, 1989.
- [26] N. H. Ibragimov, *CRC Handbook of Lie Group Analysis of Differential Equations*, vol. 3, CRC Press, Boca Raton, Fla, USA, 1996.

## Research Article

# Hydromagnetic Stagnation-Point Flow towards a Radially Stretching Convectively Heated Disk

S. Shateyi<sup>1</sup> and O. D. Makinde<sup>2</sup>

<sup>1</sup> Department of Mathematics, University of Venda, Private Bag X5050, Thohoyandou 0950, South Africa

<sup>2</sup> Institute for Advanced Research in Mathematical Modelling and Computations, Cape Peninsula University of Technology, P.O. Box 1906, Bellville 7535, South Africa

Correspondence should be addressed to S. Shateyi; stanford.shateyi@univen.ac.za

Received 16 March 2013; Revised 23 May 2013; Accepted 26 May 2013

Academic Editor: Waqar Khan

Copyright © 2013 S. Shateyi and O. D. Makinde. This is an open access article distributed under the Creative Commons Attribution License, which permits unrestricted use, distribution, and reproduction in any medium, provided the original work is properly cited.

The steady stagnation-point flow and heat transfer of an electrically conducted incompressible viscous fluid are extended to the case where the disk surface is convectively heated and radially stretching. The fluid is subjected to an external uniform magnetic field perpendicular to the plane of the disk. The governing momentum and energy balance equations give rise to nonlinear boundary value problem. Using a spectral relaxation method with a Chebyshev spectral collocation method, the numerical solutions are obtained over the entire range of the physical parameters. Emphasis has been laid to study the effects of viscous dissipation and Joule heating on the thermal boundary layer. Pertinent results on the effects of various thermophysical parameters on the velocity and temperature fields as well as local skin friction and local Nusselt number are discussed in detail and shown graphically and/or in tabular form.

## 1. Introduction

The study of boundary layer flow over stretching sheet has been a subject of great interest due to its applications in designing cooling systems such as liquid metals, MHD generators, pumps, and flow meters. Many chemical engineering processes, such as metallurgical and polymer extrusion, involve cooling of molten liquids being stretched into cooling liquids (Abel and Mahesha [1], Bataller [2], and Abdou [3], among others). Various researchers have explored the flow over stretching surfaces in different circumstances. Munawar et al. [4] presented an analytic solution of flow of viscous fluid between two stretching disks with slip boundaries. Hayat et al. [5] investigated flow and heat transfer in second grade fluid over a stretching sheet subjected to convective boundary conditions. Shateyi and Motsa [6] numerically analysed variable viscosity on magnetohydrodynamic fluid flow and heat transfer over an unsteady stretching surface with Hall effect. Makinde and Sibanda [7] investigated the effects of chemical reaction on boundary layer flow past a vertical stretching surface in the presence of internal heat generation. Recently, Ashraf and Batool [8] carried out a numerical study

of an axisymmetric steady laminar incompressible flow from an electrically conducted micropolar fluid over a stretching disk.

Stagnation-point flow appears in virtually all fields of science and engineering. A flow can be stagnated by a solid wall or a free stagnation point or a line can exist in the interior of the fluid domain. The study of stagnation-point flow was pioneered by Hiemenz in 1911 [9] who solved the two-dimensional stagnation-point problem using a similarity transformation. Motsa et al. [10] formulated the Maxwell fluid for two-dimensional stagnation flow towards a shrinking sheet and then calculated the numerical solution of transformed non linear ordinary differential equations via the successive linearisation method. Bhattacharyya et al. [11] analyzed the effects of partial slip on steady boundary layer stagnation-point flow of an incompressible fluid and heat transfer towards a shrinking sheet. This investigation explored the conditions of the nonexistence, existence, uniqueness, and duality of the solutions of self-similar equations numerically. Makinde and Charles [12] presented computational dynamics of hydromagnetic stagnation flow towards a stretching sheet. Nadeem et al. [13]

investigated by using similarity transformations the unsteady MHD boundary layer flow of a micropolar fluid near the forward stagnation point of a two-dimensional plane surface. Makinde [14] examined the hydromagnetic mixed convection stagnation point flow towards a vertical plate embedded in a highly porous medium with radiation and internal heat generation. Devi et al. [15] studied radiation effect on steady laminar hydromagnetic flow of a viscous, Newtonian, and electrically conducted fluid past a porous rotating infinite disk taking Hall current into account. Mahapatra and Nandy [16] presented a mathematical analysis for the magnetohydrodynamic (MHD) axisymmetric stagnation-point flow and heat transfer over a shrinking sheet which shrinks axisymmetrically in its own plane.

The above cited papers give more insight into the prediction of skin-friction as well as heat/mass transfer near stagnation regions of bodies in high speed flows and also in the design of thrust bearing and radial diffusers, drag reduction, transportation cooling, and thermal recovery.

The presence of a transverse magnetic field in boundary layer flows over moving surfaces is a basic and important problem in magnetohydrodynamic (MHD). The MHD flow and heat transfer for a viscous fluid over a stretching sheet has enormous applications in many engineering problems such as plasma studies, petroleum industries, and geothermal energy extractions. Chamkha, and Ahmed [17] investigated the similarity solution for an unsteady MHD stagnation-point flow of a three-dimensional porous body with heat and mass transfer. Motsa and Shateyi [18] obtained a numerical solution of MHD and rotating flow over a porous shrinking sheet by the spectral homotopy analysis method. Makinde and Aziz [19] explored the effects of the magnetic field on the viscous flow and heat transfer over a flat plate under a convective boundary condition. Butt and Ali [20] investigated the effects of magnetic field on the entropy generation during fluid flow and heat transfer due to radially stretching surface. Makinde et al. [21] analyzed the combined effects of buoyancy force, convective heating, Brownian motion, thermophoresis, and magnetic field on stagnation-point flow and heat transfer due to nanofluid flow towards a stretching sheet. Ibrahim et al. [22] analyzed the effect of magnetic field on stagnation-point flow and heat transfer due to nanofluid towards a stretching sheet.

Governing equations modelling MHD flow and heat transfer over stretching surfaces are highly nonlinear. To that end, exact solutions are impossible to obtain. Therefore, numerical solutions have always been developed, modified, and hightbred, as a bid of getting more accurate and stable solutions. The current study seeks to extend the steady stagnation-point flow and heat transfer of an electrically conducted incompressible viscous fluid to the case where the disk surface is convectively heated and radially stretching. We propose to numerically solve the present problem using a recently developed iterative method known as spectral relaxation method (SRM); see Motsa et al. [23–25]. The SRM approach is based on transforming nonlinear ordinary differential equation into an iterative scheme. The iterative scheme is then blended with Chebyshev spectral method.

## 2. Model Formulation

Consider a steady stagnation-point flow of an electrically conducted incompressible viscous fluid towards a radially stretching convectively heated disk in the presence of a transverse magnetic field of strength  $B_0$  applied parallel to the  $z$ -axis, as shown in Figure 1. The sheet is stretched with a linear velocity  $u = U_w(r) = ar$ , where  $a$  is a real number. The bottom surface of the plate is assumed to be heated by convection from a hot fluid at temperature  $T_f$ , which provides a heat transfer coefficient,  $h$ . Based on this assumption, the boundary condition for the thermal field can be written as [26–28]. The induced magnetic field due to the motion of the electrically conducted fluid is negligible. It is also assumed that the external electrical field is zero and that the electric field due to the polarization of charges is negligible.

The relevant governing equations of fluid flow and heat transfer are

$$\begin{aligned} \frac{\partial}{\partial r}(ru) + \frac{\partial}{\partial z}(rw) &= 0, \\ u \frac{\partial u}{\partial r} + w \frac{\partial u}{\partial z} &= U_\infty \frac{dU_\infty}{dr} + \nu \frac{\partial^2 u}{\partial z^2} - \frac{\sigma B_0^2 (u - U_\infty)}{\rho}, \\ u \frac{\partial T}{\partial r} + w \frac{\partial T}{\partial z} &= \frac{k}{\rho c_p} \frac{\partial^2 T}{\partial z^2} + \frac{\mu}{\rho c_p} \left( \frac{\partial u}{\partial z} \right)^2 + \frac{\sigma B_0^2 (u - U_\infty)^2}{\rho}, \end{aligned} \quad (1)$$

with

$$\begin{aligned} u &= U_w = ar, \quad w = 0, \\ -k \frac{\partial T}{\partial z} &= h(T_f - T) \quad \text{at } z = 0, \\ u &\longrightarrow U_\infty = br, \quad T \longrightarrow T_\infty \quad \text{as } z \longrightarrow \infty. \end{aligned} \quad (2)$$

*2.1. Similarity Transformation.* To make the problem amenable, following Butt and Ali [20], among others, we introduce the following nondimensional quantities:

$$\begin{aligned} \eta &= \sqrt{\frac{b}{\nu}} z, \quad u(r, z) = brf'(\eta), \\ w(r, z) &= -2\sqrt{b\nu}f(\eta), \quad \theta(\eta) = \frac{T - T_\infty}{T_w - T_\infty}, \\ \nu &= \frac{\mu}{\rho}, \quad \lambda = \frac{a}{b}, \quad \text{Bi} = \frac{h}{k} \sqrt{\frac{b}{\nu}}, \quad \text{Ha} = \frac{\sigma B_0^2}{\rho b}, \\ \text{Ec} &= \frac{U_\infty^2}{c_p (T - T_\infty)}, \quad \text{Pr} = \frac{\rho \nu c_p}{k}. \end{aligned} \quad (3)$$

Substituting (3) into (1) and (2), we obtain

$$f''' + 2ff'' - f'^2 - \text{Ha}(f' - 1) = -1, \quad (4)$$

$$\theta'' + 2\text{Pr}f\theta' + \text{PrEc}f''^2 + \text{PrEcHa}(f' - 1)^2 = 0. \quad (5)$$

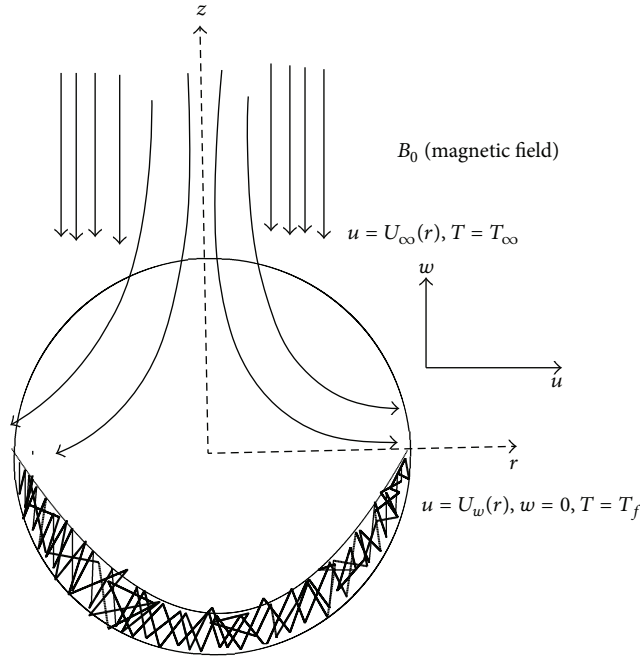


FIGURE 1: The physical model and the coordinate system for the problem.

With

$$\begin{aligned} f'(0) &= \lambda, & f(0) &= 0, \\ \theta'(0) &= \text{Bi}(\theta(0) - 1) & f'(\infty) &= 1, & \theta(\infty) &= 0. \end{aligned} \quad (6)$$

In the above equations, prime denotes differentiation with respect to  $\eta$ . The physical quantities of practical significance in this work are the local skin friction coefficient  $C_f$  and the local Nusselt number  $\text{Nu}$ , which are expressed as

$$C_f = \frac{\tau_w}{\rho U_\infty^2}, \quad \text{Nu} = \frac{r q_w}{k(T_f - T_\infty)}, \quad (7)$$

where  $C_f$  is the skin friction,  $\tau$  is the surface shear stress, and  $q_w$  is the heat flux from the plate which are given by

$$\tau_w = \mu \left. \frac{\partial u}{\partial z} \right|_{z=0}, \quad q_w = -k \left. \frac{\partial T}{\partial z} \right|_{z=0}. \quad (8)$$

Substituting (8) into (7), we obtain

$$\text{Re}_r^{1/2} C_f = f''(0), \quad \text{Re}_r^{-1/2} \text{Nu} = -\theta'(0), \quad (9)$$

where  $\text{Re}_r = U_\infty r / \nu$  is the stagnation flow Reynolds number.

### 3. Method of Solution

The set of (4) and (5) together with the boundary conditions (6) are coupled nonlinear which are to be solved numerically using a spectral relaxation method (SRM). This method involves transforming (4) and (5) into a set of linear ordinary differential equations. The entire computation procedure is

implemented using a program written in MATLAB computer language. From the process of numerical computation, the fluid velocity, temperature, the local skin friction coefficient, and the local Nusselt number are determined. The SRM algorithm starts with the assumption of having a system of  $m$  nonlinear ordinary differential equations in  $m$  unknowns functions  $z_i(\eta)$ ,  $i = 1, 2, \dots, m$  where  $\eta \in [a, b]$  is the independent variable. To solve the resultant iterative scheme, we then use the Chebyshev pseudospectral method. The details of the spectral methods can be found in (Canuto et al. [29] and Trefethen [30]). Before applying the spectral method, the domain on which the governing equation is defined to the interval  $[-1, 1]$  on which the spectral method can be implemented. We use the transformation  $\eta = (b-a)(\tau+1)/2$  to map the interval  $[a, b]$  to  $[-1, 1]$ .

Now to apply the SRM on (4) together with (5), we set  $f'(\eta) = g(\eta)$  and then write the equations as the following set of equations:

$$\begin{aligned} f' &= g, \\ g'' + 2fg' - g^2 - \text{Ha}g + \text{Ha} &= -1, \end{aligned} \quad (10)$$

$$\frac{1}{\text{Pr}} \theta'' + 2f\theta' + \text{Ec}g'^2 + \text{Ec} \text{Ha}(g-1)^2 = 0,$$

and the boundary conditions become

$$\begin{aligned} f(0) &= 0, & g(0) &= \lambda, & \theta'(0) &= \text{Bi}(\theta(0) - 1), \\ g(\infty) &= 1, & \theta(\infty) &= 0. \end{aligned} \quad (11)$$

In view of the SRM, we obtain the following iteration scheme:

$$f'_{r+1} = g_r, \quad f_{r+1}(0) = 0, \quad (12)$$

$$\begin{aligned} g''_{r+1} + 2f_{r+1}g'_{r+1} - \text{Ha}g_{r+1} &= -1 + g_r^2 - \text{Ha}, \\ g_{r+1}(0) &= \lambda, & g_{r+1}(\infty) &= 1, \end{aligned} \quad (13)$$

$$\frac{1}{\text{Pr}} \theta''_{r+1} + 2f_{r+1}\theta'_{r+1} = -\text{Ec}g_{r+1}^2 - \text{Ec} \text{Ha}(g-1)^2 = 0,$$

$$\theta_{r+1}(0) = \frac{\text{Bi}}{1 + \text{Bi}}, \quad \theta_{r+1}(\infty) = 0. \quad (14)$$

We note that the equations now form a system of linear decoupled equations which can be solved iteratively for  $r = 1, 2, \dots$ , starting from initial guesses/approximations  $(g_0(\eta), \theta(\eta))$ .

Applying the Chebyshev pseudospectral method on (12) to (14) we obtain

$$A_1 \mathbf{f}_{r+1} = B_1, \quad f_{r+1}(\tau_{\overline{N}}) = 0, \quad (15)$$

$$A_2 \mathbf{g}_{r+1} = B_2, \quad g_{r+1}(\tau_{\overline{N}}) = \lambda, \quad g_{r+1}(\tau_0) = 1, \quad (16)$$

$$A_3 \theta_{r+1} = B_3, \quad \theta_{r+1}(\tau_{\overline{N}}) = \frac{\text{Bi}}{1 + \text{Bi}}, \quad \theta_{r+1}(\tau_0) = 0, \quad (17)$$

where

$$\begin{aligned}
 A_1 &= \mathbf{D}, & B_1 &= \mathbf{g}_r, \\
 A_2 &= \mathbf{D}^2 + \text{diag}[2\mathbf{f}_{i+1}]\mathbf{D} - \text{Ha}\mathbf{I}, & B_2 &= -1 - \text{Ha} + \mathbf{g}_r^2, \\
 A_3 &= \frac{1}{\text{Pr}}\mathbf{D}^2 + \text{diag}[2\mathbf{f}_{i+1}]\mathbf{D}, \\
 B_3 &= -\text{Ec}g_{r+1}^{\prime 2} - \text{EcHa}(g-1)^2,
 \end{aligned} \tag{18}$$

where  $\mathbf{I}$  is the identity matrix of size  $(\bar{N} + 1) \times (\bar{N} + 1)$ ,  $\mathbf{f}$ ,  $\mathbf{g}$ , and  $\theta$  are the values of  $f$ ,  $g$ , and  $\theta$ , respectively, when evaluated at the grid points. Equations (13) to (15) constitute the SRM scheme. The initial approximation required to start the iterative process is

$$\begin{aligned}
 g_0(\eta) &= \lambda - 1 + \eta + (1 - \lambda)e^{-\eta}, \\
 \theta_0(\eta) &= \frac{\text{Bi}}{1 + \text{Bi}}e^{-\eta},
 \end{aligned} \tag{19}$$

which are convenient random functions that satisfy the boundary conditions. The iteration is repeated until convergence is achieved. The convergence of the SRM scheme is defined in terms of the infinity norm as

$$\text{Er} = \text{Max}(\|f_{r+1} - f_r\|; \|\theta_{r+1} - \theta_r\|). \tag{20}$$

If the iteration scheme converges, the error  $\text{Er}$  will decrease with an increase in the number of iterations. Accuracy of the scheme was established by increasing the number of collocation points  $N$  until the solutions are consistent and further increase does not change the value of the solutions.

## 4. Results and Discussion

The steady stagnation-point flow and heat transfer of an electrically conducted incompressible viscous fluid with the disk surface being convectively heated and radially stretching are numerically solved using the spectral relaxation method (SRM). We have used the **bvp4c** method to validate the SRM solution. The **bvp4c** is an in-built MATLAB solver for boundary value problems and is based on fourth-order Runge-Kutta schemes. The tolerance level for both methods was set to be  $10^{-8}$ . The figures were generated using  $N = 50$  and  $\eta_{\infty} = 15$ . Figure 2 is used to illustrate how the SRM error reduces with increased number of iterations. The plot has been generated for different values of the magnetic parameter. A steep decrease of the error is being observed for all values of  $\text{Ha}$ . The decrease in the error is an indication that the method is convergent and gives stable solutions. The convergence rate is taken to be the number of iterations the solution takes to reach a specified accuracy level. For example, in the figure it shows that when  $\text{Ha} = 4$ , the solution will converge after fifteen iterations for the given accuracy level compared to eighteen when  $\text{Ha} = 2$ .

In order to gain physical insight into the flow properties, default numerical values of the parameters encountered in the problem are assigned. Their influences on the velocity and

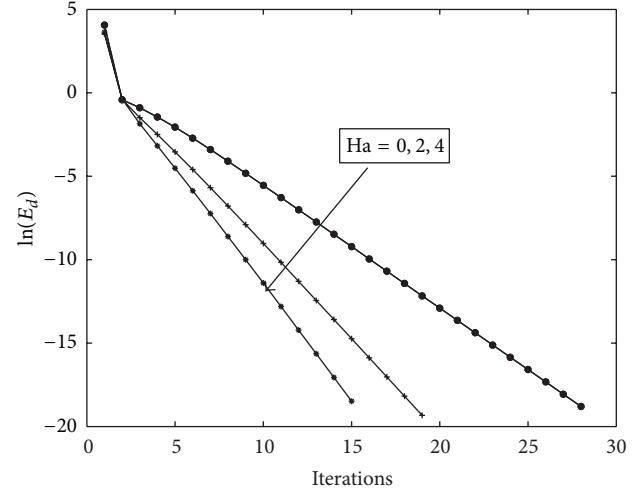


FIGURE 2: Influence of  $\text{Ha}$  on the velocity profiles when  $\lambda = 2$ ,  $\text{Pr} = 0.71$ ,  $\text{Bi} = 0.3$ , and  $\text{Ec} = 0.2$ .

TABLE 1: Values of the local Nusselt number for parameters  $\text{Bi}$ ,  $\text{Ec}$ ,  $\lambda$ , and  $\text{Ha}$ .

$\text{Bi}$	$\text{Ec}$	$\lambda$	$\text{Ha}$	$-\theta'(0)$
0.0				-0.07207353
0.2	0.3	0.3	1	0.05773461
0.5				0.18754275
2.0				0.44715903
	0.0			0.25961628
0.3	0.2	0.3	1	0.18754275
	0.5			0.07994324
		0.0		0.02032099
0.3	0.3	0.2	1	0.11131746
		0.5		0.22034202
			0.0	0.33385485
0.3	0.3	0.3	1.0	0.31735089
			5.0	0.26613250
			10.0	0.26613250

temperature profiles as well as on the skin-friction and the Nusselt number are tabulated and/or displayed graphically.

Table 1 displays the effects of the Biot number ( $\text{Bi}$ ), Eckert number ( $\text{Ec}$ ), and the velocity stretching parameter ( $\lambda$ ) on the Nusselt number ( $-\theta'(0)$ ). From this table we observe that increasing the Biot number as expected causes the local Nusselt number to increase. Values of the Biot number more than 0.1 imply that the heat convection away from the surface is much faster than the heat inside the body. This gives rise to high temperature gradients at the surface. More heat is transferred from the wall when the values of the Biot number increase thus causing the Nusselt number to increase in our current study. We also observe from this table that as the Eckert number increases, the Nusselt number decreases. Physically, an increase in the Eckert number decreases the temperature gradient between the ambient and the plate. We observe that increasing the values of the Hartman numbers

TABLE 2: Comparison of SRM solutions for  $f''(0)$  against those of the **bvp4c** for  $\lambda$  and  $Ha$  when  $Pr = 0.71$ ,  $Bi = 0.3$ , and  $Ec = 0.1$ .

$\lambda$	$Ha$	$f''(0)$ SRM	<b>bvp4c</b>
0.0		1.64532167	1.64532167
0.2	1.0	1.38320821	1.38320821
0.5		0.92353421	1.38320821
	0.0	0.78032335	0.78032335
	1.0	0.92353421	0.92353421
0.5	5.0	1.35766817	1.35766817
	10.0	1.75767520	1.75767520

leads to lowering the values of the Nusselt number. Application of a strong magnetic field reduces the flow velocity which in turn increases the temperature distributions within the fluid flow. This physically explains why heat transfer at the wall is reduced as  $Ha$  is increased. Similar observations were made by Butt and Ali [20]. Lastly, we clearly see from the table that the Nusselt number is increased when the values of the velocity parameter are increased.

Table 2 displays the influence of the Hartman number  $Ha$  and velocity parameter  $\lambda$ . The skin friction is greatly reduced by increasing the velocity parameter. As can be seen from the velocity boundary conditions,  $\lambda$  is increased by increasing the stretching parameter  $a$ . Stretching the surface radially reduces the drag force on the wall surface thus reducing the skin friction. Stretching of the surface may lead to smothering of the surface area thereby reduces the drag force on the wall. We also observe in Table 2 that the Hartman number has significant effect on the skin friction. As the magnetic strength increases, the dragging effect is clearly seen by the significant increments in the skin friction. The influence of different parameters on the velocity field  $f'(\eta)$  and temperature profile  $\theta(\eta)$  is depicted in Figures 3 to 9. In this table we observe an excellent agreement between the two methods for up to eight decimal places. However, the SRM converges much faster than the **bvp4c** both in terms of CPU time and number of iterations. This gives us much confidence in the SRM solutions.

Figure 3 depicts the effects of the Hartmann number  $Ha$  on the velocity distributions. In this figure, we observe that the velocity decreases with  $\eta$  as the values of  $Ha$  are increased. Thus, the presence of the magnetic field reduces the momentum boundary layer thickness and increases the power needed to stretch the sheet. The presence of a moderate magnetic field can be used to stabilize the flow thereby delaying the transition from laminar to turbulent. Physically, the presence of a transverse magnetic field gives rise to a drag force known as Lorentz force which results in retarding the velocity field. Similar results were arrived at by Ibrahim et al. [22].

Figure 4 displays the effect of increasing the velocity parameter  $\lambda$  on the velocity profiles. Increasing the stretching parameter causes the velocity to increase and reduces the boundary layer. The fluid flow is aided as the radially stretched surface is stretched. This explains why the velocity

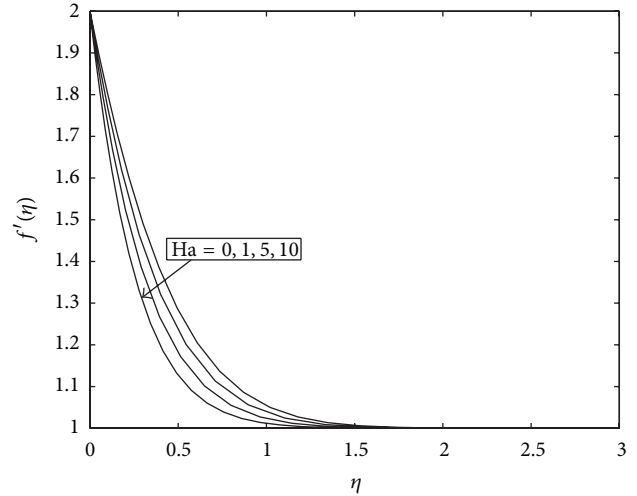


FIGURE 3: Influence of  $Ha$  on the velocity profiles when  $\lambda = 2$ ,  $Pr = 0.71$ ,  $Bi = 0.3$ , and  $Ec = 0.2$ .

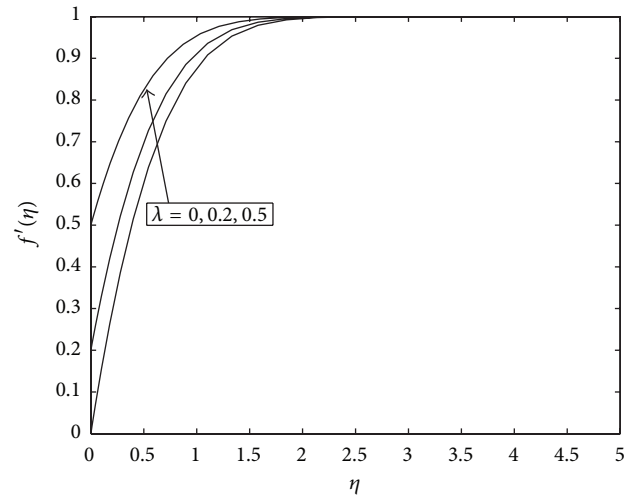


FIGURE 4: Variation of the velocity profiles with  $\lambda$  when  $Pr = 0.71$ ,  $Ha = 1$ ,  $Bi = 0.3$ , and  $Ec = 0.3$ .

increases when the stretching parameter increases. The maximum value for the velocity is a unity (one) in dimensionless variables so as the stretching parameter increases, the velocity tends to converge to this value, thus explaining why the boundary layer thickness is reduced.

In Figure 5 we depict the effect of the Biot number on the temperature profiles. The temperature distributions within the fluid flow clearly increase when the Biot number increases. By the mathematical definition of the Biot number increasing its values means that the convective heat transfer coefficient increases thereby enhancing more heat transfer from the surface. This then causes the fluid to heat up thus increasing the fluid temperature distributions. The influence of the Eckert number  $Ec$  on the temperature profiles is shown on Figure 6. We observe that the temperature is an increasing function of  $Ec$ . This is because increasing the values of the Eckert number generates heat in the fluid due to frictional

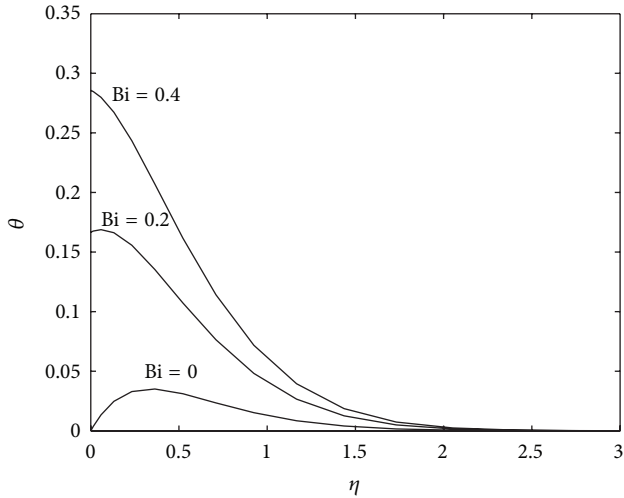


FIGURE 5: Influence of Biot number  $Bi$  on the temperature profiles when  $Pr = 0.3$ ,  $Ha = 1$ ,  $\lambda = 0.2$ , and  $Ec = 0.2$ .

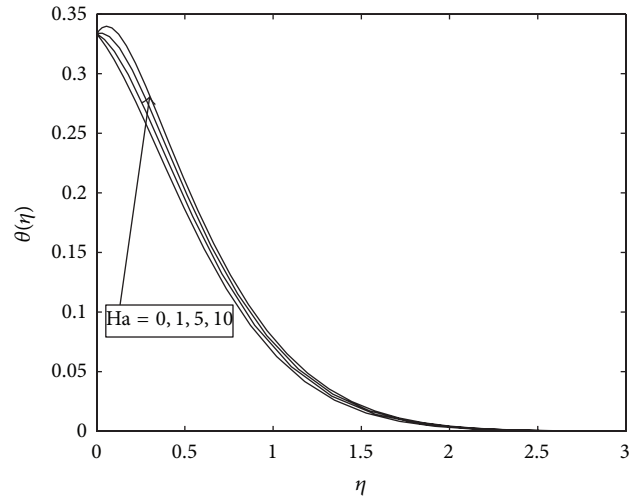


FIGURE 7: Influence of Hartmann number  $Ha$  on the temperature profiles when  $Pr = 0.3$ ,  $Bi = 0.3$ ,  $\lambda = 0.2$ , and  $Ec = 0.2$ .

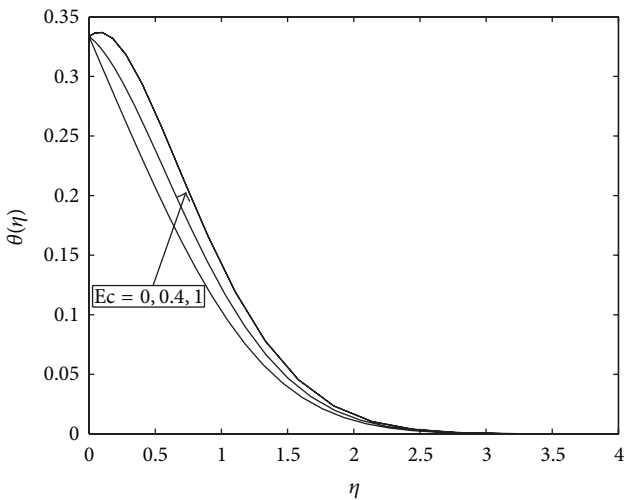


FIGURE 6: Influence of Eckert number  $Ec$  on the temperature profiles when  $Pr = 0.3$ ,  $Ha = 1$ ,  $\lambda = 0.2$ , and  $Bi = 0.3$ .

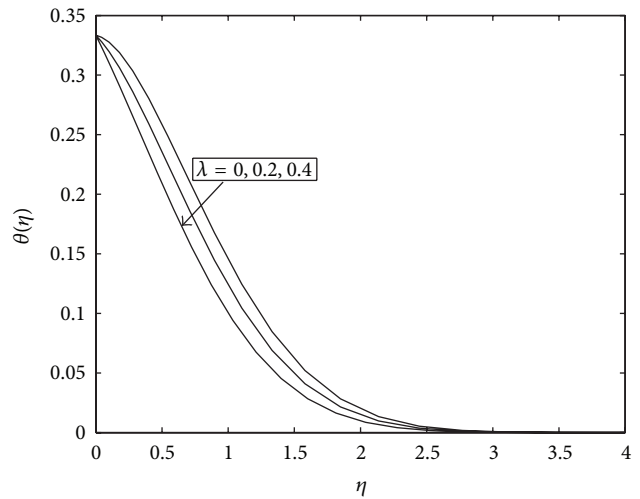


FIGURE 8: Influence of velocity parameter on the temperature profiles when  $Pr = 0.3$ ,  $Ha = 1$ ,  $Bi = 0.3$ , and  $Ec = 0.2$ .

heating. Thus the effect of increasing  $Ec$  is to enhance the temperature at any point.

The influence of the Hartmann on the fluid temperature is displayed in Figure 7. Increasing the magnetic field strength reduces the Nusselt number and hence increases the fluid temperature. Physically, the magnetic field has a stabilizing effect of the fluid velocity flow and thus increasing the temperature distribution within the fluid flow. Figure 8 displays the effect of increasing the velocity parameter  $\lambda$  on the fluid temperature. The temperature is reduced as  $\lambda$  increases. Lastly, Figure 9 depicts the effect of the Prandtl number on the temperature. It can clearly be observed that the temperature as well as the thermal boundary layer rapidly decreases with increasing values of the Prandtl number. Physically, an increase in the Prandtl number means an increase in fluid velocity which in turn causes a decrease in the temperature.

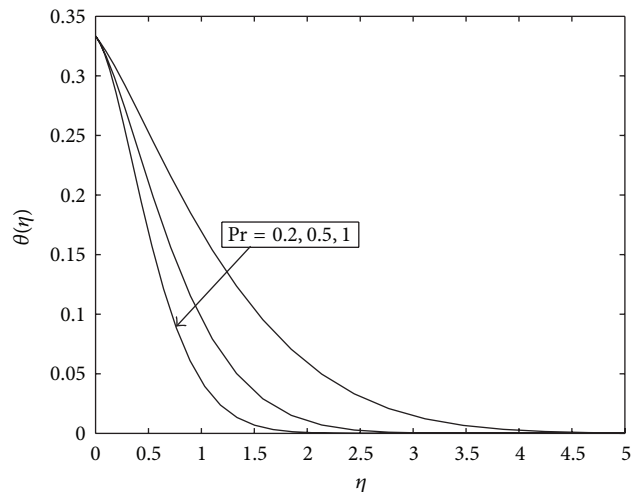


FIGURE 9: Variation of the temperature profiles with  $Pr$  when  $Bi = 0.3$ ,  $Ha = 1$ ,  $\lambda = 0.2$ , and  $Ec = 0.2$ .

## 5. Conclusion

This work is a worthwhile attempt to study the effects of convective heating, viscous dissipation, and Joule heating on the stagnation-point flow and heat transfer of an electrically conducted fluid towards a radially stretching disk. An effective relaxation spectral algorithm with Chebyshev spectral scheme has been adopted to solve the resulting system of non linear differential equations subject to the convective boundary conditions. The accuracy of the SRM is validated against the MATLAB in-built `bvp4c` routine for solving boundary value problems. The combined effects of the convective heating and the magnetic interaction parameter are studied in detail. The velocity field was found to increase as the Harthmann number and velocity parameter increase. The fluid temperature increases by increasing values of Biot number, Eckert number, and the Hartmann number; it decreases as the Prandtl number and velocity parameter increase. These findings were also observed by Hayat et al. [5] in their investigations of the flow and heat transfer in a second grade fluid over a stretching sheet subjected to convective boundary conditions. We also found in this study that the rate of heat transfer at the surface increases as the Biot number (convective parameter) increases. A similar conclusion was arrived at by Abu Bakar et al. [26].

## Nomenclature

a:	Initial stretching rate
b:	Stagnation-point flow rate
Bi:	Biot number
$B_0$ :	Magnetic field of constant strength
$C_f$ :	Skin friction coefficient
$c_p$ :	Heat capacity at constant pressure
Ec:	Eckert number
h:	Heat coefficient at the disk surface
Ha:	Hartmann number
k:	Thermal conductivity coefficient
Nu:	Local Nusselt number
Pr:	Prandtl number
$q_w$ :	Heat flux from the plate
$Re_r$ :	Stagnation flow Reynolds number
(r,z):	Polar coordinates
(u,w):	Velocity components
$U_\infty$ :	Free stream velocity
T:	Temperature
$T_f$ :	The convective fluid temperature below the moving sheet
$T_\infty$ :	Free stream temperature.

## Greek Letters

$\rho$ :	Fluid density
$\sigma$ :	Electrical conductivity
$\eta$ :	Similarity variable
$\lambda$ :	Velocity ratio parameter
$\tau$ :	Surface shear stress
$\mu$ :	Coefficient of viscosity
$\nu$ :	Kinematic viscosity
$\theta$ :	Dimensionless temperature.

## Acknowledgments

The authors wish to acknowledge financial support from the University of Venda and NRF.

## References

- [1] M. S. Abel and N. Mahesha, "Heat transfer in MHD viscoelastic fluid flow over a stretching sheet with variable thermal conductivity, non-uniform heat source and radiation," *Applied Mathematical Modelling*, vol. 32, no. 10, pp. 1965–1983, 2008.
- [2] R. C. Bataller, "Viscoelastic fluid flow and heat transfer over a stretching sheet under the effects of a non-uniform heat source, viscous dissipation and thermal radiation," *International Journal of Heat and Mass Transfer*, vol. 50, no. 15-16, pp. 3152–3162, 2007.
- [3] M. M. M. Abdou, "Effect of radiation with temperature dependent viscosity and thermal conductivity on unsteady a stretching sheet through porous media," *Nonlinear Analysis*, vol. 15, no. 3, pp. 257–270, 2010.
- [4] S. Munawar, A. Mehmood, and A. Ali, "Effects of slip on flow between stretchable disks using optical homotopy analysis method," *Canadian Journal of Pure and Applied Sciences*, vol. 1, no. 2, pp. 50–67, 2011.
- [5] T. Hayat, S. A. Shehzad, M. Qasim, and S. Obaidat, "Flow of a second grade fluid with convective boundary conditions," *Thermal Science*, vol. 15, no. 2, pp. S253–S261, 2011.
- [6] S. Shateyi and S. S. Motsa, "Variable viscosity on magnetohydrodynamic fluid flow and heat transfer over an unsteady stretching surface with Hall effect," *Boundary Value Problems*, vol. 2010, Article ID 257568, 20 pages, 2010.
- [7] O. D. Makinde and P. Sibanda, "Effects of chemical reaction on boundary layer flow past a vertical stretching surface in the presence of internal heat generation," *International Journal of Numerical Methods for Heat and Fluid Flow*, vol. 21, no. 6, pp. 779–792, 2011.
- [8] M. Ashraf and K. Batool, "MHD flow and heat transfer of a micropolar fluid over a stretchable disk," *Journal of Theoretical and Applied Mechanics*, vol. 51, no. 1, pp. 25–38, 2013.
- [9] K. Hiemenz, "Die Grenzschicht in Einem in Dem Gleichformigen Flussigkeitsstrom Eingetauchten Gerade Kreiszylinder," *Dingler Polytech Journal*, vol. 326, pp. 321–410, 1911.
- [10] S. S. Motsa, Y. Khan, and S. Shateyi, "A new numerical solution of Maxwell fluid over a shrinking sheet in the region of a stagnation point," *Mathematical Problems in Engineering*, vol. 2012, Article ID 290615, 11 pages, 2012.
- [11] K. Bhattacharyya, S. Mukhopadhyay, and G. C. Layek, "Slip effects on boundary layer stagnation-point flow and heat transfer towards a shrinking sheet," *International Journal of Heat and Mass Transfer*, vol. 54, no. 1–3, pp. 308–313, 2011.
- [12] O. D. Makinde and W. M. Charles, "Computational dynamics of hydromagnetic stagnation flow towards a stretching sheet," *Applied and Computational Mathematics*, vol. 9, no. 2, pp. 243–251, 2010.
- [13] S. Nadeem, M. Hussain, and M. Naz, "MHD stagnation flow of a micropolar fluid through a porous medium," *Meccanica*, vol. 45, no. 6, pp. 869–880, 2010.
- [14] O. D. Makinde, "Heat and mass transfer by MHD mixed convection stagnation point flow toward a vertical plate embedded in a highly porous medium with radiation and internal heat generation," *Meccanica*, vol. 47, no. 5, pp. 1173–1184, 2012.

- [15] S. P. Devi, D. Anjali, and R. Uma, "Effects of thermal radiation on hydromagnetic flow due to a porous rotating disk with hall effect," *Journal of Applied Fluid Mechanics*, vol. 5, no. 2, pp. 1–8, 2012.
- [16] T. R. Mahapatra and S. K. Nandy, "Momentum and heat transfer in MHD axisymmetric stagnation-point flow over a shrinking sheet," *Journal of Applied Fluid Mechanics*, vol. 6, no. 1, pp. 121–129, 2013.
- [17] A. J. Chamkha and S. E. Ahmed, "Similarity solution for unsteady MHD flow near a stagnation point of a three-dimensional porous body with heat and mass transfer, heat generation/absorption and chemical reaction," *Journal of Applied Fluid Mechanics*, vol. 4, no. 3, pp. 87–94, 2011.
- [18] S. S. Motsa and S. Shateyi, "A new approach for the solution of three-dimensional magnetohydrodynamic rotating flow over a shrinking sheet," *Mathematical Problems in Engineering*, vol. 2010, Article ID 586340, 15 pages, 2010.
- [19] O. D. Makinde and A. Aziz, "Boundary layer flow of a nanofluid past a stretching sheet with a convective boundary condition," *International Journal of Thermal Sciences*, vol. 50, no. 7, pp. 1326–1332, 2011.
- [20] A. S. Butt and A. Ali, "Effects of magnetic field on entropy generation in flow and heat transfer to a radially stretching surface," *Chinese Physics Letters*, vol. 30, no. 2, pp. 1–5, 2013.
- [21] O. D. Makinde, W. A. Khan, and Z. H. Khan, "Buoyancy effects on MHD stagnation point flow and heat transfer of a nanofluid past a convectively heated stretching/shrinking sheet," *International Journal of Heat and Mass Transfer*, vol. 62, pp. 526–533, 2013.
- [22] W. Ibrahim, B. Shankar, and M. M. Nandeppanavar, "MHD stagnation point flow and heat transfer due to nanofluid towards a stretching sheet," *International Journal of Heat and Mass Transfer*, vol. 56, pp. 1–9, 2013.
- [23] S. S. Motsa, P. G. Dlamini, and M. Khumalo, "Solving hyperchaotic systems using the spectral relaxation method," *Abstract and Applied Analysis*, vol. 2012, Article ID 203461, 18 pages, 2012.
- [24] S. S. Motsa, P. Dlamini, and M. Khumalo, "A new multistage spectral relaxation method for solving chaotic initial value systems," *Nonlinear Dynamics*, vol. 72, no. 1–2, pp. 265–283, 2013.
- [25] S. S. Motsa and Z. G. Makukula, "On spectral relaxation method approach for steady von Kármán flow of a Reiner-Rivlin fluid with Joule heating, viscous dissipation and suction/injection," *Central European Journal of Physics*, vol. 11, no. 3, pp. 363–374, 2013.
- [26] N. A. Abu Bakar, W. M. K. A. W. Zaimi, R. Abdul Hamid, B. Bidin, and A. Ishak, "Boundary layer flow over a stretching sheet with a convective boundary condition and slip effect," *World Applied Sciences Journal*, vol. 17, pp. 49–53, 2012.
- [27] A. Aziz, "A similarity solution for laminar thermal boundary layer over a flat plate with a convective surface boundary condition," *Communications in Nonlinear Science and Numerical Simulation*, vol. 14, no. 4, pp. 1064–1068, 2009.
- [28] A. Ishak, "Similarity solutions for flow and heat transfer over a permeable surface with convective boundary condition," *Applied Mathematics and Computation*, vol. 217, no. 2, pp. 837–842, 2010.
- [29] C. Canuto, M. Y. Hussaini, A. Quarteroni, and T. A. Zang, *Spectral Methods in Fluid Dynamics*, Springer, Berlin, Germany, 1988.
- [30] L. N. Trefethen, *Spectral Methods in MATLAB*, SIAM, Philadelphia, Pa, USA, 2000.

## Research Article

# MHD Boundary Layer Flow due to Exponential Stretching Surface with Radiation and Chemical Reaction

Y. I. Seini<sup>1</sup> and O. D. Makinde<sup>2</sup>

<sup>1</sup> Faculty of Mathematical Sciences, University for Development Studies, P.O. Box 1350, Tamale, Ghana

<sup>2</sup> Institute for Advanced Research in Mathematical Modelling and Computations, Cape Peninsula University of Technology, P.O. Box 1906, Bellville 7535, South Africa

Correspondence should be addressed to Y. I. Seini; yakubuseini@yahoo.com

Received 17 February 2013; Accepted 26 March 2013

Academic Editor: Tirivanhu Chinyoka

Copyright © 2013 Y. I. Seini and O. D. Makinde. This is an open access article distributed under the Creative Commons Attribution License, which permits unrestricted use, distribution, and reproduction in any medium, provided the original work is properly cited.

The effects of radiation and first order homogeneous chemical reaction on hydromagnetic boundary layer flow of a viscous, steady, and incompressible fluid over an exponential stretching sheet have been investigated. The governing system of partial differential equations has been transformed into ordinary differential equations using similarity variables. The dimensionless system of differential equations was then solved numerically by the Runge-Kutta method. The skin-friction coefficient and the rate of heat and mass transfers are presented in tables whilst velocity, temperature, and concentration profiles are illustrated graphically for various varying parameter values. It was found that the rate of heat transfer at the surface decreases with increasing values of the transverse magnetic field parameter and the radiation parameter.

## 1. Introduction

The effects of radiation on hydromagnetic boundary layer flow of a continuously stretching surface have attracted considerable attention in recent times due to its numerous applications in industry. It occurs frequently in manufacturing involving hot metal rolling, wire drawing, glass-fiber production, paper production, drawing of plastic films, and metal spinning, as well as metal and polymer extrusion processes. Crane [1] was the first to investigate the boundary layer flow caused by a stretching sheet moving with linearly varying velocity from a fixed point whilst the heat transfer aspect of the problem was investigated by Carragher and Crane [2] under the conditions that the temperature difference between the surface and the ambient fluid was proportional to the power of the distance from a fixed point.

Magyari and Keller [3] then investigated the steady boundary layer flow on a stretching continuous surface with exponential temperature distribution while Partha et al. [4] analyzed the effects of viscous dissipation on the mixed convection heat transfer from an exponentially stretching surface. Sajid and Hayat [5] extended the works of Partha et al. [4] to include radiation effects on the flow over exponential

stretching sheet and solved the problem analytically using the homotopy analysis method. The numerical solution for the same problem was then presented by Bidin and Nazar [6]. MHD steady flow and heat transfer on the sliding plate have been investigated by Makinde [7] whilst Ibrahim and Makinde [8] analyzed the radiation effects on chemically reacting MHD boundary layer flow of heat and mass transfer through a porous vertical flat plate. Makinde [9] earlier obtained results for the free-convection flow with thermal radiation and mass transfer past a moving vertical porous plate with Makinde and Ogulu [10] reporting on the effects of thermal radiation on heat and mass transfer of a variable viscosity fluid past a vertical porous plate permeated by transverse magnetic field. Magnetohydrodynamics has significant applications in the cooling of nuclear reactors using liquid sodium. Many processes in chemical engineering occur at high temperatures and radiation can be very significant and thus important for the design of pertinent equipment [11].

The present study considers the effect of chemical reaction on MHD boundary layer flow due to an exponential stretching surface in the presence of radiation. The paper is organized as follows: the mathematical model of the problem is described in Section 2 and the numerical method

is described in Section 3. In Section 4, we present both the numerical and graphical results with discussions. The concluding remarks are presented in Section 5.

## 2. Mathematical Model

Consider a steady two-dimensional flow of an incompressible, viscous, and electrically conducting fluid caused by a stretching surface. Assume that the plate has a surface temperature ( $T_w$ ) and concentration ( $C_w$ ) and is placed in a quiescent fluid of uniform ambient temperature ( $T_\infty$ ) and concentration ( $C_\infty$ ) (see Figure 1). A variable magnetic field  $B(x)$  is applied normally to the stretching sheet surface and the induced magnetic field is negligible. This can be justified for MHD flow at small magnetic Reynolds number. Under the usual boundary layer approximations, the flow and heat transfer with the radiation effects are governed by the following equations:

$$\frac{\partial u}{\partial x} + \frac{\partial v}{\partial y} = 0, \quad (1)$$

$$u \frac{\partial u}{\partial x} + v \frac{\partial u}{\partial y} = \nu \frac{\partial^2 u}{\partial y^2} - \frac{\sigma B^2}{\rho} u, \quad (2)$$

$$u \frac{\partial T}{\partial x} + v \frac{\partial T}{\partial y} = \frac{k}{\rho c_p} \frac{\partial^2 T}{\partial y^2} - \frac{1}{\rho c_p} \frac{\partial q_r}{\partial y} + \frac{\nu}{c_p} \left( \frac{\partial u}{\partial y} \right)^2 + \frac{\sigma B^2}{\rho c_p} u^2, \quad (3)$$

$$u \frac{\partial C}{\partial x} + v \frac{\partial C}{\partial y} = D \frac{\partial^2 C}{\partial y^2} - \gamma (C - C_\infty), \quad (4)$$

where  $u$  and  $v$  are the velocities in the  $x$ - and  $y$ -directions, respectively,  $\rho$  is the fluid density,  $\nu$  the kinematic viscosity,  $k$  the thermal conductivity, and  $c_p$  is the specific heat at constant pressure.  $T$  and  $C$  represent the fluid temperature and concentration in the boundary layer, respectively, whilst  $D$  represents the mass diffusivity,  $\gamma$  the reaction rate parameter, and  $q_r$  the radiative heat flux.

The boundary conditions for the problem are taken similarly to Ishak [12] given as

$$\begin{aligned} u &= U_w = U_0 e^{x/L}, & v &= 0, \\ T &= T_w = T_\infty + T_0 e^{x/(2L)}, \\ C &= C_w = C_\infty + C_0 e^{x/(2L)} & \text{at } y = 0, \\ u &\longrightarrow 0, & T &\longrightarrow T_\infty, \\ C &\longrightarrow C_\infty & \text{as } y \longrightarrow \infty, \end{aligned} \quad (5)$$

where  $U_0$  is the reference velocity,  $T_0$  is the reference temperature,  $C_0$  is the reference concentration, and  $L$  is the reference length. Understanding fluid radiations has been based on assumptions of some reasonable simplifications [13, 14]. These simplifications assumed that the fluid is in the optically thin limit and does not absorb its own radiation except those emitted by other boundaries. For an optically thick gas, its self-absorption rises and the situation becomes

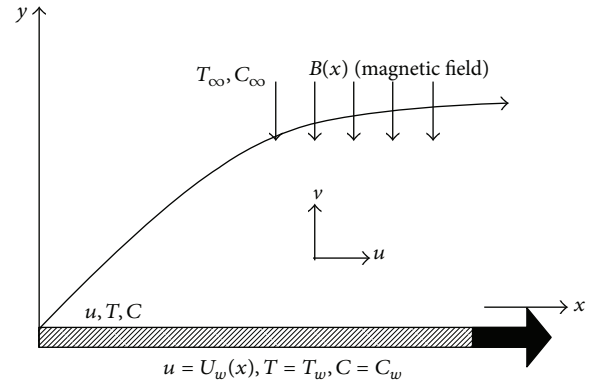


FIGURE 1: Physical configuration.

difficult. However, the problem can be simplified by using the Rosseland approximation [15–17] which simplifies the radiative heat flux to:

$$q_r = \frac{4\sigma^*}{3k^*} \frac{\partial T^4}{\partial y}, \quad (6)$$

where  $\sigma^*$  and  $k^*$  are the Stefan-Boltzmann constant and the mean absorption coefficient, respectively. This approximation is valid at points optically far from the surface and good only for intensive absorption, which is for an optically thick boundary layer, Bataller [18], Siegel and Howell [16], and Sparrow and Cess [17]. It is assumed that the temperature differences within the flow involving the term  $T^4$  may be expressed as a linear function of temperature. Hence, expanding  $T^4$  in a Taylor series about  $T_\infty$  and neglecting higher-order terms result in

$$T^4 \approx 4T_\infty^3 T - 3T_\infty^4. \quad (7)$$

Using (6) and (7) reduces (3) to:

$$\begin{aligned} u \frac{\partial T}{\partial x} + v \frac{\partial T}{\partial y} &= \left( \frac{k}{\rho c_p} + \frac{16\sigma^* T_\infty^3}{3\rho c_p k^*} \right) \frac{\partial^2 T}{\partial y^2} \\ &+ \frac{\nu}{c_p} \left( \frac{\partial u}{\partial y} \right)^2 + \frac{\sigma B^2}{\rho c_p} u^2. \end{aligned} \quad (8)$$

To obtain similarity solutions, it is assumed that the variable magnetic field  $B(x)$  is of the form:

$$B(x) = B_0 e^{x/(2L)}, \quad (9)$$

where  $B_0$  is the constant magnetic field.

The continuity equation (1) is satisfied by introducing a stream function  $\psi$  defined in the usual form as:

$$u = \frac{\partial \psi}{\partial y}, \quad v = -\frac{\partial \psi}{\partial x} \quad (10)$$

The momentum, energy, and concentration equations were transformed to ordinary differential equations using similarity variables similar to that employed by Ishak [12]:

$$\begin{aligned}
 u &= U_0 e^{x/L} f'(\eta), \\
 v &= -\left(\frac{\nu U_0}{2L}\right)^{1/2} e^{x/(2L)} (f(\eta) + \eta f'(\eta)), \\
 \eta &= y \left(\frac{U_0}{2\nu L}\right)^{1/2} e^{x/(2L)}, \\
 T &= T_\infty + T_0 e^{x/(2L)} \theta(\eta), \\
 C &= C_\infty + C_0 e^{x/(2L)} \phi(\eta),
 \end{aligned}
 \tag{11}$$

where  $\eta$  is the dimensionless similarity variable,  $f(\eta)$  is the dimensionless stream function,  $\theta(\eta)$  is the dimensionless temperature,  $\phi(\eta)$  is the dimensionless concentration, and primes denote differentiation with respect to  $\eta$ .

The transformed ordinary differential equations are

$$f''' + ff'' - 2f'^2 - Mf' = 0, \tag{12}$$

$$\left(1 + \frac{4}{3}K\right)\theta'' + \text{Pr}f\theta' - \text{Pr}f'\theta + \text{Pr}MEc f'^2 + \text{Pr}Ec f''^2 = 0,
 \tag{13}$$

$$\phi'' + \text{Sc}f\phi' - \text{Sc}f'\phi - \text{Sc}\beta\phi = 0, \tag{14}$$

in which  $M = 2\sigma B_0^2 L / (\rho U_0)$  is the magnetic parameter,  $K = 4\sigma^* T_\infty^3 / (k^* k)$  is the radiation parameter,  $\text{Pr} = \rho\nu c_p / k$  is the Prandtl number,  $\text{Ec} = U_0^2 e^{2x/L} / (c_p(T_w - T_\infty))$  is the Eckert number, and  $\text{Sc} = \nu / D$  is the Schmidt number while  $\beta = 2L\gamma / U_w$  is the reaction rate parameter.

The transformed boundary conditions are

$$\begin{aligned}
 f'(0) &= 1, & f(0) &= 0, \\
 \theta(0) &= 1, & \phi(0) &= 1, \\
 f'(\eta) &\rightarrow 0, & \theta(\eta) &\rightarrow 0, & \phi(\eta) &\rightarrow 0 \\
 && && & \text{as } \eta \rightarrow \infty.
 \end{aligned}
 \tag{15}$$

### 3. Numerical Procedure

The nonlinear differential equations (12), (13), and (14) with the boundary conditions (15) have been solved numerically using the fourth order Runge-Kutta integration scheme with a modified version of the Newton-Raphson algorithm.

We let

$$\begin{aligned}
 f &= x_1, & f' &= x_2, & f'' &= x_3, \\
 \theta &= x_4, & \theta' &= x_5, \\
 \phi &= x_6, & \phi' &= x_7.
 \end{aligned}
 \tag{16}$$

Equations (12), (13), and (14) are then reduced to systems of first order differential equations as

$$\begin{aligned}
 f' &= x'_1 = x_2, \\
 f'' &= x'_2 = x_3, \\
 f''' &= x'_3 = -x_1 x_3 + 2x_2^2 + Mx_2, \\
 \theta' &= x'_4 = x_5, \\
 \theta'' &= x'_5 = \frac{(-\text{Pr}x_1 x_5 + \text{Pr}x_2 x_4 - \text{Pr}MEc x_2^2 - \text{Pr}Ec x_3^2)}{(1 + 4K/3)}, \\
 \phi' &= x'_6 = x_7, \\
 \phi'' &= -\text{Sc}(x_1 x_7 - x_2 x_6 - \beta x_6)
 \end{aligned}
 \tag{17}$$

subject to the following initial conditions:

$$\begin{aligned}
 x_1(0) &= 0, & x_2(0) &= 1, & x_3(0) &= s_1, \\
 x_4(0) &= 1, & x_5(0) &= s_2, \\
 x_6(0) &= 1, & x_7(0) &= s_3.
 \end{aligned}
 \tag{18}$$

In the shooting method, the unspecified initial conditions  $s_1$ ,  $s_2$ , and  $s_3$  in (18) are assumed and (17) integrated numerically as an initial valued problem to a given terminal point. The accuracy of the assumed missing initial conditions was checked by comparing the calculated value of the dependent variable at the terminal point with its given value there. If differences exist, improved values of the missing initial conditions are obtained and the process repeated. The computations were done by a written program which uses a symbolic and computational computer language (maple) with a step size of  $\Delta\eta = 0.001$  selected to be satisfactory for a convergence criterion of  $10^{-7}$  in nearly all cases. The maximum value of  $\eta_\infty$  to each group of parameters was determined when the values of the unknown boundary conditions at  $\eta = 0$  do not change to successful loop with error less than  $10^{-7}$ .

### 4. Results and Discussion

The system of ordinary differential equations (12), (13), and (14) has been solved numerically using shooting technique together with the fourth order Runge-Kutta method and a modified version of the Newton-Raphson algorithm to tackle the problem [8, 20–22]. From the process of numerical computation, the main physical quantities of interest, namely, the local skin friction coefficient, the local Nusselt number and the local Sherwood numbers, which are, respectively, proportional to  $-f''(0)$ ,  $-\theta'(0)$ , and  $-\phi'(0)$ , were worked out and their numerical results presented in Table 1. It is observed that increasing the radiation parameter ( $K$ ) increases the rate of heat transfer at the surface  $-\theta'(0)$ . However, the skin friction coefficient and the rate of mass transfer are not

TABLE 1: Values of  $f''(0)$ ,  $-\theta'(0)$  and  $-\phi'(0)$  for varying values of  $K$ ,  $M$ ,  $Pr$ ,  $Sc$ ,  $Ec$  and  $\beta$ .

$K$	$M$	$Pr$	$Sc$	$Ec$	$\beta$	$-f''(0)$	$-\theta'(0)$	$-\phi'(0)$
0	1	0.71	0.24	1	1	1.629178	-0.006338	0.561835
0.1	1	0.71	0.24	1	1	1.629178	0.0069647	0.561835
0.5	1	0.71	0.24	1	1	1.629178	0.0357547	0.561835
0.1	2	0.71	0.24	1	1	1.912620	-0.276418	0.554247
0.1	5	0.71	0.24	1	1	2.581130	-0.874464	0.541547
0.1	10	0.71	0.24	1	1	3.415289	-1.536591	0.531405
0.1	1	2.14	0.24	1	1	1.629178	-0.268846	0.561835
0.1	1	5.71	0.24	1	1	1.629178	-1.153452	0.561835
0.1	1	7.10	0.24	1	1	1.629178	-1.499348	0.561835
0.1	1	0.71	1	1	1	1.629178	0.0069647	1.399541
0.1	1	0.71	2	1	1	1.629178	0.0069647	2.394415
0.1	1	0.71	2.64	1	1	1.629178	0.0069647	3.027351
0.1	1	0.71	0.24	2	1	1.629178	-0.598521	0.561835
0.1	1	0.71	0.24	3	1	1.629178	-1.204006	0.561835
0.1	1	0.71	0.24	1	2	1.629178	0.0069647	0.754006
0.1	1	0.71	0.24	1	3	1.629178	0.0069647	0.903556

TABLE 2: Values of  $\theta'(0)$  for different values of  $K$ ,  $M$  and  $Pr$  compared to previous results.

$K$	$M$	$Pr$	Magyari and Keller [3]	El-Aziz [19]	Bidin and Nazar [6]	Ishak [12]	Present study
0	0	1	-0.954782	-0.954785	-0.9548	-0.9548	-0.954811
		2			-1.4714	-1.4715	-1.471454
		3	-1.869075	-1.869074	-1.8691	-1.8691	-1.869069
		5	-2.500132	-2.500132		-2.5001	-2.500128
		10	-3.660379	-3.660372		-3.6604	-3.660369
	1	1				-0.8611	-0.861509

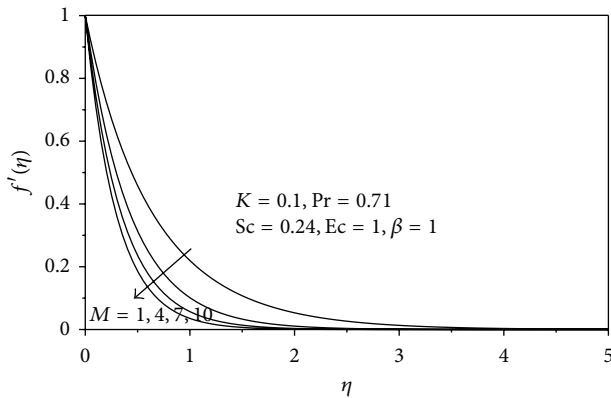


FIGURE 2: Velocity profiles for varying values of magnetic parameter ( $M$ ).

affected by the radiation parameter. The magnetic parameter is observed to increase the skin friction coefficient at the surface due to the presence of the Lorenz force. It however reduces the rate of both heat and mass transfers at the boundary for obvious reasons. Conversely, the rate of mass transfers at the surface decreases with increasing values of reaction rate and Schmidt numbers whilst the rate of heat transfer decreases with increasing values of the Eckert number. Comparison with earlier results from the literature showed a perfect agreement (see Table 2).

The velocity profiles for increasing values of the magnetic field parameter ( $M$ ) shown in Figure 2 indicate that the rate

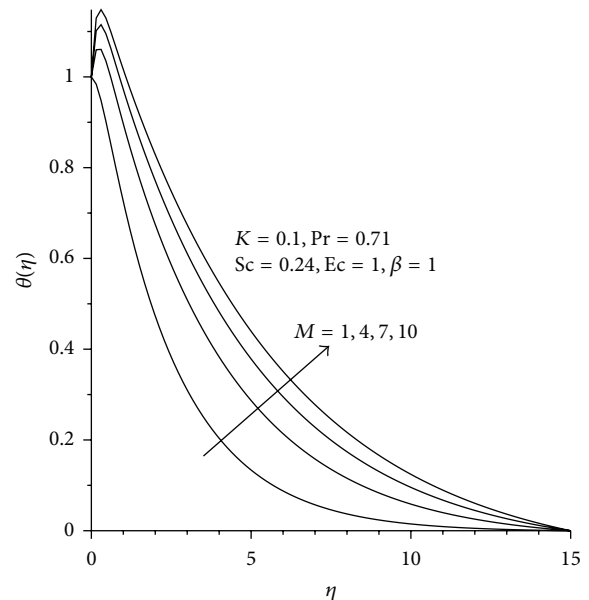


FIGURE 3: Temperature profiles for varying values of magnetic parameter ( $M$ ).

of flow is considerably reduced. This clearly reveals that the transverse magnetic field opposes the fluid transport due to increasing Lorentz force associated with increasing magnetic parameter. Figures 3 and 4 illustrate the effect of increasing the magnetic parameter on the temperature and concentration profiles, respectively. Whilst the temperature profiles

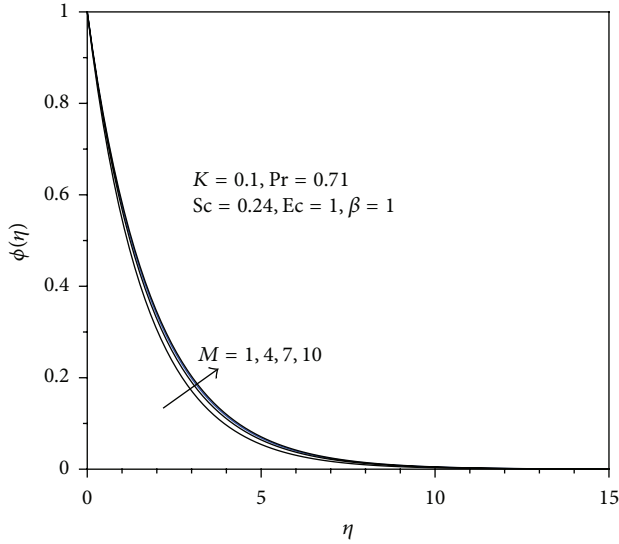


FIGURE 4: Concentration profiles for varying values of the magnetic parameter ( $M$ ).

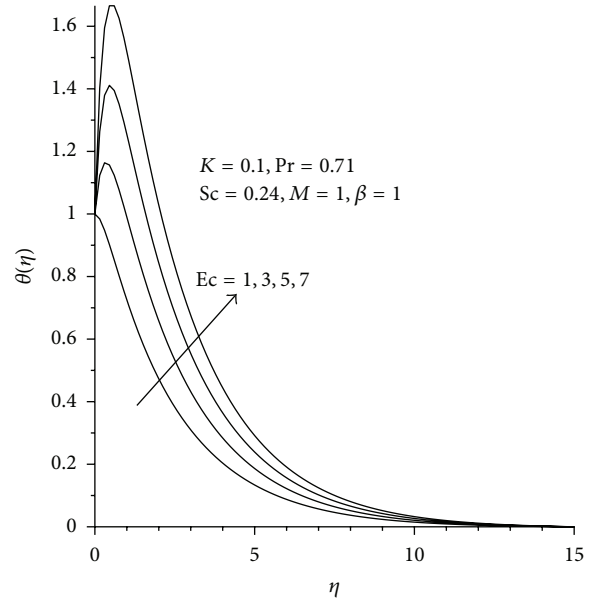


FIGURE 6: Temperature profiles for varying values of Eckert number ( $Ec$ ).

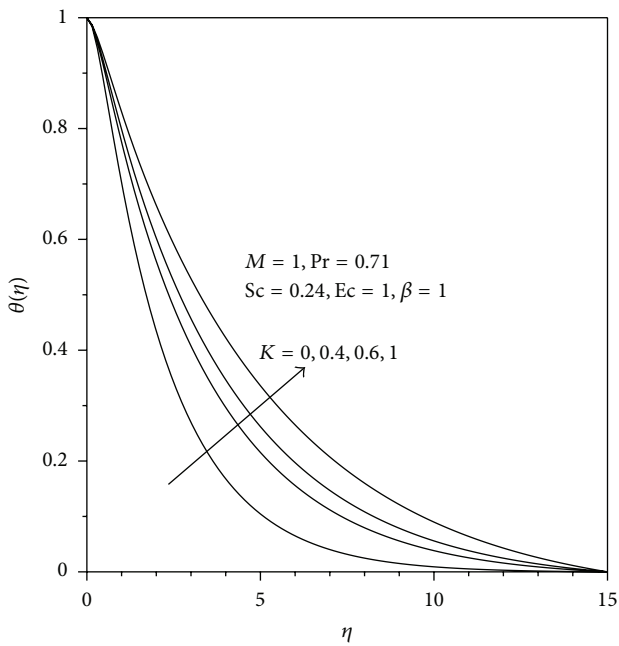


FIGURE 5: Temperature profiles for varying values of radiation parameter ( $K$ ).

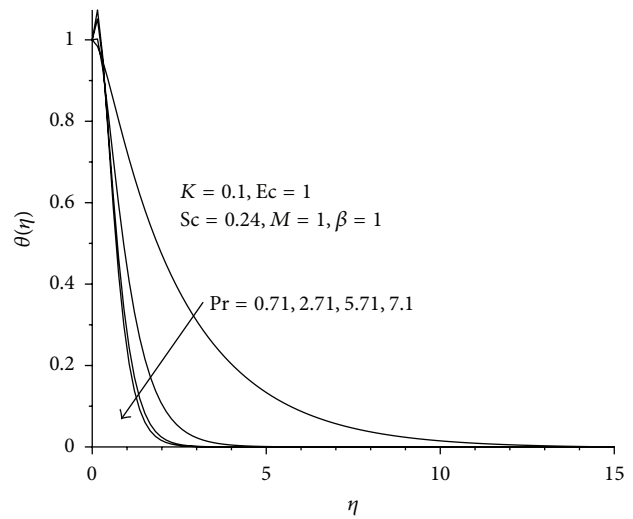


FIGURE 7: Temperature profiles for varying values of Prandtl number ( $Pr$ ).

showed an increase with increasing magnetic parameter due to Ohmic heating, the concentration profiles indicate a slight increase. It is further noted that Prandtl number ( $Pr$ ) and the radiation parameter ( $K$ ) have no effects on the velocity and chemical concentration profiles which is clearly obvious from (12) and (14). Figures 5, 6, and 7 illustrate the effects of  $K$ ,  $Ec$ , and  $Pr$ , respectively, on the temperature profiles. It is observed that increasing the radiation parameter ( $K$ ) and the Eckert number ( $Ec$ ) increases the thermal boundary layer thickness whilst the reverse is observed for increasing values of the Prandtl number ( $Pr$ ). This is due to the fact that  $Pr$  decreases the thermal diffusivity resulting in the

heat being diffused away from the surface more slowly and in consequence increases the temperature gradient at the surface. The influences of the Schmidt number ( $Sc$ ) and the reaction rate parameter ( $\beta$ ) on the concentration profiles are, respectively, illustrated in Figures 8 and 9. It can be observed that increases in both  $Sc$  and  $\beta$  reduce the concentration boundary layer. In all the illustrations (Figures 2–9), it is observed that the far field boundary conditions are satisfied asymptotically, supporting the accuracy of the numerical procedure.

### 5. Conclusions

The effect of radiation and chemical reaction on the steady MHD boundary layer flow over an exponentially stretching

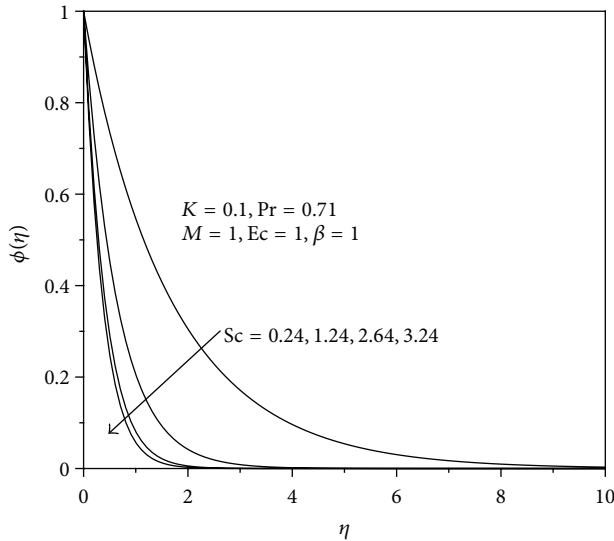


FIGURE 8: Concentration profiles for varying values of Schmidt number ( $Sc$ ).

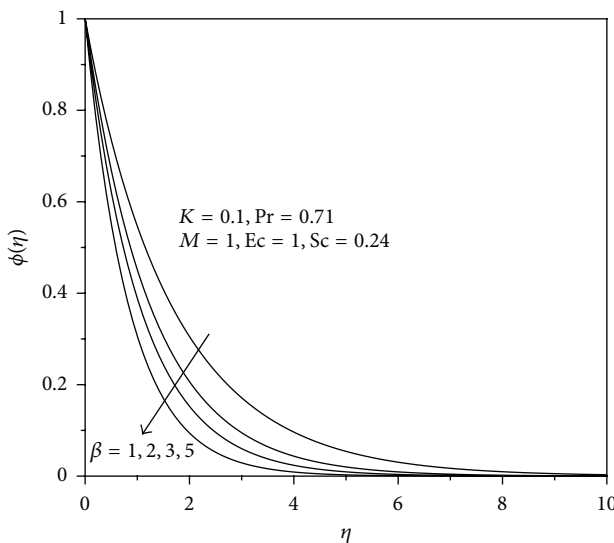


FIGURE 9: Concentration profiles for varying reaction rate parameter ( $\beta$ ).

sheet was investigated. The numerical results showed good agreement with previously reported cases available in the literature. It was found that the surface shear stress increases with increasing magnetic parameter ( $M$ ) whilst the heat transfer rate increases with Prandtl number  $Pr$ . It however decreases with both magnetic ( $M$ ) and radiation ( $K$ ) parameters. Furthermore, the chemical concentration boundary layer was found to decrease near the boundary with increasing reaction rate parameter and the Schmidt numbers.

### Acknowledgment

The authors acknowledge the contributions and comments of the reviewers in improving the paper.

### References

- [1] L. J. Crane, "Flow past a stretching plate," *Zeitschrift für angewandte Mathematik und Physik*, vol. 21, pp. 645–655, 1970.
- [2] P. Carragher and L. J. Crane, "Heat transfer on a continuous stretching sheet," *Zeitschrift für Angewandte Mathematik und Mechanik*, vol. 62, pp. 564–573, 1982.
- [3] E. Magyari and B. Keller, "Heat and mass transfer in the boundary layers on an exponentially stretching continuous surface," *Journal of Physics D*, vol. 32, no. 5, pp. 577–585, 1999.
- [4] M. K. Partha, P. V. S. N. Murthy, and G. P. Rajasekhar, "Effect of viscous dissipation on the mixed convection heat transfer from an exponentially stretching surface," *Heat and Mass Transfer*, vol. 41, no. 4, pp. 360–366, 2005.
- [5] M. Sajid and T. Hayat, "Influence of thermal radiation on the boundary layer flow due to an exponentially stretching sheet," *International Communications in Heat and Mass Transfer*, vol. 35, no. 3, pp. 347–356, 2008.
- [6] B. Bidin and R. Nazar, "Numerical solution of the boundary layer flow over an exponentially stretching sheet with thermal radiation," *European Journal of Scientific Research*, vol. 33, no. 4, pp. 710–717, 2009.
- [7] O. D. Makinde, "MHD steady flow and heat transfer on the sliding plate," *AMSE, Modeling, Measure. Control B*, vol. 70, no. 1, pp. 61–70, 2001.
- [8] S. Y. Ibrahim and O. D. Makinde, "Radiation effect on chemically reacting magnetohydrodynamics (MHD) boundary layer flow of heat and mass transfer through a porous vertical flat plate," *International Journal of Physical Sciences*, vol. 6, no. 6, pp. 1508–1516, 2011.
- [9] O. D. Makinde, "Free convection flow with thermal radiation and mass transfer past a moving vertical porous plate," *International Communications in Heat and Mass Transfer*, vol. 32, no. 10, pp. 1411–1419, 2005.
- [10] O. D. Makinde and A. Ogulu, "The effect of thermal radiation on the heat and mass transfer flow of a variable viscosity fluid past a vertical porous plate permeated by a transverse magnetic field," *Chemical Engineering Communications*, vol. 195, no. 12, pp. 1575–1584, 2008.
- [11] M. A. Seddeek, "Effects of radiation and variable viscosity on a MHD free convection flow past a semi-infinite flat plate with an aligned magnetic field in the case of unsteady flow," *International Journal of Heat and Mass Transfer*, vol. 45, no. 4, pp. 931–935, 2001.
- [12] A. Ishak, "MHD boundary layer flow due to an exponentially stretching sheet with radiation effect," *Sains Malaysiana*, vol. 40, no. 4, pp. 391–395, 2011.
- [13] E. M. Aboeldahab and M. S. El Gendy, "Radiation effect on MHD free-convective flow of a gas past a semi-infinite vertical plate with variable thermophysical properties for high-temperature differences," *Canadian Journal of Physics*, vol. 80, no. 12, pp. 1609–1619, 2002.
- [14] A. C. Cogley, W. G. Vincenty, and S. E. Gilles, "Differential approximation for radiative transfer in a non-grey gas near equilibrium," *AIAA Journal*, vol. 6, pp. 551–553, 1968.
- [15] S. Rosseland, *Theoretical Astrophysics*, Oxford University, New York, NY, USA, 1936.
- [16] R. Siegel and J. R. Howell, "Thermal radiation," in *Heat Transfer*, Washington, DC, USA, 3rd edition, 1992.
- [17] E. M. Sparrow and R. D. Cess, *Radiation Heat Transfer*, Hemisphere, Washington, DC, USA, 1978.

- [18] R. C. Bataller, "Similarity solutions for boundary layer flow and heat transfer of a FENE-P fluid with thermal radiation," *Physics Letters, Section A*, vol. 372, no. 14, pp. 2431–2439, 2008.
- [19] M. A. El-Aziz, "Viscous dissipation effect on mixed convection flow of a micropolar fluid over an exponentially stretching sheet," *Canadian Journal of Physics*, vol. 87, no. 4, pp. 359–368, 2009.
- [20] S. Y. Ibrahim and O. D. Makinde, "On MHD boundary layer flow of a chemically reacting fluid with heat and mass transfer past a stretching sheet," *International Journal of Fluid Mechanics*, vol. 2, no. 2, pp. 123–132, 2010.
- [21] S. Y. Ibrahim and O. D. Makinde, "Chemically reacting MHD boundary layer flow of heat and mass transfer over a moving vertical plate with suction," *Scientific Research and Essays*, vol. 5, no. 19, pp. 2875–2882, 2010.
- [22] S. Y. Ibrahim and O. D. Makinde, "Chemically reacting MHD boundary layer flow of heat and mass transfer past a low-heat-resistant sheet moving vertically downwards," *Scientific Research and Essays*, vol. 6, no. 22, pp. 4762–4775, 2011.

## Research Article

# Entropy Generation Analysis in a Variable Viscosity MHD Channel Flow with Permeable Walls and Convective Heating

A. S. Eegunjobi<sup>1</sup> and O. D. Makinde<sup>2</sup>

<sup>1</sup> Department of Mathematics and Statistics, Polytechnic of Namibia, Namibia's University of Science and Technology, Private Bag 13388, 13 Storch Street, Windhoek, Namibia

<sup>2</sup> Institute for Advanced Research in Mathematical Modelling and Computation, Cape Peninsula University of Technology, P.O. Box 1906, Bellville 7535, South Africa

Correspondence should be addressed to A. S. Eegunjobi; [samdet1@yahoo.com](mailto:samdet1@yahoo.com)

Received 18 February 2013; Revised 6 April 2013; Accepted 13 April 2013

Academic Editor: Tirivanhu Chinyoka

Copyright © 2013 A. S. Eegunjobi and O. D. Makinde. This is an open access article distributed under the Creative Commons Attribution License, which permits unrestricted use, distribution, and reproduction in any medium, provided the original work is properly cited.

This paper examines the effects of the thermodynamic second law on steady flow of an incompressible variable viscosity electrically conducting fluid in a channel with permeable walls and convective surface boundary conditions. The nonlinear model governing equations are solved numerically using shooting quadrature. Numerical results of the velocity and temperature profiles are utilised to compute the entropy generation number and the Bejan number. The results revealed that entropy generation minimization can be achieved by appropriate combination of the regulated values of thermophysical parameters controlling the flow systems.

## 1. Introduction

Hydromagnetic channel flows have attracted the attention of many researchers due to their numerous engineering and industrial applications. Such flow can be found in magnetohydrodynamic (MHD) generator, geothermal reservoirs, cooling of nuclear reactors, petroleum reservoirs, accelerators, pumps, flow meter, astrophysics, metallurgy, crystal growth, magnetic filtration and separation, jet printers, and microfluidic devices [1]. Several researchers have discussed MHD fluid flow under various physical situations [2–4]. Lehnert [5] presented a theoretical investigation on the behavior of electrical conducting liquid under magnetic field. Makinde and Mhone [6] investigated the combined effect of transverse magnetic field and radiative heat transfer on unsteady flow of a conducting optically thin fluid through a channel filled with saturated porous medium and nonuniform wall temperature. Seth et al. [7] studied unsteady MHD Couette flow of a viscous incompressible electrically conducting fluid between two parallel porous plates in the presence of a transverse magnetic field. Agarwal [8] analyzed

the effect of magnetic field on generalized Couette flow. The combined effects of variable viscosity and electrical conductivity on MHD generalized Couette flow and heat transfer were numerically investigated by Makinde and Onyejekwe [9].

Meanwhile, most industrial and engineering flow processes and thermal systems are unable to work at optimal level due to entropy production. Therefore, it is imperative to determine the factors that contributed to entropy generation in order to minimize their effects and maximize the flow system efficiency. The analysis of entropy generation minimization in a thermal system was pioneered by Bejan [10]. Thereafter, several researchers have theoretically studied entropy generation in thermal and flow systems under many physical situations [11–13]. Sahin and Ben-Mansour [14] reported a numerical solution of the entropy generation in a circular pipe. Hooman [15] studied the effects of different thermal boundary conditions on entropy generation in a microscale forced convection with velocity slip. The effect of Navier slip on entropy generation in a porous channel with suction/injection was investigated by Eegunjobi and

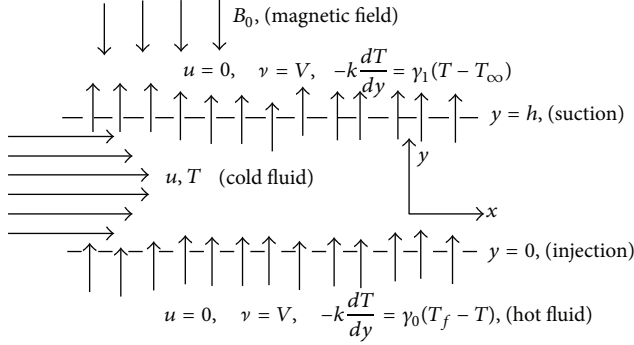


FIGURE 1: Schematic diagram of the problem.

Makinde [16]. Recently, Makinde and Eegunjobi [17] reported a numerical solution for the effects of convective heating on entropy production in a channel with permeable walls.

In this present study, the recent work of Makinde and Eegunjobi [17] is extended to include the combined effects of variable viscosity and asymmetric convective boundary conditions on the entropy generation rate in MHD porous channel flow. In the following sections, the model problem is formulated, analyzed, and numerically solved. Pertinent results are presented graphically and discussed quantitatively, with respect to various thermophysical parameters controlling the flow system.

## 2. Mathematical Model

We consider a steady, incompressible flow of an electrically conducting variable viscosity fluid between two fixed permeable parallel infinite plates of width  $h$ . The flow is fully developed and the edge effects are disregarded. A constant magnetic field of strength  $B_0$  is imposed transversely in the  $y$ -direction. In addition, both the electric field and Hall effect are not present (see Seth et al. [7], Turkyilmazoglu [18]). The applied magnetic field is assumed to be strong enough so that the induced magnetic field due to the fluid motion is weak and can be neglected. It is assumed that the lower permeable plate, where fluid injection occurs, is convectively heated; while at the upper permeable plate both fluid suction and convective heat loss take place as shown in Figure 1.

Under these assumptions, the governing equations for the momentum and energy balance in one dimension can be written as follows [7–9, 16, 17]:

$$V \frac{du}{dy} = -\frac{1}{\rho} \frac{dP}{dx} + \frac{1}{\rho} \frac{d}{dy} \left( \bar{\mu}(T) \frac{du}{dy} \right) - \frac{\sigma B_0^2 u}{\rho}, \quad (1)$$

$$V \frac{dT}{dy} = \alpha \frac{d^2 T}{dy^2} + \frac{\bar{\mu}(T)}{\rho c_p} \left( \frac{du}{dy} \right)^2 + \frac{\sigma B_0^2 u^2}{\rho c_p}. \quad (2)$$

The boundary conditions are

$$\begin{aligned} u(0) = 0, \quad -k \frac{dT}{dy}(0) &= \gamma_0 (T_f - T(0)), \\ u(h) = 0, \quad -k \frac{dT}{dy}(h) &= \gamma_1 (T(h) - T_\infty), \end{aligned} \quad (3)$$

where  $(x, y)$  is the axial and normal coordinates,  $u$  is the velocity of the fluid,  $P$  is the fluid pressure,  $V$  is the uniform suction/injection velocity at the channel walls,  $\gamma_0$  is the heat transfer coefficient at the lower plate,  $\gamma_1$  is the heat transfer coefficient at the upper plate,  $\alpha$  is the thermal diffusivity,  $\rho$  is the fluid density,  $\sigma$  is the fluid electrical conductivity,  $k$  is the thermal conductivity coefficient,  $c_p$  is the specific heat at constant pressure,  $T_f$  is the temperature of the hot fluid at the lower permeable plate,  $T$  is the channel fluid temperature, and  $T_\infty$  is the ambient temperature above the upper plate. The temperature dependent viscosity  $\bar{\mu}$  can be expressed as [9]

$$\bar{\mu}(T) = \mu_0 e^{-m(T-T_\infty)}, \quad (4)$$

where  $m$  is a viscosity variation parameter and  $\mu_0$  is the fluid dynamic viscosity at the ambient temperature. We introduce the following nondimensional quantities:

$$\begin{aligned} \eta &= \frac{y}{h}, \quad \alpha = \frac{k}{\rho c_p}, \quad w = \frac{u}{V}, \\ \theta &= \frac{T - T_\infty}{T_f - T_\infty}, \quad X = \frac{x}{h}, \quad \bar{P} = \frac{p h}{\mu_0 V}, \\ G &= -\frac{\partial \bar{P}}{\partial X}, \quad \mu = \frac{\bar{\mu}}{\mu_0}, \quad v = \frac{\mu_0}{\rho}. \end{aligned} \quad (5)$$

Substituting (5) into (1)–(4), we obtain

$$\frac{d^2 w}{d\eta^2} - \varepsilon \frac{d\theta}{d\eta} \frac{dw}{d\eta} - e^{\varepsilon\theta} \left( \text{Re} \frac{dw}{d\eta} + \text{Ha} w - G \right) = 0, \quad (6)$$

$$\frac{d^2 \theta}{d\eta^2} - \text{Re Pr} \frac{d\theta}{d\eta} + \text{Ec Pr} e^{-\varepsilon\theta} \left( \frac{dw}{d\eta} \right)^2 + \text{Ec Pr Ha} w^2 = 0, \quad (7)$$

with the boundary conditions

$$\begin{aligned} w(0) = 0, \quad \frac{d\theta}{d\eta}(0) &= \text{Bi}_0 (\theta(0) - 1), \\ w(1) = 0, \quad \frac{d\theta}{d\eta}(1) &= -\text{Bi}_1 \theta(1), \end{aligned} \quad (8)$$

where  $G$  is the pressure gradient parameter,

$$\text{Re} = Vh/\nu \text{ (Reynolds number),}$$

$$\text{Pr} = \nu/\alpha \text{ (Prandtl number),}$$

$$\text{Ec} = V^2/c_p (T_f - T_\infty) \text{ (Eckert number),}$$

$$\text{Ha} = \sigma B_0^2 h^2/\mu_0 \text{ (magnetic field parameter or square of Hartmann number),}$$

$$\begin{aligned}\varepsilon &= m(T_f - T_\infty) \text{ (variable viscosity parameter),} \\ \text{Bi}_0 &= \gamma_0 h/k \text{ (lower plate Biot number),} \\ \text{Bi}_1 &= \gamma_1 h/k \text{ (upper plate Biot number).}\end{aligned}$$

It is important to note that  $\varepsilon = 0$  corresponds to the case of constant viscosity conducting fluid. The exact solution of (6) for the fluid velocity is possible under this constant viscosity scenario and we obtain

$$w(\eta) = \frac{G}{\text{Ha}} \left[ \frac{e^{\alpha\eta} (e^\beta - 1) - e^{\beta\eta} (e^\alpha - 1)}{e^\alpha - e^\beta} + 1 \right], \quad (9)$$

where  $\alpha = (\text{Re} + \sqrt{\text{Re}^2 + 4\text{Ha}})/2$  and  $\beta = (\text{Re} - \sqrt{\text{Re}^2 + 4\text{Ha}})/2$ . Moreover, the coupled nonlinear boundary value problem represented by (6)-(7) together with their boundary conditions in (8) has been solved numerically using an efficient fourth-order Runge-Kutta method along with a shooting technique [19].

### 3. Entropy Analysis

In many engineering and industrial processes, entropy production destroys the available energy in the system. It is therefore imperative to determine the rate of entropy generation in a system, in order to optimize energy in the system for efficient operation in the system. The convection process in a channel is inherently irreversible and this causes continuous entropy generation. Wood [11] gave the local volumetric rate of entropy generation for a viscous incompressible conducting fluid in the presence of magnetic field as follows:

$$E_G = \frac{k}{T_\infty^2} \left( \frac{dT}{dy} \right)^2 + \frac{\mu}{T_\infty} \left( \frac{du}{dy} \right)^2 + \frac{\sigma B_0^2}{T_\infty} u^2. \quad (10)$$

In (10), the first term represents irreversibility due to heat transfer; the second term is entropy generation due to viscous dissipation, while the third term is local entropy generation due to the effect of the magnetic field (Joule heating or Ohmic heating). Using (5), the dimensionless form of local entropy generation rate in (10) is given as follows:

$$\text{Ns} = \frac{T_\infty^2 h^2 E_G}{k(T_f - T_\infty)^2} = \left( \frac{d\theta}{d\eta} \right)^2 + \frac{\text{Br}}{\Omega} \left[ e^{-\varepsilon\theta} \left( \frac{dw}{d\eta} \right)^2 + \text{Haw}^2 \right], \quad (11)$$

where  $\Omega = (T_f - T_\infty)/T_\infty$  is the temperature difference parameter and  $\text{Br} = \text{Ec Pr}$  is the Brinkmann number. The Bejan number (Be) is defined as

$$\text{Be} = \frac{N_1}{N_s} = \frac{1}{1 + \Phi}, \quad (12)$$

where  $N_s = N_1 + N_2$ ,  $N_1 = (d\theta/d\eta)^2$  (heat transfer irreversibility due to heat transfer),  $N_2 = (\text{Br}/\Omega)[e^{-\varepsilon\theta}(dw/d\eta)^2 + \text{Haw}^2]$  (fluid friction and magnetic field irreversibility),  $\Phi = N_2/N_1$  (irreversibility ratio).

The Bejan number (Be) as shown in (12) has a range of  $0 \leq \text{Be} \leq 1$ . If  $\text{Be} = 0$ , then the irreversibility is dominated by the combined effects of fluid friction and magnetic fields, but if  $\text{Be} = 1$ , then the irreversibility due to heat transfer dominates the flow system by the virtue of finite temperature differences.

TABLE 1: Comparison between the exact and numerical solution of velocity profile for  $G = 1$ ,  $\text{Re} = 1$ ,  $\text{Ha} = 1$ , and  $\varepsilon = 0$ .

$\eta$	Exact solution $w(\eta)$	Numerical solution $w(\eta)$
0	0	0
0.1	0.035822	0.035822
0.2	0.065264	0.065264
0.3	0.087963	0.087963
0.4	0.103449	0.103449
0.5	0.111127	0.111279
0.6	0.110257	0.110257
0.7	0.099930	0.099930
0.8	0.079042	0.079042
0.9	0.046264	0.046264
1.0	0	0

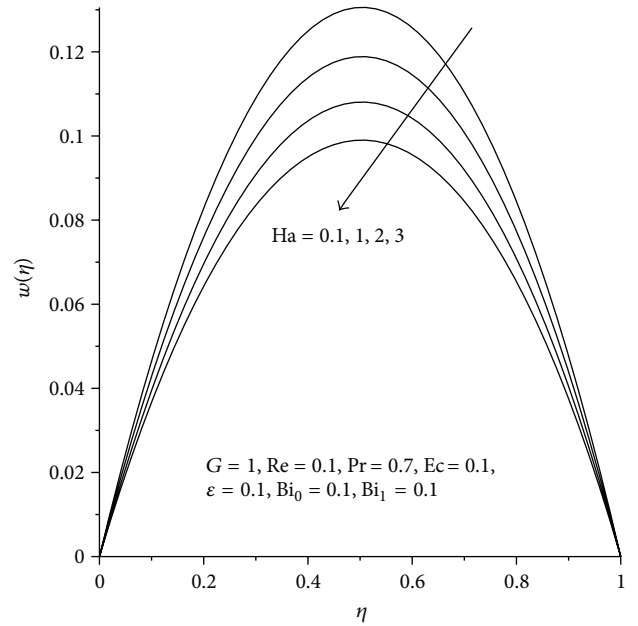
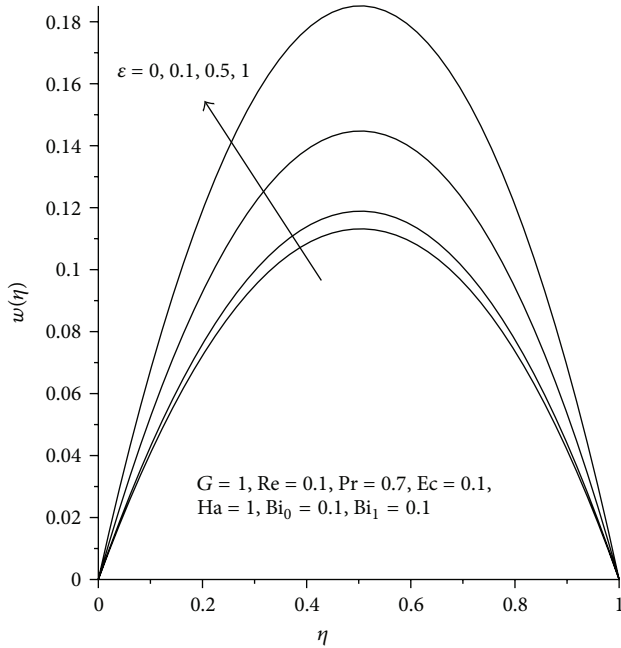
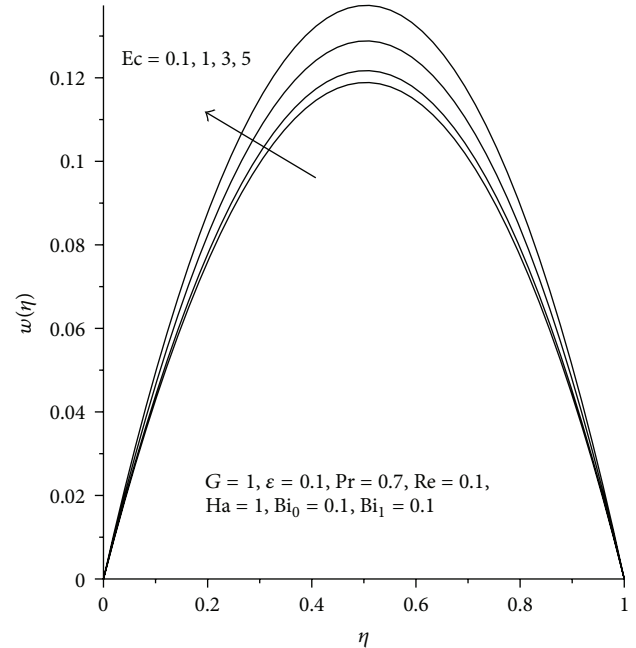
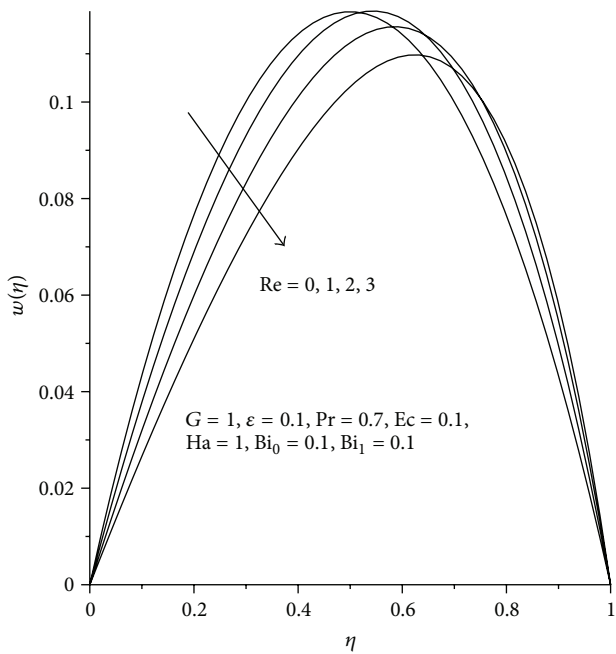
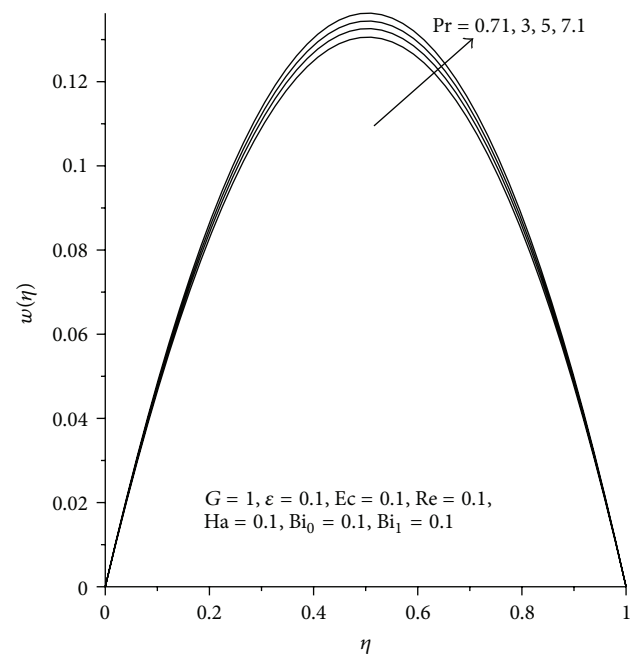


FIGURE 2: Velocity profiles increasing  $\text{Ha}$ .

## 4. Results and Discussion

The numerical results for the fluid velocity, temperature, entropy generation rate, and Bejan number distributions are reported in Table 1 and Figures 2–30. Representative values of various parameters are utilized and the Prandtl number  $\text{Pr}$  is assumed to range from  $0.71$  (Air)  $\leq \text{Pr} \leq 7.1$  (water). In order to validate the accuracy of our numerical procedure, we compare a special case of our result ( $\varepsilon = 0$ ) with the exact solution for the velocity profile in (9). The results displayed in Table 1 show perfect agreement and attest the correctness of our results.

**4.1. Effects of Parameter Variations on Velocity Profiles.** The effects of variation in key parameters on the velocity profiles are shown in Figures 2–8. Generally, the velocity profiles are parabolic in geometries with zero values at the channel

FIGURE 3: Velocity profiles increasing  $\epsilon$ .FIGURE 5: Velocity profiles with increasing  $Ec$ .FIGURE 4: Velocity profiles with increasing  $Re$ .FIGURE 6: Velocity profiles increasing  $Pr$ .

walls due to no slip condition and attain their maximum value within channel. In Figure 2, it is observed that the fluid velocity decreases with increasing magnetic field intensity ( $Ha$ ). This can be attributed to the presence of Lorentz force acting as a resistance to the flow as expected and is in perfect agreement with earlier results as reported in the literature [3–9]. As the fluid viscosity decreases as shown in Figure 3 with increasing values of  $\epsilon$ , the velocity profiles increase. The fluid velocity decreases and skews towards the upper plate as

Reynolds number ( $Re$ ) increases due to increasing injection at the lower plate and increasing suction at the upper plate as shown in Figure 4. Figures 5 and 6 show that the fluid velocity increases with increase in the values of Eckert number ( $Ec$ ) and Prandtl number ( $Pr$ ). As  $Ec$  increases, the velocity gradient increases as a result of a decrease in the fluid viscosity, consequently, the fluid velocity increases. Figures 7 and 8 show that the fluid velocity increases with increasing convective heating ( $Bi_0$ ) at the lower plate and decreases with

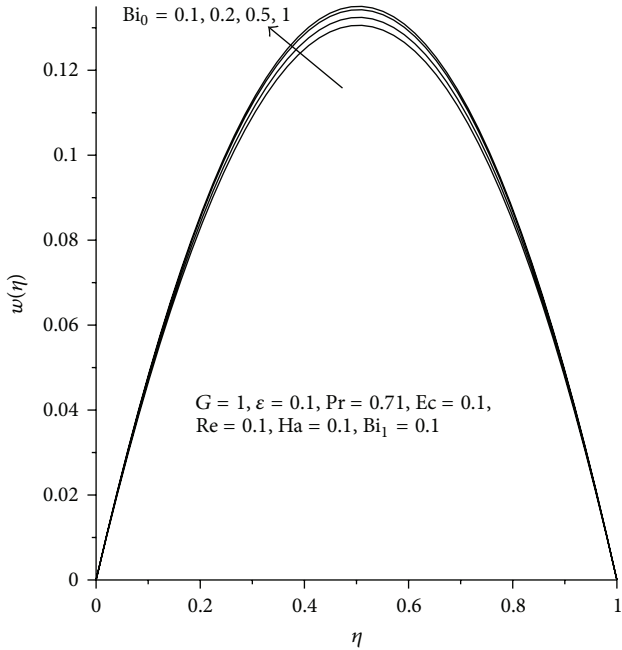


FIGURE 7: Velocity profiles with increasing  $Bi_0$ .

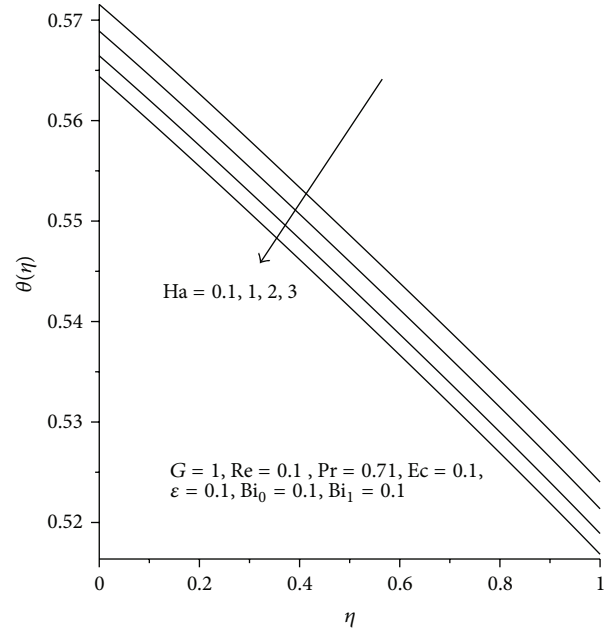


FIGURE 9: Temperature with increasing  $Ha$ .

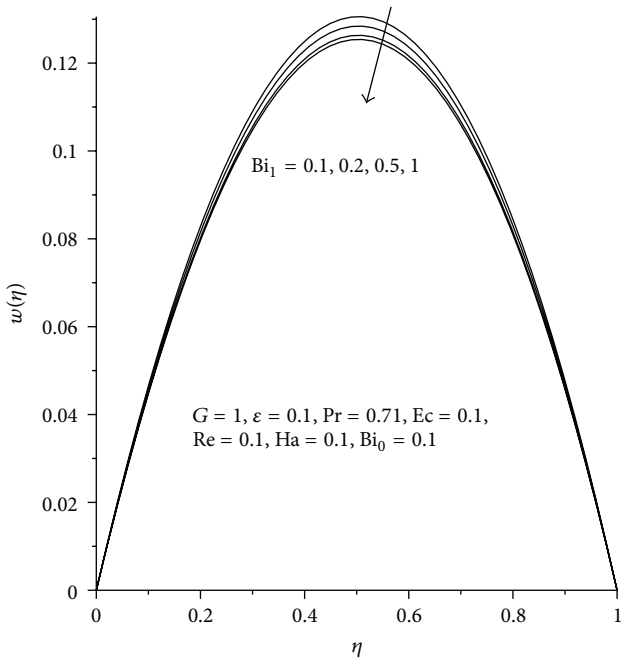


FIGURE 8: Velocity profiles with increasing  $Bi_1$ .

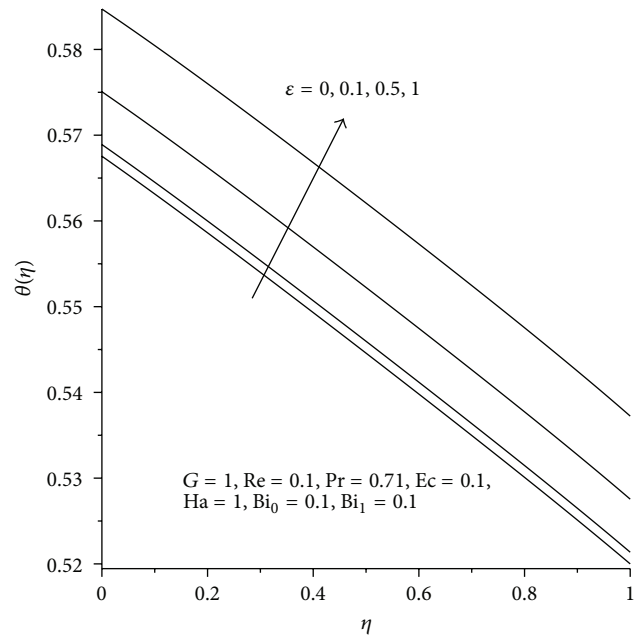


FIGURE 10: Temperature with increasing  $\epsilon$ .

increasing convective cooling ( $Bi_1$ ) at the upper plate. This is expected, since the fluid becomes lighter and flows faster with increasing temperature due to convective heating.

4.2. Effects of Parameter Variations on Temperature Profiles. Figures 9–15 demonstrate the effects of various parameters on the temperature profiles. The imposed thermal boundary conditions ensure that the fluid temperature at the lower plate

is highest due to convective heating and decreases gradually to its lowest value at the upper plate due to convective heat loss to the ambient. Figure 9 shows the influence of magnetic field ( $Ha$ ) on the flow field. As  $Ha$  increases due to increasing magnetic field intensity, the fluid temperature decreases within the channel. This decrease in the fluid temperature may be attributed to the combined effects of fluid suction and convective heat loss, despite the presence of Ohmic heating (or Lorentz heating) which serves as additional heat source to the flow system. The effects of increasing  $\epsilon$ ,  $Re$ ,

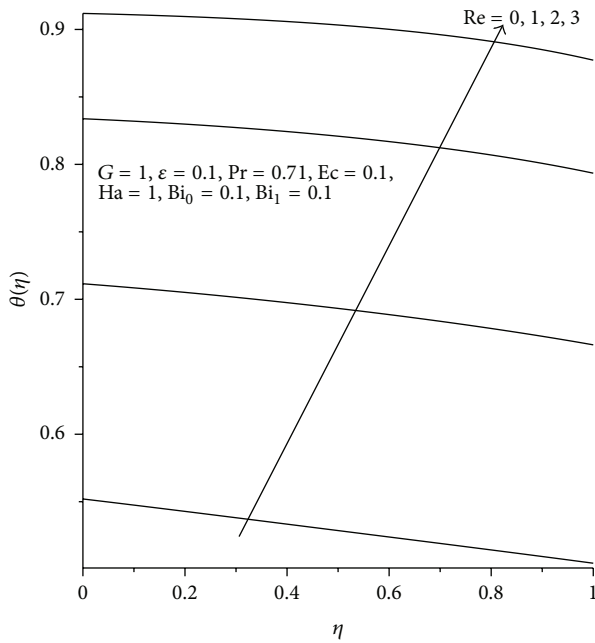


FIGURE 11: Temperature with increasing Re.

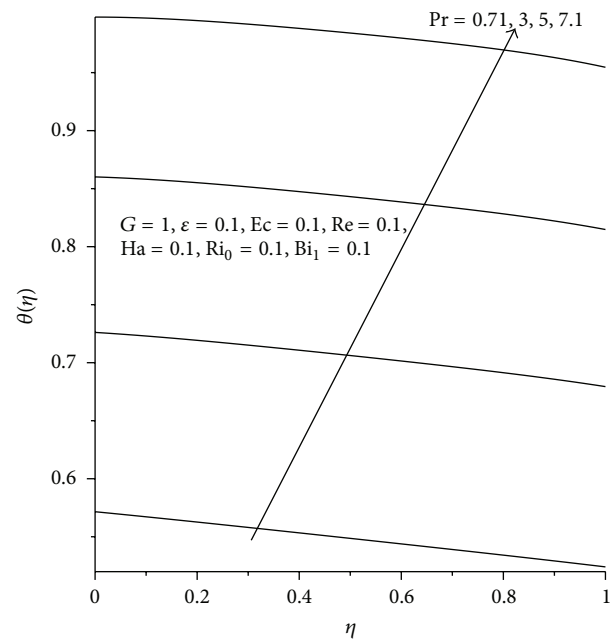


FIGURE 13: Temperature with increasing Pr.

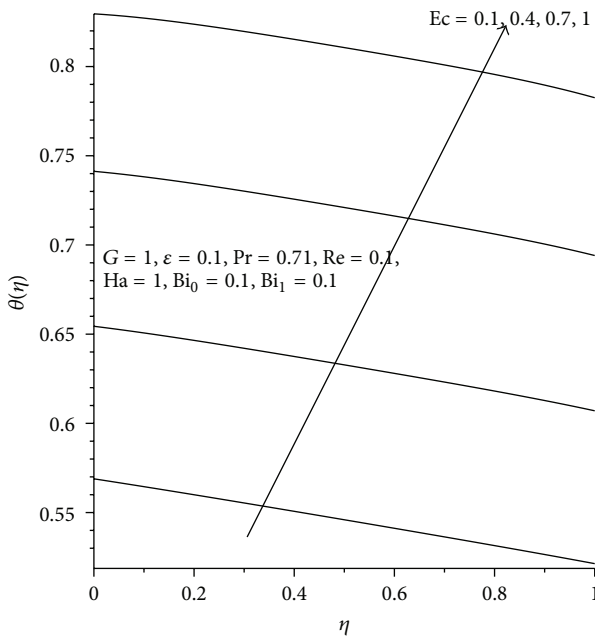
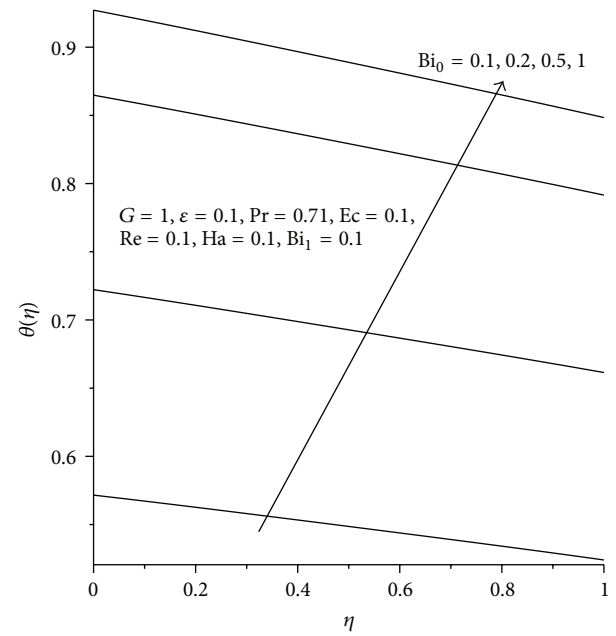


FIGURE 12: Temperature with increasing Ec.

FIGURE 14: Temperature with increasing  $Bi_0$ .

and  $Ec$  are shown in the Figures 10, 11, and 12. The rise in the fluid temperature is observed with increasing values of these parameters. This may be attributed to the facts that as  $\epsilon$ ,  $Re$ , and  $Ec$  increase, the fluid viscosity becomes lighter and viscous heating increases due to increasing convective heating at the lower plate increases leading to a rise in the fluid temperature. As the Prandtl number increases from  $Pr = 0.71$  (Air) to  $Pr = 7.1$  (water) the fluid temperature decreases as illustrated in Figure 13. In Figure 14, a rise in the fluid temperature is observed with increasing convective heating at

the lower plate as expected. Figure 15 shows the effect of increasing  $Bi_1$  on the temperature. As expected, the fluid temperature decreases due to increasing convective heat loss at the upper plate.

**4.3. Effects of Parameter Variations on Entropy Generation Rate.** The effects of key parameters variation on entropy generation rate ( $N_s$ ) are shown in Figures 16–22. Generally, the entropy production is more pronounced at the permeable channel walls and decreases towards the channel centerline

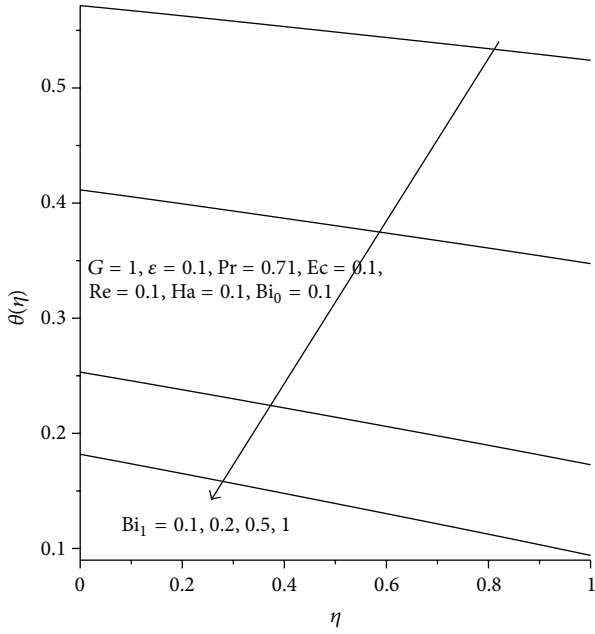


FIGURE 15: Temperature with increasing  $Bi_1$ .

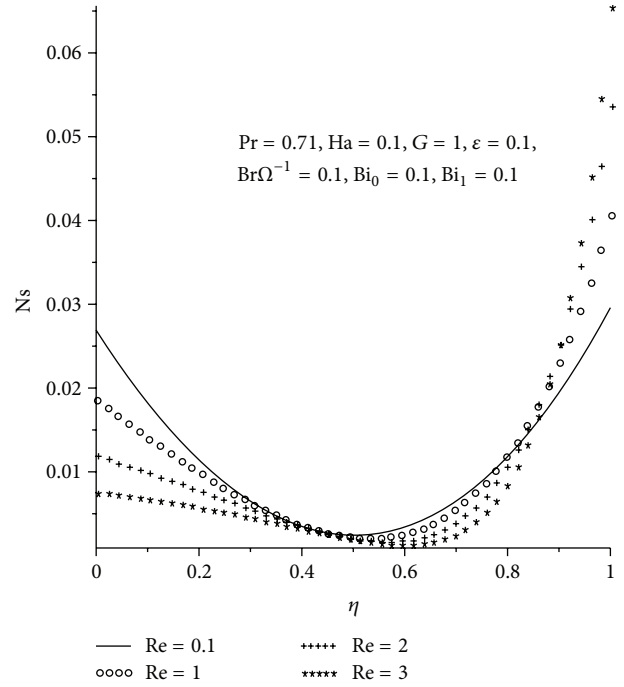


FIGURE 17:  $N_s$  with increasing  $Re$ .

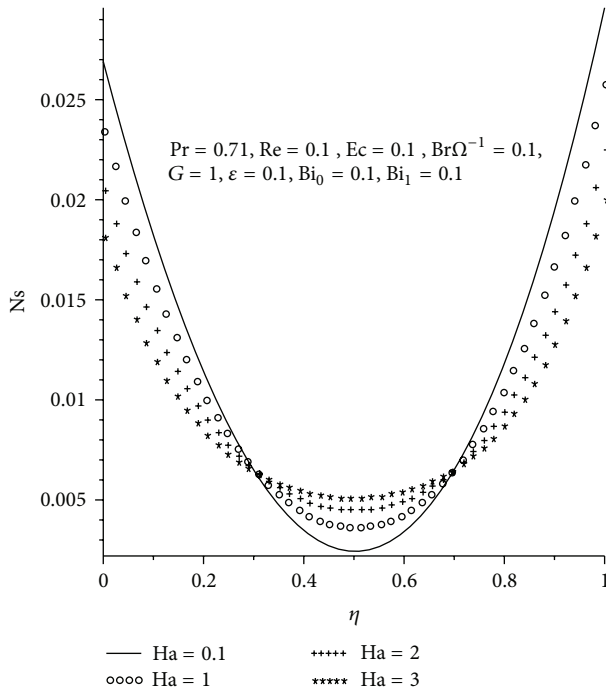


FIGURE 16:  $N_s$  with increasing  $Ha$ .

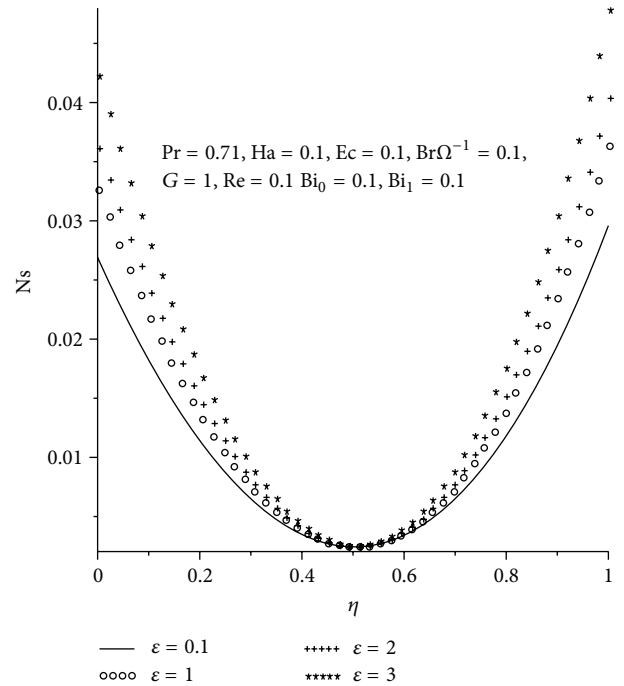


FIGURE 18:  $N_s$  with increasing  $\epsilon$ .

region. Figure 16 reveals the effect of increasing magnetic field intensity ( $Ha$ ) on entropy generation rate ( $N_s$ ). As  $Ha$  increases, the entropy generation decreases at the walls and increases at the centerline region of the channel. Meanwhile, it is interesting to note that two points exist, that is,  $\eta = 0.3$  and  $\eta = 0.7$  within the flow field where the entropy production is not affected by increasing  $Ha$ . In Figure 17, it

is observed that entropy production is enhanced with increasing suction ( $Re$ ) at the upper wall region, while a decrease in the entropy generation occurs at the lower wall with increasing fluid injection. The effects of  $\epsilon$ ,  $Br\Omega^{-1}$  and  $G$  on the entropy generation rate are shown in Figures 18–20. As the fluid viscosity decreases with increasing values of  $\epsilon$ ,

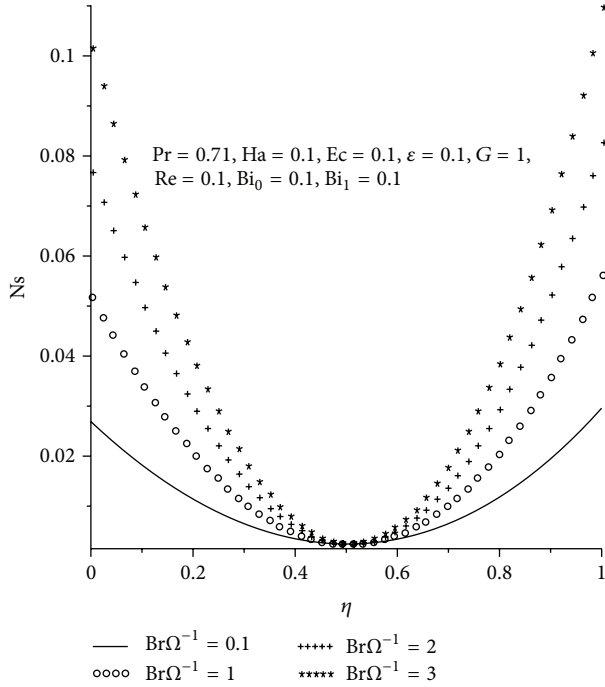


FIGURE 19:  $N_s$  with increasing  $Br\Omega^{-1}$ .

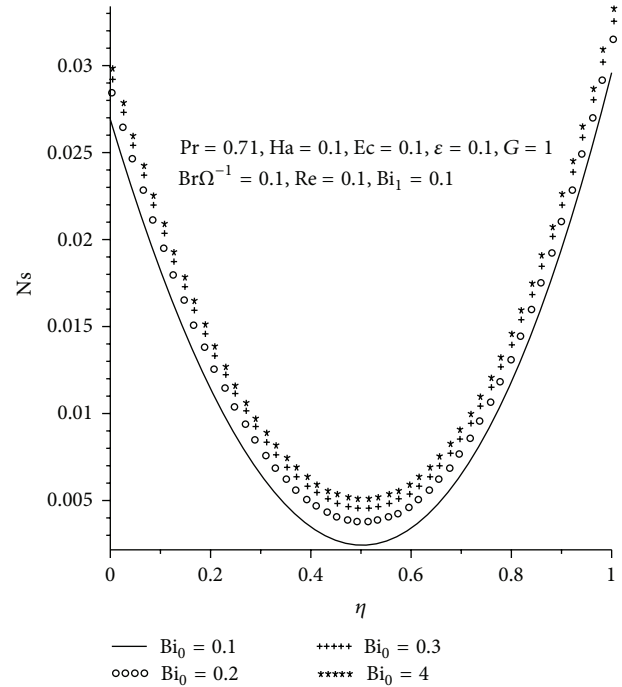


FIGURE 21:  $N_s$  with increasing  $Bi_0$ .

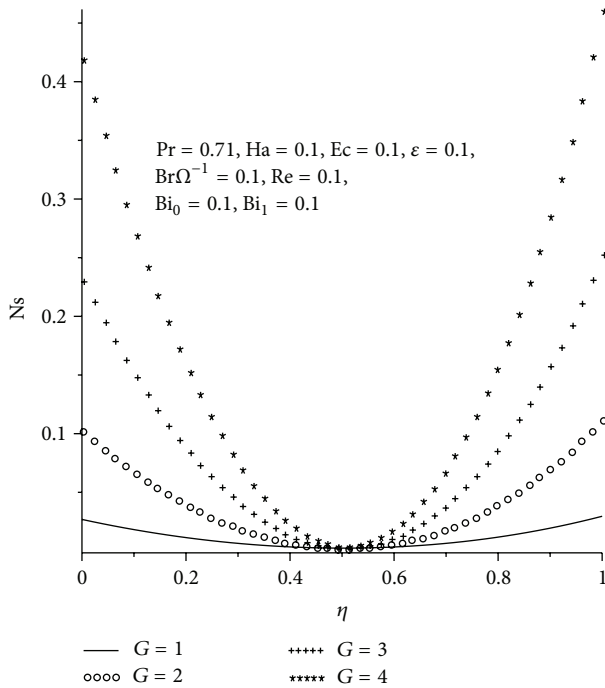


FIGURE 20:  $N_s$  with increasing  $G$ .

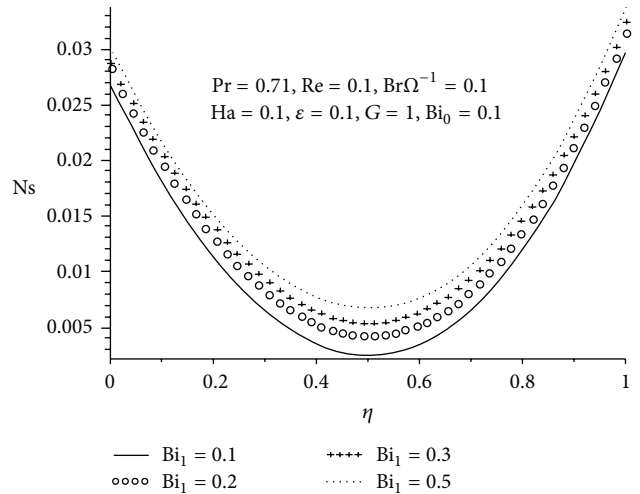


FIGURE 22:  $N_s$  with increasing  $Bi_1$ .

the entropy production increases at both walls and decreases towards the channel centerline as indicated in Figure 18. However, a point exists at  $\eta = 0.5$ , where entropy production is virtually zero. This may be attributed to the presence of zero velocity gradients at the region. A similar trend of entropy production is observed with increasing values of group

parameter ( $Br\Omega^{-1}$ ) and constant pressure gradient ( $G$ ) as demonstrated in Figures 19 and 20. Figures 21 and 22 show that the entropy generation rate increases with combined increase in convective heating at the lower wall and convective cooling at the upper wall that is, as  $Bi_0$  and  $Bi_1$  increase.

4.4. Effects of Parameter Variations on Bejan Number. Figures 23–30 illustrate the effects of different values of key parameters on Bejan number ( $Be$ ). Generally, the Bejan number is highest along the channel centerline region with irreversibility due to heat transfer dominating the flow, while near the channel walls the fluid friction and magnetic field

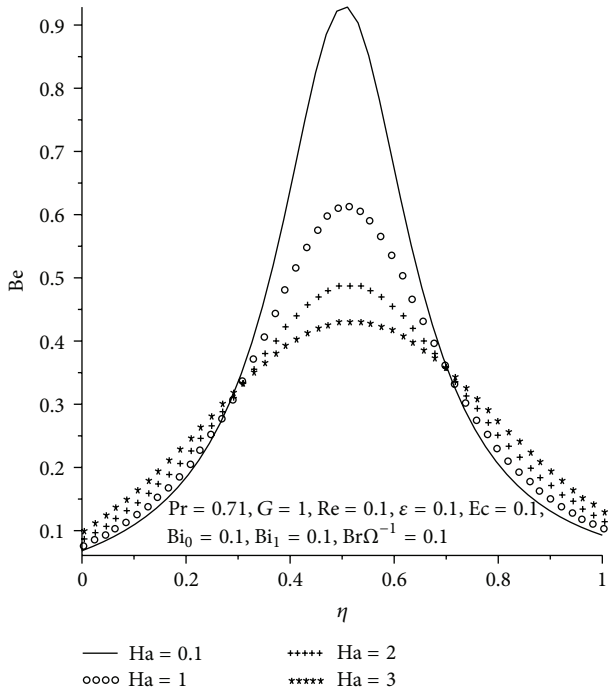


FIGURE 23: Bejan number with increasing Ha.

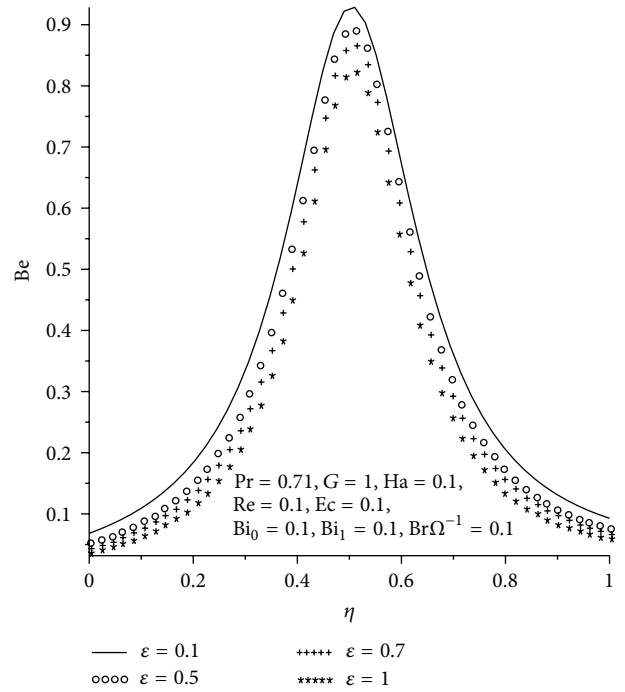


FIGURE 25: Bejan number with increasing  $\epsilon$ .

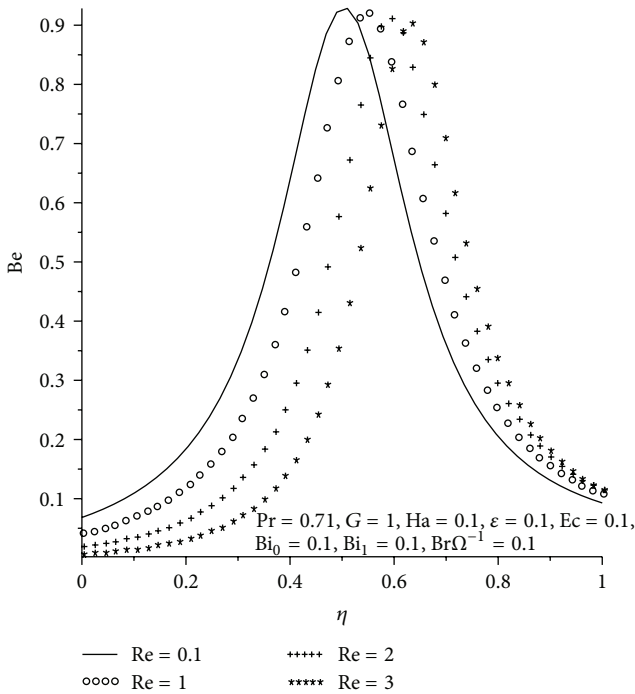


FIGURE 24: Bejan number with increasing Re.

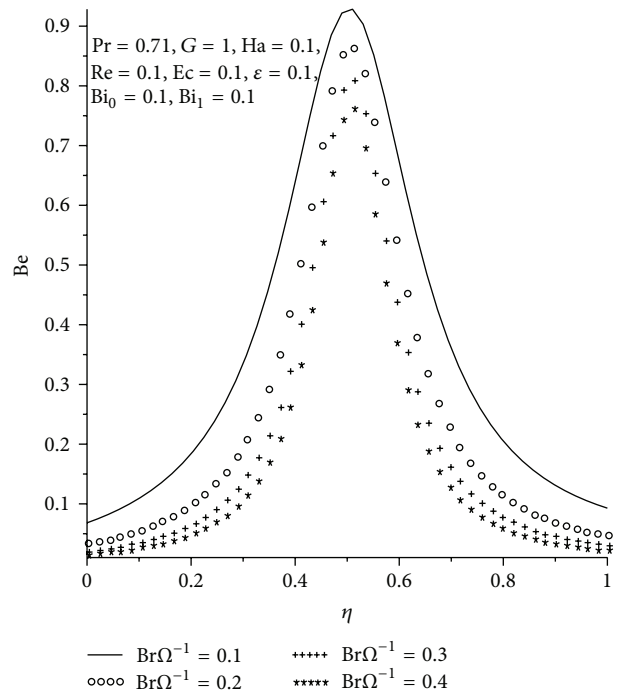


FIGURE 26: Bejan number with increasing  $Br\Omega^{-1}$ .

irreversibility dominate. Moreover, it is evident in Figure 23 that an increase in Ha results in a decrease of Be along the channel centerline. As Re increases (see Figure 24), the Bejan number decreases near the lower wall due to injection and increases toward the upper wall due to suction. Figures 25 and 26 show a general decrease in Bejan number with increasing

parameter values of  $\epsilon$  and  $Br\Omega^{-1}$  due to a decrease in fluid viscosity and an increase in viscous dissipation irreversibility. In Figures 27 and 28, an increase in the dominant influence of heat transfer irreversibility is observed as the parameter values of  $Bi_0$  and  $Bi_1$  increase, consequently, the Bejan number increases. Hence, the convective thermal boundary

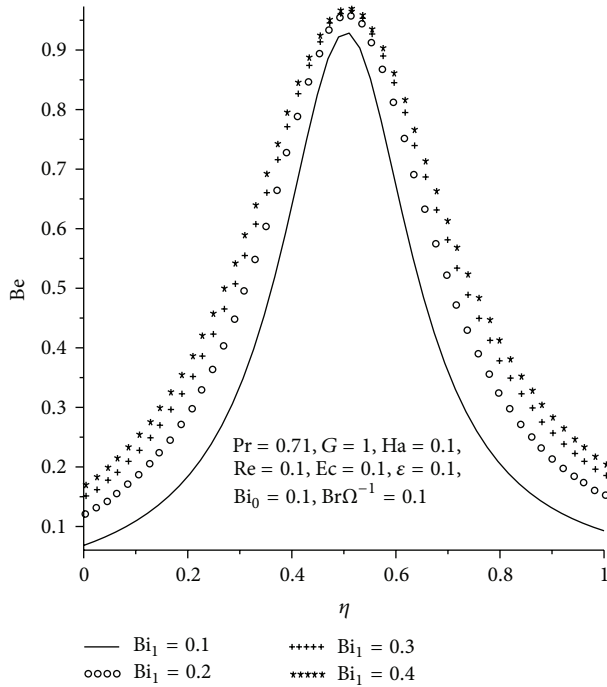


FIGURE 27: Bejan number with increasing  $Bi_1$ .

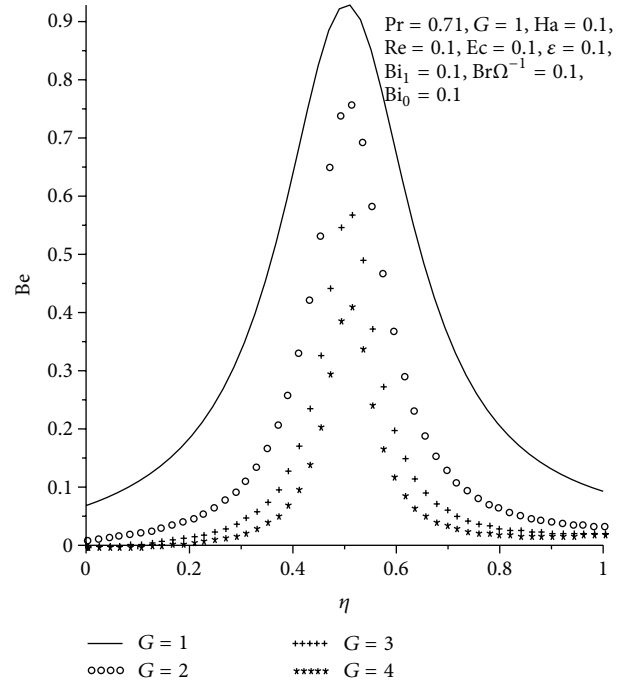


FIGURE 29: Bejan number with increasing  $G$ .

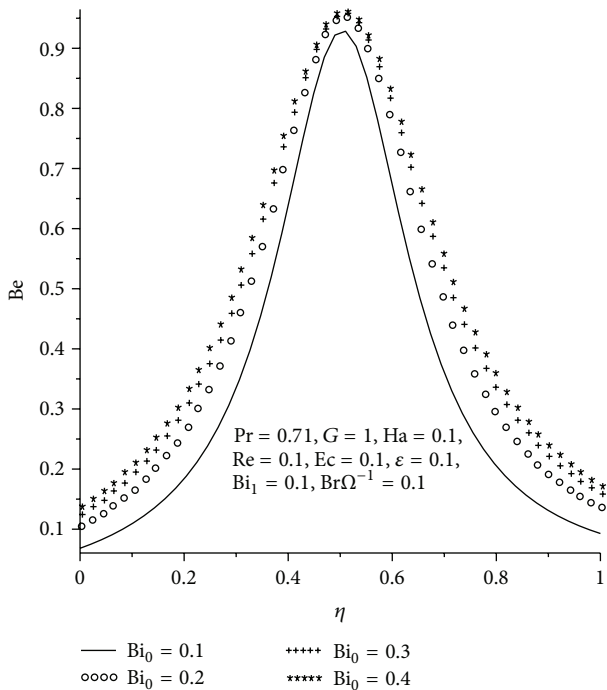


FIGURE 28: Bejan number with increasing  $Bi_0$ .

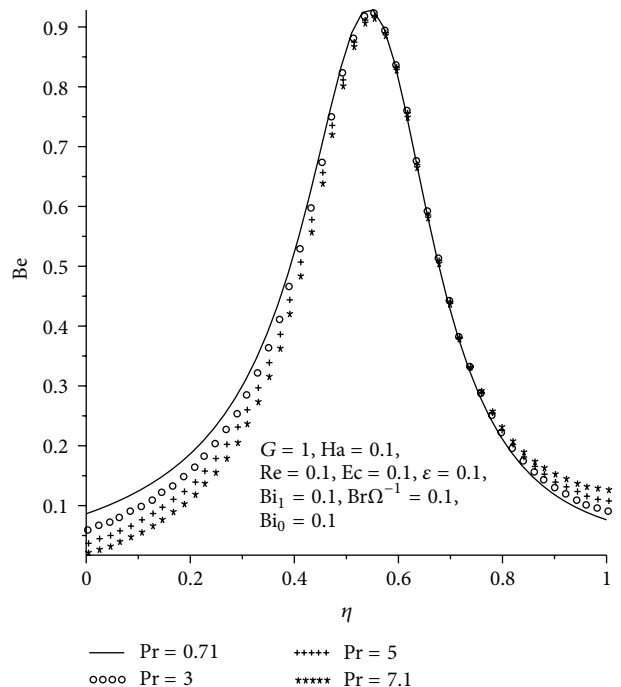


FIGURE 30: Bejan number with increasing  $Pr$ .

conditions enhance the dominant effects of heat transfer irreversibility on the flow system. An increase in the pressure gradient parameter causes a decrease in the Bejan number within the channel leading to an increase in the irreversibility due to fluid friction as shown in Figure 29. Figure 30 shows that the Bejan number slightly decreases at the lower plate and

slightly increases at the upper plate with increasing Prandtl number  $Pr$ .

## 5. Conclusion

In this paper, the effects of magnetic field on variable viscosity channel flow with suction/injection together with convective heating/cooling at the walls have been investigated. The nonlinear model problem is tackled numerically using shooting quadrature and fourth-order Runge-Kutta iteration scheme. Based on the results presented above, the following conclusions are deduced.

- (i) An increase in  $\varepsilon$ ,  $Ec$ ,  $G$ ,  $Pr$ , and  $Bi_0$  increases the velocity profiles, while an increase in  $Ha$  and  $Bi_1$  decreases the velocity profile along channel centerline region.
- (ii) An increase in  $\varepsilon$ ,  $Ec$ ,  $G$ ,  $Pr$ ,  $Re$ , and  $Bi_0$  increases the temperature profiles, while an increase in  $Ha$  and  $Bi_1$  decreases the temperature profile.
- (iii) An increase in  $\varepsilon$ ,  $Bi_0$ ,  $Bi_1$ ,  $G$ , and  $Br\Omega^{-1}$  increases the entropy generation rate. An increase in  $Re$  decreases  $Ns$  at injection wall, while at suction wall  $Ns$  increases. An increase in  $Ha$  increases  $Ns$  at both walls but decreases  $Ns$  at centre of the channel.
- (iv) An increase in  $\varepsilon$ ,  $G$ ,  $Br\Omega^{-1}$ , and  $Ha$  decreases the  $Be$  with increasing fluid friction and magnetic field irreversibility. An increase in  $Pr$  decreases  $Be$  at injection wall but increases  $Be$  at suction wall. Meanwhile increase in  $Bi_0$ ,  $Bi_1$  increases the  $Be$  with increasing effect of heat transfer irreversibility.

## Nomenclature

$C_p$ :	Specific heat at a constant pressure
$u$ :	Fluid velocity
$V$ :	Uniform suction/injection velocity
$T$ :	Fluid temperature
$Be$ :	Bejan number
$T_f$ :	Hot fluid temperature
$h$ :	Channel width
$Re$ :	Reynolds number
$Br$ :	Brinkmann number
$(x, y)$ :	Cartesian coordinates
$X$ :	Dimensionless axial coordinate
$Bi_0$ :	Lower plate Biot number
$m$ :	Variable viscosity parameter
$k$ :	Thermal conductivity
$P$ :	Fluid pressure
$E_G$ :	Volumetric rate of entropy
$Ha$ :	Square of Hartmann number
$T_\infty$ :	Ambient temperature
$G$ :	Pressure gradient
$Pr$ :	Prandtl number
$Ec$ :	Eckert number
$w$ :	Dimensionless velocity
$B_0$ :	Magnetic field strength
$Bi_1$ :	Upper plate Biot number.

## Greek Symbols

$\alpha$ :	Thermal diffusivity
$\theta$ :	Dimensionless temperature

$\Omega$ :	Temperature difference parameter
$\eta$ :	Dimensionless transverse coordinate
$\bar{\mu}(T)$ :	Temperature dependent viscosity
$\mu_0$ :	Fluid viscosity at ambient temperature
$\mu$ :	Fluid viscosity
$\phi$ :	Irreversibility ratio
$\rho$ :	Fluid density
$\sigma$ :	Electrical conductivity
$\gamma_0$ :	Lower plate heat transfer coefficient
$\gamma_1$ :	Upper plate heat transfer coefficient.

## References

- [1] R. Moreau, *Magnetohydrodynamics*, Kluwer Academic Publishers, Dordrecht, The Netherlands, 1990.
- [2] J. Hartmann and F. Lazarus, "Kongelige danske videnskabernes selskab," *Matematisk-Fysiske Meddelelser*, vol. 15, pp. 6–7, 1937.
- [3] G. W. Sutton and A. Sherman, *Engineering Magnetohydrodynamics*, McGraw Hill, 1965.
- [4] Y. Liu, L. Zheng, and X. Zhang, "Unsteady MHD Couette flow of a generalized Oldroyd-B fluid with fractional derivative," *Computers and Mathematics with Applications*, vol. 61, no. 2, pp. 443–450, 2011.
- [5] B. Lehnert, "On the behaviour of an electrically conductive liquid in a magnetic field," *Arkiv för Fysik*, vol. 5, no. 5, pp. 69–90, 1952.
- [6] O. D. Makinde and P. Y. Mhone, "Heat transfer to MHD oscillatory flow in a channel filled with porous medium," *Romanian Journal of Physics*, vol. 50, no. 9-10, pp. 931–938, 2005.
- [7] G. S. Seth, M. S. Ansari, and R. Nandkeolyar, "Unsteady hydromagnetic couette flow within a porous channel," *Tamkang Journal of Science and Engineering*, vol. 14, no. 1, pp. 7–14, 2011.
- [8] J. P. Agarwal, "On generalized incompressible couette flow in hydromagnetics," *Applied Scientific Research B*, vol. 9, no. 4-5, pp. 255–266, 1962.
- [9] O. D. Makinde and O. O. Onyejekwe, "A numerical study of MHD generalized Couette flow and heat transfer with variable viscosity and electrical conductivity," *Journal of Magnetism and Magnetic Materials*, vol. 323, no. 22, pp. 2757–2763, 2011.
- [10] A. Bejan, "Second-law analysis in heat transfer and thermal design," *Advances in Heat Transfer*, vol. 15, pp. 1–58, 1982.
- [11] L. C. Wood, *Thermodynamics of Fluid Systems*, Oxford University Press, Oxford, UK, 1975.
- [12] G. Ibanez, S. Cuevas, and M. Lopez de Haro, "Minimization of entropy generation by asymmetric convective cooling," *International Journal of Heat and Mass Transfer*, vol. 46, pp. 1321–1328, 2003.
- [13] S. Mahmud and R. A. Fraser, "Flow, thermal, and entropy generation characteristics inside a porous channel with viscous dissipation," *International Journal of Thermal Sciences*, vol. 44, no. 1, pp. 21–32, 2005.
- [14] A. Z. Sahin and R. Ben-Mansour, "Entropy generation in laminar fluid flow through a circular pipe," *Entropy*, vol. 5, no. 5, pp. 404–416, 2003.
- [15] K. Hooman, "Entropy generation for microscale forced convection: effects of different thermal boundary conditions, velocity slip, temperature jump, viscous dissipation, and duct geometry," *International Communications in Heat and Mass Transfer*, vol. 34, no. 8, pp. 945–957, 2007.

- [16] A. S. Eegunjobi and O. D. Makinde, "Effects of Navier slip on entropy generation in a porous channel with suction/injection," *Journal of Thermal Science and Technology*, vol. 7, no. 4, pp. 522–535, 2012.
- [17] O. D. Makinde and A. S. Eegunjobi, "Effects of convective heating on entropy generation rate in a channel with permeable Walls," *Entropy*, vol. 15, pp. 220–233, 2013.
- [18] M. Turkyilmazoglu, "Heat and mass transfer of MHD second order slip flow," *Computers & Fluids*, vol. 71, pp. 426–434, 2013.
- [19] T. Y. Na, *Computational Methods in Engineering Boundary Value Problems*, Academic Press, New York, NY, USA, 1979.

## Research Article

# Boundary Layer Flow Past a Wedge Moving in a Nanofluid

Waqar A. Khan<sup>1</sup> and I. Pop<sup>2</sup>

<sup>1</sup> Department of Engineering Sciences, PN Engineering College, National University of Sciences and Technology, Karachi 75350, Pakistan

<sup>2</sup> Faculty of Mathematics, University of Cluj, CP 253, 3400 Cluj, Romania

Correspondence should be addressed to Waqar A. Khan; [wkhan\\_2000@yahoo.com](mailto:wkhan_2000@yahoo.com)

Received 30 March 2013; Revised 16 April 2013; Accepted 19 April 2013

Academic Editor: Oluwole Daniel Makinde

Copyright © 2013 W. A. Khan and I. Pop. This is an open access article distributed under the Creative Commons Attribution License, which permits unrestricted use, distribution, and reproduction in any medium, provided the original work is properly cited.

The problem of steady boundary layer flow past a stretching wedge with the velocity  $u_w(x)$  in a nanofluid and with a parallel free stream velocity  $u_e(x)$  is numerically studied. It is assumed that at the stretching surface the temperature  $T$  and the nanoparticle fraction  $C$  take the constant values  $T_w$  and  $C_w$ , respectively. The ambient values (inviscid fluid) of  $T$  and  $C$  are denoted by  $T_\infty$  and  $C_\infty$ , respectively. The boundary layer governing partial differential equations of mass, momentum, thermal energy, and nanoparticles recently proposed by Kuznetsov and Nield (2006, 2009), are reduced to ordinary differential equations along with the corresponding boundary conditions. These equations are solved numerically using an implicit finite-difference method for some values of the governing parameters, such as  $\beta$ ,  $\lambda$ ,  $Pr$ ,  $Le$ ,  $N_b$ , and  $N_t$ , which are the measure of the pressure gradient, moving parameter, Prandtl number, Lewis number, the Brownian motion parameter, and the thermophoresis parameter, respectively.

## 1. Introduction

Historically, the steady laminar flow past a fixed wedge was first analyzed by Falkner and Skan [1] to illustrate the application of Prandtl's boundary layer theory. With a similarity transformation, the boundary layer equations are reduced to an ordinary differential equation, which is well known as the Falkner-Skan equation. This equation includes nonuniform flow, that is, outer flows which, when evaluated at the wall, takes the form  $ax^m$ , where  $x$  is the coordinate measured along the wedge wall and  $a$  ( $>0$ ), and  $m$  are constants. There is a large body of literature on the solutions of Falkner-Skan equation, see Hartree [2], Stewartson [3], Chen and Libby [4], Rajagopal et al. [5], Botta et al. [6], Brodie and Banks [7], Heeg et al. [8], Zaturka and Banks [9], Kuo [10], Pantokratoras [11], and so forth. Liao [12] has developed an analytical technique, named homotopy analysis method (HAM), and presented a uniformly valid analytic solution of Falkner-Skan equation for the wedge parameter  $\beta$  in the range  $-0.19884 \leq \beta \leq 2$ . This solution has been extended by Abbasbandy and Hayat [13] by including the magnetic effects. Also, there are some very recently published papers on this

problem by Liu and Chang [14], Fang and Zhang [15], and Pal and Mondal [16]. A very good list of references on this problem can be found in the recent papers by Harris et al. [17–19]. The flows predicted by the Falkner-Skan solutions are naturally assumed to be described adequately by the boundary layer equations which are parabolic in character. However, the use of the similarity method of solution cannot take account of the “initial” condition in general and so the resulting solutions are assumed to be valid, if at all, in some asymptotic sense (see Banks [20]). This is the case for the Falkner-Skan flows that has been shown rigorously by Serrin [21] for  $0 \leq \beta \leq 2$ . However, all these papers are for the Falkner-Skan boundary layer flow over a fixed wedge placed in a moving fluid. In a very interesting paper, Riley and Weidman [22] and Ishak et al. [23] have studied multiple solutions of the Falkner-Skan equation for flow past a stretching boundary when the external velocity and the boundary velocity are each proportional to the same power law of the downstream distance. Boundary layer behavior over a moving continuous solid surface is an important type of flow occurring in several engineering processes. For example, the thermal processing of sheet-like materials is

a necessary operation in the production of paper, linoleum, polymeric sheets, wire drawing, drawing of plastic films, metal spinning, roofing shingles, insulating materials, and fine-fiber Matts.

The aim of the present paper is to extend the papers by Riley and Weidman [22] and Ishak et al. [23] to the case when the wedge moves in a nanofluid. Enhancement of heat transfer is essential in improving performances and compactness of electronic devices. Usual cooling agents (water, oil, etc.) have relatively small thermal conductivities, and therefore heat transfer is not very efficient. Thus, to augment thermal characteristics very small size particles (nanoparticles) were added to fluids forming the so-called nanofluids. These suspensions of nanoparticles in fluids have physical and chemical properties depending on the concentration and the shape of particles. It was discovered that a small fraction of nanoparticles added in a base fluid leads to a large increase of the fluid thermal conductivity. The chaotic movement of the nanoparticles and sleeping between the fine particles and fluid generates the thermal dispersion effect, and this leads to an increase in the energy exchange rates in fluid. Based on the fact that for small size suspended particles (smaller than 100 nm) nanofluids behave more like a fluid than a fluid-solid mixture. Xuan and Roetzel [24] proposed a thermal dispersion model for a single-phase nanofluid. Kuznetsov and Nield [25] extended the classical boundary layer analysis of forced convection over a wedge with an attached porous substrate. In another two papers, Nield and Kuznetsov [26–28] extended the classical Cheng and Minkowycz [29] problem of boundary layer flow over a vertical flat plate in a porous medium saturated by a nanofluid and also the problem of double-diffusive natural convective boundary layer flow in a porous medium saturated by a nanofluid, presenting similarity solutions. Kuznetsov and Nield [30] extended also the Pohlhausen-Kuiken-Bejan problem to the case of a binary nanofluid using Buongiorno model and presented a similarity solution. Also, there are several very good recently published papers on nanofluids, for example, papers by Narayana and Sibanda [31] and Kameswaran et al. [32, 33]. However, the broad range of current and future applications of nanofluids is discussed in the review article by Woong and Leon [34], which includes automotive, electronics, biomedical, and heat transfer applications, besides other applications such as nanofluid detergent. In a recent review article by Saidur et al. [35], the authors also presented some applications of nanofluids in industrial, commercial, residential, and transportation sectors based on the available literatures. Recent critical reviews of the state-of-the-art of nanofluids research for heat transfer application were conducted by Mahian et al. [36] and Behar et al. [37].

In the present paper, the thermal dispersion model is similar with that proposed by Nield and Kuznetsov [28] and Kuznetsov and Nield [30]. The mentioned literature survey indicates that there is no study on the boundary layer flow past a wedge in a nanofluid. It is worth mentioning to this end that nanotechnology has been widely used in the industry since materials with sizes of nanometers possess unique physical and chemical properties.

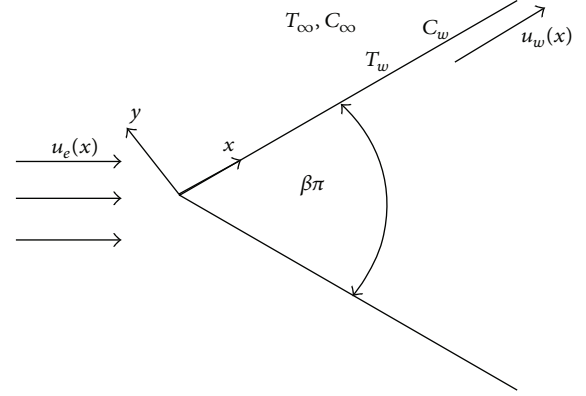


FIGURE 1: Schematic diagram of a stretching wedge.

## 2. Problem Formulation and Basic Equations

We consider the boundary layer flow past an impermeable stretching wedge moving with the velocity  $u_w(x)$  in a nanofluid, and the free stream velocity is  $u_e(x)$ , where  $x$  is the coordinate measured along the surface of the wedge as shown in Figure 1. It should be noted that the case of  $u_w(x) > 0$  corresponds to a stretching wedge surface and  $u_w(x) < 0$  corresponds to a contracting wedge surface, respectively. It is assumed that at the stretching surface, the temperature  $T$  and the nanoparticle fraction  $C$  take constant values  $T_w$  and  $C_w$ , respectively. The ambient values, attained as  $y$  tends to infinity, of  $T$  and  $C$  are denoted by  $T_\infty$  and  $C_\infty$ , respectively. Under these assumptions, it can be shown that the steady boundary layer equations of mass, momentum, thermal energy, and nanoparticles for nanofluids can be written in Cartesian coordinates  $x$  and  $y$  as, see Nield and Kuznetsov [28], and Kuznetsov and Nield [30],

$$\frac{\partial u}{\partial x} + \frac{\partial v}{\partial y} = 0, \quad (1)$$

$$u \frac{\partial u}{\partial x} + v \frac{\partial u}{\partial y} = u_e \frac{du_e}{dx} + \nu \frac{\partial^2 u}{\partial y^2}, \quad (2)$$

$$u \frac{\partial T}{\partial x} + v \frac{\partial T}{\partial y} = \alpha \frac{\partial^2 T}{\partial y^2} + \tau \left[ D_B \frac{\partial C}{\partial y} \frac{\partial T}{\partial y} + \left( \frac{D_T}{T_\infty} \right) \left( \frac{\partial T}{\partial y} \right)^2 \right], \quad (3)$$

$$u \frac{\partial C}{\partial x} + v \frac{\partial C}{\partial y} = D_B \frac{\partial^2 C}{\partial y^2} + \left( \frac{D_T}{T_\infty} \right) \frac{\partial^2 T}{\partial y^2}, \quad (4)$$

subject to the boundary conditions

$$v = 0, \quad u = u_w(x) = -\lambda u_e(x), \quad T = T_w, \quad C = C_w \quad \text{at } y = 0,$$

$$u = u_e(x), \quad T = T_\infty, \quad C = C_\infty \quad \text{as } y \rightarrow \infty. \quad (5)$$

Here  $u$  and  $v$  are velocity components along the axes  $x$  and  $y$ , respectively,  $\alpha$  is the thermal diffusivity,  $\nu$  is the kinematic

viscosity,  $D_B$  is the Brownian diffusion coefficient,  $D_T$  is the thermophoretic diffusion coefficient and  $\tau = (\rho c)_p/(\rho c)_f$  with  $\rho$  being the density,  $c$  is volumetric volume expansion coefficient, and  $\rho_p$  is the density of the particles.

In order to get similarity solutions of (1)–(5), we assume that  $u_w(x)$  and  $u_e(x)$  have the following form:

$$u_w(x) = ax^m, \quad u_e(x) = cx^m, \quad (6)$$

where  $a$ ,  $c$ , and  $m$  ( $0 \leq m \leq 1$ ) are positive constants. Therefore, the constant moving parameter  $\lambda$  in (6) is defined as  $\lambda = c/a$ , so that  $\lambda < 0$  corresponds to a stretching wedge,  $\lambda > 0$  corresponds to a contracting wedge, and  $\lambda = 0$  corresponds to a fixed wedge, respectively. Thus, we look for a similarity solution of (1)–(4) with the boundary conditions (5) of the following form:

$$\psi = \left( \frac{2u_e x v}{1+m} \right)^{1/2} f(\eta), \quad \theta(\eta) = \frac{T - T_\infty}{T_w - T_\infty},$$

$$\phi(\eta) = \frac{C - C_\infty}{C_w - C_\infty}, \quad (7)$$

$$\eta = \left( \frac{(1+m)u_e}{2xv} \right)^{1/2} y,$$

where the stream function  $\psi$  is defined in the usual way as  $u = \partial\psi/\partial y$  and  $v = -\partial\psi/\partial x$ . On substituting (7) into (2)–(4), we obtain the following ordinary differential equations:

$$f''' + ff'' + \beta(1 - f'^2) = 0, \quad (8)$$

$$\frac{1}{Pr}\theta'' + f\theta' + N_b\phi'\theta' + N_t\theta'^2 = 0, \quad (9)$$

$$\phi'' + Le f\phi' + \frac{N_t}{N_b}\theta'' = 0, \quad (10)$$

subject to the boundary conditions

$$f(0) = 0, \quad f'(0) = -\lambda, \quad \theta(0) = 1, \quad \phi(0) = 1,$$

$$f'(\infty) = 1, \quad \theta(\infty) = 0, \quad \phi(\infty) = 0, \quad (11)$$

where primes denote differentiation with respect to  $\eta$ , and the five parameters are defined by

$$\beta = \frac{2m}{1+m}, \quad Pr = \frac{\nu}{\alpha},$$

$$Le = \frac{\nu}{D_B}, \quad N_b = \frac{(\rho c)_p D_B (\phi_w - \phi_\infty)}{(\rho c)_f \nu}, \quad (12)$$

$$N_t = \frac{(\rho c)_p D_T (T_w - T_\infty)}{(\rho c)_f T_\infty \nu}.$$

Here  $\beta$ ,  $Pr$ ,  $Le$ ,  $N_b$ , and  $N_t$  are the measure of the pressure gradient, Prandtl number, Lewis number, the Brownian motion, and the thermophoresis parameters, respectively. It is important to note that this boundary value problem reduces to the classical Falkner-Skan's [1] problem of the boundary layer flow of a viscous and incompressible fluid past a fixed wedge, when  $\lambda$ ,  $N_b$ , and  $N_t$  are all zero in (9) and (10).

TABLE 1: Comparison of the values of  $f''(0)$  for several values of  $m$  when  $\lambda = 0$ .

$m$	Yih [38]	Yacob et al. [39]	White [40]	Present results
0	0.4696	0.4696	0.4696	0.4696
1/11	0.6550	0.6550	0.6550	0.6550
1/5	0.8021	0.8021	0.8021	0.8021
1/3	0.9276	0.9276	0.9277	0.9277
1/2	—	—	1.0389	1.0389
1	—	1.2326	1.2326	1.2326

TABLE 2: Comparison of the values of  $-\theta'(0)$  for various values of  $m$  when  $\lambda = N_b = N_t = 0$ .

$m$	Kuo [41]	Blasius [42]	Present
0	0.8673	0.8673	0.8769
1.0	1.1147	1.1152	1.1279

**2.1. Numerical Method.** Equations (8)–(10) with boundary conditions (11) are solved numerically using an implicit finite-difference scheme known as the Keller-box method, as described by Cebeci and Bradshaw [43, 44]. In this method, (8)–(10) are reduced to first-order equations, and using central differences, the algebraic equations are obtained. These equations are then linearized by Newton's method. The linear equations are then solved using block-tridiagonal elimination technique. The boundary conditions for  $\eta \rightarrow \infty$  are replaced by  $f'(\eta_{\max}) = 1$ ,  $\theta(\eta_{\max}) = 0$ ,  $\phi(\eta_{\max}) = 0$ , where  $\eta_{\max} = 12$ . The step size is taken as  $\Delta\eta = 0.001$ , and the convergence criteria is set to  $10^{-6}$ .

### 3. Results and Discussion

Table 1 shows the comparison of the values of  $f''(0)$  for several values of  $m$  when  $\lambda = 0$  with those reported by [38–40]. On the other hand, Table 2 compares the values of  $-\theta'(0)$  obtained from (8) and (9) for  $m = 0$  and several values of  $Pr$  when  $\lambda = N_b = N_t = 0$  with those of [41, 42]. It is seen from these tables that the results are in very good agreement. Therefore, we are deeply confident that the present numerical results are correct and very accurate.

The effect of the wedge parameter  $m$  on the dimensionless velocity is shown in Figure 2(a) for stretching wedge and in Figure 2(b) for shrinking wedge. It is observed that the dimensionless velocity at the surface increases/decreases with stretching/shrinking parameters. This is just due to increase/decrease in the stretching/shrinking velocities. In both cases, the hydrodynamic boundary layer thickness decreases with increasing wedge parameter  $m$ . The effects of Prandtl numbers on the dimensionless temperature are shown in Figures 3(a) and 3(b) for shrinking and stretching wedge, respectively. The Prandtl number is defined as the ratio of momentum diffusivity to thermal diffusivity. When  $Pr = 1$ , both momentum and thermal diffusivities are comparable, but when  $Pr > 1$ , the momentum diffusivity is greater than thermal diffusivity and the thermal boundary layer thickness decreases with increasing Prandtl number.

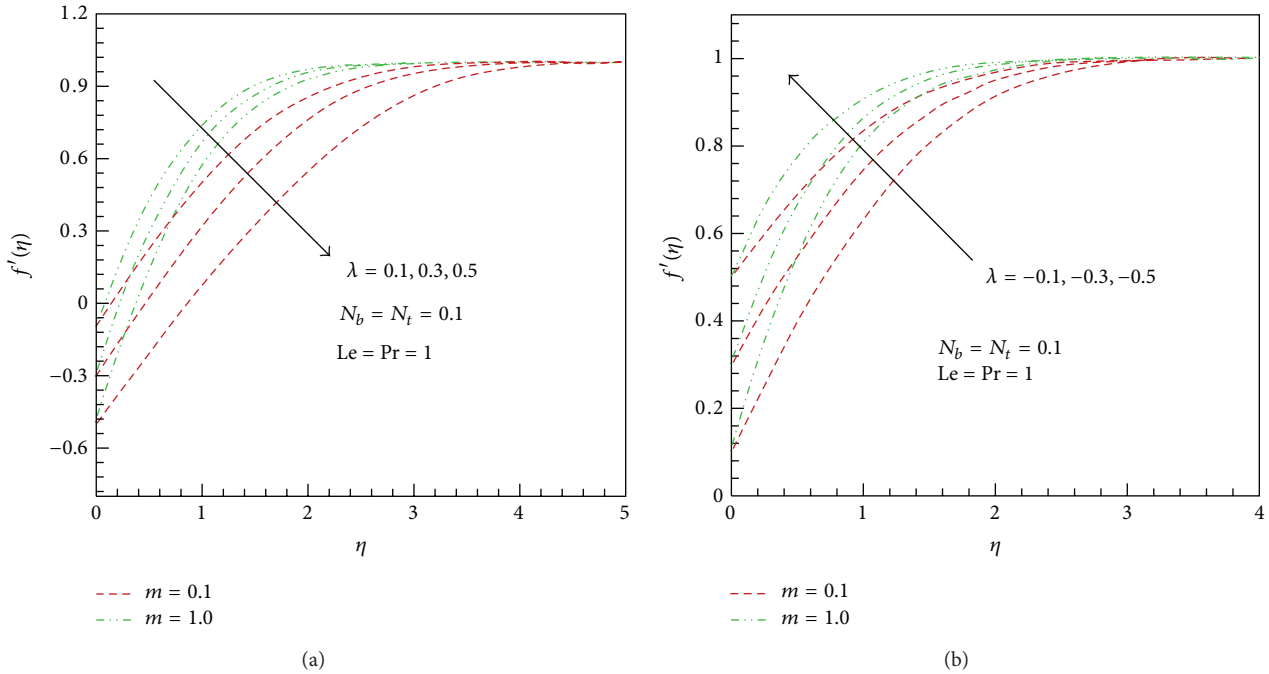


FIGURE 2: The dimensionless velocity profiles for different values of  $m$  along (a) shrinking and (b) stretching wedge.

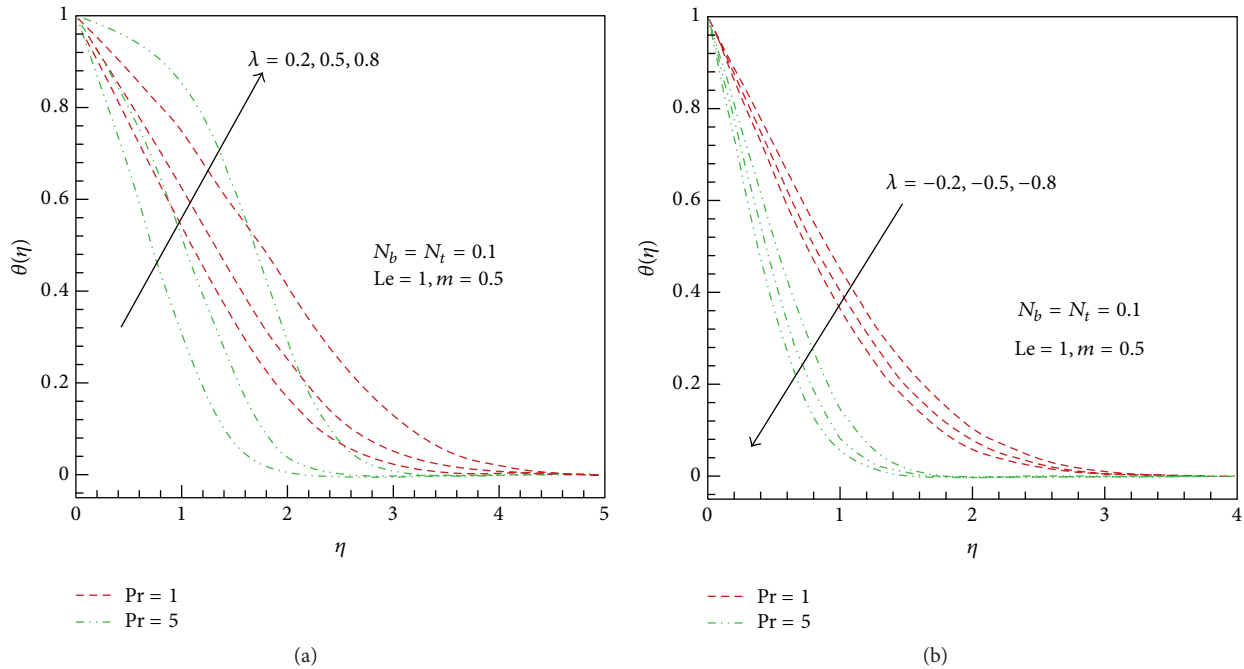


FIGURE 3: The dimensionless temperature profiles for different values of  $Pr$  along (a) shrinking and (b) stretching wedge.

This can be observed in both cases. The effects of nanofluid parameters on the dimensionless temperature are illustrated in Figures 4(a) and 4(b) for two different values of the wedge parameter. Within the thermal boundary layer, the dimensionless temperature increases with both Brownian motion and thermophoresis parameters when the wedge is shrinking. No appreciable effect of nanofluid and wedge

parameters on the thermal boundary layer thickness could be found.

Figures 5(a) and 5(b) show the variation of the dimensionless nanoparticle volume fraction with Lewis numbers for different values of wedge parameter when the wedge is fixed. It can be seen that the thickness of concentration boundary layer decreases with increasing Lewis number

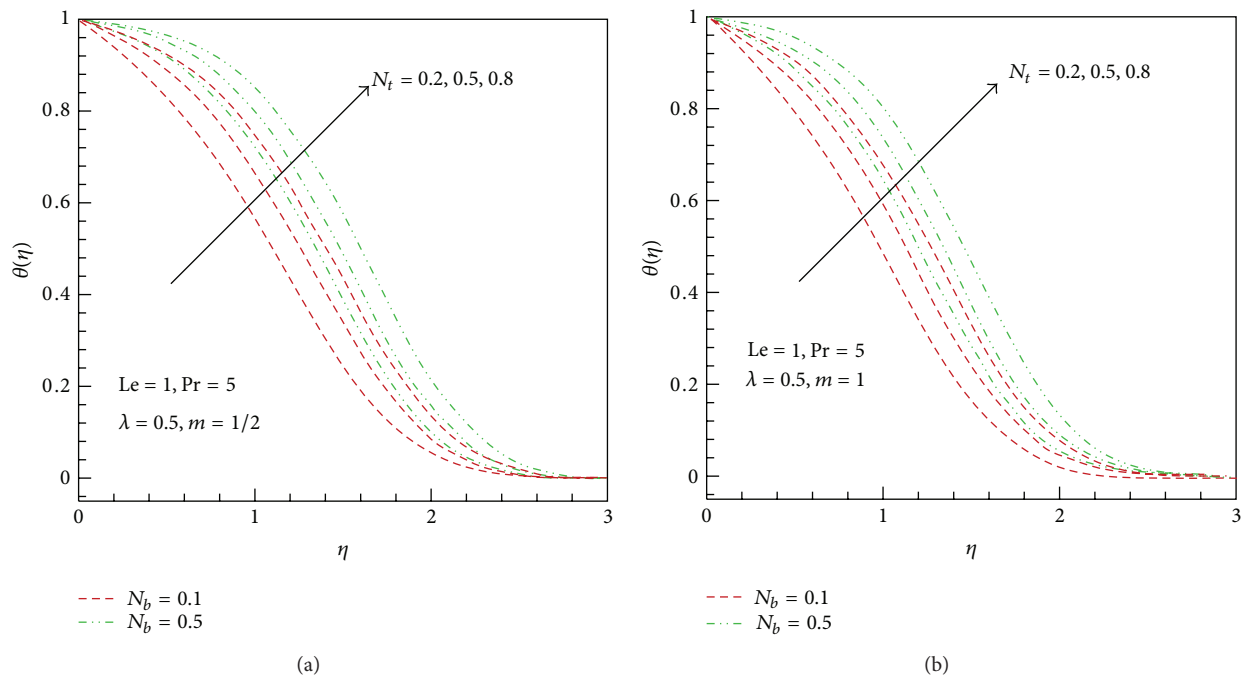


FIGURE 4: Effect of nanofluid parameters on dimensionless temperature along shrinking wedge for (a)  $m = 1/2$  and (b)  $m = 1$ .

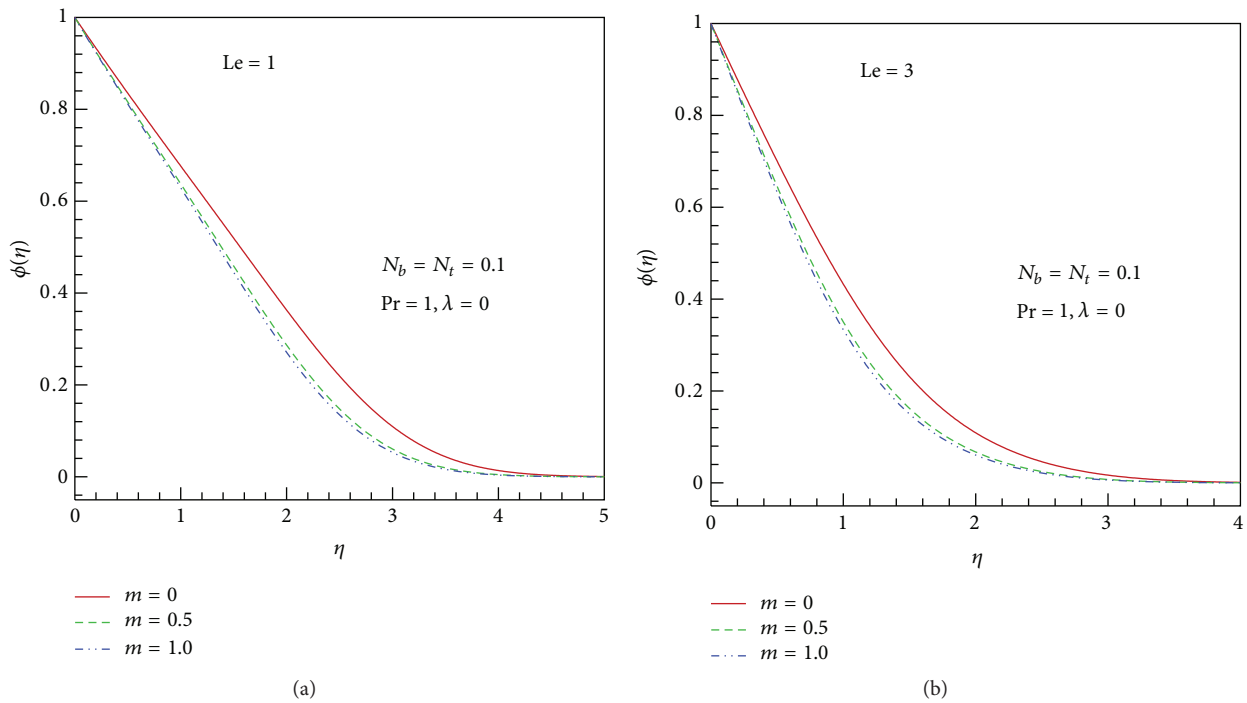


FIGURE 5: Effects of Lewis numbers on dimensionless nanoparticle volume fraction profiles for different values of  $m$  when the wedge is fixed.

and wedge parameter in both cases. Inside the concentration boundary layer, the dimensionless nanoparticle volume fraction is higher for the horizontal flat plate. The effects of nanofluid parameters on dimensionless nanoparticle

volume fraction are depicted in Figures 6(a) and 6(b) for shrinking/stretching wedge. In both cases, the concentration boundary layer thickness decreases with increasing Brownian motion and thermophoresis parameters.

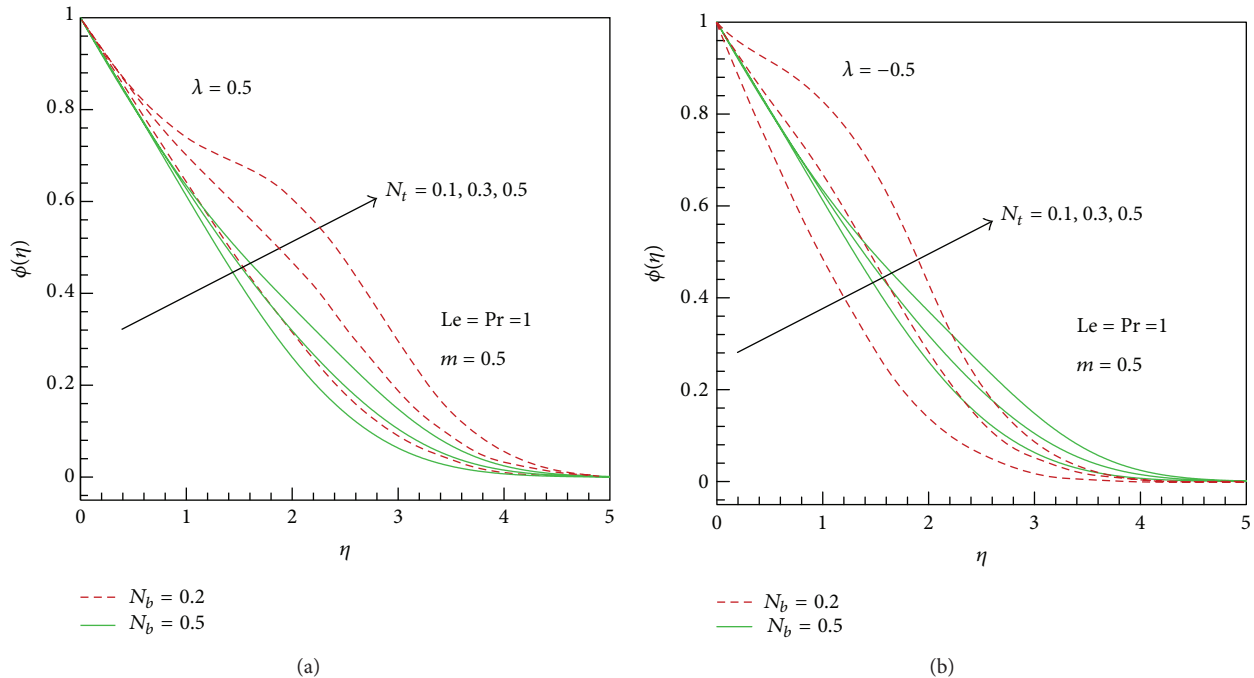


FIGURE 6: Effects of nanofluid parameters on dimensionless nanoparticle volume fraction for (a) shrinking wedge and (b) stretching wedge.

#### 4. Conclusions

Steady boundary layer flow past a moving wedge in a water-based nanofluid is studied numerically using an implicit finite-difference method for several values of the parameters  $m$ ,  $\lambda$ ,  $Pr$ ,  $Le$ ,  $N_b$ , and  $N_t$ . This problem reduces to the classical Falkner-Skan's [1] problem of the boundary layer flow of a viscous (Newtonian) fluid past a fixed wedge, when  $\lambda$ ,  $N_b$ , and  $N_t$  are all zero. The effects of all these parameters on the dimensionless velocity, temperature, and nanoparticle volume fraction are investigated and presented graphically. It is found that the

- (i) dimensionless velocity at the surface increases/decreases with stretching/shrinking parameters;
- (ii) dimensionless temperature increases with both Brownian motion and thermophoresis parameters.

#### Acknowledgment

The authors wish to thank the very competent reviewers for their valuable comments and suggestions.

#### References

- [1] V. M. Falkner and S. W. Skan, "Some approximate solutions of the boundary-layer equations," *Philosophical Magazine*, vol. 12, pp. 865–896, 1931.
- [2] D. R. Hartree, "On an equation occurring in Falkner and Skan's approximate treatment of the equations of the boundary layer," *Mathematical Proceedings of the Cambridge Philosophical Society*, vol. 33, no. 2, pp. 223–239, 1937.
- [3] K. Stewartson, "Further solutions of the Falkner-Skan equation," *Mathematical Proceedings of the Cambridge Philosophical Society*, vol. 50, pp. 454–465, 1954.
- [4] K. K. Chen and P. A. Libby, "Boundary layers with small departure from the Falkner-Skan profile," *Journal of Fluid Mechanics*, vol. 33, no. 2, pp. 273–282, 1968.
- [5] K. R. Rajagopal, A. S. Gupta, and T. Y. Na, "A note on the Falkner-Skan flows of a non-Newtonian fluid," *International Journal of Non-Linear Mechanics*, vol. 18, no. 4, pp. 313–320, 1983.
- [6] E. F. F. Botta, F. J. Hut, and A. E. P. Veldman, "The role of periodic solutions in the Falkner-Skan problem for  $\lambda > 0$ ," *Journal of Engineering Mathematics*, vol. 20, no. 1, pp. 81–93, 1986.
- [7] P. Brodie and W. H. H. Banks, "Further properties of the Falkner-Skan equation," *Acta Mechanica*, vol. 65, no. 1-4, pp. 205–211, 1987.
- [8] R. S. Heeg, D. Dijkstra, and P. J. Zandbergen, "The stability of Falkner-Skan flows with several inflection points," *Journal of Applied Mathematics and Physics*, vol. 50, no. 1, pp. 82–93, 1999.
- [9] M. B. Zaturaska and W. H. H. Banks, "A new solution branch of the Falkner-Skan equation," *Acta Mechanica*, vol. 152, no. 1-4, pp. 197–201, 2001.
- [10] B. L. Kuo, "Application of the differential transformation method to the solutions of Falkner-Skan wedge flow," *Acta Mechanica*, vol. 164, no. 3-4, pp. 161–174, 2003.
- [11] A. Pantokratoras, "The Falkner-Skan flow with constant wall temperature and variable viscosity," *International Journal of Thermal Sciences*, vol. 45, no. 4, pp. 378–389, 2006.
- [12] S. J. Liao, "A uniformly valid analytic solution of two-dimensional viscous flow over a semi-infinite flat plate," *Journal of Fluid Mechanics*, vol. 385, pp. 101–128, 1999.
- [13] S. Abbasbandy and T. Hayat, "Solution of the MHD Falkner-Skan flow by homotopy analysis method," *Communications in*

- Nonlinear Science and Numerical Simulation*, vol. 14, no. 9-10, pp. 3591–3598, 2009.
- [14] C. S. Liu and J. R. Chang, “The Lie-group shooting method for multiple-solutions of Falkner-Skan equation under suction-injection conditions,” *International Journal of Non-Linear Mechanics*, vol. 43, no. 9, pp. 844–851, 2008.
- [15] T. Fang and J. Zhang, “An exact analytical solution of the Falkner-Skan equation with mass transfer and wall stretching,” *International Journal of Non-Linear Mechanics*, vol. 43, no. 9, pp. 1000–1006, 2008.
- [16] D. Pal and H. Mondal, “Influence of temperature-dependent viscosity and thermal radiation on MHD forced convection over a non-isothermal wedge,” *Applied Mathematics and Computation*, vol. 212, no. 1, pp. 194–208, 2009.
- [17] S. D. Harris, D. B. Ingham, and I. Pop, “Unsteady heat transfer in impulsive Falkner-Skan flows: constant wall temperature case,” *European Journal of Mechanics*, vol. 21, no. 4, pp. 447–468, 2002.
- [18] S. D. Harris, D. B. Ingham, and I. Pop, “Unsteady heat transfer in impulsive Falkner-Skan flows: constant wall heat flux case,” *Acta Mechanica*, vol. 201, no. 1-4, pp. 185–196, 2008.
- [19] S. D. Harris, D. B. Ingham, and I. Pop, “Impulsive Falkner-Skan flow with constant wall heat flux: revisited,” *International Journal of Numerical Methods for Heat and Fluid Flow*, vol. 19, no. 8, pp. 1008–1037, 2009.
- [20] W. H. H. Banks, “Similarity solutions of the boundary-layer equations for a stretching wall,” *Journal of Theoretical and Applied Mechanics*, vol. 2, no. 3, pp. 375–392, 1983.
- [21] J. Serrin, “Asymptotic behavior of velocity profiles in the Prandtl boundary layer theory,” *Proceedings of the Royal Society A*, vol. 299, pp. 491–507, 1967.
- [22] N. Riley and P. D. Weidman, “Multiple solutions of the Falkner-Skan equation for flow past a stretching boundary,” *SIAM Journal on Applied Mathematics*, vol. 49, no. 5, pp. 1350–1358, 1989.
- [23] A. Ishak, R. Nazar, and I. Pop, “Falkner-Skan equation for flow past a moving wedge with suction or injection,” *Journal of Applied Mathematics & Computing*, vol. 25, no. 1-2, pp. 67–83, 2007.
- [24] Y. Xuan and W. Roetzel, “Conceptions for heat transfer correlation of nanofluids,” *International Journal of Heat and Mass Transfer*, vol. 43, no. 19, pp. 3701–3707, 2000.
- [25] A. V. Kuznetsov and D. A. Nield, “Boundary layer treatment of forced convection over a wedge with an attached porous substrate,” *Journal of Porous Media*, vol. 9, no. 7, pp. 683–694, 2006.
- [26] D. A. Nield and A. V. Kuznetsov, “The Cheng-Minkowycz problem for natural convective boundary-layer flow in a porous medium saturated by a nanofluid,” *International Journal of Heat and Mass Transfer*, vol. 52, no. 25-26, pp. 5792–5795, 2009.
- [27] A. V. Kuznetsov and D. A. Nield, “Double-diffusive natural convective boundary-layer flow of a nanofluid past a vertical plate,” *International Journal of Thermal Sciences*, vol. 50, no. 5, pp. 712–717, 2011.
- [28] D. A. Nield and A. V. Kuznetsov, “The Cheng-Minkowycz problem for the double-diffusive natural convective boundary layer flow in a porous medium saturated by a nanofluid,” *International Journal of Heat and Mass Transfer*, vol. 54, no. 1-3, pp. 374–378, 2011.
- [29] P. Cheng and W. J. Minkowycz, “Free convection about a vertical flat plate embedded in a porous medium with application to heat transfer from a dike,” *Journal of Geophysical Research*, vol. 82, no. 14, pp. 2040–2044, 1977.
- [30] A. V. Kuznetsov and D. A. Nield, “Natural convective boundary-layer flow of a nanofluid past a vertical plate,” *International Journal of Thermal Sciences*, vol. 49, no. 2, pp. 243–247, 2010.
- [31] M. Narayana and P. Sibanda, “Laminar flow of a nanoliquid film over an unsteady stretching sheet,” *International Journal of Heat and Mass Transfer*, vol. 55, no. 25-26, pp. 7552–7560, 2012.
- [32] P. K. Kameswaran, M. Narayana, P. Sibanda, and P. V. S. N. Murthy, “Hydromagnetic nanofluid flow due to a stretching or shrinking sheet with viscous dissipation and chemical reaction effects,” *International Journal of Heat and Mass Transfer*, vol. 55, no. 25-26, pp. 7587–7595, 2012.
- [33] P. K. Kameswaran, S. Shaw, P. Sibanda, and P. V. S. N. Murthy, “Homogeneous-heterogeneous reactions in a nanofluid flow due to a porous stretching sheet,” *International Journal of Heat and Mass Transfer*, vol. 57, no. 2, pp. 465–472, 2013.
- [34] K. F. V. Woong and O. D. Leon, “Applications of nanofluids: current and future,” *Advances in Mechanical Engineering*, vol. 2010, Article ID 519659, 11 pages, 2010.
- [35] R. Saidur, S. N. Kazi, M. S. Hossain, M. M. Rahman, and H. A. Mohamed, “A review on the performance of nanoparticles suspended with refrigerants and lubricating oils in refrigeration systems,” *Renewable and Sustainable Energy Reviews*, vol. 15, no. 1, pp. 310–323, 2011.
- [36] O. Mahian, A. Kianifar, S. A. Kalogirou, I. Pop, and S. Wongwises, “A review of the applications of nanofluids in solar energy,” *International Journal of Heat and Mass Transfer*, vol. 57, no. 2, pp. 582–594, 2013.
- [37] O. Behar, A. Khellaf, and K. Mohammadi, “A review of studies on central receiver solar thermal power plants,” *Renewable and Sustainable Energy Reviews*, vol. 23, pp. 12–39, 2013.
- [38] K. A. Yih, “Uniform suction/blowing effect on forced convection about a wedge: uniform heat flux,” *Acta Mechanica*, vol. 128, no. 3-4, pp. 173–181, 1998.
- [39] N. A. Yacob, A. Ishak, and I. Pop, “Falkner-Skan problem for a static or moving wedge in nanofluids,” *International Journal of Thermal Sciences*, vol. 50, no. 2, pp. 133–139, 2011.
- [40] F. M. White, *Viscous Fluid Flow*, McGraw-Hill, New York, NY, USA, 2nd edition, 1991.
- [41] B. L. Kuo, “Heat transfer analysis for the Falkner-Skan wedge flow by the differential transformation method,” *International Journal of Heat and Mass Transfer*, vol. 48, no. 23-24, pp. 5036–5046, 2005.
- [42] H. Blasius, “Grenzschichten in Flüssigkeiten mit kleiner Reibung,” *Zentralblatt Mathematical Physics*, vol. 56, pp. 1–37, 1908.
- [43] T. Cebeci and P. Bradshaw, *Momentum Transfer in Boundary Layers*, Hemisphere Publishing Corporation, New York, NY, USA, 1977.
- [44] T. Cebeci and P. Bradshaw, *Physical and Computational Aspects of Convective Heat Transfer*, Springer, New York, NY, USA, 1988.